UCLA
UCLA Electronic Theses and Dissertations

Title
The Role of the Kelvin-Helmholtz Instability in the Evolution of Magnetized Relativistic Sheared Plasma Flows

Permalink
https://escholarship.org/uc/item/7jd167rp

Author
Hamlin, Nathaniel Donald

Publication Date
2012

Peer reviewed|Thesis/dissertation

eScholarship.org Powered by the California Digital Library
University of California

UNIVERSITY OF CALIFORNIA

Los Angeles

The Role of the Kelvin-Helmholtz Instability in the Evolution of Magnetized Relativistic Sheared Plasma Flows

A dissertation submitted in partial satisfaction of the requirements for the degree Doctor of Philosophy in Physics

by

Nathaniel Donald Hamlin

2012

© Copyright by

Nathaniel Donald Hamlin

2012

ABSTRACT OF THE DISSERTATION

The Role of the Kelvin-Helmholtz Instability in the

Evolution of Magnetized Relativistic Sheared Plasma Flows

by

Nathaniel Donald Hamlin

Doctor of Philosophy in Physics

University of California, Los Angeles, 2012

Professor William I. Newman, Chair

Our objective is to explore, both analytically and by numerical simulation, the evolution of the Kelvin-Helmholtz (KH) instability in a relativistic magnetized sheared plasma flow, with applications to highly energetic astrophysical jets originating from such features as active galactic nuclei (AGN) and quasars. The Kelvin-Helmholtz instability arises in the presence of a variation in flow speed in the direction orthogonal to the flow. We use the conservative single-fluid relativistic magnetohydrodynamic (RMHD) equations of Anile (1989). Our numerical scheme uses explicit finite-differencing, which is fourth-order in space

and time, and uses a rapidly-convergent, highly accurate algorithm, developed by Newman (2002), to invert the RMHD equations. These are major improvements over previous schemes using artificial viscosity. The exact single-fluid RMHD equations are marginally stable. However, when discretized in a numerical scheme, they become unstable. Artificial viscosity is therefore needed in order to restore stability to the system. However, viscosity also models physical processes such as momentum transfer and conductivity. Diffusion can also result in an anomaly associated with relativistic effects, however we show in chapter 12 that this anomaly does not in any way affect our simulation results.

The early nonlinear regime of evolution corresponds to the formation of large vortices connected by a dual filamentary structure. In the absence of a magnetic field, these vortices persist. A magnetic field stabilizes the system, inhibiting the vortices through a series of stages. First, the vortices expel the plasma and magnetic field lines, resulting in amplified field at the vortex extremities. The magnetic field then disrupts the vortices, leading to a turbulent regime of smaller-scale structures and large-scale magnetic reconnection, followed by an approach to an equilibrium state consisting of flow-aligned vortex and current filaments whose widths are at most 1/4 the initial jet width. Qualitatively similar processes are discussed in MHD literature. We examine in detail how and to what extent these stages manifest in RMHD for a set of representative field strengths. To characterize the influence of the magnetic field, we define a relativistic extension of the Alfvenic Mach number. We observe a close complementarity between magnetic field and fluid behavior. We find qualitative agreement with observations of numerous jets, including M87, NGC 5128, 3C 273, 3C 120, HH 30, and HH 34. In particular, the knots in the radio jet M87 are believed to have amplified fields with transverse components, suggesting that these knots may exhibit vortex-

like behavior.

For stronger fields, the above inhibition stages occur more rapidly, and for sufficiently strong fields (Alfven speed greater than about 1/6 the flow speed), vortices are suppressed entirely. The jet widens to about twice the input perturbation wavelength for weak vortex-disruptive fields. Stronger fields suppress vortex rotation, magnetic reconnection, and turbulence, resulting in smaller equilibrium jet widths. These features and processes have a monotonic dependence on field strength. However, certain processes reveal bifurcations, in that they are maximized for intermediate background field strengths. Maximum jet deceleration (i.e., viscous dissipation) occurs for intermediate vortex-disruptive fields, owing to turbulent reorganization. Maximum extraction of electromagnetic energy occurs for strong vortex-disruptive fields, and is reduced for vortex-suppressing fields.

While magnetic fields tend to stabilize the system, highly relativistic flows have a destabilizing effect, for example by supporting rapidly-growing modes at wavelengths which are short compared to the length scale of the velocity shear. This sheds light on a problem that has plagued artificial viscosity simulations, such as this one, namely the difficulty in sustaining numerical simulations with Lorentz factors larger than 2.

Our numerical results uncover complex mechanisms by which the magnetic field inhibits the KH instability in RMHD, showing qualitative consistency with observations of astrophysical jets. We have also successfully unified the HD, RHD, MHD, and RMHD regimes, analytically and numerically, in both the linear analysis and nonlinear evolution.

The dissertation of Nathaniel Donald Hamlin is approved.

Margaret G. Kivelson

Ferdinand V. Coroniti

Warren B. Mori

William I. Newman, Committee Chair

University of California, Los Angeles

2012

TABLE OF CONTENTS

1 Introduction and Overview 1

1.1 Tables 1
1.2 Motivation for Research 4
1.3 Overview of the Dissertation 5

2 Prior Research on the KH Instability and Astrophysical Jets 22

2.1 Linear Regime 23
2.2 Nonlinear Regime 28
2.3 Astrophysical Jets 30
2.4 Conclusion 33

3 RMHD Transport Equations for a Fluid with Infinite Conductivity 35

3.1 Three Versions of the RMHD Equations 36
3.2 Equivalence of Versions 1 and 2 41
3.3 Equivalence of Versions 2 and 3 44
3.4 Relativistic vs Non-relativistic Fluid Equations 47
3.5 Validity of Single-fluid Model 50
3.6 Model Used in Simulations 53
3.7 Conclusion 56

4 Linear Analysis of the KH Instability: Step-function Velocity Profile 57

4.1 HD Kelvin-Helmholtz Instability 60
4.1.1 Dispersion Relation for an Unmagnetized Fluid 61
4.1.2 HD Dispersion Relation for Two Adjacent Flows 63
4.2 RHD Kelvin-Helmholtz Instability 68
4.2.1 Dispersion Relation for a Relativistic Unmagnetized Fluid 69
4.2.2 RHD Dispersion Relation for Two Adjacent Flows 73
4.3 MHD Kelvin-Helmholtz Instability 93
4.3.1 MHD Single-fluid Dispersion Relation 94
4.3.2 Non-relativistic Magnetized Kelvin-Helmholtz Instability 97
4.4 Comparison with PK83 and KP84 101
4.5 MHD KH Instability with Displacement Current 107
4.6 RMHD Kelvin-Helmholtz Instability 112
4.6.1 RMHD Single-fluid Dispersion Relation 112

4.6.2 The Relativistic Magnetized Kelvin-Helmholtz Instability 117
4.7 Numerical Solution to the RMHD Dispersion Relation 118
4.8 Conclusion 132

5 KH Instability with Velocity Shear: Launching a Mode 135

5.1 RHD KH Instability with Velocity Shear 136
5.2 RMHD KH Instability with Velocity Shear 143
5.3 RMHD ODE with a Step-function Velocity Profile 157
5.4 Underlying Structure of ODE For Pressure Eigenfunctions 159
5.5 Numerically Computing an Eigenmode 162
5.6 Conclusion 174

6 Growth Rates of the Bickley Jet Profile 176

6.1 Prior Usage of the Bickley Jet Profile 179
6.2 Comparison to Drazin and Howard (1966) 181
6.3 Dependence of Growth Rate on Magnetic Field 184
6.4 Dependence of Growth Rate on Flow Speed 190
6.5 Dependence of Growth Rate on Wave Number 194
6.6 Conclusion 198

7 Shear Profiles of the Perturbations 200

7.1 Perturbation Profiles for Unmagnetized Cases 201
7.2 Perturbation Profiles of Magnetized Cases 207
7.3 Conclusion 214

8 Numerical Method 216

8.1 Evolving the Conservation-diffusion Equations 217
8.2 Physical Significance of Magnetic Viscosity 225
8.3 Conclusion 230

9 Spatial Averages and Maximum Values Versus Time 232

9.1 Growth in the Linear Regime 234
9.2 Near-perfect Agreement in the Absence of Diffusion 248
9.3 Time-Dependence in the Nonlinear Regime 253
9.4 Nonlinear Growth in Fluctuations of the Primitive Variables 260
9.5 Oscillatory Behavior of Average Values 270

9.6 Saturation and Amplification 279
9.7 Conclusion 289

10 Displays of Simulation Results 293

10.1 Evolution in RHD 297
10.2 Weak Vortex-disruptive Field ($M_A = 41.4$) 306
10.3 Intermediate Vortex-disruptive Field ($M_A = 20.7$) 321
10.4 Strong Vortex-disruptive Field ($M_A = 10.3$) 327
10.5 Vortex-suppressing Field ($M_A = 5.145$) 332
10.6 Evolution with Periodic Boundary Conditions 340
10.7 Comparison with Jet Observations 341
10.8 RMHD Versus MHD Results 346
10.9 Alternating Symmetry of the Vorticity 347
10.10 Conclusion 348

11 Sensitivity of Results to Input Parameters 357

11.1 Zero Divergence of Magnetic Field 361
11.2 Spatio-temporal Convergence of Simulation Results 362
11.3 Dependence on System Dimensions 368
11.4 Dependence on System Width: Weaker field 374
11.5 Dependence on System Width: RHD Case 377
11.6 Convergence Between RMHD, MHD, and RHD Regimes 382
11.7 Influence of Viscosity on Nonlinear Evolution 390
11.8 Dependence on Flow Speed 407
11.9 Dependence on Perturbation Wavelength 412
11.10 Conclusion 428

12 Diffusion in Relativistic Flows: A Mathematical Anomaly 432

12.1 Lorentz-invariance and Diffusion 434
12.2 RHD Stability Analysis with Diffusion 441
12.2.1 Derivation of RHD Dispersion Relation with Diffusion 442
12.2.2 RHD Dispersion Relation in Diffusionless Case 448
12.2.3 Decaying Modes in Non-relativistic Regime 452
12.2.4 Anomalous Growing Modes in Highly Relativistic Regime 454
12.2.5 Summary of RHD Results 460
12.3 RMHD Stability Analysis with Diffusion 462

12.3.1 Derivation of RMHD Dispersion Relation with Diffusion 462
12.3.2 Stability for Equal Diffusion Coefficients 476
12.3.3 Decaying Modes in Non-relativistic Regime 477
12.3.4 Extreme Relativistic Limit 485
12.4 Conclusion 489

13 Further Research Using High Resolution Shock-capturing Methods 491

14 Summary 498

14.1 Our Model of the System 500
14.2 Stabilizing Influence of a Magnetic Field 505
14.3 Destabilizing Influence of Relativistic Effects 515
14.4 Opportunities for Future Research 517
14.5 Conclusion 518

TABLES

1.1 Commonly used acronyms . . . 2
1.2 Commonly used notation . . . 3
6.2 Comparison to Drazin and Howard (1966) . . . 182
9.1 Fractional errors in total z-momentum and energy . . . 287
11.1 Divergence of magnetic field . . . 362

FIGURES

4.1 Critical flow speed vs sound speed at $\theta = 0$ (RHD) . . . 82
4.2 Critical flow speed vs sound speed at $\theta = \pi/4$ (RHD) . . . 83
4.3 Growth rate vs flow speed and Mach number (RHD) . . . 84
4.4 Growth rate vs flow speed (RHD) . . . 85
4.5 Growth rate vs Mach number (RHD) . . . 86
4.6 Frequency and wave number vs flow speed (RHD) . . . 90
4.7 Wavelength vs Lorentz factor, $c_s = 0.57\,c$, $\theta = 0$ (RHD) . . . 93
4.8 Growth rate vs flow speed for $\theta = 0$ deg (MHD) . . . 105
4.9 Growth rate vs flow speed for $\theta = 60$ deg (MHD) . . . 105
4.10 Growth rate vs flow speed for $\theta = 78$ deg (MHD) . . . 106
4.11 Growth rates of PK83 and KP84 (MHD) . . . 106
4.12 Frequencies (RMHD) for (a) $\beta = 9$ and (b) $\beta = 2.33$ . . . 122
4.13 k_x in fluid 1 (RMHD) for (a) $\beta = 9$ and (b) $\beta = 2.33$ . . . 122
4.14 k_x in fluid 2 (RMHD) for (a) $\beta = 9$ and (b) $\beta = 2.33$ . . . 123
4.15 Max. growth rate and critical flow speeds vs field strength (RMHD) . . . 128
4.16 Max. growth rate and critical flow speeds vs field strength (MHD) . . . 128
4.17 ω and k_x vs flow speed (MHD) . . . 129
4.18 Growth rate vs Alfven speed at different flow speeds (RMHD) . . . 130

4.19 Growth rate vs M_A^{-1} at different flow speeds (RMHD) 130
4.20 Growth rate vs flow speed at different Alfven speeds (RMHD) 131
4.21 Growth rate vs Mach number at different Alfven speeds (RMHD) 131
6.1 Growth rate and phase velocity vs k_z for different sound speeds (HD) 183
6.2 Growth rate vs inverse plasma β at different flow speeds (RMHD) 185
6.3 Phase velocity vs inverse plasma β at different flow speeds (RMHD) 185
6.4 Growth rate vs Alfven speed at different flow speeds (RMHD) 188
6.5 Phase velocity vs Alfven speed at different flow speeds (RMHD) 189
6.6 Growth rate vs M_A^{-1} at different flow speeds (RMHD) 189
6.7 Growth rate and phase veloc. vs flow speed at diff. sound speeds (RHD) 191
6.8 Growth rate and phase veloc. vs Mach number at diff. sound speeds (RHD) 192
6.9 Growth rate and phase velocity vs $\gamma v_{z0}/c$ at diff. sound speeds (RHD) 194
6.10 Growth rate vs k_z at different flow speeds (RHD) 196
6.11 Phase velocity vs k_z at different flow speeds (RHD) 196
6.12 $d\omega_i/dk_z$ vs k_z at different flow speeds (RHD) 197
6.13 $d\omega_r/dk_z$ vs k_z at different flow speeds (RHD) 197
7.1 Shear profiles of δP at different flow speeds (RHD) 205
7.2 Shear profiles of $d\delta P/dx$ at different flow speeds (RHD) 205
7.3 Shear profiles of δv_x at different flow speeds (RHD) 206
7.4 Shear profiles of δv_z at different flow speeds (RHD) 206
7.6 Shear profiles of δv_x at different M_A for a flow speed of $0.7\,c$ (RMHD) 209
7.7 Shear profiles of δv_x at different M_A for a flow speed of $0.2\,c$ (RMHD) 210
7.8 Shear profiles of δv_z at different M_A for a flow speed of $0.7\,c$ (RMHD) 210
7.9 Shear profiles of δv_z at different M_A for a flow speed of $0.2\,c$ (RMHD) 211
7.10 Shear profiles of δB_x at different M_A for a flow speed of $0.7\,c$ (RMHD) 211
7.11 Shear profiles of δB_x at different M_A for a flow speed of $0.2\,c$ (RMHD) 212
7.12 Shear profiles of δB_z at different M_A for a flow speed of $0.7\,c$ (RMHD) 212

7.13 Shear profiles of δB_z at different M_A for a flow speed of $0.2\,c$ (RMHD) 213
9.1 Linear growth in δP for different values of the z-momentum viscosity 236
9.2 Linear growth in $\delta\rho$ for different values of the z-momentum viscosity 237
9.3 Linear growth curves for non-zero x-momentum viscosity 237
9.4 Linear growth curves for non-zero density and x-momentum viscosity 238
9.5 Pressure displays for non-zero density and x-momentum viscosity 239
9.6 Density displays for non-zero density and x-momentum viscosity 240
9.7 Linear growth curves for non-zero momentum and density viscosity 242
9.8 Pressure displays for non-zero momentum and density viscosity 242
9.9 Pressure displays for non-zero momentum and density viscosity 243
9.10 Density displays for non-zero momentum and density viscosity 245
9.11 Density displays for non-zero momentum and density viscosity 246
9.12 Linear growth curves for non-zero density viscosity 246
9.13 Linear growth curves for non-zero z-momentum viscosity 247
9.14 Growth in transverse velocity fluctuations vs time at different M_A 264
9.15 Growth in longit. velocity fluctuations vs time at different M_A 265
9.16 Growth in density fluctuations vs time at different M_A 265
9.17 Growth in pressure fluctuations vs time at different M_A 266
9.18 Growth in transverse field fluctuations vs time at different M_A 266
9.19 Growth in longit. field fluctuations vs time at different M_A 267
9.20 Growth in fluctuations vs time for unmagnetized case 267
9.21 Growth in fluctuations vs time for weak field ($M_A = 83$) 268
9.22 Growth in fluctuations vs time for intermediate field ($M_A = 41$) 268
9.23 Growth in fluctuations vs time for intermediate field ($M_A = 21$) 269
9.24 Growth in fluctuations vs time for intermediate field ($M_A = 10$) 269
9.25 Growth in fluctuations vs time for strong field ($M_A = 5$) 270
9.26 Average longitudinal velocity vs time at different field strengths 275

9.27 RMS transverse velocity vs time at different field strengths 275
9.28 Maximum longitudinal velocity vs time at different field strengths 276
9.29 Maximum transverse velocity vs time at different field strengths 276
9.30 Average Lorentz factor vs time at different field strengths 277
9.31 Maximum Lorentz factor vs time at different field strengths 277
9.32 Average thermal pressure vs time at different field strengths 278
9.33 Average density vs time at different field strengths 278
9.34 RMS vorticity vs time at different field strengths 282
9.35 RMS current density vs time at different field strengths 282
9.36 Avg. electromagnetic to thermal pressure vs time at different field strengths 283
9.37 Max. electromagnetic to thermal pressure vs time at different field strengths . . . 284
9.38 EM and mechanical z-momentum vs time at different M_A (flow speed $0.7\,c$) 285
9.39 EM and mechanical z-momentum vs time at different M_A (flow speed $0.5\,c$) 285
9.40 EM and mechanical energy vs time at different M_A (flow speed $0.7\,c$) 288
9.41 EM and mechanical energy vs time at different M_A (flow speed $0.5\,c$) 288
10.1 Unmagnetized evolution: $t = 7.33\,T_i = 3.26\,T = 73.7\,r_0/c = 1.35\,L_x/c_s$ 304
10.2 Unmagnetized evolution: $t = 7.94\,T_i = 3.53\,T = 79.9\,r_0/c = 1.46\,L_x/c_s$ 304
10.3 Unmagnetized evolution: $t = 9.16\,T_i = 4.08\,T = 92.2\,r_0/c = 1.68\,L_x/c_s$ 304
10.4 Unmagnetized evolution: $t = 12.21\,T_i = 5.44\,T = 122.9\,r_0/c = 2.25\,L_x/c_s$ 304
10.5 Unmagnetized evolution: $t = 14.04\,T_i = 6.25\,T = 141.3\,r_0/c = 2.58\,L_x/c_s$ 305
10.6 Unmagnetized evolution: $t = 16.49\,T_i = 7.34\,T = 165.9\,r_0/c = 3.03\,L_x/c_s$ 305
10.7 Unmagnetized evolution: $t = 27.48\,T_i = 12.23\,T = 276.5\,r_0/c = 5.05\,L_x/c_s$ 305
10.8 Unmagnetized evolution: $t = 32.97\,T_i = 14.67\,T = 331.8\,r_0/c = 6.07\,L_x/c_s$ 305
10.9 Vorticity for $B = 0$ (left) and $M_A = 41.41$ (right) at $9.8\,T_i$ 317
10.10 Vorticity for $B = 0$ (left) and $M_A = 41.41$ (right) at $12.2\,T_i$ 317
10.11 Vorticity for $B = 0$ (left) and $M_A = 41.41$ (right) at $13.4\,T_i$ 317
10.12 Various quantities at $t = 7.91\,T_i = 3.53\,T$, $M_A = 41.4$ 318

10.13 Various quantities at $t = 11.6\,T_i = 5.16\,T$, $M_A = 41.4$ 318
10.14 Various quantities at $t = 13.4\,T_i = 5.97\,T$, $M_A = 41.4$ 319
10.15 Various quantities at $t = 16.4\,T_i = 7.33\,T$, $M_A = 41.4$ 319
10.16 Various quantities at $t = 27.4\,T_i = 12.2\,T$, $M_A = 41.4$ 320
10.17 Various quantities at $t = 56.6\,T_i = 25.3\,T$, $M_A = 41.4$ 320
10.18 Vorticity at (a) $10.2\,T_i$ and (b) $13.9\,T_i$ 326
10.19 Vorticity at (a) $16.3\,T_i$ and (b) $23.5\,T_i$ 326
10.20 (a) Vorticity and (b) longitudinal velocity at $t = 37.9\,T_i$ 326
10.21 Vorticity at (a) $8.6\,T_i$ and (b) $10.9\,T_i$ 331
10.22 Vorticity at (a) $13.2T_i$ and (b) $16.7\,T_i$ 331
10.23 (a) Vorticity and (b) longitudinal velocity at $t = 27.1\,T_i$ 331
10.24 Various quantities at $t = 8.62\,T_i = 4.93\,T$, $M_A = 5.15$ 338
10.25 Various quantities at $t = 13.2\,T_i = 7.52\,T$, $M_A = 5.15$ 339
10.26 Various quantities at $t = 21.8\,T_i = 12.5\,T$, $M_A = 5.15$ 339
10.27 Laminar stream of air, Van Dyke (1982) 341
10.28 M87 (a.k.a. Virgo A, NGC 4486) 344
10.29 Centaurus A, imaged with Chandra in X-ray 344
10.30 Herbig-Haro 30 345
11.1 Time-dependencies for $\Delta t = 0.032\,r_0/c$ and $\Delta t = 0.016\,r_0/c$ 364
11.2 Vorticity displays for two time increments: $t = 17.0\,T_i$ 365
11.3 Vorticity displays at different grid resolutions: $t = 9.43\,T_i$ 366
11.4 Vorticity displays at different grid resolutions: $t = 13.7\,T_i$ 367
11.5 Vorticity displays at different grid resolutions: $t = 15.5T_i$ 367
11.6 RMS and max. vorticity for $M_A = 20.7$ for $L_x = 31.5$ (blue) and 47.25 (red) 370
11.7 Avg. and max. v_z for $M_A = 20.7$ for $L_x = 31.5$ (blue) and 47.25 (red) 370
11.8 Avg. and max. γ for $M_A = 20.7$ for $L_x = 31.5$ (blue) and 47.25 (red) 371
11.9 RMS and max. J for $M_A = 20.7$ for $L_x = 31.5$ (blue) and 47.25 (red) 371

11.10 Avg. and max. EM energy for $M_A = 20.7$ for $L_x = 31.5$ (blue), 47.25 (red) 372
11.11 Min. plasma β for $M_A = 20.7$ for $L_x = 31.5$ (blue) and 47.25 (red) 372
11.12 $M_A = 20.70, \quad t = 12.6\,T_i = 5.69\,T = 129.0\,r_0/c$ 372
11.13 $M_A = 20.70, \quad t = 15.1\,T_i = 6.77\,T = 153.6\,r_0/c$ 373
11.14 $M_A = 20.70, \quad t = 17.5\,T_i = 7.86\,T = 178.2\,r_0/c$ 373
11.15 $M_A = 20.70, \quad t = 23.5\,T_i = 10.6\,T = 239.6\,r_0/c$ 373
11.16 $M_A = 20.70, \quad t = 42.8\,T_i = 19.2\,T = 436.2\,r_0/c$ 373
11.17 $M_A = 41.41, \quad t = 12.78\,T_i = 5.70\,T = 129.0\,r_0/c$ 375
11.18 $M_A = 41.41, \quad t = 14.00\,T_i = 6.25\,T = 141.3\,r_0/c$ 375
11.19 $M_A = 41.41, \quad t = 15.21\,T_i = 6.79\,T = 153.6\,r_0/c$ 375
11.20 $M_A = 41.41, \quad t = 16.43\,T_i = 7.33\,T = 165.9\,r_0/c$ 375
11.21 $M_A = 41.41, \quad t = 21.30\,T_i = 9.50\,T = 215.0\,r_0/c$ 376
11.22 $M_A = 41.41, \quad t = 52.94\,T_i = 23.62\,T = 534.5\,r_0/c$ 376
11.23 RMS and max. vort. for $B = 0$ for $L_x = 31.5$ (blue) and 47.25 (red) 379
11.24 Avg. and max. v_z for $B = 0$ for $L_x = 31.5$ (blue) and 47.25 (red) 379
11.25 RMS and max. v_x for $B = 0$ for $L_x = 31.5$ (blue) and 47.25 (red) 380
11.26 Avg. and max. γ for $B = 0$ for $L_x = 31.5$ (blue) and 47.25 (red) 380
11.27 $B = 0, \quad t = 12.21\,T_i = 5.44\,T = 122.9\,r_0/c$ 380
11.28 $B = 0, \quad t = 14.04\,T_i = 6.25\,T = 141.3\,r_0/c$ 381
11.29 $B = 0, \quad t = 15.88\,T_i = 7.07\,T = 159.7\,r_0/c$ 381
11.30 $B = 0, \quad t = 17.10\,T_i = 7.61\,T = 172.0\,r_0/c$ 381
11.31 $B = 0, \quad t = 26.87\,T_i = 11.96\,T = 270.3\,r_0/c$ 381
11.32 Growth curves for RMHD and MHD cases 384
11.33 Vorticity and current density for RMHD (blue) and MHD (red) cases 384
11.34 Average and max. longit. veloc. for RMHD (blue) and MHD (red) cases 385
11.35 RMS and max. transverse velocity for RMHD (blue) and MHD (red) cases 385
11.36 Max. γ and min. plasma β for RMHD (blue) and MHD (red) cases 386

11.37 Vorticity displays for RMHD and MHD cases: $t = 9.38\,T_i$ 386
11.38 Vorticity displays for RMHD and MHD cases: $t = 12.3\,T_i$ 387
11.39 Vorticity displays for RMHD and MHD cases: $t = 14.0\,T_i$ 387
11.40 Vorticity displays for RHD and RMHD cases: $t = 11.3\,T_i$ 389
11.41 Vorticity displays for RHD and RMHD cases: $t = 13.7\,T_i$ 389
11.42 Viscosity-dependence of growth in velocity components: $M_A = 41$ 391
11.43 Viscosity-dependence of growth in P and B_z: $M_A = 41$ 392
11.44 Viscosity-dependence of RMS vorticity and current density: $M_A = 41$ 392
11.45 Viscosity-dependence of Max. v_z, min. plasma β: $M_A = 41$ 393
11.46 Viscosity-dependence of vorticity for $M_A = 41$: $t = 13.4\,T_i$ 394
11.47 Viscosity-dependence of vorticity for $M_A = 41$: $t = 15.2\,T_i$ 394
11.48 Viscosity-dependence of vorticity for $M_A = 41$: $t = 32.9\,T_i$ 394
11.49 Viscosity-dependence of vorticity for $M_A = 41$: $t = 52.9\,T_i$ 395
11.50 Viscosity-dependence of longitudinal velocity for $M_A = 41$: $t = 13.4\,T_i$ 395
11.51 Viscosity-dependence of longitudinal velocity for $M_A = 41$: $t = 52.9T_i$ 395
11.52 Viscosity-dependence of growth in velocity components: $M_A = 21$ 397
11.53 Viscosity-dependence of growth in P and B_z: $M_A = 21$ 397
11.54 Viscosity-dependence of RMS vorticity and current density: $M_A = 21$ 398
11.55 Viscosity-dependence of max. longit. veloc. and Lorentz factor: $M_A = 21$ 398
11.56 Viscosity-dependence of min. plasma β and avg. pressure: $M_A = 21$ 399
11.57 Viscosity-dependence of vorticity for $M_A = 21$: $t = 12.6\,T_i$ 400
11.58 Viscosity-dependence of vorticity for $M_A = 21$: $t = 15.1\,T_i$ 400
11.59 Viscosity-dependence of vorticity for $M_A = 21$: $t = 43.4\,T_i$ 400
11.60 Viscosity-dependence of longitudinal velocity for $M_A = 21$: $t = 43.4\,T_i$ 401
11.61 Viscosity-dependence of growth in velocity components: $M_A = 5.1$ 403
11.62 Viscosity-dependence of growth in P and B_z: $M_A = 5.1$ 403
11.63 Viscosity-dependence of vorticity and current density: $M_A = 5.1$ 404

11.64 Viscosity-dependence of maximum velocity components: $M_A = 5.1$ 404
11.65 Viscosity-dependence of minimum plasma β and avg. pressure: $M_A = 5.1$ 405
11.66 Viscosity-dependence of vorticity for $M_A = 5.1$: $t = 10.3\,T_i$ 406
11.67 Viscosity-dependence of vorticity for $M_A = 5.1$: $t = 17.5\,T_i$ 406
11.68 Viscosity-dependence of vorticity for $M_A = 5.1$: $t = 28.3\,T_i$ 406
11.69 Vorticity at two flow speeds, $M_A = 10.3$: $t = 10.3\,T_i$ 409
11.70 Vorticity at two flow speeds, $M_A = 10.3$: $t = 11.6\,T_i$ 409
11.71 Vorticity at two flow speeds, $M_A = 10.3$: $t = 13.8\,T_i$ 409
11.72 Vorticity at two flow speeds, $M_A = 20.7$: $t = 10.4\,T_i$ 411
11.73 Vorticity at two flow speeds, $M_A = 20.7$: $t = 12.2\,T_i$ 411
11.74 Vorticity at two flow speeds, $M_A = 20.7$: $t = 14.5\,T_i$ 412
11.75 Wavelength-dependence of growth in velocity components: $M_A = 41$ 414
11.76 Wavelength-dependence of growth in P and B_z: $M_A = 41$ 414
11.77 Wavelength-dependence of RMS vorticity and current density: $M_A = 41$ 415
11.78 Wavelength-dependence of Lorentz factor: $M_A = 41$ 415
11.79 Wavelength-dependence of maximum velocity components: $M_A = 41$ 416
11.80 Wavelength-dependence of minimum plasma β: $M_A = 41$ 416
11.81 Wavelength-dependence of vorticity for $M_A = 41.4$: $t = 12\,T_i$ 418
11.82 Wavelength-dependence of vorticity for $M_A = 41.4$: $t = 14\,T_i$ 418
11.83 Wavelength-dependence of vorticity for $M_A = 41.4$: $t = 19\,T_i$ 419
11.84 Wavelength-dependence of vorticity for $M_A = 41.4$: $t = 60\,T_i$ 419
11.85 Wavelength-dependence of longitudinal velocity for $M_A = 41.4$: $t = 60\,T_i$ 420
11.86 Wavelength-dependence of growth in velocity components: $M_A = 5.1$ 423
11.87 Wavelength-dependence of growth in P and B_z: $M_A = 5.1$ 423
11.88 Wavelength-dependence of RMS vorticity and current density: $M_A = 5.1$ 424
11.89 Wavelength-dependence of Lorentz factor: $M_A = 5.1$ 424
11.90 Wavelength-dependence of maximum velocity components: $M_A = 5.1$ 425

11.91 Wavelength-dependence of plasma β: $M_A = 5.1$ 425
11.92 Wavelength-dependence of avg. density and pressure: $M_A = 5.1$ 426
11.93 Wavelength-dependence of vorticity for $M_A = 5.1$: $t = 9.3\,T_i$ 427
11.94 Wavelength-dependence of vorticity for $M_A = 5.1$: $t = 24.5\,T_i$ 427
11.95 Wavelength-dependence of longitudinal velocity for $M_A = 5.1$: $t = 24.5\,T_i$ 428
12.1 Growth rate vs. energy viscosity for different sound speeds 454
12.2 Max. growth rate vs. flow speed for different sound speeds 459
12.3 Max. growth rate vs. covariant flow speed for different sound speeds 460

ACKNOWLEDGMENTS

This dissertation is the culmination of a six-year-long endeavor. I am tremendously grateful to my advisor, Prof. William I. Newman, for the countless hours of guidance and support he has provided throughout this process. Despite his busy schedule, he always found a way to make himself available to me, and because of this level of dedication, I am very fortunate to have had him as an advisor. I am also especially grateful to Prof. Margaret G. Kivelson, one of my thesis committee members, for all the advice and support she has provided over the years. She has been a tremendous asset to my research and to this dissertation. I would like to thank Prof. George Morales, with whom I had several meetings, and who provided numerous excellent suggestions, along with Prof. Ferdinand V. Coroniti and Prof. Warren B. Mori, each of whom are on my thesis committee, and each of whom have provided valuable advice and feedback over the years. I am also grateful to Prof. Raymond Walker and Dr. Philip Pritchett, each of whom I met with numerous times, and both of whom provided valuable advice on the study of the KH instability using numerical modeling in MHD. I would like to thank Prof. Richard Lovelace who, through numerous communications by phone and email, has helped be tremendously with my research and dissertation, along with Prof. Matt Malkan and Prof. Mark Morris, both of whom were immensely helpful in my search for astrophysical objects with which to compare my results. I am grateful to Prof. Stanley Osher and Dr. C.-C. Wu, both of whom provided valuable insight into the use of numerical schemes with which to model this problem. I also wish to thank Prof. Walter Gekelman for his helpful suggestions, and for providing my advisor and me with an eye-opening tour of his plasma research facilities.

Last but certainly not least, I would like to thank my mom Pat, my sister Kathy, my dad Chris, my step-mom Susan, and my stepsister Amanda. Each of them have provided unwavering support and encouragement throughout this long process, for which I am very fortunate, and very grateful.

VITA/BIOGRAPHICAL SKETCH

- University of California, Los Angeles, 2003 - Present (total GPA of 3.98)
  - Master of Science, Physics, December 2004
- University of California, Irvine, 1997 - 2002 (total GPA of 3.99)
  - Bachelor of Science, Summa Cum Laude, Physics, June 2002
  - Bachelor of Science, Summa Cum Laude, Mathematics, June 2002
  - Member of the Society of Physics Students
- **Employment and Research**
  - Teaching Fellow, Physics and Astronomy Dept., UCLA, Fall 2007 - Summer 2012
    - For each of 18 quarters, led three to four weekly discussion sections of introductory and advanced physics courses for 30-40 students per section.
    - Created numerous sample problems with detailed solutions. Regularly made these available to students as study guides.
  - Graduate Student Researcher, UCLA, 2005 - present
    - Prof. William I. Newman, advisor
    - Doctoral dissertation: "The Role of the Kelvin-Helmholtz Instability in the Evolution of Magnetized Relativistic Sheared Plasma Flows"
    - I numerically solve the relativistic magnetohydrodynamic (RMHD) single-fluid equations in conservative form, using a scheme which is fourth-order in space and time, and which overcomes difficulty of inverting the RMHD equations.
    - For a set of representative field strengths, I have examined how a magnetic field inhibits nonlinear Kelvin-Helmholtz vortices in RMHD.
    - Potential comparisons with jet observations, including knots in M87.
    - New analytical demonstration showing that, at highly relativistic flow speeds, artificial diffusion introduces growing modes in essentially all cases.
    - Programmed extensively in FORTRAN, PHOCAS (Physical Optics Code for Analysis and Simulation), Matlab, and Mathematica.
  - Graduate Student Researcher, UCLA, 2004 - 2005 (Prof. Ian Mclean, advisor)
    - Performed computer modeling in adaptive optics, which refers to iterative real-time corrections, in telescopes, of atmospheric distortions to images.
    - Processed Excel data from the Keck telescope and the CELT (California Extremely Large Telescope). Analyzed data using PHOCAS (Physical Optics Code for Analysis and Simulation).
  - Undergraduate Researcher, UC Irvine, 2001 - 2002 (Prof. Gary Chanan, advisor)

    - Designed wavefront reconstruction algorithm for use in adaptive optics loops in telescopes, particularly the CELT (California Extremely Large Telescope).
    - Senior honors thesis: "Optimization of Wavefront Reconstruction for Adaptive Optics"
  - Technical Staff, The Aerospace Corporation, El Segundo, CA, Summer 2001, Aug. 2002 - Aug. 2003, Summer 2004 (Dr. Richard Boucher, supervisor)
    - Computer modeling in adaptive optics. Programmed in C++ and PHOCAS.

- **Presentations**
  - "The Role of Magnetic Fields in Relativistic Astrophysical Jets" Hamlin, Nathaniel; Newman, W.I., American Astronomical Society, DDA meeting #43, #6.08, Mt. Hood, Oregon, May 2012
  - "Optimization of Interpolation of NASTRAN Finite Element Data Onto Ray-Tracing Coordinate Systems" Hamlin, N.D., Summer Hires Briefings, Electronic Systems Division, The Aerospace Corporation, El Segundo, CA, Aug. 2001
  - "Optimization of Wavefront Reconstruction for Adaptive Optics" Hamlin, N.D., UCI Undergraduate Research Symposium, Irvine, CA, May 2002

- **Awards and Honors**
  - Outstanding Teaching Award, Dept. of Physics and Astronomy, UCLA, 2009 - 2010
    - Awarded to Teaching Assistants who receive top evaluation scores by students.
  - DDA Student Stipend Award
    - Covered registration costs, plus $600 stipend, for presentation of my research at the annual meeting of the Division on Dynamical Astronomy in May 2012.
  - National Defense Science and Engineering Graduate Fellowship, 2003 - 2006
    - Tuition plus $\approx$ $23000/year for first three years of graduate study at UCLA
  - University Fellowship, $4000/year, UCLA, 2003 - 2009
  - Outstanding Student Fellowship, $100, UCLA, 2007
  - Herbert H. Chen scholarship for excellence in physics, UC Irvine, June 2000
  - Induction into Phi Beta Kappa, Sigma Pi Sigma, UC Irvine, June 2000
  - Most Outstanding Undergraduate in the School of Physical Sciences Commendation, UC Irvine, May 2000

Chapter 1

Introduction and Overview

We begin, in section 1.1, by presenting tables of acronyms and symbols which are commonly used throughout the dissertation. In section 1.2, we briefly discuss some important areas in which the Kelvin-Helmholtz (KH) instability has been studied (to be elaborated on in chapter 2), and then argue that there is considerable interest in understanding the role of the Kelvin-Helmholtz instability in the evolution of relativistic magnetized astrophysical flows. In section 1.3, we present an overview of the dissertation.

1.1 Tables

Table 1.1 contains a list of acronyms and their meanings, while table 1.2 contains a list of symbols and their meanings, along with mathematical definitions and units, where appropriate. These acronyms and symbols appear frequently throughout the dissertation.

It should be noted that throughout the dissertation, we use a system of units for charge density, current density, electric field, and magnetic field such that the factor of 4π does not appear in Maxwell's equations. Therefore, this factor also does not appear in expressions for energy density, Alfven speed (defined in table 1.2), etc..

Acronym	Meaning
AGN	active galactic nuclei
AV	artificial viscosity
HD	hydrodynamic
HLL	Harten, Lax, and van Leer
HRSC	high-resolution shock-capturing
KH	Kelvin-Helmholtz
KP84	Kivelson and Pu (1984)
LRN09	Lovelace, Romanova, and Newman (2009)
MHD	magnetohydrodynamic
MP	Miura and Pritchett
ODE	ordinary differential equation
PDE	partial differential equation
PK83	Pu and Kivelson (1983)
RHD	relativistic hydrodynamic
RMHD	relativistic magnetohydrodynamic
RMS	root-mean-square
SC	shock-capturing
TD	tangential discontinuity

Table 1.1: Commonly used acronyms

Symbol	Meaning	Expression/scaled units
$\mathbf{B}$	magnetic field in stationary frame	$[B] = \sqrt{\text{energy density}}$
$\mathbf{b}$	magnetic field in co-moving frame	$[b] = \sqrt{\text{energy density}}$
c	speed of light	unit of relativistic speed
c_s	sound speed	$c_s = \sqrt{\Gamma P/\rho}$ (non-rel.)
		$c_s = c\sqrt{\Gamma P/w}$ (relativistic)
$\mathbf{E}$	electric field in stationary frame	$\mathbf{E} = \mathbf{B} \times (\mathbf{v}/c)$
		(fluid with infinite conductivity)
M_s	Mach number (flow speed/sound speed)	$M_s = v/c_s$
M_A	relativistic Alfvenic Mach number	$M_A = (\gamma v)/(\gamma_A v_A)$
		$= (v/v_A)\sqrt{\frac{1-v_A^2/c^2}{1-v^2/c^2}}$
P	pressure in co-moving frame	$[P] =$ energy density
r_0	length scale of simulation	unit of length
$\mathbf{u}$	velocity in co-moving frame	$[u] = c$
$\mathbf{v}$	velocity in stationary frame	$[v] = c$
$\mathbf{v}_A$	Alfven velocity	$\mathbf{v}_A = \mathbf{B}/\sqrt{\rho}$ (non-rel.)
		$\mathbf{v}_A = c\mathbf{B}/\sqrt{w}$ (relativistic)
v_{z0}	background flow speed	$[v_{z0}] = c$ (relativistic)
w	enthalpy in co-moving frame	$w = \rho c^2 + P\Gamma/(\Gamma - 1)$
$\hat{x}$	shear (transverse) direction	N/A
$\hat{z}$	flow direction	N/A
$\boldsymbol{\beta}$	flow speed/(speed of light)	$\boldsymbol{\beta} = \mathbf{v}/c$
β	plasma beta	$\beta = 2P/(E^2 + B^2)$
Γ	adiabatic index	$\Gamma = C_P/C_V$
γ	Lorentz factor of flow	$\gamma = 1/\sqrt{1 - v^2/c^2}$
γ_A	Lorentz factor of Alfven speed	$\gamma_A = 1/\sqrt{1 - v_A^2/c^2}$
η_α	viscosity of quantity α	$[\eta] = r_0 c$
ρ	density in co-moving frame	$[\rho] = \sqrt{\text{energy density}}/c^2$
ω	complex frequency	$[\omega] = c/r_0$
$\bar{\omega}$	Doppler-shifted frequency	$\bar{\omega} = \omega - k_z v_{z0}$

Table 1.2: Commonly used notation

1.2 Motivation for Research

The Kelvin-Helmholtz (KH) instability arises when a perturbation is applied to a flow that exhibits a transverse (shear) variation in flow speed, either continuous or discontinuous. The KH instability was discovered independently by Lord Kelvin in 1871 and by Helmholtz in 1868. Helmholtz (1868; 1882) provided a qualitative discussion of the interaction between two vertically stratified fluids having different densities. Kelvin (1871; 1910) studied this instability in the geophysical context of wind-water interactions, or, more generally, a fluid and an air current in relative motion. This problem was further illuminated by Munk (1947), who found a critical wind velocity of 6.5 m/s above which white caps suddenly emerge. An experimental demonstration of the KH instability was provided by Francis (1954) for an air-oil interface. This has been extended to the problem of vertical stratification of air currents in the Earth's atmosphere (Chandrasekhar 1961; Case 1960; Dyson 1960; Drazin 1958; Drazin and Howard 1966). There have been many more recent studies of interactions between atmospheric air currents (Maslowe 1991; Swaters 1999; Van Dyke 1982).

The KH instability has also been widely studied in many areas of astrophysical interest, including astrophysical jets, and interactions within the Earth's magnetosphere (Pu and Kivelson 1983; Kivelson and Pu 1984; Otto and Fairfield 2000; Faganello et al. 2008). Comparisons between jet observations and simulations have suggested that the KH instability may play an important role in jet morphology, including vortices, helical structures, filamentary features, etc. (e.g., Hardee 1987, 2003, 2005, 2007; Lobanov and Zensus 2001; Bicknell and Begelman 1996). Apparent superluminal motion (i.e., behavior that gives the appearance of being greater than the speed of light, but is an effect of phase velocity),

and relativistic boosting, demonstrate that many of these jets have highly relativistic flows (e.g., Readhead 1993), while the presence of magnetic fields is strongly supported by the commonly accepted model for jet formation from active super-massive black holes (Lovelace 1976; Blandford and Payne 1982; Rees 1971; Scheuer 1974; Blandford and Rees 1974).

It is therefore of great interest to numerically simulate the KH instability in relativistic magnetized jets. However, the assumptions of relativity and magnetization greatly complicate the conservative equations used in simulations, and until 2006, the growth of the KH instability had not been accurately simulated in the RMHD regime, according to the introduction of Bucciantini and Del Zanna (2006). We solve the RMHD equations using a method which is fourth-order in space and time, instead of the second-order method previously employed, and an absolutely and more rapidly convergent scheme than has previously been available, and our results reproduce new and intriguing features of jet behavior and morphology. We shall present our numerical model of the system at the end of chapter 3, after surveying prior studies of astrophysical jets (both observational and numerical), and of the KH instability in sheared and stratified plasma flows.

1.3 Overview of the Dissertation

In chapter 2, we present an overview of prior studies of the Kelvin-Helmholtz instability, not just as it applies to astrophysical jets, but also to wind-water interactions, cloud formation, interactions between the Earth's magnetosphere and solar winds, and other space-related applications such as protostellar systems. We first discuss studies of the linear regime, then studies of the nonlinear regime, and then we elaborate on prior studies of astrophysical jets. We then present an overview of numerical methods used in prior single-fluid simulations,

particularly in the context of how they relate to the method used in the present simulation. We assume, throughout the dissertation, that the fluid being simulated is compressible, infinitely conducting, adiabatic, and has an isotropic pressure tensor. We establish the validity of these assumptions in section 3.6.

In chapter 3, we demonstrate the mathematical equivalence of three formulations of the relativistic magnetohydrodynamic (RMHD) single-fluid equations which are commonly used in the literature. This demonstrates that the formulation we use in our simulations, specifically, the covariant version of Anile (1989), is in fact equivalent to the two other formulations, where one of these is conservative but written in terms of electric and magnetic fields in the stationary reference frame, and the other is written in terms of Euler's and Maxwell's equations, and explicitly incorporates charge and current. We also show that these equations reduce to their expected counterparts in the non-relativistic limit. In the final section, we show that, for realistic physical parameters, the length scales used in the simulation are many orders of magnitude larger than length scales associated with electron and ion behavior. This demonstrates the validity of using a single-fluid model. We finally present our numerical model of the system being simulated.

In chapter 4, we discuss the linear Kelvin-Helmholtz instability for a velocity profile with a discontinuous step-function transition between two adiabatic compressible flows. The purpose of this is two-fold. First, we wish to generate growth rates which can be compared with numerical growth rates which will be generated in chapter 6 for the continuous velocity profile used in the numerical simulations. Second, we wish to demonstrate the convergence between the hydrodynamic (HD), relativistic hydrodynamic (RHD), magnetohydrodynamic

(MHD), and relativistic magnetohydrodynamic (RMHD) regimes.

In each regime, we linearize the appropriate single-fluid equations, obtaining a single-fluid dispersion relation. We then equate the perturbations to total pressure, and to normal fluid displacement, across the discontinuity, yielding a dispersion relation for predicting the KH instability. In the HD and RHD cases, we analytically solve the dispersion relation for equal and oppositely-directed flows, and find that the system is KH-unstable when the Mach number (ratio of flow speed to sound speed) has a component along the perturbation direction which is larger than $\sqrt{2}$. This corresponds to a maximum unstable flow speed (for perturbations not perpendicular to the flow), which does not exist for incompressible fluids. In the RHD case, this recovers the results of Bodo et al. (2004). We will find in chapter 6 that in the case of a continuous velocity profile, the system can be KH-unstable for much higher Mach numbers, which is in agreement with Blumen et al. (1975) and Ray (1982), among others. In chapter 12, we will recover the aforementioned single-fluid dispersion relations by a different approach, namely, linearization of the single-fluid equations in conservative form with artificial viscosity, followed by taking the inviscid limit.

We then examine the MHD regime, and show that our results agree with those of Pu and Kivelson (1983) (hereafter PK83) and Kivelson and Pu 1984 (hereafter KP84). Specifically, in addition to a maximum unstable flow speed, the magnetic field introduces a non-zero minimum unstable flow speed which is accurately predicted by the growth rate expression for a magnetized incompressible fluid. We show that in the incompressible limit, for equal densities and magnetic fields in both fluids, the system is KH-unstable when the velocity difference exceeds the Alfven speed by a factor of $\sqrt{2}$, which recovers the result of Chan-

drasekhar (1961). We then consider the MHD case where the displacement current cannot be neglected, and show how the dispersion relation is modified. We recover the result of Lovelace, Romanova, and Newman (2009) (hereafter LRN09). We finally consider a relativistic magnetized (RMHD) fluid, restricting our attention to the case where the magnetic field is aligned with the flow direction. In both the MHD and RMHD cases, the region of unstable flow speeds narrows with increasing field strength, and there is a critical field strength above which the system is stabilized. In the HD and RHD regimes, we can analytically solve the dispersion relation for predicting the KH instability. In the MHD and RMHD regimes, the dispersion relation can only be solved numerically. In all four regimes (HD, RHD, MHD, and RMHD), in the case of a step-function profile, the growth rate increases linearly with wave number, tending to infinity as the wavelength tends to zero. In chapter 6, we will consider the case of a shear variation in velocity, and generate growth rates by numerically solving a nonlinear second-order ODE, for which analytical results are not readily obtainable. From these growth rates, we will show graphically that in the case of a shear layer, there is a minimum wavelength below which the growth rate ceases to increase. This conclusion is in agreement with the results of numerous studies examining shear layers, including Chandrasekhar (1961), Ray (1982), and Miura and Pritchett (1982).

We notice that, for a step-function discontinuity, the factor of $\sqrt{2}$ emerges both as the maximum Mach number for KH instability in the HD and RHD cases, and as the minimum Alfvenic Mach number for KH instability in the incompressible limit of the MHD case. The number $\sqrt{2}$ is a common result for two-dimensional systems (i.e., systems with no variation in the third dimension), and can be thought of as the hypotenuse of a right triangle whose legs

each have a length of 1. In three-dimensional systems, the number $\sqrt{3}$ frequently emerges. For example, we will see, in chapter 4, that the maximum physically allowable relativistic adiabatic sound speed is $c/\sqrt{3}$.

In chapter 5, we extend our linear analysis to a background velocity profile that exhibits a continuous shear variation, rather than a step-function discontinuity. We assume a two-dimensional slab geometry in the $x - z$ plane, where z is the flow direction and x the shear direction. The fluid is relativistic, magnetized, and hydrodynamic (RMHD). We can therefore use the single-fluid RMHD equations given in Anile (1989). The background pressure and density are uniform. The background magnetic field is uniform and aligned with the flow direction (the z-direction). The wave vector of the perturbation is aligned with the flow direction. We linearize the single-fluid equations, first in the RHD regime, then in the RMHD regime. In each case, we derive a second-order ODE in the perturbation to the total pressure, which is in agreement with results in the literature, e.g., Miura and Pritchett (1982) and Birkinshaw (1984). To determine the eigenfrequency, and construct an eigenmode, we must numerically solve the pressure ODE. In particular, two pressure profiles, a right and left profile, are constructed by numerically integrating inward from the outer transverse boundaries. This is repeated for an array of complex eigenfrequencies, and the eigenmode is determined by the eigenfrequency for which the right and left profiles intersect smoothly at some point close to the central axis. This is known as the shooting method, and is used in Blumen (1970). We can then launch the simulation in an eigenmode of the system.

In chapter 6, we explore growth rate behavior for the background velocity profile used in the simulations, known as a "Bickley jet" profile (Bickley 1937), which has a "sech^2" shear

variation. This has the appearance of a bell, vanishing at the exterior boundaries, peaking in the center, and symmetric about the center. We find that the growth rate decreases with increasing magnetic field strength, and that the system is stabilized above a certain critical field strength (as we find in chapter 4 for a step-function discontinuity). In particular, the growth curve is a function of the relativistic Alfvenic Mach number M_A, i.e., a relativistic version of the ratio of flow speed to Alfven speed. Instability is suppressed when $M_A < 3$, i.e., when $1/M_A > 1/3$. We later demonstrate, in the numerical simulations, that the influence of the magnetic field on vortex development is accurately characterized by M_A, as defined above.

For an unmagnetized case, we plot growth rate as a function of the background flow speed amplitude. We find that growth rate increases with increasing flow speed, and abruptly drops to zero for highly relativistic flow speeds close to $0.95\,c$. Instability persists for relativistic Mach numbers well above the upper limit of 4 which is derived in chapter 4 for the case of a step-function discontinuity. This observation is consistent with the non-relativistic results of Blumen et al. (1975), Ray (1982), among others. We plot curves for several different sound speeds, and find that growth rate increases with increasing sound speed. We finally plot growth rate as a function of wave number, again for an unmagnetized case, displaying curves for several different background flow speeds. We find that for less relativistic speeds, the growth curve takes the shape of a downward-facing parabola, which is to say, there is a maximum wave number above which the growth rate ceases to increase, and there is a maximum wave number above which there is no growth, which is consistent with the non-relativistic results of Ray (1982) and Miura and Pritchett (1982). This is in contrast to the

case of a step-function velocity profile, where the growth rate increases linearly with wave number. For more relativistic flow speeds, instability at near-maximum growth extends to higher wave numbers and therefore to wavelengths which are smaller than the length scale set by the shear variation in the initial jet. This is one way in which relativistic effects tend to destabilize a system.

In chapter 7, we plot the shear profiles of perturbations corresponding to numerical eigenmodes. These are cross-sections of the initial perturbations at the start of the numerical simulation. By understanding the properties of these profiles, along with their sensitivity to such parameters as flow speed and magnetic field strength, we can better understand the evolution and parameter-sensitivity of the flow. In particular, the symmetry properties of these profiles govern the nature of the development of nonlinear vortices, and the complementarity between magnetic field and fluid behavior. Both real and imaginary parts of each perturbation have the same symmetry about the central axis, which ensures that for each quantity, the perturbation has the same symmetry at every cross-section along the flow direction.

The pressure perturbation, longitudinal (flow) velocity perturbation, and longitudinal field perturbation are each antisymmetric, while the transverse velocity and field perturbations are each symmetric, which is consistent with the sinuous mode described by Drazin and Howard (1966) for an unmagnetized incompressible fluid. The other class of modes are the varicose modes, also described by Drazin and Howard, which have the opposite symmetries. The symmetries of the pressure and velocity profiles govern the development, in the early nonlinear regime, of counter-rotating vortices. In particular, the profile symmetries

are responsible for the alternation in vortex location along the central axis. There is also a close complementarity between the flow and magnetic field behavior, which is largely because the perturbation profile of each field component has the same symmetry as the profile of the corresponding velocity component (both transverse profiles are symmetric, while both longitudinal profiles are antisymmetric).

At higher flow speeds, certain profiles show markedly larger amplitudes in their spatial variation (particularly the imaginary part of the pressure perturbation, but also to some extent the velocity perturbations). These perturbation amplitudes are largest for background flow speed amplitudes of at least $0.9\,c$. This may play a role in destabilizing the system in highly relativistic cases, in which the numerical simulation succumbs to early unphysical numerical breakdown (i.e., there is a time at which the primitive variable recovery algorithm begins to compute speeds which exceed the speed of light). In the magnetized cases, we see that for stronger background magnetic fields, the perturbation amplitudes are slightly larger in the profiles of pressure and velocity, and are markedly larger for the vortex-suppressing field, for which the larger amplitude is often accompanied by a change in shape of the profile. This may explain the bifurcations we will later observe in the dependencies of certain quantities on magnetic field strength.

In chapter 8, we discuss the numerical evolution of the system. After being launched in a numerical eigenmode, the system is evolved using the RMHD conservation-diffusion equations (Anile 1989). The numerical scheme for this is discussed in the first section. This method is fourth-order in space and time. The use of fourth-order methods gives us explicit control over the diffusion terms, which are implicitly present in second-order. The exact

single-fluid RMHD equations are marginally stable, however they become unstable when the spatial and temporal derivatives are discretized in a numerical scheme. Diffusion is therefore needed in order to restore numerical stability to the system, but also to model viscous exchanges of momentum, mass, and energy, along with a magnetic resistivity associated with electron and ion gyration in relevant astrophysical environments. At a given time step, we first invert the conserved quantities to compute the primitive variables (density, pressure, velocity, magnetic field). The magnetic field components are known immediately. However, the remaining variables cannot be solved for analytically, and must be obtained using a relaxation scheme. Such a scheme has been developed by Newman (2002), which is more accurate, efficient, and rapidly convergent than previously used schemes (Newton-Raphson, etc.). We then compute the flux quantities from the primitive variables, after which we compute the spatial derivatives of the flux quantities using the fourth-order method of lines (Schiesser 1991). We use the fourth-order Runge-Kutta method to compute the conserved quantities at the next time step. Furthermore, we use a grid consisting of 1000 distinct points in the x-direction (shear direction) and 200 points per wavelength in the z-direction (flow direction). Such a refined grid allows for greater convergence of the results than is provided by the coarser grids used in prior studies. Correspondingly, the simulation is also more temporally resolved (smaller time step), in order to satisfy the Courant-Friedrichs-Lewy (CFL) condition, which states that a given signal cannot traverse a significant fraction of a grid cell within a time step of the simulation.

In the next section of chapter 8, we calculate an approximate conductivity from the magnetic viscosity (resistivity) used in the simulations. We demonstrate that this conductivity

is on the same order of magnitude as conductivities associated with relevant astrophysical environments, including the BL Lacertae object BL Lac OJ287 (Marscher and Jorstad 2011), along with the radio jet M87 (Hines et al. 1989; Stawarz et al. 2005). This provides physical significance to the magnetic resistivity used in the simulations, apart from its role in numerical stability.

In chapter 9, we present graphs showing the time-dependence of the primitive variables (density, pressure, velocity and magnetic field components), both in the fluctuations (perturbations) of these quantities, and in their spatial averages. The initial stages of the evolution correspond to the linear regime, in which the perturbations grow exponentially, ideally at the growth rate corresponding to the eigenmode. However, the presence of artificial diffusion introduces evanescent modes, resulting in initial deviations of the growth curves from linear agreement. When the perturbations become sufficiently large compared to their background values, the growth deviates from linear behavior, corresponding to the onset of the nonlinear regime. In the early stages of the nonlinear regime, the perturbations reach a saturation level (maximum growth), after which the growth either decreases or remains at this average level. This behavior (linear regime, saturation, nonlinear regime) is qualitatively similar to the evolution of a non-relativistic MHD system, as discussed by Malagoli et al. (1996). The average density and pressure both increase over time, while the average velocity and Lorentz factor tend to decrease over time, with each of these quantities approaching an asymptotic value as the system approaches an equilibrium state. In both the perturbations and the average values, we notice nonlinear oscillations which correspond to nonlinear transverse acoustic waves propagating between the jet axis and transverse boundaries. We find that maximum

jet deceleration (and therefore maximum viscous dissipation into thermal energy) occurs for intermediate vortex-disruptive fields, due to the complexity of turbulent reorganization associated with vortex disruption.

We also plot such quantities as the RMS vorticity, RMS current density, and electromagnetic energy density, none of which exhibit the aforementioned nonlinear oscillations, but each of which exhibit a peak shortly after saturation, generally corresponding to amplification, at the vortex extremities, of field-related quantities. The peak is generally followed by a gradual decay that asymptotically approaches a small value. Collectively, these graphs show many interacting processes, among which is the transfer of energy from the bulk flow to the magnetic field in the early nonlinear regime (as the field lines are expelled by the vortices), followed by viscous dissipation into thermal energy as the field lines, and resulting filamentary features, gradually become aligned with the flow. We identify several bifurcations, i.e., energy transfer processes which are optimized for intermediate field strengths. Maximum jet deceleration, and viscous dissipation, occurs for intermediate vortex-disruptive fields. Maximum field enhancement (which maximizes electromagnetic energy and vorticity) occurs for strong vortex-disruptive fields, and is reduced for the stronger vortex-suppressing fields.

In chapter 10, we display the numerical evolution of various test cases, and discuss the behavior exhibited in the displays. In the absence of a magnetic field, the early nonlinear regime corresponds to the formation of two large counter-rotating vortices. Apart from gradual viscous dissipation, these vortices essentially persist indefinitely. Sufficiently weak fields are vortex-disruptive, which is to say, they allow vortex formation, followed by vortex inhibition through a series of stages. The first stage corresponds to field amplification at the

vortex boundaries, which results from vortex rotation, which expels plasma and magnetic field lines, leading to regions of amplified field at the vortex extremities. There is generally a remarkably close complementarity between fluid behavior and the magnetic field lines (and other quantities relating to the magnetic field, including electromagnetic pressure and current layers). In the weak-field regime, vortex twisting leads to magnetic reconnection, forming magnetic islands. This is qualitatively similar to the magnetic reconnection seen by Otto and Fairfield (2000) in their MHD studies of the Earth's magnetosphere. The next stage is vortex disruption, whereby the field exerts magnetic stresses at the vortex boundaries, leading to vortex deformation and shedding of enhanced filamentary features with alternating vorticity. The third stage corresponds to turbulent breakdown into smaller-scale structures. In the fourth and final stage, the system approaches an equilibrium state consisting of flow-aligned vortex and current filaments. The jet widens to about twice the input perturbation wavelength, and decelerates by an amount depending on field strength. These stages of vortex inhibition are qualitatively similar to those discussed in MHD literature. We examine how and to what extent these stages manifest in RMHD for a set of representative field strengths. Our simulations, and linear analysis, reveal that the extent of vortex inhibition by magnetic fields is characterized by a relativistic Alfvenic Mach number (a relativistic extension of the ratio of flow speed to Alfven speed), which we define in (6.3).

The vortex behavior, turbulent regime, filamentation, jet widening, and jet deceleration, are all in qualitative agreement with observations of numerous jets, including M87 (Bicknell et. al. 1996), NGC 5128, 3C 273 (Lobanov and Zensus 2001), 3C 120, HH 30 (Anglada 2007), and HH 34. Moreover, the field strengths we examine fall within about an order of magnitude

of one another, which is well within the range of uncertainty in estimates of field strength in astrophysical jets, obtained from synchrotron emission spectra. In particular, the radio jet M87 has a primarily flow-aligned background field, as in our simulations, with knots in which the field is believed to have transverse components (Hines et al. 1989). Stawarz et al. (2005) examined knot A, and concluded that it has an amplified field of at least 300 μG, where the surrounding jet has a field of less than 100 μG (Hines et al. 1989). If the knots exhibit vortex-like behavior, then vortex twisting of the field lines could account for the transverse components and the field amplification, which would result from field line expulsion due to vortex rotation. These magnetic field values, and associated electron and ion gyration, yield a conductivity which is consistent with the conductivity used in the simulations, as discussed at the end of chapter 8.

Stronger fields inhibit vortices more rapidly, and correspond to a more rapid transition to a filamented state, with a smaller amount of intermediate small-scale turbulence, and a narrower equilibrium jet width. A sufficiently strong field (Alfven speed exceeding about 1/6 of the flow speed amplitude) suppresses vortex formation entirely, resulting in a rapid transition to a filamented state. We also observe several bifurcations, i.e., processes which are optimized for intermediate field strengths. These are maximum viscous dissipation for intermediate vortex-disruptive fields and maximum electromagnetic energy extraction for strong fields which still allow vortex formation. Intermediate vortex-disruptive fields result in maximum flow deceleration (from $0.7\,c$ to about $0.2\,c$), and maximum viscous dissipation, resulting in a broad slow-moving equilibrium background flow. Stronger fields inhibit intermediate turbulence and viscous dissipation, and the residual mechanical energy resides in

a narrow high-speed central flow channel which is only about 1/5 of the initial jet width. The much narrower central flow channel is associated with the early vortex inhibition of strong fields, resulting in an extraction of electromagnetic energy directly from the bulk flow, and minimal diversion of mechanical energy into rotational form. The greatest extraction of electromagnetic energy occurs for the strongest fields which still allow some vortex formation. The narrow central flow overlies a slower background flow whose width, for vortex-suppressing fields, is very nearly equal to the initial jet width. For all field strengths, the flow, vorticity, and magnetic field assume equilibrium configurations that retain a memory of the initial configuration in which the system is launched (also seen in Frank et al. 1996 and Ryu et al. 2000).

In chapter 11, we examine the sensitivity of our simulation results to various input parameters. We first verify that for all field strengths, the magnetic field remains approximately divergenceless. We then verify that, for a given numerical grid, the results converge with respect to time step. We then verify that the results converge with respect to grid refinement, and find that convergence is not achieved until the grid is substantially refined (at least 750 cells in the shear direction, and at least 150 cells per wavelength in the flow direction). We note that the results are not dependent on the number of longitudinal wavelengths spanned by the simulation, and are not significantly influenced by the transverse system width. We then verify convergence of our results between the RMHD, MHD, and RHD regimes. We then study the sensitivity of our results to viscosity. In general, a higher viscosity results in slightly smaller values of quantities related to velocity and field strength, and increased thermal pressure, which is consistent with an increased amount of dissipation into thermal

energy. The overall behavior of the system has little sensitivity to viscosity, with greatest sensitivity for the moderate vortex-disruptive field $M_A = 41.4$, probably due to the complexity of the vortex disruption and turbulent breakdown. In short, we verify satisfaction of the zero-divergence condition, and find convergence of the simulation results with respect to time increment, spatial increment, system dimensions, viscosity coefficients, and between the RHD, MHD, and RMHD regimes.

For a given relativistic Alfvenic Mach number M_A, we compare simulation results for background flow speed amplitudes of $0.5\,c$ and $0.7\,c$, and find close agreement. This indicates that the quantity M_A is indeed closely correlated with the influence of a magnetic field on vortex development. We finally examine the sensitivity of the results to the wavelength of the perturbation in which the simulation is launched. For the case of a vortex-suppressing field, we find that for larger wavelengths, quantities related to magnetic field and velocity are generally larger, while the thermal pressure is generally smaller. Longer wavelengths lead to modes with larger length scales, which are therefore less correlated with the small length scales set by diffusion, thus reducing the transfer of energy into dissipative processes. We find that for a moderate vortex-disruptive field $M_A = 41.4$, equilibrium jet width and flow width both scale with the input wavelength, and that for the vortex-suppressing field $M_A = 5.1$, the width of the central flow channel, and of the central vortex filaments, both seem to scale with input wavelength, although the equilibrium jet width is independent of wavelength.

In chapter 12, we examine an anomaly associated with diffusion. The exact RMHD single-fluid equations are marginally stable. However, when discretized in a numerical scheme, they

become slightly unstable, and artificial diffusion is needed in order to restore stability to the system. An anomaly sometimes arises from the fact that the diffusion operator does not preserve the Lorentz-invariance of the single-fluid RMHD equations. In our study of the KH instability this is inconsequential, as we remain in a stationary reference frame defined by the velocity shear, and diffusion plays the role of stabilizing the system. However, for a model with a uniform background flow speed, we find that the modes introduced by diffusion decay in reference frames for which the flow is non-relativistic, but appear to grow in reference frames for which the flow is relativistic, which is of course erroneous. This mathematical exercise, however, illustrates that current mathematical models of diffusion are not well-suited to frame transformations in relativistic systems. One interesting result, nevertheless, is that when we take the diffusionless limit of our dispersion relation, we recover the relativistic acoustic that appear in Bodo et al. (2004), and the Alfven and magnetosonic modes derived in LRN09.

In chapter 13, we discuss shock-capturing schemes. Unlike our numerical scheme, these schemes do not require the use of explicit artificial viscosity to stabilize the system, and have recently been developed to successfully perform RHD simulations with Lorentz factors of up to 1000. Although shock-capturing schemes have improved stability, their accuracy is at best second-order. In recent years, these schemes have been extended to multiple dimensions, and to the RMHD regime, though with more moderate Lorentz factors generally not exceeding about 5. We suggest that one such scheme, developed by Mignone et al. (2009), could provide useful insight into our research, and useful numerical results against which to compare our results.

In chapter 14, we summarize the salient results of this study. These include the complex mechanisms by which the magnetic field inhibits KH-unstable vortices, and the manner in which these manifest for a set of representative field strengths. We also summarize our results concerning the destabilizing influence of highly relativistic flows, and our analytical demonstration that in the highly relativistic regime, diffusion essentially always introduces growing modes. We then discuss some opportunities for further exploration of this problem, including ways in which our model can potentially be extended.

Having laid out a road map for the dissertation as a whole, we now proceed to discuss some of the salient research on the KH instability, first in general, and then as it applies to astrophysical jets.

Chapter 2

Prior Research on the KH Instability and Astrophysical Jets

We now present an overview of the salient research on the KH instability (first the linear regime of evolution, then the nonlinear regime), followed by a summary of important studies of astrophysical jets, in particular as they apply to the KH instability. The Kelvin-Helmholtz (KH) instability arises when a perturbation is applied to a flow that exhibits a transverse (shear) variation in flow speed, either continuous or discontinuous. See section 1.2 for a brief discussion of the early research of the KH instability by Helmholtz (1868) in the context of vertical stratification between fluids, and by Kelvin (1871) in the context of interactions between fluids and air currents, along with related research by others. In section 2.1, dealing with the linear regime of the KH instability, we discuss studies that highlight important differences between the stability properties of a tangential (i.e., step-function) discontinuity between two flows, and a continuous shear variation used in numerical simulations. In section 2.2, we discuss studies of the nonlinear evolution of the KH instability, and compare and contrast these with our study, particularly in terms of the influence of the magnetic field and relativistic flows. In section 2.3, we present an overview of some of the salient simulations of astrophysical jets, first in the HD regime, then in the RHD and MHD regimes, and finally

in the RMHD regime. We identify specific astrophysical objects that have been described using these studies. We finally contrast these studies with our own.

2.1 Linear Regime

We now survey some of the salient research that has explored the linear regime of the KH instability. A pioneering treatment of the KH instability was performed by Chandrasekhar (1961) for incompressible fluids, both magnetized and unmagnetized. For unmagnetized fluids, he demonstrated the role of surface tension in suppressing the growth of the KH instability in a tangential discontinuity between wind and water. A tangential discontinuity (TD) does not set a length scale, and therefore the system can be unstable to any perturbation wavelength, no matter how small. For magnetized fluids, he demonstrated the analogous role of a magnetic field in suppressing the KH instability, and derived an expression for the growth rate as a function of magnetic field and velocity difference across a tangential discontinuity (TD). Consider adjacent fluids 1 and 2, where fluid j has background density, flow velocity, and magnetic field given, respectively, by ρ_j, v_{zj}, and $\mathbf{B}_j$. Let $\mathbf{k}$ denote the wave vector of the perturbation. Then the growth rate is

$$\omega_i \;=\; \sqrt{\frac{\rho_1\rho_2 k_z^2 (v_{z2}-v_{z1})^2}{(\rho_1+\rho_2)^2} - \frac{(\mathbf{B}_1\cdot\mathbf{k})^2+(\mathbf{B}_2\cdot\mathbf{k})^2}{\rho_1+\rho_2}}. \tag{2.1}$$

When we factor out the magnitude of the wave vector k, we see that the above expression sets a condition on ω_i/k, the imaginary part of phase velocity, in order for instability. This expression yields a critical velocity difference above which instability occurs. For a uniform density and uniform magnetic field aligned with the flow, this velocity difference is $\Delta v = \sqrt{2}v_A$, where v_A is the Alfven velocity. Lau and Liu (1980) demonstrated that this condition

is valid for any velocity profile in an incompressible fluid. Chandrasekhar's growth rate expression also demonstrates that when the magnetic field is everywhere parallel to the flow, it does not suppress instability to modes perpendicular to the flow. In this case, instability arises for any velocity difference. The most KH-stable system corresponds to the magnetic fields in the two regions being perpendicular, with one field being aligned with the flow, and the other perpendicular to the flow.

Numerous studies have lent further insight into instability arising from a tangential discontinuity (TD) in the velocity. Fejer (1964) and Southwood (1968) were among the first to incorporate the assumption of compressibility (i.e., finite sound speed) into a magnetized hydrodynamic (MHD) fluid with a TD. They each found separate KH-unstable modes. PK83 and KP84 made considerable advances into our understanding of the KH instability in a compressible MHD fluid with a TD, particularly as it applies to the Earth's magnetosphere, and its interaction with solar winds. They demonstrated that the assumption of compressibility has the effect of stabilizing the system for large velocity differences, so that there is a minimum and a maximum velocity difference between which instability occurs. The minimum velocity difference, and growth rate in this vicinity, are very accurately predicted by the growth rate expression for incompressible fluids derived by Chandrasekhar (1961). PK83 and KP84 also demonstrated that the unstable modes found by Southwood (1968) and Fejer (1964) are part of a larger family of unstable slow and fast magnetosonic modes. Turland and Scheuer (1976) considered a TD in a relativistic HD compressible fluid, with plane geometry, and found their models to be KH-unstable, also concluding that these results have some, albeit limited, predictive value in describing energy transfer in radio galaxies. Ferrari

et al. (1980) considered a TD in a relativistic magnetohydrodynamic (RMHD) compressible fluid, with plane geometry, in a regime in which they neglected displacement current. For weak and strong fields, they found two separate ranges of unstable Mach numbers, and for highly relativistic flows, they found that the system tends to be stable. Birkinshaw (1984) considered a TD in a relativistic HD fluid in a cylindrical geometry, finding very different results for the spatial and temporal domains, and finding poor comparison between his results and jet-like radio sources. Bodo et al. (2004) considered a TD in an RHD compressible fluid in plane geometry, and were the first to derive an analytical solution for the growth rate of the Kelvin-Helmholtz instability for flows with equal and opposite velocities. They demonstrated that the stability criterion (Mach number larger than $\sqrt{2}$) applies also to relativistic fluids, with a suitable definition of a relativistic Mach number.

The KH instability has also been studied extensively in the presence of a shear layer (i.e., transition layer) in the velocity profile. For a TD, the growth rate increases linearly with wave number, so that as the wavelength approaches zero, the growth rate goes to infinity. As Chandrasekhar (1961) demonstrated, a shear layer introduces a wavelength (i.e., wave number) above which the growth rate no longer increases, which is related to the width of the shear layer. The transition layer also typically introduces a wave number above which the system is stable, so that the dependence of growth rate on wave number has the appearance of an upside down parabola whose intercepts define the interval of unstable wave numbers. For steeper shear layers with shorter widths, this growth curve spans a larger range of wave numbers, and has a larger maximum growth rate, thereby approaching the limit of a linearly increasing growth rate for a TD, an infinitely steep profile (Blumen et al. 1975; Ray 1982).

Chandrasekhar (1961) considered several models of transition layers for which he derived either exact or approximate analytical solutions. Blumen (1970), and later Blumen et al. (1975), considered a shear layer in a 2D compressible fluid in HD. Blumen (1970) found an analytical solution for a hyperbolic tangent shear layer, with a corresponding region of KH instability. Blumen et al. (1975) showed that this region is part of a larger instability region, and further showed that a hyperbolic tangent shear layer is unstable to two-dimensional disturbances at all values of the Mach number, which is in contrast to the case of a TD, where instability is only expected for flows below a certain critical Mach number (in the frame in which the velocities are equal and opposite, $M_{\rm crit} = \sqrt{2}$ for a TD). They also showed that the growth rates generally decrease as the Mach number increases, owing to the stabilizing effects of compressibility. Ray (1982) considered a linear shear variation in a compressible fluid. As with Blumen et al. (1975), he found instability at all Mach numbers. However, unlike Blumen et al., who used a continuous profile, Ray found that the sharper linear profile has a greater destabilizing effect at smaller wavelengths.

Miura and Pritchett (1982) (hereafter MP) derived numerical eigenmodes for a sheared flow (hyperbolic tangent) in a 2D compressible MHD fluid. They numerically solved a second-order ODE in the total pressure perturbation, using the initial value method, and examined numerical growth curves. They demonstrated that growth rates decrease with a decrease in the angle between the flow and field directions, and that this decrease is larger for stronger fields. For the perpendicular case, MP showed that the sonic Mach number can simply be extended to a magnetosonic Mach number, such that the behavior is dominated by the stabilizing effects of compressibility demonstrated by Blumen (1970). MP

also discussed the effects of perturbation orientation for parallel and perpendicular magnetic field cases. When the field is perpendicular to the perturbation wave vector, only the fast magnetosonic mode is present. However, when the field has a parallel component, Alfven and slow magnetosonic modes are also unstable. MP then discussed the applicability of these results to the stability of the solar wind-magnetosphere interface. They suggested that in the presence of sheared plasma flow in the magnetosphere, the MHD KH instability can produce field-aligned currents. We observe field-aligned current filaments in the equilibrium state approached by our RMHD simulations.

Choudhury and Lovelace (1984) considered sinusoidal and linear shear profiles in a supersonic compressible HD fluid. They derived numerical eigenmodes by minimizing the ratio of forbidden to physical solutions for the pressure eigenfunction. For both profiles, they discovered that in one regime (small Mach numbers and wave numbers), there are unstable standing waves analogous to those produced for a TD, while outside this regime (larger Mach numbers and wave numbers), there are unstable traveling wave modes which are not seen in the case of a TD. For large Mach numbers, they discovered that the fastest-growing traveling waves correspond to perturbations which are nearly aligned with the flow, and that both parts of the complex eigenfrequency are increasing functions of the Mach number. Birkinshaw (1991) solved for analytical eigenmodes for a linear velocity shear in a compressible RHD fluid with a cylindrical geometry. He found a resemblance between the features of some radio jets (3C 449 and NGC 6251) and the distorted flows resulting from gradual growth of long-wavelength modes.

Having surveyed some of the important studies of the KH instability in the linear regime,

we now survey some important studies of the nonlinear evolution of the KH instability.

2.2 Nonlinear Regime

Computational advances have allowed for numerical simulation of the nonlinear evolution of the KH instability. Malagoli et al. (1996) performed a 2D MHD simulation, and identified three important stages of evolution of the KH instability. The first is linear evolution, in which perturbation amplitudes grow exponentially according to the growth rates predicted by numerical computation of the eigenmodes. The second phase corresponds to saturation of the perturbations, and the early nonlinear regime. In the second phase, the magnetic field and density interact dynamically through the formation of vortices which expel both mass and field lines, leading to regions of amplified field at the vortex extremities, and resulting in vortex stretching of the field lines. The third stage corresponds to the onset of turbulence at small length scales. As we will see later, this closely mirrors our relativistic MHD simulations. Keppens et al. (1999) obtained similar results in a 2D resistive MHD simulation with a uniform field. They also simulated anti-parallel magnetic fields, and obtained very different saturation behavior and vortex evolution. Whereas a uniform field stabilizes the linear evolution of the KH instability, a reversed field enhances the instability. This applies also in the nonlinear regime, in which the presence of magnetic field diffusion allows for magnetic reconnection events in the reversed field case, leading to tearing instabilities. As we will see later, our relativistic MHD simulations show magnetic reconnection for sufficiently weak fields. However, because our background field is uniform, significant vortex twisting must occur before the field lines reconnect.

Magnetic reconnection at the magnetospheric boundary was examined extensively by

Nykyri and Otto (2001) and Otto and Fairfield (2000). In these papers, the simulation used an MHD fluid with a 2D slab geometry and shear variations in the background profiles of density, pressure, velocity, and magnetic field. Otto and Fairfield found that the KH instability can result in mass transport of magnetosheath material, and that vortex motion can result in strongly twisted magnetic field lines, which in turn lead to magnetic reconnection and amplified current layers. These lead to detachment of filaments of high density plasma, which Otto and Fairfield concluded may explain the presence of such observed filaments in the magnetosphere. As we will see, our RMHD simulations show similar behavior with regard to reconnection, amplification, and filament fragmentation, which indicate that a similar mechanism may underlie the formation of fragmented filamentary features observed in astrophysical jets.

Baty et al. (2003) simulated the MHD KH instability in a 2D slab geometry, extending the system to span many wavelengths in the flow direction in order to observe large-scale coalescence of vortices. They examined the extent of vortex inhibition as a function of the Alfvenic Mach number (ratio of flow speed to Alfven speed). Over a wide range of magnetic fields, they observed a sequence of vortex pairing and merging events that eventually produce a vortex that spans the system. At one point, similar merging of vortices were observed in our previous relativistic simulations. However, we later discovered that in our case, these events were the result of numerical roundoff error. In our RMHD simulations, we will examine vortex inhibition as a function of a relativistic version of the Alfvenic Mach number, as we find that this parameter is closely correlated with the influence of the magnetic field on the evolution of the flow.

LRN09 studied the KH instability between the magnetopause and accretion disc of disc-accreting stars, in both the linear and nonlinear regimes, using an MHD model which includes the effects of displacement current. They determined that the most KH-unstable mode occurs when the propagation direction is azimuthal, perpendicular to the magnetic field, and derived an expression for the growth rate of the instability. They also discussed the nonlinear saturation of the KH instability, and deduced a wave number power spectrum proportional to k^{-1} of density and temperature fluctuations in the magnetopause. They also determined that when the magnetic field is perpendicular to the star's axis of rotation, it suppresses the KH instability.

We have surveyed some of the important linear and nonlinear studies of the KH instability in various physical environments. We now examine some of the salient studies of astrophysical jets, and of the KH instability as it applies to astrophysical jets.

2.3 Astrophysical Jets

As seen in much of the research mentioned above, astrophysical jets have been studied extensively in the RHD, MHD, and sometimes RMHD regimes, frequently in the context of the KH instability. Direct evidence for the existence of relativistic jet flows comes from observations of collimated parsec-scale jets moving outward from their source at speeds which seem to exceed the speed of light ("superluminal" motion), as discussed in Readhead (1993) and Zensus and Pearson (1987). AGN jets (jets arising from active galactic nuclei) are commonly thought to be formed from supermassive black holes which accrete matter onto a surrounding accretion disk (Begelman et al. 1984). The rapid rotation of the accretion disk is thought to concentrate magnetic field lines, resulting in the formation of twin collimated jets which

are perpendicular to and on opposite sides of the plane containing the disk (Blandford and Payne 1982; Rees 1971; Scheuer 1974; Blandford and Rees 1974). It is therefore reasonable to suppose that these jets are both relativistic and magnetized. These properties, along with the role of the KH instability, have been incorporated into numerous studies, as outlined below (and including some studies mentioned above).

Hardee (1979) suggested that the KH instability may play a role in the filamentary features observed in the jets 3C 449 and M87. Ray (1981) examined the twin-tail radio galaxy NGC 1265 (3C83.1B), via a linear stability analysis of a TD in an MHD compressible fluid in cylindrical coordinates, and demonstrated that its magnetic field could substantially inhibit the KH instability. Hardee (1987) applied a spatial analysis of the RHD KH instability to the study of the motions of helical components in the jet 3C 345.

Early nonlinear RHD jet simulations were performed by van Putten (1993), Duncan and Hughes (1994), and Marti and Muller (1995). Duncan and Hughes examined Lorentz factors of $\gamma = 5$ and $\gamma = 10$, finding little instability and less well-defined internal structure in the faster jet. Marti and Muller considered a jet with higher beam Mach number and Lorentz factor ($\gamma = 22.4$), and found oblique shocks and an extensive cocoon subject to KH-unstable vortices.

Lobanov and Zensus (2001) used the RHD KH instability to explain the threaded structure forming a double helix in 3C 273. They based their approach on linear perturbation analysis of the RHD KH instability in cylindrical coordinates, as developed by Hardee (1987, 2000). Lobanov (2003) also used this approach to accurately determine physical parameters of M87. Hardee (2003) and Hardee et al. (2005) successfully used the KH instability to

model the ribbons and threads in the jet in 3C 120. We will see that in the early nonlinear regime of our simulations, large vortices are connected by a dual filamentary structure which is reminiscent of the double-helix in 3C 273 and the filamentary features in 3C 120.

Until recently, relativistic magnetohydrodynamic (RMHD) nonlinear jet simulations have been computationally prohibitive. Komissarov (1999b) performed an early RMHD jet simulation after developing a numerical code which he was able to validate against standard shock-tube tests (Komissarov 1999a). He found two regimes of jet development, namely, the electromagnetically-dominated (i.e., Poynting-dominated) regime close to the central engine, often characterized by the formation of a nose cone and Mach disk, and the kinetically-dominated regime further from the central engine, often characterized by the formation of a cocoon structure around the central jet. Leismann et al. (2005) performed an RMHD simulation of an axisymmetric jet, and compared toroidal and poloidal fields, where toroidal fields encircle the jet axis and poloidal fields lie in the plane containing the jet axis. They found that, unlike poloidal fields, toroidal fields produce nose cones and are responsible for accelerating the jet along its central axis. Mignone et al. (2010) performed a three-dimensional RMHD simulation of a jet, and discovered that unlike the axisymmetric case of Leismann et al. (2005), the toroidal field does not produce a nose cone, and the jet head wanders from its central axis. Their results do not, however, exhibit good convergence upon refinement of their numerical grid. These RMHD simulations employ modest Lorentz factors generally not exceeding 5.

Our RMHD study employs a 2D slab geometry, as opposed to the cylindrical geometries used in many of the above studies. The slab geometry allows symmetric and antisymmetric

KH-unstable modes, which are analogous to the so-called pinching and helical modes, respectively, of the cylindrical geometry (referring to cylindrical Bessel functions of zeroth and first order, respectively) (Perucho et al. 2004). However, our artificial viscosity numerical scheme allows for more rapid convergence, and better absolute convergence, than the shock-capturing schemes employed in many of the above studies. Shock-capturing schemes also encounter many more difficulties when addressing the RMHD regime. Our study is more applicable to a kinetically-dominated region of a jet, which is further from the central engine. Our study also examines in detail the manner of inhibition of nonlinear KH-unstable vortices for a variety of representative field strengths, while the aforementioned recent studies are concerned with more general aspects of jet evolution. Whereas the above studies are numerical, our study is also analytical in the manner in which we demonstrate the universally destabilizing influence of artificial diffusion in the highly relativistic regime.

2.4 Conclusion

We have presented an overview of some of the salient research exploring the KH instability in the linear regime, the nonlinear regime, and as it applies to astrophysical jets. In the linear regime, these studies have highlighted important differences between a step-function velocity profile and a profile with continuous shear variation, along with important conclusions concerning the influence of a magnetic field, which we will discuss further in chapters 4 and 6. These studies have also highlighted important stages associated with nonlinear evolution, including saturation, amplification, vortex disruption, and turbulent breakdown, all of which will receive considerable elaboration and extension when we discuss our simulation results. We have also discussed studies that have revealed potentially important applications of the

KH instability to astrophysical jets, in the context of flows which are often relativistic and heavily influenced by a magnetic field. This collectively underscores the relevance of the problem we are studying. In the next chapter, we present the RMHD transport equations being used in the numerical simulations. In particular, we present three commonly-used versions, and demonstrate their mutual equivalence.

Chapter 3

RMHD Transport Equations for a Fluid with Infinite Conductivity

The literature on the subject of relativistic magnetohydrodynamics is complicated by the common usage of three formulations of the underlying single-fluid RMHD transport equations. We wish to resolve this confusion by demonstrating the mathematical equivalence of these three versions, the third of which is explicitly used in our numerical formulation and simulations. We can then conclude that each version constitutes a complete, self-consistent, closed system. These equations are discussed in Landau and Lifshitz (1959a) and Anile (1989), and used in numerous RMHD single-fluid numerical studies (Komissarov 1999a; Balsara 2001; Mignone et al. 2006, 2009, to name a few), and RMHD studies applied to astrophysical jets (Ferrari et al. 1978; Koide et al. 1996; Bucciantini and Del Zanna 2006; Zrake and MacFadyen 2012, to name a few). Consider a relativistic, magnetized, perfectly conducting, adiabatic fluid, with an isotropic pressure tensor. Let the heat function (enthalpy) be given by

$$w \;=\; \rho c^2 + \frac{\Gamma}{\Gamma - 1} P \tag{3.1}$$

where Γ is the adiabatic constant. We first present the three versions of the transport

equations for this fluid, then demonstrate their mathematical equivalence. We then demonstrate that the RMHD single-fluid equations reduce to the MHD single-fluid equations in the non-relativistic limit. Finally, we demonstrate the validity of using a single-fluid model in this study, by showing that the length scales used in our simulations are many orders of magnitude larger than the length scales associated with electron and ion behavior.

It should be noted that in this chapter, and throughout the dissertation, we use a system of units for charge density, current density, electric field, and magnetic field such that the factor of 4π does not appear in Maxwell's equations. Therefore, this factor also does not appear in expressions for energy density, Alfven speed, etc..

3.1 Three Versions of the RMHD Equations

The literature dealing with relativistic magnetohydrodynamics contains three equivalent versions of the RMHD transport equations for the fluid described above. Each version has its advantages and disadvantages. We begin with version 1, which combines the transport equations with Maxwell's equations. In section 2, version 2 is derived from version 1 by eliminating the charge and current densities and writing the transport equations in conservative form. In section 3, version 3 is obtained by converting version 2 into covariant form. Version 3, which is conservative and covariant, is the form which is explicitly used in our simulations.

We begin with version 1 of the RMHD transport equations:

$$\begin{aligned}
\frac{\partial}{\partial t}\left(\gamma\rho\right) + \boldsymbol{\nabla}\cdot\left(\gamma\rho\mathbf{v}\right) &= 0, \\
\frac{\partial}{\partial t}\left(\frac{w}{c^2}\gamma^2\mathbf{v}\right) + \boldsymbol{\nabla}\cdot\left(P\mathbf{I} + \frac{w}{c^2}\gamma^2\mathbf{v}\mathbf{v}\right) &= \rho_c\mathbf{E} + \frac{\mathbf{J}}{c}\times\mathbf{B}, \\
\frac{\partial}{\partial t}\left(w\gamma^2 - P\right) + \boldsymbol{\nabla}\cdot\left(w\gamma^2\mathbf{v}\right) &= \mathbf{J}\cdot\mathbf{E}, \\
\boldsymbol{\nabla}\times\mathbf{B} &= \frac{\mathbf{J}}{c} + \frac{1}{c}\frac{\partial\mathbf{E}}{\partial t}, \\
\boldsymbol{\nabla}\times\mathbf{E} &= -\frac{1}{c}\frac{\partial\mathbf{B}}{\partial t}, \\
\boldsymbol{\nabla}\cdot\mathbf{B} &= 0, \\
\boldsymbol{\nabla}\cdot\mathbf{E} &= \rho_c, \\
\mathbf{E} + \frac{\mathbf{v}}{c}\times\mathbf{B} &= 0.
\end{aligned} \tag{3.2}$$

This is the most familiar version, from which the other two versions are derived. However, the equations here are not in conservative form, which presents computational difficulties when attempting to numerically integrate them. The first equation, i.e., the mass continuity equation, describes mass transport, the second equation describes momentum transport (and contains the forces acting on the fluid), and the third equation describes energy transport. The fourth through seventh equations are Maxwell's equations, and the eighth equation is the assumption of infinite (i.e., perfect) conductivity. All quantities are given in the laboratory frame. This is the version we will use for deriving linear modes of the KH instability in chapters 4 and 5, as it is the easiest version to linearize. For this reason, this version is frequently used in *linear analysis* of the KH instability in RMHD studies (Ferrari et al. 1978, 1980, etc.), in the MHD approximation (LRN09; Newman and Newman 1999; PK83; KP84; Miura and Pritchett 1982; Choudhury and Lovelace 1986, etc.), and in the RHD limit (Bodo et al. 2004., etc.). This version also appears in electromagnetism textbooks such as Jackson (1975), and in plasma textbooks such as Bittencourt (2004), because this version

is the closest in form to the equations used in multiple component fluid simulations. In the case of a plasma with multiple components, one typically needs a separate mass, momentum, and energy equation for each component. Melatos and Melrose (1996) combined a two-fluid system of equations into a single-fluid system, by defining a composite mass density, charge density, etc. They obtained a system which resembled the above version, except that they did not assume infinite conductivity.

We now present version 2 of the transport equations:

$$\begin{aligned}
\frac{\partial}{\partial t}\left(\gamma\rho\right) &= -\boldsymbol{\nabla}\cdot\left(\gamma\rho\mathbf{v}\right), \\
\frac{\partial}{\partial t}\left[\frac{w}{c^2}\gamma^2\mathbf{v}+\frac{1}{c}\left(\mathbf{E}\times\mathbf{B}\right)\right] &= -\boldsymbol{\nabla}\left(P+\frac{E^2+B^2}{2}\right)-\boldsymbol{\nabla}\cdot\left(\frac{w}{c^2}\gamma^2\mathbf{vv}-\mathbf{EE}-\mathbf{BB}\right), \\
\frac{\partial}{\partial t}\left[w\gamma^2-P+\frac{1}{2}\left(E^2+B^2\right)\right] &= -\boldsymbol{\nabla}\cdot\left[w\gamma^2\mathbf{v}+\left(c\right)\left(\mathbf{E}\times\mathbf{B}\right)\right], \\
\frac{1}{c}\frac{\partial\mathbf{B}}{\partial t} &= -\boldsymbol{\nabla}\times\mathbf{E}, \\
0 &= \boldsymbol{\nabla}\cdot\mathbf{B}, \\
\mathbf{E}+\frac{\mathbf{v}}{c}\times\mathbf{B} &= 0.
\end{aligned} \tag{3.3}$$

This version is similar to the equations used in Koide et al. (1996), Nishikawa et al. (1997), among others, and also appearing in electromagnetism textbooks such as Jackson (1975). The first through third equations describe mass, momentum, and energy transport, respectively. The fourth and fifth equations are the two Maxwell's equations that don't involve charge. The sixth equation is the assumption of perfect (infinite) conductivity. The momentum and energy transport equations are written in conservative form, and for this reason, numerical simulations are more easily performed with version 2 than version 1.

We finally present version 3 of the transport equations:

$$\begin{aligned} \frac{\partial}{\partial x^\mu}\eta^\mu &= 0, \\ \frac{\partial}{\partial x^\mu}\tau^{\mu\nu} &= 0, \\ \frac{\partial}{\partial x^\mu}\mathcal{G}^{\mu\nu} &= 0, \end{aligned} \tag{3.4}$$

where

$$\begin{aligned} \eta^\mu &= \rho u^\mu, \\ \tau^{\mu\nu} &= \left(w + b^2\right) u^\mu u^\nu + \left(P + \frac{b^2}{2}\right) g^{\mu\nu} - b^\mu b^\nu, \\ \mathcal{G}^{\mu\nu} &= b^\mu u^\nu - b^\nu u^\mu, \\ u^\mu &= \gamma\left(1, \boldsymbol{\beta}\right), \\ b^0 &= \gamma\left(\boldsymbol{\beta}\cdot\mathbf{B}\right), \\ b^i &= \frac{B_i + \gamma^2\left(\boldsymbol{\beta}\cdot\mathbf{B}\right)\beta_i}{\gamma}, \\ x^\mu &= \left(ct, \mathbf{r}\right), \\ \boldsymbol{\beta} &= \frac{\mathbf{v}}{c}. \end{aligned} \tag{3.5}$$

This is the covariant version, which appears in Anile (1989), Komissarov (1999a), Balsara (2001), Leismann et al. (2005), Mignone et al. (2006, 2009), Mignone et al. (2010), Zrake and MacFadyen (2012), among others. It is also the most useful representation for numerical simulations, although unfortunately, the physical meaning of the individual terms is not as transparent as in the other two representations. Note that $g^{\mu\nu}$ is the standard metric tensor. The first of equations (3.4) describes mass transport. The time component of the second equation describes energy transport, while the spatial components of the second equation describe momentum transport. The time component of the third equation states that $\mathbf{B}$ has zero divergence, while the spatial component of the third equation is Faraday's law. $\mathbf{b}$ is the magnetic field in the rest frame of the moving fluid.

3.2 Equivalence of Versions 1 and 2

We wish to demonstrate the equivalence of versions 1 and 2 of the fluid equations in the previous section. We begin with the energy equation, which, according to version 1, can be written

$$\frac{\partial}{\partial t}\left(w\gamma^2 - P\right) \;=\; -\boldsymbol{\nabla}\cdot\left(w\gamma^2\mathbf{v}\right) + \mathbf{J}\cdot\mathbf{E}, \tag{3.6}$$

where $\mathbf{J}\cdot\mathbf{E}$ is the component of the Lorentz force corresponding to energy transport. In order to convert to conservative form, we rearrange the Lorentz force:

$$\begin{aligned}
\mathbf{J}\cdot\mathbf{E} \;&=\; \left[(c)\left(\boldsymbol{\nabla}\times\mathbf{B}\right) - \frac{\partial\mathbf{E}}{\partial t}\right]\cdot\mathbf{E} \\
&=\; \left[(c)\left(\boldsymbol{\nabla}\times\mathbf{B}\right) - \frac{\partial\mathbf{E}}{\partial t}\right]\cdot\mathbf{E} - \left[(c)\left(\boldsymbol{\nabla}\times\mathbf{E}\right) + \frac{\partial\mathbf{B}}{\partial t}\right]\cdot\mathbf{B} \\
&=\; (c)\left[(\boldsymbol{\nabla}\times\mathbf{B})\cdot\mathbf{E} - (\boldsymbol{\nabla}\times\mathbf{E})\cdot\mathbf{B}\right] - \left(\frac{\partial\mathbf{E}}{\partial t}\cdot\mathbf{E} + \frac{\partial\mathbf{B}}{\partial t}\cdot\mathbf{B}\right) \\
&=\; -(c)\boldsymbol{\nabla}\cdot(\mathbf{E}\times\mathbf{B}) - \frac{1}{2}\frac{\partial}{\partial t}\left(E^2 + B^2\right).
\end{aligned} \tag{3.7}$$

With this result, the energy equation can be written in the conservative form of version 2:

$$\frac{\partial}{\partial t}\left[w\gamma^2 - P + \frac{1}{2}\left(E^2 + B^2\right)\right] \;=\; -\boldsymbol{\nabla}\cdot\left[w\gamma^2\mathbf{v} + (c)\left(\mathbf{E}\times\mathbf{B}\right)\right]. \tag{3.8}$$

We now wish to write the momentum equation in the conservative form of version 2. The momentum equation, according to version 1, can be written

$$\frac{\partial}{\partial t}\left(\frac{w}{c^2}\gamma^2\mathbf{v}\right) \;=\; -\boldsymbol{\nabla}P - \boldsymbol{\nabla}\cdot\left(\frac{w}{c^2}\gamma^2\mathbf{v}\mathbf{v}\right) + \rho_c\mathbf{E} + \frac{\mathbf{J}}{c}\times\mathbf{B}. \tag{3.9}$$

The main expression to evaluate is

$$\frac{\mathbf{J}}{c}\times\mathbf{B} \;=\; \left(\boldsymbol{\nabla}\times\mathbf{B} - \frac{1}{c}\frac{\partial\mathbf{E}}{\partial t}\right)\times\mathbf{B}. \tag{3.10}$$

We evaluate each of the above two terms separately. The first term is

$$\begin{aligned}(\boldsymbol{\nabla}\times\mathbf{B})\times\mathbf{B} &= -\boldsymbol{\nabla}\left(\frac{1}{2}B^2\right)+(\mathbf{B}\cdot\boldsymbol{\nabla})\,\mathbf{B}\\ &= -\boldsymbol{\nabla}\left(\frac{1}{2}B^2\right)+\boldsymbol{\nabla}\cdot(\mathbf{BB})-\mathbf{B}\,(\boldsymbol{\nabla}\cdot\mathbf{B})\\ &= -\boldsymbol{\nabla}\left(\frac{1}{2}B^2\right)+\boldsymbol{\nabla}\cdot(\mathbf{BB})\,.\end{aligned}\tag{3.11}$$

The second term is

$$\begin{aligned}\left(-\frac{1}{c}\frac{\partial\mathbf{E}}{\partial t}\right)\times\mathbf{B} &= \frac{1}{c}\mathbf{B}\times\frac{\partial\mathbf{E}}{\partial t}\\ &= \frac{1}{c}\left[\frac{\partial}{\partial t}(\mathbf{B}\times\mathbf{E})-\frac{\partial\mathbf{B}}{\partial t}\times\mathbf{E}\right]\\ &= \frac{1}{c}\frac{\partial}{\partial t}(\mathbf{B}\times\mathbf{E})+(\boldsymbol{\nabla}\times\mathbf{E})\times\mathbf{E}\\ &= \frac{1}{c}\frac{\partial}{\partial t}(\mathbf{B}\times\mathbf{E})-\boldsymbol{\nabla}\left(\frac{1}{2}E^2\right)+(\mathbf{E}\cdot\boldsymbol{\nabla})\,\mathbf{E}\\ &= \frac{1}{c}\frac{\partial}{\partial t}(\mathbf{B}\times\mathbf{E})-\boldsymbol{\nabla}\left(\frac{1}{2}E^2\right)+\boldsymbol{\nabla}\cdot(\mathbf{EE})-\mathbf{E}\,(\boldsymbol{\nabla}\cdot\mathbf{E})\\ &= \frac{1}{c}\frac{\partial}{\partial t}(\mathbf{B}\times\mathbf{E})-\boldsymbol{\nabla}\left(\frac{1}{2}E^2\right)+\boldsymbol{\nabla}\cdot(\mathbf{EE})-\rho_c\mathbf{E}.\end{aligned}\tag{3.12}$$

The Lorentz force is therefore given by

$$\begin{aligned}\rho_c\mathbf{E}+\frac{\mathbf{J}}{c}\times\mathbf{B} &= \rho_c\mathbf{E}+\left(\boldsymbol{\nabla}\times\mathbf{B}-\frac{1}{c}\frac{\partial\mathbf{E}}{\partial t}\right)\times\mathbf{B}\\ &= \frac{1}{c}\frac{\partial}{\partial t}(\mathbf{B}\times\mathbf{E})-\boldsymbol{\nabla}\left(\frac{E^2+B^2}{2}\right)+\boldsymbol{\nabla}\cdot(\mathbf{EE}+\mathbf{BB})\,.\end{aligned}\tag{3.13}$$

Substituting this result into the momentum equation, we have

$$\begin{aligned}\frac{\partial}{\partial t}\left(\frac{w}{c^2}\gamma^2\mathbf{v}\right) &= -\boldsymbol{\nabla}P-\boldsymbol{\nabla}\cdot\left(\frac{w}{c^2}\gamma^2\mathbf{vv}\right)+\rho_c\mathbf{E}+\frac{\mathbf{J}}{c}\times\mathbf{B},\\ &= -\boldsymbol{\nabla}P-\boldsymbol{\nabla}\cdot\left(\frac{w}{c^2}\gamma^2\mathbf{vv}\right)+\frac{1}{c}\frac{\partial}{\partial t}(\mathbf{B}\times\mathbf{E})+\\ &\qquad\left[-\boldsymbol{\nabla}\left(\frac{E^2+B^2}{2}\right)+\boldsymbol{\nabla}\cdot(\mathbf{EE}+\mathbf{BB})\right].\end{aligned}\tag{3.14}$$

The momentum equation can now be written as

$$\frac{\partial}{\partial t}\left[\frac{w}{c^2}\gamma^2\mathbf{v}+\frac{1}{c}\left(\mathbf{E}\times\mathbf{B}\right)\right] \;=\; -\boldsymbol{\nabla}\left(P+\frac{E^2+B^2}{2}\right)-\boldsymbol{\nabla}\cdot\left(\frac{w}{c^2}\gamma^2\mathbf{vv}-\mathbf{EE}-\mathbf{BB}\right). \quad (3.15)$$

Versions 1 and 2 of the RMHD fluid equations are therefore equivalent.

3.3 Equivalence of Versions 2 and 3

We wish to demonstrate the equivalence of versions 2 and 3 of the fluid equations in section 1. To see the equivalence of the two representations, note first that

$$\begin{aligned} b^2 &= b^i b^i - b^0 b^0 \\ &= \left[\frac{B_i + \gamma^2 (\boldsymbol{\beta}\cdot\mathbf{B})\,\beta_i}{\gamma}\right]^2 - \gamma^2 (\boldsymbol{\beta}\cdot\mathbf{B})^2 \\ &= \frac{B^2}{\gamma^2} + 2(\boldsymbol{\beta}\cdot\mathbf{B})^2 - \gamma^2 (\boldsymbol{\beta}\cdot\mathbf{B})^2 \left(1-\beta^2\right) \\ &= \frac{B^2}{\gamma^2} + (\boldsymbol{\beta}\cdot\mathbf{B})^2 . \end{aligned} \tag{3.16}$$

The conserved electromagnetic energy in version 3 is given by

$$\begin{aligned} b^2 u^0 u^0 + \frac{1}{2} b^2 g^{00} - b^0 b^0 &= b^2\left(\gamma^2 - \frac{1}{2}\right) - \gamma^2 (\boldsymbol{\beta}\cdot\mathbf{B})^2 \\ &= -\frac{B^2}{2\gamma^2} - \frac{(\boldsymbol{\beta}\cdot\mathbf{B})^2}{2} + B^2 \\ &= -\frac{B^2}{2}\left(1-\beta^2\right) - \frac{(\boldsymbol{\beta}\cdot\mathbf{B})^2}{2} + B^2 \\ &= \frac{B^2\beta^2 - (\boldsymbol{\beta}\cdot\mathbf{B})^2 + B^2}{2} \\ &= \frac{E^2 + B^2}{2}, \end{aligned} \tag{3.17}$$

which is consistent with the left side of the energy equation in version 2. The electromagnetic energy flux in version 3 is given by

$$\begin{aligned} b^2 u^0 u^i + \frac{1}{2} b^2 g^{0i} - b^0 b^i &= b^2\gamma^2\beta_i - \gamma (\boldsymbol{\beta}\cdot\mathbf{B})\, b^i \\ &= \left[\frac{B^2}{\gamma^2} + (\boldsymbol{\beta}\cdot\mathbf{B})^2\right]\gamma^2\beta_i - \gamma (\boldsymbol{\beta}\cdot\mathbf{B})\,\frac{B_i + \gamma^2 (\boldsymbol{\beta}\cdot\mathbf{B})\,\beta_i}{\gamma} \\ &= B^2\beta_i - (\boldsymbol{\beta}\cdot\mathbf{B})\,\beta_i \\ &= \left[(\mathbf{B}\times\boldsymbol{\beta})\times\mathbf{B}\right]_i \\ &= (\mathbf{E}\times\mathbf{B})_i , \end{aligned} \tag{3.18}$$

which is consistent with the right side of the energy equation in version 2. The conserved electromagnetic momentum in version 3 is given by

$$\begin{aligned} b^2 u^i u^0 + \frac{1}{2} b^2 g^{i0} - b^i b^0 &= b^2 u^0 u^i + \frac{1}{2} b^2 g^{0i} - b^0 b^i \\ &= (\mathbf{E} \times \mathbf{B})_i , \end{aligned} \tag{3.19}$$

which is consistent with the left side of the momentum equation in version 2. To evaluate the electromagnetic momentum flux in version 3, we must first make the following simplification:

$$\begin{aligned} & B^2 \boldsymbol{\beta} \beta_i + \beta^2 \mathbf{B} B_i - (\boldsymbol{\beta} \cdot \mathbf{B}) (\mathbf{B} \beta_i + \boldsymbol{\beta} B_i) \\ &= \left[B^2 \boldsymbol{\beta} - \mathbf{B} (\boldsymbol{\beta} \cdot \mathbf{B}) \right] \beta_i + \left[\beta^2 \mathbf{B} - \boldsymbol{\beta} (\boldsymbol{\beta} \cdot \mathbf{B}) \right] B_i \\ &= \left[(\mathbf{B} \times \boldsymbol{\beta}) \times \mathbf{B} \right] \beta_i + \left[(\boldsymbol{\beta} \times \mathbf{B}) \times \boldsymbol{\beta} \right] B_i \\ &= (\mathbf{E} \times \mathbf{B}) \beta_i - (\mathbf{E} \times \boldsymbol{\beta}) B_i \\ &= \mathbf{E} \times (\mathbf{B} \beta_i - \boldsymbol{\beta} B_i) \\ &= \left[(B_i \beta_j - B_j \beta_i)^2 + (B_i \beta_k - B_k \beta_i)^2 \right] \hat{\mathbf{e}}_i - E_i E_j \hat{\mathbf{e}}_j - E_i E_k \hat{\mathbf{e}}_k \\ &= \left(E^2 - E_i^2 \right) \hat{\mathbf{e}}_i - E_i E_j \hat{\mathbf{e}}_j - E_i E_k \hat{\mathbf{e}}_k \\ &= E^2 \hat{\mathbf{e}}_i - \mathbf{E} E_i . \end{aligned} \tag{3.20}$$

Using this result, the electromagnetic momentum flux in version 3 is given by

$$\begin{aligned} & b^2 \mathbf{u} u^i + \frac{1}{2} b^2 \hat{\mathbf{e}}_i - \mathbf{b} b^i \\ &= \left[\frac{B^2}{\gamma^2} + (\boldsymbol{\beta} \cdot \mathbf{B})^2 \right] \left(\gamma^2 \boldsymbol{\beta} \beta_i + \frac{1}{2} \hat{\mathbf{e}}_i \right) - \left[\frac{B_i + \gamma^2 (\boldsymbol{\beta} \cdot \mathbf{B}) \beta_i}{\gamma} \right] \left[\frac{\mathbf{B} + \gamma^2 (\boldsymbol{\beta} \cdot \mathbf{B}) \boldsymbol{\beta}}{\gamma} \right] \\ &= \frac{B^2 - E^2}{2} \hat{\mathbf{e}}_i + \left[\frac{B^2}{\gamma^2} + (\boldsymbol{\beta} \cdot \mathbf{B})^2 \right] \gamma^2 \boldsymbol{\beta} \beta_i - \frac{\mathbf{B} B_i}{\gamma^2} - \gamma^2 (\boldsymbol{\beta} \cdot \mathbf{B})^2 \boldsymbol{\beta} \beta_i - \\ &\qquad (\boldsymbol{\beta} \cdot \mathbf{B}) (\mathbf{B} \beta_i + \boldsymbol{\beta} B_i) \\ &= \frac{B^2 - E^2}{2} \hat{\mathbf{e}}_i - \mathbf{B} B_i + B^2 \boldsymbol{\beta} \beta_i + \beta^2 \mathbf{B} B_i - (\boldsymbol{\beta} \cdot \mathbf{B}) (\mathbf{B} \beta_i + \boldsymbol{\beta} B_i) \\ &= \frac{B^2 - E^2}{2} \hat{\mathbf{e}}_i - \mathbf{B} B_i + E^2 \hat{\mathbf{e}}_i - \mathbf{E} E_i \\ &= \frac{E^2 + B^2}{2} \hat{\mathbf{e}}_i - \mathbf{E} E_i - \mathbf{B} B_i , \end{aligned} \tag{3.21}$$

which is consistent with the right side of the momentum equation in version 2. Combining these results, versions 2 and 3 of the RMHD fluid equations are therefore equivalent. There-

fore, all three versions are equivalent to one another. Having demonstrated the equivalence of three versions of the relativistic fluid equations, we now demonstrate that in the appropriate limits, they reduce to the non-relativistic equations.

3.4 Relativistic vs Non-relativistic Fluid Equations

The KH instability has been studied extensively in the non-relativistic regime (PK83; KP84; Ray 1982; Miura and Pritchett 1982; Malagoli et al. 1996; Ryu et al. 2000, among others). We therefore wish to demonstrate that the relativistic and non-relativistic MHD fluid equations are consistent with one another. We begin with version 1 of the relativistic MHD equations:

$$\begin{aligned}
\frac{\partial}{\partial t}\left(\gamma\rho\right) + \boldsymbol{\nabla}\cdot\left(\gamma\rho\mathbf{v}\right) &= 0, \\
\frac{\partial}{\partial t}\left(\frac{w}{c^2}\gamma^2\mathbf{v}\right) + \boldsymbol{\nabla}\cdot\left(P\mathbf{I} + \frac{w}{c^2}\gamma^2\mathbf{v}\mathbf{v}\right) &= \rho_c\mathbf{E} + \frac{\mathbf{J}}{c}\times\mathbf{B}, \\
\frac{\partial}{\partial t}\left(w\gamma^2 - P\right) + \boldsymbol{\nabla}\cdot\left(w\gamma^2\mathbf{v}\right) &= \mathbf{J}\cdot\mathbf{E}, \\
\boldsymbol{\nabla}\times\mathbf{B} &= \frac{1}{c}\mathbf{J} + \frac{1}{c}\frac{\partial\mathbf{E}}{\partial t}, \\
\boldsymbol{\nabla}\times\mathbf{E} &= -\frac{1}{c}\frac{\partial\mathbf{B}}{\partial t}, \\
\boldsymbol{\nabla}\cdot\mathbf{B} &= 0, \\
\boldsymbol{\nabla}\cdot\mathbf{E} &= \rho_c, \\
\mathbf{E} + \frac{\mathbf{v}}{c}\times\mathbf{B} &= 0,
\end{aligned} \tag{3.22}$$

where w is the heat function, given by

$$w = \rho c^2 + \frac{\Gamma P}{\Gamma - 1}. \tag{3.23}$$

The first equation describes mass continuity, the second momentum transport, and the third energy transport. The fourth through seventh equations are Maxwell's laws, and the eighth equation is the assumption of infinite conductivity. We seek to write these equations in the non-relativistic limit, i.e., the limit in which the Lorentz factor $\gamma \approx 1$. The mass transport equation in this limit becomes simply

$$\begin{aligned}
0 &= \frac{\partial}{\partial t}\left(\gamma\rho\right) + \boldsymbol{\nabla}\cdot\left(\gamma\rho\mathbf{v}\right) \\
&= \frac{\partial\rho}{\partial t} + \boldsymbol{\nabla}\cdot\left(\rho\mathbf{v}\right).
\end{aligned} \tag{3.24}$$

Before addressing the other equations, we first wish to write the relativistic heat function multiplied by γ^2 in terms of the non-relativistic heat function.

$$\begin{aligned} w\gamma^2 &= \left(\rho c^2 + \frac{\Gamma}{\Gamma-1}P\right)\gamma^2, \\ &\approx \left(\rho c^2 + \frac{\Gamma}{\Gamma-1}P\right)\gamma, \\ &\approx \gamma\rho c^2 + \frac{\Gamma}{\Gamma-1}P, \\ &= \frac{\rho c^2}{\sqrt{1-\frac{v^2}{c^2}}} + \frac{\Gamma}{\Gamma-1}P, \\ &\approx \rho c^2\left(1+\frac{1}{2}\frac{v^2}{c^2}\right) + \frac{\Gamma}{\Gamma-1}P, \\ &= \rho c^2 + \frac{1}{2}\rho v^2 + \frac{\Gamma}{\Gamma-1}P, \\ &\equiv \rho c^2 + w_0, \end{aligned} \tag{3.25}$$

where w_0 is the non-relativistic heat function, given by

$$w_0 \equiv \frac{1}{2}\rho v^2 + \frac{\Gamma}{\Gamma-1}P. \tag{3.26}$$

In the non-relativistic limit, the left side of the relativistic momentum transport equation therefore becomes

$$\begin{aligned} &\frac{\partial}{\partial t}\left(\frac{w}{c^2}\gamma^2\mathbf{v}\right) + \boldsymbol{\nabla}\cdot\left(P\mathbf{I} + \frac{w}{c^2}\gamma^2\mathbf{v}\mathbf{v}\right) \\ &\qquad\approx \frac{\partial}{\partial t}\left[\left(\rho + \frac{w_0}{c^2}\right)\mathbf{v}\right] + \boldsymbol{\nabla}\cdot\left[P\mathbf{I} + \left(\rho + \frac{w_0}{c^2}\right)\mathbf{v}\mathbf{v}\right] \\ &\qquad\approx \frac{\partial}{\partial t}\left(\rho\mathbf{v}\right) + \boldsymbol{\nabla}\cdot\left(P\mathbf{I} + \rho\mathbf{v}\mathbf{v}\right), \end{aligned} \tag{3.27}$$

and the left side of the relativistic energy transport equation becomes

$$\frac{\partial}{\partial t}\left(w\gamma^2 - P\right) + \boldsymbol{\nabla}\cdot\left(w\gamma^2\mathbf{v}\right) \tag{3.28}$$

$$\begin{aligned}
&\approx \frac{\partial}{\partial t}\left(\rho c^2 + w_0 - P\right) + \boldsymbol{\nabla}\cdot\left[\left(\rho c^2 + w_0\right)\mathbf{v}\right] \\
&= c^2\left[\frac{\partial \rho}{\partial t} + \boldsymbol{\nabla}\cdot(\rho\mathbf{v})\right] + \frac{\partial}{\partial t}(w_0 - P) + \boldsymbol{\nabla}\cdot(w_0\mathbf{v}) \\
&= \frac{\partial}{\partial t}(w_0 - P) + \boldsymbol{\nabla}\cdot(w_0\mathbf{v}) \qquad (3.29) \\
&= \frac{\partial}{\partial t}\left(\frac{1}{2}\rho v^2 + \frac{P}{\Gamma - 1}\right) + \boldsymbol{\nabla}\cdot\mathbf{v}\left(\frac{1}{2}\rho v^2 + \frac{\Gamma P}{\Gamma - 1}\right).
\end{aligned}$$

We see that equations (3.27) and (3.29) are the familiar non-relativistic expressions for momentum and energy transport. We now consider the right sides of the momentum and energy transport equations in the non-relativistic limit. First, we assume that the conductivity is infinite, and the non-relativistic plasma frequencies are low. That is, the characteristic length and time scales are large compared to the ion gyroradius and gyroperiod. In this case, we have zero displacement current, i.e.,

$$\frac{\partial \mathbf{E}}{\partial t} \approx 0. \tag{3.30}$$

so that the non-relativistic Ampere's law becomes simply

$$\begin{aligned}
\boldsymbol{\nabla}\times\mathbf{B} &= \frac{\mathbf{J}}{c} + \frac{1}{c}\frac{\partial \mathbf{E}}{\partial t} \\
&\approx \frac{\mathbf{J}}{c}.
\end{aligned} \tag{3.31}$$

We also assume electrical neutrality on a macroscopic scale, so that the macroscopic charge density ρ_c approximately vanishes. Using these results, the right side of the non-relativistic momentum equation becomes

$$\begin{aligned}
\rho_c\mathbf{E} + \frac{\mathbf{J}}{c}\times\mathbf{B} &\approx (\boldsymbol{\nabla}\times\mathbf{B})\times\mathbf{B} \\
&= -\boldsymbol{\nabla}\left(\frac{1}{2}B^2\right) + (\mathbf{B}\cdot\boldsymbol{\nabla})\,\mathbf{B}.
\end{aligned} \tag{3.32}$$

Combining these results, we now have a set of non-relativistic MHD equations for a perfectly conducting fluid:

$$\begin{aligned} \frac{\partial \rho}{\partial t} + \boldsymbol{\nabla} \cdot (\rho \mathbf{v}) &= 0 \\ \frac{\partial}{\partial t}(\rho \mathbf{v}) + \boldsymbol{\nabla} \cdot (P\mathbf{I} + \rho \mathbf{v}\mathbf{v}) &= -\boldsymbol{\nabla}\left(\frac{1}{2}B^2\right) + (\mathbf{B} \cdot \boldsymbol{\nabla})\,\mathbf{B}, \\ \frac{\partial}{\partial t}\left(\frac{1}{2}\rho v^2 + \frac{P}{\Gamma - 1}\right) + \boldsymbol{\nabla} \cdot \mathbf{v}\left(\frac{1}{2}\rho v^2 + \frac{\Gamma P}{\Gamma - 1}\right) &= \mathbf{J} \cdot \left(\mathbf{B} \times \frac{\mathbf{v}}{c}\right). \end{aligned} \tag{3.33}$$

We have recovered the familiar MHD equations used in numerous papers (e.g. Miura and Pritchett 1982; PK83; KP84). We therefore see that the RMHD single-fluid transport equations reduce to the expected non-relativistic result. Having examined the single-fluid equations, we now wish to demonstrate the validity of using them to model our system.

3.5 Validity of Single-fluid Model

To demonstrate the validity of using a single-fluid model, we wish to demonstrate that the length scales in our simulations are many orders of magnitude larger than the length scales associated with electron and ion gyroradii, and the ratio of thermal velocity to plasma frequency, which in itself defines a length scale. The velocities in our simulations are with respect to the speed of light $c = 3 \times 10^{10}$ cm/s. The lengths are with respect to the scale length r_0 which appears in the background velocity profile $v_z(x) = v_{z0}\,\mathrm{sech}^2(x/r_0)$ used in the simulations. r_0 is approximately half a jet radius, or between 0.1 and 1 parsec, which is about 10^{18} cm. In the foregoing calculations, we assume the ions are protons, as is thought to be the case in most jets. The ranges of densities and magnetic fields correspond approximately to values derived in various articles from observations of AGN jets, quasars, and BL Lacertae objects.

The length scale associated with the electron plasma frequency is approximately

$$\begin{aligned} l_{pe} &= \frac{c}{\omega_{pe}} = c\sqrt{\frac{m_e}{4\pi n_e e^2}} \\ &= (3\times 10^{10})\sqrt{\frac{9.11\times 10^{-28}}{4\pi(4.8\times 10^{-10})^2 n_e}} = \frac{5.32\times 10^{5}\ \mathrm{cm}^{-1/2}}{\sqrt{n_e}}. \end{aligned} \tag{3.34}$$

The ratio corresponding to electron plasma frequency is approximately

$$\frac{l_{pe}}{r_0} = \frac{5.32\times 10^{-13}\ \mathrm{cm}^{-3/2}}{\sqrt{n_e}}. \tag{3.35}$$

For electron densities ranging from 10^{-12} cm^{-3} to 10^{-4} cm^{-3}, we have

$$5.32\times 10^{-11} \le \frac{l_{pe}}{r_0} \le 5.32\times 10^{-7}. \tag{3.36}$$

The length scale associated with the ion plasma frequency is approximately

$$\begin{aligned} l_{pi} &= \frac{c}{\omega_{pi}} = c\sqrt{\frac{m_i}{4\pi n_i e^2}} \\ &= (3\times 10^{10})\sqrt{\frac{1.67\times 10^{-24}}{4\pi(4.8\times 10^{-10})^2 n_i}} = \frac{2.28\times 10^{7}\ \mathrm{cm}^{-1/2}}{\sqrt{n_i}}. \end{aligned} \tag{3.37}$$

The ratio corresponding to ion plasma frequency is approximately

$$\frac{l_{pi}}{r_0} = \frac{2.28\times 10^{-11}\ \mathrm{cm}^{-3/2}}{\sqrt{n_i}}. \tag{3.38}$$

For ion densities ranging from 10^{-12} cm^{-3} to 10^{-4} cm^{-3}, we have

$$2.28\times 10^{-9} \le \frac{l_{pi}}{r_0} \le 2.28\times 10^{-5}. \tag{3.39}$$

The length scale associated with the electron gyrofrequency can be approximated as

$$l_{ce} \;=\; \frac{c}{\omega_{ce}} \;=\; \frac{m_e c^2}{eB} \;=\; \frac{(9.11\times 10^{-28})(3\times 10^{10})^2}{(4.8\times 10^{-10})B} \;=\; \frac{1708 \text{ G cm}}{B}. \tag{3.40}$$

The ratio corresponding to electron gyrofrequency is approximately

$$\frac{l_{ce}}{r_0} \;=\; \frac{1.71\times 10^{-15} \text{ G}}{B}. \tag{3.41}$$

For magnetic fields ranging from 10^{-6} G to 1 G, we have

$$1.71\times 10^{-15} \;\leq\; \frac{l_{ce}}{r_0} \;\leq\; 1.71\times 10^{-9}. \tag{3.42}$$

The length scale associated with the ion gyrofrequency can be approximated as

$$l_{ci} \;=\; \frac{c}{\omega_{ci}} \;=\; \frac{m_i c^2}{eB} \;=\; \frac{(1.67\times 10^{-24})(3\times 10^{10})^2}{(4.8\times 10^{-10})B} \;=\; \frac{3.13\times 10^{6} \text{ G cm}}{B}. \tag{3.43}$$

The ratio corresponding to ion gyrofrequency is approximately

$$\frac{l_{ci}}{r_0} \;=\; \frac{3.13\times 10^{-12} \text{ G}}{B}. \tag{3.44}$$

For magnetic fields ranging from 10^{-6} G to 1 G, we have

$$3.13\times 10^{-12} \;\leq\; \frac{l_{ci}}{r_0} \;\leq\; 3.13\times 10^{-6}. \tag{3.45}$$

The run time for a typical simulation is about

$$\tau_{\text{run}} \;\approx\; 300\frac{r_0}{c} \;=\; 10^{10} \text{ s}. \tag{3.46}$$

We can now approximate the ratio of the run time to the period associated with the ion plasma frequency:

$$\omega_{pi}\tau_{\rm run} \approx \frac{4\pi n_i e^2}{m_i}(10^{10}\ {\rm s}) = \frac{4\pi n_i (4.8\times 10^{-10})^2}{1.67\times 10^{-24}}(10^{10}\ {\rm s}) = (1.73\times 10^{16}\ {\rm cm}^3)\ n_i. \quad (3.47)$$

For ion densities ranging from 10^{-12} cm^{-3} to 10^{-4} cm^{-3}, we have

$$1.73\times 10^4 \le \omega_{pi}\tau_{\rm run} \le 1.73\times 10^{12}. \quad (3.48)$$

These comparisons collectively demonstrate that for the relevant ranges of densities and magnetic field strengths, the length scales in our simulation are many orders of magnitude larger than the length scales associated with electron and ion behavior, thereby demonstrating the validity of using a single-fluid model in our simulations. Another important observation is that for typical parameters, the Larmor frequencies are on the order of 100 s^{-1}, which is about 10 orders of magnitude larger than c/r_0, corresponding to frequencies of typical KH-unstable perturbations examined in our study. It is therefore highly unlikely that these KH -unstable perturbations would generate resonance in gyrating particles. We also discuss this in section 8.2 of chapter 8.

Having justified our use of the single-fluid RMHD equations, and surveyed the salient research on the KH instability in sheared plasma flows, we are now in a position to present our model of the system.

3.6 Model Used in Simulations

The fluid in this study is relativistic, magnetized, and hydrodynamic (RMHD). The fluid is also compressible, infinitely conducting, adiabatic, and has an isotropic pressure tensor. These are the assumptions made in most single-fluid MHD and RMHD studies (Miura and

Pritchett 1982; Frank et al. 1996; Malagoli et al. 1996; Ryu et al. 2000; Otto et al. 2000, among others), including those that involve simulations of jets (Duncan and Hughes 1994; Koide et al. 1996; Mignone et al. 2010, among others). Some magnetic resistivity is included in the form of artificial viscosity. However, we will show at the end of chapter 8 that for physically realistic length scales, this resistivity corresponds to a conductivity which is at least three orders of magnitude larger than frequencies typical of the system (i.e., growth rates, eigenfrequencies, etc.). Therefore, the formal inclusion of Ohmic dissipation is not necessary, and the conductivity is effectively infinite. We also show at the end of chapter 8 that the conductivity modeled by magnetic viscosity is consistent with electron and ion gyration within relevant astrophysical environments (i.e., regions of astrophysical jets at sufficient distances from the nucleus). In assuming an isotropic pressure tensor, we assume that thermal electron and ion interactions are random, i.e., that they do not occur more strongly in a certain preferred direction with respect to the magnetic field. This assumption is valid because, as we show at the end of chapter 3, the length scales associated with electron and ion behavior are much smaller than the length scales relevant to the simulation. Viscous exchanges of momentum, mass, and energy are instead dominated by interactions of small eddies (Tennekes and Lumley 1973), whose sizes are intermediate between the molecular level and the level of structures arising from the simulation. We can therefore use the single-fluid RMHD equations given in Landau and Lifshitz (1959a) and Anile (1989).

We assume a two-dimensional slab geometry in the $x - z$ plane, where z is the flow direction and x the shear direction. The background pressure and density are uniform. The background magnetic field is uniform and aligned with the flow direction (the z-direction). The

background velocity has the "Bickley jet" shear variation (Bickley 1937):

$$v_z(x) \;=\; v_{z0}\,\mathrm{sech}^2(x/r_0). \tag{3.49}$$

This profile, also sometimes referred to as the "sech^2" velocity profile, has the appearance of a Gaussian profile, vanishing asymptotically at the exterior boundaries, peaking in the center, and symmetric about the center. The boundary conditions are periodic in the x and z-directions. However, the salient research of the Kelvin-Helmholtz instability, as it applies to compressible, magnetized, or relativistic fluids, has not thus far used a Bickley jet profile, nor has it been applied to astrophysical jets. Rather, prior studies (Miura and Pritchett 1982; Frank et al. 1996; Otto and Fairfield 2000; Malagoli et al. 1996, among others) have often used a slab geometry with a single transition layer between jet and ambient medium, typically a hyperbolic tangent profile. Our background profiles are symmetric about the central axis, which means that the numerical solutions should exhibit certain symmetry properties about the central axis which should be preserved through time. This provides a way of verifying that our solutions sustain their numerical accuracy as they evolve. Other studies have used a cylindrical geometry (Marti et al. 1995; Koide et al. 1996; Leismann et al. 2005; Hardee 2003; Hardee 2005; Mignone et al. 2010, among others), which allows for a more complete exploration of the jet cross section. However, the RMHD cylindrical studies tend to focus on more general aspects of jet evolution, rather than the specific role of the KH instability. This is largely due to the many numerical difficulties that arise when the relativistic magnetohydrodynamic (RMHD) conservation-diffusion equations are modeled in cylindrical geometry in the presence of a velocity shear. By allowing for the use of a slab geometry, the Bickley jet profile avoids many of these difficulties, while spanning

an entire cross section of the jet, and providing a built-in mechanism for validating the numerical accuracy of the solutions by ascertaining that certain symmetry properties remain intact throughout the evolution. One example is a condition of alternating symmetry of the vorticity, which we describe in section 6.1 of chapter 6.

3.7 Conclusion

We have demonstrated the mutual equivalence of three commonly-used versions of the single-fluid RMHD transport equations, and shown that in the non-relativistic limit they reduce to the MHD transport equations used in many non-relativistic studies. We have also demonstrated the validity of using a single-fluid model, by showing that for physically relevant astrophysical parameters, the length scales of the simulation are many orders of magnitude larger than the length scales associated with electron and ion behavior. Having also presented our model of the system, we can now discuss properties of linear modes of the KH instability. We begin, in the following chapter, by restricting our discussion to the case of a transverse step-function discontinuity in the flow velocity, in all four regimes (HD, RHD, MHD, RMHD). We derive important results, and show how they converge between the different regimes. We will then proceed, in chapter 5, to generalize our discussion to the case of a continuous shear variation in flow velocity.

Chapter 4

Linear Analysis of the KH Instability: Step-function Velocity Profile

In this chapter, we wish to derive and solve linear dispersion relations for predicting the Kelvin-Helmholtz (KH) instability in the case of a tangential discontinuity, i.e., step-function velocity profile. We frequently use a general reference frame in which the flow speeds are non-zero on both sides of the discontinuity, which is related by a Doppler shift (in the non-relativistic case) or Lorentz shift (in the relativistic case) to the frame in which one fluid is stationary (i.e., the ambient medium). We then wish to solve the dispersion relations, and from this our aim is two-fold. We wish to derive growth rate results which we can compare with numerical growth rates to be generated in chapter 6 for the continuous "sech^2" velocity profile used in numerical simulations. This profile has the appearance of a bell, vanishing at the exterior boundaries, peaking in the center, and symmetric about the center. Second, we wish to demonstrate convergence between the hydrodynamic (HD), relativistic hydrodynamic (RHD), magnetohydrodynamic (MHD), and relativistic magnetohydrodynamic (RMHD) regimes.

We perform our analysis first (section 4.1) for a non-relativistic unmagnetized fluid (HD),

then (section 4.2) for a relativistic unmagnetized fluid (RHD), then (sections 4.3 and 4.5) for a non-relativistic magnetized fluid (MHD), and finally (sections 4.6 and 4.7) for a relativistic magnetized fluid (RMHD). In each regime, we linearize the appropriate single-fluid equations, obtaining a single-fluid dispersion relation. We then equate the perturbations to total pressure, and to normal fluid displacement, across the discontinuity, yielding a dispersion relation for predicting the KH instability. In the HD and RHD cases, we analytically solve this dispersion relation in the frame of equal and oppositely-directed flows, and in both regimes, find that the system is stabilized when the Mach number (ratio of flow speed to sound speed) exceeds $\sqrt{2}$ (specifically, the projection of the Mach number onto the perturbation direction). For the RHD case, this recovers the stability results found in Bodo et al. (2004). In chapter 6, when we analyze numerical growth rates for a continuous sech^2 background velocity profile, we will see that for flow-aligned perturbations, instability extends to much higher Mach numbers than predicted by the step-function analysis, which is also observed in the MHD results of Miura and Pritchett (1982). However, in both models, growth rate increases with increasing sound speed. We also examine the normal wave vectors in equal and oppositely-directed flows. Here, the system of equations now assumes a complex form, and is Hermitian. The frequency is either purely imaginary (in the unstable regime) or purely real (in the stable regime). The normal wave vectors in the two flows are complex conjugates of one another in the unstable regime. We discover that in the highly relativistic KH-stable regime, one of these tends to infinity. The appearance of modes with vanishingly small wavelengths might be one manifestation of the tendency of highly relativistic flows to destabilize the system.

In the MHD case, we again derive a dispersion relation for predicting the KH instability, this time with a magnetized non-relativistic fluid. As with the HD and RHD cases, there is a maximum unstable flow speed for a given perturbation direction. However, the magnetic field also introduces a non-zero minimum unstable flow speed, which is accurately predicted by the growth rate expression for a magnetized incompressible fluid. These results are generated in section 4.3, by numerically solving the dispersion relation using Mathematica, and, in section 4.4, we recover the results of PK83 and KP84. Our successful comparison indicates that we have a valid algorithm for generating growth rates via Mathematica, which we can extend to the relativistic regime. In section 4.5, we consider a fluid with non-relativistic flow speed and sound speed, but relativistic Alfven speed, so that the effect of the displacement current must be included in deriving the dispersion relation. We recover the result of LRN09. In section 4.6, we consider the fully relativistic magnetized (RMHD) case, restricting our attention to the case where the magnetic field is aligned with the flow direction. The MHD and RMHD dispersion relations for equal and oppositely directed flows have the same aforementioned Hermiticity properties as the results for the unmagnetized cases.

In the RMHD case, the dispersion relation is solved numerically using Mathematica, and the results are presented in section 4.7. In particular, we investigate the dependence of the stability of the system on flow speed and on magnetic field strength. We find that in the case of a flow-aligned perturbation, the magnetic field eliminates the instability at all flow speeds if the magnetic pressure is greater than the thermal pressure. Also, the corresponding non-relativistic results are similar, except that the stabilization of the system occurs at a smaller value of the magnetic field. In the case of an oblique perturbation, an increasing

magnetic field can reduce but not eliminate the instability, no matter how strong it is.

We also compute RMHD growth rates for the sound speed $c_s = 0.57\,c$ used in the simulations. We find that there are critical Alfven velocities above which instability is suppressed, and that these values are consistently less than the values predicted by Chandrasekhar (1961) for an incompressible fluid. This is consistent with the numerical results to be obtained in chapter 6 for the sech^2 background velocity profile. In the case of the sech^2 velocity profile, however, we will see that the influence of the magnetic field on the growth curves is heavily dependent on the relativistic Alfvenic Mach number (a relativistic version of the ratio of the ratio of flow speed to Alfven speed). Little such dependence exists for a step-function velocity profile.

We uncover another important difference between the step-function velocity profile and continuous profiles. For a step-function profile, the growth rate increases linearly with wave number, and therefore tends to infinity as the wave number tends to infinity (wavelength tends to zero). For a continuous profile, however, we will see in chapter 6 that there is a wave number above which the growth rate ceases to increase, i.e., a wave number corresponding to maximum growth. This conclusion is in agreement with the results of numerous papers examining shear layers, including Ray (1982) and Miura and Pritchett (1982).

We first consider the HD regime, for which the flow is neither relativistic nor magnetized.

4.1 HD Kelvin-Helmholtz Instability

We begin by examining the KH instability in a non-relativistic unmagnetized HD fluid, which we assume is compressible and adiabatic. We begin by deriving a dispersion relation

for adiabatic sound waves in a uniform flow. We then use this result to derive a dispersion relation for predicting the KH instability in two adjacent flows with equal and opposite flow directions. We solve this dispersion relation analytically for the growth rate, and recover the familiar result that the system is unstable only for $M < \sqrt{2}$, where M is the Mach number in the frame of equal and oppositely-directed flow speeds.

4.1.1 Dispersion Relation for an Unmagnetized Fluid

Consider a non-relativistic unmagnetized adiabatic fluid flowing in the positive z-direction at a speed v_z. The fluid also has density ρ and pressure P. We define the non-relativistic adiabatic sound speed c_s by

$$c_s^2 \;=\; \frac{dP}{d\rho} \;=\; \frac{\Gamma \tilde{P}}{\tilde{\rho}}, \tag{4.1}$$

where Γ is the adiabatic constant. The HD fluid equations we wish to linearize are

$$\begin{aligned} \frac{\partial \rho}{\partial t} + \boldsymbol{\nabla} \cdot (\rho \mathbf{v}) \;&=\; 0, \\ \rho \left(\frac{\partial}{\partial t} + \boldsymbol{\nabla} \cdot \mathbf{v} \right) \mathbf{v} + \boldsymbol{\nabla} P \;&=\; 0, \\ c_s^2 \;=\; \frac{dP}{d\rho} \;&=\; \frac{\Gamma \tilde{P}}{\tilde{\rho}}. \end{aligned} \tag{4.2}$$

The first equation in (4.2), the mass continuity equation, describes mass transport. The second equation is Euler's equation. The third equation is the adiabatic assumption, where c_s is the sound speed. We assume each quantity has the linearized form

$$q = \tilde{q} + \delta q e^{i(\mathbf{k}\cdot\mathbf{r} - \omega t)}. \tag{4.3}$$

Substituting the linearizations into the energy equation, we obtain

$$-\omega\delta\rho + \tilde{\rho}\mathbf{k}\cdot\delta\mathbf{v} + k_z\tilde{v}_z\delta\rho \;=\; 0, \tag{4.4}$$

which can be simplified to give

$$-\bar{\omega}\delta\rho + \tilde{\rho}\mathbf{k}\cdot\delta\mathbf{v} \;=\; 0, \tag{4.5}$$

where $\bar{\omega} \equiv \omega - k_z\tilde{v}_z$. From (4.1), we have

$$c_s^2 \;=\; \frac{\delta P}{\delta\rho}, \qquad \text{or} \qquad \delta\rho \;=\; \frac{\delta P}{c_s^2}. \tag{4.6}$$

Substituting this into (4.5), we have

$$-\bar{\omega}\frac{\delta P}{c_s^2} + \tilde{\rho}\mathbf{k}\cdot\delta\mathbf{v} \;=\; 0. \tag{4.7}$$

The linearized version of Euler's equation is

$$-\tilde{\rho}\bar{\omega}\delta\mathbf{v} + \mathbf{k}\delta P \;=\; 0. \tag{4.8}$$

Solving for the velocity perturbations in the above equations, we have

$$\delta\mathbf{v} \;=\; \frac{\mathbf{k}\delta P}{\tilde{\rho}\bar{\omega}}. \tag{4.9}$$

Substituting these results into (4.7), we have

$$-\frac{\bar{\omega}}{c_s^2} + \frac{k_x^2}{\bar{\omega}} + \frac{k_y^2}{\bar{\omega}} + \frac{k_z^2}{\bar{\omega}} \;=\; 0, \tag{4.10}$$

which, upon simplification, gives

$$\bar{\omega}^2 \;=\; c_s^2(k_x^2 + k_y^2 + k_z^2). \tag{4.11}$$

This is the familiar dispersion relation for non-relativistic adiabatic sound waves. In the next subsection, we use these results to derive and solve a dispersion relation for a tangential discontinuity between two flows.

4.1.2 HD Dispersion Relation for Two Adjacent Flows

We now consider two adjacent flows of a non-relativistic unmagnetized fluid. We derive a dispersion relation for the Kelvin-Helmholtz instability between these flows, and solve the dispersion relation analytically, obtaining a growth rate in the event of instability. We then show that there is an upper-critical Mach number above which the system is unconditionally stable. All of these results are in agreement with the non-relativistic limit of Bodo et al. (2004), and the unmagnetized limit of PK83 and KP84.

The boundary between the two flows is the $y-z$ plane. Below the $y-z$ plane (denoted region 1), the unperturbed flow velocity is $\tilde{v}_z$ in the *positive* z-direction. Above the $y-z$ plane (denoted region 2), the unperturbed flow velocity is $\tilde{v}_z$ in the *negative* z-direction. That is, the two flow velocities are equal and opposite. The fluid has uniform unperturbed density $\tilde{\rho}$ and uniform unperturbed pressure $\tilde{P}$. As before, we perturb these quantities, and write them in linearized form. The linearized density, pressure, x-velocity, and y-velocity, are, for $j = 1, 2$,

$$
\begin{aligned}
\rho_j(x,y,z,t) &= \tilde{\rho} + \delta\rho \exp\left[i\left(k_{xj}x + k_y y + k_z z - \omega t\right)\right], \\
P_j(x,y,z,t) &= \tilde{P} + \delta P \exp\left[i\left(k_{xj}x + k_y y + k_z z - \omega t\right)\right], \\
v_{xj}(x,y,z,t) &= \delta v_{xj} \exp\left[i\left(k_{xj}x + k_y y + k_z z - \omega t\right)\right], \\
v_{yj}(x,y,z,t) &= \delta v_{yj} \exp\left[i\left(k_{xj}x + k_y y + k_z z - \omega t\right)\right].
\end{aligned} \tag{4.12}
$$

The linearized z-velocity is

$$
\begin{aligned}
v_{z1}(x,y,z,t) &= \tilde{v}_z + \delta v_{z1} \exp\left[i\left(k_{x1}x + k_y y + k_z z - \omega t\right)\right], \\
v_{z2}(x,y,z,t) &= -\tilde{v}_z + \delta v_{z2} \exp\left[i\left(k_{x2}x + k_y y + k_z z - \omega t\right)\right].
\end{aligned} \tag{4.13}
$$

Based on the results of subsection 4.1.1, the normal wave vector in each region is given by

$$
\begin{aligned}
k_{x1} &= \sqrt{\left(\frac{\omega - k_z\tilde{v}_z}{c_s}\right)^2 - k_z^2 - k_y^2}, \\
k_{x2} &= \sqrt{\left(\frac{\omega + k_z\tilde{v}_z}{c_s}\right)^2 - k_z^2 - k_y^2},
\end{aligned} \tag{4.14}
$$

where

$$
c_s = \sqrt{\frac{\Gamma\tilde{P}}{\tilde{\rho}}}. \tag{4.15}
$$

We insert the linearized forms of the primitive variables into the HD equations presented in subsection 4.1.1, and arrive at the following:

$$
\begin{aligned}
\delta\rho &= \frac{\delta P}{c_s^2}, \\
\delta v_{xj} &= \frac{k_{xj}\delta P}{\tilde{\rho}\left(\omega - k_z\tilde{v}_{zj}\right)}, \\
\delta v_{yj} &= \frac{k_y\delta P}{\tilde{\rho}\left(\omega - k_z\tilde{v}_{zj}\right)}, \\
\delta v_{zj} &= \frac{k_z\delta P}{\tilde{\rho}\left(\omega - k_z\tilde{v}_{zj}\right)},
\end{aligned} \tag{4.16}
$$

where $\tilde{v}_{z1} = \tilde{v}_z$ and $\tilde{v}_{z2} = -\tilde{v}_z$. To arrive at a dispersion relation, we require that the normal components of the fluid displacements be equal on both sides of the boundary (Chandrasekhar 1961):

$$\frac{\delta v_{x1}}{\omega - k_z \tilde{v}_z} = \frac{\delta v_{x2}}{\omega + k_z \tilde{v}_z}. \tag{4.17}$$

Using the expressions for δv_{x1} and δv_{x2}, this condition can be rewritten

$$\frac{k_{x1}\delta P}{\tilde{\rho}\left(\omega - k_z \tilde{v}_z\right)^2} = \frac{k_{x2}\delta P}{\tilde{\rho}\left(\omega + k_z \tilde{v}_z\right)^2}, \tag{4.18}$$

or simply

$$\frac{k_{x1}}{\left(\omega - k_z \tilde{v}_z\right)^2} = \frac{k_{x2}}{\left(\omega + k_z \tilde{v}_z\right)^2}. \tag{4.19}$$

We now insert our expressions for k_{x1} and k_{x2}, square both sides, and cross-multiply. We arrive at

$$\left[\left(\frac{\omega - k_z \tilde{v}_z}{c_s}\right)^2 - k_z^2 - k_y^2\right]\left(\omega + k_z \tilde{v}_z\right)^4 = \left[\left(\frac{\omega + k_z \tilde{v}_z}{c_s}\right)^2 - k_z^2 - k_y^2\right]\left(\omega - k_z \tilde{v}_z\right)^4. \tag{4.20}$$

This is the non-relativistic version of the dispersion relation presented in Bodo et al. (2004). To simplify the solution process, we divide both sides of this equation by $k_z^6 c_s^4$, and introduce the definitions

$$\phi \equiv \frac{\omega}{k_z c_s}, \qquad M \equiv \frac{\tilde{v}_z}{c_s}, \qquad \alpha \equiv \frac{k_y}{k_z}. \tag{4.21}$$

The dispersion relation can now be written

$$\left[(\phi - M)^2 - 1 - \alpha^2\right](\phi + M)^4 \;=\; \left[(\phi + M)^2 - 1 - \alpha^2\right](\phi - M)^4 . \tag{4.22}$$

We can now write the dispersion relation as the fifth-order polynomial

$$\phi\left[A_1\left(\frac{\phi}{M}\right)^4 + A_2\left(\frac{\phi}{M}\right)^2 + A_3\right] \;=\; 0, \tag{4.23}$$

where

$$\begin{aligned} A_1 &\equiv M^2, \\ A_2 &\equiv -2\left(M^2 + 1 + \alpha^2\right), \\ A_3 &\equiv M^2 - 2 - 2\alpha^2. \end{aligned} \tag{4.24}$$

The solutions to (4.23) are

$$\begin{aligned} \phi &= 0, \\ \frac{\phi^2}{M^2} &= \frac{-A_2 \pm \sqrt{A_2^2 - 4A_1A_3}}{2A_1}. \end{aligned} \tag{4.25}$$

We now introduce the additional definitions

$$\begin{aligned} \cos\theta &\equiv \frac{1}{\sqrt{1+\alpha^2}}, \\ \mathcal{M}_e &\equiv M\cos\theta. \end{aligned} \tag{4.26}$$

$\mathcal{M}_e$ is the projection of the Mach number onto the wave vector. The solutions can now be written in the form

$$\begin{aligned} \phi &= 0, \\ \frac{\phi^2}{M^2} &= \frac{\mathcal{M}_e^2 + 1 \pm \sqrt{(\mathcal{M}_e^2+1)^2 + \mathcal{M}_e^2\left(2 - \mathcal{M}_e^2\right)}}{\mathcal{M}_e^2}. \end{aligned} \tag{4.27}$$

These are the non-relativistic limit of the roots found in Bodo et al. (2004). Among the second set of solutions, only the one with the minus sign can potentially yield the Kelvin-Helmholtz instability, in which case the growth rate is given by

$$\omega_i \;=\; k_z \tilde{v}_z \sqrt{\frac{\sqrt{(\mathcal{M}_e^2+1)^2 + \mathcal{M}_e^2\,(2-\mathcal{M}_e^2)} - \mathcal{M}_e^2 - 1}{\mathcal{M}_e^2}}. \tag{4.28}$$

An important feature of this expression is that for fixed $\tilde{v}_z$, growth rate increases linearly with increasing k_z. This can be understood intuitively by thinking of k_z as representing the sharpness of an "edge" in the interface between the two fluids. As we make k_z larger, this edge becomes sharper and sharper, which will only make the system more unstable. This dependence of growth rate on k_z applies only to a step-function discontinuity in the velocity profile. As we will see in chapter 6, when the velocity profile undergoes a continuous shear variation, there is a critical wave number above which the growth rate no longer increases.

From expression (4.28), instability can only occur when the expression inside the radical is larger than $(\mathcal{M}_e^2+1)^2$. This can only occur if $\mathcal{M}_e^2 < 2$, i.e., if $\mathcal{M}_e < \sqrt{2}$. That is to say, the projection of the Mach number onto the perturbation wave vector must be less than $\sqrt{2}$. This is the condition for instability, and can be rewritten as follows:

$$\begin{aligned} \mathcal{M}_e &< \sqrt{2}, \\ \frac{\tilde{v}_z}{c_s}\cos\theta &< \sqrt{2}, \\ \tilde{v}_z &< \frac{c_s\sqrt{2}}{\cos^2\theta}. \end{aligned} \tag{4.29}$$

Therefore, the criterion for instability also presents an upper limit on the flow speed $\tilde{v}_z$ of each fluid, i.e., a maximum unstable flow speed. This maximum unstable flow speed

increases with an increase in the sound speed or with an increase in the angle θ between the perturbation direction and flow direction. By increasing either of these quantities, we can increase the region of instability.

We have derived a dispersion relation for a tangential discontinuity separating two fluids in HD, and analytically solved it, enabling us to predict the occurrence of the KH instability. We now perform the same analysis in the relativistic (RHD) regime.

4.2 RHD Kelvin-Helmholtz Instability

We seek to derive, interpret, and then extend the analysis of the RHD Kelvin-Helmholtz instability presented in Bodo et al. (2004). We first consider a single relativistic unmagnetized adiabatic compressible fluid. We derive a dispersion relation for this scenario, and show that it is the dispersion relation for relativistic adiabatic sound waves given in Bodo et al. (2004). We then consider two adjacent flows of the given fluid. The two flows have equal and oppositely directed relativistic flow speeds, but the same density and pressure (and therefore sound speed). This is the scenario considered in Bodo et al. (2004). We derive the dispersion relation for predicting the Kelvin-Helmholtz instability between the two flows, and analytically solve the dispersion relation for the growth rate. We then demonstrate that there is a critical relativistic Mach number, and a corresponding critical flow velocity (dependent on sound speed), above which the system is unconditionally stable. This demonstration is provided both analytically and graphically. The dispersion relation, growth rate, and stability condition, are all in agreement with Bodo et al. (2004), and references therein. These results are also consistent with the those of Bicknell et al. (1996) in the limit of a slab geometry. When, in chapter 6, we examine numerical growth rates for a continuous velocity

profile, we will find that instability exists for Mach numbers much larger than the maximum unstable value for a step-function profile.

We then examine the behavior of the normal wave vector as functions of the flow speed, both for unstable flow speeds and for stable flow speeds. We discover that for unstable flow speeds (those below the maximum unstable flow speed), the angular frequency is purely imaginary, and its curve has the shape of a downward-facing parabola, meaning that a maximum growth rate is achieved at a certain flow speed. The normal wave vector k_x has equal real parts and equal but opposite imaginary parts in the two fluids. For stable flow speeds (those above the maximum unstable flow speed), the frequency and normal wave vectors are purely real. As the flow speed approaches c, k_x in fluid 1 approaches zero, while k_x in fluid 2 grows rapidly with the Lorentz factor. Therefore, in the highly relativistic regime, we have very long wavelengths in fluid 1, and very short wavelengths in fluid 2. The emergence of vanishingly small wavelengths might be one manifestation of the tendency of highly relativistic flows to destabilize a system.

4.2.1 Dispersion Relation for a Relativistic Unmagnetized Fluid

Consider a relativistic unmagnetized adiabatic fluid flowing in the positive z-direction at a speed v_z. The fluid also has density ρ and pressure P. We define the heat function w, the internal energy ϵ, and the relativistic adiabatic sound speed c_s, by

$$\begin{aligned} w &= \rho c^2 + \frac{\Gamma}{\Gamma - 1} P, \\ \epsilon &= \rho c^2 + \frac{P}{\Gamma - 1}, \qquad (4.30) \\ c_s^2 &= c^2 \frac{dP}{d\epsilon} = c^2 \frac{\Gamma P}{w}, \qquad (4.31) \end{aligned}$$

where Γ is the adiabatic constant. The RHD fluid equations we wish to linearize are

$$\begin{aligned} \frac{\partial}{\partial t}\left(w\gamma^2 - P\right) + \boldsymbol{\nabla}\cdot\left(w\gamma^2\mathbf{v}\right) &= 0, \\ \frac{w}{c^2}\gamma^2\left(\frac{\partial}{\partial t} + \boldsymbol{\nabla}\cdot\mathbf{v}\right)\mathbf{v} + \left(\boldsymbol{\nabla} + \frac{\mathbf{v}}{c^2}\frac{\partial}{\partial t}\right)P &= 0, \\ \frac{dP}{d\epsilon} &= \frac{c_s^2}{c^2}. \end{aligned} \tag{4.32}$$

The first equation in (4.32) describes energy transport. The second equation is the relativistic version of Euler's equation, as given by Bodo et al. (2004). The third equation is the adiabatic assumption, where c_s is the sound speed. We assume each quantity has the linearized form

$$q = \tilde{q} + \delta q e^{i(\mathbf{k}\cdot\mathbf{r} - \omega t)}. \tag{4.33}$$

Let us also define a speed c_w, where

$$\frac{c_w^2}{c^2} = \frac{dP}{dw} = \frac{dP}{d\left(\epsilon + P\right)} = \frac{1}{(d\epsilon/dP) + 1} = \frac{1}{(c^2/c_s^2) + 1} = \frac{c_s^2}{c^2 + c_s^2}. \tag{4.34}$$

The linearized version of (4.34) is then

$$\frac{c_w^2}{c^2} = \frac{\delta P}{\delta w}. \tag{4.35}$$

We also note that

$$\delta\left(\gamma^2\right) = \delta\left(\frac{1}{1 - v_z^2/c^2}\right) = \frac{1}{\left(1 - v_z^2/c^2\right)^2}\left(\frac{2\tilde{v}_z\delta v_z}{c^2}\right) = \frac{2\gamma^4\tilde{v}_z\delta v_z}{c^2}. \tag{4.36}$$

Substituting the linearizations into the energy equation, we obtain

$$-\omega\left(\gamma^2\delta w - \delta P\right) - \tilde{w}\omega\frac{2\gamma^4\tilde{v}_z\delta v_z}{c^2} + \tilde{w}\gamma^2\mathbf{k}\cdot\delta\mathbf{v} + k_z\tilde{v}_z\gamma^2\delta w + \tilde{w}k_z\tilde{v}_z\frac{2\gamma^4\tilde{v}_z\delta v_z}{c^2} = 0, \tag{4.37}$$

which can be simplified to give

$$-\gamma^2\bar{\omega}\delta w + \omega\delta P + \tilde{w}\gamma^2\mathbf{k}\cdot\delta\mathbf{v} - \frac{2\gamma^4\tilde{v}_z\tilde{w}\bar{\omega}}{c^2}\delta v_z \;=\; 0, \tag{4.38}$$

where $\bar{\omega} \equiv \omega - k_z\tilde{v}_z$. From (4.35), we have $\delta w \;=\; c^2\delta P/c_w^2$. Substituting this into the above result, and dividing by c^2, we have

$$-\gamma^2\bar{\omega}\frac{\delta P}{c_w^2} + \frac{\omega}{c^2}\delta P + \frac{\tilde{w}\gamma^2}{c^2}\mathbf{k}\cdot\delta\mathbf{v} - \frac{2\gamma^4\tilde{v}_z\tilde{w}\bar{\omega}}{c^4}\delta v_z \;=\; 0. \tag{4.39}$$

The linearized version of Euler's equation is

$$\begin{aligned} -\frac{\tilde{w}}{c^2}\gamma^2\bar{\omega}\delta v_x + k_x\delta P \;&=\; 0, \\ -\frac{\tilde{w}}{c^2}\gamma^2\bar{\omega}\delta v_y + k_y\delta P \;&=\; 0, \\ -\frac{\tilde{w}}{c^2}\gamma^2\bar{\omega}\delta v_z + \left(k_z - \frac{\omega\tilde{v}_z}{c^2}\right)\delta P \;&=\; 0. \end{aligned} \tag{4.40}$$

Solving for the velocity perturbations in the above equations, we have

$$\begin{aligned} \delta v_x \;&=\; \frac{c^2 k_x\delta P}{\tilde{w}\gamma^2\bar{\omega}}, \\ \delta v_y \;&=\; \frac{c^2 k_y\delta P}{\tilde{w}\gamma^2\bar{\omega}}, \\ \delta v_z \;&=\; \frac{c^2\delta P}{\tilde{w}\gamma^2\bar{\omega}}\left(k_z - \frac{\omega\tilde{v}_z}{c^2}\right). \end{aligned} \tag{4.41}$$

Substituting these results into the linearized energy equation, we have

$$-\frac{\gamma^2\bar{\omega}}{c_w^2} + \frac{\omega}{c^2} + \frac{k_x^2}{\bar{\omega}} + \frac{k_y^2}{\bar{\omega}} + \frac{k_z}{\bar{\omega}}\left(k_z - \frac{\omega\tilde{v}_z}{c^2}\right) - \frac{2\gamma^2\tilde{v}_z}{c^2}\left(k_z - \frac{\omega\tilde{v}_z}{c^2}\right) \;=\; 0, \tag{4.42}$$

which, upon simplification, gives

$$-\frac{\gamma^2\bar{\omega}^2}{c_w^2}+\frac{\omega\bar{\omega}}{c^2}+k_x^2+k_y^2+\left(k_z-\frac{2\gamma^2\bar{\omega}\tilde{v}_z}{c^2}\right)\left(k_z-\frac{\omega\tilde{v}_z}{c^2}\right) \;=\; 0. \tag{4.43}$$

This expression can be simplified as follows:

$$\begin{aligned}
k_x^2+k_y^2 &= -\bar{\omega}\left(\frac{\omega}{c^2}-\frac{\gamma^2\bar{\omega}}{c_w^2}\right)-\left(k_z-\frac{2\gamma^2\bar{\omega}\tilde{v}_z}{c^2}\right)\left(k_z-\frac{\omega\tilde{v}_z}{c^2}\right)\\
&= -\gamma^2\bar{\omega}\left[\frac{\omega}{c^2}\left(1-\frac{\tilde{v}_z^2}{c^2}\right)-\frac{\bar{\omega}}{c_w^2}\right]-\gamma^2\left[k_z\left(1-\frac{\tilde{v}_z^2}{c^2}\right)-\frac{2\bar{\omega}\tilde{v}_z}{c^2}\right]\left(k_z-\frac{\omega\tilde{v}_z}{c^2}\right)\\
&= \gamma^2\frac{\bar{\omega}^2}{c_w^2}-\gamma^2\left(k_z-\frac{\omega\tilde{v}_z}{c^2}\right)^2-\gamma^2\frac{\omega\bar{\omega}}{c^2}\left(1-\frac{\tilde{v}_z^2}{c^2}\right)+\gamma^2\frac{\bar{\omega}\tilde{v}_z}{c^2}\left(k_z-\frac{\omega\tilde{v}_z}{c^2}\right)\\
&= \gamma^2\bar{\omega}^2\left(\frac{1}{c_w^2}-\frac{1}{c^2}\right)-\gamma^2\left(k_z-\frac{\omega\tilde{v}_z}{c^2}\right)^2.
\end{aligned} \tag{4.44}$$

Therefore, we have

$$\gamma^2\bar{\omega}^2\left(\frac{1}{c^2}-\frac{1}{c_w^2}\right)+k_x^2+k_y^2+\gamma^2\left(k_z-\frac{\omega\tilde{v}_z}{c^2}\right)^2 \;=\; 0. \tag{4.45}$$

Now, using

$$\frac{1}{c_s^2} \;=\; \frac{1}{c_w^2}-\frac{1}{c^2}, \tag{4.46}$$

we have, finally,

$$-\frac{\gamma^2\bar{\omega}^2}{c_s^2}+k_x^2+k_y^2+\gamma^2\left(k_z-\frac{\omega\tilde{v}_z}{c^2}\right)^2 \;=\; 0, \tag{4.47}$$

which is the dispersion relation given in Bodo et al. (2004). Having derived the single-fluid dispersion relation for acoustic waves in RHD, in the next subsection we use these results in deriving a dispersion relation for a tangential discontinuity between two fluids in RHD.

4.2.2 RHD Dispersion Relation for Two Adjacent Flows

We now consider the case presented in Bodo et al. (2004). Specifically, we consider two adjacent flows of a relativistic unmagnetized fluid. We derive a dispersion relation for the Kelvin-Helmholtz instability between these flows, and solve the dispersion relation analytically, obtaining a growth rate in the event of instability. We then show, both graphically and analytically, that there is an upper-critical relativistic Mach number above which the system is unconditionally stable. Corresponding to this upper-critical Mach number is a maximum unstable flow speed, which depends on sound speed. All of these results are in agreement with those presented in Bodo et al. (2004).

The boundary between the two flows is the $y-z$ plane. Below the $y-z$ plane (denoted region 1), the unperturbed flow velocity is $\tilde{v}_z$ in the *positive* z-direction. Above the $y-z$ plane (denoted region 2), the unperturbed flow velocity is $\tilde{v}_z$ in the *negative* z-direction. That is, the two flow velocities are equal and opposite. The fluid has uniform unperturbed density $\tilde{\rho}$ and uniform unperturbed pressure $\tilde{P}$. As before, we perturb these quantities, and write them in linearized form. The linearized density, pressure, x-velocity, and y-velocity, are, for $j = 1, 2$,

$$\begin{aligned}
\rho_j(x,y,z,t) &= \tilde{\rho} + \delta\rho \exp\left[i\left(k_{xj}x + k_y y + k_z z - \omega t\right)\right], \\
P_j(x,y,z,t) &= \tilde{P} + \delta P \exp\left[i\left(k_{xj}x + k_y y + k_z z - \omega t\right)\right], \\
v_{xj}(x,y,z,t) &= \delta v_{xj} \exp\left[i\left(k_{xj}x + k_y y + k_z z - \omega t\right)\right], \\
v_{yj}(x,y,z,t) &= \delta v_{yj} \exp\left[i\left(k_{xj}x + k_y y + k_z z - \omega t\right)\right].
\end{aligned} \tag{4.48}$$

The linearized z-velocity is

$$\begin{aligned}
v_{z1}(x,y,z,t) &= \tilde{v}_z + \delta v_{z1} \exp\left[i\left(k_{x1}x + k_y y + k_z z - \omega t\right)\right], \\
v_{z2}(x,y,z,t) &= -\tilde{v}_z + \delta v_{z2} \exp\left[i\left(k_{x2}x + k_y y + k_z z - \omega t\right)\right].
\end{aligned} \tag{4.49}$$

Based on the results of subsection 4.2.1, the normal wave vector in each region is given by

$$\begin{aligned} k_{x1} &= \sqrt{\gamma^2\left(\frac{\omega - k_z\tilde{v}_z}{c_s}\right)^2 - \gamma^2\left(k_z - \frac{\omega\tilde{v}_z}{c^2}\right)^2 - k_y^2}, \\ k_{x2} &= \sqrt{\gamma^2\left(\frac{\omega + k_z\tilde{v}_z}{c_s}\right)^2 - \gamma^2\left(k_z + \frac{\omega\tilde{v}_z}{c^2}\right)^2 - k_y^2}, \end{aligned} \tag{4.50}$$

where

$$\begin{aligned} \gamma &= \frac{1}{\sqrt{1 - \tilde{v}_z^2/c^2}}, \\ c_s &= c\sqrt{\frac{\Gamma\tilde{P}}{\tilde{w}}}, \\ \tilde{w} &= \tilde{\rho}c^2 + \frac{\Gamma}{\Gamma - 1}\tilde{P}. \end{aligned} \tag{4.51}$$

We insert the linearized forms of the primitive variables into the RHD equations presented in subsection 4.2.1, and arrive at the following:

$$\begin{aligned} \delta\rho &= \left[\frac{1}{c_s^2} - \frac{1}{c^2\left(\Gamma - 1\right)}\right]\delta P, \\ \delta v_{xj} &= \frac{c^2 k_{xj}\delta P}{\tilde{w}\gamma^2\left(\omega - k_z\tilde{v}_{zj}\right)}, \\ \delta v_{yj} &= \frac{c^2 k_y\delta P}{\tilde{w}\gamma^2\left(\omega - k_z\tilde{v}_{zj}\right)}, \\ \delta v_{zj} &= \frac{c^2\delta P}{\tilde{w}\gamma^2\left(\omega - k_z\tilde{v}_{zj}\right)}\left(k_z - \frac{\omega\tilde{v}_{zj}}{c^2}\right), \end{aligned} \tag{4.52}$$

where $\tilde{v}_{z1} = \tilde{v}_z$ and $\tilde{v}_{z2} = -\tilde{v}_z$. To arrive at a dispersion relation, we require that the normal components of the fluid displacements be equal on both sides of the boundary (Chandrasekhar 1961):

$$\frac{\delta v_{x1}}{\omega - k_z\tilde{v}_z} = \frac{\delta v_{x2}}{\omega + k_z\tilde{v}_z}. \tag{4.53}$$

Using the expressions for δv_{x1} and δv_{x2}, this condition can be rewritten

$$\frac{c^2 k_{x1} \delta P}{\tilde{w}\gamma^2 \left(\omega - k_z \tilde{v}_z\right)^2} = \frac{c^2 k_{x2} \delta P}{\tilde{w}\gamma^2 \left(\omega + k_z \tilde{v}_z\right)^2}, \tag{4.54}$$

or simply

$$\frac{k_{x1}}{\left(\omega - k_z \tilde{v}_z\right)^2} = \frac{k_{x2}}{\left(\omega + k_z \tilde{v}_z\right)^2}. \tag{4.55}$$

We now insert our expressions for k_{x1} and k_{x2}, square both sides, and cross-multiply. We arrive at

$$\left[\gamma^2 \left(\frac{\omega - k_z \tilde{v}_z}{c_s}\right)^2 - \gamma^2 \left(k_z - \frac{\omega \tilde{v}_z}{c^2}\right)^2 - k_y^2\right] \left(\omega + k_z \tilde{v}_z\right)^4 = \left[\gamma^2 \left(\frac{\omega + k_z \tilde{v}_z}{c_s}\right)^2 - \gamma^2 \left(k_z + \frac{\omega \tilde{v}_z}{c^2}\right)^2 - k_y^2\right] \left(\omega - k_z \tilde{v}_z\right)^4. \tag{4.56}$$

This is the same dispersion relation presented in Bodo et al. (2004). To simplify the solution process, we divide both sides of this equation by $k_z^6 c_s^4 \gamma^2$, and introduce the definitions

$$\phi \equiv \frac{\omega}{k_z c_s}, \qquad M \equiv \frac{\tilde{v}_z}{c_s}, \qquad \alpha \equiv \frac{k_y}{k_z}, \qquad \beta \equiv \frac{\tilde{v}_z}{c}. \tag{4.57}$$

The dispersion relation can now be written

$$\left[(\phi - M)^2 - \left(1 - \frac{\phi M c_s^2}{c^2}\right)^2 - \alpha^2 \left(1 - \beta^2\right)\right] (\phi + M)^4 = \left[(\phi + M)^2 - \left(1 + \frac{\phi M c_s^2}{c^2}\right)^2 - \alpha^2 \left(1 - \beta^2\right)\right] (\phi - M)^4. \tag{4.58}$$

We also define a relativistic Mach number $\mathcal{M}$ by

$$\mathcal{M} \equiv M\sqrt{\frac{1-c_s^2/c^2}{1-\beta^2}}. \tag{4.59}$$

We can now write the dispersion relation as a fifth-order polynomial in ϕ (i.e., ϕ multiplied by a fourth-order polynomial in ϕ):

$$\phi\left[A_1\left(\frac{\phi}{M}\right)^4 + A_2\left(\frac{\phi}{M}\right)^2 + A_3\right] = 0, \tag{4.60}$$

where

$$\begin{aligned} A_1 &\equiv \mathcal{M}^2 + 2\beta^2, \\ A_2 &\equiv -2\left(\mathcal{M}^2 + 1 + \alpha^2 - \beta^2\right), \\ A_3 &\equiv \mathcal{M}^2 - 2 - 2\alpha^2. \end{aligned} \tag{4.61}$$

The solutions to (4.60) are

$$\begin{aligned} \phi &= 0, \\ \frac{\phi^2}{M^2} &= \frac{-A_2 \pm \sqrt{A_2^2 - 4A_1A_3}}{2A_1}. \end{aligned} \tag{4.62}$$

We now introduce the additional definitions

$$\cos\theta \equiv \frac{1}{\sqrt{1+\alpha^2}}, \qquad \mathcal{M}_e \equiv \mathcal{M}\cos\theta, \qquad \beta_e \equiv \beta\cos\theta. \tag{4.63}$$

$\mathcal{M}_e$ and β_e are the projections of the Mach number and flow velocity, respectively, onto the wave vector. The solutions can now be written in the form

$$\begin{aligned} \phi &= 0, \\ \frac{\phi^2}{M^2} &= \frac{S_2 \pm \sqrt{S_2^2 + \left(\mathcal{M}_e^2 + 2\beta_e^2\right)\left(2 - \mathcal{M}_e^2\right)}}{\mathcal{M}_e^2 + 2\beta_e^2}. \end{aligned} \tag{4.64}$$

where

$$S_2 \equiv \mathcal{M}_e^2 + 1 - \beta_e^2. \tag{4.65}$$

These are the same roots found in Bodo et al. (2004). Among the second set of solutions, only the one with the minus sign can potentially yield the Kelvin-Helmholtz instability, in which case the growth rate is given by

$$\omega_i = k_z \tilde{v}_z \sqrt{\frac{\sqrt{S_2^2 + (\mathcal{M}_e^2 + 2\beta_e^2)(2 - \mathcal{M}_e^2)} - S_2}{\mathcal{M}_e^2 + 2\beta_e^2}}. \tag{4.66}$$

An important feature of this expression is that for fixed $\tilde{v}_z$, growth rate increases linearly with increasing k_z. This can be understood intuitively by thinking of k_z as representing the sharpness of an "edge" in the interface between the two fluids. As we make k_z larger, this edge becomes sharper and sharper, which will only make the system more unstable. This dependence of growth rate on k_z applies only to a step-function discontinuity in the velocity profile. As we will see in chapter 6, when the velocity profile undergoes a continuous shear variation, there is a critical wave number above which the growth rate no longer increases.

From expression (4.66), instability can only occur when the expression inside the radical is larger than S_2^2. This can only occur if $\mathcal{M}_e^2 < 2$, i.e., if $\mathcal{M}_e < \sqrt{2}$. That is to say, the projection of the relativistic Mach number onto the perturbation wave vector must be less than $\sqrt{2}$. This is the condition for instability, and can be rewritten as follows:

$$
\begin{aligned}
\mathcal{M}_e &< \sqrt{2}, \qquad \text{or} \\
\frac{\tilde{v}_z}{c_s}\sqrt{\frac{1-c_s^2/c^2}{1-\tilde{v}_z^2/c^2}}\cos\theta &< \sqrt{2}, \qquad \text{which yields} \\
\left(\frac{\tilde{v}_z}{c_s}\right)^2\left(1-\frac{c_s^2}{c^2}\right)\cos^2\theta &< 2\left(1-\frac{\tilde{v}_z^2}{c^2}\right), \qquad \text{which yields} \\
\tilde{v}_z^2\left(c^2-c_s^2\right)\cos^2\theta &< 2\,c_s^2\left(c^2-\tilde{v}_z^2\right), \qquad \text{which yields} \\
\tilde{v}_z &< c_s c\sqrt{\frac{2}{(c^2-c_s^2)\cos^2\theta+2\,c_s^2}}.
\end{aligned} \tag{4.67}
$$

Therefore, the criterion for instability also presents an upper limit on the flow speed $\tilde{v}_z$ of each fluid, i.e., a maximum unstable flow speed. This maximum unstable flow speed increases with an increase in the sound speed or with an increase in the angle θ between the perturbation direction and flow direction. By increasing either of these quantities, we can increase the region of instability. The maximum allowable sound speed is $c_s = c/\sqrt{3}$. Therefore, for a polarization angle θ, the maximum unstable flow speed is obtained by substituting $c_s = c/\sqrt{3}$ into (4.67):

$$
\tilde{v}_{z,\max} = \frac{c}{\sqrt{3}}\sqrt{\frac{2}{(1-1/3)\cos^2\theta+2/3}} = \frac{c}{\sqrt{3}}\sqrt{\frac{3}{\cos^2\theta+1}} = \frac{c}{\sqrt{\cos^2\theta+1}}. \tag{4.68}
$$

The corresponding maximum unstable Lorentz factor is

$$
\gamma_{\max} = \frac{1}{\sqrt{1-\tilde{v}_{z,\max}^2/c^2}} = \frac{\sqrt{\cos^2\theta+1}}{\cos\theta}. \tag{4.69}
$$

For $\theta = 0$, i.e., the perturbation polarized along the flow direction, the maximum unstable flow speed and Lorentz factor are $c/\sqrt{2}$ and $\sqrt{2}$, respectively. As the perturbation direction is rotated away from the flow direction, this critical flow speed increases, reaching c in the limit of a perturbation perpendicular to the flow direction. This means that in order to have

instability at highly relativistic flow velocities, the perturbation direction must be oblique to the flow direction, i.e., must have a component in the y-direction. When all other variables are fixed, the growth rate vs $\tilde{v}_z$ is a concave downward parabola with intercepts at $\tilde{v}_z = 0$ and at the maximum unstable $\tilde{v}_z$ given by (4.67). It is also important to note that the ω that solves the dispersion relation is either purely real, corresponding to stability, or purely imaginary, corresponding to instability. ω never has both real and imaginary components. This is a consequence of the Hermiticity of the system.

We seek to graphically illustrate the validity of our stability results. To do this, We plot below the growth rate distribution as a function of sound speed (horizontal axis) and flow speed (vertical axis). The component of the wave vector tangential to the interface is fixed at

$$\begin{aligned} k_{yz} &= \sqrt{k_y^2 + k_z^2} = 5\, c^{-1}(1\text{ s})^{-1}, \\ k_z &= k_{yz}\cos\theta. \end{aligned} \tag{4.70}$$

We display growth rate plots first for polarization vector parallel to flow direction ($\theta = 0$, figures 4.1), and then for an oblique polarization of $\theta = 45$ degrees (figures 4.2). In both cases, we see that the instability region is *bounded by an upper curve that corresponds precisely to equation* (4.67) *for the upper-critical flow velocity*. For each polarization angle, there are three graphs, arranged as follows. The top left graph is a gray-scale distribution, where white indicates maximum growth rate, and black indicates minimum growth rate. The top right graph is the corresponding contour plot, where each contour corresponds to a specific value of the growth rate. That is to say, everywhere along a given contour, the growth rate is a constant value. The bottom graph displays the critical velocity curve predicted by

equation (4.67) for the given polarization angle, which agrees with the upper boundary of the instability regions in the growth rate distributions. These stability results are in agreement with those of Bodo et al. (2004).

We now seek to recover the plot given in Bodo et al. (2004). We plot the growth rate "phase velocity" ϕ as a function of β_e (horizontal axis) and $\mathcal{M}_e$ (vertical axis). The left plot is a gray-scale distribution, for which the minimum growth rate is black, and the maximum growth rate is white. The right plot is a contour plot, where each curve represents a constant value of ϕ. For these plots, the polarization angle $\theta = 0$, which means that the polarization vector is polarized parallel to the flow. We therefore have

$$\phi \;=\; M\sqrt{\frac{\sqrt{S_2^2 + (\mathcal{M}^2 + 2\beta^2)\,(2 - \mathcal{M}^2)} - S_2}{\mathcal{M}^2 + 2\beta^2}}, \tag{4.71}$$

where

$$\begin{aligned} M &= \sqrt{\mathcal{M}^2\,(1-\beta^2) + \beta^2}, \\ S_2 &= \mathcal{M}^2 + 1 - \beta^2, \\ \mathcal{M}^2 &= \mathcal{M}_e^2, \\ \beta^2 &= \beta_e^2. \end{aligned} \tag{4.72}$$

The plots shown in figure 4.3 *agree with the contour plot presented in Bodo et al. (2004).* We are only interested in the growth rate within the region where the adiabatic sound speed does not exceed its physically allowable maximum value of $c/\sqrt{3}$. The plots in figure 4.3 are therefore restricted to the physically allowable region $c_s \leq c/\sqrt{3}$.

The physically allowable region agrees with the one presented in the contour plot in Bodo et al. (2004). The above graphs confirm that we indeed have unconditional stability (zero growth) for $\mathcal{M}_e > \sqrt{2}$, which is also a conclusion in Bodo et al. (2004).

We now wish to compute growth rates of the step-function profile that can be compared with the numerical growth rates used in the simulations. We use a flow-aligned perturbation for which $k_z = 0.8$ inverse light seconds, and $k_y = 0$, as in the simulations (although

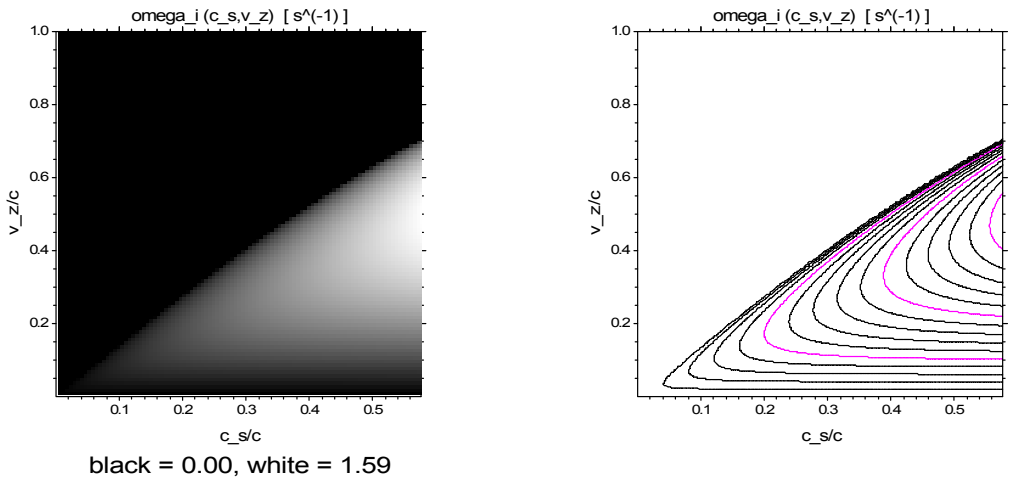

$$\omega_i(c_s, \tilde{v}_z), \qquad \theta = 0$$

Critical flow velocity at $\theta = 0$

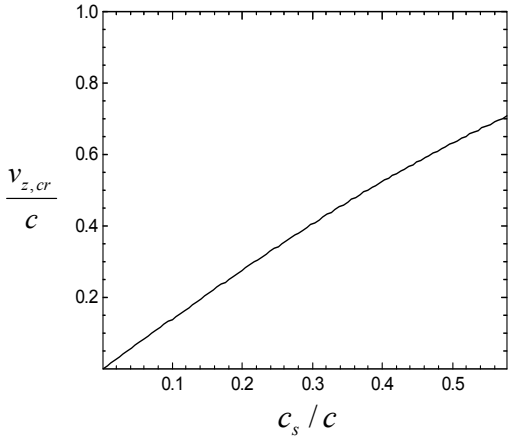

$$\frac{v_{z,cr}}{c} = c_s \sqrt{\frac{2}{\left(c^2 - c_s^2\right)\cos^2(0) + 2c_s^2}}$$

Figure 4.1: Critical flow speed vs sound speed at $\theta = 0$ (RHD)

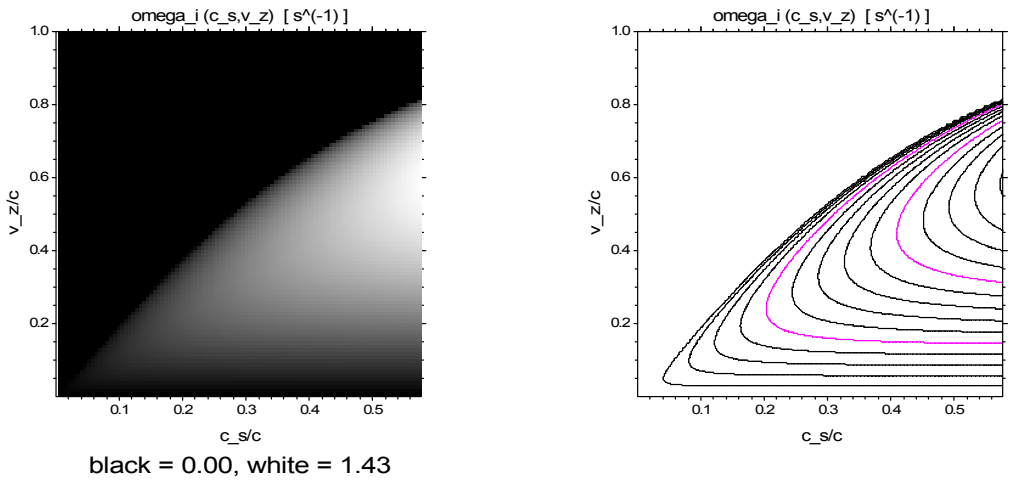

$$\omega_i(c_s, \tilde{v}_z), \qquad \theta = \pi/4$$

Critical flow velocity at $\theta = \frac{\pi}{4}$

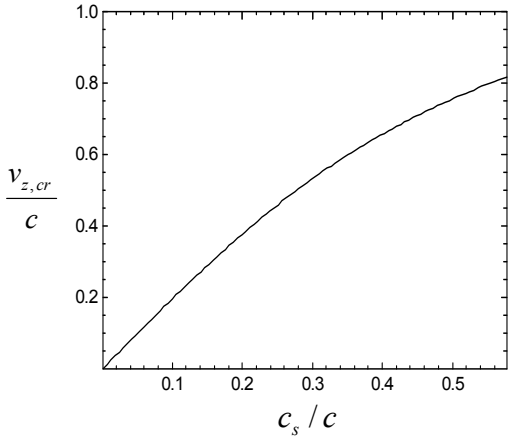

$$\frac{v_{z,cr}}{c} = c_s \sqrt{\frac{2}{\left(c^2 - c_s^2\right)\cos^2\left(\frac{\pi}{4}\right) + 2c_s^2}}$$

Figure 4.2: Critical flow speed vs sound speed at $\theta = \pi/4$ (RHD)

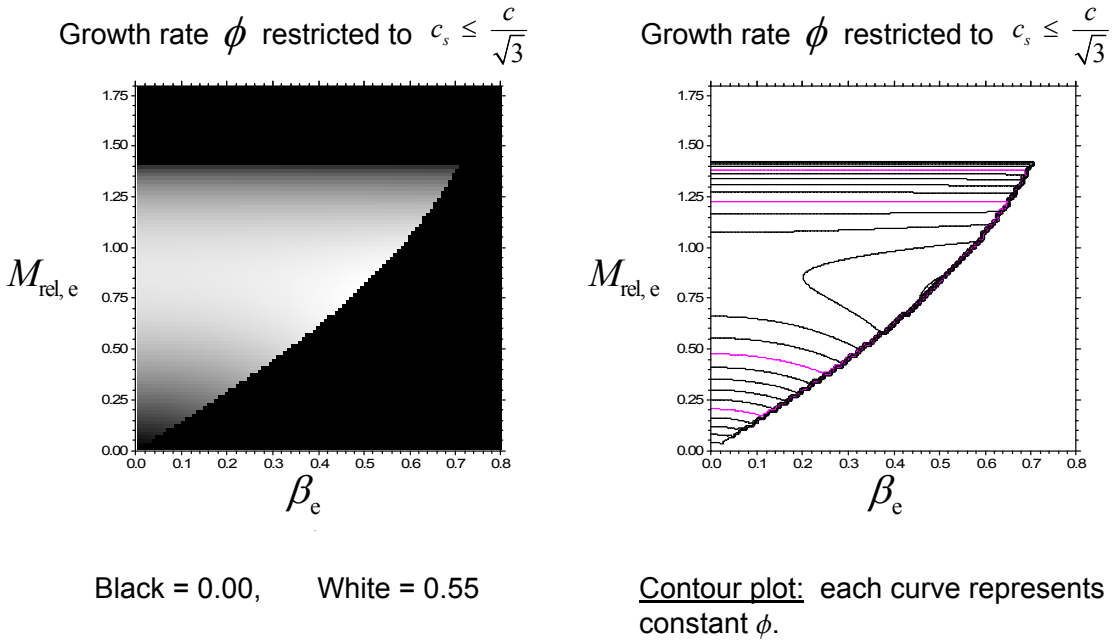

Figure 4.3: Growth rate vs flow speed and Mach number (RHD)

the simulations define lengths not in terms of light seconds but in terms of a length scale introduced by the shear variation in velocity). If v_{z0} and $-v_{z0}$ are the equal and opposite flow velocities in the stationary frame, then the relative flow velocity u_{z0} (in the co-moving frame of one fluid) is given by

$$u_{z0} = \frac{2v_{z0}}{1 + v_{z0}^2/c^2}. \tag{4.73}$$

The relativistic Mach numbers in the stationary frame (M_s) and the co-moving frame ($M_{s,\text{rel}}$) are given by

$$M_s = \frac{v_{z0}\gamma}{c_s\gamma_s} = \frac{v_{z0}}{c_s}\sqrt{\frac{1 - c_s^2/c^2}{1 - v_{z0}^2/c^2}}, \tag{4.74}$$

$$M_{s,\text{rel}} = \frac{u_{z0}\gamma_u}{c_s\gamma_s} = \frac{u_{z0}}{c_s}\sqrt{\frac{1 - c_s^2/c^2}{1 - u_{z0}^2/c^2}}, \tag{4.75}$$

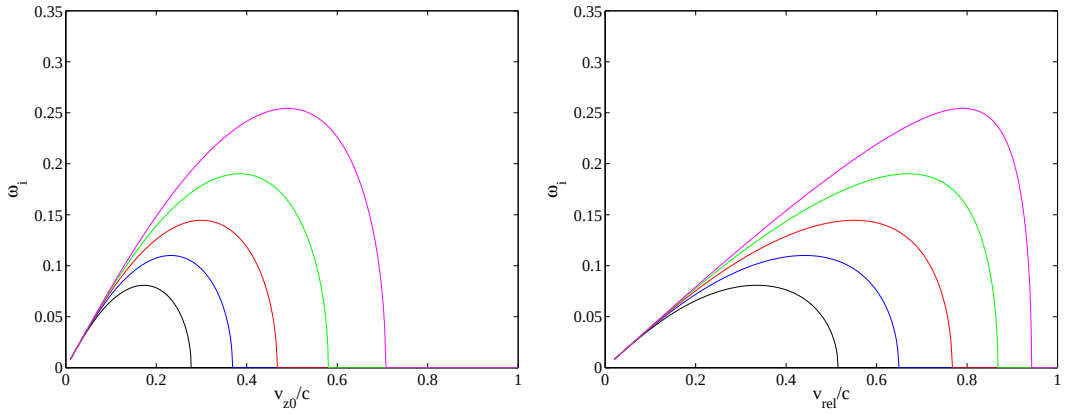

Figure 4.4: Growth rate vs flow speed (RHD)
$c_s/c = 0.2$ (black), 0.27 (blue), 0.35 (red), 0.45 (green), $1/\sqrt{3}$ (magenta)

where γ_u is the Lorentz factor corresponding to u_{z0}. For purposes of future comparison with numerical growth curves, the relative flow velocity and Mach number, in the co-moving frame of one fluid, are more applicable. Figures 4.4 display the growth rate as a function of flow velocity, where each curve corresponds to a different sound speed. The figure on the left is in the frame of equal and opposite flow speeds (the stationary frame), while the figure on the right is in the co-moving frame of one fluid.

Figures 4.5 display the growth rate as a function of relativistic Mach number in the stationary frame (left graph), and the co-moving frame (right graph).

We see that, for flow-aligned perturbations, and independent of sound speed, the maximum unstable Mach number is $\sqrt{2}$ in the frame of equal and opposite flows. In the co-moving frame of one fluid, the maximum unstable Mach number is 4 for the maximum sound speed $(c/\sqrt{3})$, and decreases as sound speed decreases. This is in agreement with Bodo et al. (2004). Also, as sound speed increases, growth rate increases, which is the trend we will observe in the numerical growth rates for a continuous velocity profile. The growth rates associated with the continuous profile will be consistently less than those observed with

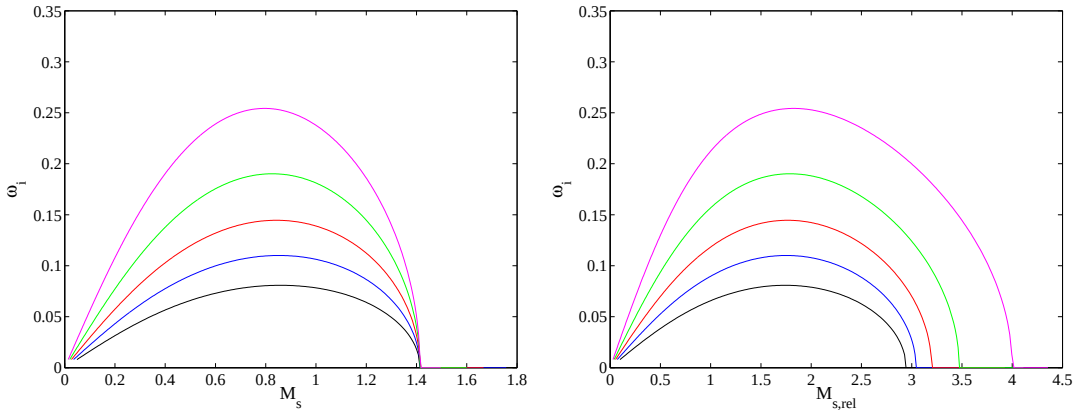

Figure 4.5: Growth rate vs Mach number (RHD)
$c_s/c = 0.2$ (black), 0.27 (blue), 0.35 (red), 0.45 (green), $1/\sqrt{3}$ (magenta)

the step-function discontinuity, which is indicative of the stabilizing influence of a smooth transition in velocity. However, in the case of the continuous (sech^2) profile, there is no maximum unstable Mach number, and we find instability at Mach numbers much larger than 4 (see chapter 6). Furthermore, as sound speed decreases, the maximum unstable Mach number becomes larger, not smaller, in the case of a sech^2 profile. Again, this analysis pertains specifically to flow-aligned perturbations. For oblique perturbations, the critical value of $\sqrt{2}$ pertains to the projection of the Mach number onto the perturbation direction.

We now wish to compare the normal wave vectors in the two fluids in the unstable regime. The cases of growth correspond to positive imaginary ω, i.e., $\omega = i\omega_i$, where $\omega_i > 0$. For such a case, the squared normal wave vector in fluid 1 is

$$\begin{aligned} k_{x1}^2 &= \gamma^2 \left[\frac{\left(i\omega_i - k_z \tilde{v}_z\right)^2}{c_s^2} - \left(k_z - \frac{i\omega_i \tilde{v}_z}{c^2} \right)^2 \right] - k_y^2 \\ &= \left(k_{x1}^2\right)_r + i \left(k_{x1}^2\right)_i , \end{aligned} \tag{4.76}$$

where

$$
\begin{aligned}
\left(k_{x1}^2\right)_r &= \gamma^2\left[\frac{k_z^2\tilde{v}_z^2-\omega_i^2}{c_s^2}-k_z^2+\left(\frac{\omega_i\tilde{v}_z}{c^2}\right)^2\right]-k_y^2 \\
&= \gamma^2\left[k_z^2\left(\frac{\tilde{v}_z^2}{c_s^2}-1\right)-\omega_i^2\left(\frac{1}{c_s^2}-\frac{\tilde{v}_z^2}{c^4}\right)\right]-k_y^2, \qquad (4.77)\\
\left(k_{x1}^2\right)_i &= -2\gamma^2\omega_i k_z\tilde{v}_z\left(\frac{1}{c_s^2}-\frac{1}{c^2}\right).
\end{aligned}
$$

The squared normal wave vector in fluid 2 is

$$
\begin{aligned}
k_{x2}^2 &= \gamma^2\left[\frac{\left(i\omega_i+k_z\tilde{v}_z\right)^2}{c_s^2}-\left(k_z+\frac{i\omega_i\tilde{v}_z}{c^2}\right)^2\right]-k_y^2 \\
&= \left(k_{x2}^2\right)_r+i\left(k_{x2}^2\right)_i, \qquad (4.78)
\end{aligned}
$$

where

$$
\begin{aligned}
\left(k_{x2}^2\right)_r &= \gamma^2\left[\frac{k_z^2\tilde{v}_z^2-\omega_i^2}{c_s^2}-k_z^2+\left(\frac{\omega_i\tilde{v}_z}{c^2}\right)^2\right]-k_y^2 \\
&= \gamma^2\left[k_z^2\left(\frac{\tilde{v}_z^2}{c_s^2}-1\right)-\omega_i^2\left(\frac{1}{c_s^2}-\frac{\tilde{v}_z^2}{c^4}\right)\right]-k_y^2 \\
&= \left(k_{x1}^2\right)_r, \qquad (4.79)\\
\left(k_{x2}^2\right)_i &= 2\gamma^2\omega_i k_z\tilde{v}_z\left(\frac{1}{c_s^2}-\frac{1}{c^2}\right) \\
&= -\left(k_{x1}^2\right)_i. \qquad (4.80)
\end{aligned}
$$

We can therefore make a general comparison of the squared normal wave vectors in the two fluids if ω is imaginary. Specifically, the real parts are equal, while the imaginary parts are equal and opposite. We now seek to determine what this implies about the relationship between k_{x1} and k_{x2}. To do this, we note that the squared normal wave vectors have equal magnitudes and opposite phases. Specifically, we write k_{x1}^2 as

$$k_{x1}^2 = \left(k_{x1,r}^2 + k_{x1,i}^2\right) \exp\left(i\phi_{1sq}\right). \tag{4.81}$$

We now write k_{x2}^2 as

$$\begin{aligned} k_{x2}^2 &= \left(k_{x2,r}^2 + k_{x2,i}^2\right) \exp\left(i\phi_{2sq}\right) \\ &= \left(k_{x1,r}^2 + k_{x1,i}^2\right) \exp\left(i\phi_{2sq}\right) \\ &= \left(k_{x1,r}^2 + k_{x1,i}^2\right) \exp\left(-i\phi_{1sq}\right). \end{aligned} \tag{4.82}$$

The normal wave vectors are then given by

$$\begin{aligned} k_{x1} &= \sqrt{k_{x1,r}^2 + k_{x1,i}^2} \exp\left(i\frac{\phi_{1sq}}{2}\right) \\ &= \sqrt{k_{x1,r}^2 + k_{x1,i}^2} \left[\cos\left(\frac{\phi_{1sq}}{2}\right) + i\sin\left(\frac{\phi_{1sq}}{2}\right)\right], \end{aligned} \tag{4.83}$$

$$\begin{aligned} k_{x2} &= \sqrt{k_{x1,r}^2 + k_{x1,i}^2} \exp\left(-i\frac{\phi_{1sq}}{2}\right) \\ &= \sqrt{k_{x1,r}^2 + k_{x1,i}^2} \left[\cos\left(\frac{\phi_{1sq}}{2}\right) - i\sin\left(\frac{\phi_{1sq}}{2}\right)\right]. \end{aligned} \tag{4.84}$$

Comparing the real and imaginary parts of the normal wave vectors, we see that

$$\begin{aligned} k_{x1,r} &= k_{x2,r}, \\ k_{x1,i} &= -k_{x2,i}. \end{aligned} \tag{4.85}$$

This result is a consequence of the Hermiticity of the system, and is consistent with waves that undergo spatial decay away from the boundary, and vanish as $x \to \infty$ and as $x \to -\infty$. Note that in taking the square roots of the normal wave vectors, we chose the branch cut for which the phase of k_{xj} would lie in the same quadrant as the phase of k_{xj}^2. If we chose each branch cut to lie in the opposite quadrant as its square, we would still have the same results as above. If, however, we were inconsistent, and chose the branch cut of k_{x1} to lie in

the opposite quadrant as k_{x1}^2, while keeping the quadrants the same for k_{x2}, we would obtain normal wave vectors with opposite real parts and equal imaginary parts.

We now plot, in figures 4.6, the dependence on flow speed of the angular frequency ω and the normal wave vector k_x. Explicit expressions for these quantities are provided below. Each quantity is complex, and each graph shows both real and imaginary parts simultaneously. The real part is the black curve, while the imaginary part is the gray curve. For k_x, the value in fluid 1 is plotted on the left, while the value in fluid 2 is plotted on the right. The input parameters for the plots are as follows:

$$\begin{aligned} \tilde{\rho} &= 0.5 \times 10^{-24}\ \mathrm{g/cm^3}, \\ \tilde{P} &= 10.0\, c^2 \times 10^{-24}\ \mathrm{g/cm^3}, \\ c_s &= 0.57\, c, \\ k_z &= 2.0\, c^{-1}\mathrm{s}^{-1}, \\ k_y &= 0\, c^{-1}\mathrm{s}^{-1}. \end{aligned} \tag{4.86}$$

Note that because $k_y = 0$, we have $\theta = 0$. The maximum unstable flow speed corresponding to this case is

$$\tilde{v}_z = c c_s \sqrt{\frac{2}{c^2 + c_s^2}} = 0.704\, c. \tag{4.87}$$

The region from 0 to $0.704\, c$ corresponds to instability, while the region from $0.704\, c$ to c corresponds to stability. For unstable flow speeds, only the imaginary part of ω is non-zero, while for stable flow speeds, only the real part of ω is non-zero. Each graph exhibits a "kink" at the critical flow speed.

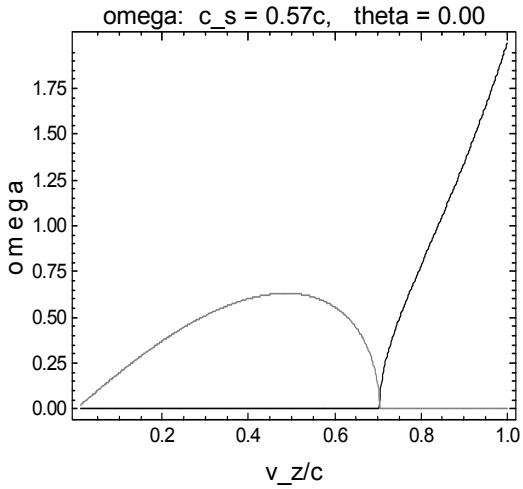

black = real, gray = imag.

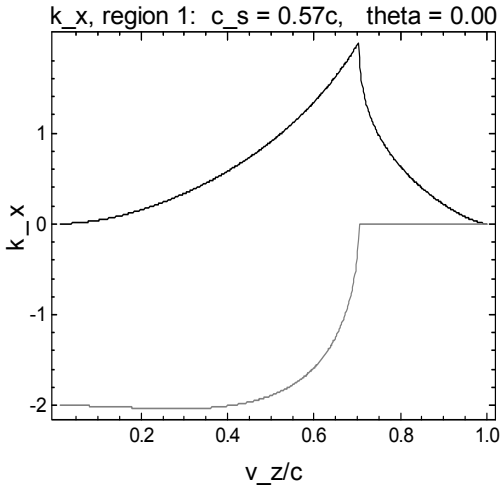

black = real, gray = imag.

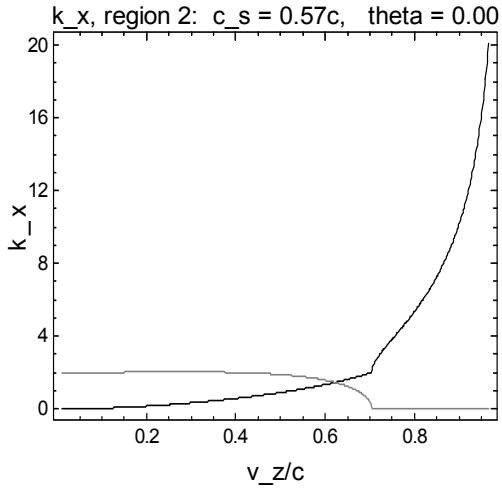

black = real, gray = imag.

Figure 4.6: Frequency and wave number vs flow speed (RHD)

Explicitly, the above quantities are as follows:

$$\begin{aligned}
\omega &= k_z \tilde{v}_z \sqrt{\frac{S_2 - \sqrt{S_2^2 + (\mathcal{M}_e^2 + 2\beta_e^2)(2 - \mathcal{M}_e^2)}}{\mathcal{M}_e^2 + 2\beta_e^2}}, \qquad \text{where} \\
S_2 &= 1 + \mathcal{M}_e^2 - \beta_e^2 \\
k_{x1} &= \sqrt{\gamma^2 \frac{(\omega - k_z \tilde{v}_z)^2}{c_s^2} - \gamma^2 \left(k_z - \frac{\omega \tilde{v}_z}{c^2} \right)^2 - k_y^2}, \\
k_{x2} &= \sqrt{\gamma^2 \frac{(\omega + k_z \tilde{v}_z)^2}{c_s^2} - \gamma^2 \left(k_z + \frac{\omega \tilde{v}_z}{c^2} \right)^2 - k_y^2}.
\end{aligned} \tag{4.88}$$

Several observations can be made from the previously mentioned graphs. First, we consider the *region of instability*. The angular frequency is purely imaginary, and this imaginary part is positive, signifying growth. The growth curve has the shape of a downward-facing parabola, meaning that a maximum growth rate is reached at a certain flow speed. At $\tilde{v}_z = 0$ and at the maximum unstable flow speed, the growth rate is zero. As we determined earlier, the real parts of k_x are the same in both fluids, while the imaginary parts of k_x are equal and opposite.

We now consider the *region of stability*. In this region all quantities are purely real, and have no imaginary part. The angular frequency ω increases monotonically from 0 to 2 s^{-1}. Recall that we had $k_z = 2.0\, c^{-1}\mathrm{s}^{-1}$. Furthermore, ω depends linearly on k_z, which means that ω/k_z will always approach c as $\tilde{v}_z$ approaches c. All velocity perturbations tend to zero as $\tilde{v}_z$ approaches c. However, only in fluid 1 does k_x tend to zero in the highly relativistic limit. k_x in region 2, on the other hand, tends to infinity. This means that at highly relativistic velocities, we have huge wavelengths in one fluid, and very small wavelengths in the other fluid. The reason for this is that the Lorentz factor tends to infinity as the flow speed approaches c. However, in this limit, in fluid 1 (see above expression for k_{x1}) the

Lorentz factor is multiplied by something that tends to zero more quickly, so that the product tends to zero. In fluid 2 (see above expression for k_{x2}), the Lorentz factor is multiplied by a non-zero quantity, and therefore the product tends to infinity. This highly relativistic behavior can be seen more clearly by plotting the wavelength in each fluid as a function of the Lorentz factor for the flow velocity, as is done in figures 4.7. Note that in fluid 1, we can only go out to a Lorentz factor of around 33. Above this, the wavelength in fluid 1 is too large to be computed accurately without using more refined methods.

In fluid 2, the wavelength approaches zero as the Lorentz factor approaches infinity (i.e., as the flow velocity approaches the speed of light). This illustrates the tendency of highly relativistic flows to break synchronicity between longitudinal and transverse motions, so that high Lorentz factors tend to excite modes with vanishingly small wavelengths. In chapter 6, when we consider the sech^2 profile, we will see that highly relativistic velocities excite modes with near-maximum growth at wavelengths shorter than the length scale set by the velocity shear. These are two possible manifestations of the destabilizing influence of highly relativistic flows. No amount or combination of diffusion can sustain a numerical simulation with a bulk flow Lorentz factor exceeding roughly 2.

In both the HD and RHD cases, we have found that the system is only unstable for Mach numbers less than $\sqrt{2}$ in the stationary frame, and less than 4 in the co-moving frame of one fluid. This is only valid when the velocity profile exhibits a step-function discontinuity between two flows. When the velocity profile exhibits a continuous shear variation, the region of instability generally extends to much larger Mach numbers, as we will see in chapter 6.

We have examined the KH instability in the HD and RHD regimes. In the next section,

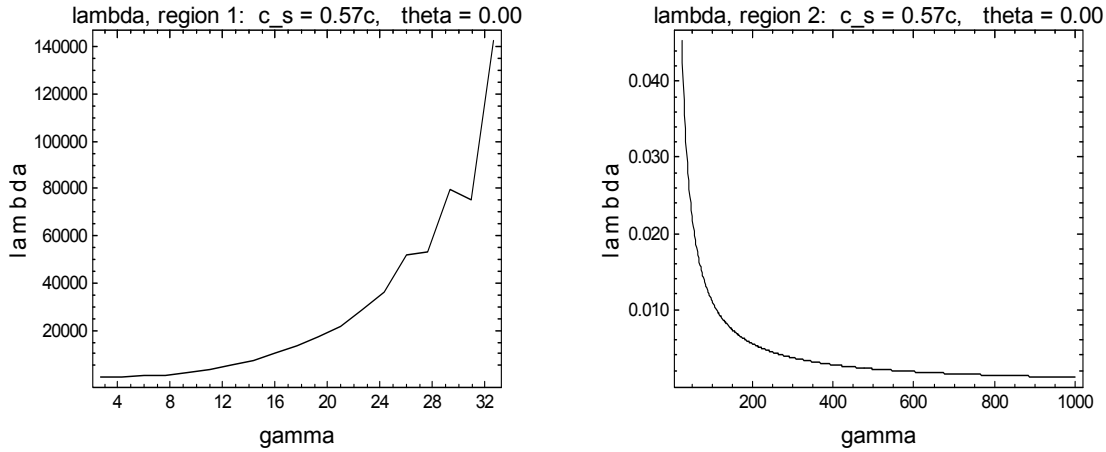

(a) fluid 1 (b) fluid 2

Figure 4.7: Wavelength vs Lorentz factor, $c_s = 0.57\,c$, $\theta = 0$ (RHD)

we introduce a magnetic field, and examine the stability of a tangential discontinuity in the MHD regime.

4.3 MHD Kelvin-Helmholtz Instability

We now consider a magnetized non-relativistic (MHD) fluid. As before, we first derive a dispersion relation for a uniform background flow by linearizing the single-fluid equations. We then introduce a step-function discontinuity in the background density, velocity, and pressure, and derive a linear dispersion relation for predicting the KH instability between the two flows. In section 4.4, we solve the dispersion relation using Mathematica, and demonstrate that we recover the results of PK83 and KP84. In particular, we verify that in the presence of a magnetic field, for a given perturbation orientation, the region of instability

is bounded by a lower and upper-critical flow velocity. The lower-critical velocity, and growth rates at lower velocities, are accurately predicted by the expression for MHD growth rates of an incompressible fluid, as in Chandrasekhar (1961). However, at higher flow speeds, compressibility has a stabilizing effect. In the limit of zero magnetic field, the lower-critical velocity is simply zero. In section 4.5, we deal with the case of a relativistic Alfven velocity, for which the displacement current must be included.

We begin by deriving the dispersion relation for single-fluid MHD modes with a uniform background flow.

4.3.1 MHD Single-fluid Dispersion Relation

We consider a magnetized non-relativistic compressible perfectly conducting fluid. We also assume for this section that the Alfven velocity is non-relativistic, so that the effect of the displacement current can be neglected. The dynamics of this fluid are generally described by the MHD equations

$$\begin{aligned}
\frac{\partial \rho}{\partial t} + \boldsymbol{\nabla} \cdot (\rho \mathbf{v}) &= 0, \\
\left(\frac{\partial}{\partial t} + \mathbf{v} \cdot \boldsymbol{\nabla} \right) \mathbf{v} &\approx -\boldsymbol{\nabla} P + \frac{\mathbf{J}}{c} \times \mathbf{B}, \\
\boldsymbol{\nabla} \times \mathbf{B} &\approx \frac{\mathbf{J}}{c}, \\
\boldsymbol{\nabla} \cdot \mathbf{B} &= 0, \\
\boldsymbol{\nabla} \times \mathbf{E} &= -\frac{1}{c} \frac{\partial \mathbf{B}}{\partial t}, \\
\mathbf{E} + \frac{\mathbf{v}}{c} \times \mathbf{B} &= 0, \\
c_s^2 &= \frac{dP}{d\rho}.
\end{aligned} \tag{4.89}$$

The first equation describes continuity of mass. The second equation is Euler's equation. The third through fifth equations are Maxwell's equations, while the sixth equation is the

assumption of infinite conductivity. The seventh equation is the adiabatic assumption. These equations can be combined to yield four equations relating just the pressure, density, velocity, and magnetic field:

$$\begin{aligned}
\frac{\partial \rho}{\partial t} + \boldsymbol{\nabla} \cdot (\rho \mathbf{v}) &= 0, \\
\left(\frac{\partial}{\partial t} + \mathbf{v} \cdot \boldsymbol{\nabla} \right) \mathbf{v} &\approx -\boldsymbol{\nabla} P + (\boldsymbol{\nabla} \times \mathbf{B}) \times \mathbf{B}, \\
\frac{\partial \mathbf{B}}{\partial t} &= \boldsymbol{\nabla} \times (\mathbf{v} \times \mathbf{B}) \\
&= (\mathbf{B} \cdot \boldsymbol{\nabla}) \mathbf{v} - \mathbf{B} (\boldsymbol{\nabla} \cdot \mathbf{v}) - (\mathbf{v} \cdot \boldsymbol{\nabla}) \mathbf{B}, \\
c_s^2 &= \frac{dP}{d\rho}.
\end{aligned} \tag{4.90}$$

We now consider a single fluid with uniform unperturbed density $\tilde{\rho}$, uniform unperturbed pressure $\tilde{P}$, flowing with uniform unperturbed velocity $\tilde{v}_z$ in the z-direction. The fluid is immersed in a uniform unperturbed magnetic field $\mathbf{B}$. We perturb each of these quantities as follows:

$$Q(\mathbf{r}, t) = \tilde{Q} + \delta Q e^{i(\mathbf{k} \cdot \mathbf{r} - \omega t)}. \tag{4.91}$$

We insert this perturbed form into equations (4.90), thereby yielding the following linearized equations:

$$\begin{aligned}
-(\omega - k_z \tilde{v}_z) \, \delta \rho + \tilde{\rho} \, (\mathbf{k} \cdot \delta \mathbf{v}) &= 0, \\
-(\omega - k_z \tilde{v}_z) \, \delta \mathbf{v} &= -\mathbf{k} \left(\delta P + \tilde{\mathbf{B}} \cdot \delta \mathbf{B} \right) + (\mathbf{B} \cdot \mathbf{k}) \delta \mathbf{B}, \\
-\omega \delta B &= \mathbf{k} \times \left(\tilde{\mathbf{v}} \times \delta \mathbf{B} + \delta \mathbf{v} \times \tilde{\mathbf{B}} \right), \\
c_s^2 &= \frac{\delta P}{\delta \rho}.
\end{aligned} \tag{4.92}$$

Upon solving the above system of linearized equations, we find that the velocity perturbations are given in terms of the pressure perturbation by

$$\delta \mathbf{v} \;=\; \frac{\left(\omega - k_z \tilde{v}_z\right)^2 \mathbf{k} - k^2 \left(\mathbf{v}_A \cdot \mathbf{k}\right) \mathbf{v_A}}{\tilde{\rho}\left(\omega - k_z \tilde{v}_z\right)\left[\left(\omega - k_z \tilde{v}_z\right)^2 - v_A^2 k^2\right]} \delta P, \tag{4.93}$$

where the Alfven velocity is given by

$$\mathbf{v}_A \;=\; \frac{\tilde{\mathbf{B}}}{\sqrt{\tilde{\rho}}}. \tag{4.94}$$

We now substitute this result into the linearized continuity equation, and employ the adiabatic condition. This leads to the following dispersion relation:

$$\left(\omega - k_z \tilde{v}_z\right)^4 - \left(\omega - k_z \tilde{v}_z\right)^2 k^2 (c_s^2 + v_A^2) + c_s^2 k^2 (\mathbf{v}_A \cdot \mathbf{k})^2 \;=\; 0. \tag{4.95}$$

For purposes of defining the modes, we now introduce the total pressure P_b, given by

$$P_b \;=\; P + \frac{B^2}{2}. \tag{4.96}$$

For a characteristic frequency ω that solves the dispersion relation, we can write the corresponding mode in terms of the total pressure perturbation:

$$\begin{aligned}
\delta P \;&=\; \frac{\bar{\omega}^2 - v_A^2 k^2}{\bar{\omega}^2 - \left(\mathbf{v}_A \cdot \mathbf{k}\right)^2} \delta P_b, \\
\delta \rho \;&=\; \frac{1}{c_s^2} \frac{\bar{\omega}^2 - v_A^2 k^2}{\bar{\omega}^2 - \left(\mathbf{v}_A \cdot \mathbf{k}\right)^2} \delta P_b, \\
\delta \mathbf{v} \;&=\; \frac{\bar{\omega}^2 \mathbf{k} - k^2 \left(\mathbf{v}_A \cdot \mathbf{k}\right) \mathbf{v}_A}{\tilde{\rho}\bar{\omega}\left[\bar{\omega}^2 - \left(\mathbf{v}_A \cdot \mathbf{k}\right)^2\right]} \delta P_b, \\
\delta B_\alpha \;&=\; \frac{v_{A\alpha}\left(k^2 - k_\alpha^2\right) - k_\alpha \left(\mathbf{v}_A \cdot \mathbf{k} - v_{A\alpha} k_\alpha\right)}{\sqrt{\tilde{\rho}}\left[\bar{\omega}^2 - \left(\mathbf{v}_A \cdot \mathbf{k}\right)^2\right]} \delta P_b,
\end{aligned} \tag{4.97}$$

where $\alpha = \{x, y, z\}$, and $\bar{\omega} \equiv \omega - k_z \tilde{v}_z$. Having derived a single-fluid dispersion relation in MHD, we now apply this result to the case of a tangential discontinuity between two fluids.

4.3.2 Non-relativistic Magnetized Kelvin-Helmholtz Instability

We now consider the same fluid as in the previous section, but in addition we introduce a discontinuity in the x-direction in magnetic field, velocity, and density. Each of these quantities is still assumed to be uniform on both sides of the discontinuity. The equations from the previous section now hold in both half-planes. Furthermore, we have several boundary constraints, one of which involves the fluid displacement, given by

$$\left(\frac{\partial}{\partial t} + \mathbf{v}\cdot\boldsymbol{\nabla}\right)\xi \;=\; \mathbf{v}. \tag{4.98}$$

First, the component of the fluid displacement normal to the discontinuity must both be equal on either side (Chandrasekhar 1961):

$$\xi_{x1} \;=\; \xi_{x2}. \tag{4.99}$$

Second, the total pressure perturbation (thermal and magnetic pressure) must be equal on either side. This gives the following relation among the unperturbed quantities:

$$\begin{aligned} \tilde{P}_{b,1} \;&=\; \tilde{P}_{b,2}, \qquad \text{or} \\ \tilde{P}_1 + \frac{\tilde{B}_1^2}{2} \;&=\; \tilde{P}_2 + \frac{\tilde{B}_2^2}{2}. \end{aligned} \tag{4.100}$$

These two conditions must also be applied to the perturbed quantities:

$$\begin{aligned} \delta P_{b,1} \;&=\; \delta P_{b,2}, \\ \frac{\delta v_{x1}}{\omega - k_z\tilde{v}_{z1}} \;&=\; \frac{\delta v_{x2}}{\omega - k_z\tilde{v}_{z2}}. \end{aligned} \tag{4.101}$$

We also have boundary conditions on the electric and magnetic fields. Because we assume the fluid is infinitely conducting, the electric field is given by

$$\mathbf{E} \;=\; \mathbf{B} \times \frac{\mathbf{v}}{c}. \tag{4.102}$$

The unperturbed electric field is therefore

$$\tilde{\mathbf{E}} \;=\; \tilde{B}_y \frac{\tilde{v}}{c}\, \hat{x} - \tilde{B}_x \frac{\tilde{v}}{c}\, \hat{y}. \tag{4.103}$$

The third condition is equality of the components of the magnetic field normal to the boundary, i.e., in the shear direction. For the unperturbed quantities, this gives simply

$$\tilde{B}_{x1} \;=\; \tilde{B}_{x2}. \tag{4.104}$$

The fourth condition is equality of the components of the electric field tangential to the boundary, which for the unperturbed quantities gives

$$\begin{aligned} \tilde{E}_{y1} \;&=\; \tilde{E}_{y2}, \\ \tilde{B}_{x1}\tilde{v}_1 \;&=\; \tilde{B}_{x2}\tilde{v}_2. \end{aligned} \tag{4.105}$$

Combining these two conditions, we see that the only way to have two distinct unperturbed flow velocities on either side of the boundary is to set $\tilde{B}_x = 0$ everywhere, so that there is no component of the magnetic field in the shear direction. That is, the magnetic field is polarized in the $y - z$ plane.

To complete the dispersion relation, we must solve for each k_{xj} in terms of the other variables, which is done using the dispersion relation derived in the previous section. The solution for k_{xj}, for $j = 1, 2$, is

$$k_{xj}^2 \;=\; \frac{\bar{\omega}_j^4}{\bar{\omega}_j^2 \left(v_{Aj}^2 + c_{sj}^2\right) - c_{sj}^2 \left(v_{Ay,j} k_y + v_{Az,j} k_z\right)} - k_{yz}^2, \tag{4.106}$$

where $k_{yz}^2 \equiv k_y^2 + k_z^2$. With these values of k_{xj}, the dispersion relation for a magnetic field *perpendicular to the shear direction* is given by (13) with $v_{Ax,j} = 0$:

$$\frac{\sqrt{k_{x1}^2}}{\tilde{\rho}_1 \left[\bar{\omega}_1^2 - (v_{Ay,1}k_y + v_{Az,1}k_z)^2\right]} = \frac{-\sqrt{k_{x2}^2}}{\tilde{\rho}_2 \left[\bar{\omega}_2^2 - (v_{Ay,2}k_y + v_{Az,2}k_z)^2\right]}. \tag{4.107}$$

The "$-$" sign is included because we expect the solution to vanish as $x \to \pm\infty$. Suppose fluid 1 occupies the half-space of negative x, and fluid 2 occupies the half-space of positive x. Then in order to satisfy the above boundary condition, we must have

$$\begin{aligned} k_{x1} &= -\sqrt{k_{x1}^2}, \\ k_{x2} &= \sqrt{k_{x2}^2}. \end{aligned} \tag{4.108}$$

For a given k_y and k_z, the dispersion relation (4.107) generates several values of ω. Corresponding to each ω is a mode whose perturbation amplitudes are obtained by applying the relationships (4.97) separately to each fluid, with δP_b, k_y, and k_z the same in both fluids.

In the limit of *incompressible* fluids, the density ρ is constant, and $c_s^2 = dP/d\rho$. The incompressible limit therefore corresponds to $c_s \to \infty$. Applying this limit to our expression for k_x, we obtain

$$\begin{aligned} k_x^2 &= -k_y^2 + k_z^2, \qquad \text{or simply} \\ k_x^2 + k_y^2 + k_z^2 &= 0. \end{aligned} \tag{4.109}$$

Therefore, we must have equal normal wave vectors in both fluids. That is, $k_{x1} = k_{x2}$. Therefore, the dispersion relation becomes

$$\frac{k_x}{\tilde{\rho}_1 \left[(\omega - k_z\tilde{v}_{z1})^2 - (\mathbf{v}_{A1} \cdot \mathbf{k})^2\right]} = \frac{-k_x}{\tilde{\rho}_2 \left[(\omega - k_z\tilde{v}_{z2})^2 - (\mathbf{v}_{A2} \cdot \mathbf{k})^2\right]}. \tag{4.110}$$

This dispersion relation can be analytically solved for the growth rate:

$$\omega_i \;=\; \sqrt{\frac{\tilde{\rho}_1\tilde{\rho}_2}{\left(\tilde{\rho}_1+\tilde{\rho}_2\right)^2}k_z^2\left(\tilde{v}_{z2}-\tilde{v}_{z1}\right)^2-\frac{1}{\tilde{\rho}_1+\tilde{\rho}_2}\left[\tilde{\rho}_1\left(\tilde{\mathbf{v}}_{A1}\cdot\mathbf{k}\right)^2+\tilde{\rho}_2\left(\tilde{\mathbf{v}}_{A2}\cdot\mathbf{k}\right)^2\right]}, \tag{4.111}$$

where, as before,

$$\tilde{\mathbf{v}}_{Aj}\cdot\mathbf{k} \;=\; v_{Ay,j}k_y+v_{Az,j}k_z. \tag{4.112}$$

The critical velocity difference above which instability occurs is therefore given by

$$\left(\tilde{v}_{z2}-\tilde{v}_{z1}\right)_c^2 \;=\; \frac{\tilde{\rho}_1+\tilde{\rho}_2}{k_z^2}\left[\frac{\left(\tilde{\mathbf{v}}_{A1}\cdot\mathbf{k}\right)^2}{\tilde{\rho}_2}+\frac{\left(\tilde{\mathbf{v}}_{A2}\cdot\mathbf{k}\right)^2}{\tilde{\rho}_1}\right]. \tag{4.113}$$

This result agrees with the result of Chandrasekhar (1961). As long as the difference in flow velocities is sufficiently small, the above dispersion relation and growth rate are approximately correct in the compressible case. In particular, the lower-critical velocity for instability in the compressible case is approximately given by expression (4.113) for the incompressible case. At large velocity differences, however, the incompressible case continues to give instability, whereas the compressible case exhibits an upper-critical velocity difference above which the system is stable, for a given perturbation direction. Compressibility therefore stabilizes the system for large velocity differences (PK83; KP84; Southwood 1968, and references therein). For large relative velocities, the instability is inhibited by the necessity for the perturbation to perform a large amount of work against the mechanical energy of the background (bulk) flow. This effect is not present when the Mach number approaches zero, as in the incompressible case.

Having derived a dispersion relation for predicting the KH instability in the MHD regime, we now wish to compare our growth rate results with those of PK83 and KP84, which demonstrates the validity of our numerical algorithm for solving this dispersion relation.

4.4 Comparison with PK83 and KP84

Through the use of root-finding algorithms in Mathematica, we obtain linear results for the non-relativistic MHD Kelvin-Helmholtz instability. We wish to compare these results with the results presented in PK83 and KP84. By doing this, we can validate our method of analysis in the non-relativistic regime. Once this is done, modified versions of these same algorithms can then be used to obtain stability results in the relativistic case, discussed in later sections. As derived in subsection 4.3.2, the dispersion relation for the MHD Kelvin-Helmholtz instability is

$$\frac{\sqrt{k_{x1}^2}}{\tilde{\rho}_1\left[\bar{\omega}_1^2-\left(v_{Ay,1}k_y+v_{Az,1}k_z\right)^2\right]} \;=\; \frac{-\sqrt{k_{x2}^2}}{\tilde{\rho}_2\left[\bar{\omega}_2^2-\left(v_{Ay,2}k_y+v_{Az,2}k_z\right)^2\right]}, \tag{4.114}$$

where, for $j = 1, 2$,

$$k_{xj}^2 \;=\; \frac{\bar{\omega}_j^4}{\bar{\omega}_j^2\left(v_{Aj}^2+c_{sj}^2\right)-c_{sj}^2\left(v_{Ay,j}k_y+v_{Az,j}k_z\right)}-k_y^2-k_z^2. \tag{4.115}$$

We choose, as our velocity scale, $c_0 = 0.001\,c$, where c is the speed of light. We use the following parameters, which are consistent with the test case of PK83 and KP84:

$$
\begin{aligned}
\Gamma &= 2 \qquad \text{(adiabatic constant)}, \\
\tilde{\rho}_1 &= 1.0 \times 10^{-24}\ \text{g/cm}^{-3}, \\
\tilde{\rho}_2 &= 10.0 \times 10^{-24}\ \text{g/cm}^{-3}, \\
\beta_1 &= \tilde{P}_1 \left(\frac{\tilde{B}_1^2}{2} \right)^{-1} = 0.64, \\
\beta_2 &= \tilde{P}_2 \left(\frac{\tilde{B}_2^2}{2} \right)^{-1} = 2.5, \\
\frac{\tilde{B}_2^2}{2} &= \frac{c_0^2 \times 10^{-24}}{2}\ \text{g/cm}^{-3}, \\
k_{yz} &= \sqrt{k_y^2 + k_z^2} = 1.0\ c^{-1}\ (1\ \text{s})^{-1}.
\end{aligned}
\tag{4.116}
$$

Note that β_j is the ratio of magnetic pressure to thermal pressure. To obtain the remaining parameters, we invoke equilibrium of total pressure at the interface:

$$
\begin{aligned}
\tilde{P}_1 + \frac{\tilde{B}_1^2}{2} &= \tilde{P}_2 + \frac{\tilde{B}_2^2}{2}, \\
(\beta_1 + 1)\, \frac{\tilde{B}_1^2}{2} &= (\beta_2 + 1)\, \frac{\tilde{B}_2^2}{2}, \\
\frac{\tilde{B}_1^2}{\tilde{B}_2^2} &= \frac{\beta_2 + 1}{\beta_1 + 1}.
\end{aligned}
\tag{4.117}
$$

This gives us the remaining parameters, for $j = 1, 2$ where needed:

$$
\begin{aligned}
\frac{\tilde{B}_1^2}{2} &= \frac{1}{2} \left(\frac{\beta_2 + 1}{\beta_1 + 1} \right) c_0^2 \times 10^{-24}\ \text{g/cm}^{-3}, \\
\tilde{P}_j &= \beta_j \frac{\tilde{B}_j^2}{2}, \\
c_{sj}^2 &= \frac{\Gamma \tilde{P}_j}{\tilde{\rho}_j}, \\
\mathbf{v}_{Aj} &= \frac{\tilde{\mathbf{B}}_j}{\sqrt{\tilde{\rho}_j}}.
\end{aligned}
\tag{4.118}
$$

We further assume that the magnetic field in both fluids is parallel to the flow direction, as is the case with the nightside magnetopause in PK83 and KP84:

$$\mathbf{B}_1 \;=\; B_{z1}\,\hat{z}, \qquad \mathbf{B}_2 \;=\; B_{z2}\,\hat{z}. \tag{4.119}$$

We define θ as the angle between the flow direction and the direction of the wave vector of the perturbation.

$$k_z \;=\; k_{yz}\cos\theta, \qquad k_y \;=\; k_{yz}\sin\theta. \tag{4.120}$$

We first perform a comparison for a flow aligned perturbation, for which $\theta = 0$, so that $k_z = k_{yz}$ and $k_y = 0$. In figure 4.8, we present two plots. The left plot is of the scaled growth rate $\omega_i/(k_{yz}v_{A1})$ as a function of the scaled flow speed $\tilde{v}_z/v_{A1}$. The right plot is of the base-10 log of $\omega_i/(k_{yz}v_{A1})$ as a function of $\tilde{v}_z/v_{A1}$. Note that each plot contains two concave-downward parabolas. The left parabola is referred to, in PK83 and KP84, as the slow mode, while the right parabola is referred to as the fast mode.

We present the same graphs for oblique perturbation directions of $\theta = 60$ deg, in figures 4.9, and $\theta = 78$ deg, in figures 4.10, which are the directions considered in PK83 and KP84, for the nightside magnetopause. Note that the horizontal axes are different than for the previous graphs, due to the range of flow speeds being extended. However, the lower-critical speed of the fast mode has very little dependence on perturbation direction. We see that as the perturbation becomes more oblique, the fast mode becomes more dominant, and the slow mode essentially fades away.

For the three directions considered above, the corresponding results from page 847 of PK83 and KP84 are shown in figure 4.11. We see that these results are in agreement with figures 4.9 and 4.10 (in particular, the logarithmic plots on the right).

Based on our successful comparison, we see that we have a reliable algorithm for computing linear growth rates of the MHD Kelvin-Helmholtz instability. We may now proceed with more confidence in extending our algorithm to the relativistic regime. We have also recovered the expected influence of compressibility on MHD growth rates, as described in the previous section. Specifically, at lower flow speeds, the growth rates (and lower-critical flow velocity) are accurately predicted by the growth rate expression for incompressible fluids (see subsection 4.3.2). At higher growth rates, compressibility stabilizes the system, introducing an upper-critical velocity. In the next section, we consider the effects of displacement current on the MHD dispersion relation for predicting the KH instability.

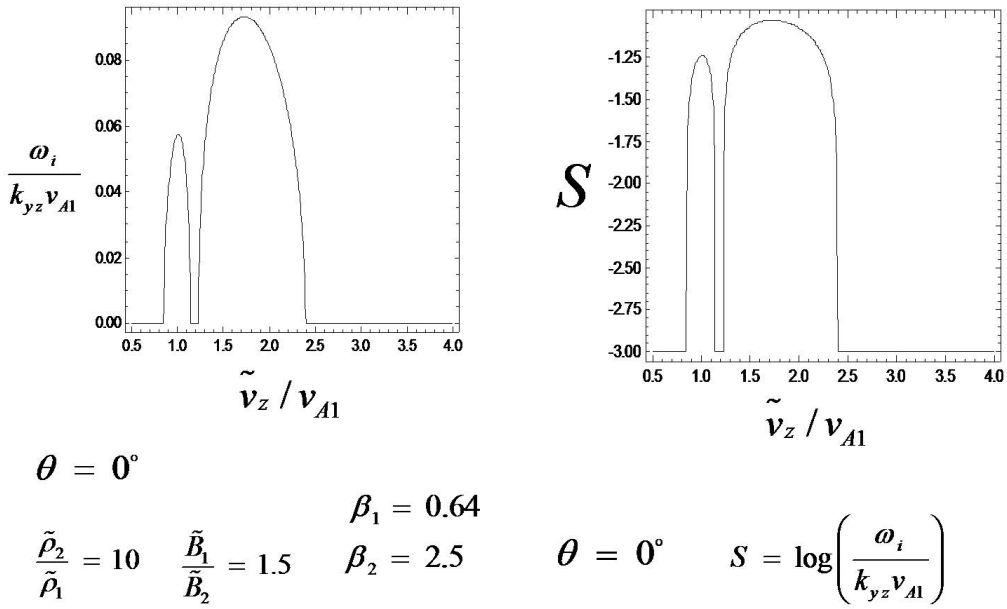

Figure 4.8: Growth rate vs flow speed for $\theta = 0$ deg (MHD)

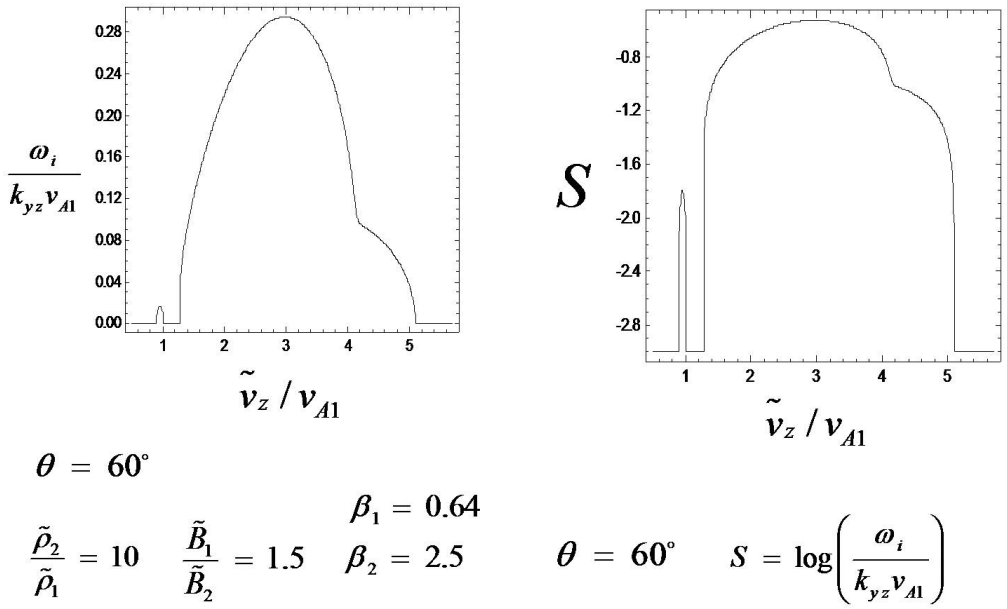

Figure 4.9: Growth rate vs flow speed for $\theta = 60$ deg (MHD)

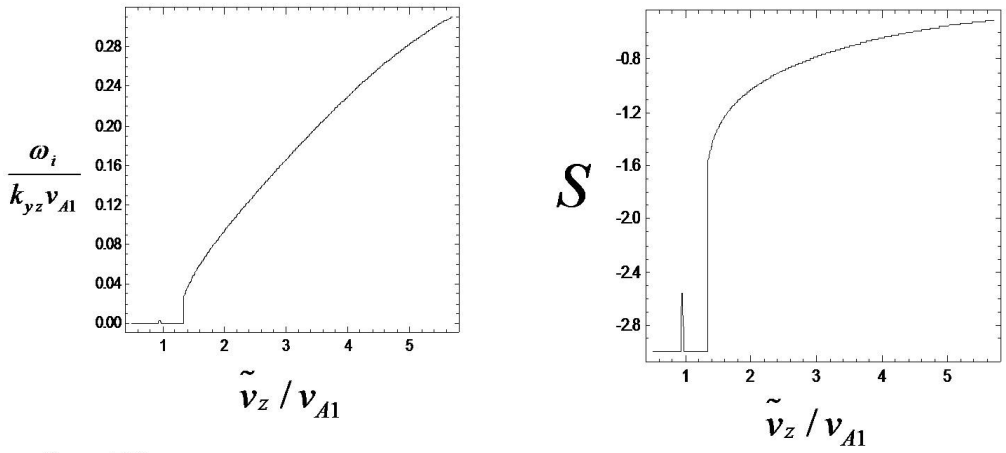

$\theta = 78^\circ$

$\beta_1 = 0.64$

$\frac{\tilde{\rho}_2}{\tilde{\rho}_1} = 10 \quad \frac{\tilde{B}_1}{\tilde{B}_2} = 1.5 \quad \beta_2 = 2.5 \quad \theta = 78^\circ \quad S = \log\left(\frac{\omega_i}{k_{yz} v_{A1}}\right)$

Figure 4.10: Growth rate vs flow speed for $\theta = 78$ deg (MHD)

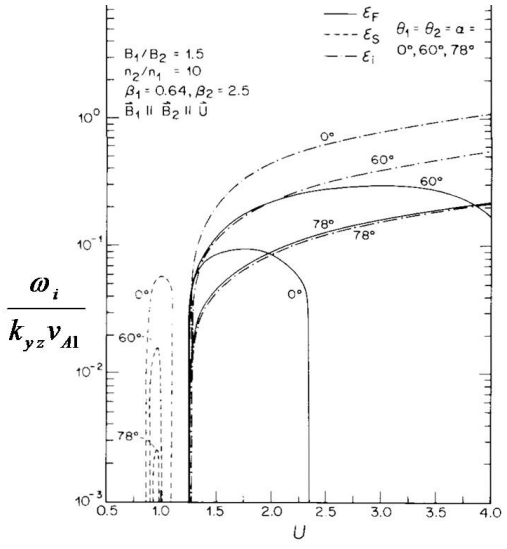

$U = \frac{\tilde{v}_z}{v_{A1}} \qquad \tilde{B}_1 \parallel \tilde{B}_2 \parallel \tilde{v}_z$

Figure 4.11: Growth rates of PK83 and KP84 (MHD)

4.5 MHD KH Instability with Displacement Current

We again consider two magnetized fluids with non-relativistic flow velocities, and non-relativistic sound speeds, but we now allow for the Alfven velocities to be relativistic, as would be the case for a magnetically-dominated or low-density jet. In order to ensure that the phase speed, flow speed, and Alfven speed not exceed the speed of light, we must incorporate the contribution from the displacement current into the MHD fluid equations for a single fluid. Our results are in agreement with the results of LRN09. As we did previously, we first linearize the MHD equations:

$$\begin{aligned}
\frac{\partial \rho}{\partial t} + \boldsymbol{\nabla} \cdot (\rho \mathbf{v}) &= 0, \\
\rho \left(\frac{\partial}{\partial t} + \boldsymbol{\nabla} \cdot \mathbf{v} \right) \mathbf{v} + \boldsymbol{\nabla} P &= \rho_c \mathbf{E} + \frac{\mathbf{J}}{c} \times \mathbf{B}, \\
\boldsymbol{\nabla} \times \mathbf{E} &= -\frac{1}{c} \frac{\partial \mathbf{B}}{\partial t}, \\
\boldsymbol{\nabla} \times \mathbf{B} &= \frac{\mathbf{J}}{c} + \frac{1}{c} \frac{\partial \mathbf{E}}{\partial t}, \\
\boldsymbol{\nabla} \cdot \mathbf{B} &= 0, \\
\boldsymbol{\nabla} \cdot \mathbf{E} &= \rho_c, \\
\mathbf{E} + \frac{\mathbf{v}}{c} \times \mathbf{B} &= 0, \\
\frac{\partial P}{\partial \rho} &= c_s^2.
\end{aligned} \tag{4.121}$$

The first equation describes mass continuity, while the second equation is Euler's equation. The third through sixth equations are Maxwell's laws, the seventh equation is the assumption of infinite conductivity, and the eighth equation is the adiabatic assumption. The non-relativistic sound speed c_s is given, as before, by

$$c_s = \sqrt{\frac{\partial P}{\partial \rho}} = \sqrt{\frac{\Gamma P}{\rho}}. \tag{4.122}$$

We now consider a single fluid with uniform unperturbed density $\tilde{\rho}$, uniform unperturbed pressure $\tilde{P}$, flowing with uniform unperturbed velocity $\tilde{v}_z$ in the z-direction. The fluid is immersed in a uniform unperturbed magnetic field $\tilde{B}_z$ in the z-direction. We perturb each of these quantities as follows:

$$Q(\mathbf{r},t) \;=\; \tilde{Q} + \delta Q e^{i(\mathbf{k}\cdot\mathbf{r}-\omega t)}. \tag{4.123}$$

The process of linearizing the equations is greatly simplified by assuming that the magnetic field and flow direction are both aligned. Because of this, there is no unperturbed electric field. Therefore, the linearized Lorentz force due to the electric field is zero:

$$\begin{aligned}\delta\left(\rho_c\mathbf{E}\right) \;&=\; \delta\left[\left(\boldsymbol{\nabla}\cdot\mathbf{E}\right)\mathbf{E}\right] \\ &=\; \left(\mathbf{k}\cdot\delta\mathbf{E}\right)\tilde{\mathbf{E}} \;=\; \left(\mathbf{k}\cdot\delta\mathbf{E}\right)\left(\tilde{\mathbf{B}}\times\frac{\tilde{\mathbf{v}}}{c}\right) \;=\; \left(\mathbf{k}\cdot\delta\mathbf{E}\right)\left(\tilde{B}_y\frac{\tilde{v}_z}{c}\right) \;=\; 0.\end{aligned} \tag{4.124}$$

For purposes of linearization, we would like to write the fluid equations entirely in terms of ρ, P, $\mathbf{v}$, and $\mathbf{B}$. We do this as follows:

$$\begin{aligned}\frac{\partial\rho}{\partial t}+\boldsymbol{\nabla}\cdot\left(\rho\mathbf{v}\right) \;&=\; 0, \\ \rho\left(\frac{\partial}{\partial t}+\boldsymbol{\nabla}\cdot\mathbf{v}\right)\mathbf{v}+\boldsymbol{\nabla}P \;&=\; -\frac{\boldsymbol{\nabla}\left(B^2\right)}{2}+\left(\mathbf{B}\cdot\boldsymbol{\nabla}\right)\mathbf{B}+h_1, \\ \frac{\partial\mathbf{B}}{\partial t} \;&=\; \left(\mathbf{B}\cdot\boldsymbol{\nabla}\right)\mathbf{v}-\mathbf{B}\left(\boldsymbol{\nabla}\cdot\mathbf{v}\right)-\left(\mathbf{v}\cdot\boldsymbol{\nabla}\right)\mathbf{B}, \\ \frac{\partial P}{\partial\rho} \;&=\; c_s^2,\end{aligned} \tag{4.125}$$

where

$$h_1 \;\equiv\; \frac{1}{c^2}\left[\frac{\partial\mathbf{B}}{\partial t}\left(\mathbf{B}\cdot\mathbf{v}\right)-\mathbf{v}\left(\mathbf{B}\cdot\frac{\partial\mathbf{B}}{\partial t}\right)+\mathbf{B}\left(\mathbf{B}\cdot\frac{\partial\mathbf{v}}{\partial t}\right)-\frac{\partial\mathbf{v}}{\partial t}B^2\right]. \tag{4.126}$$

Upon substituting the linearizations (4.123) into (4.125), the fluid equations become

$$\begin{aligned} \frac{\delta P}{\delta \rho} &= c_s^2, \\ -\left(\omega - k_z \tilde{v}_z\right) \delta\rho + (\mathbf{k} \cdot \delta\mathbf{v})\tilde{\rho} &= 0, \\ -\tilde{\rho}\left(\omega - k_z \tilde{v}_z\right) \delta\mathbf{v} + \mathbf{k}\delta P &= -\mathbf{k}\left(\tilde{\mathbf{B}} \cdot \delta\mathbf{B}\right) + \left(\tilde{\mathbf{B}} \cdot \mathbf{k}\right) \delta\mathbf{B} + \delta h_1, \\ -\left(\omega - k_z \tilde{v}_z\right) \delta\mathbf{B} &= \left(\tilde{\mathbf{B}} \cdot \mathbf{k}\right) \delta\mathbf{v} - \tilde{\mathbf{B}}\left(\mathbf{k} \cdot \delta\mathbf{v}\right), \end{aligned} \tag{4.127}$$

where

$$\delta h_1 = \frac{\omega}{c^2}\left[-\tilde{B}_z \tilde{v}_z \delta\mathbf{B} + \tilde{\mathbf{v}}\left(\tilde{\mathbf{B}} \cdot \delta\mathbf{B}\right) - \tilde{\mathbf{B}}\left(\tilde{\mathbf{B}} \cdot \delta\mathbf{v}\right) + \delta\mathbf{v}\tilde{B}^2\right]. \tag{4.128}$$

In general, the total pressure the fluid experiences should incorporate both the magnetic and electric fields:

$$P_b = P + \frac{E^2 + B^2}{2}. \tag{4.129}$$

However, because the unperturbed electric field is zero, the electric field does not appear in the total pressure perturbation, which therefore is the same as in the previous section:

$$\delta P_b = \delta P + \tilde{\mathbf{B}} \cdot \delta\mathbf{B}. \tag{4.130}$$

By solving the linearized equations, we find that the primitive variable perturbations are related as follows to the electromagnetic pressure perturbation:

$$
\begin{aligned}
\delta P &= \frac{\bar{\omega}^2 - v_{Az}^2(k^2 - \omega^2/c^2)}{\bar{\omega}^2 - v_{Az}^2\left(k_z^2 - \omega^2/c^2\right)}\delta P_b, \\
\delta\rho &= \left(\frac{1}{c_s^2}\right)\frac{\bar{\omega}^2 - v_{Az}^2(k^2 - \omega^2/c^2)}{\bar{\omega}^2 - v_{Az}^2\left(k_z^2 - \omega^2/c^2\right)}\delta P_b, \\
\delta v_x &= \frac{\bar{\omega}k_x}{\tilde{\rho}\left[\bar{\omega}^2 - v_{Az}^2\left(k_z^2 - \omega^2/c^2\right)\right]}\delta P_b, \\
\delta v_y &= \frac{\bar{\omega}k_y}{\tilde{\rho}\left[\bar{\omega}^2 - v_{Az}^2\left(k_z^2 - \omega^2/c^2\right)\right]}\delta P_b, \\
\delta v_z &= \frac{\left[\bar{\omega}^2 - v_{Az}^2(k^2 - \omega^2/c^2)\right]k_z}{\tilde{\rho}\bar{\omega}\left[\bar{\omega}^2 - v_{Az}^2\left(k_z^2 - \omega^2/c^2\right)\right]}\delta P_b, \\
\delta B_x &= -\frac{k_x k_z v_{Az}}{\sqrt{\tilde{\rho}}\left[\bar{\omega}^2 - v_{Az}^2\left(k_z^2 - \omega^2/c^2\right)\right]}\delta P_b, \\
\delta B_y &= -\frac{k_y k_z v_{Az}}{\sqrt{\tilde{\rho}}\left[\bar{\omega}^2 - v_{Az}^2\left(k_z^2 - \omega^2/c^2\right)\right]}\delta P_b, \\
\delta B_z &= \frac{(k_x^2 + k_y^2)v_{Az}}{\sqrt{\tilde{\rho}}\left[\bar{\omega}^2 - v_{Az}^2\left(k_z^2 - \omega^2/c^2\right)\right]}\delta P_b,
\end{aligned}
\tag{4.131}
$$

where

$$
c_s^2 \;=\; \frac{\Gamma\tilde{P}}{\tilde{\rho}}, \qquad v_{Az} \;=\; \frac{\tilde{B}_z}{\sqrt{\tilde{\rho}}}, \qquad \bar{\omega} \;\equiv\; \omega - k_z\tilde{v}_z. \tag{4.132}
$$

We also obtain the following single-fluid MHD dispersion relation for a flow-aligned unperturbed magnetic field:

$$
\bar{\omega}^4 - \bar{\omega}^2\left[k^2c_s^2 + \left(k^2 - \frac{\omega^2}{c^2}\right)v_{Az}^2\right] + c_s^2v_{Az}^2k_z^2\left(k^2 - \frac{\omega^2}{c^2}\right) \;=\; 0. \tag{4.133}
$$

In the limit of non-relativistic Alfven velocities, this dispersion relation reduces to the MHD single-fluid dispersion relation given in the previous section, and in PK83 and KP84. The above dispersion relation can also be written in the form

$$
\bar{\omega}^2(k_x^2 + k_y^2 + k_s^2) - v_{Az}^2k_s^2\left(k^2 - \frac{\omega^2}{c^2}\right) \;=\; 0, \tag{4.134}
$$

where

$$k_s^2 \equiv k_z^2 - \frac{\bar{\omega}^2}{c_s^2}. \tag{4.135}$$

This dispersion relation is equivalent to the result of LRN09.

We now introduce a discontinuity at $x = 0$, so that there are now two fluids, each with its own unperturbed density, pressure, z-directed flow velocity, and z-directed magnetic field. From the first boundary condition at the interface, the total electromagnetic pressure must be equal on both sides of the interface. This must therefore also hold for the electromagnetic pressure perturbation:

$$\delta P_{b1} = \delta P_{b2}. \tag{4.136}$$

The perturbation amplitudes are computed by applying equations (4.131) separately to each fluid, with δP_b, k_y, and k_z the same in each fluid. In particular, the normal velocity perturbation in fluid j is

$$\delta v_{xj} = \frac{\bar{\omega}_j k_{xj}}{\tilde{\rho}_j \left[\bar{\omega}_j^2 - v_{Az,j}^2 \left(k_z^2 - \omega^2/c^2\right)\right]} \delta P_b. \tag{4.137}$$

We now invoke the second boundary condition, and equate the normal fluid displacements on either side of the interface (Chandrasekhar 1961). The resulting dispersion relation is

$$\begin{aligned} \frac{\delta v_{x1}}{\bar{\omega}_1} &= \frac{\delta v_{x2}}{\bar{\omega}_2}, \qquad \text{which yields} \\ \frac{\sqrt{k_{x1}^2}}{\tilde{\rho}_1 \left[\bar{\omega}_1^2 - \left(k_z^2 - \omega^2/c^2\right) v_{Az,1}^2\right]} &= \frac{-\sqrt{k_{x2}^2}}{\tilde{\rho}_2 \left[\bar{\omega}_2^2 - \left(k_z^2 - \omega^2/c^2\right) v_{Az,2}^2\right]}, \end{aligned} \tag{4.138}$$

where we solve for k_{xj}^2 in the single-fluid MHD dispersion relation (4.134):

$$k_{xj}^2 = \frac{v_{Az,j}^2 k_{sj}^2 \left(k_y^2 + k_z^2 - \omega^2/c^2\right) - \bar{\omega}_j^2 (k_y^2 + k_{sj}^2)}{\bar{\omega}_j^2 - v_{Az,j}^2 k_{sj}^2}, \qquad \text{where}$$

$$k_{sj}^2 \equiv k_z^2 - \frac{\bar{\omega}_j^2}{c_{sj}^2}. \tag{4.139}$$

In the limit of non-relativistic Alfven velocities, this dispersion relation reduces to the MHD Kelvin-Helmholtz dispersion relation from the previous section, and given in PK83 and KP84. Having examined the MHD regime, we now derive the corresponding dispersion relation for a tangential discontinuity in the RMHD regime.

4.6 RMHD Kelvin-Helmholtz Instability

We now wish to derive a dispersion relation for predicting the Kelvin-Helmholtz instability between two magnetized fluids in the *relativistic* regime. Our results are consistent with the dispersion relation presented in Ferrari et al. (1978 and 1980), and the results of Ray (1981) in the limit of a slab geometry. Our RMHD dispersion relation also has the correct RHD (Bodo et al. 2004), and MHD (PK83; KP84) limits.

4.6.1 RMHD Single-fluid Dispersion Relation

As we did in the non-relativistic case, we first linearize the relativistic MHD fluid equations for a single fluid:

$$
\begin{aligned}
\frac{\partial}{\partial t}\left(w\gamma^2 - P\right) + \boldsymbol{\nabla}\cdot\left(w\gamma^2\mathbf{v}\right) &= 0, \\
\frac{w}{c^2}\gamma^2\left(\frac{\partial}{\partial t} + \boldsymbol{\nabla}\cdot\mathbf{v}\right)\mathbf{v} + \left(\boldsymbol{\nabla} + \frac{\mathbf{v}}{c^2}\frac{\partial}{\partial t}\right)P &= \rho_c\mathbf{E} + \frac{\mathbf{J}}{c}\times\mathbf{B}, \\
\boldsymbol{\nabla}\times\mathbf{E} &= -\frac{1}{c}\frac{\partial\mathbf{B}}{\partial t}, \\
\boldsymbol{\nabla}\times\mathbf{B} &= \frac{\mathbf{J}}{c} + \frac{1}{c}\frac{\partial\mathbf{E}}{\partial t}, \\
\boldsymbol{\nabla}\cdot\mathbf{B} &= 0, \\
\boldsymbol{\nabla}\cdot\mathbf{E} &= \rho_c, \\
\mathbf{E} + \frac{\mathbf{v}}{c}\times\mathbf{B} &= 0, \\
\frac{\partial P}{\partial\epsilon} &= \frac{c_s^2}{c^2},
\end{aligned}
\tag{4.140}
$$

where we define the relativistic internal energy by

$$
\epsilon = \rho c^2 + \frac{P}{\Gamma - 1}, \tag{4.141}
$$

and the relativistic enthalpy by

$$
w = \rho c^2 + \frac{\Gamma}{\Gamma - 1}P = \epsilon + P. \tag{4.142}
$$

The first equation describes transport of mechanical energy, while the second equation is Euler's equation. The third through sixth equations are Maxwell's laws, the seventh equation is the assumption of infinite conductivity, and the eighth equation is the adiabatic assumption. c_s is the relativistic sound speed, given by

$$
c_s = c\sqrt{\frac{\partial P}{\partial\epsilon}} = c\sqrt{\frac{\Gamma P}{w}}. \tag{4.143}
$$

We now consider a single fluid with uniform unperturbed density $\tilde{\rho}$, uniform unperturbed pressure $\tilde{P}$, flowing with uniform unperturbed velocity $\tilde{v}_z$ in the z-direction. The fluid is immersed in a uniform unperturbed magnetic field $\tilde{B}_z$ in the z-direction. We perturb each of these quantities as follows:

$$Q(\mathbf{r},t) \;=\; \tilde{Q} + \delta Q e^{i(\mathbf{k}\cdot\mathbf{r}-\omega t)}. \tag{4.144}$$

The process of linearizing the equations is greatly simplified by assuming that the magnetic field and flow direction are both aligned. Because of this, there is no unperturbed electric field. Therefore, the linearized Lorentz force due to the electric field is zero:

$$\begin{aligned}\delta\left(\rho_c\mathbf{E}\right) \;&=\; \delta\left[\left(\boldsymbol{\nabla}\cdot\mathbf{E}\right)\mathbf{E}\right] \\ &=\; \left(\mathbf{k}\cdot\delta\mathbf{E}\right)\tilde{\mathbf{E}} \;=\; \left(\mathbf{k}\cdot\delta\mathbf{E}\right)\left(\tilde{\mathbf{B}}\times\frac{\tilde{\mathbf{v}}}{c}\right) \;=\; \left(\mathbf{k}\cdot\delta\mathbf{E}\right)\left(\tilde{B}_y\frac{\tilde{v}_z}{c}\right) \;=\; 0.\end{aligned} \tag{4.145}$$

For purposes of linearization, we would like to write the fluid equations entirely in terms of ρ, P, w, $\mathbf{v}$, and $\mathbf{B}$. We do this as follows:

$$\begin{aligned}\frac{\partial}{\partial t}\left(w\gamma^2 - P\right) + \boldsymbol{\nabla}\cdot\left(w\gamma^2\mathbf{v}\right) \;&=\; 0, \\ \frac{w}{c^2}\gamma^2\left(\frac{\partial}{\partial t} + \boldsymbol{\nabla}\cdot\mathbf{v}\right)\mathbf{v} + \left(\boldsymbol{\nabla} + \frac{\mathbf{v}}{c^2}\frac{\partial}{\partial t}\right)P \;&=\; -\frac{\boldsymbol{\nabla}\left(B^2\right)}{2} + \left(\mathbf{B}\cdot\boldsymbol{\nabla}\right)\mathbf{B} + h_1, \\ \frac{\partial\mathbf{B}}{\partial t} \;&=\; \left(\mathbf{B}\cdot\boldsymbol{\nabla}\right)\mathbf{v} - \mathbf{B}\left(\boldsymbol{\nabla}\cdot\mathbf{v}\right) - \left(\mathbf{v}\cdot\boldsymbol{\nabla}\right)\mathbf{B}, \\ \frac{\partial P}{\partial\epsilon} \;&=\; \frac{c_s^2}{c^2},\end{aligned} \tag{4.146}$$

where

$$h_1 \equiv\; \frac{1}{c^2}\left[\frac{\partial\mathbf{B}}{\partial t}\left(\mathbf{B}\cdot\mathbf{v}\right) - \mathbf{v}\left(\mathbf{B}\cdot\frac{\partial\mathbf{B}}{\partial t}\right) + \mathbf{B}\left(\mathbf{B}\cdot\frac{\partial\mathbf{v}}{\partial t}\right) - \frac{\partial\mathbf{v}}{\partial t}B^2\right]. \tag{4.147}$$

Upon substituting the linearizations (4.144) into (4.146), the fluid equations become

$$\begin{aligned}
\frac{\delta P}{\delta \epsilon} &= \frac{c_s^2}{c^2}, \\
\left(\frac{\omega - \gamma^2\bar{\omega}}{c^2} - \frac{\gamma^2\bar{\omega}}{c_s^2}\right)\delta P + \gamma^2\frac{\tilde{w}}{c^2}\mathbf{k}\cdot\delta\mathbf{v} &= 2\frac{\tilde{w}}{c^2}\bar{\omega}\gamma^4\frac{\tilde{v}_z\delta v_z}{c^2}, \\
-\frac{\tilde{w}}{c^2}\gamma^2\left(\omega - k_z\tilde{v}_z\right)\delta\mathbf{v} + \left(\mathbf{k} - \omega\frac{\tilde{\mathbf{v}}}{c^2}\right)\delta P &= -\mathbf{k}\left(\tilde{\mathbf{B}}\cdot\delta\mathbf{B}\right) + \left(\tilde{\mathbf{B}}\cdot\mathbf{k}\right)\delta\mathbf{B} + \delta h_1, \qquad (4.148) \\
-\left(\omega - k_z\tilde{v}_z\right)\delta\mathbf{B} &= \left(\tilde{\mathbf{B}}\cdot\mathbf{k}\right)\delta\mathbf{v} - \tilde{\mathbf{B}}\left(\mathbf{k}\cdot\delta\mathbf{v}\right),
\end{aligned}$$

where

$$\delta h_1 = \frac{\omega}{c^2}\left[-\tilde{B}_z\tilde{v}_z\delta\mathbf{B} + \tilde{\mathbf{v}}\left(\tilde{\mathbf{B}}\cdot\delta\mathbf{B}\right) - \tilde{\mathbf{B}}\left(\tilde{\mathbf{B}}\cdot\delta\mathbf{v}\right) + \delta\mathbf{v}\tilde{B}^2\right]. \qquad (4.149)$$

Because the fluid is relativistic, the total pressure it experiences should incorporate both the magnetic and electric fields:

$$P_b = P + \frac{E^2 + B^2}{2}. \qquad (4.150)$$

However, because the unperturbed electric field is zero, the electric field does not appear in the total pressure perturbation, which therefore is the same as its non-relativistic counterpart:

$$\delta P_b = \delta P + \tilde{\mathbf{B}}\cdot\delta\mathbf{B}. \qquad (4.151)$$

By solving the linearized equations (4.148), we find that the primitive variable perturbations are related as follows to the electromagnetic pressure perturbation:

$$
\begin{aligned}
\delta P &= \frac{\gamma^2\bar{\omega}^2 - v_{Az}^2(k^2-\omega^2/c^2)}{\gamma^2\bar{\omega}^2 - v_{Az}^2\left(k_z^2-\omega^2/c^2\right)}\delta P_b, \\
\delta\rho &= \left[\frac{1}{c_s^2} - \frac{1}{c^2\left(\Gamma-1\right)}\right]\frac{\gamma^2\bar{\omega}^2 - v_{Az}^2(k^2-\omega^2/c^2)}{\gamma^2\bar{\omega}^2 - v_{Az}^2\left(k_z^2-\omega^2/c^2\right)}\delta P_b, \\
\delta v_x &= \frac{\bar{\omega}k_x}{\tilde{w}\left[\gamma^2\bar{\omega}^2 - v_{Az}^2\left(k_z^2-\omega^2/c^2\right)\right]}\delta P_b, \\
\delta v_y &= \frac{\bar{\omega}k_y}{\tilde{w}\left[\gamma^2\bar{\omega}^2 - v_{Az}^2\left(k_z^2-\omega^2/c^2\right)\right]}\delta P_b, \\
\delta v_z &= \frac{\left[\gamma^2\bar{\omega}^2 - v_{Az}^2(k^2-\omega^2/c^2)\right]k_z'}{\tilde{w}\gamma^2\bar{\omega}\left[\gamma^2\bar{\omega}^2 - v_{Az}^2\left(k_z^2-\omega^2/c^2\right)\right]}\delta P_b, \\
\delta B_x &= -\frac{k_x k_z v_{Az}}{\sqrt{\tilde{w}}\left[\gamma^2\bar{\omega}^2 - v_{Az}^2\left(k_z^2-\omega^2/c^2\right)\right]}\delta P_b, \\
\delta B_y &= -\frac{k_y k_z v_{Az}}{\sqrt{\tilde{w}}\left[\gamma^2\bar{\omega}^2 - v_{Az}^2\left(k_z^2-\omega^2/c^2\right)\right]}\delta P_b, \\
\delta B_z &= \frac{(k_x^2+k_y^2)v_{Az}}{\sqrt{\tilde{w}}\left[\gamma^2\bar{\omega}^2 - v_{Az}^2\left(k_z^2-\omega^2/c^2\right)\right]}\delta P_b,
\end{aligned}
\tag{4.152}
$$

where

$$
\begin{aligned}
c_s^2 &= c^2\frac{\Gamma\tilde{P}}{\tilde{w}}, \\
v_{Az} &= (c)\frac{\tilde{B}_z}{\sqrt{\tilde{w}}}, \\
\bar{\omega} &\equiv \omega - k_z\tilde{v}_z, \\
k_z' &\equiv \gamma\left(k_z - \frac{\omega\tilde{v}_z}{c^2}\right).
\end{aligned}
\tag{4.153}
$$

We also obtain the following single-fluid RMHD dispersion relation for a flow-aligned unperturbed magnetic field:

$$
\gamma^4\bar{\omega}^4 - \gamma^2\bar{\omega}^2\left[(k_x^2+k_y^2+k_z'k_z')c_s^2 + \left(k^2-\frac{\omega^2}{c^2}\right)v_{Az}^2\right] + c_s^2v_{Az}^2k_z'k_z'\left(k^2-\frac{\omega^2}{c^2}\right) = 0. \tag{4.154}
$$

In the non-relativistic limit, this dispersion relation reduces to the MHD single-fluid dispersion relation given in the previous section, and in LRN09. The above dispersion

relation can also be written in the form

$$\gamma^2\bar{\omega}^2(k_x^2+k_y^2+k_s^2)-v_{Az}^2k_s^2\left(k^2-\frac{\omega^2}{c^2}\right) \;=\; 0, \tag{4.155}$$

where

$$k_s^2 \;\equiv\; \gamma^2\left(k_z-\frac{\omega\tilde{v}_z}{c^2}\right)^2-\gamma^2\frac{\bar{\omega}^2}{c_s^2}. \tag{4.156}$$

4.6.2 The Relativistic Magnetized Kelvin-Helmholtz Instability

We now introduce a discontinuity at $x = 0$, so that there are two fluids, each with its own unperturbed density, pressure, z-directed flow velocity, and z-directed magnetic field. From the first boundary condition at the interface, the total electromagnetic pressure must be equal on both sides of the interface. This must therefore also hold for the electromagnetic pressure perturbation:

$$\delta P_{b1} \;=\; \delta P_{b2}. \tag{4.157}$$

The perturbation amplitudes are computed by applying equations (4.152) separately to each fluid, with δP_b, k_y, and k_z the same in both fluids. In particular, the normal velocity perturbation in fluid j is

$$\delta v_{xj} \;=\; \frac{\bar{\omega}_j k_{xj}}{\tilde{w}_j\left[\gamma_j^2\bar{\omega}_j^2-v_{Az,j}^2\left(k_z^2-\omega^2/c^2\right)\right]}\delta P_b. \tag{4.158}$$

We now invoke the second boundary condition, and equate the normal fluid displacements on either side of the interface (Chandrasekhar 1961). The resulting dispersion relation is

$$\begin{aligned} \frac{\delta v_{x1}}{\bar{\omega}_1} &= \frac{\delta v_{x2}}{\bar{\omega}_2}, \qquad \text{which yields} \\ \frac{\sqrt{k_{x1}^2}}{\tilde{w}_1 \left[\gamma_1^2 \bar{\omega}_1^2 - (k_z^2 - \omega^2/c^2)\, v_{Az,1}^2\right]} &= \frac{-\sqrt{k_{x2}^2}}{\tilde{w}_2 \left[\gamma_2^2 \bar{\omega}_2^2 - (k_z^2 - \omega^2/c^2)\, v_{Az,2}^2\right]}, \end{aligned} \tag{4.159}$$

where we solve for k_{xj}^2 in the single-fluid RMHD dispersion relation derived above:

$$\begin{aligned} k_{xj}^2 &= \frac{v_{Az,j}^2 k_{sj}^2 \left(k_y^2 + k_z^2 - \omega^2/c^2\right) - \gamma_j^2 \bar{\omega}_j^2 (k_y^2 + k_{sj}^2)}{\gamma_j^2 \bar{\omega}_j^2 - v_{Az,j}^2 k_{sj}^2}, \qquad \text{where} \\ k_{sj}^2 &\equiv \gamma_j^2 \left(k_z - \frac{\omega \tilde{v}_{zj}}{c^2}\right)^2 - \gamma_j^2 \frac{\bar{\omega}_j^2}{c_{sj}^2}. \end{aligned} \tag{4.160}$$

This dispersion relation is consistent with the one presented in Ferrari et al. (1978 and 1980), and the dispersion relation presented by Ray (1981) in the limit of a slab geometry. In the limit of no magnetic field, it reduces to the RHD dispersion relation in Bodo et al. (2004). In the non-relativistic magnetized limit, this dispersion relation reduces to the MHD Kelvin-Helmholtz dispersion relation from the previous section, which is consistent with PK83 and KP84, and Southwood (1968).

We have now derived dispersion relations for a tangential discontinuity between two flows in each of the four regimes, namely HD, RHD, MHD, and RMHD. We now proceed to numerically solve the RMHD dispersion relation, and examine the stability properties of the resulting linear modes.

4.7 Numerical Solution to the RMHD Dispersion Relation

We now wish to numerically solve the RMHD dispersion relation for predicting the Kelvin-Helmholtz instability, derived in the previous section. This will allow us to characterize the

influence of the magnetic field and flow speed on the stability of the system. We restrict the foregoing analysis to flow-aligned perturbations (i.e., perturbations for which $k_y = 0$), as this is the criterion satisfied by the perturbations in which we will later launch our numerical simulations. We find that, as with the MHD case, for flow-aligned perturbations there is generally a range of unstable flow speeds, bounded by a lower and an upper-critical flow speed. We then determine the dependence of these critical flow speeds on the magnetic field strength. We find that the magnetic field eliminates the instability if the magnetic pressure is greater than the thermal pressure. We compare these results to non-relativistic (NR) cases, and find that in the NR flow-aligned case, the magnetic field eliminates the instability when the magnetic pressure comprises only 40% of the total pressure, compared to 50% in the relativistic case. We then generate growth rate results for the sound speed of $0.57\,c$ and the wave number of 0.8 inverse light seconds used in the numerical simulations. These results can be compared with the numerical growth rates generated in chapter 6 for the sech^2 velocity profile.

We first wish to characterize the dependence of ω and the normal wave vector k_x on flow velocity. We will find many similarities with the relativistic unmagnetized case presented in section 4.2, which contributes to the validation of our analysis. We consider the following scenario:

$$\begin{aligned} k_z &= 2\ c^{-1}(1\ \mathrm{s})^{-1}, \qquad k_y = 0, \\ \tilde{\rho} &= 0.5 \times 10^{-24}\ \mathrm{g/cm}^{-3}, \\ \tilde{P} + \frac{\tilde{B}^2}{2} &= 10\,c^2 \times 10^{-24}\ \mathrm{g/cm}^{-3}, \\ \tilde{v}_{z1} &= \tilde{v}_z, \qquad \tilde{v}_{z2} = -\tilde{v}_z. \end{aligned} \tag{4.161}$$

In the studies that follow, we vary the magnetic field, thus varying the magnetic pres-

sure and thermal pressure, but keeping the total pressure at a constant value of $10\,c^2 \times 10^{-24}$ g/cm^{-3}. To represent the fraction of total pressure consisting of magnetic pressure, we define the parameter

$$\alpha_B \;=\; \frac{\tilde{B}^2/2}{\tilde{P}+\tilde{B}^2/2} \;=\; \frac{1}{\beta+1}, \tag{4.162}$$

where $\beta = 2\tilde{P}/\tilde{B}^2$ is the plasma β. When the magnetic field is increased, keeping total pressure constant, the plasma β decreases. We can also write

$$\beta \;=\; \frac{1}{\alpha_B} - 1. \tag{4.163}$$

In figures 4.12(a) and (b), we plot the real and imaginary frequencies, as a function of flow speed (equal and opposite in each fluid), for an (a) weak field ($\beta = 9$) and (b) strong field ($\beta = 2.33$). In figures 4.13(a) and (b), we plot the real and imaginary values of k_x in fluid 1, as a function of flow speed, for an (a) weak and (b) strong field. In figures 4.14(a) and (b), we plot the real and imaginary values of k_x in fluid 2, as a function of flow speed, for an (a) weak and (b) strong field. As these graphs show, the increase in the magnetic field decreases the interval of unstable flow speeds, and also decreases the maximum absolute imaginary parts of ω and k_x in the region of unstable flow speeds. This latter value is close to the local maximum value of the real part of k_x in fluid 1, reached at the maximum unstable flow speed. In the limit of no magnetic field, these values are equal to k_z, the wave vector component along the flow direction. However, the magnetic field has little effect on the behavior of the real part of the normal wave vector at highly relativistic flow speeds. It seems that regardless of the strength of the magnetic field, as the Lorentz factor increases in the stable region, the

real normal wave vector in region 2 approaches infinity, while the real normal wave vector in fluid 1 approaches 0. This means that, for any magnetic field strength, highly relativistic flow speeds can excite modes at arbitrarily small wavelengths, i.e., wavelengths which would be too small to be resolved by the grid used in a numerical simulation. This is one possible manifestation of numerical destabilization at highly relativistic flow speeds.

Recall that in the unmagnetized case, in the *unstable region* only, the real parts of k_x are equal, while the imaginary parts of k_x are equal and opposite. We expect to observe this in the magnetized case as well, as long as the magnetic fields are equal in both fluids. This is indeed observed, as shown by figures 4.13 and 4.14. In the region of low flow speeds, $k_{x1,i}$ and $k_{x2,i}$ approach either 2 or -2 inverse light seconds, while $k_{x1,r} = 0$ and $k_{x2,r} = 0$. Recall that $k_z = 2$ inverse light seconds. Therefore, we see that we have a region of low flow speeds where, for fluids $j = 1, 2$,

$$k_{xj}^2 + k_y^2 + k_z^2 \;=\; 0. \tag{4.164}$$

Recall that in this case $k_y = 0$. The above equation corresponds to the limit of an incompressible fluid. Such a limit can only exist at non-relativistic flow speeds. We finally observe that the basic properties of the ω and k_x curves are the same as those of the corresponding curves presented in section 4.2 for the unmagnetized relativistic case. As described above, the magnetic field merely modifies the extent to which these properties are observed.

In figures 4.15, we plot certain quantities as functions of α_B, where α_B varies from 0 (no magnetic field, infinite β) to 0.495 (0.5 corresponds to equal magnetic and thermal pressure, i.e., $\beta = 1$). Recall that α_B is proportional to the amount of magnetic pressure,

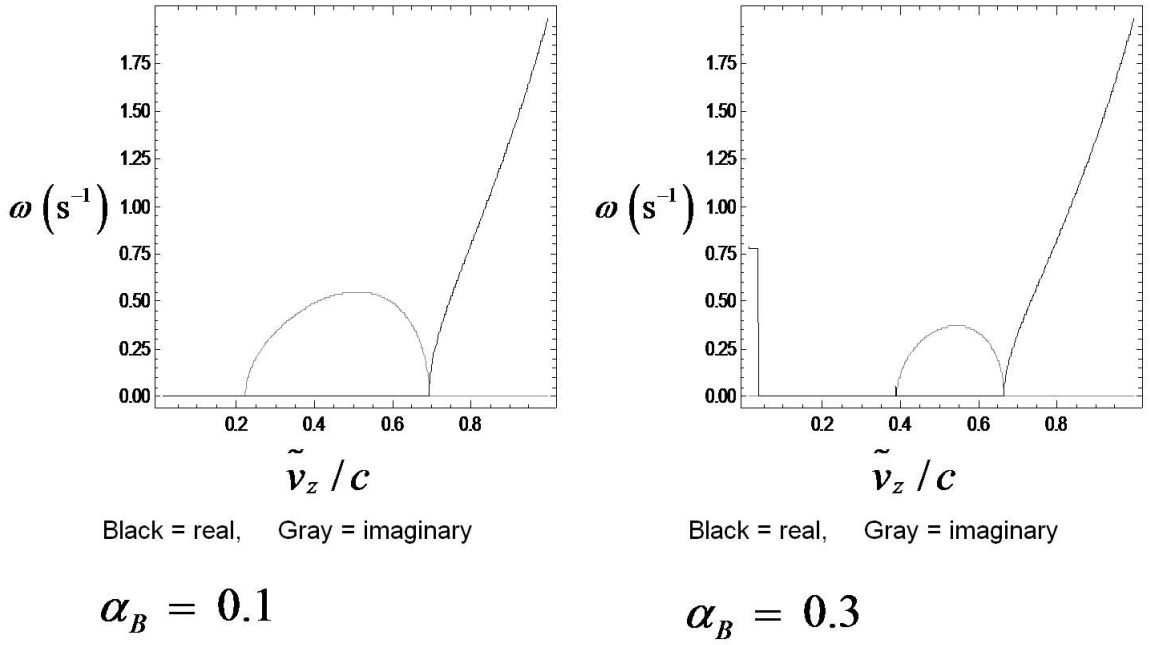

Figure 4.12: Frequencies (RMHD) for (a) $\beta = 9$ and (b) $\beta = 2.33$

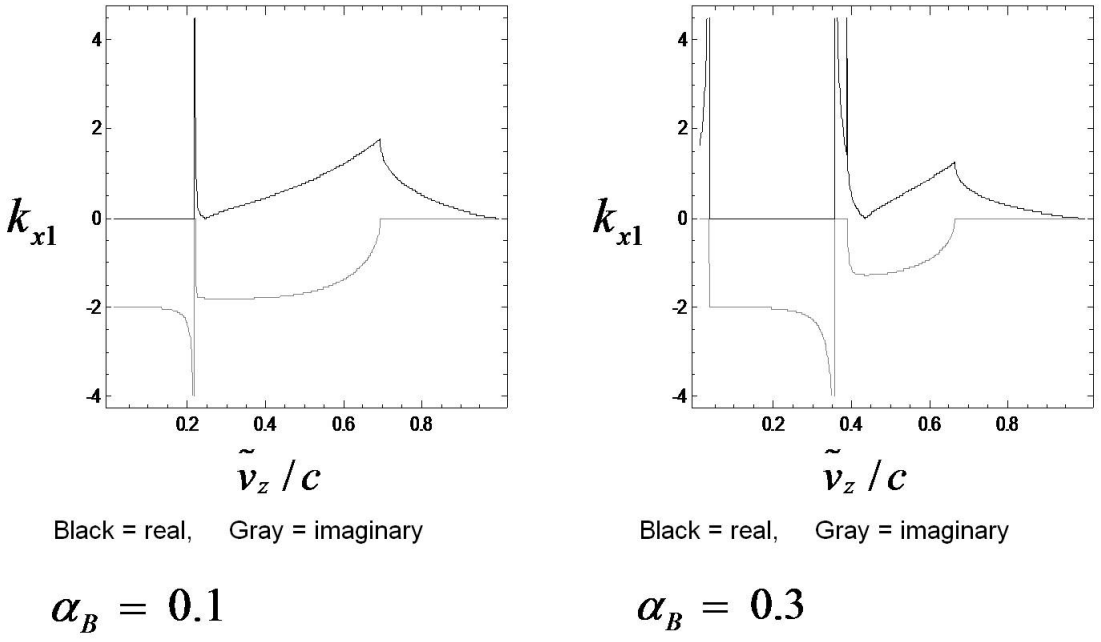

Figure 4.13: k_x in fluid 1 (RMHD) for (a) $\beta = 9$ and (b) $\beta = 2.33$

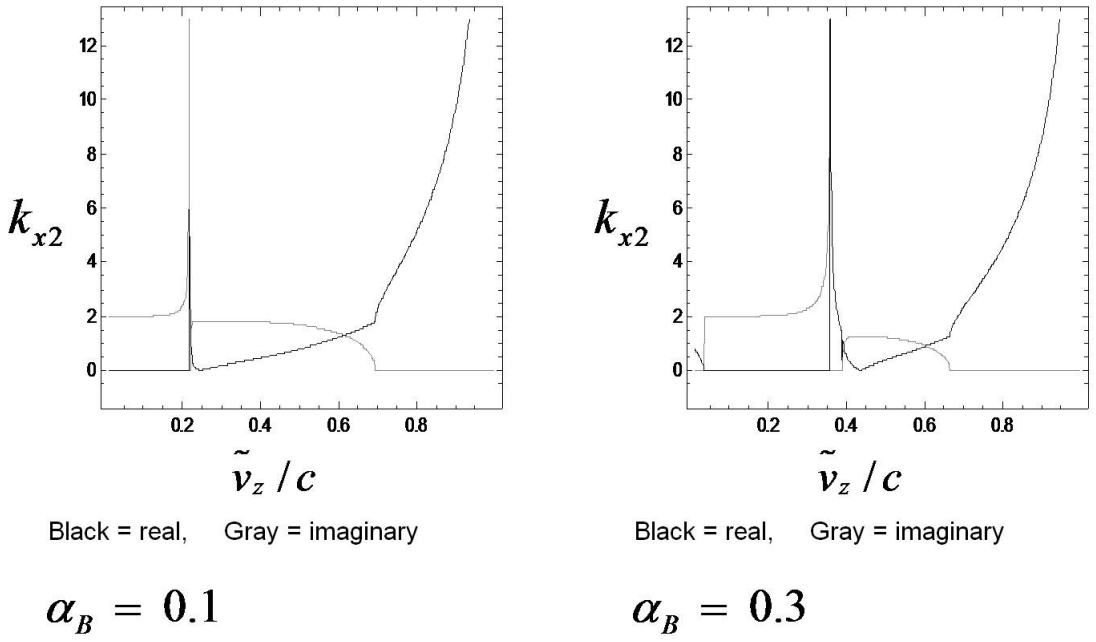

Figure 4.14: k_x in fluid 2 (RMHD) for (a) $\beta = 9$ and (b) $\beta = 2.33$

or strength of the magnetic field. Figure 4.15(a) shows the maximum growth rate as a function of α_B. Figure 4.15(b) shows three critical flow speeds as functions of α_B. The bottom curve is the lower-critical, or minimum unstable, flow speed. The middle curve is the flow speed corresponding to maximum growth. The top curve is the upper-critical, or maximum unstable, flow speed. The unstable region is therefore the region between the bottom and top curves. As the magnetic field increases (increasing α_B), the lower and upper-critical flow speeds move closer together, approaching equality as α_B approaches 0.5 ($\beta \to 1$). The maximum growth rate also decreases, approaching zero as α_B approaches 0.5 ($\beta \to 1$). This demonstrates the ability of the magnetic field to not only reduce but eliminate the Kelvin-Helmholtz instability in the relativistic regime for flow-aligned perturbations. Furthermore, there is no Kelvin-Helmholtz instability predicted by linear theory for flow-

aligned perturbations in the magnetically dominated ($\alpha_B > 0.5$, i.e., $\beta < 1$) relativistic regime. These results are consistent with Ferrari et al. (1980), and with Ray (1981), in the limit of a slab geometry.

We now present results for the corresponding case in the *non-relativistic* regime. Instead of being in units of c, speeds are now in units of c_0, where we choose $c_0 = 0.001\,c$. Correspondingly, lengths are in units of thousandths of a light second. The parameters are now

$$\begin{aligned} k_z &= 2\,c_0^{-1}(1\text{ s})^{-1}, \qquad k_y = 0, \\ \rho_0 &= 0.5\times 10^{-24}\text{ g/cm}^{-3}, \\ P_{\rm tot} &= \tilde{P} + \frac{\tilde{B}^2}{2} = 10\,c_0^2\times 10^{-24}\text{ g/cm}^{-3}, \\ \tilde{v}_{z1} &= \tilde{v}_z, \qquad \tilde{v}_{z2} = -\tilde{v}_z. \end{aligned} \tag{4.165}$$

We vary the fractional magnetic pressure α_B, and with each value we adjust the density so that the ratio of flow speed to sound speed and ratio of flow speed to Alfven speed are the same as the corresponding relativistic values. That is, we do the following for each α_B:

$$\begin{aligned} \tilde{P} &= (1-\alpha_B)P_{\rm tot}, \qquad \tilde{B}_z = \sqrt{2\alpha_B P_{\rm tot}}, \\ c_s &= \sqrt{\frac{\Gamma\tilde{P}}{\tilde{\rho}}}, \qquad v_{Az} = \frac{\tilde{B}_z}{\sqrt{\tilde{\rho}}}. \end{aligned} \tag{4.166}$$

We now present, in figures 4.16, the *non-relativistic* plots as functions of α_B, and compare these to the above relativistic plots. We see that the qualitative behavior is the same for the growth rate and critical speeds. However, in the non-relativistic case, the instability is quenched out at a smaller value of $\alpha_B = 0.4$ ($\beta = 1.5$), where in the relativistic case this

occurs at $\alpha_B = 0.5$ ($\beta = 1$). If in each case we normalize α_B relative to its instability-suppressing value, the values of the growth rates and critical speeds are quite similar in the relativistic and non-relativistic cases. In fact, in both the non-relativistic and relativistic cases, a comparison of figures 4.15(b) and 4.16(b) shows that the three critical speeds converge to a normalized value of around 0.57, which is approximately equal to $1/\sqrt{3}$. This is equal to the maximum allowable relativistic sound speed of $c/\sqrt{3}$.

Again, for the *non-relativistic* case, we present graphs, in figures 4.17, of the frequency and normal wave vector k_x as functions of the flow velocity. As with the relativistic case, the real part is the black curve while the imaginary part is the gray curve. The behavior is similar qualitatively to the corresponding curves in the relativistic case. In both cases, as the flow speed increases in the stable region, the normal wave vector in region 1 decreases to zero, while that in region 2 increases monotonically. However, in the non-relativistic case, the rate of increase of k_{x2} is slower, and bounded. In the relativistic case, k_{x2} blows up with the Lorentz factor as the flow speed approaches c.

We now return to the relativistic case, and for purposes of future comparisons with numerical growth rates, we keep the thermal pressure constant, rather than the magnetic plus thermal pressure. We consider a sound speed $c_s = 0.57\,c$, near its relativistic limit of $c/\sqrt{3}$, and a wave number $k_z = 0.8$ inverse light seconds ($k_y = 0$), which are the parameters used in the numerical simulations, though the simulations use a different (sech^2) velocity profile. We first plot the growth rate as a function of Alfven speed for different bulk flow speeds. We recall the relationship between the flow velocities v_{z0} and $-v_{z0}$ in the stationary frame, and the flow velocity u_{z0} of one flow relative to the other:

$$u_{z0} \;=\; \frac{2v_{z0}}{1+v_{z0}^2/c^2}. \tag{4.167}$$

For purposes of later comparison with numerical growth rates, the relative flow velocity is more applicable than the velocities in the stationary frame. Figures 4.18 show the growth rates as a function of Alfven velocity v_{Az}/c, where each curve corresponds to a specific flow speed u_{z0}.

We note that for each flow speed, there is a critical Alfven velocity above which the system is stabilized. Chandrasekhar (1961) predicted that for an incompressible fluid, the ratio of relative flow speed to critical Alfven speed is $\sqrt{2}$. We see from figures 4.18 that in our model, this ratio is consistently less than $\sqrt{2}$. This is due, in part, to the stabilizing effects of compressibility. We will observe the same phenomenon when we examine, in chapter 6, the numerical growth rates obtained with a sech^2 velocity profile.

We now plot, in figures 4.19, the scaled growth rate (relative to maximum) as a function of the inverse relativistic Alfvenic Mach number in the co-moving frame of one fluid. We define this Mach number by

$$M_{A,\mathrm{rel}} \;=\; \frac{u_{z0}\gamma_u}{v_{Az}\gamma_A} \;=\; \frac{u_{z0}}{v_{Az}}\sqrt{\frac{1-v_{Az}^2/c^2}{1-u_{z0}^2/c^2}}, \tag{4.168}$$

where γ_u and γ_A are the Lorentz factors corresponding to u_{z0} and v_{Az}, respectively. Our definition of M_A is analogous to the definition of a relativistic sonic Mach number in Bodo et al. (2004). When we plot numerical growth rates for the sech^2 velocity profile in chapter 6, we will discover that the influence of the magnetic field on the growth curve is heavily dependent on the relativistic Alfvenic Mach number M_A, so that the growth curves for different flow

speeds very nearly overlay one another when plotted as a function of M_A^{-1}. Figures 4.19 show that this does not occur for the case of a step-function discontinuity.

We now plot, in figures 4.20, the growth rate as a function of flow velocity, where each curve corresponds to a specific Alfven speed. The left graph is plotted as a function of the flow speed v_{z0} in the stationary frame, while the right graph is plotted as a function of the relative flow speed u_{z0}. We see that for each Alfven speed, there is a lower and upper-critical flow velocity for instability, and that as the Alfven speed (magnetic field strength) increases, the lower-critical velocity increases, and the upper-critical velocity decreases, though the former effect is more pronounced than the latter. As field strength increases, the region of instability shrinks, and the growth rates decrease.

We now consider the dependence of growth rate on the relativistic Mach number M_s in the stationary frame (left graph), and $M_{s,\mathrm{rel}}$ in the frame of one fluid relative to the other (right graph). Recall that these are given by

$$M_s = \frac{v_{z0}\gamma}{c_s\gamma_s} = \frac{v_{z0}}{c_s}\sqrt{\frac{1-c_s^2/c^2}{1-v_{z0}^2/c^2}}, \tag{4.169}$$

$$M_{s,\mathrm{rel}} = \frac{u_{z0}\gamma_u}{c_s\gamma_s} = \frac{u_{z0}}{c_s}\sqrt{\frac{1-c_s^2/c^2}{1-u_{z0}^2/c^2}}. \tag{4.170}$$

The maximum upper-critical Mach number, occurring in the unmagnetized case (black curve), has a value of $\sqrt{2}$ in the stationary frame (left graph), and 4 in the co-moving frame of one fluid (right graph). These results are in agreement with Bodo et al. (2004) (again, for flow-aligned perturbations). We will see, when we examine numerical growth rates for a continuous velocity profile (the sech^2 profile) in chapter 6, that there is growth at Mach numbers much larger than the aforementioned upper-critical value of 4.

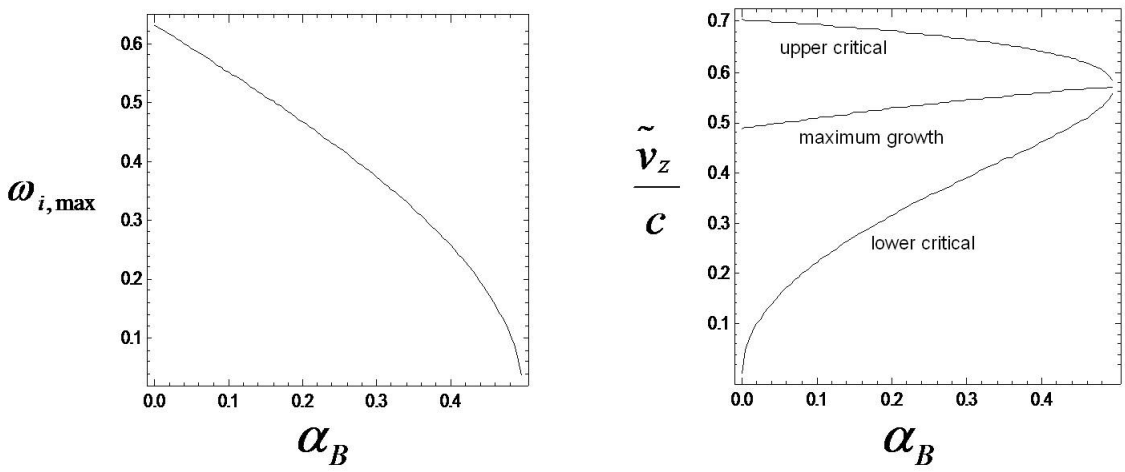

Figure 4.15: Max. growth rate and critical flow speeds vs field strength (RMHD)

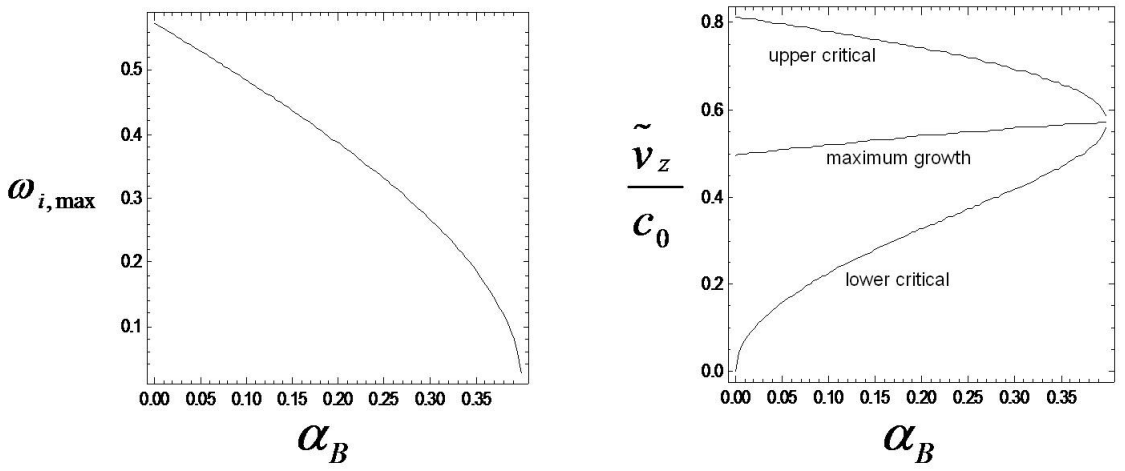

Figure 4.16: Max. growth rate and critical flow speeds vs field strength (MHD)

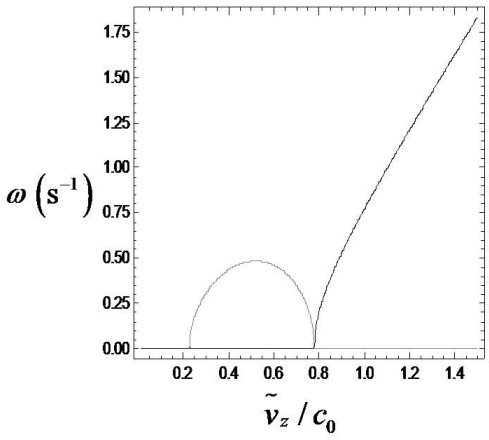

(a)

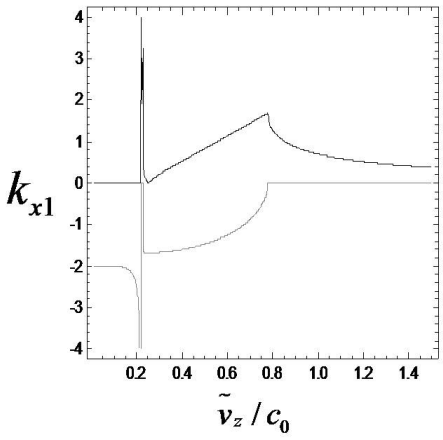

(b)

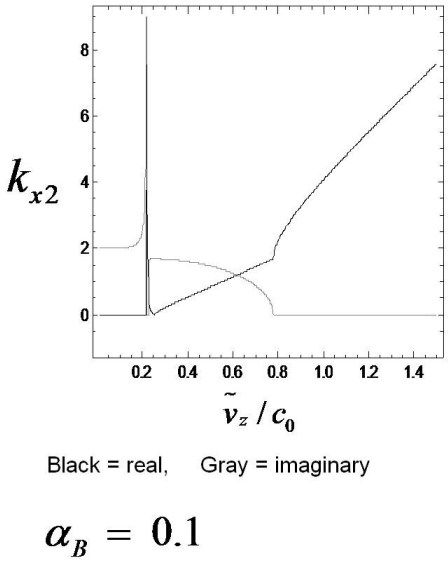

(c)

Figure 4.17: ω and k_x vs flow speed (MHD)

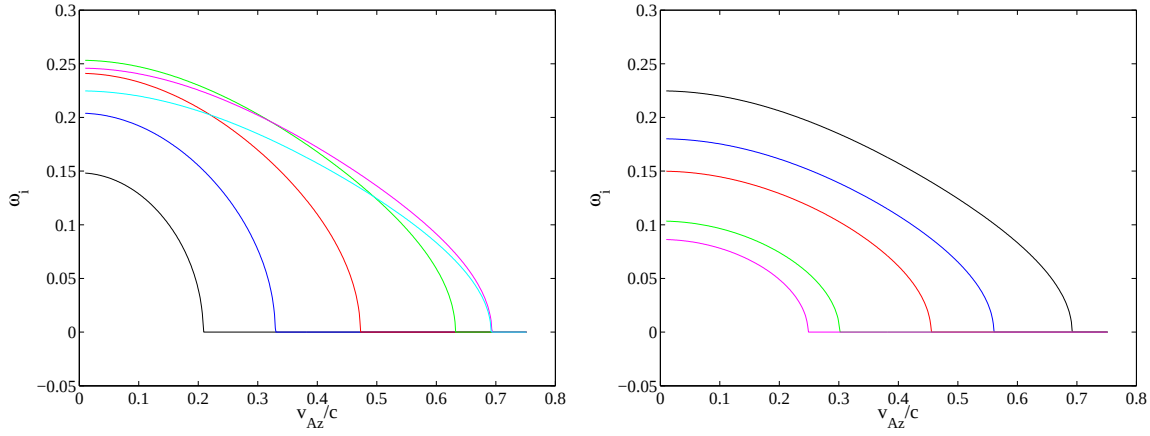

Figure 4.18: Growth rate vs Alfven speed at different flow speeds (RMHD)
left: $u_{z0}/c = 0.38$ (black), 0.55 (blue), 0.69 (red),
0.8 (green), 0.84 (magenta), 0.88 (cyan)
right: $u_{z0}/c = 0.88$ (black), 0.91 (blue), 0.92 (red), 0.935 (green), 0.937 (magenta)

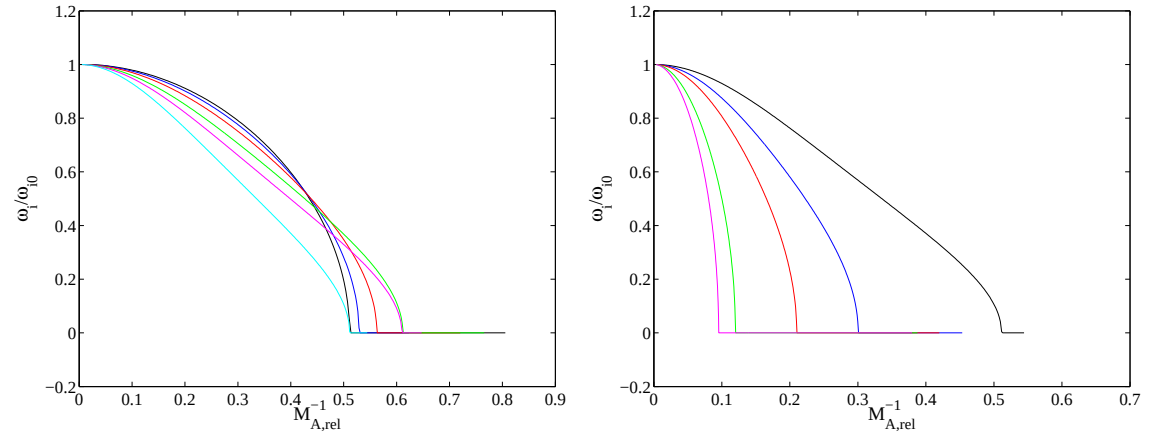

Figure 4.19: Growth rate vs M_A^{-1} at different flow speeds (RMHD)
left: $u_{z0}/c = 0.38$ (black), 0.55 (blue), 0.69 (red),
0.8 (green), 0.84 (magenta), 0.88 (cyan)
right: $u_{z0}/c = 0.88$ (black), 0.91 (blue), 0.92 (red), 0.935 (green), 0.937 (magenta)

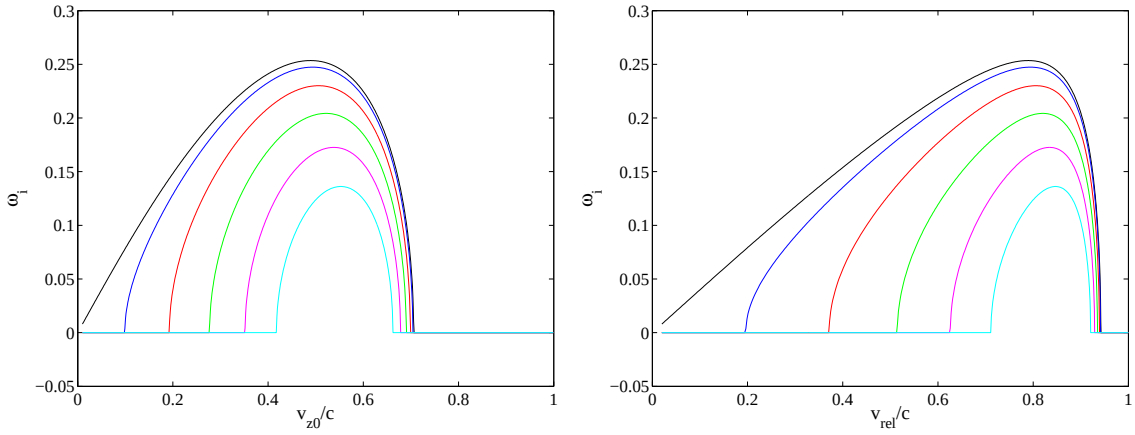

(a) stationary frame (b) co-moving frame

Figure 4.20: Growth rate vs flow speed at different Alfven speeds (RMHD)
$v_{Az}/c = 0$ (black), 0.1 (blue), 0.2 (red), 0.3 (green), 0.4 (magenta), 0.5 (cyan)

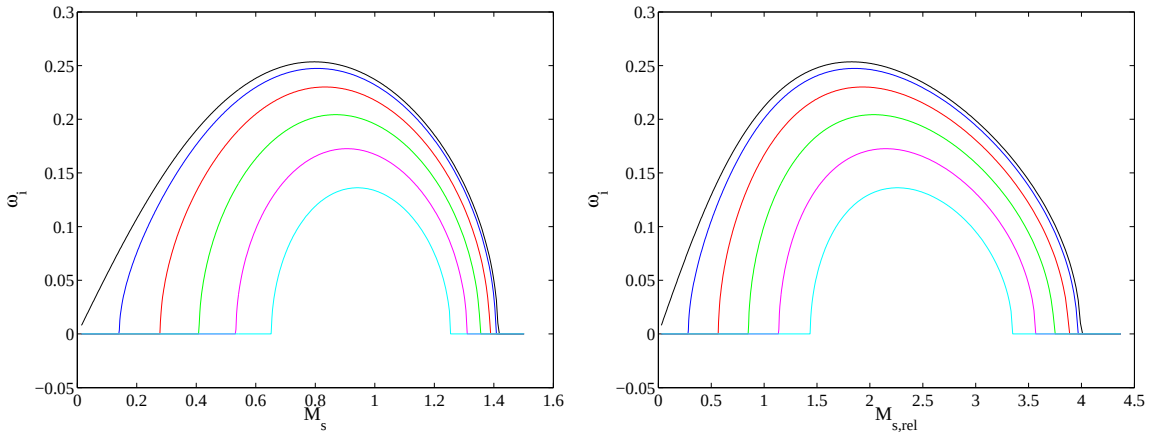

(a) stationary frame (b) co-moving frame

Figure 4.21: Growth rate vs Mach number at different Alfven speeds (RMHD)
$v_{Az}/c = 0$ (black), 0.1 (blue), 0.2 (red), 0.3 (green), 0.4 (magenta), 0.5 (cyan)

4.8 Conclusion

We have studied the KH instability for a step-function discontinuity in the HD, RHD, MHD, and RMHD regimes, in each case deriving dispersion relations which agree with familiar results. We restricted much of our analysis to flow-aligned perturbations, as these are the perturbations in which our numerical simulations will be launched. In the HD regime, we have recovered the familiar result that instability is suppressed when the Mach number, defined in terms of the equal and oppositely directed flow speed in each fluid, exceeds $\sqrt{2}$. In the RHD regime, we have recovered the result of Bodo et al. (2004), which states that for flow-aligned perturbations, instability is suppressed when a relativistic version of this Mach number exceeds $\sqrt{2}$, which, in the rest frame of one fluid, corresponds to a critical Mach number of 4. When, in chapter 6, we examine growth rates for the sech^2 velocity profile used in the numerical simulations, we will see that instability to flow-aligned perturbations extends to Mach numbers much larger than 4. In the MHD regime, we have recovered the results of PK83 and KP84, showing that for a given perturbation orientation, a magnetic field introduces a non-zero lower and upper-critical flow speed for instability, where the lower-critical flow speed is accurately predicted by the growth rate expression for an incompressible fluid.

In the RMHD regime, we have examined the case for which the background magnetic field, and perturbation wave vector, are both aligned with the flow, as this is the geometry we will later employ on our simulations. We have shown that, in both RMHD and MHD regimes, as field strength increases, the maximum growth rate decreases, as does the region of unstable flow speeds, where the lower-critical flow speed increases more rapidly than the upper-critical

flow speed. In the RMHD case, the magnetic field completely suppresses the instability when the plasma β is less than 1, i.e., when magnetic pressure exceeds thermal pressure. In the MHD case, this complete suppression occurs for $\beta < 1.5$. This is qualitatively similar to what we will see in chapter 6 for a sech^2 profile. However, we will see that in the case of a sech^2 profile, the dependence of growth rate on field strength is heavily correlated with a relativistic version of the Alfvenic Mach number, which we have seen is not the case for a step-function discontinuity. Also, for a step-function discontinuity, growth rate increases linearly with perturbation wave number. For a shear profile, such as the sech^2 profile, we will see in chapter 6 that there is a critical wave number corresponding to maximum growth.

For the RHD, MHD, and RMHD regimes, in the frame of equal and opposite flow speeds, we also examined the behavior of the normal wave vectors k_x in each fluid. We found that the region of instability exhibits Hermiticity, in that k_x in this region has equal real parts and equal and opposite imaginary parts, between the two flows. However, in the stable region, k_x in one region approaches infinity as the flow speed approaches the speed of light. This supports the notion that highly relativistic flows tend to produce modes with very small wavelengths, i.e., too small to be resolved by a numerical grid. This will also manifest in the growth rate behavior to be discussed for the sech^2 profile in chapter 6. All of this is associated with the desynchronization between longitudinal and transverse motions that occurs in highly relativistic flows, leading to numerical instability.

We finally recall that we encountered the value $\sqrt{2}$ in two different instances: as the maximum KH-unstable Mach number in the HD and RHD cases, for flow-aligned perturbations, and also as the minimum Alfvenic Mach number for KH instability in the incompressible

limit of the MHD case. This is correlated with the fact that our system is two-dimensional, exhibiting variation in the flow direction, and normal to the fluid interface. $\sqrt{2}$ is a common result in two-dimensional systems, which makes intuitive sense when we view this value as the hypotenuse of a right triangle whose legs each have a length of 1. We also found that the maximum physically allowable relativistic sound speed is $c/\sqrt{3}$. This result does not restrict spatial variation to a particular direction or plane, and therefore is three-dimensional. The value $\sqrt{3}$ frequently emerges in three-dimensional systems.

Having considered the case of a discontinuous velocity profile, we now consider the more general case of a shear variation in velocity, including the sech^2 profile. In chapter 5, when we linearize the RMHD equations in the presence of shear variation in velocity, what we will obtain is not a polynomial dispersion relation (as we derived in this chapter) but rather a second-order ODE which must generally be solved numerically.

Chapter 5

KH Instability with Velocity Shear: Launching a Mode

We have thus far considered how to characterize an eigenmode of the KH instability for a step-function velocity profile which varies discontinuously between two fluids. In this case, each fluid had plane wave solutions, and by invoking boundary conditions at the fluid interface, we were able, in chapter 4, to derive a dispersion relation which is an algebraic function of ω. In the unmagnetized HD and RHD cases, we were able to solve this dispersion relation analytically. In a numerical simulation, however, a discontinuous transition results in numerical instability, and we must instead resort to a background velocity profile which varies continuously in the shear direction. This has the added benefit of providing a minimum length scale of perturbation wavelengths below which the system is stable. A continuously varying shear profile is the subject of this chapter. By linearizing the fluid equations, we derive a second-order differential equation (ODE) of the total pressure perturbation as a function of x, the shear coordinate. Due to the continuous variation of the background velocity profile, the pressure ODE does not have simple plane wave solutions, and in fact is not analytically solvable. It must instead be solved numerically in order to obtain an eigenmode with which to launch a simulation. We derive the pressure ODE for the RHD

case (thermal pressure) in the section 5.1, and for the RMHD case (thermal plus magnetic pressure) in section 5.2. In section 5.3, we demonstrate that in the limit of a step-function discontinuity, our RMHD pressure ODE yields the dispersion relation derived in chapter 4. In section 5.4, we demonstrate that the pressure ODEs in each of the four regimes (HD, RHD, MHD, and RMHD) have a common fundamental self-adjoint structure. In section 5.5, we describe the numerical method used to solve the pressure ODE, thereby yielding a linear eigenmode with which to perturb the system at the start of the simulation. As before, we use a single-fluid model, where the fluid is adiabatic, compressible, isotropic in pressure, and when magnetized, has infinite conductivity. Our results for the pressure ODE are in agreement with those in the existing literature, including Bodo et al. (2004), LRN09, and Miura and Pritchett (1982). In the case of a step-function velocity profile, our results reduce to the plane-wave solutions derived in the previous chapter.

We begin, in section 5.1, by showing how we linearize the RHD equations, in the presence of a velocity shear, to derive the second-order ODE whose solutions correspond to eigenmodes in RHD.

5.1 RHD KH Instability with Velocity Shear

We wish to derive a linear mode of the RHD KH instability, where the velocity exhibits a continuous shear variation instead of a step-function discontinuity. The result will be a second-order ODE in the perturbation to the thermal pressure. In a later section in this chapter, we then show how to numerically solve this ODE in order to obtain the eigenfrequency and eigenmodes.

We consider a relativistic fluid which is compressible, adiabatic, and isotropic. No magnetic field is present. Such a fluid obeys the following equations:

$$\begin{aligned} \frac{\partial}{\partial t}(\gamma\rho) + \boldsymbol{\nabla}\cdot(\gamma\rho\mathbf{v}) &= 0, \\ w\gamma^2\left(\frac{\partial}{\partial t} + \mathbf{v}\cdot\boldsymbol{\nabla}\right)\mathbf{v} + c^2\left(\boldsymbol{\nabla} + \frac{\mathbf{v}}{c^2}\frac{\partial}{\partial t}\right)P &= 0, \\ \left(\frac{\partial}{\partial t} + \mathbf{v}\cdot\boldsymbol{\nabla}\right)P &= \frac{\Gamma P}{w}\left(\frac{\partial}{\partial t} + \mathbf{v}\cdot\boldsymbol{\nabla}\right)\epsilon, \end{aligned} \tag{5.1}$$

where

$$\Gamma = \frac{4}{3}, \qquad \text{adiabatic constant,} \tag{5.2}$$

$$\gamma = \frac{1}{\sqrt{1 - v^2/c^2}}, \qquad \text{Lorentz factor,} \tag{5.3}$$

$$\epsilon = \rho c^2 + \frac{P}{\Gamma - 1}, \qquad \text{internal energy,} \tag{5.4}$$

$$w = \rho c^2 + \frac{\Gamma P}{\Gamma - 1}, \qquad \text{enthalpy,} \tag{5.5}$$

$$c_s^2 = c^2\frac{\partial P}{\partial \epsilon} = c^2\frac{\Gamma P}{w}, \qquad \text{relativistic sound speed.} \tag{5.6}$$

The first of equations (5.1) is the mass continuity equation. The second is Euler's equation, which describes the forces acting on the fluid. The third equation invokes the adiabatic assumption. In chapter 3, we demonstrated that the magnetized version of these equations is equivalent to the conservative form of Anile (1989), i.e., the form used in the numerical simulations. However, here, we have combined the energy equation with the adiabatic equation of state. By linearizing these equations, we wish to derive the relations characterizing a linear mode of the KH instability in RHD. We restrict our attention to the $x - z$ plane, so that there are no components, nor is there any evolution, in the y-direction. The fluid has a uniform unperturbed density $\tilde{\rho}$, a uniform unperturbed pressure $\tilde{P}$, and flows in the

z-direction with some unperturbed velocity profile $\tilde{v}_z(x)$, where x is the direction transverse, or shear, to the flow.

This is the equilibrium situation. We then perturb the fluid with a perturbation aligned with the flow, having wave number k_z. In the linear regime, the system subsequently evolves as follows:

$$\begin{aligned}
\rho(x,z,t) &= \tilde{\rho} + \delta\rho_0(x)\exp[i(k_z z - \omega t)], && (5.7)\\
P(x,z,t) &= \tilde{P} + \delta P_0(x)\exp[i(k_z z - \omega t)], && (5.8)\\
v_x(x,z,t) &= \delta v_{x0}(x)\exp[i(k_z z - \omega t)], && (5.9)\\
v_z(x,z,t) &= \tilde{v}_z(x) + \delta v_{z0}(x)\exp[i(k_z z - \omega t)]. && (5.10)
\end{aligned}$$

It should be noted that in the foregoing analysis, the prime symbol denotes differentiation with respect to x.

To simplify the linearization of the system, we first make the definitions

$$\begin{aligned}
\bar{\omega}(x) &\equiv \omega - k_z\tilde{v}_z(x), && (5.11)\\
\omega_a(x)^2 &\equiv \gamma(x)^2\bar{\omega}(x)^2. && (5.12)
\end{aligned}$$

To solve for δv_x and δv_z in terms of δP, we use Euler's equation. This can be written

$$w\gamma^2\left(\frac{\partial}{\partial t} + \mathbf{v}\cdot\boldsymbol{\nabla}\right)\mathbf{v} + c^2\left(\boldsymbol{\nabla} + \frac{\mathbf{v}}{c^2}\frac{\partial}{\partial t}\right)P = 0. \quad (5.13)$$

Linearizing the x-component of the above equation, we have

$$-i\tilde{w}\gamma(x)^2\bar{\omega}(x)\delta v_x + c^2\delta P' = 0. \quad (5.14)$$

We can now readily solve for δv_x in terms of δP:

$$\delta v_x = \frac{-ic^2\delta P'}{\tilde{w}\gamma(x)^2\bar{\omega}(x)}. \quad (5.15)$$

We now linearize the z-component of Euler's equation:

$$\begin{aligned} -i\tilde{w}\gamma(x)^2\bar{\omega}(x)\delta v_z + \tilde{w}\gamma(x)^2\delta v_x\tilde{v}_z'(x) + i\left(c^2k_z - \omega\tilde{v}_z(x)\right)\delta P &= 0, \qquad \text{which yields} \\ \delta v_z &= \frac{c^2[k_z - \omega\tilde{v}_z(x)/c^2]\delta P}{\tilde{w}\gamma(x)^2\bar{\omega}(x)} - \frac{c^2\tilde{v}_z'(x)\delta P'}{\tilde{w}\omega_a(x)^2} = \frac{c^2\bar{k}_z(x)\delta P}{\tilde{w}\gamma(x)^2\bar{\omega}(x)} - \frac{c^2\tilde{v}_z'(x)\delta P'}{\tilde{w}\omega_a(x)^2}. \end{aligned} \tag{5.16}$$

We can now write δv_z in terms of δP:

$$\delta v_z = \frac{c^2\bar{k}_z(x)\delta P}{\tilde{w}\gamma(x)^2\bar{\omega}(x)} - \frac{c^2\tilde{v}_z'(x)\delta P'}{\tilde{w}\omega_a(x)^2} \equiv C_1(x)\delta P' + C_0(x)\delta P, \tag{5.17}$$

where

$$C_1(x) \equiv -\frac{c^2\tilde{v}_z'(x)}{\tilde{w}\omega_a(x)^2}, \tag{5.18}$$

$$C_0(x) \equiv \frac{c^2\bar{k}_z(x)}{\tilde{w}\gamma(x)^2\bar{\omega}(x)}. \tag{5.19}$$

To derive an ODE in terms of δP, we linearize the equation of mass continuity:

$$\frac{\partial}{\partial t}(\gamma\rho) + \boldsymbol{\nabla}\cdot(\gamma\rho\mathbf{v}) = 0, \tag{5.20}$$

which can be rewritten

$$\frac{\partial}{\partial t}(\gamma\rho) + \gamma\rho(\boldsymbol{\nabla}\cdot\mathbf{v}) + (\mathbf{v}\cdot\boldsymbol{\nabla})(\gamma\rho) = 0. \tag{5.21}$$

Linearizing this equation, we have

$$\begin{aligned} 0 &= -i\omega\left[\gamma(x)\delta\rho + \frac{\tilde{\rho}\gamma(x)^3\tilde{v}_z(x)\delta v_z}{c^2}\right] + \tilde{\rho}\gamma(x)(\delta v_x' + ik_z\delta v_z) \\ &\quad + ik_z\tilde{v}_z(x)\left[\gamma(x)\delta\rho + \frac{\tilde{\rho}\gamma(x)^3\tilde{v}_z(x)\delta v_z}{c^2}\right] + \delta v_x\frac{\tilde{\rho}\gamma(x)^3\tilde{v}_z(x)\tilde{v}_z'(x)}{c^2}, \qquad \text{or} \\ 0 &= \bar{\omega}(x)\gamma(x)\delta\rho + \left[\frac{\bar{\omega}(x)\tilde{\rho}\gamma(x)^3\tilde{v}_z(x)}{c^2} - \tilde{\rho}\gamma(x)k_z\right]\delta v_z + i\frac{\tilde{\rho}\gamma(x)^3\tilde{v}_z(x)\tilde{v}_z'(x)}{c^2}\delta v_x + i\tilde{\rho}\gamma(x)\delta v_x' \\ &\equiv \bar{\omega}(x)\gamma(x)\delta\rho + (k\rho)_s(x)\delta v_z + i\frac{\tilde{\rho}\gamma(x)^3\tilde{v}_z(x)\tilde{v}_z'(x)}{c^2}\delta v_x + i\tilde{\rho}\gamma(x)\delta v_x', \end{aligned} \tag{5.22}$$

where

$$(k\rho)_s(x) \equiv \frac{\bar{\omega}(x)\tilde{\rho}\gamma(x)^3\tilde{v}_z(x)}{c^2} - \tilde{\rho}\gamma(x)k_z. \tag{5.23}$$

We wish to write the above equation in terms of δP_b. To do this, we first write $\delta\rho$ in terms of δP:

$$\frac{c_s^2}{c^2} = \frac{\delta P}{\delta\epsilon} = \frac{\delta P}{c^2\delta\rho + \delta P/(\Gamma-1)}, \tag{5.24}$$

$$\delta\rho = \delta P\left[\frac{1}{c_s^2} - \frac{1}{c^2(\Gamma-1)}\right], \tag{5.25}$$

where c_s is the relativistic sound speed and $\delta\epsilon$ is the perturbation to the system's internal energy. We also have

$$\begin{aligned}
\delta v_x &= \frac{-ic^2\bar{\omega}(x)\delta P'}{\tilde{w}\omega_a(x)^2}, \\
\delta v_x' &= \frac{-ic^2}{\tilde{w}}\left[\frac{\bar{\omega}(x)}{\omega_a(x)^2}\delta P'' + \left(\frac{-k_z\tilde{v}_z'}{\omega_a(x)^2} + \bar{\omega}(x)f_a'(x)\right)\delta P'\right],
\end{aligned} \tag{5.26}$$

where

$$f_a'(x) \equiv \frac{d}{dx}\left[\frac{1}{\omega_a(x)^2}\right]. \tag{5.27}$$

Recall that we further have

$$\delta v_z = C_1(x)\delta P' + C_0(x)\delta P, \tag{5.28}$$

with the $C_j(x)$ coefficients defined above. Inserting these results into our linearized mass continuity equation, we have

$$0 = F_2(x)\delta P'' + F_1(x)\delta P' + F_0(x)\delta P, \tag{5.29}$$

where $F_0(x)$ is given by

$$\begin{aligned}
F_0(x) &= \bar{\omega}(x)\gamma(x)\left[\frac{1}{c_s^2} - \frac{1}{c^2(\Gamma-1)}\right] + (k\rho)_s(x)C_0(x) \\
&= \frac{c^2\bar{\omega}(x)\gamma(x)\tilde{\rho}}{\tilde{w}c_s^2} + \left[\frac{\bar{\omega}(x)\tilde{\rho}\gamma(x)^3\tilde{v}_z(x)}{c^2} - \tilde{\rho}\gamma(x)k_z\right]\frac{\bar{k}_z(x)}{\tilde{w}\gamma(x)^2\bar{\omega}(x)} \\
&= \frac{\tilde{\rho}}{\tilde{w}\gamma(x)\bar{\omega}(x)}\left[\frac{\gamma(x)^2\bar{\omega}(x)^2}{c_s^2} - \bar{k}_z(x)\left(k_z - \gamma(x)^2\frac{\bar{\omega}(x)\tilde{v}_z(x)}{c^2}\right)\right] \\
&= \frac{\tilde{\rho}}{\tilde{w}\gamma(x)\bar{\omega}(x)}\left[\frac{\gamma(x)^2\bar{\omega}(x)^2}{c_s^2} - \gamma(x)^2\bar{k}_z(x)^2\right] \\
&= \frac{\tilde{\rho}}{\tilde{w}\gamma(x)\bar{\omega}(x)}\gamma(x)^2\left[\frac{\bar{\omega}(x)^2}{c_s^2} - \bar{k}_z(x)^2\right]. \qquad (5.30)
\end{aligned}$$

In the above manipulation, we used the following results:

$$\begin{aligned}
\bar{k}_z(x)\left[k_z - \gamma(x)^2\frac{\bar{\omega}(x)\tilde{v}_z(x)}{c^2}\right] &= \gamma(x)^2\bar{k}_z(x)\left[\frac{k_z}{\gamma(x)^2} - \frac{\bar{\omega}(x)\tilde{v}_z(x)}{c^2}\right] \\
&\approx \gamma(x)^2\bar{k}_z(x)\left[k_z\left(1 - \frac{\tilde{v}_z(x)^2}{c^2}\right) - \frac{\bar{\omega}(x)\tilde{v}_z(x)}{c^2}\right] \\
&= \gamma(x)^2\bar{k}_z(x)^2 - \gamma(x)^2\bar{k}_z(x)k_z\frac{\tilde{v}_z(x)^2}{c^2} + \gamma(x)^2\bar{k}_z(x)k_z\frac{\tilde{v}_z(x)^2}{c^2} \\
&= \gamma(x)^2\bar{k}_z(x)^2, \\
c_s^2 &= c^2\frac{\Gamma\tilde{P}}{\tilde{w}}, \\
\tilde{w} = \tilde{\rho}c^2 + \frac{\Gamma\tilde{P}}{\Gamma-1} &= \tilde{\rho}c^2 + \frac{1}{\Gamma-1}\left(\frac{\tilde{w}c_s^2}{c^2}\right), \qquad \text{which yields} \\
\tilde{\rho}c^2 &= \tilde{w} - \frac{1}{\Gamma-1}\left(\frac{\tilde{w}c_s^2}{c^2}\right), \qquad \text{or} \\
\frac{\tilde{\rho}c^2}{\tilde{w}c_s^2} &= \frac{1}{c_s^2} - \frac{1}{c^2(\Gamma-1)}. \qquad (5.31)
\end{aligned}$$

$F_1(x)$ is given by

$$
\begin{aligned}
F_1(x) &= (k\rho)_s(x)C_1(x) \\
&\quad + \frac{\tilde{\rho}\gamma(x)^3\tilde{v}_z(x)\tilde{v}_z'(x)}{c^2}\left[\frac{\bar{\omega}(x)}{\tilde{w}\omega_a(x)^2}\right] + \frac{\tilde{\rho}\gamma(x)}{\tilde{w}}\left[\frac{-k_z\tilde{v}_z'(x)}{\omega_a(x)^2} + \bar{\omega}(x)f_a'(x)\right] \\
&= -\left[\frac{\bar{\omega}(x)\tilde{\rho}\gamma(x)^3\tilde{v}_z(x)}{c^2} - \tilde{\rho}\gamma(x)k_z\right]\left[\frac{\tilde{v}_z'(x)}{\tilde{w}\omega_a(x)^2}\right] \\
&\quad + \frac{\tilde{\rho}\gamma(x)^3\tilde{v}_z(x)\tilde{v}_z'(x)}{c^2}\left[\frac{\bar{\omega}(x)}{\tilde{w}\omega_a(x)^2}\right] + \frac{\tilde{\rho}\gamma(x)}{\tilde{w}}\left[\frac{-k_z\tilde{v}_z'(x)}{\omega_a(x)^2} + \bar{\omega}(x)f_a'(x)\right] \\
&= \frac{\tilde{\rho}\gamma(x)\bar{\omega}(x)f_a'(x)}{\tilde{w}}. \qquad (5.32)
\end{aligned}
$$

$F_2(x)$ is given by

$$
F_2(x) = \frac{\tilde{\rho}\gamma(x)\bar{\omega}(x)}{\tilde{w}\omega_a(x)^2}. \qquad (5.33)
$$

We therefore have the simplification

$$
F_2(x)\delta P'' + F_1(x)\delta P' = A(x)\left[\frac{\delta P'}{\omega_a(x)^2}\right]', \qquad (5.34)
$$

where

$$
A(x) = \frac{\tilde{\rho}\gamma(x)\bar{\omega}(x)}{\tilde{w}}. \qquad (5.35)
$$

We can now rewrite our pressure ODE as

$$
\begin{aligned}
A(x)\left[\frac{\delta P'}{\omega_a(x)^2}\right]' + F_0(x)\delta P &= 0, \qquad \text{where} \\
F_0(x) &= \frac{\tilde{\rho}}{\tilde{w}\gamma(x)\bar{\omega}(x)}\gamma(x)^2\left[\frac{\bar{\omega}(x)^2}{c_s^2} - \bar{k}_z(x)^2\right], \\
A(x) &= \frac{\tilde{\rho}\gamma(x)\bar{\omega}(x)}{\tilde{w}}, \qquad (5.36)
\end{aligned}
$$

or, equivalently,

$$\begin{aligned}
\omega_a(x)^2\left[\frac{\delta P'}{\omega_a(x)^2}\right]' + k_x(x)^2\delta P &= 0, \qquad \text{where} \\
k_x(x)^2 &= \gamma(x)^2\left[\frac{\bar{\omega}(x)^2}{c_s^2} - \bar{k}_z(x)^2\right], \\
\omega_a(x)^2 &= \gamma(x)^2\bar{\omega}(x)^2. \qquad (5.37)
\end{aligned}$$

The above expression for k_x is in agreement with that of Bodo et al. (2004), and the unmagnetized limit of LRN09. The above pressure ODE is in agreement with the unmagnetized limit of Miura and Pritchett (1982).

We have derived the second-order pressure ODE that yields eigenmodes of the system in RHD. We now proceed to do the same for the RMHD regime.

5.2 RMHD KH Instability with Velocity Shear

We again consider a sheared relativistic velocity profile, but also introduce a magnetic field. We wish to derive a linear mode of the KH instability in relativistic magnetohydrodynamics (RMHD). We consider a fluid which is compressible, adiabatic, isotropic, and infinitely conducting. Such a fluid obeys the following equations:

$$\begin{aligned}
\frac{\partial}{\partial t}(\gamma\rho) + \boldsymbol{\nabla}\cdot(\gamma\rho\mathbf{v}) &= 0, \\
\frac{w}{c^2}\gamma^2\left(\frac{\partial}{\partial t} + \mathbf{v}\cdot\boldsymbol{\nabla}\right)\mathbf{v} + \left(\boldsymbol{\nabla} + \frac{\mathbf{v}}{c^2}\frac{\partial}{\partial t}\right)P &= \rho_c\mathbf{E} + \frac{\mathbf{J}}{c}\times\mathbf{B}, \\
\left(\frac{\partial}{\partial t} + \mathbf{v}\cdot\boldsymbol{\nabla}\right)P &= \frac{\Gamma P}{w}\left(\frac{\partial}{\partial t} + \mathbf{v}\cdot\boldsymbol{\nabla}\right)\epsilon, \\
\boldsymbol{\nabla}\times\mathbf{B} &= \frac{\mathbf{J}}{c} + \frac{1}{c}\frac{\partial\mathbf{E}}{\partial t}, \\
\boldsymbol{\nabla}\times\mathbf{E} &= -\frac{1}{c}\frac{\partial\mathbf{B}}{\partial t}, \\
\boldsymbol{\nabla}\cdot\mathbf{B} &= 0, \\
\mathbf{E} + \frac{\mathbf{v}}{c}\times\mathbf{B} &= 0, \qquad (5.38)
\end{aligned}$$

where

$$\Gamma = \frac{4}{3}, \qquad \text{adiabatic constant,} \tag{5.39}$$

$$\gamma = \frac{1}{\sqrt{1 - v^2/c^2}}, \qquad \text{Lorentz factor,} \tag{5.40}$$

$$\epsilon = \rho c^2 + \frac{P}{\Gamma - 1}, \qquad \text{internal energy,} \tag{5.41}$$

$$w = \rho c^2 + \frac{\Gamma P}{\Gamma - 1}, \qquad \text{enthalpy,} \tag{5.42}$$

$$c_s^2 = c^2 \frac{\partial P}{\partial \epsilon} = c^2 \frac{\Gamma P}{w}, \qquad \text{relativistic sound speed,} \tag{5.43}$$

where c_s^2 is the relativistic sound speed, and ϵ is the internal energy. The first of equations (5.38) describes mass transport (i.e., the mass continuity equation). The second is Euler's equation, the right side of which is the Lorentz force. The third equation invokes the adiabatic assumption. The fourth, fifth, and sixth equations are Maxwell's equations. The seventh equation invokes the assumption of infinite conductivity. In chapter 3, we demonstrated that these equations are equivalent to the conservative form of Anile (1989), i.e., the form used in the numerical simulations. However, here, we have combined the energy equation with the adiabatic equation of state. By linearizing these equations, we wish to derive the relations characterizing a linear mode of the KH instability in RMHD. We restrict our attention to the $x - z$ plane, so that there are no components, nor is there any evolution, in the y-direction. We consider a fluid which is compressible, adiabatic, isotropic, and infinitely conducting. The fluid has a uniform unperturbed density $\tilde{\rho}$, a uniform unperturbed pressure $\tilde{P}$, and flows in the z-direction with some unperturbed velocity profile $\tilde{v}_z(x)$, where x is the direction transverse, or shear, to the flow. The fluid is immersed in a uniform unperturbed magnetic field $\mathbf{B} = \tilde{B}_z \hat{z}$ aligned with the flow direction. This is the equilibrium situation. We then perturb the fluid with a perturbation aligned with the flow, having wave number

k_z. In the linear regime, the system subsequently evolves as follows:

$$\begin{aligned}
\rho(x,z,t) &= \tilde{\rho} + \delta\rho_0(x)\exp[i(k_z z - \omega t)], && (5.44)\\
P(x,z,t) &= \tilde{P} + \delta P_0(x)\exp[i(k_z z - \omega t)], && (5.45)\\
v_x(x,z,t) &= \delta v_{x0}(x)\exp[i(k_z z - \omega t)], && (5.46)\\
v_z(x,z,t) &= \tilde{v}_z(x) + \delta v_{z0}(x)\exp[i(k_z z - \omega t)], && (5.47)\\
B_x(x,z,t) &= \delta B_{x0}(x)\exp[i(k_z z - \omega t)], && (5.48)\\
B_z(x,z,t) &= \tilde{B}_z + \delta B_{z0}(x)\exp[i(k_z z - \omega t)]. && (5.49)
\end{aligned}$$

It should be noted that in the foregoing analysis, the prime symbol denotes differentiation with respect to x. We wish to express these perturbations in terms of the perturbation to the total stress P_b, where

$$\begin{aligned}
P_b &= P + \frac{E^2 + B^2}{2},\\
\delta P_b &= \delta P + \mathbf{E}\cdot\delta\mathbf{E} + \tilde{B}_z\delta B_z = \delta P + \tilde{B}_z\delta B_z. && (5.50)
\end{aligned}$$

The contribution from the electric field is zero. We see this from our assumption of a perfectly conducting fluid:

$$\begin{aligned}
\mathbf{E} + \frac{\mathbf{v}}{c}\times\mathbf{B} &= 0,\\
\mathbf{E} &= \frac{\mathbf{B}\times\mathbf{v}}{c}. && (5.51)
\end{aligned}$$

Restricting our analysis to two dimensions, we see that the perturbation to the squared electric field is

$$\begin{aligned}
\mathbf{E}\cdot\delta\mathbf{E} &= E_x\delta E_x + E_y\delta E_y + E_z\delta E_z\\
&= E_y\delta E_y = \frac{1}{c^2}(B_z v_x - B_x v_z)\delta(B_z v_x - B_x v_z) = 0, && (5.52)
\end{aligned}$$

since both $B_z v_x$ and $B_x v_z$ vanish in zeroth order.

To solve for δB_x and δB_z in terms of δv_x and δv_z, we use Faraday's law in conjunction with the assumption of infinite conductivity and zero divergence in the magnetic field:

$$\begin{aligned} \frac{1}{c}\frac{\partial \mathbf{B}}{\partial t} &= -\boldsymbol{\nabla} \times \mathbf{E}, \\ \mathbf{E} + \frac{\mathbf{v}}{c} \times \mathbf{B} &= 0, \\ \boldsymbol{\nabla} \cdot \mathbf{B} &= 0. \end{aligned} \tag{5.53}$$

Inserting the second of these equations into the first, we have

$$\begin{aligned} \frac{\partial \mathbf{B}}{\partial t} &= \boldsymbol{\nabla} \times (\mathbf{v} \times \mathbf{B}) \\ &= (\mathbf{B} \cdot \boldsymbol{\nabla})\mathbf{v} + \mathbf{v}(\boldsymbol{\nabla} \cdot \mathbf{B}) - (\mathbf{v} \cdot \boldsymbol{\nabla})\mathbf{B} - \mathbf{B}(\boldsymbol{\nabla} \cdot \mathbf{v}). \end{aligned} \tag{5.54}$$

Linearizing the x-component of the above equation, we have

$$\begin{aligned} -i\omega\delta B_x &= ik_z\tilde{B}_z\delta v_x - ik_z\tilde{v}_z(x)\delta B_x, \qquad \text{or} \\ \omega\delta B_x &= -k_z\tilde{B}_z\delta v_x + k_z\tilde{v}_z(x)\delta B_x, \qquad \text{which yields} \\ \delta B_x &= -\frac{k_z\tilde{B}_z\delta v_x}{\omega - k_z\tilde{v}_z(x)} = -\frac{k_z\tilde{B}_z\delta v_x}{\bar{\omega}(x)}, \end{aligned} \tag{5.55}$$

where

$$\bar{\omega}(x) \equiv \omega - k_z\tilde{v}_z(x).$$

Linearizing the z-component of (5.54), we have

$$\begin{aligned} -i\omega\delta B_z &= ik_z\tilde{B}_z\delta v_z + \tilde{v}_z(x)(\boldsymbol{\nabla} \cdot \mathbf{B}) + \delta B_x\tilde{v}_z'(x) - ik_z\tilde{v}_z(x)\delta B_z - \tilde{B}_z(\delta v_x' + ik_z\delta v_z) \\ &= \delta B_x\tilde{v}_z'(x) + \tilde{v}_z(x)(\boldsymbol{\nabla} \cdot \mathbf{B}) - ik_z\tilde{v}_z(x)\delta B_z - \tilde{B}_z\delta v_x', \qquad \text{which yields} \\ \tilde{v}_z(x)(\boldsymbol{\nabla} \cdot \mathbf{B}) &= -i\bar{\omega}(x)\delta B_z + \tilde{B}_z\delta v_x' - \delta B_x\tilde{v}_z'(x), \qquad \text{or} \\ 0 &= -i\bar{\omega}(x)\delta B_z + \tilde{B}_z\delta v_x' - \delta B_x\tilde{v}_z'(x). \end{aligned} \tag{5.56}$$

We arrive at this same equation by directly imposing the condition of zero divergence on $\mathbf{B}$:

$$
\begin{aligned}
0 \;=\; \boldsymbol{\nabla}\cdot\mathbf{B} \;&=\; ik_z\delta B_z + \delta B_x' \\
&=\; ik_z\delta B_z - k_z\tilde{B}_z\left[\frac{\delta v_x}{\bar{\omega}(x)}\right]' \\
&=\; ik_z\delta B_z - k_z\tilde{B}_z\left[\frac{\delta v_x'}{\bar{\omega}(x)} + \frac{k_z\tilde{v}_z'(x)\delta v_x}{\bar{\omega}(x)^2}\right], \qquad \text{which yields} \\
0 \;&=\; -i\delta B_z + \tilde{B}_z\left[\frac{\delta v_x'}{\bar{\omega}(x)} + \frac{k_z\tilde{v}_z'(x)\delta v_x}{\bar{\omega}(x)^2}\right], \qquad \text{or} \\
0 \;&=\; -i\bar{\omega}(x)\delta B_z + \tilde{B}_z\left[\delta v_x' + \frac{k_z\tilde{v}_z'(x)\delta v_x}{\bar{\omega}(x)}\right] \qquad (5.57)
\end{aligned}
$$

Substituting (5.55) into (5.57), we recover (5.56):

$$
0 \;=\; -i\bar{\omega}(x)\delta B_z + \tilde{B}_z\delta v_x' - \delta B_x\tilde{v}_z'(x). \qquad (5.58)
$$

Solving this equation for δB_z, we obtain

$$
\delta B_z \;=\; (i)\frac{\delta B_x\tilde{v}_z'(x) - \tilde{B}_z\delta v_x'}{\bar{\omega}(x)}.
$$

Before invoking Euler's equation, we first solve Ampere's law for the current density:

$$
\begin{aligned}
\boldsymbol{\nabla}\times\mathbf{B} \;&=\; \frac{\mathbf{J}}{c} + \frac{1}{c}\frac{\partial\mathbf{E}}{\partial t}, \qquad \text{which gives} \\
\frac{\mathbf{J}}{c} \;&=\; \boldsymbol{\nabla}\times\mathbf{B} - \frac{1}{c}\frac{\partial\mathbf{E}}{\partial t} \;=\; \boldsymbol{\nabla}\times\mathbf{B} - \frac{1}{c}\frac{\partial}{\partial t}\left(\frac{\mathbf{B}\times\mathbf{v}}{c}\right). \qquad (5.59)
\end{aligned}
$$

The magnetic force is therefore

$$
\begin{aligned}
\frac{\mathbf{J}}{c}\times\mathbf{B} \;&=\; (\boldsymbol{\nabla}\times\mathbf{B})\times\mathbf{B} - \frac{1}{c^2}\frac{\partial}{\partial t}(\mathbf{B}\times\mathbf{v})\times\mathbf{B} \\
&=\; (\boldsymbol{\nabla}\times\mathbf{B})\times\mathbf{B} + \frac{1}{c^2}\mathbf{B}\times\frac{\partial}{\partial t}(\mathbf{B}\times\mathbf{v}) \\
&=\; (\boldsymbol{\nabla}\times\mathbf{B})\times\mathbf{B} + \frac{1}{c^2}\left[\frac{\partial\mathbf{B}}{\partial t}(\mathbf{B}\cdot\mathbf{v}) - \mathbf{v}\left(\frac{\partial\mathbf{B}}{\partial t}\cdot\mathbf{B}\right) + \mathbf{B}\left(\frac{\partial\mathbf{B}}{\partial t}\cdot\mathbf{v}\right) - \frac{\partial\mathbf{v}}{\partial t}B^2\right] \\
&=\; -\boldsymbol{\nabla}\left(\frac{B^2}{2}\right) + (\mathbf{B}\cdot\boldsymbol{\nabla})\mathbf{B} \\
&\qquad + \frac{1}{c^2}\left[\frac{\partial\mathbf{B}}{\partial t}(\mathbf{B}\cdot\mathbf{v}) - \mathbf{v}\left(\frac{\partial\mathbf{B}}{\partial t}\cdot\mathbf{B}\right) + \mathbf{B}\left(\frac{\partial\mathbf{B}}{\partial t}\cdot\mathbf{v}\right) - \frac{\partial\mathbf{v}}{\partial t}B^2\right]. \qquad (5.60)
\end{aligned}
$$

Euler's equation can now be written

$$\frac{w}{c^2}\gamma^2\left(\frac{\partial}{\partial t}+\mathbf{v}\cdot\boldsymbol{\nabla}\right)\mathbf{v}+\left(\boldsymbol{\nabla}+\frac{\mathbf{v}}{c^2}\frac{\partial}{\partial t}\right)P \;=\; \frac{\mathbf{J}}{c}\times\mathbf{B}$$
$$-\boldsymbol{\nabla}\left(\frac{B^2}{2}\right)+(\mathbf{B}\cdot\boldsymbol{\nabla})\mathbf{B}+\frac{1}{c^2}\left[\frac{\partial\mathbf{B}}{\partial t}(\mathbf{B}\cdot\mathbf{v})-\mathbf{v}\left(\frac{\partial\mathbf{B}}{\partial t}\cdot\mathbf{B}\right)+\mathbf{B}\left(\frac{\partial\mathbf{B}}{\partial t}\cdot\mathbf{v}\right)-\frac{\partial\mathbf{v}}{\partial t}B^2\right]. \tag{5.61}$$

Linearizing the x-component of the above equation, we have

$$\begin{aligned}-i\frac{\tilde{w}}{c^2}\gamma(x)^2\bar{\omega}(x)\delta v_x+\delta P' &= -\tilde{B}_z\delta B_z+ik_z\tilde{B}_z\delta B_x-\frac{i\omega}{c^2}\left[\tilde{B}_z\tilde{v}_z(x)\delta B_x-\tilde{B}_z^2\delta v_x\right]\\ &= -\tilde{B}_z\delta B_z+\frac{i\omega}{c^2}\tilde{B}_z^2\delta v_x-\frac{i(k_z-\omega\tilde{v}_z(x)/c^2)\tilde{B}_z^2k_z}{\bar{\omega}(x)}\delta v_x.\end{aligned} \tag{5.62}$$

In the above manipulations, we used equation (5.55) for δB_x in terms of δv_x. This equation can now be written in terms of the perturbation to the total stress:

$$\begin{aligned}\delta P_b' &= \delta P'+\tilde{B}_z\delta B_z'\\ &= i\left[\frac{\tilde{w}}{c^2}\gamma(x)^2\bar{\omega}(x)+\left(\frac{\omega}{c^2}-\frac{\bar{k}_z(x)k_z}{\bar{\omega}(x)}\right)\tilde{B}_z^2\right]\delta v_x, \qquad \text{where}\\ \bar{k}_z(x) &\equiv k_z-\frac{\omega\tilde{v}_z(x)}{c^2}.\end{aligned} \tag{5.63}$$

We can now readily solve for δv_x in terms of δP_b:

$$\begin{aligned}\delta v_x &= \frac{-ic^2\bar{\omega}(x)\delta P_b'}{\tilde{w}\gamma(x)^2\bar{\omega}(x)^2+[\omega\bar{\omega}(x)-c^2k_z\bar{k}_z(x))\tilde{B}_z^2}\\ &= \frac{-ic^2\bar{\omega}(x)\delta P_b'}{\tilde{w}[\gamma(x)^2\bar{\omega}(x)^2-v_{Az}^2(k_z^2-\omega^2/c^2)]} \;\equiv\; \frac{-ic^2\bar{\omega}(x)\delta P_b'}{\tilde{w}\omega_a(x)^2},\end{aligned} \tag{5.64}$$

where

$$v_{Az} \;\equiv\; c\frac{\tilde{B}_z}{\sqrt{\tilde{w}}}, \tag{5.65}$$

$$\omega_a(x)^2 \;\equiv\; \gamma(x)^2\bar{\omega}(x)^2-v_{Az}^2(k_z^2-\omega^2/c^2). \tag{5.66}$$

Inserting (5.55) into (5.64), we see that δB_x is given by

$$\delta B_x \;=\; -\frac{k_z \tilde{B}_z}{\bar{\omega}(x)}\delta v_x \;=\; i\frac{c^2 k_z \tilde{B}_z \delta P_b'}{\tilde{w}\omega_a(x)^2}.$$

We now linearize the z-component of Euler's equation:

$$\begin{aligned} &-i\frac{\tilde{w}}{c^2}\gamma(x)^2\bar{\omega}(x)\delta v_z + \frac{\tilde{w}}{c^2}\gamma(x)^2\delta v_x \tilde{v}_z'(x) + i\left[k_z - \frac{\omega\tilde{v}_z(x)}{c^2}\right]\delta P \;= \\ &\quad -ik_z\tilde{B}_z\delta B_z + ik_z\tilde{B}_z\delta B_z - \frac{i\omega}{c^2}\left[\tilde{B}_z\tilde{v}_z(x)\delta B_z - \tilde{v}_z(x)\tilde{B}_z\delta B_z + \tilde{B}_z^2\delta v_z - \tilde{B}_z^2\delta v_z\right] \;=\; 0. \end{aligned}$$

Solving the above equation for δv_z, we obtain

$$\delta v_z \;=\; \frac{c^2[k_z - \omega\tilde{v}_z(x)/c^2]\delta P}{\tilde{w}\gamma(x)^2\bar{\omega}(x)} - \frac{c^2\tilde{v}_z'(x)\delta P_b'}{\tilde{w}\omega_a(x)^2} \;=\; \frac{c^2\bar{k}_z(x)\delta P}{\tilde{w}\gamma(x)^2\bar{\omega}(x)} - \frac{c^2\tilde{v}_z'(x)\delta P_b'}{\tilde{w}\omega_a(x)^2}. \tag{5.67}$$

To express δv_z in terms of δP_b, we first need to write δP in terms of δP_b:

$$\delta P \;=\; \delta P_b - \tilde{B}_z\delta B_z, \tag{5.68}$$

where we need to write δB_z in terms of δP_b:

$$\begin{aligned} \delta B_z \;&=\; (i)\frac{\delta B_x\tilde{v}_z'(x) - \delta v_x'\tilde{B}_z}{\bar{\omega}(x)} \\ &=\; -\frac{c^2 k_z\tilde{v}_z'(x)\tilde{B}_z\delta P_b'}{\tilde{w}\bar{\omega}(x)\omega_a(x)^2} - \frac{c^2\tilde{B}_z}{\tilde{w}\bar{\omega}(x)}\left[\frac{\bar{\omega}(x)\delta P_b'' - k_z\tilde{v}_z'(x)\delta P_b'}{\omega_a(x)^2} + \bar{\omega}(x)\delta P_b'\frac{\partial}{\partial x}\left(\frac{1}{\omega_a(x)^2}\right)\right] \\ &=\; -\frac{c^2\tilde{B}_z}{\tilde{w}}\left[\frac{\delta P_b''}{\omega_a(x)^2} + \frac{\partial}{\partial x}\left(\frac{1}{\omega_a(x)^2}\right)\delta P_b'\right] \\ &\equiv\; -\frac{c^2\tilde{B}_z}{\tilde{w}}\left[\frac{\delta P_b''}{\omega_a(x)^2} + f_a'(x)\delta P_b'\right], \end{aligned} \tag{5.69}$$

where

$$f_a'(x) \;\equiv\; \frac{\partial}{\partial x}\left(\frac{1}{\omega_a(x)^2}\right). \tag{5.70}$$

Therefore, we have, for δP in terms of δP_b,

$$\delta P \;=\; \delta P_b - \tilde{B}_z \delta B_z \;=\; \frac{c^2 \tilde{B}_z^2}{\tilde{w}} \left[\frac{\delta P_b''}{\omega_a(x)^2} + f_a'(x) \delta P_b' \right] + \delta P_b. \tag{5.71}$$

We can now write δv_z in terms of δP_b:

$$\delta v_z \;=\; \frac{c^2 \bar{k}_z(x) \delta P}{\tilde{w}\gamma(x)^2 \bar{\omega}(x)} - \frac{c^2 \tilde{v}_z'(x) \delta P_b'}{\tilde{w}\omega_a(x)^2} \;\equiv\; C_2(x)\delta P_b'' + C_1(x)\delta P_b' + C_0(x)\delta P_b, \tag{5.72}$$

where

$$\begin{aligned} C_2(x) \;&\equiv\; \frac{c^4 \tilde{B}_z^2 \bar{k}_z(x)}{\tilde{w}^2 \gamma(x)^2 \bar{\omega}(x) \omega_a(x)^2}, \\ C_1(x) \;&\equiv\; \frac{c^4 \tilde{B}_z^2 \bar{k}_z(x) f_a'(x)}{\tilde{w}^2 \gamma(x)^2 \bar{\omega}(x)} - \frac{c^2 \tilde{v}_z'(x)}{\tilde{w}\omega_a(x)^2}, \\ C_0(x) \;&\equiv\; \frac{c^2 \bar{k}_z(x)}{\tilde{w}\gamma(x)^2 \bar{\omega}(x)}. \end{aligned} \tag{5.73}$$

To derive an ODE in terms of δP_b, we linearize the equation of mass continuity:

$$\frac{\partial}{\partial t}(\gamma\rho) + \boldsymbol{\nabla} \cdot (\gamma\rho \mathbf{v}) \;=\; 0, \tag{5.74}$$

which can be rewritten

$$\frac{\partial}{\partial t}(\gamma\rho) + \gamma\rho(\boldsymbol{\nabla} \cdot \mathbf{v}) + (\mathbf{v} \cdot \boldsymbol{\nabla})(\gamma\rho) \;=\; 0. \tag{5.75}$$

Linearizing this equation, we have

$$\begin{aligned} 0 \;&=\; -i\omega \left[\gamma(x)\delta\rho + \frac{\tilde{\rho}\gamma(x)^3 \tilde{v}_z(x) \delta v_z}{c^2} \right] + \tilde{\rho}\gamma(x)(\delta v_x' + i k_z \delta v_z) \\ &\quad + i k_z \tilde{v}_z(x) \left[\gamma(x)\delta\rho + \frac{\tilde{\rho}\gamma(x)^3 \tilde{v}_z(x)\delta v_z}{c^2} \right] + \delta v_x \frac{\tilde{\rho}\gamma(x)^3 \tilde{v}_z(x) \tilde{v}_z'(x)}{c^2}, \qquad \text{or} \\ 0 \;&=\; \bar{\omega}(x)\gamma(x)\delta\rho + \left[\frac{\bar{\omega}(x)\tilde{\rho}\gamma(x)^3 \tilde{v}_z(x)}{c^2} - \tilde{\rho}\gamma(x) k_z \right] \delta v_z + i \frac{\tilde{\rho}\gamma(x)^3 \tilde{v}_z(x)\tilde{v}_z'(x)}{c^2} \delta v_x + i\tilde{\rho}\gamma(x)\delta v_x' \\ &\equiv\; \bar{\omega}(x)\gamma(x)\delta\rho + (k\rho)_s(x)\delta v_z + i \frac{\tilde{\rho}\gamma(x)^3 \tilde{v}_z(x)\tilde{v}_z'(x)}{c^2} \delta v_x + i\tilde{\rho}\gamma(x)\delta v_x', \end{aligned} \tag{5.76}$$

where

$$(k\rho)_s(x) \;\equiv\; \frac{\bar{\omega}(x)\tilde{\rho}\gamma(x)^3\tilde{v}_z(x)}{c^2} - \tilde{\rho}\gamma(x)k_z.$$

We wish to write the above equation in terms of δP_b. To do this, we first write $\delta\rho$ in terms of δP:

$$\frac{c_s^2}{c^2} \;=\; \frac{\delta P}{\delta\epsilon} \;=\; \frac{\delta P}{c^2\delta\rho + \delta P/(\Gamma-1)}, \tag{5.77}$$

which yields

$$\delta\rho \;=\; \delta P\left[\frac{1}{c_s^2} - \frac{1}{c^2(\Gamma-1)}\right], \tag{5.78}$$

where c_s is the relativistic sound speed and $\delta\epsilon$ is the perturbation to the system's internal energy. Now recall that

$$\delta P \;=\; \delta P_b - \tilde{B}_z\delta B_z \;=\; \frac{c^2\tilde{B}_z^2}{\tilde{w}}\left[\frac{\delta P_b''}{\omega_a(x)^2} + f_a'(x)\delta P_b'\right] + \delta P_b.$$

We therefore have

$$\delta\rho \;=\; \left[\frac{c^2\tilde{B}_z^2}{\tilde{w}}\left(\frac{\delta P_b''}{\omega_a(x)^2} + f_a'(x)\delta P_b'\right) + \delta P_b\right]\left[\frac{1}{c_s^2} - \frac{1}{c^2(\Gamma-1)}\right].$$

We also have

$$\begin{aligned}
\delta v_x \;&=\; \frac{-ic^2\bar{\omega}(x)\delta P_b'}{\tilde{w}\omega_a(x)^2}, \\
\delta v_x' \;&=\; \frac{-ic^2}{\tilde{w}}\left[\frac{\bar{\omega}(x)}{\omega_a(x)^2}\delta P_b'' + \left(\frac{-k_z\tilde{v}_z'}{\omega_a^2} + \bar{\omega}(x)f_a'(x)\right)\delta P_b'\right].
\end{aligned} \tag{5.79}$$

Recall that we further have

$$\delta v_z \;=\; C_2(x)\delta P_b'' + C_1(x)\delta P_b' + C_0(x)\delta P_b,$$

with the $C_j(x)$ coefficients defined in (5.73). Inserting these results into our linearized mass continuity equation, we have

$$0 \;=\; F_2(x)\delta P_b'' + F_1(x)\delta P_b' + F_0(x)\delta P_b,$$

where $F_0(x)$ is given by

$$\begin{aligned}
F_0(x) &= \bar{\omega}(x)\gamma(x)\left[\frac{1}{c_s^2} - \frac{1}{c^2(\Gamma-1)}\right] + (k\rho)_s(x)C_0(x) \\
&= \frac{c^2\bar{\omega}(x)\gamma(x)\tilde{\rho}}{\tilde{w}c_s^2} + \left[\frac{\bar{\omega}(x)\tilde{\rho}\gamma(x)^3\tilde{v}_z(x)}{c^2} - \tilde{\rho}\gamma(x)k_z\right]\frac{c^2\bar{k}_z(x)}{\tilde{w}\gamma(x)^2\bar{\omega}(x)} \\
&= \frac{c^2\tilde{\rho}}{\tilde{w}\gamma(x)\bar{\omega}(x)}\left[\frac{\gamma(x)^2\bar{\omega}(x)^2}{c_s^2} - \bar{k}_z(x)\left(k_z - \gamma(x)^2\frac{\bar{\omega}(x)\tilde{v}_z(x)}{c^2}\right)\right] \\
&= \frac{c^2\tilde{\rho}}{\tilde{w}\gamma(x)\bar{\omega}(x)}\left[\frac{\gamma(x)^2\bar{\omega}(x)^2}{c_s^2} - \gamma(x)^2\bar{k}_z(x)^2\right] \\
&= \frac{c^2\tilde{\rho}}{\tilde{w}\gamma(x)\bar{\omega}(x)}\gamma(x)^2\left[\frac{\bar{\omega}(x)^2}{c_s^2} - \bar{k}_z(x)^2\right]. \qquad (5.80)
\end{aligned}$$

In the above manipulation, we used the following results:

$$
\begin{aligned}
\bar{k}_z(x)\left[k_z-\gamma(x)^2\frac{\bar{\omega}(x)\tilde{v}_z(x)}{c^2}\right] &= \gamma(x)^2\bar{k}_z(x)\left[\frac{k_z}{\gamma(x)^2}-\frac{\bar{\omega}(x)\tilde{v}_z(x)}{c^2}\right] \\
&\approx \gamma(x)^2\bar{k}_z(x)\left[k_z\left(1-\frac{\tilde{v}_z(x)^2}{c^2}\right)-\frac{\bar{\omega}(x)\tilde{v}_z(x)}{c^2}\right] \\
&= \gamma(x)^2\bar{k}_z(x)^2-\gamma(x)^2\bar{k}_z(x)k_z\frac{\tilde{v}_z(x)^2}{c^2}+\gamma(x)^2\bar{k}_z(x)k_z\frac{\tilde{v}_z(x)^2}{c^2} \\
&= \gamma(x)^2\bar{k}_z(x)^2, \\
c_s^2 &= c^2\frac{\Gamma\tilde{P}}{\tilde{w}}, \\
\tilde{w} = \tilde{\rho}c^2+\frac{\Gamma\tilde{P}}{\Gamma-1} &= \tilde{\rho}c^2+\frac{1}{\Gamma-1}\left(\frac{\tilde{w}c_s^2}{c^2}\right), \qquad \text{which yields} \\
\tilde{\rho}c^2 &= \tilde{w}-\frac{1}{\Gamma-1}\left(\frac{\tilde{w}c_s^2}{c^2}\right), \qquad \text{or} \\
\frac{\tilde{\rho}c^2}{\tilde{w}c_s^2} &= \frac{1}{c_s^2}-\frac{1}{c^2(\Gamma-1)}.
\end{aligned} \tag{5.81}
$$

$F_1(x)$ is given by

$$
\begin{aligned}
F_1(x) &= \frac{c^2\bar{\omega}(x)\gamma(x)\tilde{B}_z^2f_a'(x)}{\tilde{w}}\left[\frac{1}{c_s^2}-\frac{1}{c^2(\Gamma-1)}\right]+(k\rho)_s(x)C_1(x) \\
&\quad +\tilde{\rho}\gamma(x)^3\tilde{v}_z(x)\tilde{v}_z'(x)\left[\frac{\bar{\omega}(x)}{\tilde{w}\omega_a(x)^2}\right]+\frac{\tilde{\rho}c^2\gamma(x)}{\tilde{w}}\left[\frac{-k_z\tilde{v}_z'(x)}{\omega_a(x)^2}+\bar{\omega}(x)f_a'(x)\right] \\
&= \frac{c^2\bar{\omega}(x)\gamma(x)\tilde{B}_z^2f_a'(x)}{\tilde{w}}\frac{\tilde{\rho}c^2}{\tilde{w}c_s^2} \\
&\quad +\left[\frac{\bar{\omega}(x)\tilde{\rho}\gamma(x)^3\tilde{v}_z(x)}{c^2}-\tilde{\rho}\gamma(x)k_z\right]\left[\frac{c^2\tilde{B}_z^2\bar{k}_z(x)f_a'(x)}{\tilde{w}^2\gamma(x)^2\bar{\omega}(x)}-\frac{c^2\tilde{v}_z'(x)}{\tilde{w}\omega_a(x)^2}\right] \\
&\quad +\tilde{\rho}\gamma(x)^3\tilde{v}_z(x)\tilde{v}_z'(x)\left[\frac{\bar{\omega}(x)}{\tilde{w}\omega_a(x)^2}\right]+\frac{\tilde{\rho}c^2\gamma(x)}{\tilde{w}}\left[\frac{-k_z\tilde{v}_z'(x)}{\omega_a(x)^2}+\bar{\omega}(x)f_a'(x)\right] \\
&= \bar{\omega}(x)\gamma(x)v_{Az}^2f_a'(x)\frac{\tilde{\rho}c^2}{\tilde{w}c_s^2}+\left[\frac{\bar{\omega}(x)\tilde{\rho}\gamma(x)^3\tilde{v}_z(x)}{c^2}-\tilde{\rho}\gamma(x)k_z\right]\frac{c^2v_{Az}^2\bar{k}_z(x)f_a'(x)}{\tilde{w}\gamma(x)^2\bar{\omega}(x)} \\
&\quad +\frac{\tilde{\rho}c^2\gamma(x)\bar{\omega}(x)f_a'(x)}{\tilde{w}}.
\end{aligned} \tag{5.82}
$$

$F_2(x)$ is given by

$$
\begin{aligned}
F_2(x) &= \frac{c^2\bar{\omega}(x)\gamma(x)\tilde{B}_z^2}{\tilde{w}\omega_a(x)^2}\left[\frac{1}{c_s^2}-\frac{1}{c^2(\Gamma-1)}\right]+(k\rho)_s(x)C_2(x)+\frac{c^2\tilde{\rho}\gamma(x)\bar{\omega}(x)}{\tilde{w}\omega_a(x)^2}\\
&= \frac{c^2\bar{\omega}(x)\gamma(x)\tilde{B}_z^2}{\tilde{w}\omega_a(x)^2}\left(\frac{\tilde{\rho}c^2}{\tilde{w}c_s^2}\right)+\left[\frac{\bar{\omega}(x)\tilde{\rho}\gamma(x)^3\tilde{v}_z(x)}{c^2}-\tilde{\rho}\gamma(x)k_z\right]\left[\frac{c^2\tilde{B}_z^2\bar{k}_z(x)}{\tilde{w}\gamma(x)^2\bar{\omega}(x)\omega_a(x)^2}\right]\\
&\quad+\frac{\tilde{\rho}c^2\gamma(x)\bar{\omega}(x)}{\tilde{w}\omega_a(x)^2}\\
&= \frac{\bar{\omega}(x)\gamma(x)v_{Az}^2}{\omega_a(x)^2}\left(\frac{\tilde{\rho}c^2}{\tilde{w}c_s^2}\right)+\left[\frac{\bar{\omega}(x)\tilde{\rho}\gamma(x)^3\tilde{v}_z(x)}{c^2}-\tilde{\rho}\gamma(x)k_z\right]\left[\frac{c^2v_{Az}^2\bar{k}_z(x)}{\tilde{w}\gamma(x)^2\bar{\omega}(x)\omega_a(x)^2}\right]\\
&\quad+\frac{\tilde{\rho}c^2\gamma(x)\bar{\omega}(x)}{\tilde{w}\omega_a(x)^2}. \qquad (5.83)
\end{aligned}
$$

We therefore have the simplification

$$
F_2(x)\delta P_b''+F_1(x)\delta P_b' = A(x)\left[\frac{\delta P_b'}{\omega_a(x)^2}\right]',
$$

where

$$
\begin{aligned}
A(x) &= \frac{c^2\tilde{\rho}\gamma(x)\bar{\omega}(x)}{\tilde{w}}+\frac{c^2\tilde{\rho}\gamma(x)\bar{\omega}(x)v_{Az}^2}{\tilde{w}c_s^2}+\left[\frac{\bar{\omega}(x)\tilde{\rho}\gamma(x)^3\tilde{v}_z(x)}{c^2}-\tilde{\rho}\gamma(x)k_z\right]\frac{c^2v_{Az}^2\bar{k}_z(x)}{\tilde{w}\gamma(x)^2\bar{\omega}(x)}\\
&= \frac{c^2\tilde{\rho}\gamma(x)\bar{\omega}(x)}{\tilde{w}}\left[1+\frac{v_{Az}^2}{c_s^2}+\frac{v_{Az}^2\bar{k}_z(x)\tilde{v}_z(x)}{\bar{\omega}(x)c^2}-\frac{v_{Az}^2\bar{k}_z(x)k_z}{\gamma(x)^2\bar{\omega}(x)^2}\right]\\
&= \frac{c^2\tilde{\rho}}{\tilde{w}\gamma(x)\bar{\omega}(x)}\left[\gamma(x)^2\bar{\omega}(x)^2\left(1+\frac{v_{Az}^2}{c_s^2}\right)-v_{Az}^2\bar{k}_z(x)\left(k_z-\frac{\gamma(x)^2\bar{\omega}(x)\tilde{v}_z(x)}{c^2}\right)\right]\\
&= \frac{c^2\tilde{\rho}}{\tilde{w}\gamma(x)\bar{\omega}(x)}\left[\gamma(x)^2\bar{\omega}(x)^2\left(1+\frac{v_{Az}^2}{c_s^2}\right)-v_{Az}^2\gamma(x)^2\bar{k}_z(x)^2\right]\\
&= \frac{c^2\tilde{\rho}}{\tilde{w}\gamma(x)\bar{\omega}(x)}\left[\gamma(x)^2\bar{\omega}(x)^2+v_{Az}^2\gamma(x)^2\left(\frac{\bar{\omega}(x)^2}{c_s^2}-\bar{k}_z(x)^2\right)\right]. \qquad (5.84)
\end{aligned}
$$

We can now rewrite our pressure ODE as

$$
\begin{aligned}
A(x)\left[\frac{\delta P_b'}{\omega_a(x)^2}\right]'+F_0(x)\delta P_b &= 0, \qquad \text{where}\\
F_0(x) &= \frac{c^2\tilde{\rho}}{\tilde{w}\gamma(x)\bar{\omega}(x)}\gamma(x)^2\left[\frac{\bar{\omega}(x)^2}{c_s^2}-\bar{k}_z(x)^2\right],\\
A(x) &= \frac{c^2\tilde{\rho}}{\tilde{w}\gamma(x)\bar{\omega}(x)}\left[\gamma(x)^2\bar{\omega}(x)^2+v_{Az}^2\gamma(x)^2\left(\frac{\bar{\omega}(x)^2}{c_s^2}-\bar{k}_z(x)^2\right)\right], \qquad (5.85)
\end{aligned}
$$

or, equivalently,

$$\begin{aligned}
\omega_b(x)^2\left[\frac{\delta P_b'}{\omega_a(x)^2}\right]' + k_d(x)^2\delta P_b &= 0, \qquad \text{where} \\
k_d(x)^2 &= \gamma(x)^2\left[\frac{\bar{\omega}(x)^2}{c_s^2} - \bar{k}_z(x)^2\right], \\
\omega_b(x)^2 &= \gamma(x)^2\bar{\omega}(x)^2 + v_{Az}^2\gamma(x)^2\left(\frac{\bar{\omega}(x)^2}{c_s^2} - \bar{k}_z(x)^2\right), \\
\omega_a(x)^2 &= \gamma(x)^2\bar{\omega}(x)^2 - v_{Az}^2(k_z^2 - \omega^2/c^2), \\
\bar{k}_z(x) &= k_z - \frac{\omega\tilde{v}_z(x)}{c^2}, \\
\delta P_b &= \delta P + \tilde{B}_z\delta B_z. \qquad (5.86)
\end{aligned}$$

We can now multiply both sides of the above ODE by $\omega_a(x)^2/\omega_b(x)^2$. We obtain

$$\omega_a(x)^2\left[\frac{\delta P_b'}{\omega_a(x)^2}\right]' + k_x(x)^2\delta P_b = 0, \qquad (5.87)$$

where

$$\begin{aligned}
k_x(x)^2 &= \frac{\omega_a(x)^2}{\omega_b(x)^2}k_d(x)^2 \\
&= \frac{\gamma(x)^2\bar{\omega}(x)^2 - v_{Az}^2(k_z^2 - \omega^2/c^2)}{\gamma(x)^2\bar{\omega}(x)^2 + v_{Az}^2 k_d(x)^2}[k_d(x)^2]. \qquad (5.88)
\end{aligned}$$

This ODE reduces in the non-relativistic MHD limit to the pressure ODE given in Miura and Pritchett (1982). The expression for $k_d(x)^2$ is also equivalent to the dispersion relation given in LRN09. The above ODE is written in terms of the perturbation to total pressure. However, from the linearization process, we also have the following expressions for the perturbations of the remaining quantities in terms of the perturbation to total pressure:

$$
\begin{aligned}
\delta v_x &= \frac{-ic^2\bar{\omega}(x)\delta P_b'}{\tilde{w}\omega_a(x)^2}, \\
\delta v_z &= C_2(x)\delta P_b'' + C_1(x)\delta P_b' + C_0(x)\delta P_b, \qquad \text{where} \\
C_2(x) &\equiv \frac{c^4\tilde{B}_z^2\bar{k}_z(x)}{\tilde{w}^2\gamma(x)^2\bar{\omega}(x)\omega_a(x)^2}, \\
C_1(x) &\equiv \frac{c^4\tilde{B}_z^2\bar{k}_z(x)f_a'(x)}{\tilde{w}^2\gamma(x)^2\bar{\omega}(x)} - \frac{\tilde{v}_z'(x)}{\tilde{w}\omega_a(x)^2}, \\
C_0(x) &\equiv \frac{\bar{k}_z(x)}{\tilde{w}\gamma(x)^2\bar{\omega}(x)}, \qquad \text{and}
\end{aligned}
$$

$$
\begin{aligned}
\delta B_x &= \frac{ic^2k_z\tilde{B}_z\delta P_b'}{\tilde{w}\omega_a(x)^2}, \\
\delta B_z &= -\frac{c^2\tilde{B}_z}{\tilde{w}}\left[\frac{\delta P_b''}{\omega_a(x)^2} + f_a'(x)\delta P_b'\right], \\
\delta P &= \frac{c^2\tilde{B}_z^2}{\tilde{w}}\left[\frac{\delta P_b''}{\omega_a(x)^2} + f_a'(x)\delta P_b'\right] + \delta P_b, \\
\delta\rho &= \delta P\left[\frac{1}{c_s^2} - \frac{1}{c^2(\Gamma-1)}\right].
\end{aligned} \tag{5.89}
$$

These expressions allow us to define the perturbation profiles of the eigenmode in which the system is launched at the start of the simulation. In the limit of zero magnetic field, the above ODE reduces to the corresponding RHD differential equation in the thermal pressure:

$$
\begin{aligned}
\omega_a(x)^2\left[\frac{\delta P'}{\omega_a(x)^2}\right]' + k_d(x)^2\delta P &= 0, \qquad \text{where} \\
k_d(x)^2 &= \gamma(x)^2\left[\frac{\bar{\omega}(x)^2}{c_s^2} - \bar{k}_z(x)^2\right], \\
\omega_a(x)^2 &= \gamma(x)^2\bar{\omega}(x)^2.
\end{aligned} \tag{5.90}
$$

We have derived the second-order ODE in total pressure whose solution yields eigenmodes of the system in RMHD. We now wish to show that in the limit of a step-function (tangential) discontinuity, this ODE recovers the results obtained in chapter 4.

5.3 RMHD ODE with a Step-function Velocity Profile

We consider the RMHD result from the previous section, and wish to recover the dispersion relation for a step-function velocity profile, which was derived in chapter 4. Let region 1 correspond to $x > 0$, and region to correspond to $x < 0$. The velocity profile has the form

$$\begin{aligned} v_z(x) &= v_{z1}, \qquad x > 0, \\ v_z(x) &= v_{z2}, \qquad x < 0. \end{aligned} \tag{5.91}$$

For notational simplicity, let $S = \delta P_b$ denote the perturbation to total pressure. For a step-function profile, the RMHD pressure ODE (5.87) reduces to two constant-coefficient ODEs, one in each half-space:

$$\begin{aligned} \frac{d^2S}{dx^2} + k_{x1}^2 S &= 0, \qquad x > 0, \\ \frac{d^2S}{dx^2} + k_{x2}^2 S &= 0, \qquad x < 0, \end{aligned} \tag{5.92}$$

where the normal wave vectors are given, from (5.88), by

$$k_{xj}^2 = \frac{\gamma_j^2 \bar{\omega}_j^2 - v_{Az}^2 (k_z^2 - \omega^2/c^2)}{\gamma_j^2 \bar{\omega}_j^2 + v_{Az}^2 k_{dj}^2}, \tag{5.93}$$

and, for $j = 1, 2$,

$$\bar{\omega}_j = \omega - k_z v_{zj}, \tag{5.94}$$

$$\gamma_j = \frac{1}{\sqrt{1 - v_{zj}^2/c^2}}, \tag{5.95}$$

$$k_{dj}^2 = \gamma_j^2 \left[\frac{\bar{\omega}_j^2}{c_s^2} - \left(k_z - \frac{\omega v_{zj}}{c^2} \right)^2 \right]. \tag{5.96}$$

The general solutions to (5.92) are, again for $j = 1, 2$,

$$S_j(x) \;=\; S_{j0}\exp(ik_{xj}x). \tag{5.97}$$

In order to relate the S_{j0} and derive an algebraic dispersion relation, we must apply boundary conditions to $S(x)$ at $x = 0$. To determine these conditions, we note that at $x = 0$, $S(x)$ must satisfy the RMHD pressure ODE (5.87):

$$\omega_a^2(x)\frac{d}{dx}\left[\frac{1}{\omega_a(x)^2}\frac{dS}{dx}\right] + k_x^2(x)S \;=\; 0. \tag{5.98}$$

In order for (5.98) to hold at $x = 0$, we must have continuity, at $x = 0$, of S, and of the left-hand term inside the brackets. The boundary conditions are therefore

$$\begin{aligned} S_1(0) \;&=\; S_2(0), \\ \frac{S_1'(0)}{\omega_{a1}^2} \;&=\; \frac{S_2'(0)}{\omega_{a2}^2}, \end{aligned} \tag{5.99}$$

where, for $j = 1, 2$,

$$\omega_{aj}^2 \;=\; \gamma_j^2\bar{\omega}_j^2 - v_{Az}^2\left(k_z^2 - \frac{\omega^2}{c^2}\right). \tag{5.100}$$

The first boundary condition states that the total pressure (i.e., thermal plus electromagnetic) must be equal across the discontinuity. The second condition states that the normal fluid displacements must be equal across the discontinuity (Chandrasekhar 1961). Substituting the general solutions (5.97) into the boundary conditions (5.99), we obtain

$$S_{10} \;=\; S_{20}, \tag{5.101}$$

$$\frac{k_{x1}S_{10}}{\omega_{a1}^2} \;=\; \frac{k_{x2}S_{20}}{\omega_{a2}^2}, \tag{5.102}$$

or simply

$$\frac{k_{x1}}{\omega_{a1}^2} = \frac{k_{x2}}{\omega_{a2}^2}. \tag{5.103}$$

This is precisely the dispersion relation obtained in chapter 4 for an RMHD fluid with a step-function discontinuity. The non-relativistic limit of this dispersion relation recovers the result of LRN09.

We have demonstrated that the second-order ODE in total pressure recovers the expected results obtained in chapter 4 in the limit of a tangential discontinuity. We now wish to demonstrate that this pressure ODE has the same underlying structure in the HD, RHD, MHD, and RMHD regimes.

5.4 Underlying Structure of ODE For Pressure Eigenfunctions

In comparing our results for the unmagnetized and magnetized cases, we observe a central underlying form for the second-order ODE satisfied by the perturbation to the total pressure when a Kelvin-Helmholtz instability is introduced in a jet with sheared boundaries. There are four cases: hydrodynamic (HD), relativistic HD (RHD), magnetohydrodynamic (MHD), and relativistic MHD (RMHD). Recall that the fluid is adiabatic, compressible, and when magnetized, infinitely conducting. The density and pressure have uniform respective values $\tilde{\rho}$ and $\tilde{P}$. The unperturbed velocity is in the z-direction, and has some shear variation $\tilde{v}_z(x)$ in the x-direction.

The following second-order ODE is used with the shooting method in order to numerically construct the eigenfunction profiles of the pressure perturbation:

$$\Omega^2(x)\frac{d}{dx}\left[\frac{1}{\Omega^2(x)}\frac{d\delta P_b}{dx}\right] + k_x^2(x)\delta P_b(x) \;=\; 0, \tag{5.104}$$

where δP_b is the perturbation to the total stress from thermal pressure and, if present, magnetic pressure.

In the hydrodynamic (HD) case, $\Omega^2(x)$ corresponds to Doppler-shifted traveling waves, while the expression for $k_x^2(x)$ corresponds to non-relativistic adiabatic sound waves:

$$\begin{aligned}
\delta P_b(x) &= \delta P(x), \qquad \text{thermal pressure,} \\
\Omega^2(x) &= (\omega - k_z\tilde{v}_z(x))^2, \\
k_x^2(x) &= \frac{(\omega - k_z\tilde{v}_z(x))^2}{c_s^2} - k_z^2 - k_y^2, \qquad \text{where} \\
c_s^2 &= \frac{\Gamma\tilde{P}}{\tilde{\rho}}.
\end{aligned} \tag{5.105}$$

In the relativistic hydrodynamic (RHD) case, $\Omega^2(x)$ corresponds to Lorentz-shifted traveling waves, while the expression for $k_x^2(x)$ corresponds to relativistic adiabatic sound waves, with Lorentz-shifts in the frequency and wave vector:

$$\begin{aligned}
\delta P_b(x) &= \delta P(x), \qquad \text{thermal pressure,} \\
\Omega^2(x) &= \gamma(x)^2(\omega - k_z\tilde{v}_z(x))^2, \\
k_x(x)^2 &= \frac{\gamma(x)^2(\omega - k_z\tilde{v}_z(x))^2}{c_s^2} - \gamma(x)^2\left(k_z - \frac{\omega\tilde{v}_z(x)}{c^2}\right)^2 - k_y^2,
\end{aligned} \tag{5.106}$$

where

$$\begin{aligned}
\gamma(x) &= \frac{1}{\sqrt{1 - \tilde{v}_z(x)/c^2}}, \\
c_s^2 &= c^2\frac{\Gamma\tilde{P}}{\tilde{w}}, \\
\tilde{w} &= \tilde{\rho}c^2 + \frac{\Gamma}{\Gamma - 1}\tilde{P}.
\end{aligned} \tag{5.107}$$

In the magnetohydrodynamic (MHD) case, $\Omega^2(x)$ corresponds to Alfven waves, while the expression for $k_x^2(x)$ corresponds to slow and fast magnetosonic waves. This result is in agreement with Miura and Pritchett (1982) and LRN09 in the limit in which we can neglect displacement current.

$$\begin{aligned}
\delta P_b(x) &= \delta P(x) + \tilde{\mathbf{B}} \cdot \delta \mathbf{B}, \qquad \text{thermal and magnetic pressure,} \\
\Omega^2(x) &= \bar{\omega}(x)^2 - \left(\mathbf{v}_A \cdot \mathbf{k}\right)^2, \\
k_x(x)^2 &= \frac{\bar{\omega}(x)^4}{\Omega^2(x) c_s^2 + \bar{\omega}(x)^2 v_A^2} - k_z^2 - k_y^2, \qquad \text{where} \\
\\
\bar{\omega}(x) &= \omega - k_z \tilde{v}_z(x), \\
\mathbf{v}_A &= \frac{\tilde{\mathbf{B}}}{\sqrt{\tilde{\rho}}}, \qquad c_s^2 = \frac{\Gamma \tilde{P}}{\tilde{\rho}}.
\end{aligned} \tag{5.108}$$

In the relativistic magnetohydrodynamic (RMHD) case, we consider a flow-aligned magnetic field ($\tilde{B}_y = 0$). $\Omega^2(x)$ corresponds to Lorentz-shifted Alfven waves with displacement current causing a shift of k_z^2, while the expression for $k_x^2(x)$ corresponds to slow and fast relativistic magnetosonic waves:

$$\begin{aligned}
\delta P_b(x) &= \delta P(x) + \tilde{\mathbf{B}} \cdot \delta \mathbf{B}, \qquad \text{thermal and magnetic pressure} \\
\Omega^2(x) &= \gamma(x)^2 \bar{\omega}(x)^2 - v_{Az}^2 \left(k_z^2 - \frac{\omega^2}{c^2} \right), \\
k_x^2(x) &= \frac{\gamma(x)^2 \bar{\omega}(x)^2 k_d(x)^2 - \omega_d(x)^2 \left(k_y^2 + k_z^2 - \omega^2/c^2 \right)}{\gamma(x)^2 \bar{\omega}(x)^2 + \omega_d(x)^2},
\end{aligned} \tag{5.109}$$

where

$$
\begin{aligned}
\omega_d(x)^2 &= \gamma(x)^2 v_{Az}^2 \left(\frac{\bar{\omega}(x)^2}{c_s^2} - \bar{k}_z(x)^2 \right), \\
k_d(x)^2 &= \gamma(x)^2 \left(\frac{\bar{\omega}(x)^2}{c_s^2} - \bar{k}_z(x)^2 \right) - k_y^2, \\
\bar{\omega}(x) &= \omega - k_z \tilde{v}_z(x), \\
\bar{k}_z(x) &= k_z - \frac{\omega \tilde{v}_z(x)}{c^2}, \\
v_{Az} &= \frac{\tilde{B}_z}{\sqrt{\tilde{w}}}, \\
\gamma(x) &= \frac{1}{\sqrt{1 - \tilde{v}_z(x)/c^2}}, \qquad c_s^2 = c^2 \frac{\Gamma \tilde{P}}{\tilde{w}}.
\end{aligned} \tag{5.110}
$$

Another important observation is that the above pressure ODEs converge to one another in the appropriate limits. The unmagnetized limit of the RMHD ODE recovers the RHD ODE. The non-relativistic limit of the RMHD ODE recovers the MHD ODE. The non-relativistic (unmagnetized) limits of the RHD (MHD) ODEs each recover the HD ODE.

We have demonstrated that the second-order ODE in total pressure has the same underlying structure in the HD, RHD, MHD, and RMHD regimes. We now describe the process by which we numerically solve this ODE in order to construct a numerical eigenmode of the system, i.e., the eigenmode in which the system is launched at the start of the simulation.

5.5 Numerically Computing an Eigenmode

In the previous sections, we obtained the self-adjoint ODE

$$
\omega_a(x)^2 \left[\frac{\delta P_b'}{\omega_a(x)^2} \right]' + k_x(x)^2 \delta P_b = 0, \tag{5.111}
$$

where

$$
\delta P_b = \delta P + \tilde{B}_z \delta B_z, \qquad \text{in RMHD, and} \tag{5.112}
$$

$$
\delta P_b = \delta P, \qquad \text{in RHD.} \tag{5.113}
$$

We wish to numerically solve this ODE using what is known as the *shooting method*, which is discussed in Blumen (1970). In so doing, we will obtain an eigenmode of the system. At some location $x = x_m$, $-L_x/2 < x_m < L_x/2$, we divide the system into left and right regions. For a given eigenfrequency ω, we use the fourth-order Runge-Kutta method to numerically compute $\delta P_b(x)$ in the two regions: a left profile in the region $x \leq x_m$, and a right profile in the region $x \geq x_m$. Our goal is to find the eigenfrequency ω for which the numerically computed left and right profiles of $\delta P_b(x)$ converge smoothly at $x = x_m$. We have then defined a numerical eigenmode. This is the eigenmode that will serve as our initial perturbation at the start of the simulation. Because we are integrating inward from the outer boundaries, our direction of integration ensures that the irregular solutions damp out, and the regular solutions prevail. We have also repeated this method for progressively more refined meshes (smaller spatial increments), and verified convergence of the eigenfrequency. We use at least 1001 grid points in our simulations, corresponding to a highly refined grid.

We now show how to compute the numerical profiles for a given eigenfrequency ω. We begin by defining the coefficients

$$\begin{aligned} C_1(x) &= k_x(x)^2 = \frac{\gamma(x)^2\bar{\omega}(x)^2 - v_{Az}^2(k_z^2 - \omega^2/c^2)}{\gamma(x)^2\bar{\omega}(x)^2 + v_{Az}^2 k_d(x)^2}[k_d(x)^2], \\ C_2(x) &= \omega_a(x)^2 = \gamma(x)^2\bar{\omega}(x)^2 - v_{Az}^2(k_z^2 - \omega^2/c^2). \end{aligned} \tag{5.114}$$

In the RHD case, these reduce to

$$\begin{aligned} C_1(x) &= k_d(x)^2 = \gamma(x)^2\left[\frac{\bar{\omega}(x)^2}{c_s^2} - \bar{k}_z(x)^2\right], \\ C_2(x) &= \omega_a(x)^2 = \gamma(x)^2\bar{\omega}(x)^2. \end{aligned} \tag{5.115}$$

Our ODE is now

$$C_2(x)\left[\frac{\delta P_b(x)'}{C_2(x)}\right]' + C_1(x)\delta P_b(x) \;=\; 0. \tag{5.116}$$

We then write this second-order equation as a system of two first-order equations in the variables $S(x) = \delta P_b(x)$ and $Q(x) = \delta P_b'(x)/C_2(x)$.

$$\begin{aligned} S'(x) &= C_2(x)Q(x), \\ Q'(x) &= -\frac{C_1(x)S(x)}{C_2(x)}. \end{aligned} \tag{5.117}$$

Suppose there are n_x spatial points from $x = -L_x/2$ to $x = L_x/2$. We first choose an index n_f satisfying $1 < n_f < n_x$, and the corresponding x_m satisfying $-L_x/2 < x_m < L_x/2$. In general, x_m should be close, but unequal, to zero. We then compute the left profiles, in the region $x \leq x_m$. We start at the spatial increment $n = 1$, corresponding to $x = -L_x/2$, and proceed to $n = n_f$, corresponding to $x = x_m$. In what follows, we use the subscript l to denote "left", meaning that we're computing the left-hand profiles. S_{l1} and Q_{l1} are given by

$$\begin{aligned} S_{l1} &= \delta P_{b0}, \\ Q_{l1} &= 0. \end{aligned} \tag{5.118}$$

δP_{b0} is a small but non-zero user-specified value that controls the amplitude of the perturbation at $x = x_m$. Suppose that at spatial index n we have Q_{ln} and S_{ln}. We wish to compute $Q_{l,n+1}$ and $S_{l,n+1}$ at spatial index $n + 1$.

Because we're using the fourth-order Runge-Kutta method, the above computation is made in four iterations. Therefore, we wish to define four spatial locations ranging from x_n to $x_{n+1} = x_n + \Delta x$. We first define the vector

$$f = \left(0, \frac{1}{2}, \frac{1}{2}, 1\right). \tag{5.119}$$

This vector is motivated by the coefficients of the Runge-Kutta method being used. We can then define intermediate spatial locations

$$\begin{aligned} x_{l,n+i/4} &= -\frac{L_x}{2} + \Delta x(n - 1 + f_i), \\ x_{l,n+i/4+j} &= x_{l,n+i/4} + j\Delta x, \\ x_{l,n+i/4-j} &= x_{l,n+i/4} - j\Delta x. \end{aligned} \tag{5.120}$$

We can now make the following definitions:

$$\begin{aligned} \gamma_{lj} &= \frac{1}{\sqrt{1 - \tilde{v}_z(x_{lj})^2/c^2}}, \\ \bar{k}_{z,lj} &= k_z - \frac{\omega \tilde{v}_z(x_{lj})}{c^2}, \\ \bar{\omega}_{lj} &= \omega - k_z \tilde{v}_z(x_{lj}), \\ k^2_{dl,j} &= \gamma^2_{lj}\left(\frac{\bar{\omega}^2_{lj}}{c_s^2} - \bar{k}^2_{z,lj}\right), \\ C_{1l,j} &= \frac{\gamma^2_{lj}\bar{\omega}^2_{lj} - v^2_{Az}(k_z^2 - \omega^2/c^2)}{\gamma^2_{lj}\bar{\omega}^2_{lj} + v^2_{Az}k^2_{dl,j}}[k^2_{dl,j}], \\ C_{2l,j} &= \gamma^2_{lj}\bar{\omega}^2_{lj} - v^2_{Az}(k_z^2 - \omega^2/c^2). \end{aligned} \tag{5.121}$$

In the RHD case, the last two definitions reduce to

$$\begin{aligned} C_{1l,j} &= k^2_{dl,j}, \\ C_{2l,j} &= \gamma^2_{lj}\bar{\omega}^2_{lj}. \end{aligned} \tag{5.122}$$

This allows us to define the coefficients C_{1l} and C_{2l} at intermediate spatial locations. In the RMHD case, we have

$$\begin{aligned} C_{1l,n+i/4} &= \frac{\gamma^2_{l,n+i/4}\bar{\omega}^2_{l,n+i/4} - v^2_{Az}(k_z^2 - \omega^2/c^2)}{\gamma^2_{l,n+i/4}\bar{\omega}^2_{l,n+i/4} + v^2_{Az}k^2_{dl,n+i/4}}[k^2_{dl,n+i/4}], \\ C_{2l,n+i/4} &= \gamma^2_{l,n+i/4}\bar{\omega}^2_{l,n+i/4} - v^2_{Az}(k_z^2 - \omega^2/c^2). \end{aligned} \tag{5.123}$$

In the RHD case, we have

$$\begin{aligned} C_{1l,n+i/4} &= k^2_{dl,\,n+i/4}, \\ C_{2l,n+i/4} &= \gamma^2_{l,n+i/4}\bar{\omega}^2_{l,n+i/4}. \end{aligned} \tag{5.124}$$

We now loop from $i = 1$ to $i = 4$, and at each value of i we compute the following:

$$i > 1: \qquad \begin{pmatrix} S_{l,n+i/4} \\ Q_{l,n+i/4} \end{pmatrix} = \begin{pmatrix} S_{ln} \\ Q_{ln} \end{pmatrix} + \Delta x \sum_{j=1}^{i-1} \alpha_{ij} \frac{d}{dx} \begin{pmatrix} S \\ Q \end{pmatrix}_{l,n+j/4}, \tag{5.125}$$

$$\text{all } i: \qquad \frac{d}{dx} \begin{pmatrix} S \\ Q \end{pmatrix}_{l,n+i/4} = \begin{pmatrix} C_{2l,n+i/4} Q_{l,n+i/4} \\ -C_{1l,n+i/4} S_{l,n+i/4} / C_{2l,n+i/4} \end{pmatrix}. \tag{5.126}$$

The values of Q_l and S_l at the spatial increment $n + 1$ are then given by

$$\begin{pmatrix} S_{l,n+1} \\ Q_{l,n+1} \end{pmatrix} = \begin{pmatrix} S_{ln} \\ Q_{ln} \end{pmatrix} + \Delta x \sum_{i=1}^{4} \beta_i \frac{d}{dx} \begin{pmatrix} S \\ Q \end{pmatrix}_{l,n+i/4}.$$

Once we have gone from $n = 1$ to n_f, we have computed the S_{ln} and Q_{ln} in the region $x \le x_m$. That is, we have computed the left-hand profiles. Let us denote our results at $x = x_m$ as follows:

$$\begin{aligned} S_{\text{left}}(x_m) &= S_{l,n_f}, \\ Q_{\text{left}}(x_m) &= Q_{l,n_f}. \end{aligned} \tag{5.127}$$

The method used is the "classic" fourth-order Runge-Kutta method. Its α and β coefficients are defined as follows:

$$\begin{aligned} &\alpha_{21} = 1/2, \quad \alpha_{32} = 1/2, \quad \alpha_{43} = 1, \quad \alpha_{ij} = 0 \ \text{ otherwise, and} \\ &\beta_1 = 1/6, \quad \beta_2 = 1/3, \quad \beta_3 = 1/3, \quad \beta_4 = 1/6. \end{aligned} \tag{5.128}$$

We now compute the right profiles, in the region $x \ge x_m$. We start at the spatial increment $n = 1$, which now corresponds to $x = L_x/2$, and proceed to $n = n_x + 1 - n_f$,

corresponding to $x = x_m$. In what follows, we use the subscript r to denote "right," meaning that we're computing the right-hand profiles. S_{r1} and Q_{r1} are the same as S_{l1} and Q_{l1}, the values at the left boundary. That is,

$$\begin{aligned} S_{r1} &= S_{l1} = \delta P_{b0}, \\ Q_{r1} &= Q_{l1} = 0. \end{aligned} \tag{5.129}$$

Suppose that at spatial index n we have Q_{rn} and S_{rn}. We wish to compute $Q_{r,n+1}$ and $S_{r,n+1}$ at spatial index $n + 1$.

Because we're using the fourth-order Runge-Kutta method, the above computation is made in four iterations. Therefore, we wish to define four spatial locations ranging from x_n to $x_{n+1} = x_n - \Delta x$. We first define the vector

$$f = \left(0, \frac{1}{2}, \frac{1}{2}, 1\right).$$

This vector is motivated by the coefficients of the Runge-Kutta method being used. We can then define intermediate spatial locations

$$\begin{aligned} x_{r,n+i/4} &= \frac{L_x}{2} - \Delta x(n - 1 + f_i), \\ x_{r,n+i/4+j} &= x_{r,n+i/4} - j\Delta x, \\ x_{r,n+i/4-j} &= x_{r,n+i/4} + j\Delta x. \end{aligned} \tag{5.130}$$

Note that as the index increases, the value of x *decreases*. We can now make the following definitions:

$$
\begin{aligned}
\gamma_{rj} &= \frac{1}{\sqrt{1-\tilde{v}_z(x_{rj})^2/c^2}}, \\
\bar{k}_{z,rj} &= k_z - \frac{\omega\tilde{v}_z(x_{rj})}{c^2}, \\
\bar{\omega}_{rj} &= \omega - k_z\tilde{v}_z(x_{rj}), \\
k^2_{dr,j} &= \gamma^2_{rj}\left(\frac{\bar{\omega}^2_{rj}}{c_s^2} - \bar{k}^2_{z,rj}\right), \\
C_{1r,j} &= \frac{\gamma^2_{rj}\bar{\omega}^2_{rj} - v^2_{Az}(k_z^2-\omega^2/c^2)}{\gamma^2_{rj}\bar{\omega}^2_{rj} + v^2_{Az}k^2_{dr,j}}[k^2_{dr,j}], \\
C_{2r,j} &= \gamma^2_{rj}\bar{\omega}^2_{rj} - v^2_{Az}(k_z^2-\omega^2/c^2).
\end{aligned}
\tag{5.131}
$$

In the RHD case, the last two definitions reduce to

$$
\begin{aligned}
C_{1r,j} &= k^2_{dr,j}, \\
C_{2r,j} &= \gamma^2_{rj}\bar{\omega}^2_{rj}.
\end{aligned}
\tag{5.132}
$$

This allows us to define the coefficients C_{1r} and C_{2r} at intermediate spatial locations. In the RMHD case, we have

$$
\begin{aligned}
C_{1r,n+i/4} &= \frac{\gamma^2_{r,n+i/4}\bar{\omega}^2_{r,n+i/4} - v^2_{Az}(k_z^2-\omega^2/c^2)}{\gamma^2_{r,n+i/4}\bar{\omega}^2_{r,n+i/4} + v^2_{Az}k^2_{dr,n+i/4}}[k^2_{dr,n+i/4}], \\
C_{2r,n+i/4} &= \gamma^2_{r,n+i/4}\bar{\omega}^2_{r,n+i/4} - v^2_{Az}(k_z^2-\omega^2/c^2).
\end{aligned}
\tag{5.133}
$$

In the RHD case, we have

$$
\begin{aligned}
C_{1r,n+i/4} &= k^2_{dr,n+i/4}, \\
C_{2r,n+i/4} &= \gamma^2_{r,n+i/4}\bar{\omega}^2_{r,n+i/4}.
\end{aligned}
\tag{5.134}
$$

We now loop from $i = 1$ to $i = 4$, and at each value of i we compute the following:

$$
i > 1: \qquad \begin{pmatrix} S_{r,n+i/4} \\ Q_{r,n+i/4} \end{pmatrix} = \begin{pmatrix} S_{rn} \\ Q_{rn} \end{pmatrix} - \Delta x \sum_{j=1}^{i-1} \alpha_{ij} \frac{d}{dx} \begin{pmatrix} S \\ Q \end{pmatrix}_{r,n+j/4}, \tag{5.135}
$$

$$
\text{all } i: \qquad \frac{d}{dx}\begin{pmatrix} S \\ Q \end{pmatrix}_{r,n+i/4} = \begin{pmatrix} C_{2r,n+i/4}Q_{r,n+i/4} \\ -C_{1r,n+i/4}S_{r,n+i/4}/C_{2r,n+i/4} \end{pmatrix}. \tag{5.136}
$$

The values of Q_r and S_r at the spatial increment $n+1$ are then given by

$$\begin{pmatrix} S_{r,n+1} \\ Q_{r,n+1} \end{pmatrix} = \begin{pmatrix} S_{rn} \\ Q_{rn} \end{pmatrix} - \Delta x \sum_{i=1}^{4} \beta_i \frac{d}{dx} \begin{pmatrix} S \\ Q \end{pmatrix}_{r,n+i/4}. \tag{5.137}$$

Once we have gone from $n = 1$ to $n_x + 1 - n_f$, we have computed the S_{rn} and Q_{rn} in the region $x \geq x_m$. That is, we have computed the right-hand profiles. Let us denote our results at $x = x_m$ as follows:

$$\begin{aligned} S_{\text{right}}(x_m) &= S_{r,n_x+1-n_f}, \\ Q_{\text{right}}(x_m) &= Q_{r,n_x+1-n_f}. \end{aligned} \tag{5.138}$$

If we have chosen ω correctly, then the left and right-hand profiles should converge smoothly at $x = x_m$. That is, we should have

$$\begin{aligned} S_{\text{left}}(x_m) &= S_{\text{right}}(x_m), \\ Q_{\text{left}}(x_m) &= Q_{\text{right}}(x_m). \end{aligned} \tag{5.139}$$

Another way to state this is to say that the Wronskian corresponding to the input ω should be zero at $x = x_m$:

$$0 = W(x_m) = S_{\text{left}}(x_m) Q_{\text{right}}(x_m) - S_{\text{right}}(x_m) Q_{\text{left}}(x_m). \tag{5.140}$$

We wish to find the value of ω for which the Wronskian vanishes. The method for doing this depends on the profile of the velocity shear. Consider a hyperbolic tanh profile of the form

$$\tilde{v}_z(x) = v_{0z} \tanh(\kappa x). \tag{5.141}$$

In the limit $\kappa \to \infty$, this becomes the step-function profile considered earlier, between $-v_{0z}$ and v_{0z}. Therefore, in this limit, the behavior of the growth rates approaches the behavior of the growth rates for a step-function profile. The above tanh profile retains the Hermitian properties of the antisymmetric step-function profile. Therefore, here again, we can expect the frequency ω to either be purely real (stable) or purely imaginary (unstable). Furthermore, the Wronskian is purely real. Once we have decided whether to search for stability or instability, the search is one-dimensional, which means it can be facilitated with the use of the secant method. We begin with two initial guesses of the growth rate, α_1 and α_2. The corresponding values of the Wronskian are, respectively, W_1 and W_2. The line passing through these two points has the equation

$$W(\alpha) \;=\; W_1 + \frac{W_2 - W_1}{\alpha_2 - \alpha_1}(\alpha - \alpha_1). \tag{5.142}$$

The next estimate of the growth rate is the value α_3 for which $W(\alpha_3)$ is equal to zero. That is, we have

$$\begin{aligned} W_1 + \frac{W_2 - W_1}{\alpha_2 - \alpha_1}(\alpha_3 - \alpha_1) \;&=\; 0, \qquad \text{which yields} \\ \alpha_3 \;&=\; \alpha_1 - \frac{\alpha_2 - \alpha_1}{W_2 - W_1}(W_1). \end{aligned} \tag{5.143}$$

We then repeat this process, but now starting with α_2 and α_3 corresponding to W_2 and W_3. The best estimate of the growth rate is the value α_{j+1} for which W_j and W_{j+1} differ negligibly. We see that when the search is over a one-dimensional space, we have a systematic way of determining the desired frequency.

Consider now the"Bickley" jet velocity profile (Bickley 1937). Its definition, originally given in section 3.6, is

$$\tilde{v}_z(x) \;=\; v_{0z}\mathrm{sech}^2(\kappa x). \tag{5.144}$$

This is the profile which will be used in the nonlinear simulations shown later. It lacks the Hermiticity of the tanh profile. Therefore, each eigenmode is characterized by a frequency with non-zero *real* and *imaginary* parts, so the search for this frequency is now two-dimensional, across the entire complex frequency plane. This means we can no longer use the secant method. We search for zeros of the absolute value $|W|$ of the Wronskian. We iteratively refine the frequency grid over which we search, zooming in on regions where $|W|$ is locally minimized. Through the above algorithm, we obtain an eigenvalue for which the absolute value of the Wronskian is zero at $x = x_m$.

We're not quite done. The maximum value of δP_b is probably either too large or too small compared to the unperturbed quantities. Let $|\delta P_b|_i$ be the current maximum magnitude of δP_b, occurring at $x = x_{\max}$. Let $|\delta P_b|_f$ be the desired maximum magnitude of δP_b. In order to have this, we simply multiply the computed profiles by the scale factor g_0, given by

$$g_0 \;=\; \frac{|\delta P_b|_f}{|\delta P_b|_i}.$$

The perturbations of δP_b and $\delta P_b'$ are given, for $1 \le n \le n_f$, by

$$\begin{aligned} \delta P_{bn} &= g_0 S_{ln}, \\ \delta P'_{bn} &= g_0 Q_{ln}. \end{aligned} \tag{5.145}$$

For $1 \le n \le n_x + 1 - n_f$, the perturbations are given by

$$\begin{aligned} \delta P_{b,n_x+1-n} &= g_0 S_{rn}, \\ \delta P'_{b,n_x+1-n} &= g_0 Q_{rn}. \end{aligned} \tag{5.146}$$

Once these stress perturbations are computed, we can readily compute the numerical shear profiles of the perturbations $\delta\rho_j$, δv_{xj}, δv_{zj}, δP_j, δB_{xj}, and δB_{zj}, for $1 \leq j \leq n_x$.

In the RMHD case, we first compute δv_{xj} and δB_{xj} at each of these spatial points:

$$\begin{aligned}
\delta v_{xj} &= -i\frac{c^2\bar{\omega}_j\delta P'_{bj}}{\tilde{w}\omega_{aj}^2}, \\
\delta B_{xj} &= -\frac{k_z\tilde{B}_z}{\bar{\omega}_j}\delta v_{xj} = (i)\frac{c^2k_z\tilde{B}_z\delta P'_{bj}}{\tilde{w}\omega_{aj}^2}.
\end{aligned} \tag{5.147}$$

We then loop through the spatial points a second time, allowing us to compute $\delta v'_x$ using fourth-order finite-differencing schemes, since we now know δv_x at multiple locations. This in turn allows us to compute δB_z, and from this, the remaining perturbations.

$$\begin{aligned}
\delta B_{zj} &= (i)\frac{\delta B_{xj}\tilde{v}'_{zj} - \tilde{B}_z\delta v'_{xj}}{\bar{\omega}_j}, \\
\delta P_j &= \delta P_{bj} - \tilde{B}_z\delta B_{zj}, \\
\delta v_{zj} &= \frac{c^2\bar{k}_{zj}\delta P_{bj}}{\tilde{w}\gamma_j^2\bar{\omega}_j} - \frac{c^2\tilde{v}'_{zj}\delta P'_{bj}}{\tilde{w}\omega_{aj}^2}, \\
\delta\rho_j &= \delta P_j\left[\frac{1}{c_s^2} - \frac{1}{c^2(\Gamma-1)}\right].
\end{aligned} \tag{5.148}$$

The intermediate quantities are computed as follows:

$$\begin{aligned}
x_j &= -\frac{L_x}{2} + \Delta x(j-1), \\
\omega_{aj}^2 &= \gamma_j^2\bar{\omega}_j^2 - v_{Az}^2(k_z^2 - \omega^2/c^2), \\
\bar{\omega}_j &= \omega - k_z\tilde{v}_{zj}, \\
\bar{k}_{zj} &= k_z - \frac{\omega\tilde{v}_{zj}}{c^2}.
\end{aligned} \tag{5.149}$$

In the RHD case, we compute the following:

$$
\begin{aligned}
\delta P_j &= \delta P_{bj}, \\
\delta v_{xj} &= -i\frac{c^2 \delta P'_{bj}}{\tilde{w}\gamma_j^2 \bar{\omega}_j^2}, \\
\delta v_{zj} &= \frac{c^2 \bar{k}_{zj} \delta P_{bj}}{\tilde{w}\gamma_j^2 \bar{\omega}_j} - \frac{c^2 \tilde{v}'_{zj} \delta P'_{bj}}{\tilde{w}\gamma_j^2 \bar{\omega}_j^2}, \\
\delta \rho_j &= \delta P_j \left[\frac{1}{c_s^2} - \frac{1}{c^2(\Gamma - 1)} \right].
\end{aligned} \tag{5.150}
$$

Assume our total initial perturbation consists of a superposition of N_m modes. The jth mode corresponds to an input wave number k_{zj}, a corresponding eigenfrequency

$$
\omega_j = \omega_{rj} + i\omega_{ij}, \tag{5.151}
$$

and eigenfunctions

$$
\delta\rho_j(x),\ \delta P_j(x),\ \delta v_{xj}(x),\ \delta v_{zj}(x),\ \delta B_{xj}(x),\ \delta B_{zj}(x). \tag{5.152}
$$

Let mode j have amplitude C_j. Let the spatial grid, in the $x-z$ plane, be defined as follows:

$$
\begin{aligned}
\Delta x &= \frac{L_x}{n_x - 1}, \\
\Delta z &= \frac{L_z}{n_z - 1}, \\
x_{j_1} &= -\frac{L_x}{2} + (\Delta x)(j_1 - 1), \qquad 1 \le j_1 \le n_x, \\
z_{j_2} &= (\Delta z)(j_2 - 1), \qquad 1 \le j_2 \le n_z.
\end{aligned} \tag{5.153}
$$

Then the initial distributions are as follows:

$$
\begin{aligned}
\rho(x_{j_1}, z_{j_2}, 0) &= \tilde{\rho} + \sum_{j_0=1}^{N_m} C_{j_0} \delta\rho_{j_0}(x_{j_1}) \exp[ik_{z,j_0} z_{j_2}], \\
P(x_{j_1}, z_{j_2}, 0) &= \tilde{P} + \sum_{j_0=1}^{N_m} C_{j_0} \delta P_{j_0}(x_{j_1}) \exp[ik_{z,j_0} z_{j_2}], \\
v_x(x_{j_1}, z_{j_2}, 0) &= \sum_{j_0=1}^{N_m} C_{j_0} \delta v_{x,j_0}(x_{j_1}) \exp[ik_{z,j_0} z_{j_2}], \\
v_z(x_{j_1}, z_{j_2}, 0) &= \tilde{v}_z(x_{j_1}) + \sum_{j_0=1}^{N_m} C_{j_0} \delta v_{z,j_0}(x_{j_1}) \exp[ik_{z,j_0} z_{j_2}], \\
B_x(x_{j_1}, z_{j_2}, 0) &= \sum_{j_0=1}^{N_m} C_{j_0} \delta B_{x,j_0}(x_{j_1}) \exp[ik_{z,j_0} z_{j_2}], \\
B_z(x_{j_1}, z_{j_2}, 0) &= \tilde{B}_z + \sum_{j_0=1}^{N_m} C_{j_0} \delta B_{z,j_0}(x_{j_1}) \exp[ik_{z,j_0} z_{j_2}].
\end{aligned} \tag{5.154}
$$

We evolve only the real parts of these initial distributions. This is the general method for perturbing the system in a superposition of eigenmodes, thereby initializing the simulation. We should note, however, that the simulations in our study are launched in a single eigenmode, namely, the mode with the fastest growth rate. We have now described the numerical method by which we solve the second-order ODE in total pressure perturbation and construct the numerical eigenmode of the perturbation in which the system is launched at the start of the simulation.

5.6 Conclusion

For a continuously varying background velocity profile in RHD and RMHD, we have derived a second-order ODE in the perturbation to total pressure. We have demonstrated that this ODE has the same underlying self-adjoint form in the HD, RHD, MHD, and RMHD regimes. The non-relativistic limit of our RMHD result is in agreement with LRN09, and with the

result of Miura and Pritchett (1982). For a step-function velocity profile, the pressure ODE recovers the results of the previous chapter in each of the four regimes, including the results of Bodo et al. (2004) in RHD. We have then demonstrated how to numerically solve the pressure ODE by using the shooting method to integrate inward from the outer transverse boundaries (Blumen 1970; Miura and Pritchett 1982; Frank et al. 1996). This process is repeated over an array of complex eigenfrequencies, and a mode corresponds to a frequency for which the right and left pressure perturbation profiles converge smoothly at a point near the axis. By inserting this frequency into expressions (5.147) and (5.148), we have obtained the corresponding eigenfunction profiles of the thermal pressure, density, velocity components, and magnetic field components. We have now defined a numerical eigenmode in which to launch the system at the start of a simulation. We have also described how to launch a superposition of eigenmodes.

In chapter 6, we numerically solve the pressure ODE for the case of a sech^2 background velocity profile, which is the profile used in the simulations. We plot the dependence of numerical growth rate and phase velocity on various parameters, and uncover important stability properties.

Chapter 6

Growth Rates of the Bickley Jet Profile

We wish to examine the growth rate behavior of the KH instability for a velocity shear profile corresponding to the Bickley jet, namely, a background flow velocity given by $v_z(x) = v_{z0}\,\mathrm{sech}^2(x/r_0)$ (Bickley 1937), as this is the profile used in the numerical simulations. We assume a uniform background density ρ_0, background pressure P_0, and flow-aligned magnetic field B_{z0}. The system is assumed to span a length L_x, with N_x grid points, in the shear direction, corresponding to the interval $-L_x/2 \leq x \leq L_x/2$. The system is perturbed, and the wave vector of the perturbation has a component k_z in the flow direction. For a given set of these parameters, the corresponding complex eigenfrequency of maximum growth is computed numerically, as described in chapter 5. For each growth rate and eigenmode we compute, we use at least 1001 spatial grid points in the shear direction, to ensure convergence of our results. Throughout this chapter, we refer to "sinuous" and "varicose" modes, also used in Drazin and Howard (1966) in their linear stability analysis of the Bickley jet. "Sinuous" modes have antisymmetric pressure perturbation profiles, while "varicose" modes have symmetric pressure perturbation profiles. The sinuous and varicose modes also have opposite symmetries in the profiles of the remaining quantities (velocity, magnetic field, etc.). The

growth rates plotted in each case correspond to the fastest-growing sinuous mode, as opposed to the slower-growing varicose modes, since we select for sinuous modes in our simulations. Varicose modes occur at low growth rates ($\omega_i < 0.01\, c/r_0$), and regularly spaced values of ω_r, in the complex frequency plane. When the growth rate of the desired sinuous mode becomes too low ($\omega_i < 0.01\, c/r_0$), it becomes difficult for the search algorithm to distinguish the sinuous mode from the varicose modes. This accounts for most of the discontinuous behavior occasionally observed, at low growth rates, in the graphs that follow. Sinuous and varicose modes were discussed, in the HD regime, by Drazin and Howard (1966).

In section 6.1, we provide an overview of prior usage of the Bickley jet profile. In section 6.2, we recover the results of Drazin and Howard (1966), in the unmagnetized, non-relativistic regime. In section 6.3, we plot, in the relativistic regime, growth rate versus background magnetic-to-thermal pressure ratio (inverse plasma β) for various flow velocities. We find that growth rate decreases with increasing field strength, and that the system is stabilized above a certain field strength, corresponding to a critical inverse β which, for each flow speed, is considerably less than one in a pressure-dominated system (sound speed near its relativistic maximum of $c/\sqrt{3}$), but comparable to or larger than one in a density-dominated system (mildly relativistic sound speed). The corresponding critical Alfven velocities are approximately the same for both pressure and density-dominated systems (i.e., independent of sound speed). For more relativistic flow speeds, the growth rates are higher, and a stronger magnetic field is required in order to stabilize the system. Also, for sufficiently small Lorentz factors, the fractional decrease in growth rate is primarily a function of a relativistic Alfvenic Mach number M_A, which we have defined analogously to the manner in which Bodo et al. (2004) defined a relativistic sonic Mach number. The system is stabilized for $M_A^{-1} > \approx 1/3$.

This critical value is a consequence of the choice of a sech^2 background velocity profile.

In section 6.4, we plot unmagnetized growth rate versus flow speed for various sound speeds, and find that, regardless of sound speed, a flow speed very close to c is required in order to suppress instability. At higher sound speeds, the growth rate is larger, and increases with increasing flow speed. At lower sound speeds, the growth rate is approximately constant over a large range of flow speeds. In section 6.5, we plot growth rate versus the wave number k_z for various flow speeds. In each case, the k_z that maximizes the growth rate is slightly less than 1. We also find that, as the flow speed becomes more relativistic, instability extends to higher values of k_z, resulting in the excitation of modes with shorter wavelengths. When the flow speed is highly relativistic, modes are excited at wavelengths which are smaller than the length scale set by shear variation, which is one manifestation of the destabilizing tendencies of relativistic flows.

Throughout this chapter, we assume that the perturbation wave vector is aligned with the flow (i.e., has no component in the y-direction, which is orthogonal to the plane of the flow), as this is the nature of the perturbation in which the numerical simulations are launched.

Another important point is that the KH-unstable wave frequencies in the relativistic regime have frequencies on the order of c/r_0, which, as discussed in section 8.2, corresponds to about 10^{-8} s^{-1}. As discussed in sections 3.5 and 8.2, this is about 10 orders of magnitude smaller than the Larmor frequency. It is therefore highly unlikely that our KH-unstable modes would generate resonance with gyrating particles.

We begin by discussing the prior usage of the Bickley jet profile, which has thus far been primarily restricted to incompressible fluids in hydrodynamics. Our simulations incorporate compressibility, magnetization, and relativity.

6.1 Prior Usage of the Bickley Jet Profile

The salient research of the Kelvin-Helmholtz instability, as it applies to compressible, magnetized, or relativistic fluids, has not thus far used a Bickley jet profile, nor has it been applied to astrophysical jets. Rather, prior studies (Miura and Pritchett 1982; Frank et al. 1996; Otto and Fairfield 2000; Malagoli et al. 1996, among others) have often used a slab geometry with a single transition layer between jet and ambient medium, typically a hyperbolic tangent profile. Our background profiles are symmetric about the central axis, which means that the numerical solutions should exhibit certain symmetry properties about the central axis which should be preserved through time. This provides a way of verifying that our solutions sustain their numerical accuracy as they evolve. Other studies have used a cylindrical geometry (Marti et al. 1995; Koide et al. 1996; Leismann et al. 2005; Hardee 2005; Mignone et al. 2010, among others), which allows for a more complete exploration of the jet cross section. However, the RMHD cylindrical studies tend to focus on more general aspects of jet evolution, rather than the specific role of the KH instability. This is largely due to the many numerical difficulties that arise when the RMHD conservation-diffusion equations are modeled in cylindrical geometry in the presence of a velocity shear. By allowing for the use of a slab geometry, the Bickley jet profile avoids many of these difficulties, while spanning an entire cross section of the jet, and providing a built-in mechanism for validating the numerical accuracy of the solutions by ascertaining that certain symmetry properties are preserved throughout the evolution. One example is a condition on the vorticity $\Omega(x, z, t)$, i.e., the curl of the velocity. This condition reads

$$\Omega(x, z, t) \;=\; -\Omega(-x, z + \lambda/2, t), \tag{6.1}$$

where $\lambda = 2\pi/k_z$ is the longitudinal wavelength of the perturbation in which the system is launched. As we describe in chapter 11, we have verified that the system remains spatially periodic in the longitudinal direction, with wavelength λ, so that to very high accuracy we satisfy the condition

$$\Omega(x, z, t) \;=\; \Omega(x, z + \lambda, t). \tag{6.2}$$

We provide a physical interpretation of condition (6.1) in section 7.1, and discuss it in the context of numerical accuracy in section 10.9 of chapter 10.

Thus far, the Bickley jet has been used in meteorological and oceanographic studies of incompressible, non-relativistic, unmagnetized fluids. Bickley (1937) originally derived this profile as a solution to the Prandtl boundary layer equations (i.e., the HD single-fluid equations in the presence of a viscous boundary layer). Savic (1941) used the Bickley jet to model vortex motion in gaseous jets. This profile was also used by Lipps (1962) to study the stability of mid-latitude atmospheric jets, by Stern (1961) to study oceanic thermocline jets (the "thermocline" layer is the depth corresponding to the largest temperature gradient), and to examine wakes behind large obstacles (e.g., Mattingly et al. 1972). These studies, and others, focused on solving the Navier-Stokes equation written as a vorticity equation in terms of a stream function ψ, whose gradient is perpendicular to the velocity field $\mathbf{v}$, i.e., $\mathbf{v} = \hat{\mathbf{n}} \times \boldsymbol{\nabla}\psi$, where $\hat{\mathbf{n}}$ is normal to the plane of the flow. Linearizing this equation yields the Rayleigh equation. Solutions of this equation, i.e., modes, can be divided into two classes. Modes with even eigenfunctions (of the stream function) are called sinuous, while modes with odd eigenfunctions are called varicose. Drazin and Howard (1966) found approximate analytical expressions, and accurate numerical eigenfrequencies, for both types of modes.

Our numerical method of eigenmode construction, discussed in chapter 5, recovers these results very accurately. Lipps found several modes whose critical levels (where flow speed and phase velocity are equal) occur at the inflection points of the profile. Howard and Drazin (1964) found a sinuous neutral mode whose critical level lies at $x = 0$, where the profile is maximized, and where the stream function is singular. Maslowe (1991) demonstrated that the mode found by Howard and Drazin is part of the lower stability boundary of the varicose mode found by Lipps. Swaters (1999) examined the nonlinear evolution of a family of sinuous modes which lie in the vicinity of the mode discovered by Howard and Drazin.

In our numerical simulations, we expand the usage of the Bickley jet profile to fluids which are compressible, magnetized, and relativistic. We select for sinuous, rather than varicose, modes, as the sinuous modes have higher growth rates. We begin by demonstrating that our algorithm for eigenmode construction, explained in chapter 5, recovers the growth rates obtained by Drazin and Howard (1966) in the HD regime.

6.2 Comparison to Drazin and Howard (1966)

Drazin and Howard (1966) computed complex frequencies for an incompressible fluid in HD, with a velocity profile $v_z(x) = v_{z0}\,\mathrm{sech}^2(x/r_0)$. For comparison, we use a large enough sound speed to approximate incompressibility ($c_s = 18.3\,v_{z0}$), having found that our results converge at this sound speed. We use a system length of $L_x = 31.5\,r_0$. We compute frequencies at the same wave numbers used by Drazin and Howard (1966), and report the comparisons in table 6.2. Specifically, we compare results for the sinuous mode (antisymmetric pressure perturbation profiles), not the varicose mode (symmetric pressure perturbation profiles), as we use sinuous modes in the simulations. Let $\phi = \omega r_0/v_{z0}$. ϕ_r and ϕ_i denote our results,

$k_z r_0$	ϕ_r	ϕ_r(DH)	ϕ_i	ϕ_i(DH)
0.2	0.0334	0.0332	0.0512	0.0514
0.3	0.0688	0.0687	0.0801	0.0801
0.4	0.112	0.112	0.105	0.105
0.5	0.162	0.162	0.126	0.126
0.6	0.217	0.217	0.141	0.142
0.7	0.276	0.277	0.152	0.153
0.8	0.339	0.339	0.159	0.158
0.9	0.406	0.406	0.161	0.161
1.0	0.475	0.475	0.159	0.159
1.2	0.623	0.624	0.145	0.145
1.4	0.783	0.783	0.119	0.119
1.6	0.955	0.955	0.0844	0.0848
1.8	1.113	1.138	0.0480	0.0432

Table 6.1: Comparison to Drazin and Howard (1966)

while ϕ_r(DH) and ϕ_i(DH) denote the results of Drazin and Howard (1966).

These results agree very closely, which indicates that the numerical growth rates are being generated correctly in the HD regime. Figures 6.1 show plots of growth rate and phase velocity versus wave number for a set of different sound speeds. In each case, there is a maximum growth rate. With decreasing sound speed, this maximum value decreases, and occurs at a lower wave number. The growth rates decrease with decreasing sound speeds (i.e., as the fluid becomes more compressible). A decreasing sound speed corresponds to a larger density relative to pressure, i.e., a background flow with a larger amount of mechanical energy and inertia. At a lower sound speed, a perturbation must therefore perform more work against the bulk flow in order to extract energy and grow. From figure 6.1(b), we notice that the phase velocity is larger for smaller sound speeds, which again is due to the correspondence between smaller sound speeds and larger amounts of mechanical energy (and inertia) in the bulk flow. A noteworthy observation is that the phase velocity remains roughly

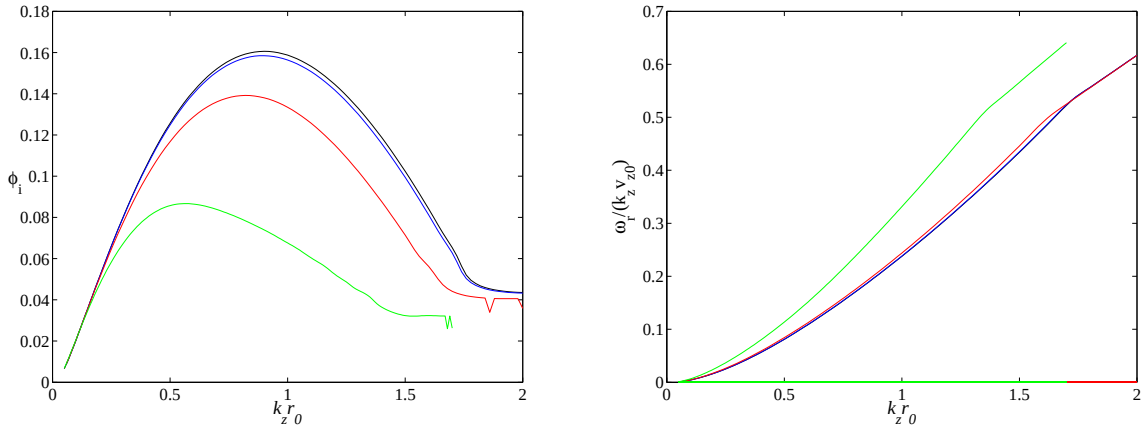

(a) growth rate

(b) phase velocity

Figure 6.1: Growth rate and phase velocity vs k_z for different sound speeds (HD)
$c_s/v_{z0} = 9.13$ (black), 2.89 (blue), 0.913 (red), 0.408 (green)

the same for sound speeds of $9.13\, v_{z0}$ and $0.913\, v_{z0}$, and all values in between. However, when we decrease the sound speed from $0.913\, v_{z0}$ to $0.408\, v_{z0}$, the phase velocity increases abruptly. Evidently, this is the interval of sound speeds within which the inertial effects of the bulk flow become significantly more important (i.e., within which the background density passes some critical value). This effect is very pronounced for the phase velocities, but also occurs to some extent with the growth rates, which are noticeably less at $c_s = 0.408\, v_{z0}$ than at the higher sound speeds. The incompressible case, considered by Drazin and Howard (1966) in the above table, corresponds most closely to the black curve, for which the ratio of sound speed to flow speed is largest.

We have verified that our algorithm for eigenmode construction reproduces the results of Drazin and Howard (1966) in the HD regime. We now proceed to examine the dependence of the numerical growth rate on various parameters. We begin with the dependence on the strength of the magnetic field.

6.3 Dependence of Growth Rate on Magnetic Field

Figures 6.2 displays growth rate (in units of c/r_0) as a function of the magnetic-to-thermal pressure ratio $\beta_0^{-1} = B_{z0}^2/(2P_0)$ (i.e., the inverse background plasma beta) for several flow velocities, each flow velocity corresponding to a specific curve. Figure 6.2(a) corresponds to the pressure-dominated case (relativistic sound speed), while figure 6.2(b) corresponds to a density-dominated case (non-relativistic sound speed). In both cases, we see that for higher flow speeds, the growth rates are generally higher, as is the strength of the magnetic field required to suppress instability. The critical ratio at $0.9\,c$ is nearly double its value at $0.8\,c$, which in turn is more than triple its value at $0.5\,c$. This illustrates the rapid increase of this ratio as the flow speed becomes more relativistic.

In the *pressure-dominated case*, we see that even for highly relativistic flow speeds, the critical ratio is substantially less than 1, which is to say, instability is suppressed for background magnetic pressures which are considerably less than the background thermal pressures. In the *density-dominated case*, instability is suppressed for much higher magnetic pressures which are generally larger than the thermal pressure. In fact, the ratio of critical β_0^{-1} between the two cases is approximately equal to the ratio of the enthalpies. We will see below that in both cases (pressure-dominated and density-dominated), instability is suppressed at approximately the same Alfven velocities, where the Alfven velocity is the magnetic field divided by the square root of enthalpy. Figures 6.3 display the corresponding ratio of phase velocity to flow speed, $\omega_r/(k_z v_{z0})$.

Figures 6.4 display growth rate (in units of c/r_0) for the same parameters as in figures 6.2, but this time as a function of the Alfven speed $v_A = B_{z0}/\sqrt{w_0}$. We see that

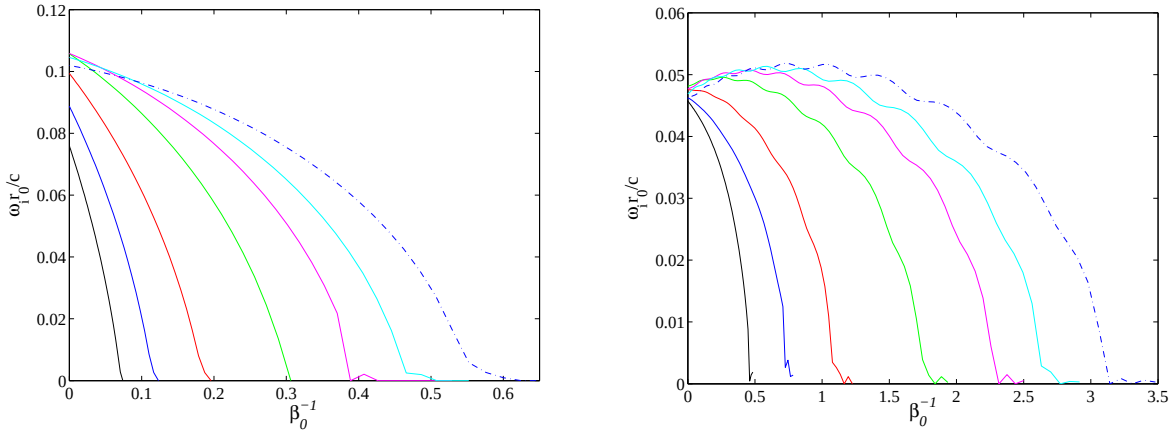

(a) $P_0/(\rho_0 c^2) = 50$ (b) $P_0/(\rho_0 c^2) = 0.05$

Figure 6.2: Growth rate vs inverse plasma β at different flow speeds (RMHD)
$v_{z0}/c = 0.5$ (black), 0.6 (blue), 0.7 (red), 0.8 (green)
$v_{z0}/c = 0.85$ (magenta), 0.875 (cyan), 0.9 (dashed blue)

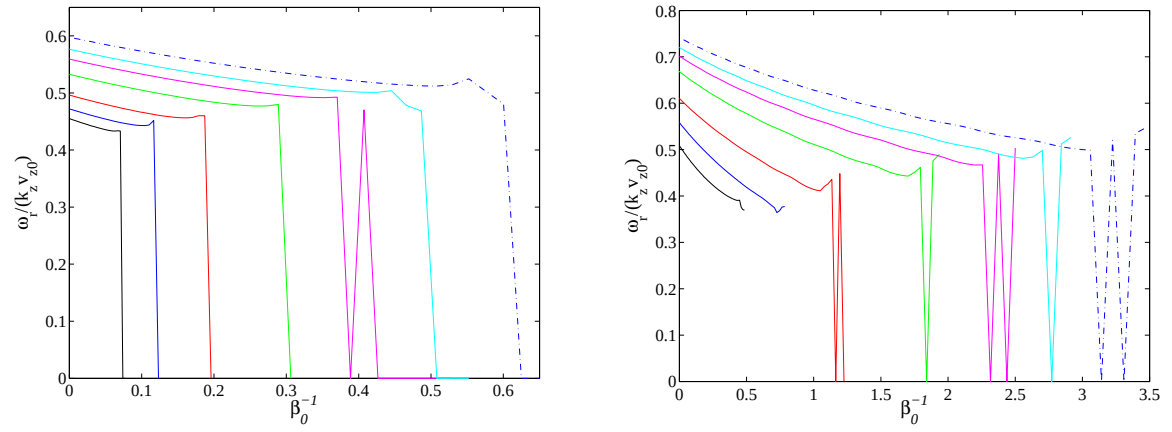

(a) $P_0/(\rho_0 c^2) = 50$ (b) $P_0/(\rho_0 c^2) = 0.05$

Figure 6.3: Phase velocity vs inverse plasma β at different flow speeds (RMHD)
$v_{z0}/c = 0.5$ (black), 0.6 (blue), 0.7 (red), 0.8 (green)
$v_{z0}/c = 0.85$ (magenta), 0.875 (cyan), 0.9 (dashed blue)

the critical instability-suppressing Alfven velocities are approximately the same in both the pressure-dominated and density-dominated cases. Figures 6.5 display the corresponding ratio of phase velocity to flow speed. For both pressure and density-dominated systems, this ratio is higher for larger flow speeds, and varies little with magnetic field strength in the pressure-dominated case, but has more field strength dependence in the density-dominated case. The phase velocities are also consistently larger for the density-dominated case, indicating that phase velocity increases with a decrease in sound speed. We also see that the phase velocity is consistently less than the flow speed. For highly relativistic flow speeds, the growth rate changes very little for weaker field strengths, and decreases very rapidly only as we approach the critical field strength for suppression of the instability. For two adjacent incompressible flows with a difference v_{z0} in flow speeds, and uniform flow-aligned Alfven velocity v_A, instability is suppressed when $v_A/v_{z0} > \sqrt{2}$ (Chandrasekhar 1961). The critical Alfven velocities shown in figures 6.4 are consistently less than this, which might be explained in part by the stabilizing influence of compressibility. In fact, for $v_{z0} <\approx 0.8\,c$, the suppression of instability occurs when $M_A^{-1} >\approx 1/3$, where M_A is a relativistic version of the Alfvenic Mach number, which we define by

$$M_A \;=\; \frac{v_{z0}\gamma}{v_A\gamma_A} \;=\; \frac{v_{z0}}{v_A}\sqrt{\frac{1-v_A^2/c^2}{1-v_{z0}^2/c^2}}, \tag{6.3}$$

where v_{z0} is the amplitude of the background flow speed, v_A is the background Alfven speed, and γ and γ_A are the Lorentz factors corresponding to the flow speed and Alfven speed, respectively. Our definition of M_A is analogous to the manner in which Bodo et al. (2004) defined a relativistic version of the sonic Mach number. We have discovered that, for

moderately relativistic flow speeds (i.e., $v_{z0} <\approx 0.8\,c$), M_A is strongly correlated with the influence of the magnetic field on growth rate. The fractional decrease in growth rate has a strong correlation with M_A, independently of other parameters. This is seen in figure 6.6, where the growth rate is plotted as a function of M_A^{-1} for each of the flow speeds considered above. Specifically, the dependent variable is the ratio of the growth rate to its corresponding value in the unmagnetized case. The curves very closely overlay one another, and have a common instability threshold of $M_A^{-1} \approx 1/3$. This correspondence, however, breaks down for $v_{z0} > 0.8\,c$. The correlation of growth rate with M_A is considerably closer for the pressure-dominated system (figure 6.6(a)) than for the density-dominated system (figure 6.6(b)). In our numerical simulations, we will see that M_A is the governing parameter in describing the extent of influence of the magnetic field on vortex formation. The critical stabilizing value of $M_A^{-1} = 1/3$ is a consequence of the use of a sech^2 background velocity profile.

In the plots of phase velocity versus inverse plasma β in figures 6.3, and versus Alfven speed v_A in figures 6.5, we notice an abrupt discontinuity in each of the curves, which corresponds to the value of β^{-1} or v_A at which the growth rate has dropped to zero, and above which there is no instability, as shown by the corresponding plots of growth rate. In some of the phase velocity curves, we notice spikes that occur after the stabilizing value of β^{-1} or v_A. These correspond to a family of varicose modes which exist in the region of low growth rates in the frequency plane. Recall that we are interested in the fastest-growing sinuous mode. When the growth rate of this mode is too low ($\omega_i < 0.01\,c$), the search algorithm has difficulty distinguishing the sinuous mode from the varicose modes.

We have examined the influence of the magnetic field on numerical growth rates. We

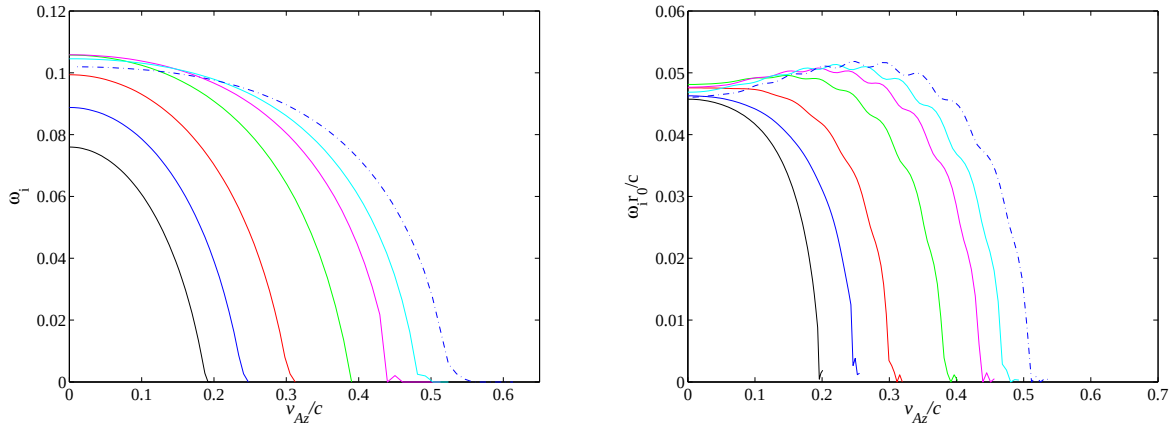

(a) $P_0/(\rho_0 c^2) = 50$ (b) $P_0/(\rho_0 c^2) = 0.05$

Figure 6.4: Growth rate vs Alfven speed at different flow speeds (RMHD)
$v_{z0}/c = 0.5$ (black), 0.6 (blue), 0.7 (red), 0.8 (green)
$v_{z0}/c = 0.85$ (magenta), 0.875 (cyan), 0.9 (dashed blue)

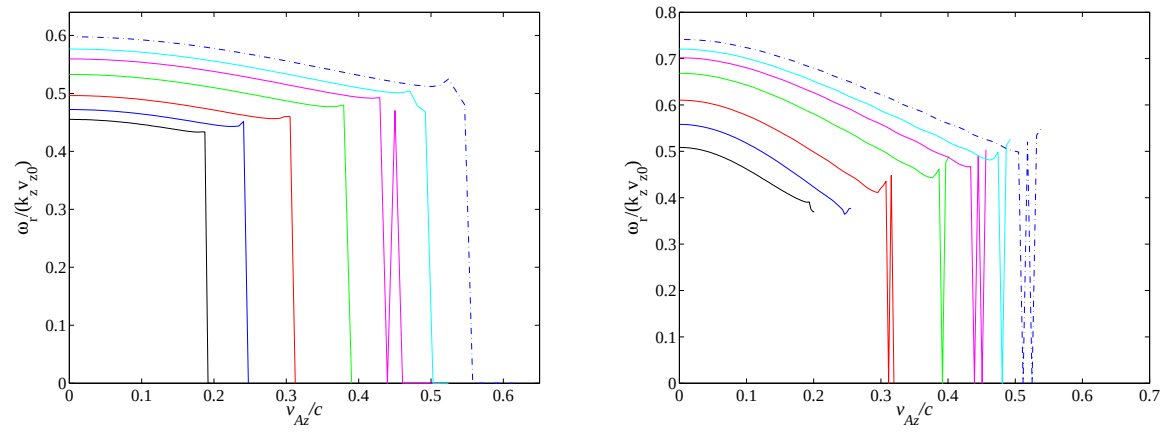

(a) $P_0/(\rho_0 c^2) = 50$ (b) $P_0/(\rho_0 c^2) = 0.05$

Figure 6.5: Phase velocity vs Alfven speed at different flow speeds (RMHD)
$v_{z0}/c = 0.5$ (black), 0.6 (blue), 0.7 (red), 0.8 (green)
$v_{z0}/c = 0.85$ (magenta), 0.875 (cyan), 0.9 (dashed blue)

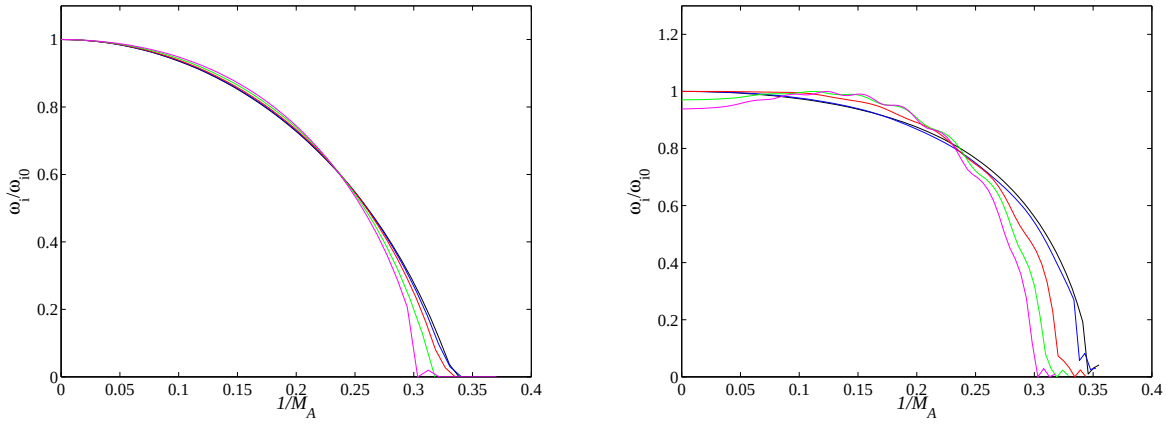

(a) $P_0/(\rho_0 c^2) = 50$ (b) $P_0/(\rho_0 c^2) = 0.05$

Figure 6.6: Growth rate vs M_A^{-1} at different flow speeds (RMHD)
$v_{z0}/c = 0.5$ (black), 0.6 (blue), 0.7 (red), 0.8 (green), 0.85 (magenta)

now turn our attention to an unmagnetized system, and examine the dependence of growth rate and phase velocity on the background flow speed (in particular, its amplitude, reached at the center of the velocity profile).

6.4 Dependence of Growth Rate on Flow Speed

Figure 6.7(a) displays growth rate (in units of c/r_0) as a function of flow speed for different values of the sound speed. There is no magnetic field. At all sound speeds, instability persists into the highly relativistic regime. As the sound speed increases, the growth rates increase. As with the hydrodynamic case in figure 6.1(a), figure 6.7(a) illustrates the stabilizing influence of a small sound speed (greater compressibility) for the *relativistic* case. Under these circumstances, the density is more dominant over the pressure, and the perturbation must perform a greater amount of work against the mechanical energy of the background flow. Figure 6.7(b) displays the corresponding ratio of phase velocity to flow speed. This ratio increases as flow velocity increases, which is consistent with our observations for the non-relativistic case in the first section. For smaller sound speeds, the phase velocity is larger,

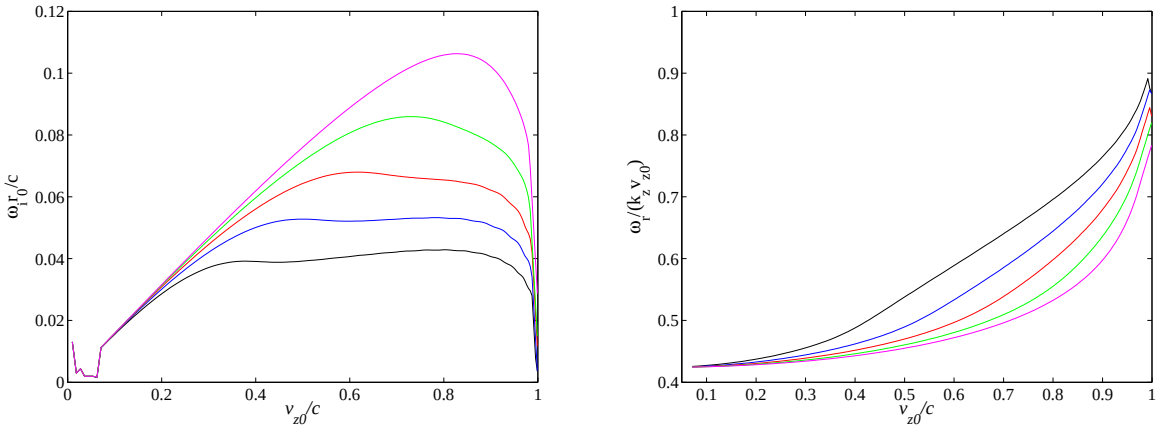

(a) (b)

Figure 6.7: Growth rate and phase veloc. vs flow speed at diff. sound speeds (RHD)
$c_s/c = 0.2$ (black), 0.27 (blue), 0.35 (red), 0.45 (green), $1/\sqrt{3}$ (magenta)
$B_{z0} = 0, \qquad k_z = 0.8/r_0$

which is consistent with the non-relativistic case shown in figure 6.1(b). As flow speed increases or sound speed decreases, the phase velocity becomes more comparable to the flow speed. As with the non-relativistic case considered in the first section, the decrease in sound speed corresponds to a larger density, giving the bulk flow greater inertia, and hence a greater influence on the pattern speed of the emergent features. At low flow speeds, we notice two spikes. These correspond to a family of varicose modes (symmetric shear profiles of pressure perturbation), which exist at low growth rates and a set of regularly spaced values of ω_r. For sufficiently low flow speeds, the growth rates are very low, as seen by figure 6.7(a), and therefore it is difficult to distinguish the sinuous mode from the varicose modes. Recall that for a given set of parameters, we seek to recover the fastest-growing sinuous mode.

Figures 6.8 display growth rate and phase velocity to flow speed, respectively, as functions of the relativistic Mach number, given by

$$M_s \;=\; \frac{v_{z0}}{c_s}\left(\frac{\gamma}{\gamma_s}\right) \;=\; \frac{v_{z0}}{c_s}\sqrt{\frac{1-c_s^2/c^2}{1-v_{z0}^2/c^2}}. \tag{6.4}$$

Figure 6.8(a) shows that for smaller sound speeds, the instability region extends to higher Mach numbers. This is consistent with our observation from figure 6.7(a) that the upper critical flow velocity is larger than $0.9\,c$, independent of sound speed. Bodo et al. (2004) demonstrated that for a tangential discontinuity, in the frame in which two adjacent flows have equal and opposite velocities, instability to flow-aligned perturbations is suppressed for relativistic Mach numbers larger than $\sqrt{2}$, independent of sound speed. This Mach number is in terms of the individual flow speeds. When we transform to the frame in which one of the fluids is stationary, which more closely corresponds to the profile $v_{z0}\mathrm{sech}^2(x/r_0)$, the maximum critical Mach number, for any sound speed, is 4. In our case, the critical Mach numbers are considerably larger than this, and have a strong dependence on sound speed. Instability therefore exists at much larger Mach numbers, and therefore much higher flow speeds, for the sech^2 profile than for the case of two adjacent flows, particularly at low sound speeds. We see from figure 6.8(b) that the ratio of phase velocity to flow speed is a function of the Mach number, not of the sound speed and flow speed individually.

In figures 6.9, we plot the (a) growth rate and (b) phase velocity for the same sound speeds, but this time as a function of the covariant velocity $u_{z0} = \gamma v_{z0}/c$, where $\gamma = (1-v_{z0}^2/c^2)^{-1/2}$ is the Lorentz factor. Note that in the highly relativistic regime, the covariant velocity and Lorentz factor are approximately equal. Figure 6.9(a) illustrates that for any sound speed, the growth rate decreases with increasing flow speed in the highly relativistic regime. The most rapid decrease seems to occur for Lorentz factors ranging from about

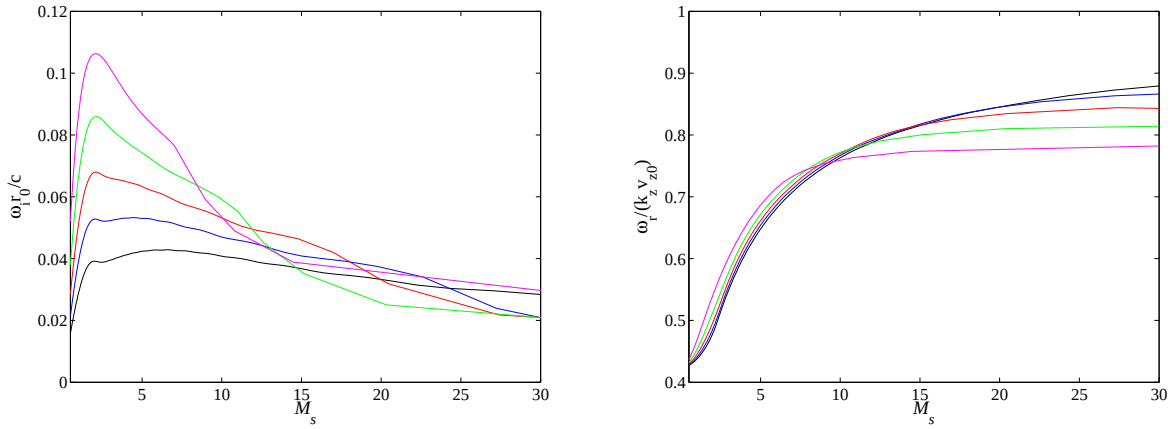

(a) (b)

Figure 6.8: Growth rate and phase veloc. vs Mach number at diff. sound speeds (RHD)
$c_s/c = 0.2$ (black), 0.27 (blue), 0.35 (red), 0.45 (green), $1/\sqrt{3}$ (magenta)
$B_{z0} = 0, \qquad k_z = 0.8/r_0$

2 to about 20, and the subsequent decrease is more gradual. Most of the curves exhibit a kink, or noticeable change in behavior, at around $\gamma = 20$. This most likely corresponds to some sort of transition from sinuous modes (antisymmetric pressure profiles) to varicose modes (symmetric pressure profiles). That is, for flow speeds less than about $\gamma = 20$, the fastest-growing modes are sinuous, but figure 6.9(a) shows that this growth rate decreases rapidly from $\gamma = 2$ to about $\gamma = 20$. As shown in figure 6.9(b), this corresponds to a rapid increase in the sinuous phase velocity.

At about $\gamma = 20$, the growth rate of the sinuous mode drops below the growth rates of the varicose modes, which, for $\gamma < 20$, seem to have much less dependence on flow speed than the growth rate of the sinuous mode. For γ larger than roughly 20, the fastest-growing mode is now a varicose mode. For $c_s = 0.35\,c$, the transition in growth behavior occurs at a larger value of $\gamma \approx 33$, as shown by the red curve in figure 6.9(a). After the transition, the phase velocity of the varicose mode changes very little, as shown in figure 6.9(b). In particular, this figure shows that the ratio of phase velocity to flow speed seems to asymptotically

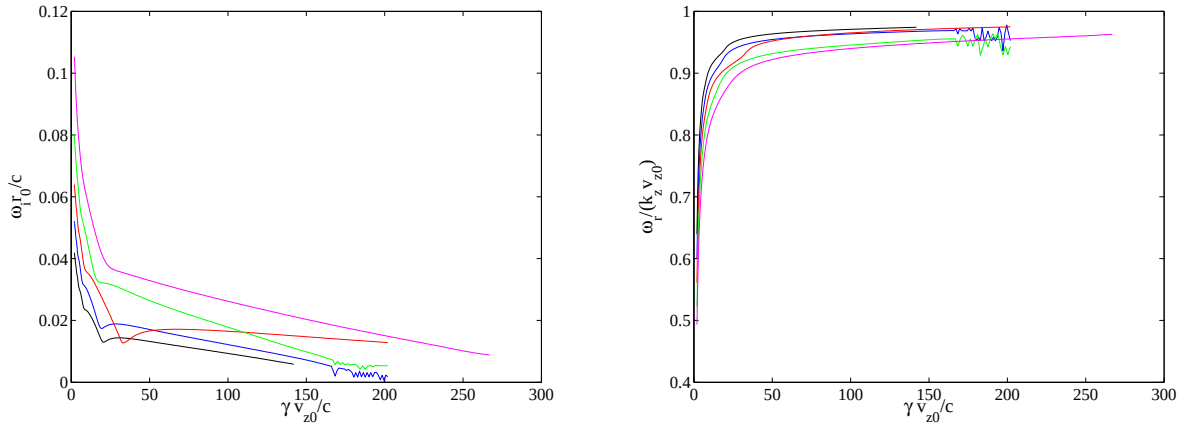

(a) (b)

Figure 6.9: Growth rate and phase velocity vs $\gamma v_{z0}/c$ at diff. sound speeds (RHD)
$c_s/c = 0.2$ (black), 0.27 (blue), 0.35 (red), 0.45 (green), $1/\sqrt{3}$ (magenta)
$B_{z0} = 0, \qquad k_z = 0.8/r_0$

approach unity as the flow speed approaches the speed of light (as the Lorentz factor goes to infinity). Figures 6.9 also show that, even when the growth rate behavior is altered for highly relativistic flow speeds, the growth rates are still higher, and the phase velocities lower, for higher sound speeds. This is what we found previously for moderately relativistic flow speeds.

We see that in the highly relativistic regime, the system becomes more KH-stable to perturbations with wave numbers on the order of $1/r_0$, which is the approximate wave number corresponding to maximum growth for moderately relativistic flow speeds. However, we show in the next section that highly relativistic flow speeds can render the system less KH-stable to perturbations with higher wave numbers, i.e., smaller wavelengths.

6.5 Dependence of Growth Rate on Wave Number

Figure 6.10 displays growth rate (in units of c/r_0) as a function of the wave number k_z (in units of $1/r_0$), again for several values of the flow speed. As with the HD case, the

growth curve has a concave-downward shape, with a wave number corresponding to maximum growth and a larger wave number above which the system is stabilized. This wave number corresponds to a wavelength which is on the order of the width of shear variation (which in our model is half the initial jet width, or about $2\,r_0$). This is in contrast to the case of a step-function velocity profile considered earlier, for which the growth rate increases linearly with k_z. We see that with an increase in flow speed, there is an increase in the peak growth rate and in the range of instability. However, the former trend breaks down for flow speeds larger than $0.8\,c$, and the maximum growth rate is noticeably less at $0.9\,c$ than at $0.85\,c$. Maximum growth occurs at roughly $k_z = 0.8/r_0$, and this critical wave number is independent of flow speed for speeds less than around $0.85\,c$. However, at $0.9\,c$, maximum growth occurs at roughly $k_z = 0.7/r_0$. As the flow speed becomes more relativistic, the growth rate decreases more slowly for larger k_z, and this decrease becomes more linear, suggesting the emergence of a complex phase velocity, which is discussed below. At the highly relativistic flow speed of $0.98\,c$, the growth rates are somewhat lower, but growth rate no longer decreases with increasing k_z, and instead continues a gradual *increase*. At $0.98\,c$, the system is not stabilized until k_z exceeds approximately $5.36/r_0$, corresponding to a wavelength of $2\pi/k_z = 1.17\,r_0$, which is narrower than the width of shear variation ($\approx 2\,r_0$) At highly relativistic velocities, we have near-maximum growth at wavelengths smaller than the width of shear variation. This is one manifestation of the tendency of relativistic effects to destabilize the system, and a possible contributing factor to the numerical breakdown observed at Lorentz factors larger than about 2. The growth behavior is qualitatively different for highly relativistic flows, which is due to the rapid increase in the Lorentz factor, resulting in higher relativistic boosting in the flow direction.

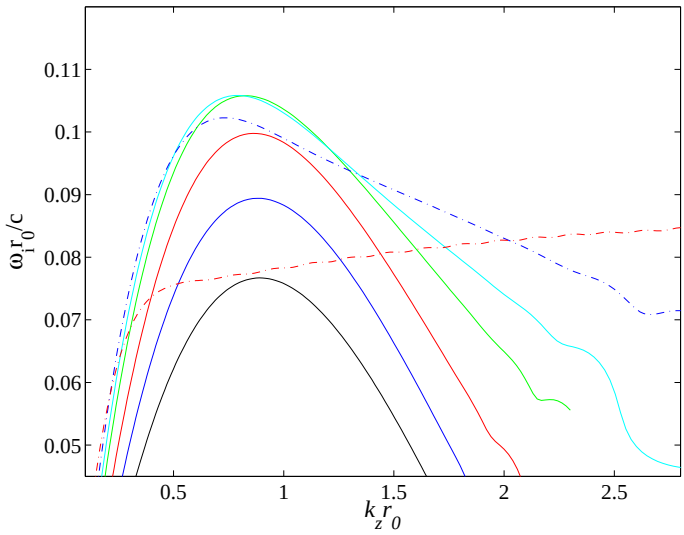

Figure 6.10: Growth rate vs k_z at different flow speeds (RHD)
$v_{z0}/c = 0.5$ (black), 0.6 (blue), 0.7 (red), 0.8 (green), 0.85 (cyan)
$v_{z0}/c = 0.9$ (dashed blue), 0.98 (dashed red), $P_0/(\rho_0 c^2) = 50$, $B_{z0} = 0$

When we compare figures 6.10 and 6.11, we notice that at a given flow speed, there is a change in the behavior of phase velocity when the corresponding growth curve drops to zero. Again, this is due to the presence, in the complex plane, of a family of varicose modes at low growth rates ($\omega_i < 0.01\, c/r_0$). Recall that the search algorithm attempts to recover the fastest-growing sinuous mode in each case. When the growth rate of this mode becomes too low, however, it becomes difficult to distinguish this mode from the varicose modes.

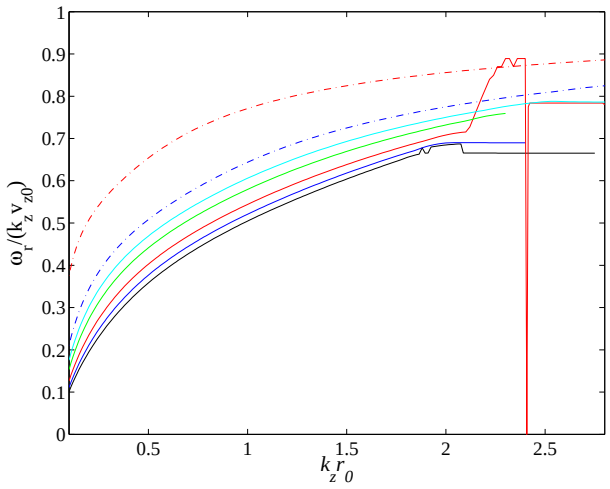

Figure 6.11: Phase velocity vs k_z at different flow speeds (RHD)
$v_{z0}/c = 0.5$ (black), 0.6 (blue), 0.7 (red), 0.8 (green), 0.85 (cyan)
$v_{z0}/c = 0.9$ (dashed blue), 0.98 (dashed red), $P_0/(\rho_0 c^2) = 50$, $B_{z0} = 0$

Figure 6.12 displays $d\omega_i/dk_z$, and figure 6.13 displays $d\omega_r/dk_z$, both as functions of k_z, for the cases considered in figures 6.10 and 6.11. These figures show that at highly relativistic flow speeds, and sufficiently large k_z, the group velocities approach a characteristic complex phase velocity. As the flow speed approaches c within this regime, the real component of the group velocity approaches c, while the imaginary component approaches 0 from the negative region.

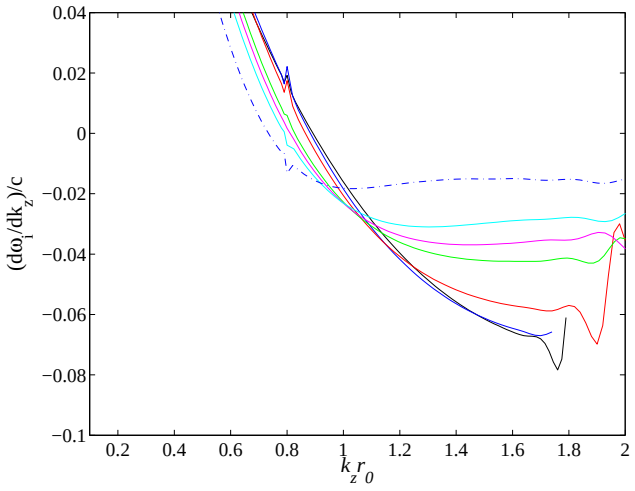

Figure 6.12: $d\omega_i/dk_z$ vs k_z at different flow speeds (RHD)
$v_{z0}/c = 0.5$ (black), 0.6 (blue), 0.7 (red), 0.8 (green), 0.825 (magenta)
$v_{z0}/c = 0.85$ (cyan), 0.9 (dashed blue), $P_0/(\rho_0 c^2) = 50$, $B_{z0} = 0$

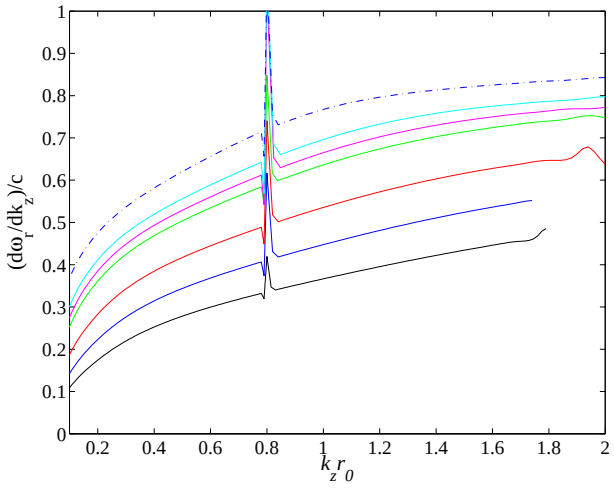

Figure 6.13: $d\omega_r/dk_z$ vs k_z at different flow speeds (RHD)
$v_{z0}/c = 0.5$ (black), 0.6 (blue), 0.7 (red), 0.8 (green), 0.825 (magenta)
$v_{z0}/c = 0.85$ (cyan), 0.9 (dashed blue), $P_0/(\rho_0 c^2) = 50$, $B_{z0} = 0$

6.6 Conclusion

In conclusion, we see that in the presence of a shear variation in the velocity profile, KH instability to flow-aligned perturbations extends to much higher Mach numbers than the upper limits corresponding to a step function discontinuity (discussed in chapter 4). For sound speeds near the relativistic limit of $c/\sqrt{3}$, the growth rate increases as the flow speed becomes more relativistic, and reaches a maximum only at a flow speed of around $0.95\,c$. This stands in contrast to the commonly held notion that relativistic flows tend to have a stabilizing effect. We see that the influence of the magnetic field is closely correlated with a relativistic extension of the Alfvenic Mach number, which we have defined analogously to the definition of a relativistic sonic Mach number used in Bodo et al. (2004). Consequently, a stronger magnetic field is required to suppress the instability at higher flow speeds, and higher densities. As discussed in the introduction to this chapter, the wave frequencies are many orders of magnitude smaller than typical Larmor frequencies, making it highly unlikely

for these KH-unstable modes to exhibit resonance with gyrating particles.

Another important difference from the case of a step-function discontinuity involves the dependence of growth rate on wave number. For a step-function discontinuity, the growth rate increases linearly with wave number, while in the case of shear variation, the growth rate ceases to increase above a certain wave number, i.e., the shear variation sets a length scale. For mildly relativistic flows, the growth rate decreases to zero with increasing wave number, and the system is stable above a wave number for which the wavelength is roughly the width of shear variation. For highly relativistic flows, relativistic boosting changes the shape of the growth curves, and instability with near maximum growth extends to wavelengths which are smaller than the width of shear variation. This relativistic destabilization offers insight into the early unphysical breakdown ($v > c$), in the linear regime, of simulations with flow speeds exceeding $0.9\,c$. This is a problem that for over 20 years has plagued simulations using artificial viscosity, such as ours (Marti and Muller 2003).

Chapter 7

Shear Profiles of the Perturbations

We have considered the growth rates of eigenmodes of a system with a background velocity profile $v_{z0}\,\mathrm{sech}^2(x/r_0)$. We now consider the behavior of the shear profiles of the corresponding eigenfunctions of these eigenmodes. These profiles are cross sections of the initial perturbations at the start of the simulation. Therefore, their sensitivity to flow velocity and magnetic field could explain the sensitivity, to these parameters, of the subsequent numerical evolution. We first consider unmagnetized cases, in order to isolate relativistic effects. We then consider magnetized cases at several different flow speeds.

We find that the symmetry properties of the pressure and velocity profiles have a close correlation with the pattern of vortex development in the early nonlinear regime of evolution. These symmetries also play a major role in the complementarity between the nonlinear evolution of the magnetic field and the flow. In particular, this complementarity arises in part from the fact that the transverse field and velocity profiles are both symmetric, while the longitudinal field and velocity perturbations are both antisymmetric. At more relativistic flow speeds, the perturbation profiles tend to exhibit larger amplitudes of spatial variation, which may contribute to an instability associated with highly relativistic velocities. There is also a noticeable change in profile shape, of each perturbation, for magnetic fields which

are strong enough to suppress vortex formation. This may illuminate the nature of the bifurcation between the weaker, vortex-disruptive, and stronger, vortex-suppressing regimes of field strength.

For each perturbation profile $\delta q_0(x)$, the real and imaginary parts of $\delta q_0(x)$ both have the same symmetry (whether symmetric or antisymmetric). This is due to the symmetric nature of the background velocity profile $v_{z0}\mathrm{sech}^2(x/r_0)$. As a result, a given perturbation has the same symmetry at all cross-sections along the flow direction. This emerges from the perturbation distribution in the xz-plane:

$$\delta q(x,z) \;=\; \mathrm{Re}[\delta q_0(x)\exp(ik_z z)] \;=\; \delta q_{0r}(x)\cos(k_z z) - \delta q_{0i}(x)\sin(k_z z) \tag{7.1}$$

If $\delta q_{0r}(x)$ and $\delta q_{0i}(x)$ are both symmetric, $\delta q(x,z)$ is symmetric for any z. If $\delta q_{0r}(x)$ and $\delta q_{0i}(x)$ are both antisymmetric, $\delta q(x,z)$ is antisymmetric for any z. This preservation of symmetry (or antisymmetry), along the flow direction, has important consequences for the evolution of the flow, and its complementarity with the field, as we will see below.

We begin by considering the perturbation profiles of pressure and velocity for unmagnetized cases, examining both the symmetries of these profiles and their dependence on the background flow speed.

7.1 Perturbation Profiles for Unmagnetized Cases

Figures 7.1 through 7.4 show plots of the shear profiles of the normalized perturbation eigenfunctions for unmagnetized RHD cases. Each plot simultaneously displays the profiles corresponding to background flow speeds $v_{z0}/c = 0.9$, 0.85, 0.8, 0.7, and 0.5, to illustrate the

influence, on the profiles, of the relativistic nature of the flow. It should be noted that the shear profiles are unchanged when the system length is widened or when the spatial increment is halved, indicating that these profiles have converged with respect to system length and spatial step. The pressure and longitudinal velocity perturbations are both antisymmetric, while the transverse (x) velocity perturbation is symmetric. This is a consequence of choosing sinuous modes of the sech^2 profile, as opposed to varicose modes, which have the opposite symmetries, as discussed in chapter 6, and Drazin and Howard (1966). Recall that the velocity perturbations can be written as follows in terms of the pressure perturbation (where the prime symbol denotes differentiation with respect to x, the shear direction):

$$\delta v_x = \frac{-ic^2\delta P'}{\tilde{w}\gamma^2(\omega - k_z v_{z0})}, \tag{7.2}$$

$$\delta v_z = \frac{-c^2 v_z'\delta P' + c^2(k_z - \omega v_{z0}/c^2)(\omega - k_z v_{z0})\delta P}{\tilde{w}\gamma^2(\omega - k_z v_{z0})}. \tag{7.3}$$

Note also that, near the axis at $x = 0$, the curves overlay one another almost exactly, indicating that, in this region, the perturbation profiles have very little sensitivity to the background flow speed. The sensitivity to flow speed only occurs at sufficient distances from the central axis (i.e., for $|x| >\approx 2\,r_0$). Where the profiles are sensitive to flow speed, the local amplitudes either increase with increasing flow speed, as with Im(δP), Im($d\delta P/dx$), Re(δv_x), Im(δv_x), and Re(δv_z), or decrease with increasing flow speed, as with Re($d\delta P/dx$) and Im(δv_z). That is, there is no bifurcation in the dependence of perturbation amplitude on flow speed. The most pronounced increase in amplitude, with increasing flow speed, occurs in the plot of Im(δP) versus x, and we generally observe larger-amplitude variations in the profiles at more relativistic flow speeds, particularly at a background flow speed amplitude of

$0.9\,c$. These profiles define the perturbation at the start of the simulation. Large-amplitude spatial variations in these profiles are a likely contributing factor in explaining early numerical instability that arises at highly relativistic flow speeds.

The symmetries of the perturbation profiles play an important role in vortex development in the early nonlinear regime of evolution. The early stages of vortex formation are shown in figure 7.5, where the flow is directed upward (positive z-direction), and the x-axis is the transverse direction. Each display (vorticity and longitudinal velocity) spans one wavelength of the perturbation in the z-direction. Each display corresponds to 7.94 growth times, denoted T_i, where $T_i = 10.1\,r_0/c$, i.e., 10.1 clock times. Saturation of the linear perturbations occurs after 8 to 10 growth times. At the onset of nonlinear evolution, the antisymmetric pressure perturbations, and symmetric transverse velocity perturbations, have grown to a point where there are appreciable thermal and transverse mechanical stresses, causing the flow to bend by different amounts at different points along the flow, depending on the magnitude and direction of the transverse velocity (whether in the positive or negative transverse direction). Where the transverse velocity is a maximum in the positive transverse (x) direction, the flow is maximally displaced in the positive x-direction. A quarter-wavelength upstream from this point, the transverse velocity is zero, and the flow is not displaced. A quarter-wavelength further upstream, the transverse velocity is a maximum in the negative x-direction, and the flow is maximally displaced in the negative x-direction. This initial twisting of the flow is shown in figure 7.5(b).

This results in the formation of counter-rotating vortices on opposite sides of the flow axis, which are spaced half a wavelength apart along the flow direction. The vortices form

around regions of low density and pressure, which, due to the antisymmetry of the pressure perturbations, are also spaced a half-wavelength apart. These vortices are shown in figure 7.5(a), which displays the curl of the velocity. Because the y-axis points into the page, the red vortex corresponds to clockwise fluid circulation, and the blue vortex to counterclockwise fluid circulation. By the above mechanism, we see that the antisymmetry of pressure perturbation, and symmetry of transverse velocity perturbation, play a vital role in the half-wavelength displacement, along the flow axis, of counter-rotating vortices. This corresponds to the symmetries of a sinuous mode. If the transverse velocity were antisymmetric, as in a varicose mode, the transverse mechanical stresses would be oppositely directed on either side of the axis, and would separate the flow into pairs of adjacent vortices.

If we denote the vorticity $\Omega(x, z, t)$, we can express its alternating symmetry as follows:

$$\Omega(x, z, t) \;=\; -\Omega(-x, z + \lambda/2, t), \tag{7.4}$$

where $\lambda = 2\pi/k_z$ is the longitudinal wavelength of the perturbation in which the simulation is launched. By determining the accuracy with which this condition is satisfied at a given time in the simulation, we can assess the accuracy of the numerical results. As we discuss in section 10.9 of chapter 10, this condition is indeed satisfied in each case we examine.

Having examined perturbation profiles in the absence of a magnetic field, we now examine the influence of magnetic fields of various strengths.

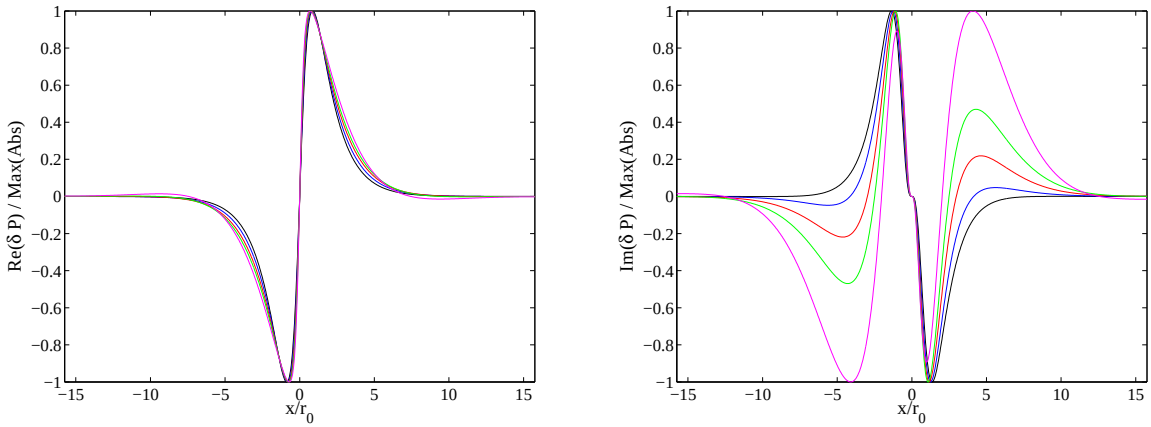

(a) Re(δP) (b) Im(δP)

Figure 7.1: Shear profiles of δP at different flow speeds (RHD)
$v_{z0}/c = 0.5$ (black), 0.7 (blue), 0.8 (red), 0.85 (green), 0.9 (magenta)
$P_0/(\rho_0 c^2) = 50, \qquad B_{z0} = 0$

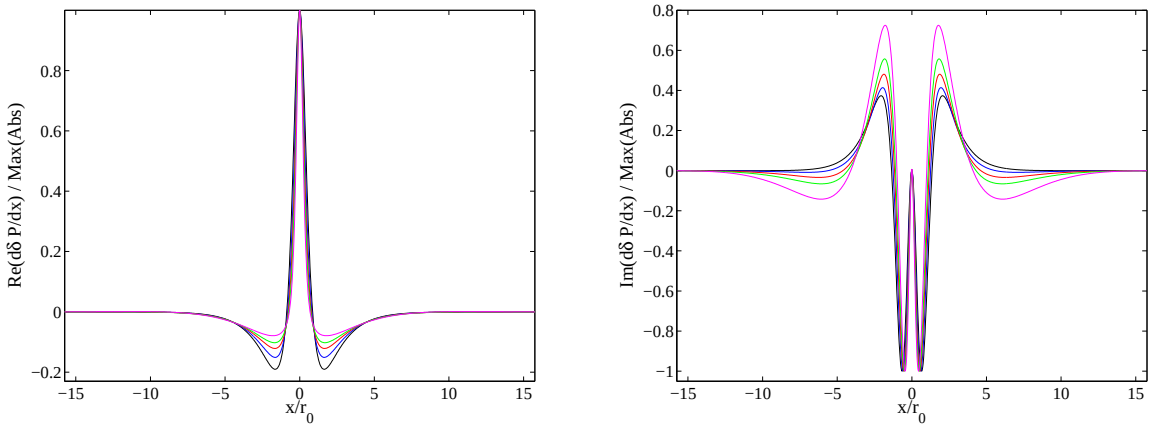

(a) Re($d\delta P/dx$) (b) Im($d\delta P/dx$)

Figure 7.2: Shear profiles of $d\delta P/dx$ at different flow speeds (RHD)
$v_{z0}/c = 0.5$ (black), 0.7 (blue), 0.8 (red), 0.85 (green), 0.9 (magenta)
$P_0/(\rho_0 c^2) = 50, \qquad B_{z0} = 0$

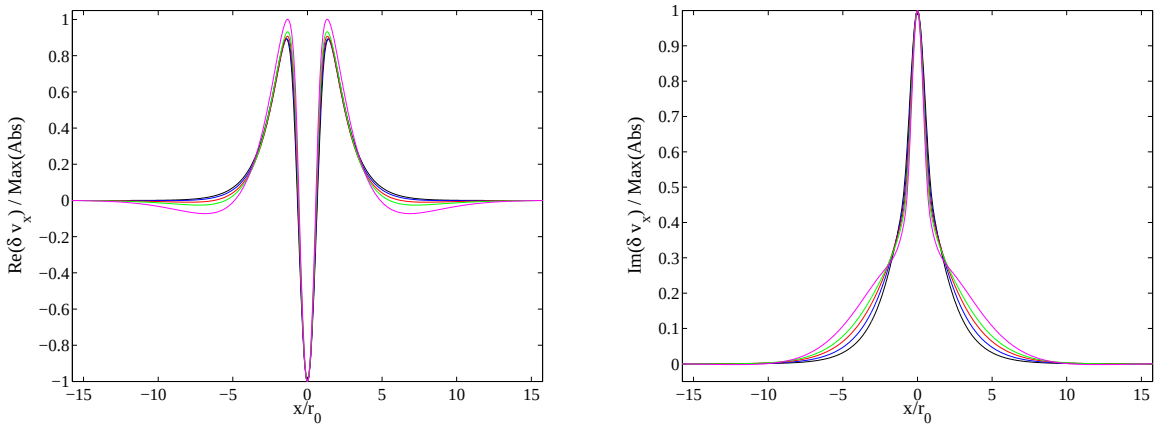

(a) $\mathrm{Re}(\delta v_x)$ (b) $\mathrm{Im}(\delta v_x)$

Figure 7.3: Shear profiles of δv_x at different flow speeds (RHD)
$v_{z0}/c = 0.5$ (black), 0.7 (blue), 0.8 (red), 0.85 (green), 0.9 (magenta)
$P_0/(\rho_0 c^2) \;=\; 50, \qquad B_{z0} \;=\; 0$

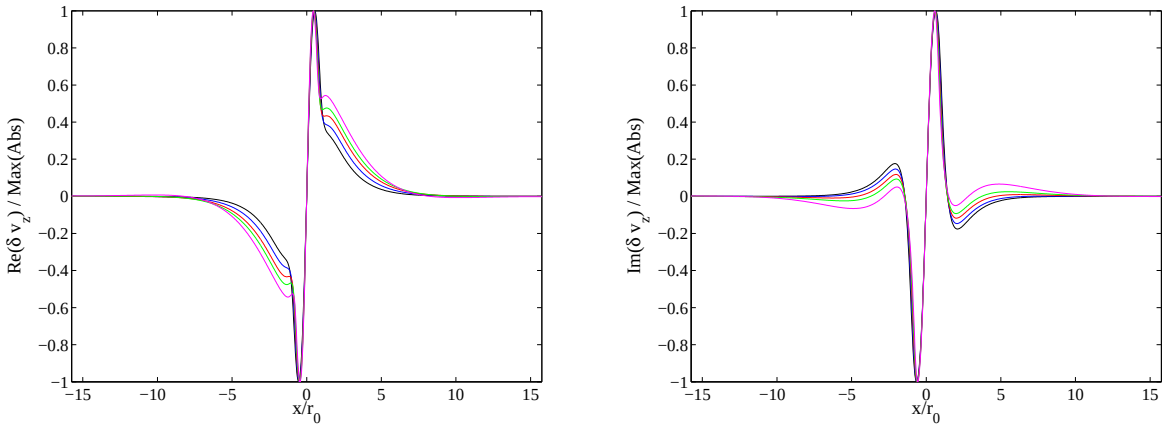

(a) $\mathrm{Re}(\delta v_z)$ (b) $\mathrm{Im}(\delta v_z)$

Figure 7.4: Shear profiles of δv_z at different flow speeds (RHD)
$v_{z0}/c = 0.5$ (black), 0.7 (blue), 0.8 (red), 0.85 (green), 0.9 (magenta)
$P_0/(\rho_0 c^2) \;=\; 50, \qquad B_{z0} \;=\; 0$

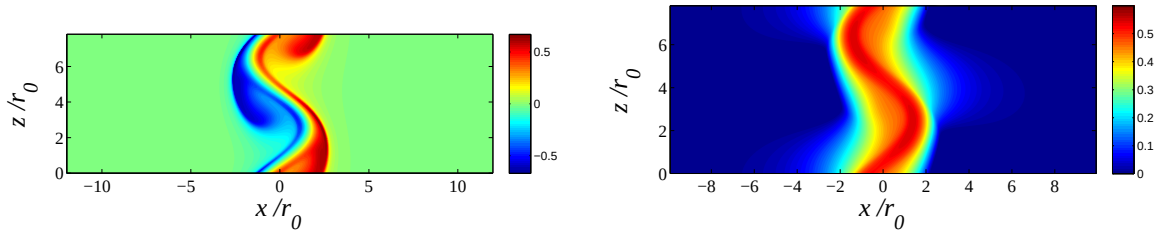

(a) vorticity (b) longitudinal velocity

Figure 7.5: $t = 7.94\,T_i = 3.53\,T = 79.9\,r_0/c = 1.46\,L_x/c_s, \qquad 0.7\,c\,\mathrm{sech}^2(x/r_0)$

7.2 Perturbation Profiles of Magnetized Cases

We now consider the influence of a magnetic field on the perturbation profiles of the velocity and magnetic field components. Again, these perturbation profiles are cross-sections of the initial perturbations at the start of the simulation. Again, the shear profiles are unchanged when the system length is widened or when the spatial increment is halved, indicating that these profiles have converged with respect to system length and spatial step. Each of the figures below contain multiple curves, each curve corresponding to a specific value of the relativistic Alfvenic Mach number M_A, given by (6.3). A black curve corresponds to the unmagnetized case, a cyan curve to the case $M_A = 82.83$, a red curve to the case $M_A = 41.41$, a green curve to the case $M_A = 20.70$, a magenta curve to the case $M_A = 10.34$, and a blue curve to the case $M_A = 5.145$. For each perturbation, we display graphs for background flow speed amplitudes of $0.7\,c$ and $0.2\,c$. Each of the modes graphed have also been evolved well into the nonlinear regime, as will be discussed later. δv_x and δB_x, the perturbations to transverse velocity and field, both have symmetric shear profiles. On the other hand, δv_z and δB_z, the perturbations to longitudinal velocity and field, both have antisymmetric shear profiles. This, again, is a consequence of choosing sinuous modes of the sech^2 profile, as opposed to varicose modes, which have the opposite symmetries (Drazin and Howard 1966). One important observation is that for each quantity being considered, the graphs for both flow speeds ($0.7\,c$ and $0.2\,c$) are remarkably self-similar, differing only in amplitudes. This indicates that within the moderately relativistic regime, relativity has very little influence on the form of the spatial variation of the initial perturbations.

There is another fundamental observation that underlies each of the graphs below. Specif-

ically, for each quantity plotted, the curves corresponding to Alfvenic Mach numbers of 82.83, 41.41, 20.70, and 10.34 are very similar, and overlap very closely. These fields are in the vortex-disruptive regime, which is to say, they still allow vortex formation in the early nonlinear regime of evolution, and only disrupt the vortices after a certain amount of vortex development. However, the curve corresponding to $M_A = 5.145$, the strongest field, has a noticeably different shape from the other curves. For instance, we see substantially larger amplitudes in the spatial variation of the velocity components. This field ($M_A = 5.145$), in contrast to the others, is in the vortex-suppressing regime, which is to say, it does not allow complete vortex formation. The vortex-suppressing field also corresponds to a noticeably lower growth rate, which is only about 75% of the growth rates of the weaker fields, while the weaker fields correspond to growth rates which are within a few percentage points of one another. We see that a large fractional reduction in growth rate corresponds to noticeable deviations in the perturbation profiles. We will later see, in chapter 9, that the magnetic field is enhanced in the early nonlinear regime of evolution, and that this enhancement is largest for strongly vortex-disruptive fields ($M_A = 10.34$), but is considerably less for vortex-suppressing fields ($M_A = 5.145$). That is, field enhancement increases with increasing field throughout the vortex-disruptive regime, and then decreases in the vortex-suppressive regime. Evidently, the ability of a field to suppress vortex formation, and the nature of field enhancement in early nonlinear evolution, are both closely correlated with the influence the field has on the growth rate and spatial variation of the initial perturbations.

Note that the perturbation profiles are symmetric in transverse velocity and transverse field, and antisymmetric in longitudinal velocity and longitudinal field. The background

profiles of the longitudinal field and longitudinal velocity are both symmetric. We see that the velocity and field components have common symmetry properties in their transverse profiles. This allows for a close complementarity between the behavior of the flow and the behavior of the field throughout the nonlinear evolution. This complementarity is shown in figures 7.14, which display the vorticity, i.e., curl of the velocity field, overlaid with contours of the magnetic field. This corresponds to the vortex-disruptive field $M_A = 41.4$, where figure 7.14(a) displays an early stage of vortex formation at 10.3 growth times, and figure 7.14(b) displays an early stage of vortex disruption at 12.2 growth times. One growth time T_i is $10.1\, r_0/c$, i.e., 10.1 clock times. Saturation of the linear perturbations occurs after about 8 to 10 growth times.

We begin by considering the profiles of the real and imaginary parts of δv_x, the perturbation to transverse velocity, first at $0.7\, c$ (figure 7.6) and then at $0.2\, c$ (figure 7.7).

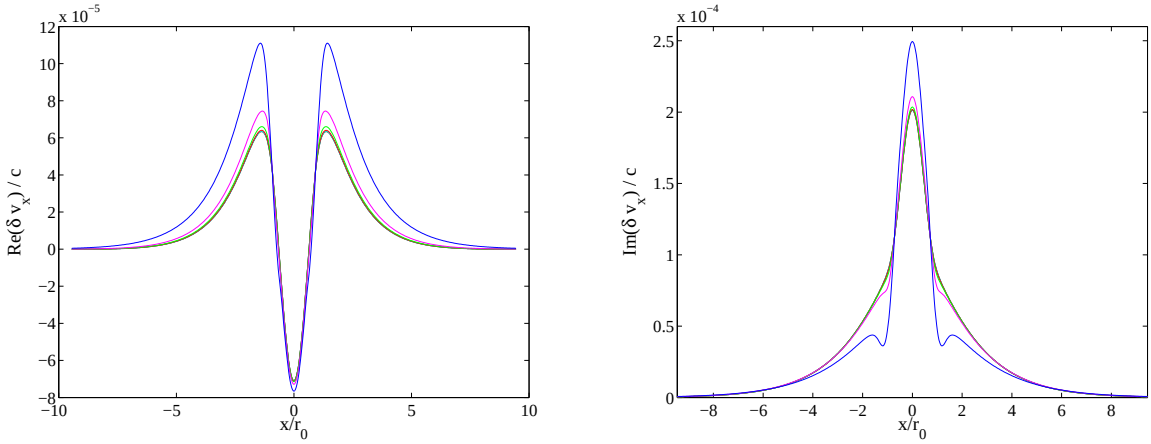

(a) Re(δv_x) (b) Im(δv_x)

Figure 7.6: Shear profiles of δv_x at different M_A for a flow speed of $0.7\, c$ (RMHD)
$M_A = \infty$ (black), 82.83 (cyan), 41.41 (red), 20.70 (green), 10.34 (magenta), 5.145 (blue)
$P_0/(\rho_0 c^2) = 50, \qquad v_{z0} = 0.7\, c\, \mathrm{sech}^2(x/r_0)$

We now consider the profiles of the real and imaginary parts of δB_x, the perturbation in

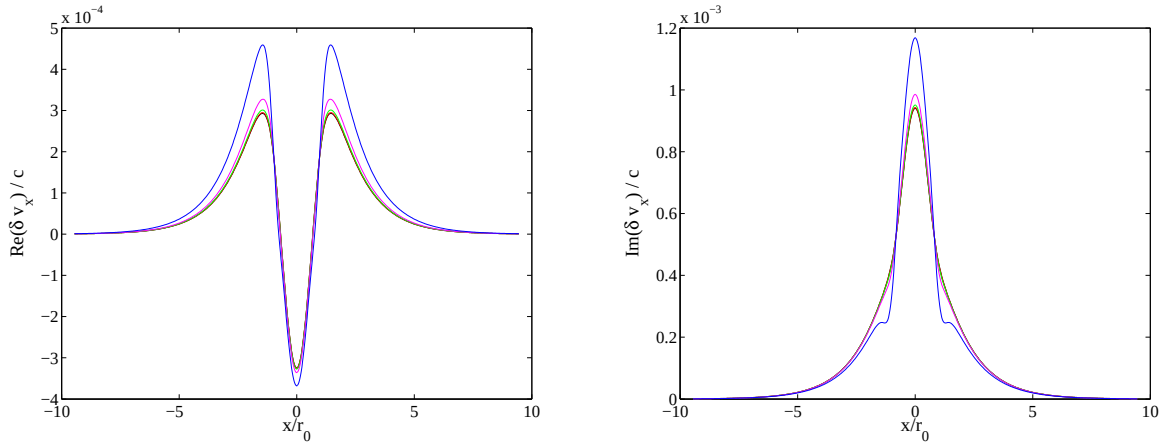

(a) Re(δv_x) (b) Im(δv_x)

Figure 7.7: Shear profiles of δv_x at different M_A for a flow speed of $0.2\,c$ (RMHD)
$M_A = \infty$ (black), 82.83 (cyan), 41.41 (red), 20.70 (green), 10.34 (magenta), 5.145 (blue)
$P_0/(\rho_0 c^2) \;=\; 50, \qquad v_{z0} \;=\; 0.2\,c\,\mathrm{sech}^2(x/r_0)$

We now consider the profiles of the real and imaginary parts of δv_z, the perturbation in flow velocity, first at $0.7\,c$ (figure 7.8) and then at $0.2\,c$ (figure 7.9).

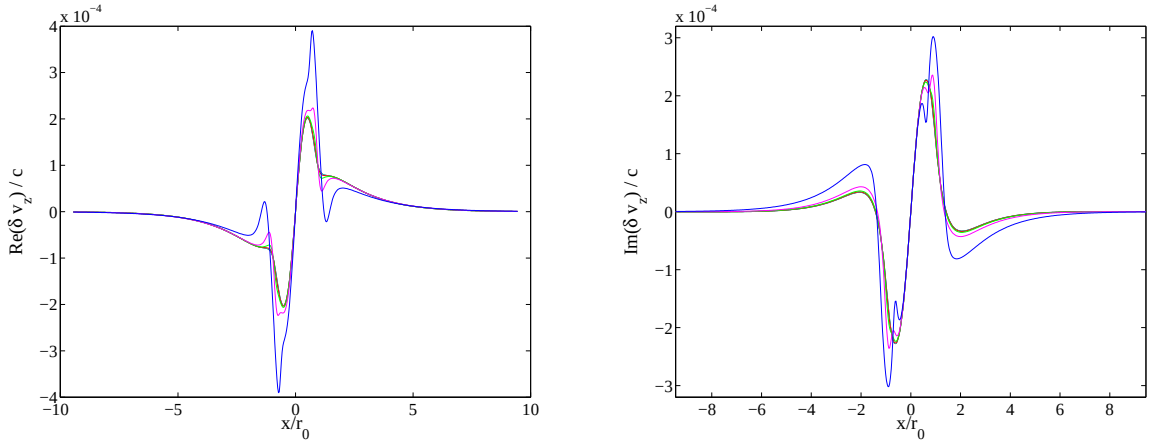

(a) Re(δv_z) (b) Im(δv_z)

Figure 7.8: Shear profiles of δv_z at different M_A for a flow speed of $0.7\,c$ (RMHD)
$M_A = \infty$ (black), 82.83 (cyan), 41.41 (red), 20.70 (green), 10.34 (magenta), 5.145 (blue)
$P_0/(\rho_0 c^2) \;=\; 50, \qquad v_{z0} \;=\; 0.7\,c\,\mathrm{sech}^2(x/r_0)$

transverse field, first at $0.7\,c$ (figure 7.10) and then at $0.2\,c$ (figure 7.11). Note that these graphs are normalized with respect to the perturbation amplitude. The field perturbations are approximately proportional to the strength of the field, i.e., the inverse of M_A.

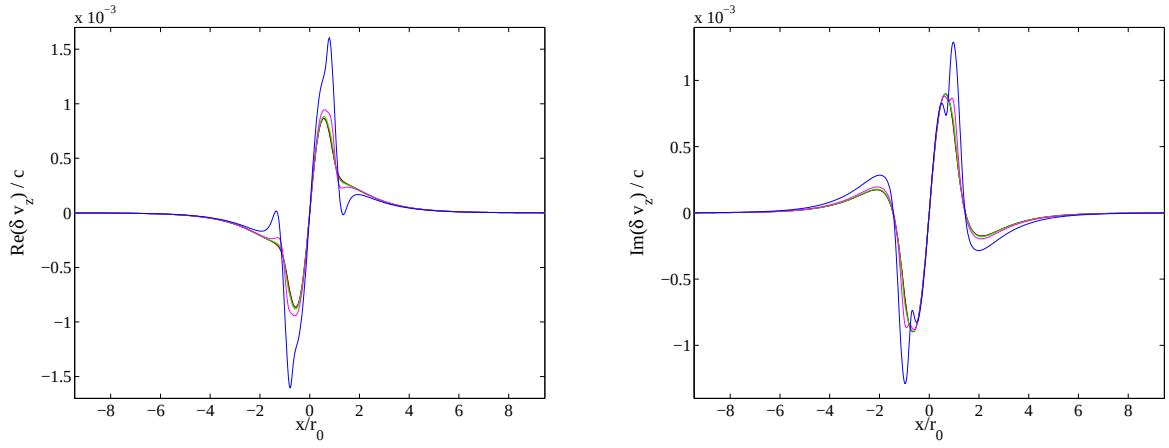

(a) Re(δv_z) (b) Im(δv_z)

Figure 7.9: Shear profiles of δv_z at different M_A for a flow speed of $0.2\,c$ (RMHD)
$M_A = \infty$ (black), 82.83 (cyan), 41.41 (red), 20.70 (green), 10.34 (magenta), 5.145 (blue)
$P_0/(\rho_0 c^2) = 50, \qquad v_{z0} = 0.2\,c\ \mathrm{sech}^2(x/r_0)$

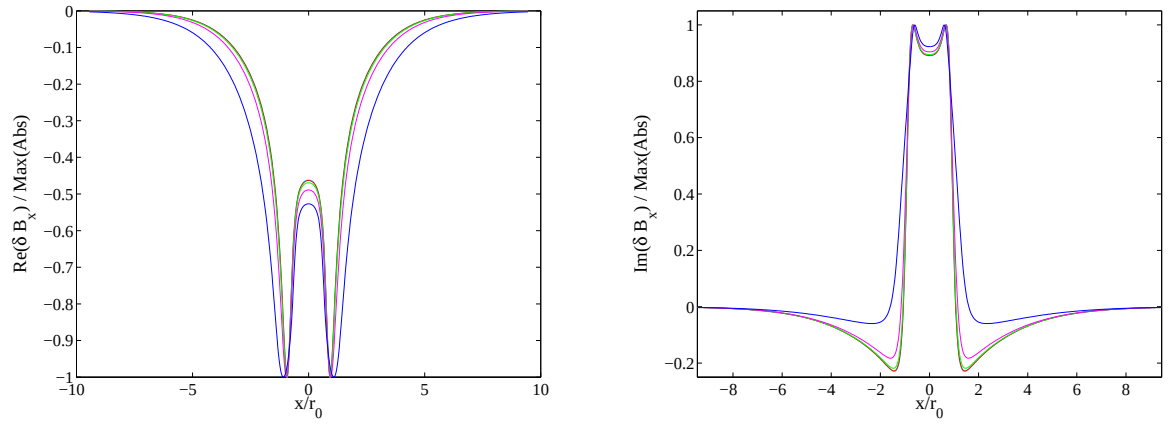

(a) Re(δB_x) (b) Im(δB_x)

Figure 7.10: Shear profiles of δB_x at different M_A for a flow speed of $0.7\,c$ (RMHD)
$M_A = \infty$ (black), 82.83 (cyan), 41.41 (red), 20.70 (green), 10.34 (magenta), 5.145 (blue)
$P_0/(\rho_0 c^2) = 50, \qquad v_{z0} = 0.7\,c\ \mathrm{sech}^2(x/r_0)$

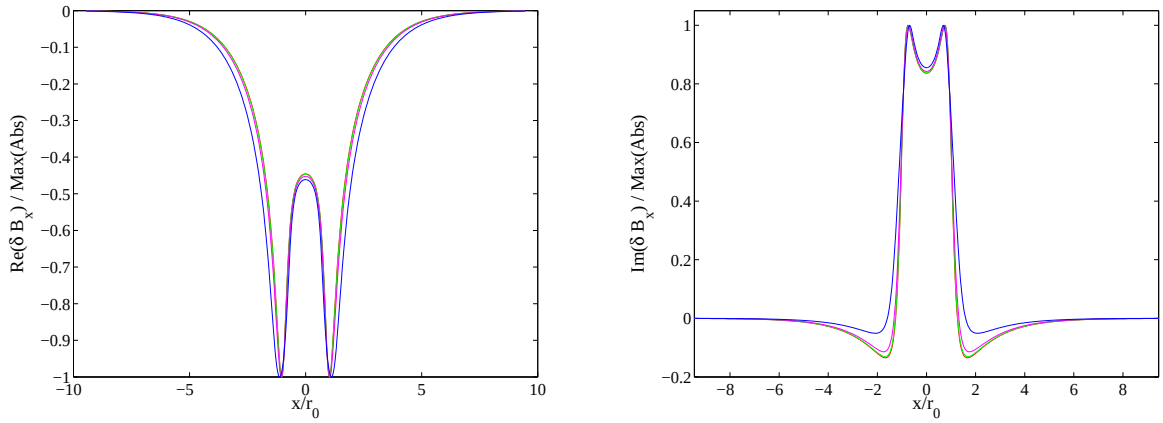

(a) Re(δB_x) (b) Im(δB_x)

Figure 7.11: Shear profiles of δB_x at different M_A for a flow speed of $0.2\,c$ (RMHD)
$M_A = \infty$ (black), 82.83 (cyan), 41.41 (red), 20.70 (green), 10.34 (magenta), 5.145 (blue)
$P_0/(\rho_0 c^2) \;=\; 50, \qquad v_{z0} \;=\; 0.2\,c\,\mathrm{sech}^2(x/r_0)$

We finally consider the profiles of the real and imaginary parts of δB_z, the perturbation in longitudinal field, first at $0.7\,c$ (figure 7.12) and then at $0.2\,c$ (figure 7.13). Note that these graphs are also normalized with respect to the perturbation amplitude. The field perturbations are, again, approximately proportional to the strength of the field, i.e., the inverse of M_A.

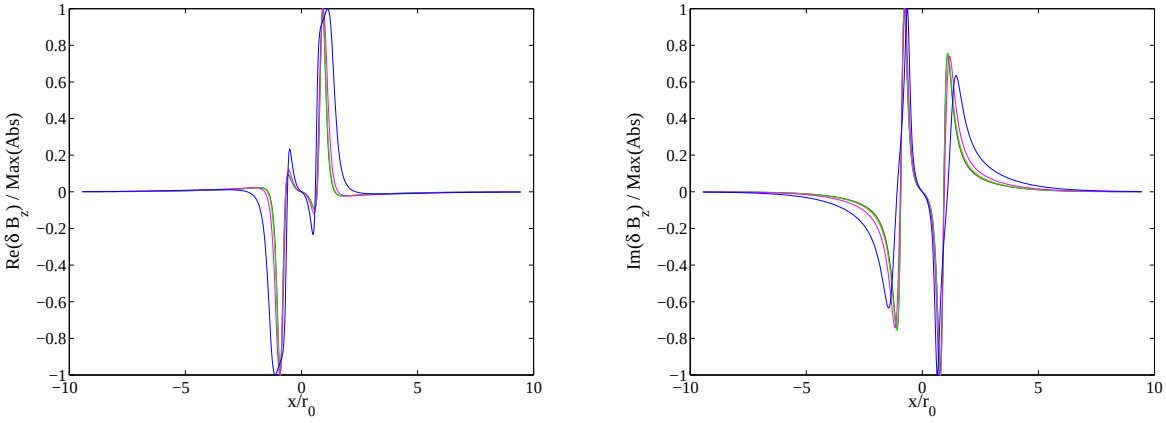

(a) Re(δB_z) (b) Im(δB_z)

Figure 7.12: Shear profiles of δB_z at different M_A for a flow speed of $0.7\,c$ (RMHD)
$M_A = \infty$ (black), 82.83 (cyan), 41.41 (red), 20.70 (green), 10.34 (magenta), 5.145 (blue)
$P_0/(\rho_0 c^2) \;=\; 50, \qquad v_{z0} \;=\; 0.7\,c\,\mathrm{sech}^2(x/r_0)$

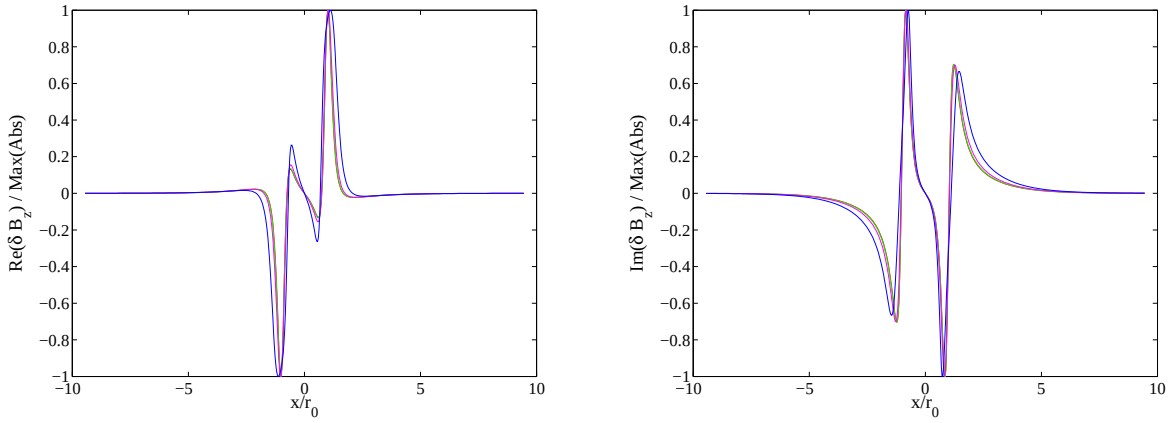

(a) Re(δB_z) (b) Im(δB_z)

Figure 7.13: Shear profiles of δB_z at different M_A for a flow speed of $0.2\,c$ (RMHD) $M_A = \infty$ (black), 82.83 (cyan), 41.41 (red), 20.70 (green), 10.34 (magenta), 5.145 (blue) $P_0/(\rho_0 c^2) = 50, \qquad v_{z0} = 0.2\,c\,\mathrm{sech}^2(x/r_0)$

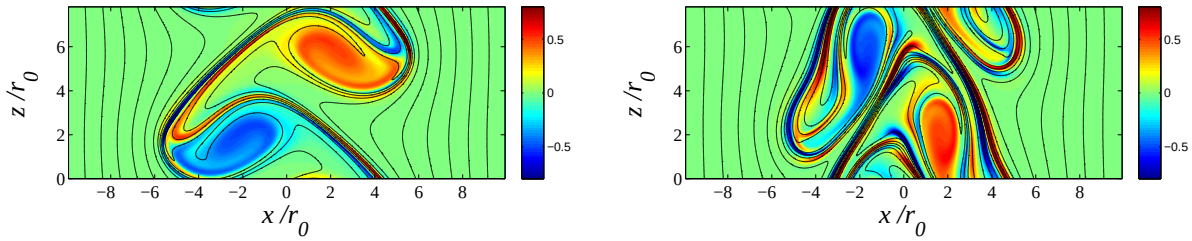

(a) $t = 10.34\,T_i = 4.62\,T = 104.4\,r_0/c$ $= 1.91\,L_x/c_s = 0.079\,L_x/v_A, \quad \beta_{\min} = 4.11$

(b) $t = 12.17\,T_i = 5.43\,T = 122.9\,r_0/c$ $= 2.25\,L_x/c_s = 0.092\,L_x/v_A, \quad \beta_{\min} = 1.94$

Figure 7.14: $M_A = 41.41, \qquad v_{Az}/c = 0.0237, \qquad \beta = 888.3, \qquad v_{z0} = 0.7c$

7.3 Conclusion

We have examined the shear profiles of the perturbations, which are cross-sections of the initial perturbations in which the simulation is launched. The perturbation profiles have converged with respect to system width and spatial step. We have seen that the pressure perturbations are initially antisymmetric, while the transverse velocity perturbations are initially symmetric. However, we will observe that in the nonlinear regime of the simulations, there emerge transversely propagating sound waves which are symmetric in the pressure and antisymmetric in the transverse velocity. Also, the density perturbations are antisymmetric. However, density diffusion introduces a density depletion layer which is symmetric about the jet axis (also noticed in the RMHD analysis of Mignone et al. 2009, and the MHD analysis of Frank et al. 1996). This indicates that certain features emerge whose symmetry is opposite the symmetry imposed by the perturbations.

In the unmagnetized cases, the perturbation profiles were plotted simultaneously for different background flow speeds. We noticed that at larger flow speeds, the profiles typically exhibit larger amplitudes of spatial variation, particularly in the case of the imaginary part of the pressure perturbation. This is especially evident at flow speeds greater than or equal to $0.9\,c$, and may partially explain why, at these highly relativistic flow speeds, the numerical simulation undergoes early unphysical breakdown (speeds exceeding the speed of light, negative densities, etc.), a problem that has plagued artificial viscosity simulations for over 20 years (Marti and Muller 2003). In general, large-amplitude spatial variations tend to generate numerical instability. In the pressure and velocity profiles of the magnetized cases, the perturbation amplitudes increase with increasing magnetic field strength (decreasing M_A),

and the amplitudes are noticeably larger for the strongest, vortex-suppressing field, for which $M_A = 5.145$. For the strongest fields (those which suppress nonlinear vortex formation), the perturbation profiles have a somewhat different shape than the profiles of the weaker fields (those which allow vortex formation, followed by disruption). This observation is correlated with a substantially reduced growth rate for vortex-suppressing fields. The deviation in profile behavior may also be correlated with a bifurcation in the nature of field enhancement in the early nonlinear regime of evolution, which will be explored in chapter 9. Throughout the vortex-disruptive regime, field enhancement increases with increasing field strength. However, in the vortex-suppressing regime, field enhancement decreases.

We have observed common symmetry properties in the transverse profiles of the velocity and magnetic field components. This creates the conditions necessary for a close complementarity between the flow and the magnetic field during nonlinear evolution, as we will observe in our simulation results. Before we discuss simulation results, however, we must first describe the numerical scheme for evolving the simulation, which we do in the next chapter.

Chapter 8

Numerical Method

We now describe the numerical method for evolving the RMHD single-fluid equations of Anile (1989) in conservative form. We use explicit finite-differencing in combination with artificial viscosity. The exact single-fluid RMHD equations are marginally stable, but become unstable when discretized in a numerical scheme. Artificial viscosity is needed in order to restore stability to the system, and also has physical significance. The momentum viscosity represents viscous exchanges of momentum between microscopic eddy structures (Tennekes and Lumley 1973). Our scheme has fourth-order accuracy in both space and time, and uses a rapidly convergent algorithm developed by Newman (2002) to recover the primitive variables from conserved quantities. In section 8.2, we demonstrate the physical significance of the magnetic viscosity (resistivity), by showing that it corresponds to a conductivity associated with electron and ion gyration within a range of physically realistic astrophysical parameters. In particular, we make comparisons to the environment of the BL Lacertae object BL Lac OJ287 discussed in Marscher and Jorstad (2011). In first and second-order methods, viscosity is implicitly present in the form of truncation error. The use of fourth-order spatial and temporal methods gives us explicit control over these viscosity terms.

We begin, in the first section, by describing our numerical scheme.

8.1 Evolving the Conservation-diffusion Equations

Here, we describe the numerical method for evolving a system in relativistic MHD. We begin by physically motivating the RMHD single-fluid conservative equations. Within a given volume of fluid, the total rate of change of a given conserved quantity is equal to the flux of that quantity through the boundaries of that volume. Let C_i is the density of a given conserved quantity, and F_{ij} the flux density of that quantity in the direction $\hat{\mathbf{e}}_j$. Let $d\tau$ denote a volume element of the volume under consideration (i.e., the volume over which we integrate C_i), and let da_j denote the jth component of the area vector normal to a given location on the surface bounding this volume. Then mathematically, we have

$$\frac{\partial}{\partial t}\int C_i d\tau + \oint F_{ij} da_j \;=\; 0. \tag{8.1}$$

With the use of the Divergence Theorem, we can rewrite (8.1) as follows:

$$\frac{\partial}{\partial t}\int C_i d\tau + \int \frac{\partial F_{ij}}{\partial x_j} d\tau \;=\; 0. \tag{8.2}$$

When we remove the volume integrals, the RMHD conservation equations take the general form

$$\frac{\partial C_i}{\partial t} + \frac{\partial F_{ij}}{\partial x_j} \;=\; 0, \tag{8.3}$$

where the x_j refer to the x, y, and z directions of a Cartesian coordinate system. This is the form of the single-fluid RMHD equations used in Landau and Lifshitz (1959a), Anile (1989), and Komissarov (1999). C_j are the conserved quantities. F_{ij} are the corresponding flux quantities. If there is no net flux through the boundaries of a given volume of fluid,

then the corresponding conserved quantity is conserved within that volume. This is true of the boundaries of our numerical system, which is a slab in the $x - z$ plane. It therefore follows that throughout our simulations, the total conserved quantities (integrated over the numerical system) are in fact conserved. These are the C_j listed below in equation (8.6).

When we incorporate viscosity, the RMHD conservation-diffusion equations take the general form

$$\frac{\partial C_i}{\partial t} + \frac{\partial F_{ij}}{\partial x_j} \;=\; \eta_i \frac{\partial^2 C_i}{\partial x_j^2}. \tag{8.4}$$

The term on the right represents artificial viscosity, which does not influence the conservative nature of the equations, and which is included for purposes of numerical stability, but also has physical significance. The exact RMHD single-fluid equations are marginally stable. However, when we discretize the spatial and temporal derivatives in a numerical scheme, these equations become unstable. We therefore need to include diffusion in order to restore stability to the system. Because diffusion is second-order in space, the use of fourth-order spatial and temporal methods gives us explicit control over the viscosity coefficients, which in turn represent physical processes. The momentum viscosity represents viscous exchanges of momentum between microscopic eddy structures (Tennekes and Lumley 1973). The magnetic viscosity corresponds to a conductivity associated with electron gyration around the magnetic field lines, as discussed in the next section. Diffusion can produce certain anomalies associated with relativistic effects, as we discuss in chapter 12, in which we also discuss why these anomalies do not emerge in our numerical simulations.

To advance the system one time step, we compute the primitive variables from the con-

served quantities, using a highly accurate, efficient, and convergent algorithm developed by Newman (2002). We then compute the necessary spatial derivatives using the fourth-order method of lines. We finally compute the conserved quantities at the next time step using the fourth-order Runge-Kutta method. Being a one-step method, the Runge-Kutta method is superior to multi-step methods in several respects (Ralston 2001). It allows for more versatility in modifying such parameters as the time step. The Runge-Kutta method is also self-starting. However, one-step methods are somewhat more computationally expensive. We first make the definitions

$$\begin{aligned} w &= \rho c^2 + \frac{\Gamma P}{\Gamma - 1}, \\ u^0 &= \gamma, \\ u^i &= \gamma \beta_i, \\ b^0 &= \mathbf{B} \cdot \boldsymbol{\beta}, \\ b^i &= \frac{B_i + b^0 u^i}{u^0}, \\ b^2 &= b_1 b_1 + b_2 b_2 + b_3 b_3 - b_0 b_0, \end{aligned} \tag{8.5}$$

where w is the enthalpy and Γ is the adiabatic constant. In this section, the speed of light c is normalized to unity. The conserved quantities are then given by

$$\begin{aligned} C_1 &= \rho u^0, \\ C_2 &= (w + b_\alpha b^\alpha) u^0 u^1 - b^0 b^1, \\ C_3 &= (w + b_\alpha b^\alpha) u^0 u^2 - b^0 b^2, \\ C_4 &= (w + b_\alpha b^\alpha) u^0 u^3 - b^0 b^3, \\ C_5 &= (w + b_\alpha b^\alpha) u^0 u^0 - \left(P + \frac{1}{2} b_\alpha b^\alpha \right) - b^0 b^0, \\ C_6 &= B_1, \\ C_7 &= B_2, \\ C_8 &= B_3. \end{aligned} \tag{8.6}$$

The first quantity represents mass density. The second, third, and fourth components are the

components of the momentum density. The fifth component is the energy density. The sixth, seventh, and eighth components are the components of the magnetic field in the stationary frame.

The corresponding flux quantities are given by

$$\begin{aligned}
F_{1i} &= \rho u^i, \\
F_{2i} &= (w + b_\alpha b^\alpha) u^2 u^i - \left(P + \frac{1}{2} b_\alpha b^\alpha \right) \delta_{2i} - b^2 b^i, \\
F_{3i} &= (w + b_\alpha b^\alpha) u^3 u^i - \left(P + \frac{1}{2} b_\alpha b^\alpha \right) \delta_{3i} - b^3 b^i, \\
F_{4i} &= (w + b_\alpha b^\alpha) u^4 u^i - \left(P + \frac{1}{2} b_\alpha b^\alpha \right) \delta_{4i} - b^4 b^i, \\
F_{5i} &= (w + b_\alpha b^\alpha) u^0 u^i - b^0 b^i, \\
F_{62} &= v_1 B_2 - v_2 B_1, \\
F_{63} &= v_1 B_3 - v_3 B_1, \\
F_{71} &= v_2 B_1 - v_1 B_2, \\
F_{73} &= v_2 B_3 - v_3 B_2, \\
F_{81} &= v_3 B_1 - v_1 B_3, \\
F_{82} &= v_3 B_2 - v_2 B_3, \\
F_{61} &= F_{72} = F_{83} = 0.
\end{aligned} \tag{8.7}$$

Let Δt denote the time increment of the simulation. Let Δx, Δy, and Δz denote the spatial increments in the x, y, and z directions, respectively. Suppose we know the conserved quantities at time step n and wish to compute them at time-step $n+1$. We use the fourth-order Runge-Kutta method. We loop from $i = 1$ to $i = 4$, and at each value of i we compute the following, for $i > 1$:

$$\mathbf{C}^{n+i/4} = \mathbf{C}^n + \Delta t \sum_{j=1}^{i-1} \alpha_{ij} \frac{\partial \mathbf{C}^{n+j/4}}{\partial t}. \tag{8.8}$$

The value of $\mathbf{C}^{n+1}$, i.e., $\mathbf{C}$ at the time increment $n+1$, is then given by

$$\mathbf{C}^{n+1} \;=\; \mathbf{C}^n + \Delta t \sum_{i=1}^{4} \beta_i \frac{\partial \mathbf{C}^{n+i/4}}{\partial t}. \tag{8.9}$$

The method used is the "classic" fourth-order Runge-Kutta method. The α coefficients for this method are defined as follows:

$$\alpha_{21} = 1/2, \quad \alpha_{32} = 1/2, \quad \alpha_{43} = 1, \quad \alpha_{ij} = 0, \quad \text{otherwise.} \tag{8.10}$$

The β coefficients are defined as follows:

$$\beta_1 = 1/6, \quad \beta_2 = 1/3, \quad \beta_3 = 1/3, \quad \beta_4 = 1/6. \tag{8.11}$$

We clearly need a method for estimating

$$\left(\frac{\partial C_m}{\partial t}\right)^{n+(l+1)/4}$$

at $l = 0, 1, 2,$ and 3, from the known quantity $C_m^{n+l/4}$. To do this, we must estimate the spatial derivatives at time step $n + l/4$. The primitive variables are recovered from the conserved quantities using an algorithm developed by Newman (2002). This method reduces a system of five equations to a single cubic polynomial in the pressure P, and is one order of magnitude faster than Newton-based methods used to solve equivalent systems. The algorithm is as follows (methods for solving the cubic equation are described in such articles as McKelvey (1984) and Nickalls (1993)). We first denote the momentum density, momentum density squared, and the quantity T, by

$$
\begin{aligned}
m^i &= (w + b_\alpha b^\alpha)u^0 u^i - b^0 b^i, \\
mm &= C_2^2 + C_3^2 + C_4^2, \\
T^2 &= (C_2 B_2 + C_3 B_3 + C_4 B_4)^2.
\end{aligned} \tag{8.12}
$$

We begin by making an initial guess for P, which is generally its unperturbed (equilibrium) value. We denote this P_0. We then compute

$$
\begin{aligned}
a &= C_5 + P_0 + \frac{B^2}{2}, \\
d &= \frac{1}{2}\left(mmB^2 - T^2\right).
\end{aligned} \tag{8.13}
$$

We must now verify that P satisfies the condition

$$
a \geq \left(\frac{27d}{4}\right)^{1/3}. \tag{8.14}
$$

We now make the following computations:

$$
\begin{aligned}
\phi &= \cos^{-1}\left[\frac{1}{a}\sqrt{\frac{27d}{4a}}\right], \\
U_1 &= \frac{a}{3} - \frac{2a}{3}\cos\left(\frac{2\phi}{3} + \frac{2\pi}{3}\right), \\
L &= U_1 - B^2, \\
\beta^2 &= \frac{mmL^2 - T^2(B^2 + 2L)}{L^2(B^2 + L)^2}, \\
u^0 &= \frac{1}{\sqrt{1 - \beta^2}}, \\
w &= \frac{L}{u^0 u^0}, \\
\rho &= \frac{C_1}{u^0}, \\
P_1 &= \frac{\Gamma - 1}{\Gamma}(w - \rho c^2).
\end{aligned} \tag{8.15}
$$

We repeat this process, using P_1 as an input instead of P_0. This generates a third value P_2. We now perform convergence checks on P_0, P_1, and P_2, making sure that the magnitude of the difference between two successive estimates of P is less than a sufficiently small number of around 10^{-12}. We can then compute the Lipshitz constant R, given by

$$R = \frac{P_2 - P_1}{P_1 - P_0}. \tag{8.16}$$

We then compute the Aitken accelerant P_{Aitken}, given by

$$P_{\text{Aitken}} = P_0 + \frac{P_1 - P_0}{1 - R}. \tag{8.17}$$

We perform convergence checks on P_0, P_1, P_2, and P_{Aitken}. If necessary, we repeat the algorithm, using P_{Aitken} as the new P_0, and continue to do so until the convergence checks are satisfied.

The quantities P, ρ, w, β^2, u^0, and $\vec{B}$ are now known. To compute the remaining quantities, we do the following:

$$\begin{aligned} S &= \frac{T}{wu^0u^0}, \\ \beta_i &= \frac{m^i + SB^i}{wu^0u^0 + B^2}, \qquad i = 1, 2, 3, \\ u^i &= \beta^i u^0, \qquad i = 1, 2, 3. \end{aligned} \tag{8.18}$$

Let Δx denote the spatial increment in x, Δy the increment in y, and Δz the increment in z. Suppose there are N_x grid cells, so that $L_x = (N_x - 1)\Delta x$. To estimate the spatial derivatives of a quantity G, we use the method of lines, which employs the method of asymptotic matching. Consider the $(n + l/4)$th time step, and (i, j, k)th spatial location. In

the following two equations, the j, k indices are omitted from the superscripts, but implicitly understood. In general, the fourth-order method of lines is used (Schiesser 1991). In fourth-order, the first derivative of the flux quantity F_{m1}, with respect to x, is given by

$$\left(\frac{\partial F_{m1}}{\partial x}\right)^{i,n+l/4} \approx \frac{1}{\Delta x}\left(\frac{-1}{12}F_{m1}^{i+2,n+l/4} + \frac{2}{3}F_{m1}^{i+1,n+l/4} - \frac{2}{3}F_{m1}^{i-1,n+l/4} + \frac{1}{12}F_{m1}^{i-2,n+l/4}\right). \quad (8.19)$$

We must also compute the diffusion terms. The second derivative of the conserved quantity C_m with respect to x, again in fourth-order, is given by

$$\begin{aligned}\left(\frac{\partial^2 C_m}{\partial x^2}\right)^{i,n+l/4} \approx\ & \frac{1}{\Delta x^2}\left(\frac{-1}{12}C_m^{i+2,n+l/4} + \frac{4}{3}C_m^{i+1,n+l/4}\right) \\ & + \frac{1}{\Delta x^2}\left(-\frac{5}{2}C_m^{i,n+l/4} + \frac{4}{3}C_m^{i-1,n+l/4} - \frac{1}{12}C_m^{i-2,n+l/4}\right). \end{aligned} \quad (8.20)$$

We use periodic boundary conditions in each spatial direction. Therefore, when $i = N_x - 1$, we replace $i + 2$ with 2, and $i + 1$ with N_x. When $i = N_x$, we replace $i + 2$ with 2 and $i + 1$ with 1. When $i = 1$, we replace $i - 2$ with $N_x - 2$ and $i - 1$ with $N_x - 1$. When $i = 2$, we replace $i - 2$ with $N_x - 1$ and $i - 1$ with 1. What we have said about x applies in the same manner to y and z. In practice, the simulation is performed in two dimensions, with finite spatial extent in the x and z directions only.

We can now estimate the desired time derivative, at the given spatial location, using the conservation-diffusion equation:

$$\left(\frac{\partial C_m}{\partial t}\right)^{i,j,k,n+(l+1)/4} = -\left(\frac{\partial F_{mh}}{\partial x_h}\right)^{i,j,k,n+l/4} + \eta_m\left(\frac{\partial^2 C_m}{\partial x_h^2}\right)^{i,j,k,n+l/4}. \quad (8.21)$$

We now repeat the process described in equations (8.12) through (8.21) to obtain the necessary intermediate time derivatives of the C_m. We then use equation (8.9) to evaluate the

conserved quantities C_m at the next time step of the simulation. This is the process by which we advance the numerical simulation through each time step. Having described our numerical algorithm, we now describe the physical significance of the magnetic viscosity used in this algorithm.

8.2 Physical Significance of Magnetic Viscosity

We demonstrate that the magnetic viscosity (i.e., resistivity) used in the simulations corresponds to a conductivity which is consistent with electron and ion gyrations in astrophysical environments relevant to our study, including the BL Lacertae object OJ287 examined by Marscher and Jorstad (2011), and the radio jet M87 examined by Hines et al. (1989) and Stawarz et al. (2005). As we will show, these objects correspond to conductivities on the order of 10^{-5} s^{-1}, which is within an order of magnitude of the conductivity derived from the magnetic viscosity used in the numerical simulations. We use the following fundamental constants, which are quoted here for reference:

$$\begin{aligned} c &= 3 \times 10^{10} \text{ cm/s}, \\ e &= 4.8 \times 10^{-10} \text{ statc}, \\ m_e &= 9.11 \times 10^{-28} \text{ g}, \\ m_p &= 1.67 \times 10^{-24} \text{ g}, \\ k_B &= 1.38 \times 10^{-16} \text{ ergs/K}. \end{aligned} \tag{8.22}$$

We first estimate the conductivity corresponding to the magnetic viscosity used in the simulations. A typical magnetic viscosity in the numerical simulations is $\eta = \chi r_0 c \approx 0.001\, r_0 c$, where lengths on the numerical grid are measured in units of r_0, and velocities are measured in units of the speed of light c. In particular, the background velocity profile varies as $v_{z0}\,\mathrm{sech}^2(x/r_0)$, so the simulation length unit r_0 is on the order of half a jet radius. We use

Jackson (1975) to estimate the corresponding conductivity:

$$\sigma_{\text{visc}} \approx \frac{c^2}{\eta} = \frac{c^2}{\chi r_0 c} \approx 1000\frac{c}{r_0}. \tag{8.23}$$

In the simulations, typical frequencies are on the order of c/r_0, so the above result is approximately consistent with the assumption of effectively infinite conductivity. A typical jet radius is on the order of a parsec, or 10^{18} cm, so we have

$$\sigma_{\text{visc}} \approx 1000\frac{3 \times 10^{10}}{10^{18}} = 3 \times 10^{-5}\ \text{s}^{-1}. \tag{8.24}$$

We denote σ_{visc} as the conductivity corresponding to the magnetic viscosity used in the simulations. We now compute a conductivity that would be typical of BL Lacertae OJ287, using the magnetic field value of 5 μG derived in Marscher and Jorstad (2011), along with parameters typical of jet environments, and therefore plausible for BL Lacertae OJ287. We then repeat the process for a field of around 100 μG, which is an estimate of the field in the radio jet M87 (Hines et al. 1989 and Stawarz et al. 2005). We assume the conductivity to be dominated by electrons of mass m_e, charge e, number density n, and having a Larmor frequency ω_{lar} which is much larger than their collision frequency ν with the protons. The conductivity of the plasma can be approximated as (Bittencourt 2004):

$$\sigma = \frac{ne^2\omega_{\text{lar}}}{m_e[\omega_{\text{lar}}^2 + (\nu - i\omega)^2]}, \tag{8.25}$$

where $\omega \approx c/r_0 \approx 10^{-8}\ \text{s}^{-1}$. We will see that $\omega_{\text{lar}} >> \omega$. Also, as will be shown later, $\omega_{\text{lar}} >> \nu$. We therefore have

$$\sigma \approx \frac{ne^2}{m_e\omega_{\text{lar}}}. \tag{8.26}$$

This can be further simplified as follows:

$$\sigma \approx \frac{ne^2}{m_e\omega_{\rm lar}} \approx \frac{ne^2}{m_e}\left(\frac{m_e c}{eB}\right) \tag{8.27}$$

$$= \frac{nec}{B} \approx \frac{(4.8\times10^{-10})(3\times10^{10})(n)}{B} = \frac{(14.4\ {\rm cm^3 G\,s^{-1}})(n)}{B}. \tag{8.28}$$

In terms of the plasma β, we have

$$P \approx \frac{\beta B^2}{8\pi}. \tag{8.29}$$

Let α be defined by

$$P = \alpha\rho c^2 \approx \alpha n m_p c^2, \tag{8.30}$$

where we assume that the mass density is dominated by the contribution from protons. For a typical jet environment in which the sound speed is near its relativistic limit, we have $\alpha \approx 50$. The number density of electrons (and protons) is therefore related to the magnetic field by

$$n \approx \frac{P}{\alpha m_p c^2} \approx \frac{\beta B^2}{8\pi\alpha m_p c^2} \approx \frac{(26.5\ {\rm cm^{-3}G^{-2}})\beta B^2}{\alpha}. \tag{8.31}$$

Inserting this result into our expression for σ, we have

$$\sigma \approx \frac{14.4\,n}{B} \approx (14.4)(26.5\ {\rm G^{-1}s^{-1}})\frac{\beta B}{\alpha} \approx [380\ ({\rm G\ s})^{-1}]\,\frac{\beta B}{\alpha}. \tag{8.32}$$

We assume a plasma β of around unity. We obtain the following values from the magnetic field used in Marscher and Jorstad (2011) in their study of the BL Lac object OJ287:

$$B \approx 5 \times 10^{-6} \text{ G}, \qquad \beta \approx 1, \tag{8.33}$$

$$\alpha = \frac{P}{\rho c^2} \approx 50, \tag{8.34}$$

$$P \approx \frac{\beta B^2}{8\pi} \approx 1 \times 10^{-12} \text{ dynes/cm}^2, \tag{8.35}$$

$$n \approx (26.5 \text{ cm}^{-3}\text{G}^{-2})\frac{\beta B^2}{\alpha} \approx 1.3 \times 10^{-11} \text{ cm}^{-3}, \tag{8.36}$$

$$\omega_{\text{lar}} = \frac{eB}{m_e c} \approx 88 \text{ s}^{-1}, \tag{8.37}$$

$$\sigma \approx [380 \text{ (G s)}^{-1}] \frac{\beta B}{\alpha} \approx 3.8 \times 10^{-5} \text{ s}^{-1}, \tag{8.38}$$

$$\frac{\sigma}{\sigma_{\text{visc}}} \approx \frac{3.8 \times 10^{-5}}{3 \times 10^{-5}} \approx 1.3. \tag{8.39}$$

We therefore have very good agreement between the conductivity σ_{visc}, corresponding to the magnetic viscosity used in the simulations, and the conductivity σ of BL Lac object OJ287, estimated from the magnetic field quoted in Marscher and Jorstad (2011).

Hines et al. (1989) and Stawarz et al. (2005) both deduced a magnetic field value on the order of 10^{-4} G in one of the knots of extragalactic radio jet M87. In this case, we obtain approximate agreement between conductivities (from the numerical viscosity and from the jet) if we assume a more pressure-dominated system, where

$$\alpha = \frac{P}{\rho c^2} \approx 500. \tag{8.40}$$

The knots in M87 are in fact believed to be overpressured (Bicknell and Begelman 1996). It is reasonable to assume that for a larger magnetic field, the pressure will be correspondingly larger, in order to maintain a plasma β of order unity. This corresponds to a sound speed which is even closer to its relativistic limit of $c/\sqrt{3}$. The corresponding parameters in this case are as follows:

$$B \approx 10^{-4}\ \mathrm{G}, \qquad \beta \approx 1, \tag{8.41}$$

$$\alpha = \frac{P}{\rho c^2} \approx 500, \tag{8.42}$$

$$P \approx \frac{\beta B^2}{8\pi} \approx 4 \times 10^{-10}\ \mathrm{dynes/cm^2}, \tag{8.43}$$

$$n \approx (26.5\ \mathrm{cm^{-3}G^{-2}})\frac{\beta B^2}{\alpha} \approx 5.3 \times 10^{-10}\ \mathrm{cm^{-3}}, \tag{8.44}$$

$$\omega_{\mathrm{lar}} = \frac{eB}{m_e c} \approx 1.8 \times 10^3\ \mathrm{s^{-1}}, \tag{8.45}$$

$$\sigma \approx [380\ (\mathrm{G\ s})^{-1}]\,\frac{\beta B}{\alpha} \approx 7.6 \times 10^{-5}\ \mathrm{s^{-1}}, \tag{8.46}$$

$$\frac{\sigma}{\sigma_{\mathrm{visc}}} \approx \frac{7.6 \times 10^{-5}}{3 \times 10^{-5}} \approx 2.5. \tag{8.47}$$

We see that in a jet with a 10^{-4} G field, we have good agreement between the conductivities deduced from the magnetic viscosity and from the fields measured in Hines et al. (1989) and Stawarz et al. (2005) for M87. Note that for typical parameters the Larmor frequency is on the order of 100 $\mathrm{s^{-1}}$, which is about 10 orders of magnitude larger than frequencies typical of the perturbations being simulated. It is therefore highly unlikely that the KH-destabilization being studied would generate resonance in gyrating particles.

We verify below that the Larmor frequency is much larger than the collision frequency. The collision frequency is given approximately by

$$\nu = n\Pi\frac{v_{\mathrm{th}}}{\sqrt{3}} < n\Pi c, \tag{8.48}$$

where Π is the collisional cross-section. The next term is the thermal velocity in a given direction, which certainly cannot exceed c. We assume an impact parameter with the protons on the order of a Bohr radius, i.e., $a_0 = 10^{-8}$ cm. The cross section is therefore approximately

$$\Pi \approx \pi a_0^2 \approx \pi \times 10^{-16}\ \mathrm{cm^2}. \tag{8.49}$$

The collision frequency is bounded as follows:

$$\nu \approx n\Pi c = n(\pi \times 10^{-16})(3 \times 10^{10}) = n\pi \times 10^{-6}\ \mathrm{s}^{-1}. \tag{8.50}$$

For typical particle densities in the range $10^{-12} < n < 10^{-4}$ cm^{-3}, the corresponding range of collision frequencies is

$$\pi \times 10^{-18} < \nu < \pi \times 10^{-10} \tag{8.51}$$

We therefore have $\nu << \omega_{\mathrm{lar}}$ for even the smallest Larmor frequency calculated above. That is, the collision frequency is much less than the Larmor frequency, and hence we are justified in our assumption that the conductivity is dominated by electron and ion gyration. We also have $\nu << \omega$, where $\omega \approx 10^{-8}$ s^{-1} are frequencies typical of the KH-unstable waves in our study. We are therefore justified in our assumption that the plasma is approximately collisionless.

We have demonstrated that the magnetic viscosity (resistivity) used in the simulations corresponds, within a range of realistic physical parameters, to conductivities associated with electron and ion gyration in the environments of relevant astrophysical objects, including the BL Lacertae object BL Lac OJ287 explored by Marscher and Jorstad (2011), and the extragalactic radio jet M87 explored by Hines et al. (1989) and Stawarz et al. (2005).

8.3 Conclusion

We have described the numerical method used to evolve the simulation in time, which, as we have seen, numerically solves the single-fluid RMHD equations in conservative form, using fourth-order finite-differencing to estimate spatial derivatives of flux quantities, the

fourth-order Runge-Kutta method to compute the conserved quantities at the next time step, and a highly accurate, rapidly convergent algorithm developed by Newman (2002) to recover the primitive variables from the conserved quantities. This scheme has fourth-order accuracy in space and time. Artificial viscosity is used for numerical stability, but also has physical significance, as the momentum viscosity models viscous exchanges of momentum between small-scale eddies, between molecular and integral length scales (Tennekes and Lumley 1973), and the magnetic viscosity (i.e., resistivity) models electron and ion gyration for realistic parameters of relevant astrophysical environments. Another important result is that for typical parameters, the Larmor frequency is on the order of 100 s^{-1} while typical perturbation frequencies are on the order of 10^{-8} s^{-1}. This means it is highly unlikely that the perturbations being simulated would exhibit resonance with particles gyrating about the magnetic field lines.

Another class of schemes, known as high-resolution shock-capturing (HRSC) schemes, do not require the use of artificial viscosity, though they are not as rapidly convergent as the scheme being used, and are difficult to employ in the RMHD regime. Nevertheless, Mignone et al. (2009) have developed an HRSC scheme, for use in the RMHD regime, that overcomes many of these difficulties. As we will discuss in chapter 13, a useful path of future research would be to compare results generated in this study with results generated using the scheme of Mignone et al. (2009). We now present the results of our numerical simulations.

Chapter 9

Spatial Averages and Maximum Values Versus Time

We have described (chapter 5) the algorithm for computing a numerical eigenmode in which to launch a simulation, and (chapter 8) the scheme used to advance the numerical simulation in time. We are now in a position to examine the results of our simulations. In this chapter, we present plots showing the time-dependence of various spatially-averaged or maximized quantities. We begin with the primitive variables (density, pressure, velocity and magnetic field components), and examine the time-dependence both in the fluctuations (perturbations) of these quantities, and in their spatial averages. In section 9.1, we consider the linear regime, i.e., the initial stages of the evolution, in which the perturbations grow exponentially, ideally at the growth rate corresponding to the eigenmode. As we demonstrate in section 9.2, the real-valued initial perturbation distribution consists of only one positive growth rate. However, the presence of artificial diffusion introduces evanescent modes, resulting in initial deviations of the growth curves from linear agreement. When the perturbations become sufficiently large compared to their background values, the growth deviates from linear behavior, corresponding to the onset of the nonlinear regime. This is what we consider in section 9.4. In the early stages of the nonlinear regime, the perturbations reach a saturation

level (maximum growth), after which the growth either decreases or remains at this average level. In section 9.5, we consider the average values of the primitive variables, which are not strongly correlated with the fluctuation behavior. The average density and pressure both increase over time, while the average velocity and Lorentz factor tend to decrease over time, with each of these quantities approaching an asymptotic value as the system approaches an equilibrium state.

In both the perturbations and the average values, we notice nonlinear oscillations which correspond to nonlinear transverse acoustic waves propagating between the jet axis and transverse boundaries, particularly in the unmagnetized and weakly magnetized cases, and for more highly relativistic flows. An important point is that the period of these oscillations is dependent on the transverse system width, which is a numerical parameter. However, as we will show in sections 11.3 through 11.5, these acoustic oscillations do not significantly affect the evolution of the flow and its interaction with the magnetic field, the important properties of which are independent of system width.

In section 9.6, we plot such quantities as the RMS vorticity, RMS current density, and electromagnetic energy density, none of which exhibit the aforementioned nonlinear oscillations, but each of which exhibit a peak shortly after saturation, generally corresponding to amplification, at the vortex extremities, of field-related quantities. The peak is generally followed by a decay which asymptotically approaches some equilibrium value (usually zero). Collectively, these plots show many interacting processes, among which is the transfer of energy from the bulk flow to the magnetic field in the early nonlinear regime (as the field lines are expelled by the vortices), followed by viscous dissipation into thermal energy as the

field lines, and resulting filamentary features, gradually become aligned with the flow. We finally examine the numerical accuracy with which the total z-momentum and total energy are conserved, as shown in table 9.1.

We begin by discussing the initial evolution of the system through the linear regime.

9.1 Growth in the Linear Regime

In its initial equilibrium state, the system has a uniform background density and pressure, and, when magnetized, a uniform background magnetic field in the z-direction. The background flow velocity has a shear variation of the form $v_{z0}\,\mathrm{sech}^2(x/r_0)$. To launch the simulation, the system is perturbed in a numerically-derived linear eigenmode of the system, as described in chapter 5. For a given perturbation wave number k_z, there are multiple modes, each with its own complex eigenfrequency and therefore growth rate (the "sinuous" and "varicose" modes, so named because of their opposite symmetries, described in chapters 6 and 7). However, we select the sinuous mode with the fastest growth rate, and as we show in section **??**, this is the only positive growth rate that emerges in the real-valued initial perturbation distributions. As a means of validating the numerical code, we need to compare the linear growth of the primitive variables (density, pressure, velocity, and when present, magnetic field) with the growth rate of the fastest-growing eigenmode. In the absence of diffusion, the growth of the primitive variables, in the linear regime, shows excellent agreement with linear theory.

However, we must include diffusion in order to provide numerical stability to the system, particularly in the nonlinear regime. Diffusion is also physically realistic, as it models

viscous exchanges of mass, momentum, and energy between interacting small-scale eddies (Tennekes and Lumley 1973). Most of the numerical simulations use equal amounts of x and z-momentum viscosity, as momentum diffusion is generally isotropic. Density viscosity is also included in order to prevent the densities from becoming negative in the nonlinear regime. In the magnetized cases, magnetic viscosity models a conductivity which is consistent with electron and ion gyrations in relevant astrophysical environments (see section 8.2).

However, diffusion also causes initial deviations from linear agreement in the growth of the primitive variables, and these can be noticeably larger than the deviations caused by the slower-growing modes described above. We wish to isolate the effects of the individual viscosity coefficients on linear growth, and identify the physical driving mechanisms of the evanescent modes that underly the linear deviations. We do this by considering first x-momentum viscosity in isolation, then equal amounts of x-momentum and density viscosity, and finally equal amounts of x-momentum, density, and z-momentum viscosity. The first two cases are not entirely realistic physically, as we would generally expect to have comparable amounts of momentum viscosity in both components. However, this procedure will allow us to isolate the evanescent modes introduced by each viscosity coefficient. We will see that the modes introduced by viscosity are either evanescent, or have much smaller growth rates than that of the numerical mode. Therefore, in the later stages of the linear regime, the modes introduced by diffusion effectively disappear, and the numerical mode ultimately dominates, since it has the fastest growth rate.

The fluid is unmagnetized, with a background flow velocity of $v_{z0}(x) = 0.7\,c\,\mathrm{sech}^2(x/r_0)$,

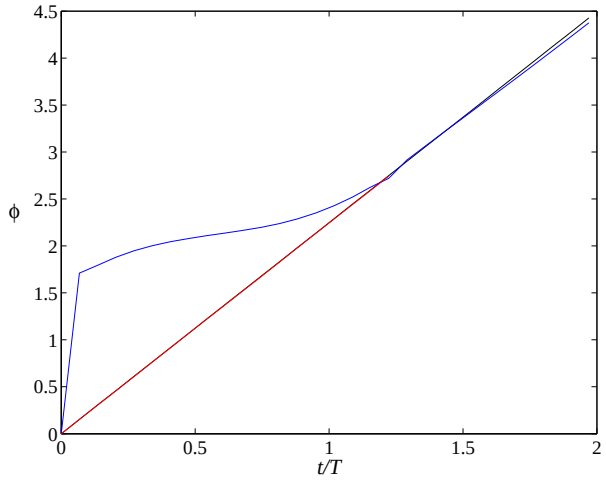

Figure 9.1: Linear growth in δP for different values of the z-momentum viscosity theoretical (Black), $\eta_z = 0.00025\, r_0 c$ (Blue), $\eta_z = 0$ (Red)
Pressure growth, $v_{z0}(x) = 0.7\, c\, \mathrm{sech}^2(x/r_0)$, $\eta_x = \eta_\rho = 0.00025\, r_0 c$

a uniform background pressure to density ratio of $P_0/(\rho_0 c^2) = 50$, and a wave number $k_z = 0.8/r_0$. The complex frequency is $\omega = (0.278 + 0.099i)\, c/r_0$, and the period is $2\pi/\omega_r = 22.6\, r_0/c$. The results are summarized in the growth curves in figures 9.1 and 9.2, and explained more fully in what follows.

We begin with a viscosity of $0.00025\, r_0 c$ only in the transverse (x) component of momentum. This does not introduce any deviation from linear agreement, as shown by the growth curves in figure 9.3.

We now consider the same case as above, except we introduce a density viscosity equal to the x-momentum viscosity ($0.00025\, r_0 c$). As shown in figure 9.4, the pressure growth curve still shows excellent linear agreement, as do the velocity growth curves. However, we now notice a large deviation in the density agreement. Furthermore, this is not a numerically stable combination of viscosities, as seen by the early numerical breakdown after only 1.3 periods. We now examine displays of the linear evolution. The z-direction (vertical), is the

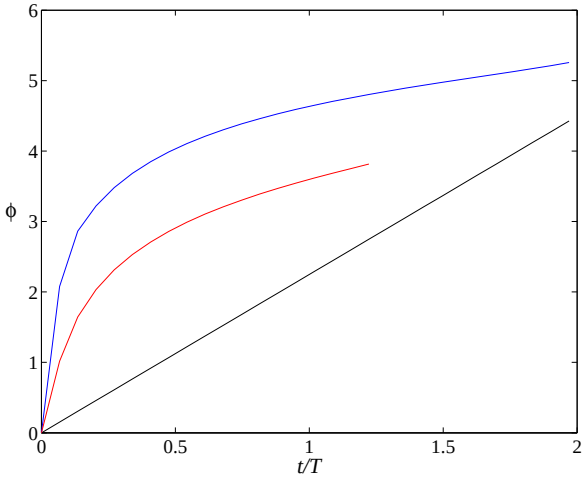

Figure 9.2: Linear growth in $\delta\rho$ for different values of the z-momentum viscosity theoretical (Black), $\eta_z = 0.00025\, r_0 c$ (Blue), $\eta_z = 0$ (Red)
Density growth, $v_{z0}(x) = 0.7\, c\, \mathrm{sech}^2(x/r_0)$, $\eta_x = \eta_\rho = 0.00025\, r_0 c$

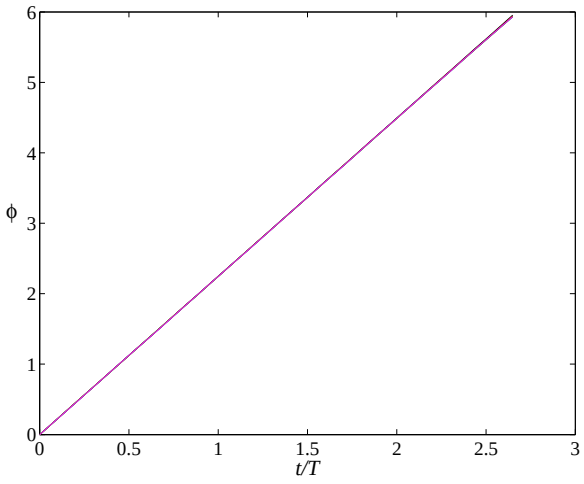

Figure 9.3: Linear growth curves for non-zero x-momentum viscosity theoretical (Black), ρ (Blue), v_x (Red), v_z (Green), P (Magenta)
$v_{z0}(x) = 0.7\, c\, \mathrm{sech}^2(x/r_0)$, $\eta_x = 0.00025\, r_0 c$

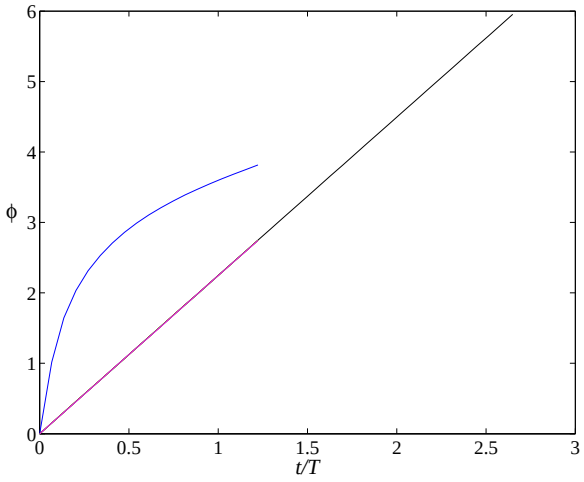

Figure 9.4: Linear growth curves for non-zero density and x-momentum viscosity theoretical (Black), ρ (Blue), v_x (Red), v_z (Green), P (Magenta)
$v_{z0}(x) \;=\; 0.7\,c\,\mathrm{sech}^2(x/r_0), \qquad \eta_\rho \;=\; \eta_x \;=\; 0.00025\,r_0 c$

flow direction, where the flow is directed upward, and the displays show only one wavelength of the perturbation, although the system spans two perturbation wavelengths (for the cases shown). In some simulations, not shown in this chapter, the system spans up to five perturbation wavelengths, however in each case the system remains spatially periodic in the flow direction, with negligible differences in behavior from one wavelength to the next. The pressure displays in figures 9.5 show linear behavior, where the pattern speed of the flow is approximately equal to the phase velocity of $0.347\,c$.

Each display is labeled underneath with the minimum and maximum values of the quantity being displayed. The minimum value corresponds to dark blue coloration, while the maximum value corresponds to dark red coloration, and the values in between are assigned colors according to the visible spectrum. At later times in the linear evolution, the range of values is typically larger, due to growth of the perturbations, so the color scales do not correspond to the same values from one display to the next.

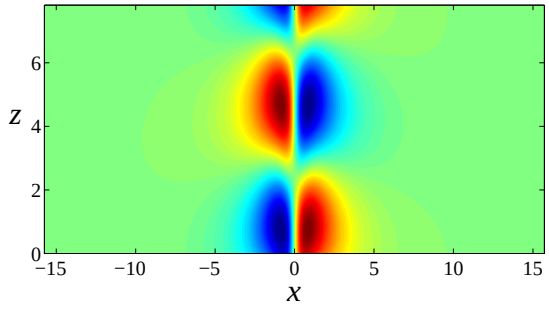

(a) $t = 1.536\, r_0/c = 0.068\, T$
$4.999 \leq P \leq 5.001$

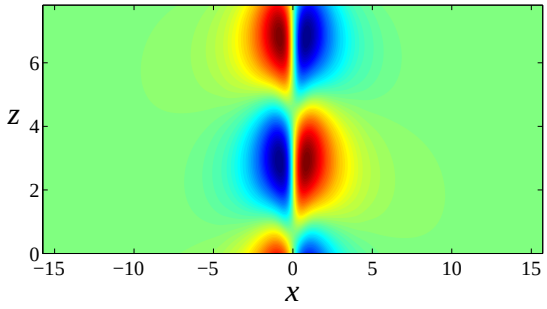

(b) $t = 7.680\, r_0/c = 0.340\, T$
$4.998 \leq P \leq 5.002$

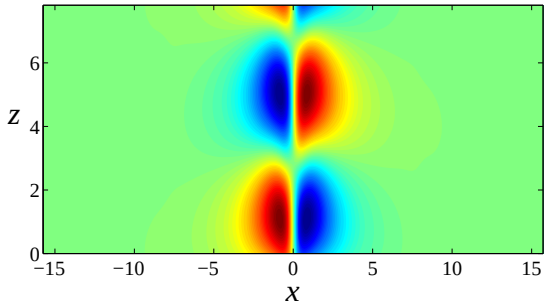

(c) $t = 13.82\, r_0/c = 0.611\, T$
$4.996 \leq P \leq 5.004$

Figure 9.5: Pressure displays for non-zero density and x-momentum viscosity
Pressure, $v_{z0}(x) = 0.7\, c\, \mathrm{sech}^2(x/r_0)$, $\eta_\rho = \eta_x = 0.00025\, r_0 c$

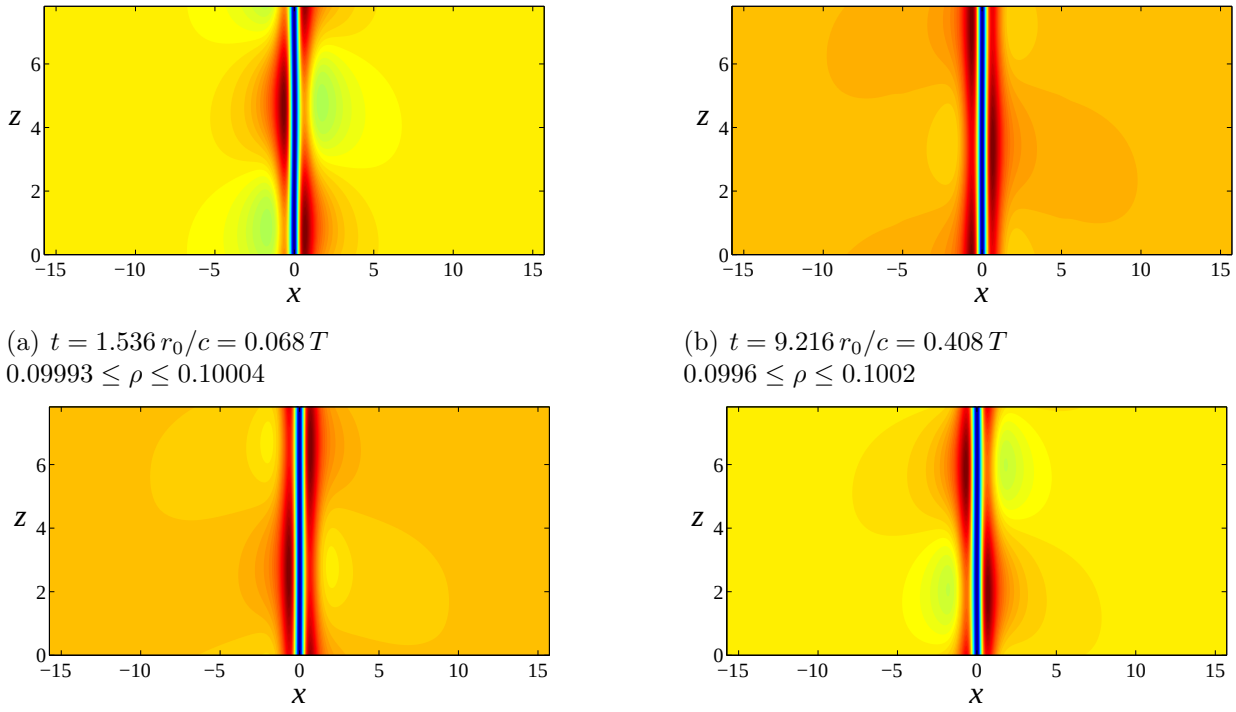

(a) $t = 1.536\, r_0/c = 0.068\, T$
$0.09993 \leq \rho \leq 0.10004$

(b) $t = 9.216\, r_0/c = 0.408\, T$
$0.0996 \leq \rho \leq 0.1002$

(c) $t = 18.432\, r_0/c = 0.815\, T$
$0.0992 \leq \rho \leq 0.1004$

(d) $t = 27.65\, r_0/c = 1.223\, T$
$0.0988 \leq \rho \leq 0.1007$

Figure 9.6: Density displays for non-zero density and x-momentum viscosity
Density, $\quad v_{z0}(x) \;=\; 0.7\, c\, \mathrm{sech}^2(x/r_0), \quad \eta_\rho \;=\; \eta_x \;=\; 0.00025\, r_0 c$

In the density displays in figures 9.6, we observe that the density viscosity has introduced a density depletion layer around the central axis, which is evidently responsible for the large linear deviation in density growth. As illustrated by the density displays below, this depletion layer persists throughout the linear regime. There is evidently a rapid initial expulsion of matter from the central axis. This has a profound effect on the density growth, but very little effect on the growth of the other quantities. Central regions of low density were also found in the MHD simulations of Frank et al. (1996) and the RMHD simulations of Mignone et al. (2009).

We now introduce momentum viscosity in the flow direction, also equal to $0.00025\, r_0 c$. As seen in the growth curves in figure 9.7, the z-momentum viscosity is responsible for

initial linear deviations in the growth of pressure and the velocity. As seen in the pressure displays in figures 9.8 and 9.9, the z-momentum diffusion creates two oppositely directed transverse plane waves that propagate from the central axis to the outer boundaries in x, at which point they are reflected back inward, and converge once again at the central axis. The propagation speed is about $0.6\,c$, which is very close to the sound speed for this case ($0.58\,c$). As the transverse waves return inward, their amplitudes decay, and the pressure returns to its background value. The generation of the transverse waves results in the initial linear deviation, and their decay results in the asymptotic approach of the growth curve to its expected linear behavior. The momentum and pressure therefore respond much more sharply to the z-momentum viscosity than to the x-momentum viscosity, which suggests strong relativistic boosting in the flow direction. As shown by the density displays in figures 9.10 and 9.11, the resulting transverse waves have a small amplitude compared to the density depletion layer.

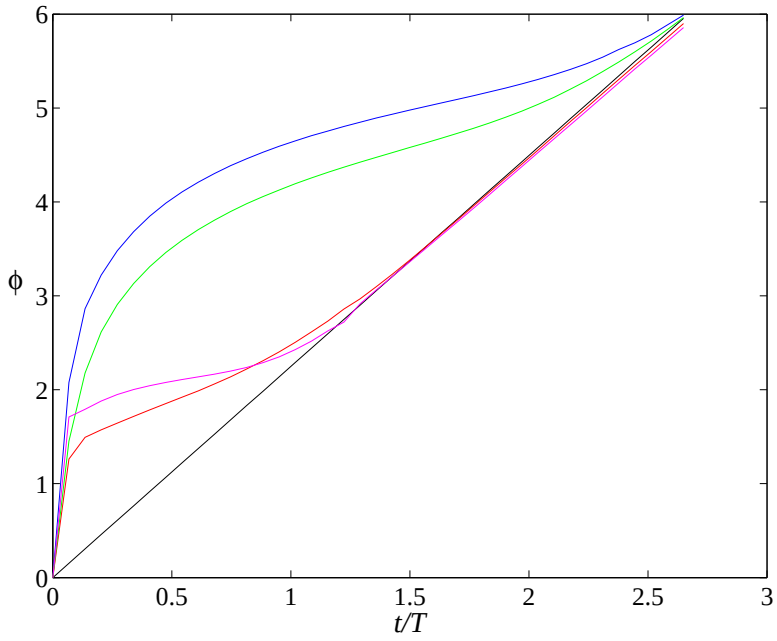

Figure 9.7: Linear growth curves for non-zero momentum and density viscosity theoretical (Black), ρ (Blue), v_x (Red), v_z (Green), P (Magenta) $v_{z0}(x) = 0.7\,c\,\mathrm{sech}^2(x/r_0)$, $\eta_\rho = \eta_x = \eta_z = 0.00025\,r_0 c$

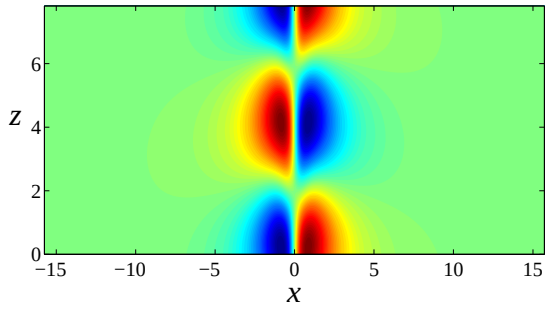

(a) $t = 0$ $\quad 4.999 \le P \le 5.001$

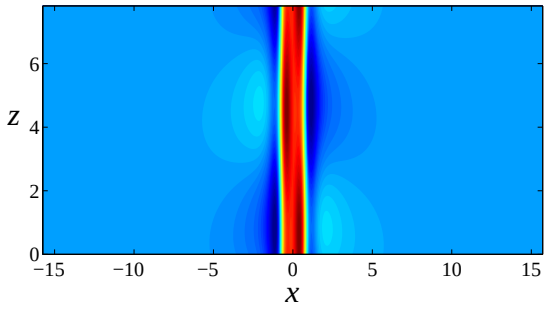

(b) $t = 1.536\,r_0/c = 0.068\,T$
$4.997 \le P \le 5.007$

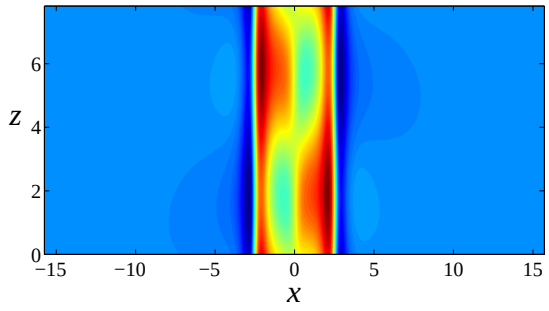

(c) $t = 4.608\,r_0/c = 0.204\,T$
$4.998 \le P \le 5.007$

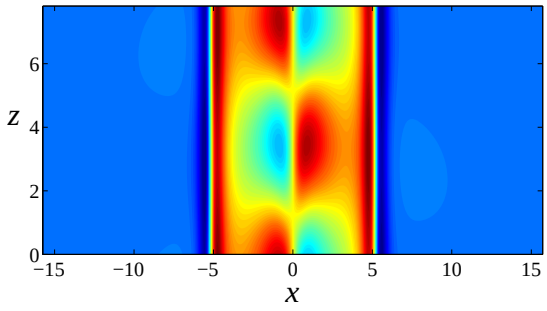

(d) $t = 9.216\,r_0/c = 0.408\,T$
$4.998 \le P \le 5.006$

Figure 9.8: Pressure displays for non-zero momentum and density viscosity Pressure, $v_{z0}(x) = 0.7\,c\,\mathrm{sech}^2(x/r_0)$, $\eta_\rho = \eta_x = \eta_z = 0.00025\,r_0 c$

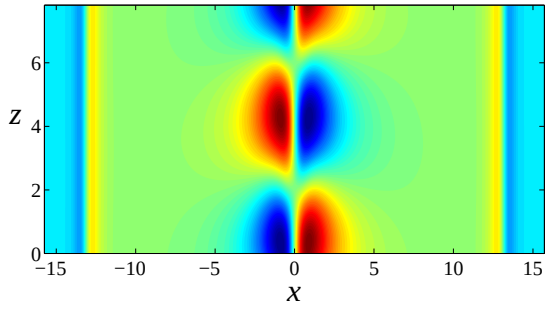

(a) $t = 23.04\, r_0/c = 1.019\, T$
$4.993 \le P \le 5.012$

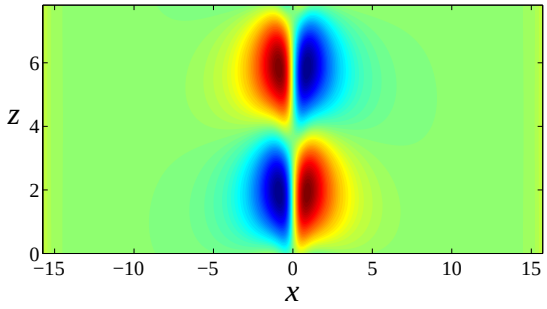

(b) $t = 27.65\, r_0/c = 1.223\, T$
$4.988 \le P \le 5.018$

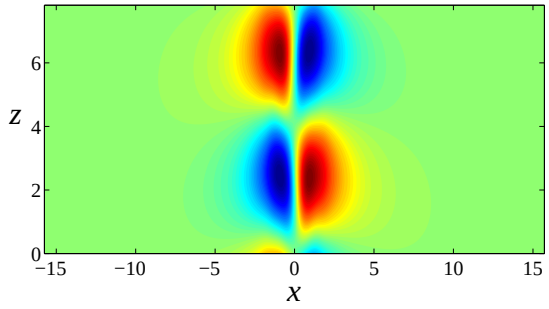

(c) $t = 52.22\, r_0/c = 2.310\, T$
$4.834 \le P \le 5.168$

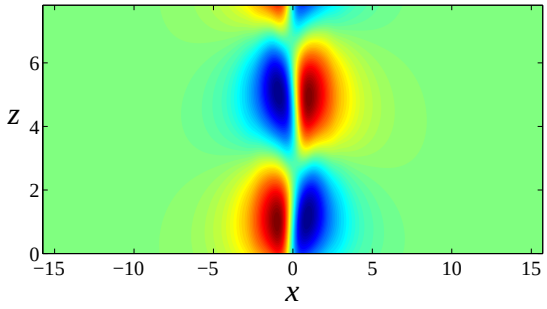

(d) $t = 59.90\, r_0/c = 2.650\, T$
$4.660 \le P \le 5.356$

Figure 9.9: Pressure displays for non-zero momentum and density viscosity
Pressure, $v_{z0}(x) = 0.7\, c\, \mathrm{sech}^2(x/r_0)$, $\eta_\rho = \eta_x = \eta_z = 0.00025\, r_0 c$

These cases correspond to a maximum background flow speed of $0.7\,c$, but when the maximum flow speed is instead $0.5\,c$, we obtain the same results as described above. At a less relativistic maximum flow speed $0.2\,c$, the effect of the density viscosity is the same, however the z-momentum viscosity no longer introduces transverse plane waves. This latter effect, therefore, is a relativistic one. In figure 9.12, only the density viscosity is non-zero, and has the same impact as concluded above. This case is much more numerically stable than the case in which both density and x-momentum viscosity are non-zero. In figure 9.13, only the z-momentum viscosity is non-zero, and its effect is the same as we saw previously. This latter case is numerically unstable, with numerical breakdown after fewer than two periods. Many of these cases are somewhat unreasonable physically, but again, our purpose is to isolate the manner in which each viscosity influences the growth. In most of the numerical simulations, we use equal non-zero x and z-momentum viscosities, assuming isotropy in the momentum, and a non-zero density viscosity in order to prevent the densities from becoming negative in the nonlinear regime. As we will see in the sections that follow, these simulations show deviations from linear agreement. We have shown the manner in which the viscosities are responsible for these deviations.

In this section, we have shown that in the linear regime of evolution, the perturbations grow at approximately the numerical growth rate of the eigenmode in which the system is launched. However, we have seen that artificial diffusion introduces evanescent modes which result in deviation from linear agreement. In particular, the density diffusion (included to prevent densities from becoming negative) introduces a narrow region of low density around the central axis, resulting in a large deviation in density growth. The diffusion in longitudinal

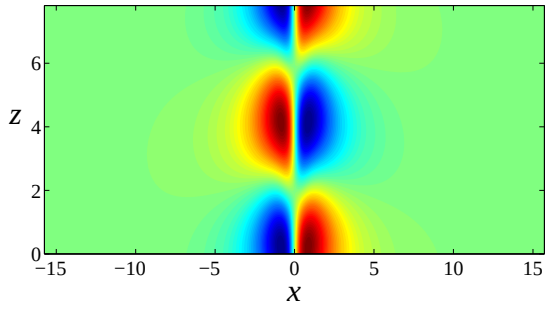

(a) $t = 0$ s $\quad 0.09999 \leq \rho \leq 0.10001$

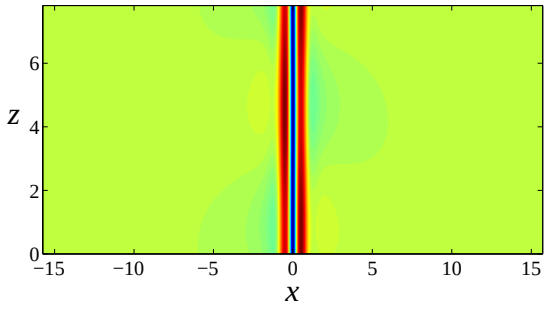

(b) $t = 1.536\, r_0/c = 0.068\, T$
$0.0998 \leq \rho \leq 0.1002$

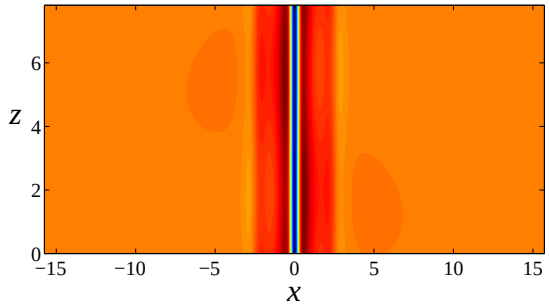

(c) $t = 4.608\, r_0/c = 0.204\, T$
$0.0992 \leq \rho \leq 0.1002$

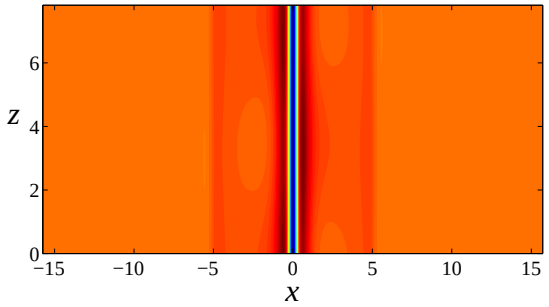

(d) $t = 9.216\, r_0/c = 0.408\, T$
$0.0986 \leq \rho \leq 0.1004$

Figure 9.10: Density displays for non-zero momentum and density viscosity
Density, $\quad v_{z0}(x) = 0.7\, c\, \mathrm{sech}^2(x/r_0), \quad \eta_\rho = \eta_x = \eta_z = 0.00025\, r_0 c$

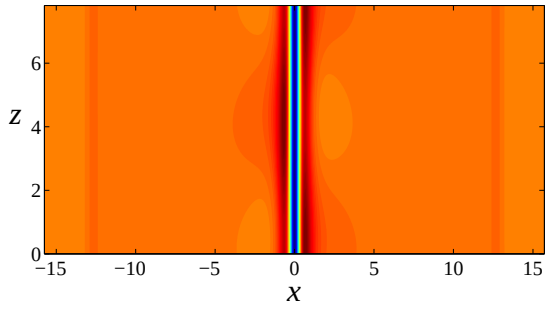

(a) $t = 23.04\, r_0/c = 1.019\, T$
$0.0970 \leq \rho \leq 0.1010$

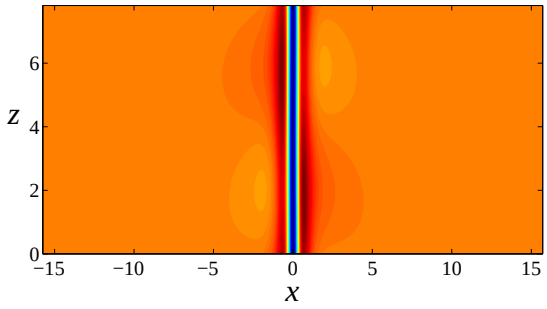

(b) $t = 27.65\, r_0/c = 1.223\, T$
$0.0966 \leq \rho \leq 0.1012$

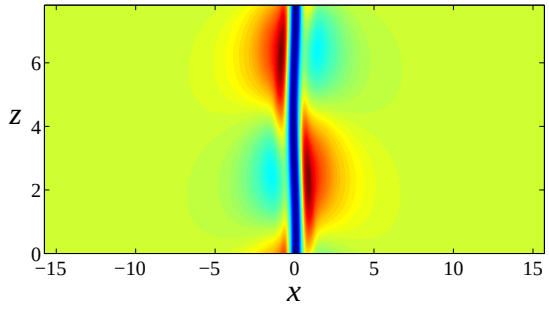

(c) $t = 52.22\, r_0/c = 2.310\, T$
$0.0947 \leq \rho \leq 0.1041$

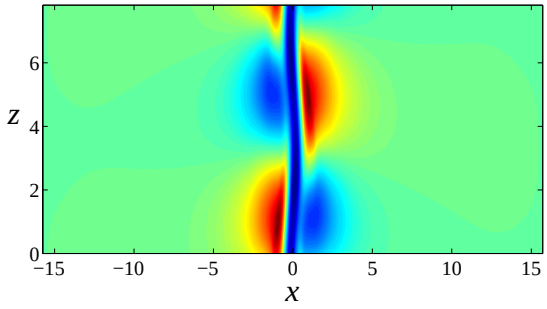

(d) $t = 59.90\, r_0/c = 2.650\, T$
$0.0938 \leq \rho \leq 0.1071$

Figure 9.11: Density displays for non-zero momentum and density viscosity
Density, $v_{z0}(x) = 0.7\, c\, \mathrm{sech}^2(x/r_0)$, $\eta_\rho = \eta_x = \eta_z = 0.00025\, r_0 c$

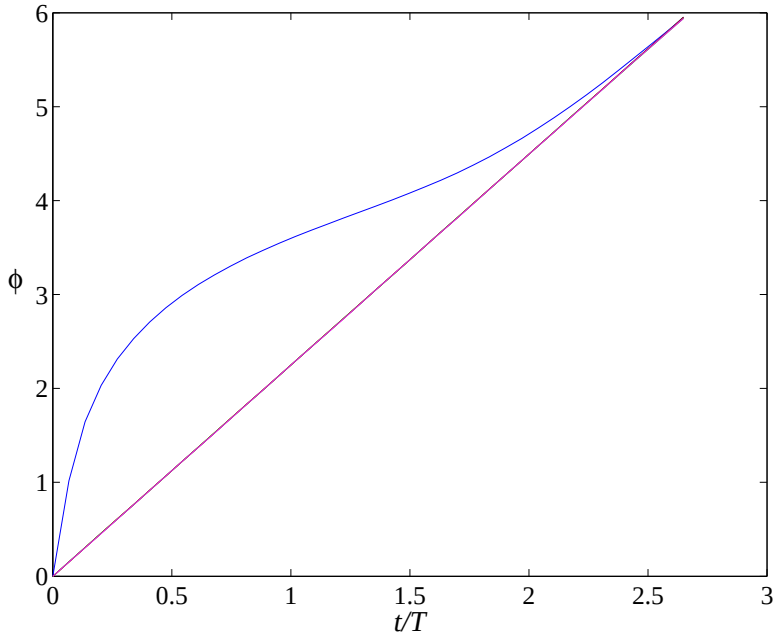

Figure 9.12: Linear growth curves for non-zero density viscosity
theoretical (Black), ρ (Blue), v_x (Red), v_z (Green), P (Magenta)
$v_{z0}(x) = 0.7\, c\, \mathrm{sech}^2(x/r_0)$, $\eta_\rho = 0.00025\, r_0 c$

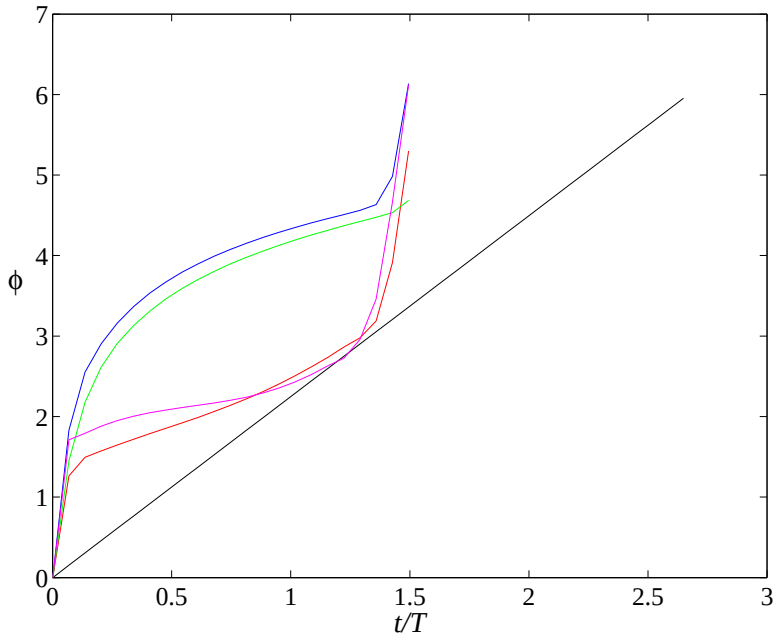

Figure 9.13: Linear growth curves for non-zero z-momentum viscosity theoretical (Black), ρ (Blue), v_x (Red), v_z (Green), P (Magenta)
$v_{z0}(x) \;=\; 0.7\,c\,\mathrm{sech}^2(x/r_0), \qquad \eta_z \;=\; 0.00025\,r_0 c$

momentum introduces a pair of transverse acoustic waves which propagate between the jet axis and transverse boundaries, resulting in deviations in the growth of density, pressure, and both velocity components. The transverse momentum viscosity, on the other hand, does not introduce noticeable waves of any sort, and has much less of an impact on the system than the longitudinal momentum viscosity. Having examined the influence of diffusion on the linear behavior of the perturbations, we can now turn our attention to the nonlinear behavior.

The perturbations eventually grow to a point where their amplitudes are no longer negligible compared to the values of the background quantities, and we can no longer neglect terms which are higher than first-order. This marks the transition from the linear to the nonlinear regime. The early stages of nonlinear evolution involve saturation of each of the

perturbed quantities. In the sections that follow, we incorporate magnetic fields, and consider the temporal behavior, associated with nonlinear evolution, of not only perturbations but also average (or RMS) values. Before we do this, we examine analytically the reasons for near-perfect linear agreement in the absence of diffusion.

9.2 Near-perfect Agreement in the Absence of Diffusion

We have seen that in the absence of diffusion, there is near-perfect agreement with linear growth, and therefore that deviations from linear behavior are due to evanescent modes introduced by diffusion. We seek to explain this near-perfect agreement by analytically examining the properties of the numerical modes resulting from the linearization described in chapter 5. Our analysis will show that our real-valued initial perturbation distribution does not consist of modes with multiple positive growth rates.

We seek to show analytically that when the system is linearized in the absence of diffusion, the initial distributions are a superposition of modes that contain only one growth rate. In the absence of diffusion, the linearization (see chapter 5) yields a second-order ODE in the perturbation to total pressure (taking $k_y = 0$ so that the perturbation is aligned with the flow, as in the simulations):

$$\Omega^2(x,\omega)\frac{d}{dx}\left[\frac{1}{\Omega^2(x,\omega)}\frac{d\delta P_b}{dx}\right] + k_x^2(x,\omega)\delta P_b(x) \;=\; 0, \tag{9.1}$$

where

$$
\begin{aligned}
\delta P_b(x) &= \delta P(x) + \tilde{\mathbf{B}} \cdot \delta \mathbf{B}, \qquad \text{thermal and magnetic pressure} \\
\Omega^2(x,\omega) &= \gamma(x)^2(\omega - k_z \tilde{v}_z(x))^2 - v_{Az}^2 \left(k_z^2 - \frac{\omega^2}{c^2} \right), \\
k_x^2(x,\omega) &= \frac{k_d(x,\omega)^2 \Omega^2(x,\omega)}{\gamma(x)^2(\omega - k_z \tilde{v}_z(x))^2 + k_d^2(x,\omega) v_{Az}^2},
\end{aligned} \tag{9.2}
$$

and

$$
\begin{aligned}
k_d^2(x,\omega) &= \gamma(x)^2 \left[\frac{(\omega - k_z \tilde{v}_z(x))^2}{c_s^2} - \left(k_z - \frac{\omega \tilde{v}_z(x)}{c^2} \right)^2 \right], \\
v_{Az} &= \frac{\tilde{B}_z}{\sqrt{4\pi \tilde{w}}}, \\
\gamma(x) &= \frac{1}{\sqrt{1 - \tilde{v}_z(x)/c^2}}, \qquad c_s^2 = c^2 \frac{\Gamma \tilde{P}}{\tilde{w}}.
\end{aligned} \tag{9.3}
$$

where $\delta P_b(x)$ is the complex shear profile of the total pressure. The corresponding perturbation to the initial distribution is

$$
\begin{aligned}
\delta P_b(x,z) &= \mathrm{Re}[\delta P_b(x) \exp(i k_z z)] \\
&= \frac{1}{2} \left[\delta P_b(x) \exp(i k_z z) + \delta P_b^*(x) \exp(-i k_z z) \right],
\end{aligned} \tag{9.4}
$$

where $\delta P_b(x)$ is a solution to equation (9.1) corresponding to eigenfrequency ω, and $\delta P_b^*(x)$ is a solution to equation (9.1) corresponding to some eigenfrequency ω'. That is, for some ω', we have

$$
\Omega^2(x,\omega') \frac{d}{dx} \left[\frac{1}{\Omega^2(x,\omega')} \frac{d \delta P_b^*}{dx} \right] + k_x^2(x,\omega') \delta P_b^*(x) = 0. \tag{9.5}
$$

In order for $\delta P_b^*(x)$ to satisfy (9.1), we must have

$$[\Omega^2(x,\omega)]^* \frac{d}{dx}\left[\frac{1}{[\Omega^2(x,\omega)]^*}\frac{d\delta P_b^*}{dx}\right] + [k_x^2(x,\omega)]^*\delta P_b^*(x) \;=\; 0. \tag{9.6}$$

Combining (9.5) and (9.6), we must satisfy the conditions

$$\begin{aligned} \Omega^2(x,\omega') &= [\Omega^2(x,\omega)]^*, \\ k_x^2(x,\omega') &= [k_x^2(x,\omega)]^*. \end{aligned} \tag{9.7}$$

We first explicitly evaluate the right-hand sides of conditions (9.7). We have

$$\begin{aligned} \Omega^2(x,\omega) &= \gamma^2(\omega - k_z v_{z0})^2 - v_{Az}^2\left(k_z^2 - \frac{\omega^2}{c^2}\right) \\ &= \gamma^2\left[(\omega_r - k_z v_{z0})^2 - \omega_i^2 + 2i\omega_i(\omega_r - k_z v_{z0})\right] - v_{Az}^2\left[k_z^2 - \frac{\omega_r^2 - \omega_i^2 + 2i\omega_r\omega_i}{c^2}\right], \end{aligned} \tag{9.8}$$

so that

$$\begin{aligned} [\Omega^2(x,\omega)]^* &= \gamma^2[(\omega - k_z v_{z0})^2]^* - v_{Az}^2\left[\left(k_z^2 - \frac{\omega^2}{c^2}\right)\right]^* \\ &= \gamma^2\left[(\omega_r - k_z\tilde{v}_z(x))^2 - \omega_i^2 - 2i\omega_i(\omega_r - k_z\tilde{v}_z(x))\right] - v_{Az}^2\left[k_z^2 - \frac{\omega_r^2 - \omega_i^2 - 2i\omega_r\omega_i}{c^2}\right]. \end{aligned} \tag{9.9}$$

For $[k_x^2(x,\omega)]^*$, we have

$$[k_x^2(x,\omega)]^* \;=\; \frac{[k_d^2(x,\omega)]^*[\Omega^2(x,\omega)]^*}{\gamma(x)^2(\omega^* - k_z\tilde{v}_z(x))^2 + [k_d^2(x,\omega)]^* v_{Az}^2}, \tag{9.10}$$

where

$$[k_d^2(x,\omega)]^* = \gamma(x)^2\left[\frac{(\omega^* - k_z\tilde{v}_z(x))^2}{c_s^2} - \left(k_z - \frac{\omega^*\tilde{v}_z(x)}{c^2}\right)^2\right], \qquad \text{where} \tag{9.11}$$

$$(\omega^* - k_z\tilde{v}_z(x))^2 = (\omega_r - k_z\tilde{v}_z(x))^2 - \omega_i^2 - 2i\omega_i(\omega_r - k_z\tilde{v}_z(x)), \qquad \text{and} \tag{9.12}$$

$$\left(k_z - \frac{\omega^*\tilde{v}_z(x)}{c^2}\right)^2 = \left(k_z - \frac{\omega_r\tilde{v}_z(x)}{c^2}\right)^2 - \frac{\omega_i^2\tilde{v}_z(x)^2}{c^4} + (2i)\frac{\omega_i\tilde{v}_z(x)}{c^2}\left(k_z - \frac{\omega_r\tilde{v}_z(x)}{c^2}\right). \tag{9.13}$$

We first consider $\omega' = \omega^*$. We have

$$\begin{aligned}
\Omega^2(x,\omega^*) &= \gamma^2(\omega^* - k_z v_{z0})^2 - v_{Az}^2\left(k_z^2 - \frac{(\omega^*)^2}{c^2}\right) \\
&= \gamma^2[(\omega - k_z v_{z0})^2]^* - v_{Az}^2\left[\left(k_z^2 - \frac{\omega^2}{c^2}\right)\right]^* = [\Omega^2(x,\omega)]^*, \\
k_d^2(x,\omega^*) &= \gamma(x)^2\left[\frac{(\omega^* - k_z\tilde{v}_z(x))^2}{c_s^2} - \left(k_z - \frac{\omega^*\tilde{v}_z(x)}{c^2}\right)^2\right] = [k_d^2(x,\omega)]^*.
\end{aligned} \tag{9.14}$$

Inserting these results into expression (9.10) for $[k_x^2(x,\omega)]^*$, we obtain

$$k_x^2(x,\omega^*) = [k_x^2(x,\omega)]^*. \tag{9.15}$$

We combine this result with the result from (9.14), namely,

$$\Omega^2(x,\omega^*) = [\Omega^2(x,\omega)]^*. \tag{9.16}$$

Conditions (9.7) are therefore satisfied, which shows that $\delta P_b^*(x)$ is a solution of (9.1) corresponding to $\omega' = \omega^*$.

Conditions (9.7) are also satisfied if we choose $\omega' = -\omega^*$, provided we replace k_z with $-k_z$. $-\omega^*$ differs from ω in the sign of the real part. Therefore, in order to maintain the direction of the longitudinal phase velocity ω_r/k_z, we must also flip the sign of k_z. This amounts to an exchange of the coefficients $\exp(ik_z z)$ and $\exp(-ik_z z)$ in expression (9.4) for $\delta P_b(x,z)$. For $\omega' = -\omega^*$ and k_z replaced with $-k_z$, we have

$$(\omega' + k_z\tilde{v}_z(x))^2 \;=\; (-\omega^* + k_z\tilde{v}_z(x))^2 \;=\; (\omega^* - k_z\tilde{v}_z(x))^2 \tag{9.17}$$

$$\left(-k_z - \frac{\omega'\tilde{v}_z(x)}{c^2}\right)^2 \;=\; \left(-k_z + \frac{\omega^*\tilde{v}_z(x)}{c^2}\right)^2 \;=\; \left(k_z - \frac{\omega^*\tilde{v}_z(x)}{c^2}\right)^2 \tag{9.18}$$

$$(-k_z)^2 - \frac{(\omega')^2}{c^2} \;=\; (-k_z)^2 - \frac{(-\omega^*)^2}{c^2} \;=\; k_z^2 - \frac{(\omega^*)^2}{c^2}. \tag{9.19}$$

Combining (9.17) and (9.19), we have satisfied

$$\Omega^2(x, -\omega^*, -k_z) \;=\; [\Omega^2(x, \omega, k_z)]^*. \tag{9.20}$$

Combining (9.17) and (9.18), we have satisfied

$$k_d^2(x, -\omega^*, -k_z) \;=\; [k_d^2(x, \omega, k_z)]^*. \tag{9.21}$$

Combining (9.17), (9.20), and (9.21), we have satisfied

$$k_x^2(x, -\omega^*, -k_z) \;=\; [k_x^2(x, \omega, k_z)]^*. \tag{9.22}$$

From (9.20) and (9.22), we have satisfied conditions (9.7). In summary, if $\delta P_b(x)$ is a solution of (9.1) with eigenfrequency ω, then $\delta P_b^*(x)$ is a solution of (9.1) with eigenfrequency ω^*, or

with eigenfrequency $-\omega^*$ and k_z replaced by $-k_z$ in order to maintain the direction of the longitudinal phase velocity. Either way, we see that the superposition of $\delta P_b(x)$ and $\delta P_b^*(x)$, in order to construct the real-valued initial perturbation distribution $\delta P_b(x,z)$ via equation (9.4), only involves a single positive growth rate, which explains the close agreement with linear theory in the absence of diffusion.

Having examined the linear regime, we now proceed to discuss temporal behavior in the nonlinear regime of evolution.

9.3 Time-Dependence in the Nonlinear Regime

We now turn our attention to the temporal behavior of various quantities in the nonlinear regime. We first plot the nonlinear evolution of the fluctuations of the primitive variables (density, velocity, pressure, and magnetic field), in section 9.4. We notice oscillations in the growth curves. These correspond to a series of nonlinear transverse acoustic waves, which propagate back and forth between the jet axis and transverse boundaries. We also plot the time-dependence of certain spatially-averaged quantities, including the aforementioned primitive variables, in section 9.5. Many of these plots show the same nonlinear oscillations. These oscillations are dependent on the location of the transverse boundaries. However, as we will show in sections 11.3 through 11.5, they do not significantly influence the evolution of the flow. The average density and pressure both tend to increase over time, with the fastest increase occurring shortly after saturation. The average flow speed and Lorentz factor tend to decrease over time. Each of these quantities approach an asymptotic value as the system tends toward equilibrium, where the asymptote depends on the magnetic field strength, and to a lesser extent, on the viscosity.

In the plots in section 9.6, we will notice a peak in the given quantity, occurring shortly after the saturation stage, typically followed by quasi-exponential decay. This occurs in the plots of vorticity, RMS current density, RMS electromagnetic energy density, among other quantities. The peaks generally correspond to amplification of field-related quantities as the field lines and plasma are expelled by vortices during their formation, resulting in concentration of field lines at the vortex extremities (we will see displays of this in chapter 10). The vortices extract mechanical energy from the bulk flow, resulting in abrupt deceleration of the flow (seen in the above plots of flow speed and Lorentz factor), and use energy this to perform work against the magnetic field lines, thereby converting this energy into electromagnetic form. This electromagnetic energy then undergoes gradual viscous dissipation into thermal energy as the system relaxes to an equilibrium state consisting of flow-aligned filaments. These stages of evolution are also described in the MHD results of Frank et al. (1996), Malagoli et al. (1996), and Baty et al. (2003).

Collectively, these plots illustrate how the magnetic field modulates the transfer of momentum and energy between the bulk flow and the field, along with viscous dissipation into thermal energy. The plots shed light on many complex mechanisms, as seen, for example, in the bifurcations in the dependence on field strength. That is, maximum field amplification, flow deceleration, and viscous dissipation all occur for intermediate vortex-disruptive fields, not for the strongest or weakest fields. This means that these processes are modulated not only by the extent of vortex formation, but also by the rapidness and complexity of vortex disruption. Most plots simultaneously display curves for multiple values of the relativistic Alfvenic Mach number, given by

$$M_A \;=\; \frac{v_{z0}\gamma}{v_A\gamma_A} \;=\; \frac{v_{z0}}{v_A}\sqrt{\frac{1-v_A^2/c^2}{1-v_{z0}^2/c^2}}, \tag{9.23}$$

where v_{z0} is the amplitude of the background flow speed, v_A is the background relativistic Alfven speed, and γ and γ_A are the respective Lorentz factors. The Alfven speed is given by

$$v_A \;=\; \frac{B_{z0}}{\sqrt{\rho_0 + (P_0/c^2)\Gamma/(\Gamma-1)}}, \tag{9.24}$$

where Γ is the adiabatic index, here assumed to be 4/3, owing to the sound speed being approximately at its relativistic maximum value of $c/\sqrt{3}$. For each Alfvenic Mach number, we display plots at two different maximum background flow speeds, $v_{z0} = 0.7\,c$ and $v_{z0} = 0.5\,c$, and find striking similarity between the plots at the two flow speeds. This demonstrates that within a range of moderately relativistic flow speeds, the relativistic Alfvenic Mach number is closely correlated with the influence of the magnetic field on the evolution of the system. The above Alfvenic Mach number is a relativistic extension of the non-relativistic version (v_{z0}/v_A) used by Baty et al. (2003) in their MHD study, in 2D slab geometry, of the nonlinear KH instability.

In the sections that follow, we plot the time-dependence of quantities of physical interest, where each quantity corresponds to a given pair of plots, with $v_{z0} = 0.7\,c$ the left graph and $v_{z0} = 0.5\,c$ the right graph. Each graph contains multiple curves, each curve corresponding to a specific value of the Alfvenic Mach number M_A. The same values of M_A are studied at both flow speeds (i.e., in all plots). The independent variable in all plots is the time in units of the linear growth time. We first consider the time-dependence in the growth of

fluctuations in the primitive variables (density, velocity, pressure, and magnetic field). We will see that these quantities first pass through a linear regime in which the perturbations grow at a certain expected linear growth rate. There is then a transition to a nonlinear regime, followed shortly by saturation of each of the perturbation amplitudes. We then consider the time-dependence of quantities which are spatially averaged or maximized over the numerical grid. In both the fluctuations and average values of the velocity components, density, and pressure, we will notice oscillations in the nonlinear regime. We will see that these correspond to nonlinear transverse sound waves which, for weak fields, move back and forth between the jet axis and transverse boundaries. The period of oscillation is the sound transit time. We finally consider the time-dependence of certain quantities which reach a maximum value at or shortly after saturation, and then undergo a quasi-exponential decay toward an equilibrium state. These include the RMS vorticity, RMS current density, electromagnetic to thermal pressure (i.e., inverse plasma β), electromagnetic energy, and electromagnetic longitudinal momentum.

We list below the parameters for the cases to be considered in the sections that follow, where ϵ has units of energy density. The primitive variables, sound speed, Mach number, and plasma β are background values that characterize the equilibrium at the start of the simulation. At a given time in the simulation, the minimum plasma β is often several orders of magnitude less than the background β.

The parameters specific to all cases are as follows:

$$
\begin{aligned}
\rho_0 c^2 &= 0.1\,\epsilon, \qquad P_0 = 5\,\epsilon, \\
c_s &= 0.576\,c, \\
k_z &= 0.8\,r_0^{-1}, \\
L_x/c_s &= 31.5\,r_0/(0.576\,c) = 54.70\,r_0/c \qquad \text{(sound transit time)}, \\
-15.75\,r_0 \le x \le 15.75\,r_0, &\qquad 0 \le z \le \frac{2\pi}{k_z}, \\
N_x &= 1001, \qquad N_z = 201, \\
\Delta t &= 0.032\,r_0/c, \qquad \Delta x = 0.0315\,r_0, \qquad \Delta z = 0.0393\,r_0. \qquad (9.25)
\end{aligned}
$$

The parameters specific to simulations performed with $v_{z0}(x) = 0.7\,c\,\mathrm{sech}^2(x/r_0)$ are as

follows:

$$
\begin{aligned}
M_A \;=\; \infty, \qquad \beta \;=\; \infty: \qquad \omega_{i0} \;&=\; 0.0994\, c/r_0, \quad T_i \;=\; 10.06\, r_0/c, \\
T_i \;=\; \frac{1}{\omega_i} \;&=\; 10.06\, r_0/c, \qquad T \;=\; \frac{2\pi}{\omega_r} \;=\; 22.61\, r_0/c,
\end{aligned}
$$

$$
\begin{aligned}
(M_A, \beta, v_A/c) \;&=\; (82.83,\ 3553,\ 0.0118): \quad \omega_i \;=\; 0.0993\, c/r_0 \;=\; 0.9991\, \omega_{i0}, \\
T_i \;=\; \frac{1}{\omega_i} \;&=\; 10.07\, r_0/c, \qquad T \;=\; \frac{2\pi}{\omega_r} \;=\; 22.61\, r_0/c,
\end{aligned}
$$

$$
\begin{aligned}
(M_A, \beta, v_A/c) \;&=\; (41.41,\ 888.3,\ 0.0237): \quad \omega_i \;=\; 0.0990\, c/r_0 \;=\; 0.9965\, \omega_{i0}, \\
T_i \;=\; \frac{1}{\omega_i} \;&=\; 10.10\, r_0/c, \qquad T \;=\; \frac{2\pi}{\omega_r} \;=\; 22.63\, r_0/c,
\end{aligned}
$$

$$
\begin{aligned}
(M_A, \beta, v_A/c) \;&=\; (20.70,\ 222.1,\ 0.0473): \quad \omega_i \;=\; 0.0980\, c/r_0 \;=\; 0.986\, \omega_{i0}, \\
T_i \;=\; \frac{1}{\omega_i} \;&=\; 10.20\, r_0/c, \qquad T \;=\; \frac{2\pi}{\omega_r} \;=\; 22.68\, r_0/c,
\end{aligned}
$$

$$
\begin{aligned}
(M_A, \beta, v_A/c) \;&=\; (10.34,\ 55.52,\ 0.0947): \quad \omega_i \;=\; 0.0937\, c/r_0 \;=\; 0.943\, \omega_{i0}, \\
T_i \;=\; \frac{1}{\omega_i} \;&=\; 10.67\, r_0/c, \qquad T \;=\; \frac{2\pi}{\omega_r} \;=\; 22.89\, r_0/c,
\end{aligned}
$$

$$
\begin{aligned}
(M_A, \beta, v_A/c) \;&=\; (5.145,\ 13.88,\ 0.1893): \quad \omega_i \;=\; 0.0738\, c/r_0 \;=\; 0.743\, \omega_{i0}, \\
T_i \;=\; \frac{1}{\omega_i} \;&=\; 13.55\, r_0/c, \qquad T \;=\; \frac{2\pi}{\omega_r} \;=\; 23.70\, r_0/c,
\end{aligned}
$$

$$
\begin{aligned}
10^4(\eta_\rho, \eta_x, \eta_z, \eta_{Bx}, \eta_{Bz}) \;&=\; (0.25, 0.25, 0.25, 1.2, 1.2)\, r_0 c, \qquad \text{magnetized}, \\
\eta_\rho \;=\; \eta_x \;=\; \eta_z \;&=\; 0.00025\, r_0 c, \qquad \text{unmagnetized}.
\end{aligned} \tag{9.26}
$$

The parameters specific to simulations performed with $v_{z0}(x) \;=\; 0.5\, c\, \mathrm{sech}^2(x/r_0)$ are as

follows:

$$
\begin{aligned}
M_A \;&=\; \infty, \qquad \beta \;=\; \infty : \qquad \omega_{i0} \;=\; 0.0760\, c/r_0, \quad T_i \;=\; 13.16\, r_0/c, \\
T_i \;&=\; \frac{1}{\omega_i} \;=\; 13.16\, r_0/c, \qquad T \;=\; \frac{2\pi}{\omega_r} \;=\; 34.51\, r_0/c,
\end{aligned}
$$

$$
\begin{aligned}
(M_A, \beta, v_A/c) \;&=\; (82.83,\ 10240,\ 0.0070) : \quad \omega_i \;=\; 0.0759\, c/r_0 \;=\; 0.9991\, \omega_{i0}, \\
T_i \;&=\; \frac{1}{\omega_i} \;=\; 13.17\, r_0/c, \qquad T \;=\; \frac{2\pi}{\omega_r} \;=\; 34.52\, r_0/c,
\end{aligned}
$$

$$
\begin{aligned}
(M_A, \beta, v_A/c) \;&=\; (41.41,\ 2560,\ 0.0139) : \quad \omega_i \;=\; 0.0757\, c/r_0 \;=\; 0.9963\, \omega_{i0}, \\
T_i \;&=\; \frac{1}{\omega_i} \;=\; 13.21\, r_0/c, \qquad T \;=\; \frac{2\pi}{\omega_r} \;=\; 34.53\, r_0/c,
\end{aligned}
$$

$$
\begin{aligned}
(M_A, \beta, v_A/c) \;&=\; (20.70,\ 640,\ 0.0279) : \quad \omega_i \;=\; 0.0749\, c/r_0 \;=\; 0.985\, \omega_{i0}, \\
T_i \;&=\; \frac{1}{\omega_i} \;=\; 13.36\, r_0/c, \qquad T \;=\; \frac{2\pi}{\omega_r} \;=\; 34.57\, r_0/c,
\end{aligned}
$$

$$
\begin{aligned}
(M_A, \beta, v_A/c) \;&=\; (10.34,\ 160,\ 0.0558) : \quad \omega_i \;=\; 0.0715\, c/r_0 \;=\; 0.940\, \omega_{i0}, \\
T_i \;&=\; \frac{1}{\omega_i} \;=\; 14.00\, r_0/c, \qquad T \;=\; \frac{2\pi}{\omega_r} \;=\; 34.73\, r_0/c,
\end{aligned}
$$

$$
\begin{aligned}
(M_A, \beta, v_A/c) \;&=\; (5.145,\ 40,\ 0.1115) : \quad \omega_i \;=\; 0.0565\, c/r_0 \;=\; 0.744\, \omega_{i0}, \\
T_i \;&=\; \frac{1}{\omega_i} \;=\; 17.69\, r_0/c, \qquad T \;=\; \frac{2\pi}{\omega_r} \;=\; 35.34\, r_0/c,
\end{aligned}
$$

$$
\begin{aligned}
\eta_\rho \;&=\; \eta_x \;=\; \eta_z \;=\; 0.00025\, r_0 c, \\
\eta_{Bx} \;&=\; \eta_{Bz} \;=\; 0.0006\, r_0 c.
\end{aligned}
\tag{9.27}
$$

9.4 Nonlinear Growth in Fluctuations of the Primitive Variables

We begin by plotting the growth in fluctuations of the primitive variables (density, pressure, velocity, and magnetic field). At a given time t, the growth in fluctuations of a quantity $Q(x, z, t)$, which has a background distribution $Q_0(x, z)$, is given by

$$\phi_Q \;=\; \ln\left(\frac{\mathrm{RMS}|Q(x,z,t) - Q_0(x,z)|}{\mathrm{RMS}|Q(x,z,0) - Q_0(x,z)|}\right). \tag{9.28}$$

The growth of a given quantity describes the magnitude of its fluctuations from a mean value, and does not contain information about the time-dependence of the mean value of that quantity. This is a separate issue which will be addressed in the next section. Each of figures 9.14 through 9.19 displays the time-dependence of the growth of a given primitive variable. Each graph contains multiple curves, each curve corresponding to a specific value of the Alfvenic Mach number M_A. The same values of M_A are studied at two maximum background flow speeds, with $v_{z0} = 0.7\,c$ the left graph and $v_{z0} = 0.5\,c$ the right graph. In the linear regime, each growth curve grows at the linear growth rate of the numerically computed eigenmode in which the system is launched. The linear deviations are due to transient modes introduced by the artificial viscosity, which is included for numerical stability. However, the density and momentum viscosity also model viscous exchanges between small eddies (Tennekes and Lumley 1973), and the magnetic viscosity models a resistivity associated with gyrations of electrons and protons about the magnetic field lines (see the last section of chapter 8).

Saturation of density, pressure, and transverse velocity perturbations occur after about

7 growth times for the strong-field ($M_A = 5.145$) case, and occurs later for the cases with weaker fields, requiring about 10 growth times for the unmagnetized case. In each case, the field components are the last of the perturbations to saturate. This is true at both flow speeds, $0.5\,c$ and $0.7\,c$. The density, pressure, and velocity component perturbations saturate at between 7 and 8 powers of e in the case with $v_{z0} = 0.7\,c$, and at between 6 and 7 powers of e in the case with $v_{z0} = 0.5\,c$. This can be explained in terms of the higher flow speed having the higher growth rate, and in terms of the mechanism of saturation. In the linear regime, a single linear mode is present. As the perturbations become sufficiently large, relative to the background values, additional, nonlinear modes begin to influence the evolution of the system, so that energy is extracted from the linear mode and deposited into these additional modes, until the linear mode and emergent modes have comparable energy. The linear mode no longer dominates the evolution of the system, resulting in saturation. A linear mode with a higher growth rate has more energy, and therefore allows more growth to take place before this energy is deposited into nonlinear modes.

As seen in figures 9.18 and 9.19, for both flow speeds, the magnetic field perturbations saturate at about 8 to 9 powers of e, with the transverse field component reaching a slightly higher level than the longitudinal component, and the saturation levels decreasing with increasing field (decreasing M_A). At both flow speeds, the longitudinal velocity and magnetic field components do not exhibit oscillations in the linear regime. The field components each exhibit a slow nonlinear decrease corresponding to gradual decay of field perturbations, while the longitudinal velocity remains at the level at which it saturates. The magnetic field components saturate at a higher level, and are generally the last to saturate. This is due

largely to centrifugal expulsion of the field lines to vortex extremities, resulting in further amplification of the field and field perturbations as electromagnetic energy is extracted from the mechanical energy of the bulk flow. Weaker fields are amplified by a larger fraction of their background field strength, which is why they saturate at higher levels. The subsequent decay of field perturbations corresponds to the viscous dissipation of electromagnetic energy into thermal form. This behavior is characteristic of vortex-disruptive fields, but not fields which completely suppress vortex formation.

However, the results are somewhat different for the strongest, vortex-suppressing, field, corresponding to $M_A = 5.145$. In this case, the saturation levels of all perturbations are nearly the same, and occur after nearly the same number of growth times (about 8.2 growth times for $v_{z0} = 0.7\,c$, and 7.8 growth times for $v_{z0} = 0.5\,c$). We notice from figures 9.18 and 9.19 that in the vortex-suppressing case (the cyan-colored curves), the field component perturbations have both leveled off after about 40 growth times. This corresponds to alignment of the field lines with the flow direction, after the system has reached an equilibrium state consisting of flow-aligned vortex and current filaments. For the weaker fields, the simulations were not propagated to the point where this level of field alignment was achieved, which is why the growth curves continue to decrease.

The density, pressure, and transverse velocity perturbations undergo nonlinear oscillations which correspond to nonlinear transverse sound waves. For weak fields, these waves travel back and forth between the jet axis and transverse boundaries. At a given maximum of pressure growth, the pressure is maximized along the jet axis. At the next minimum, the pressure is more evenly distributed. At the next maximum, the pressure is maximized at

the transverse boundaries. At the next minimum, the pressure is once again more evenly distributed, and so on. The oscillation period is approximately equal to the sound transit time (about 5.4 growth times for $v_{z0} = 0.7\,c$ and about 4.2 growth times for $v_{z0} = 0.5\,c$). The oscillations have somewhat larger amplitude for $v_{z0} = 0.7\,c$ than for $v_{z0} = 0.5\,c$, and are suppressed for stronger fields ($M_A = 10.34$ or 5.145), indicating that these nonlinear acoustic waves are enhanced by relativity. These waves take the form of pressure and density waves, and are most apparent for weaker fields, and higher (more relativistic) background flow speeds.

It should be noted that the period of these oscillations is equal to the sound transit time across the transverse width of the system, and is therefore dependent on the location of the transverse boundaries, i.e., a numerical constraint. However, as we will show in sections 11.3 through 11.5 of chapter 11, these acoustic oscillations do not significantly influence the evolution of the flow.

An important observation is that at a given relativistic Alfvenic Mach number M_A, corresponding growth curves are very similar at $0.7\,c$ and $0.5\,c$. This indicates that within a regime of moderately relativistic flow speeds, this Alfvenic Mach number is closely correlated with the influence of a magnetic field on linear and nonlinear fluctuations. Frank et al. (1996) and Baty et al. (2003) described field strength in terms of the non-relativistic Alfvenic Mach number.

Each of figures 9.20 through 9.25 corresponds to a given value of the magnetic field, and simultaneously displays the growth curves for the density (black), transverse velocity (blue), longitudinal velocity (red), pressure (green), transverse magnetic field (magenta), and

longitudinal magnetic field (cyan). In the unmagnetized case, the density and pressure curves are practically indistinguishable in the nonlinear regime. As the field strength increases, there is an increase in the disparity between the nonlinear behavior of the density and pressure curves, and an increasingly closer correspondence between the transverse velocity and pressure curves.

Having examined the time-dependence of the growth in fluctuations of the primitive variables, we now proceed, in the next section, to examine the time-dependence of the average values of these, and related, quantities.

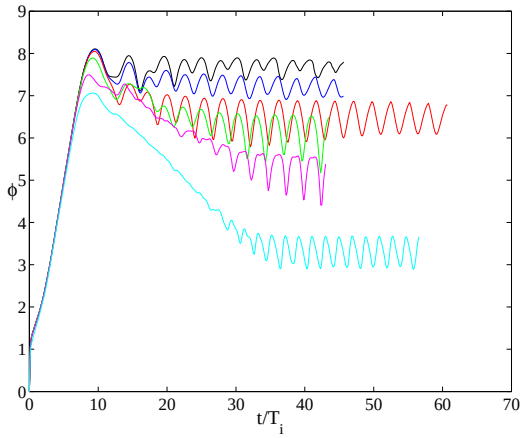

(a) $v_{z0}(x) = 0.7\,c\,\mathrm{sech}^2(x/r_0)$

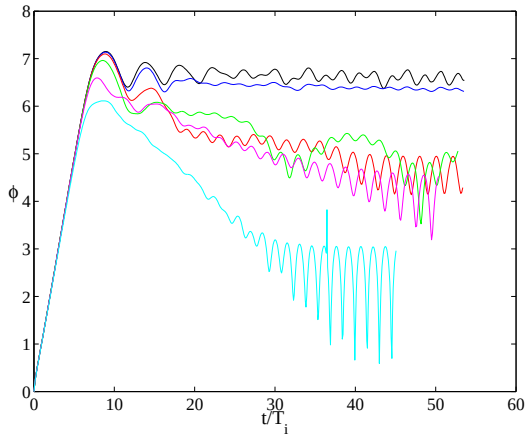

(b) $v_{z0}(x) = 0.5\,c\,\mathrm{sech}^2(x/r_0)$

Figure 9.14: Growth in transverse velocity fluctuations vs time at different M_A
$M_A = \infty$ (Black), 82.8 (Blue), 41.4 (Red), 20.7 (Green), 10.3 (Magenta), 5.15 (Cyan)

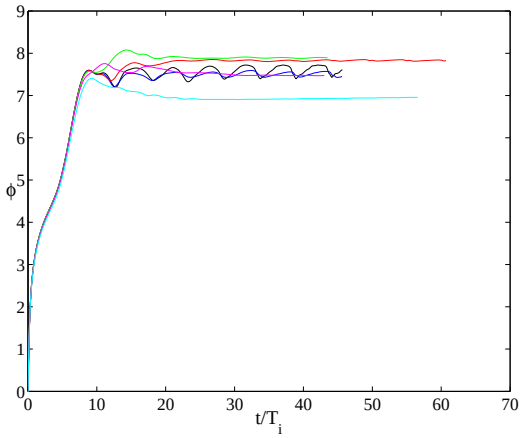

(a) $v_{z0}(x) = 0.7\,c\,\mathrm{sech}^2(x/r_0)$

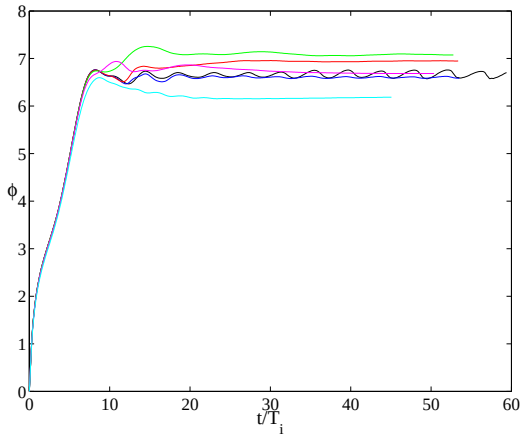

(b) $v_{z0}(x) = 0.5\,c\,\mathrm{sech}^2(x/r_0)$

Figure 9.15: Growth in longit. velocity fluctuations vs time at different M_A
$M_A = \infty$ (Black), 82.8 (Blue), 41.4 (Red), 20.7 (Green), 10.3 (Magenta), 5.15 (Cyan)

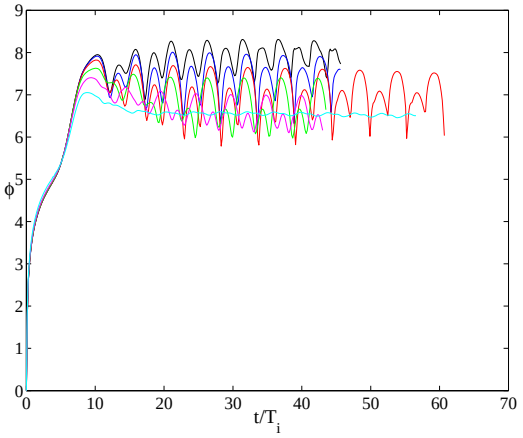

(a) $v_{z0}(x) = 0.7\,c\,\mathrm{sech}^2(x/r_0)$

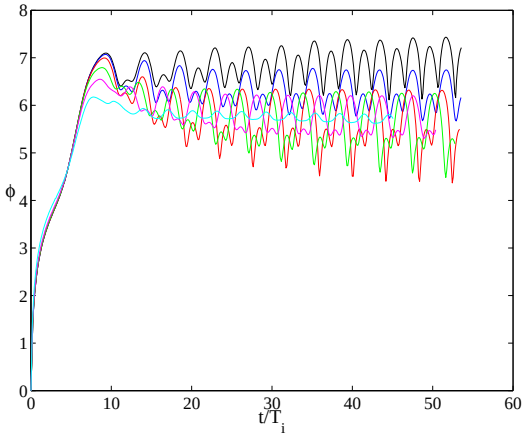

(b) $v_{z0}(x) = 0.5\,c\,\mathrm{sech}^2(x/r_0)$

Figure 9.16: Growth in density fluctuations vs time at different M_A
$M_A = \infty$ (Black), 82.8 (Blue), 41.4 (Red), 20.7 (Green), 10.3 (Magenta), 5.15 (Cyan)

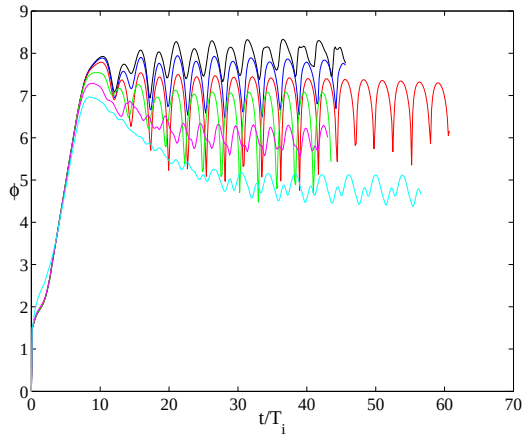

(a) $v_{z0}(x) = 0.7\,c\,\mathrm{sech}^2(x/r_0)$

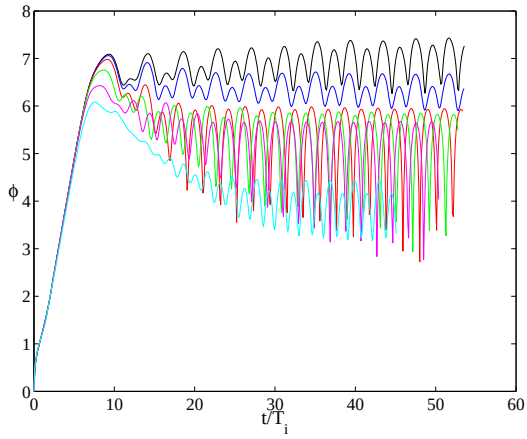

(b) $v_{z0}(x) = 0.5\,c\,\mathrm{sech}^2(x/r_0)$

Figure 9.17: Growth in pressure fluctuations vs time at different M_A
$M_A = \infty$ (Black), 82.8 (Blue), 41.4 (Red), 20.7 (Green), 10.3 (Magenta), 5.15 (Cyan)

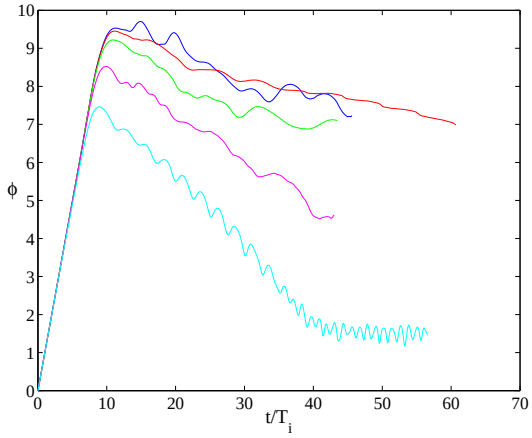

(a) $v_{z0}(x) = 0.7\,c\,\mathrm{sech}^2(x/r_0)$

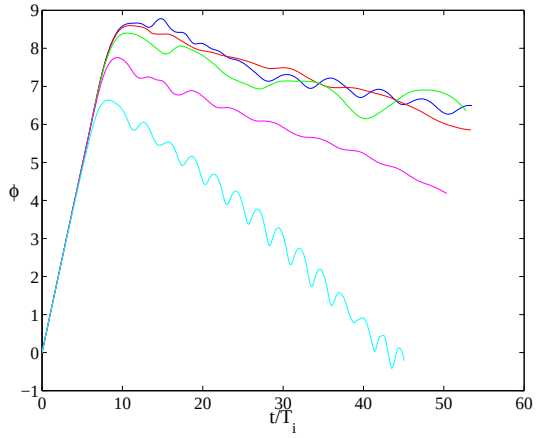

(b) $v_{z0}(x) = 0.5\,c\,\mathrm{sech}^2(x/r_0)$

Figure 9.18: Growth in transverse field fluctuations vs time at different M_A
$M_A = \infty$ (Black), 82.8 (Blue), 41.4 (Red), 20.7 (Green), 10.3 (Magenta), 5.15 (Cyan)

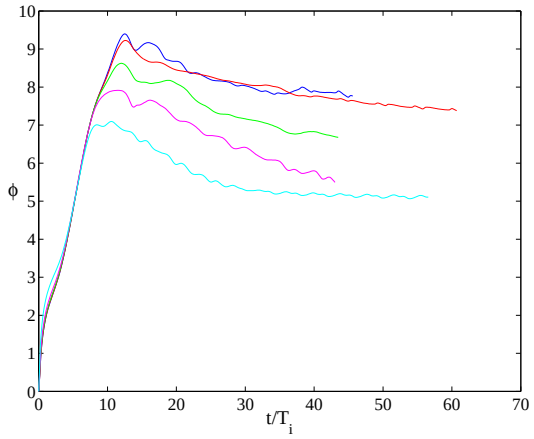

(a) $v_{z0}(x) = 0.7\,c\,\mathrm{sech}^2(x/r_0)$

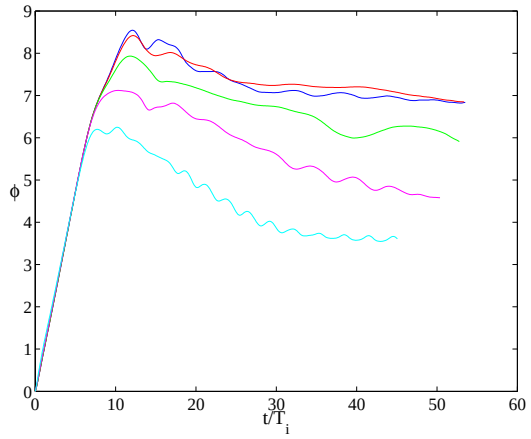

(b) $v_{z0}(x) = 0.5\,c\,\mathrm{sech}^2(x/r_0)$

Figure 9.19: Growth in longit. field fluctuations vs time at different M_A
$M_A = \infty$ (Black), 82.8 (Blue), 41.4 (Red), 20.7 (Green), 10.3 (Magenta), 5.15 (Cyan)

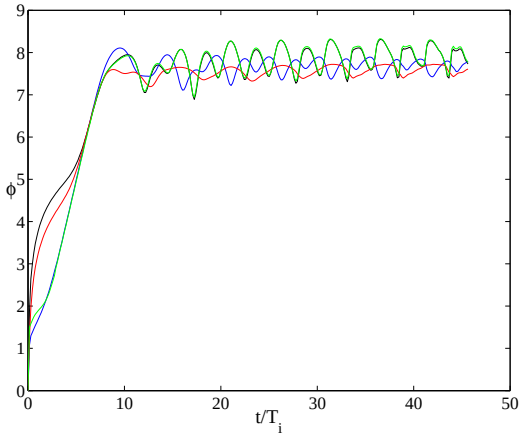

(a) $v_{z0}(x) = 0.7\,c\,\mathrm{sech}^2(x/r_0)$

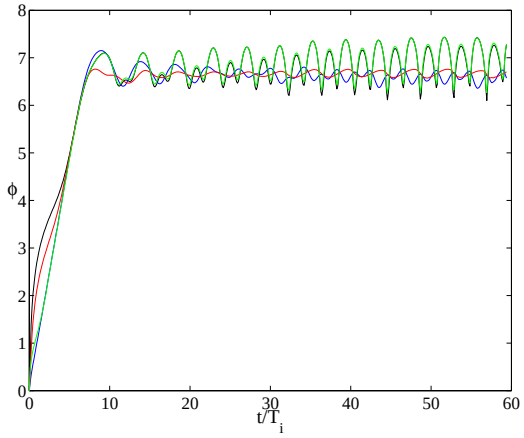

(b) $v_{z0}(x) = 0.5\,c\,\mathrm{sech}^2(x/r_0)$

Figure 9.20: Growth in fluctuations vs time for unmagnetized case
ρ (Black), v_x (Blue), v_z (Red), P (Green), $M_A = \infty$

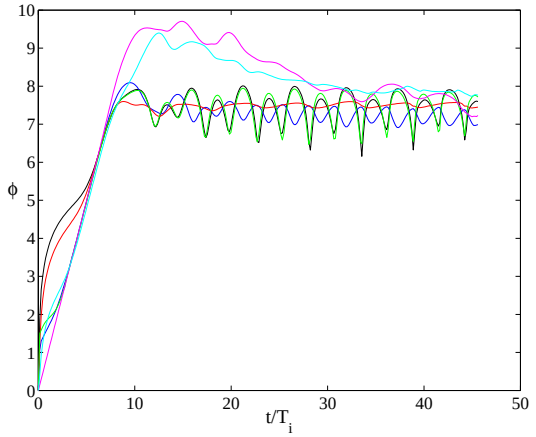

(a) $v_{z0}(x) = 0.7\,c\,\mathrm{sech}^2(x/r_0)$

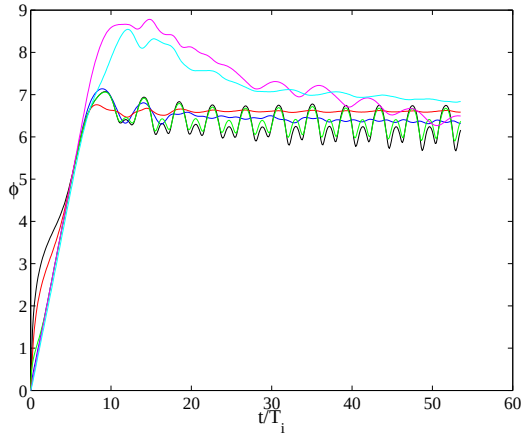

(b) $v_{z0}(x) = 0.5\,c\,\mathrm{sech}^2(x/r_0)$

Figure 9.21: Growth in fluctuations vs time for weak field ($M_A = 83$)
ρ (Black), v_x (Blue), v_z (Red), P (Green), B_x (Magenta), B_z (Cyan), $M_A = 82.83$

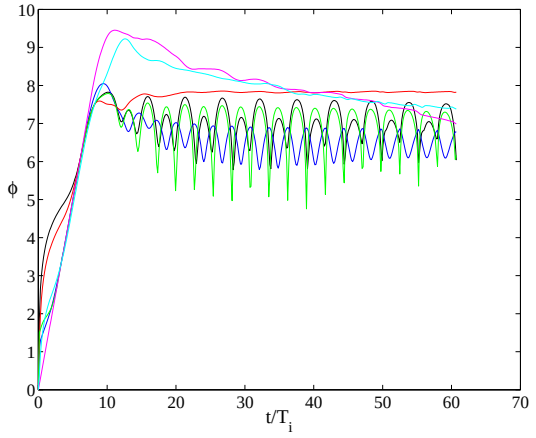

(a) $v_{z0}(x) = 0.7\,c\,\mathrm{sech}^2(x/r_0)$

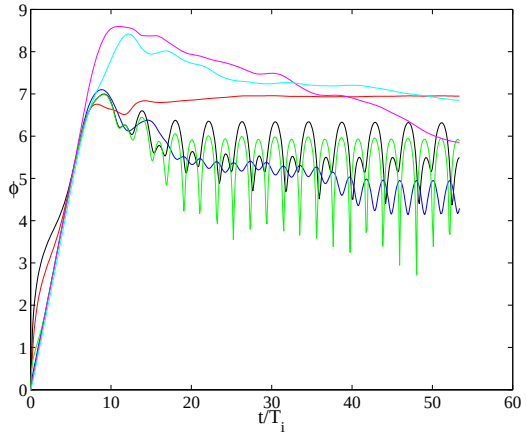

(b) $v_{z0}(x) = 0.5\,c\,\mathrm{sech}^2(x/r_0)$

Figure 9.22: Growth in fluctuations vs time for intermediate field ($M_A = 41$)
ρ (Black), v_x (Blue), v_z (Red), P (Green), B_x (Magenta), B_z (Cyan), $M_A = 41.41$

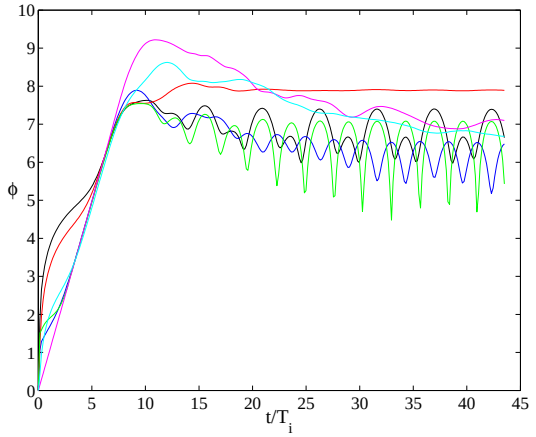

(a) $v_{z0}(x) = 0.7\,c\,\mathrm{sech}^2(x/r_0)$

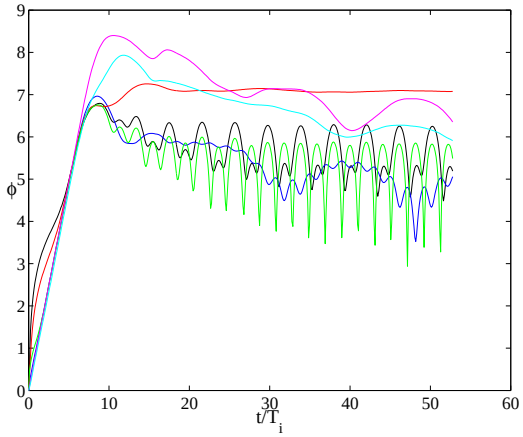

(b) $v_{z0}(x) = 0.5\,c\,\mathrm{sech}^2(x/r_0)$

Figure 9.23: Growth in fluctuations vs time for intermediate field ($M_A = 21$)
ρ (Black), v_x (Blue), v_z (Red), P (Green), B_x (Magenta), B_z (Cyan), $M_A = 20.70$

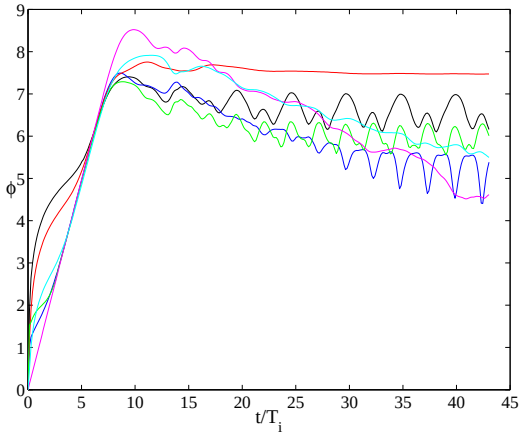

(a) $v_{z0}(x) = 0.7\,c\,\mathrm{sech}^2(x/r_0)$

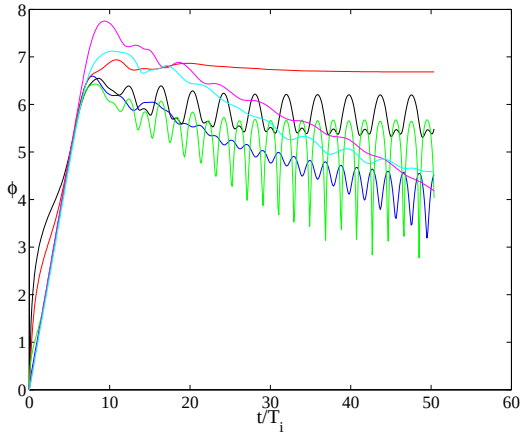

(b) $v_{z0}(x) = 0.5\,c\,\mathrm{sech}^2(x/r_0)$

Figure 9.24: Growth in fluctuations vs time for intermediate field ($M_A = 10$)
ρ (Black), v_x (Blue), v_z (Red), P (Green), B_x (Magenta), B_z (Cyan), $M_A = 10.34$

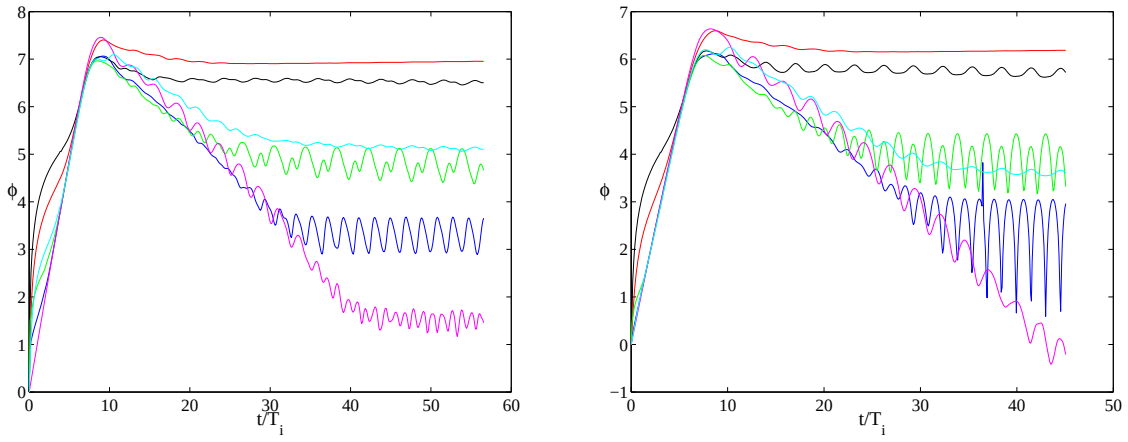

(a) $v_{z0}(x) = 0.7\,c\,\mathrm{sech}^2(x/r_0)$ (b) $v_{z0}(x) = 0.5\,c\,\mathrm{sech}^2(x/r_0)$

Figure 9.25: Growth in fluctuations vs time for strong field ($M_A = 5$)
ρ (Black), v_x (Blue), v_z (Red), P (Green), B_x (Magenta), B_z (Cyan), $M_A = 5.145$

9.5 Oscillatory Behavior of Average Values

Having studied the growth behavior of various fluctuations, we now consider the time-dependence of average values of certain quantities, through the linear and nonlinear regimes. We begin, in this section, by plotting certain quantities which have nonlinear oscillatory behavior that mirrors the oscillations in the growth of the fluctuations of velocity, density, and pressure. These oscillations are due largely to the back and forth motion of nonlinear transverse sound waves, which propagate between the jet axis and transverse boundaries at an average velocity that approximates the sound speed of $0.576\,c$, as described below. Although these oscillations are influenced by the finite width of the numerical system, we will show in sections 11.3 through 11.5 of chapter 11 that they do not significantly influence the evolution of the flow. The transverse system width does not influence observations that do not explicitly refer to oscillations. For example, we will discuss the bifurcation in energy dissipation, which is maximized for intermediate field strengths, and all aspects of this

discussion are independent of system width.

Throughout this section, and the sections that follow, each row consists of two plots, with the left plot corresponding to a central background flow speed of $v_{z0} = 0.7\,c$, and the right plot corresponding to a central background flow speed of $v_{z0} = 0.5\,c$. By comparing the right and left plots, it is evident that the influence of the magnetic field, in terms of the relativistic Alfvenic Mach number M_A, is very similar at both flow speeds. This reinforces the idea that the influence of the magnetic field, on nonlinear evolution, is very closely correlated with M_A. In the non-relativistic (MHD) studies of Frank et al. (1996) and Baty et al. (2003), among others, the magnetic field strength is reported in terms of the non-relativistic Alfvenic Mach number.

In figures 9.26, we plot the time-dependence of the average longitudinal velocity. In figures 9.28, we plot the time-dependence of the maximum longitudinal velocity. We also plot the time-dependence of the transverse velocity, the RMS values in figures 9.27 and the maximum values in figures 9.29 (the average transverse velocity is zero, to within an accuracy of $10^{-15}\,c$). The averages are taken over the range $-7.875\,r_0 \leq x \leq 7.875\,r_0$, as the fluid velocity is negligible outside of this range. Of particular interest is the oscillatory behavior in the average velocities. The average longitudinal velocity oscillates with a period of about $5.2\,T_i$, i.e., 5.2 growth times, in the $v_{z0} = 0.7\,c$ unmagnetized case, and a period of about $4.8\,T_i$ in the unmagnetized $v_{z0} = 0.5\,c$ case. As the magnetic field becomes stronger, the oscillation period decreases, and this effect is more pronounced in the $v_{z0} = 0.5\,c$ case than the $v_{z0} = 0.7\,c$ case. In the $v_{z0} = 0.5\,c$ case, the RMS transverse velocity has an oscillation period of about 4.7 growth times, but in the $v_{z0} = 0.7\,c$ case, this oscillation

period is about 2.6 growth times, which is almost exactly half of the period of oscillations of the longitudinal velocity. In figures 9.30 and 9.31, we plot the average and maximum Lorentz factors, respectively. In figures 9.32 and 9.33, we plot the spatially-averaged thermal pressure and density, respectively, relative to their background values. The oscillation periods of the average Lorentz factor, density, and pressure, are roughly the same as the period observed for the average flow speed. The oscillation amplitudes decrease with increasing field strength in both the $v_{z0} = 0.7\,c$ and $v_{z0} = 0.5\,c$ cases.

The oscillation period of about 5 growth times is about equal to the period of oscillations of nonlinear unmagnetized longitudinal velocity fluctuations, and twice the oscillation period of fluctuations of transverse velocity, density, and pressure, which are associated with the back and forth motion of nonlinear transverse sound waves, between the jet axis and transverse boundaries. We therefore see that the breathing of these transverse waves is coupled not only to oscillations in the fluctuations of velocity, density, and pressure, but also to oscillations in their average values. At a given local maximum of pressure and density, these quantities are maximized along the jet axis, and the longitudinal velocity is at a local minimum. At the next pressure and density local minimum, these quantities are more evenly distributed. At the next local maximum, the pressure and density are maximized at the transverse boundaries, and the longitudinal velocity is at a local maximum. At the next local pressure minimum, the pressure and density are once again more evenly distributed, and so on. In this way, the oscillation corresponds to a breathing motion. The nonlinear oscillation period of average longitudinal velocity is therefore equal to the transit time for sound waves (about $55\,r_0/c$, or 2.4 periods, or 5 growth times), while the oscillation period of

average pressure is half the sound transit time. The oscillation period of *transverse* velocity is equal to that for the average pressure, as seen by comparing figures 9.27 to 9.32. Maximum outward transverse velocity occurs after the pressure is maximized around the central axis. Maximum inward transverse velocity occurs after the pressure is maximized at the outer boundaries. As with the fluctuation curves in the previous section, the nonlinear oscillations have consistently larger amplitudes at a background flow speed of $v_{z0} = 0.7\,c$ than at $v_{z0} = 0.5\,c$, reinforcing the notion that these nonlinear acoustic oscillations are enhanced by the relativistic nature of the flow.

It should again be emphasized that the oscillation mechanisms described above are dependent on the transverse system width, which is a numerical parameter of the system. For larger system widths, the period of acoustic oscillations is correspondingly larger. However, as we will show in sections 11.3 through 11.5, these oscillations do not significantly influence the evolution of the flow, and its interaction with the magnetic field. Furthermore, the transverse system width does not significantly influence the time-averaged values of the quantities being plotted (i.e., when we average the oscillations over time). The conclusions that do not explicitly refer to oscillations (such as those in the paragraphs that follow) are therefore unaffected by the transverse width of the system.

For all field strengths, the average and maximum Lorentz factor and flow speed both decrease over time, and the average thermal pressure and density both increase over time. Both of these trends (increase in thermal pressure, decrease in Lorentz factor) are consistent with the viscous dissipation of mechanical bulk flow energy, and electromagnetic energy, into thermal energy.

We also notice from these figures that as field strength increases from $M_A = 83$ to 41 to 21, there is a decrease in the equilibrium values of the average longitudinal velocity and average Lorentz factor (and in the corresponding maximum values). However, as the field strength continues to increase from $M_A = 21$ to 10 to 5, these equilibrium values now increase, rather than continue to decrease, as shown in figures 9.26, 9.28, 9.30, and 9.31. This signifies a bifurcation in field behavior, where maximum deceleration occurs for intermediate vortex-disruptive fields ($M_A = 41$ or 21). This same bifurcation is also evident in the plots of average pressure and average density shown in figures 9.32 and 9.33, where there is an increase in equilibrium pressure and density as field strength increases from $M_A = 83$ to 41 to 21, and then decreases from $M_A = 21$ to 10 to 5. As with deceleration, maximum dissipation into thermal energy occurs for intermediate vortex-disruptive fields ($M_A = 41$ or 21). This bifurcation can largely be attributed to the complexity of vortex disruption, which is closely followed by turbulent breakdown into smaller-scale structures. Intermediate vortex-disruptive fields allow extensive vortex formation followed by rapid disruption, a combination which maximizes the complexity of turbulent breakdown, thereby maximizing viscous dissipation of bulk flow energy into thermal energy. At $M_A = 81$, vortex disruption does not occur rapidly enough, and at $M_A = 10$ or 5, the field is too strong to allow sufficient vortex development, so neither of these regimes create the conditions necessary for optimally complex breakdown and reorganization. The equilibrium values of RMS and maximum *transverse* velocity, on the other hand, decrease with increasing field strength, with no evident bifurcation, as shown in figures 9.27 and 9.29. The transverse motions of the flow are strongly correlated with the extent of vortex formation and nonlinear jet broadening, both of which are inversely correlated with background magnetic field strength,

as we will see in chapter 10.

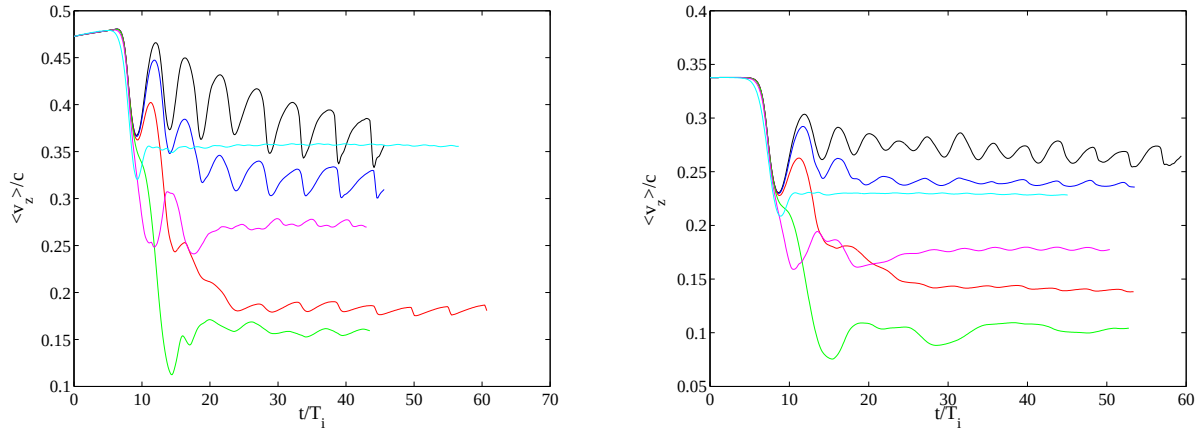

(a) $v_{z0}(x) = 0.7\,c\,\mathrm{sech}^2(x/r_0)$ (b) $v_{z0}(x) = 0.5\,c\,\mathrm{sech}^2(x/r_0)$

Figure 9.26: Average longitudinal velocity vs time at different field strengths
Average v_z at $M_A = \infty$ (black), 83 (blue), 41 (red), 21 (green), 10 (magenta), 5 (cyan)

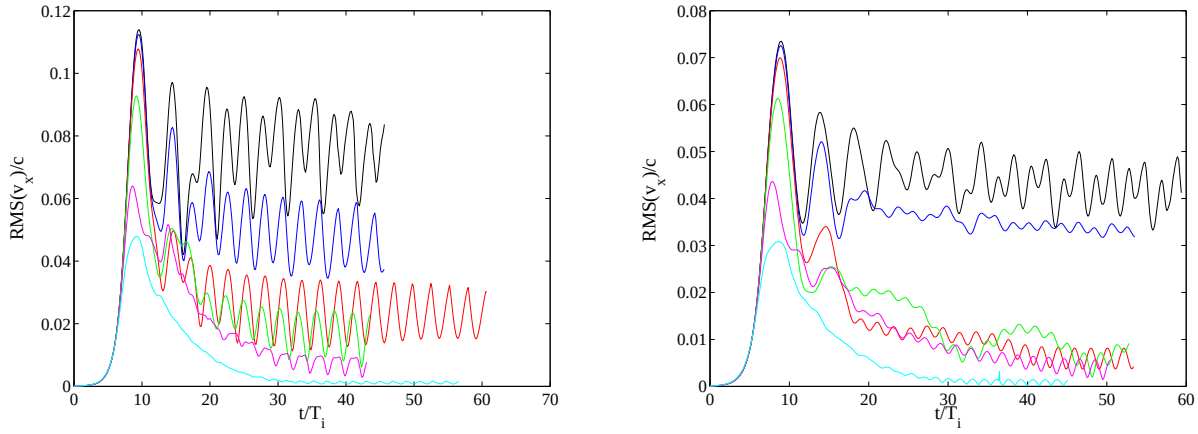

(a) $v_{z0}(x) = 0.7\,c\,\mathrm{sech}^2(x/r_0)$ (b) $v_{z0}(x) = 0.5\,c\,\mathrm{sech}^2(x/r_0)$

Figure 9.27: RMS transverse velocity vs time at different field strengths
RMS v_x at $M_A = \infty$ (black), 83 (blue), 41 (red), 21 (green), 10 (magenta), 5 (cyan)

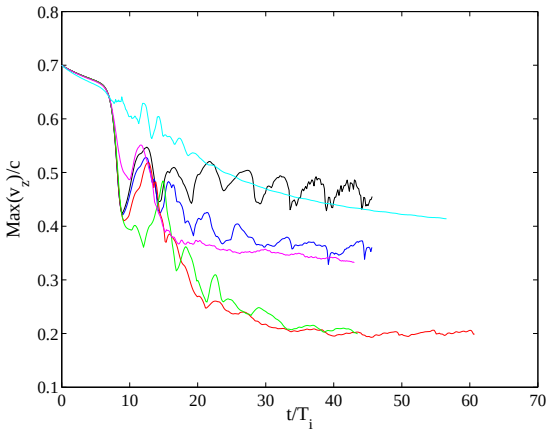

(a) $v_{z0}(x) = 0.7\,c\,\mathrm{sech}^2(x/r_0)$

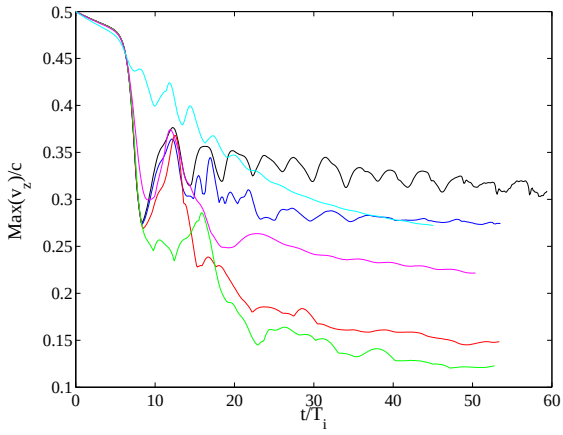

(b) $v_{z0}(x) = 0.5\,c\,\mathrm{sech}^2(x/r_0)$

Figure 9.28: Maximum longitudinal velocity vs time at different field strengths
Max. v_z at $M_A = \infty$ (black), 83 (blue), 41 (red), 21 (green), 10 (magenta), 5 (cyan)

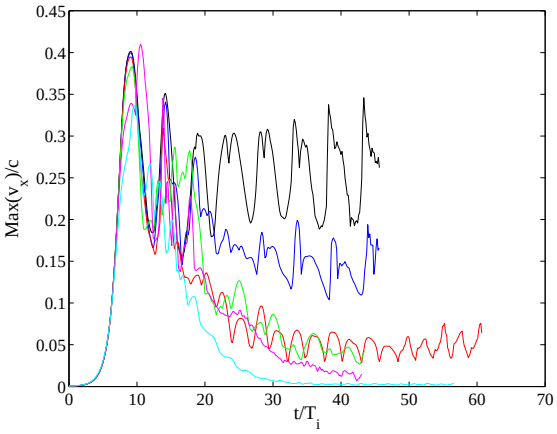

(a) $v_{z0}(x) = 0.7\,c\,\mathrm{sech}^2(x/r_0)$

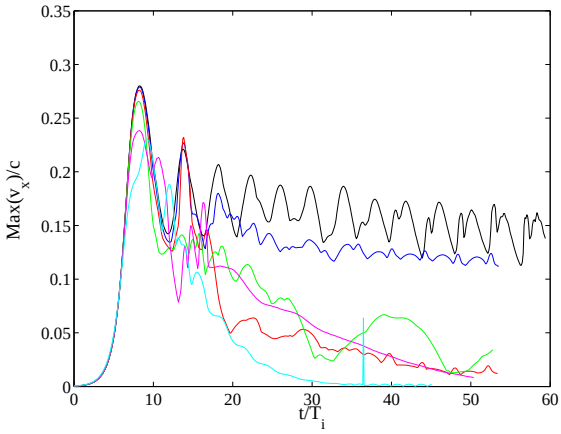

(b) $v_{z0}(x) = 0.5\,c\,\mathrm{sech}^2(x/r_0)$

Figure 9.29: Maximum transverse velocity vs time at different field strengths
Max. v_x at $M_A = \infty$ (black), 83 (blue), 41 (red), 21 (green), 10 (magenta), 5 (cyan)

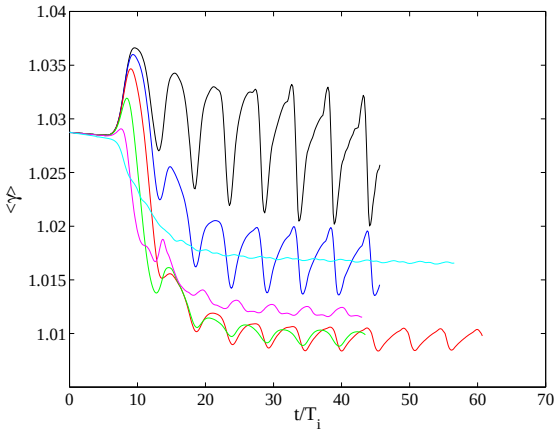

(a) $v_{z0}(x) = 0.7\,c\,\mathrm{sech}^2(x/r_0)$

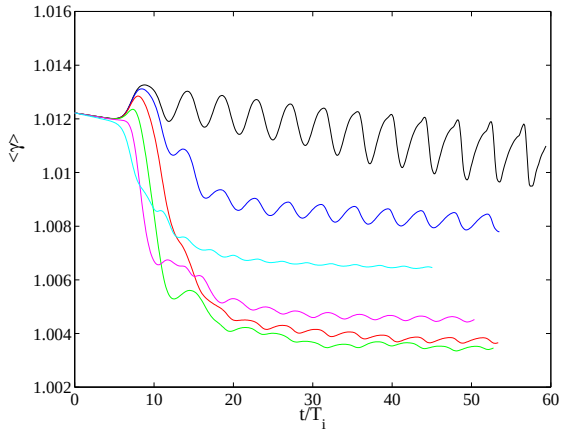

(b) $v_{z0}(x) = 0.5\,c\,\mathrm{sech}^2(x/r_0)$

Figure 9.30: Average Lorentz factor vs time at different field strengths
$M_A = \infty$ (black), 82.8 (Blue), 41.4 (Red), 20.7 (Green), 10.3 (Magenta), 5.15 (cyan)

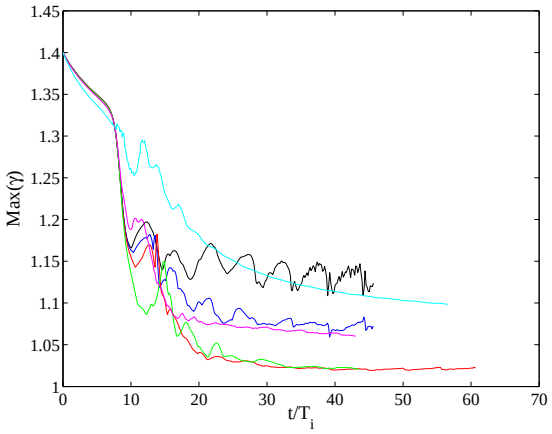

(a) $v_{z0}(x) = 0.7\,c\,\mathrm{sech}^2(x/r_0)$

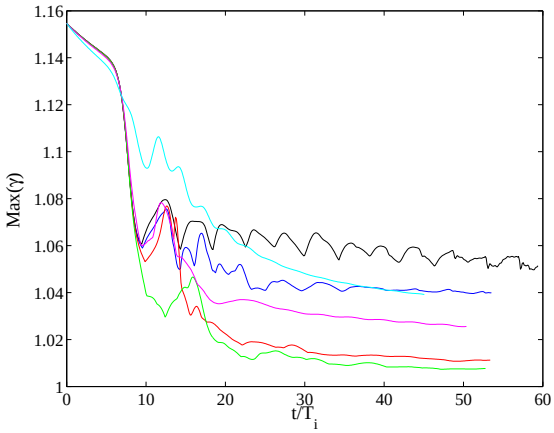

(b) $v_{z0}(x) = 0.5\,c\,\mathrm{sech}^2(x/r_0)$

Figure 9.31: Maximum Lorentz factor vs time at different field strengths
Max. γ at $M_A = \infty$ (black), 83 (blue), 41 (red), 21 (green), 10 (magenta), 5 (cyan)

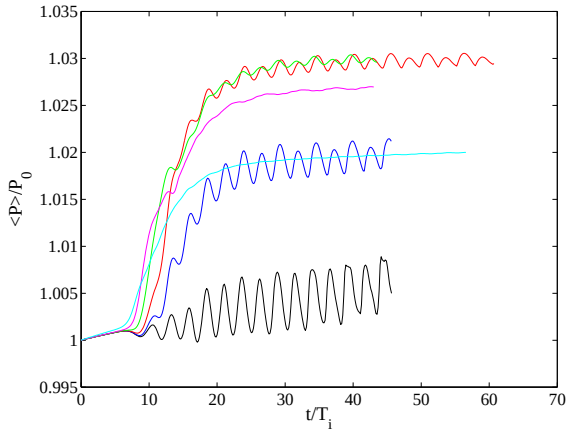

(a) $v_{z0}(x) = 0.7\,c\,\mathrm{sech}^2(x/r_0)$

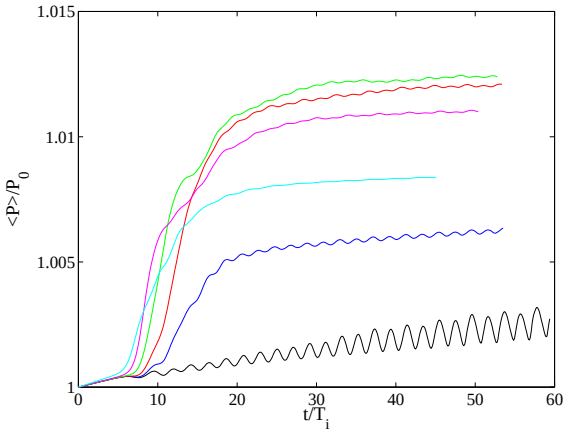

(b) $v_{z0}(x) = 0.5\,c\,\mathrm{sech}^2(x/r_0)$

Figure 9.32: Average thermal pressure vs time at different field strengths $M_A = \infty$ (black), 82.8 (Blue), 41.4 (Red), 20.7 (Green), 10.3 (Magenta), 5.15 (cyan)

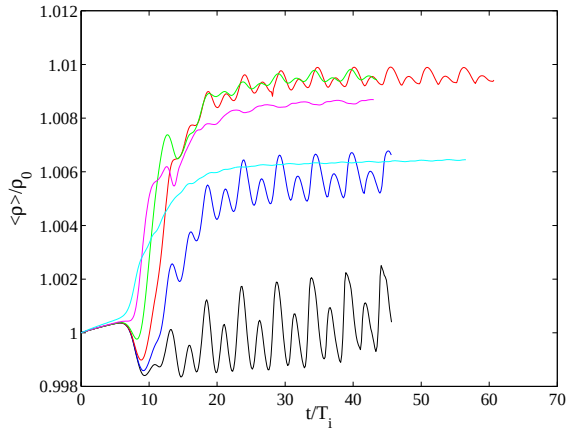

(a) $v_{z0}(x) = 0.7\,c\,\mathrm{sech}^2(x/r_0)$

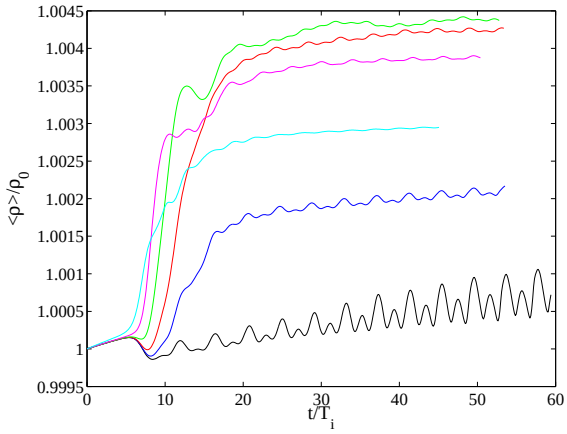

(b) $v_{z0}(x) = 0.5\,c\,\mathrm{sech}^2(x/r_0)$

Figure 9.33: Average density vs time at different field strengths $M_A = \infty$ (black), 82.8 (Blue), 41.4 (Red), 20.7 (Green), 10.3 (Magenta), 5.15 (cyan)

9.6 Saturation and Amplification

We now turn our attention to quantities that reach a well-defined maximum value at or shortly after saturation, and subsequently decrease as mechanical and electromagnetic energy are dissipated in the form of heat. These maxima correspond closely to the formation of large vortices, which generate centrifugal forces that expel matter and magnetic field lines, concentrating the field lines into amplified fields at the vortex extremities. These amplified fields correspond to amplified vorticity, current layers, and electromagnetic energy and momentum, each of which reach a maximum, and subsequently undergo a quasi-exponential decay as the vortices break down into smaller-scale structures, corresponding to a cascade of energy to smaller length scales, and viscous dissipation into thermal energy. The maxima frequently extend into the early stages of vortex disruption by the magnetic field. This overall behavior, which we further explore in chapter 10, is in agreement with the MHD results of Malagoli et al. (1996) and Baty et al. (2003), along with the RMHD results of Bucciantini and Del Zanna (2006).

In figures 9.34, we plot the time-dependence of the RMS vorticity at $v_{z0} = 0.7\,c$ (left graph) and $v_{z0} = 0.5\,c$ (right graph). In figures 9.35, we plot the time-dependence of the RMS current density at $v_{z0} = 0.7\,c$ (left graph) and $v_{z0} = 0.5\,c$ (right graph). Each graph contains multiple curves, each curve corresponding to a specific value of the Alfvenic Mach number M_A. The same values of M_A are studied at both flow speeds (i.e., in all plots).

In figures 9.36, we plot the spatially averaged ratio of electromagnetic to thermal pressure, $(E^2 + B^2)/(2P)$, in units of the corresponding background value (which, it should be noted, is different for each magnetic field). In figures 9.37, we plot the maximum value of this

ratio. Note that because most of the electromagnetic pressure is magnetic, this ratio is approximately the inverse of the plasma β.

We also plot the relative electromagnetic and thermo-mechanical longitudinal (z) momentum. These are given, respectively, by

$$\begin{aligned} p_{\mathrm{mech,z}} &= \frac{w}{c^2}\gamma^2 v_z, \qquad w = \rho c^2 + \frac{\Gamma P}{\Gamma - 1}, \\ p_{\mathrm{em,z}} &= \frac{(\mathbf{E}\times\mathbf{B})_z}{c} = \frac{E_y B_z}{c} = \frac{(B_z v_x - B_x v_z)B_z}{c^2}. \end{aligned} \tag{9.29}$$

In figures 9.38(a) and 9.39(a), we plot, as a function of time, the spatially averaged fraction of electromagnetic to total longitudinal (z) momentum, given by

$$\frac{p_{\mathrm{em,z}}}{p_{\mathrm{tot,z}}} = \frac{(B_z v_x - B_x v_z)B_z}{w\gamma^2 v_z + (B_z v_x - B_x v_z)B_z}. \tag{9.30}$$

In figures 9.38(b) and 9.39(b), we plot, as a function of time, the spatially averaged fraction of thermo-mechanical to longitudinal (z) momentum, given by

$$\frac{p_{\mathrm{mech,z}}}{p_{\mathrm{tot,z}}} = \frac{w\gamma^2 v_z}{w\gamma^2 v_z + (B_z v_x - B_x v_z)B_z}. \tag{9.31}$$

The total z-momentum of the system remains roughly constant over time. That is,

$$p_{\mathrm{tot,z}} = \frac{w}{c^2}\gamma^2 v_z + (B_z v_x - B_x v_z)\frac{B_z}{c^2} = \text{constant}. \tag{9.32}$$

As shown in table 9.1, this quantity remains roughly constant over time. We expect this, since $p_{\mathrm{tot,z}}$ is one of the conserved quantities in the conservative RMHD equations, and there is no net flux of conserved quantities through the boundaries of the system.

In the previous section, we observed a bifurcation in the dissipation of energy into thermal form, which is maximized for intermediate vortex-disruptive fields. In this section, we observe a second bifurcation, this time with regard to the extraction of electromagnetic energy from the bulk flow, which is maximized for strong vortex-disruptive fields. The RMS vorticity (figure 9.34), maximum electromagnetic to thermal pressure (figure 9.37), and electromagnetic momentum (figure 9.38) each have maximum peaks corresponding to a strong vortex-disruptive field, $M_A = 10$. This indicates that the amplification of vorticity, correlated with the extraction of electromagnetic energy and momentum from the bulk flow, are each optimized for rapid vortex inhibition, i.e., when the tension in the magnetic field lines is able to extract electromagnetic energy directly from the bulk flow, with a minimal amount of it being diverted into rotational form. However, for the vortex-suppressing field $M_A = 5.1$, figures 9.34, 9.37, and 9.38 show smaller peaks, indicating that some vortex formation is required in order to optimize the extraction of electromagnetic energy. The RMS current density, on the other hand (figure 9.35), has a maximum peak for a weak vortex-disruptive field, $M_A = 41$. The current density is governed by the curl of the magnetic field, not the magnitude of the field itself. That is, current amplification is maximized when we maximize the shear across the field lines, which occurs during the concentration of field lines which are expelled by rotating vortices. Therefore, optimum current amplification requires vortex formation and development, while the other quantities are governed by processes related to

the magnitude of the background field. However, the bifurcations show that none of these processes are optimized by complete vortex suppression ($M_A = 5$) or maximum vortex development ($M_A = 83$). It should be noted, from figure 9.36(b.), that this bifurcation does not occur when considering the electromagnetic to thermal pressure relative to its background value $B_{z0}^2/(2P_0)$. Here, we see that for stronger and stronger fields, the amplification of this ratio is a smaller and smaller fraction of its background value.

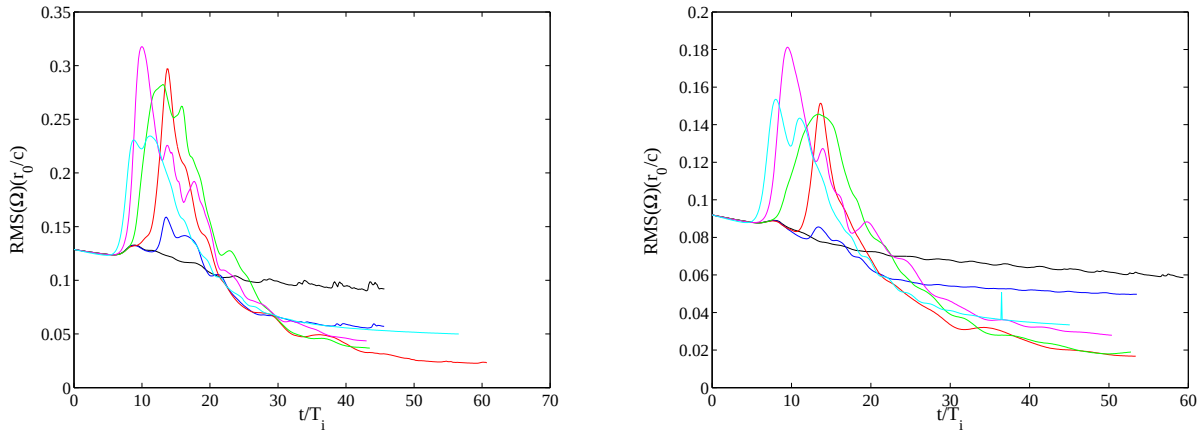

(a) $v_{z0}(x) = 0.7\,c\,\mathrm{sech}^2(x/r_0)$ (b) $v_{z0}(x) = 0.5\,c\,\mathrm{sech}^2(x/r_0)$

Figure 9.34: RMS vorticity vs time at different field strengths
Vorticity at $M_A = \infty$ (black), 83 (blue), 41 (red), 21 (green), 10 (magenta), 5 (cyan)

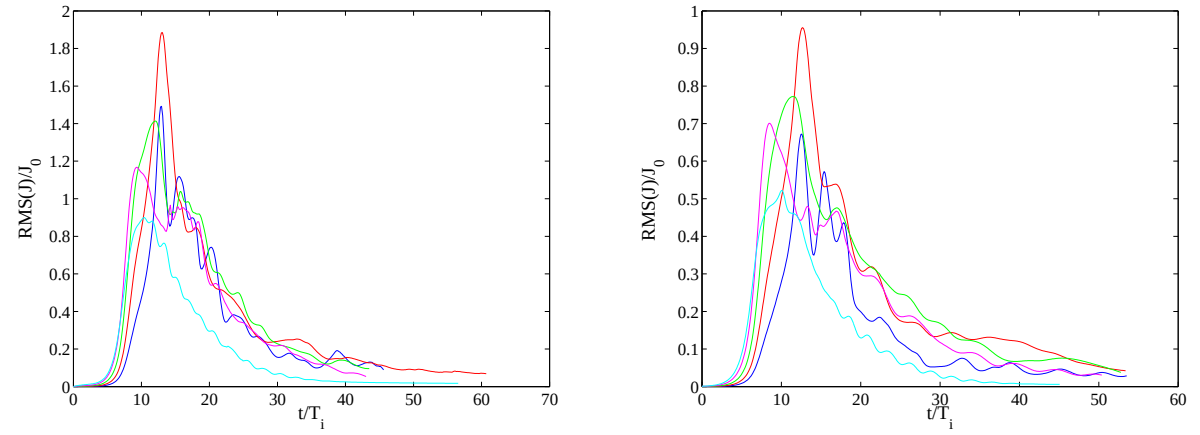

(a) $v_{z0}(x) = 0.7\,c\,\mathrm{sech}^2(x/r_0)$ (b) $v_{z0}(x) = 0.5\,c\,\mathrm{sech}^2(x/r_0)$

Figure 9.35: RMS current density vs time at different field strengths
Curr. dens. at $M_A = \infty$ (black), 83 (blue), 41 (red), 21 (green), 10 (magenta), 5 (cyan)

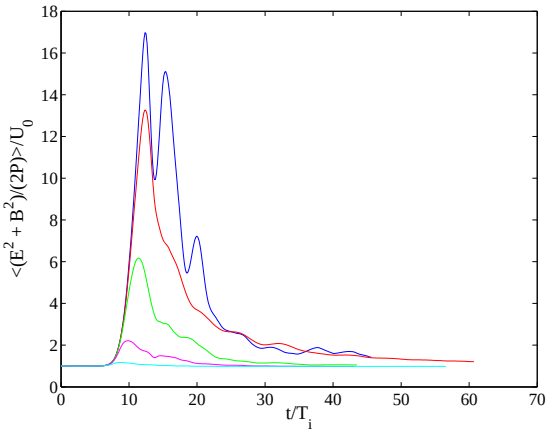

(a) $v_{z0}(x) = 0.7\,c\,\mathrm{sech}^2(x/r_0)$

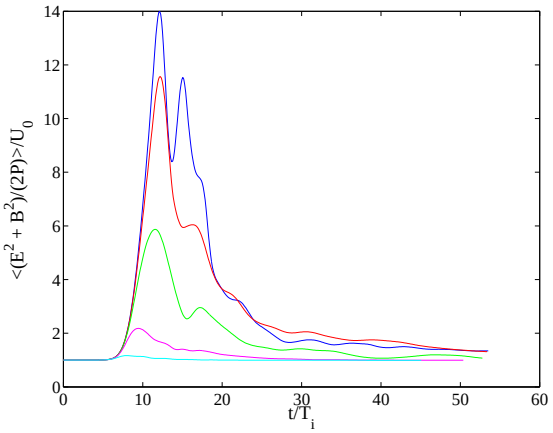

(b) $v_{z0}(x) = 0.5\,c\,\mathrm{sech}^2(x/r_0)$

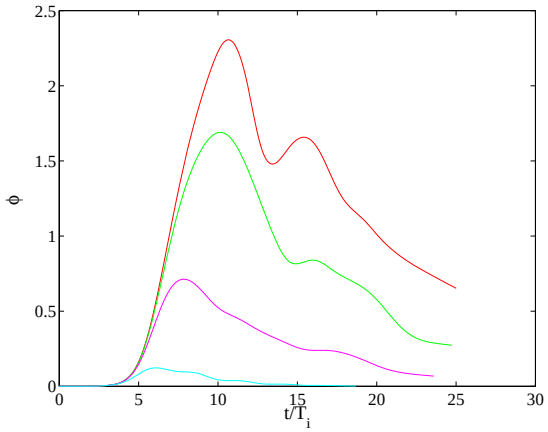

(c) $v_{z0}(x) = 0.2\,c\,\mathrm{sech}^2(x/r_0)$

Figure 9.36: Avg. electromagnetic to thermal pressure vs time at different field strengths $M_A = 82.83$ (Blue), 41.41 (Red), 20.70 (Green), 10.34 (Magenta), 5.145 (Cyan) Average electromagnetic to thermal pressure (relative to background value)

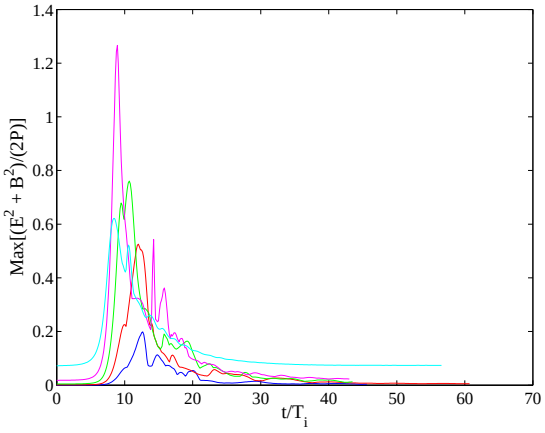

(a) $v_{z0}(x) = 0.7\,c\,\mathrm{sech}^2(x/r_0)$

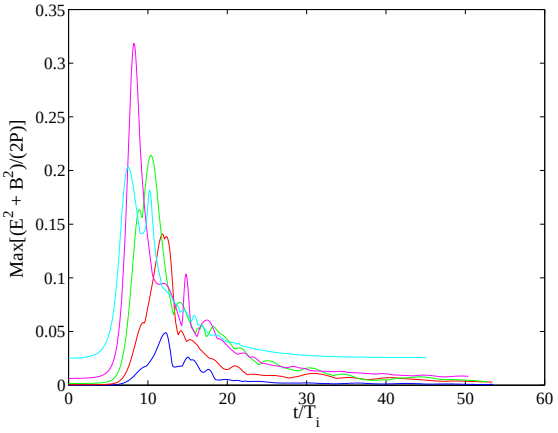

(b) $v_{z0}(x) = 0.5\,c\,\mathrm{sech}^2(x/r_0)$

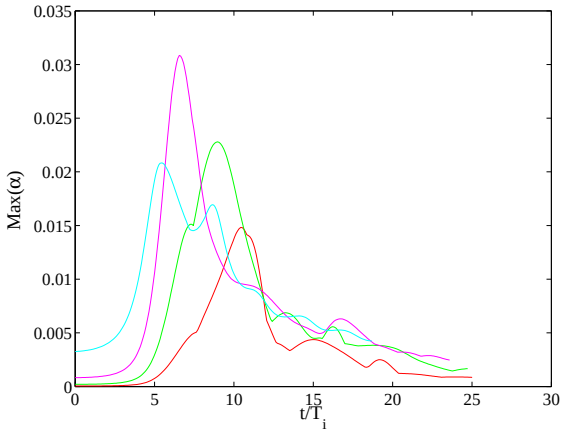

(c) $v_{z0}(x) = 0.2\,c\,\mathrm{sech}^2(x/r_0)$

Figure 9.37: Max. electromagnetic to thermal pressure vs time at different field strengths $M_A = 82.83$ (Blue), 41.41 (Red), 20.70 (Green), 10.34 (Magenta), 5.145 (Cyan)

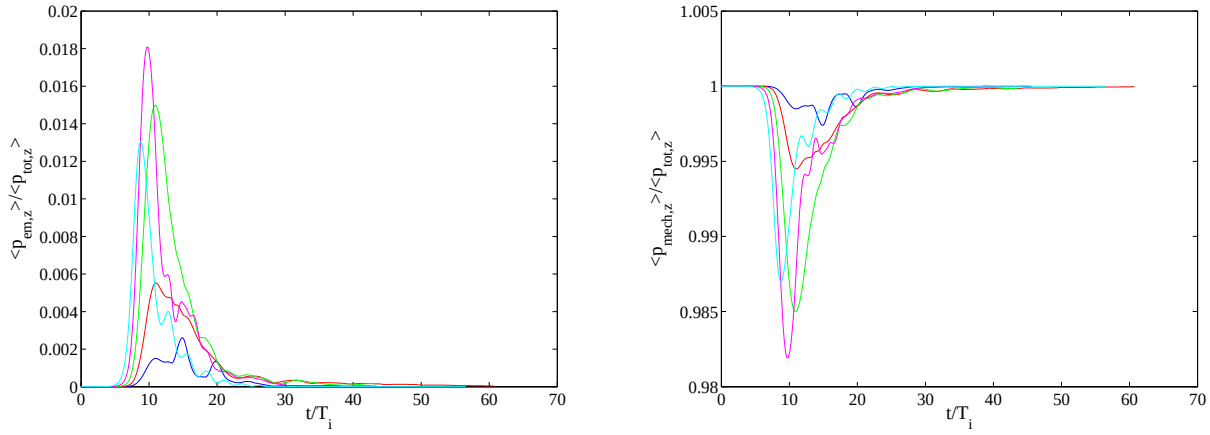

(a) average electromagnetic to total z-momentum

(b) average thermo-mechanical to total z-momentum

Figure 9.38: EM and mechanical z-momentum vs time at different M_A (flow speed $0.7\,c$)
M_A = 82.83 (Blue), 41.41 (Red), 20.70 (Green), 10.34 (Magenta), 5.145 (Cyan)
$v_{z0}(x) = 0.7\,c\,\mathrm{sech}^2(x/r_0)$

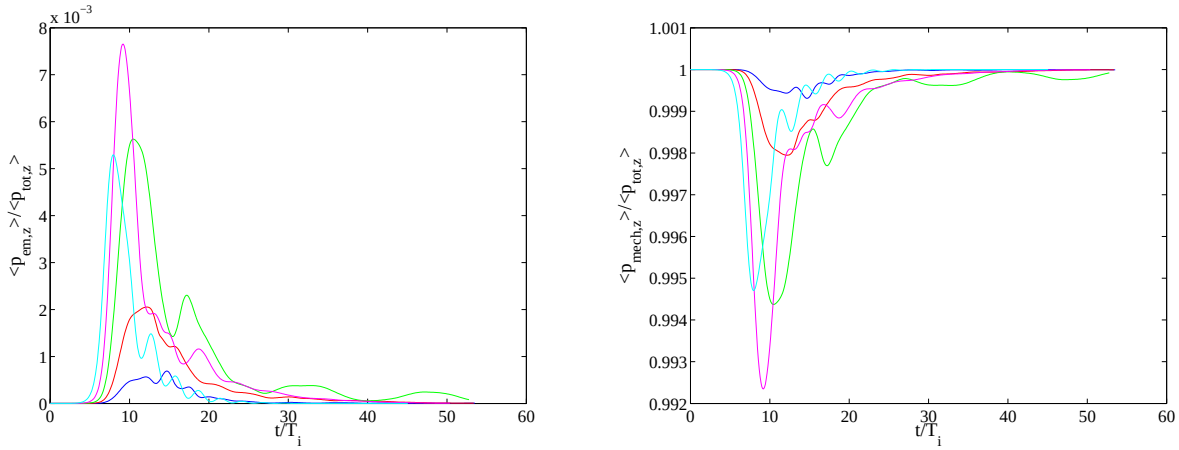

(a) average electromagnetic to total z-momentum

(b) average thermo-mechanical to total z-momentum

Figure 9.39: EM and mechanical z-momentum vs time at different M_A (flow speed $0.5\,c$)
M_A = 82.83 (Blue), 41.41 (Red), 20.70 (Green), 10.34 (Magenta), 5.145 (Cyan)
$v_{z0}(x) = 0.5\,c\,\mathrm{sech}^2(x/r_0)$

We now consider the relative thermo-mechanical and electromagnetic energy, given, respectively, by

$$\begin{aligned} U_{\text{mech}} &= w\gamma^2 - P, \qquad w = \rho c^2 + \frac{\Gamma P}{\Gamma - 1}, \\ U_{\text{em}} &= \frac{E^2 + B^2}{2} = \frac{1}{2}\left[\frac{(B_z v_x - B_x v_z)^2}{c^2} + B_x^2 + B_z^2\right]. \end{aligned} \tag{9.33}$$

In figures 9.40(a) and 9.41(a), we plot, as a function of time, the spatially averaged fraction of electromagnetic to total energy, given by

$$\frac{U_{\text{em}}}{U_{\text{tot}}} = \frac{(E^2 + B^2)/2}{w\gamma^2 - P + (E^2 + B^2)/2}. \tag{9.34}$$

In figures 9.40(b) and 9.41(b), we plot, as a function of time, the spatially averaged fraction of thermo-mechanical to total energy, given by

$$\frac{U_{\text{mech}}}{U_{\text{tot}}} = \frac{w\gamma^2 - P}{w\gamma^2 - P + (E^2 + B^2)/2}. \tag{9.35}$$

The total energy of the system is given by

$$U_{\text{tot}} = w\gamma^2 - P + \frac{E^2 + B^2}{2} = \text{constant}. \tag{9.36}$$

Like the total z-momentum, the total energy is a conserved quantity. As with all conserved quantities, we do not expect it change over time, since there is no net flux of any conserved quantity through the system boundaries. By determining the variation of these quantities

M_A	ϵ_p	ϵ_U
82.83	1.03×10^{-14}	9.11×10^{-15}
41.41	1.85×10^{-8}	7.41×10^{-8}
20.70	7.34×10^{-15}	8.40×10^{-15}
10.34	8.79×10^{-15}	9.35×10^{-15}
5.145	8.43×10^{-15}	8.02×10^{-15}

Table 9.1: Fractional errors in total z-momentum and energy

over time, we have one method of verifying the accuracy of our numerical scheme. We define the following fractional error parameters:

$$\epsilon_p = \frac{\mathrm{RMS}\left(< p_{z,\mathrm{tot}} > - << p_{z,\mathrm{tot}} >>\right)}{<< p_{z,\mathrm{tot}} >>}, \tag{9.37}$$

$$\epsilon_U = \frac{\mathrm{RMS}\left(< U_{\mathrm{tot}} > - << U_{\mathrm{tot}} >>\right)}{<< U_{\mathrm{tot}} >>}. \tag{9.38}$$

where $p_{z,\mathrm{tot}}$ is given by (9.32). $< Q >$ denotes a spatial average of Q, and $<< Q >>$ denotes an average of Q over space and time (approximately the first 45 growth times). Table 9.1 gives the values of these error parameters for each of the magnetic field strengths plotted, and corresponding to a maximum background flow speed of $0.7\,c$. The fractional errors are generally on the order of 10^{-15}, which indicates that these quantities are conserved to very high accuracy. For the case $M_A = 41.4$, the fractional error is on the order of 10^{-8}, which indicates somewhat less accuracy. This is due to a few specific times at which the quantities deviate from the temporal mean by somewhat larger amounts, though the largest fractional deviation is on the order of 10^{-6}.

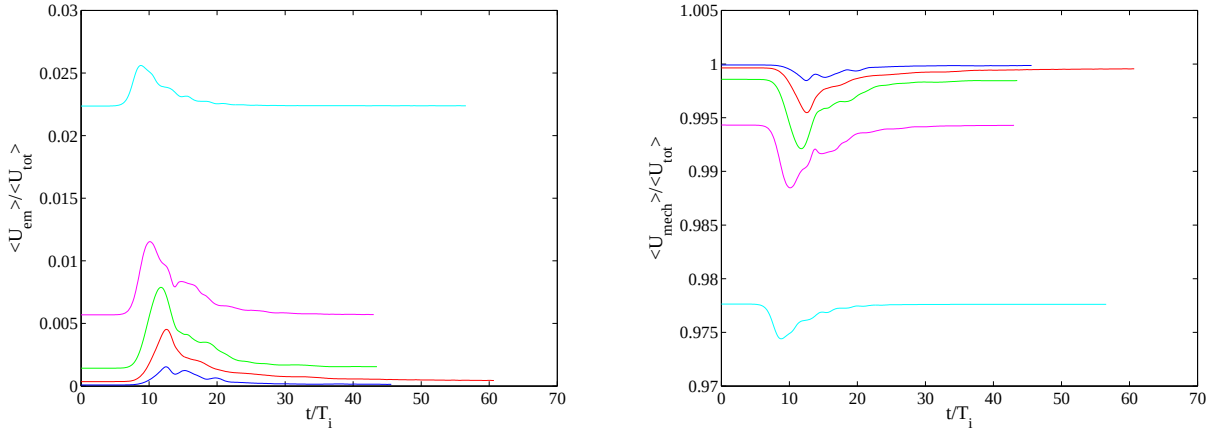

(a) average electromagnetic to total energy (b) average thermo-mechanical to total energy

Figure 9.40: EM and mechanical energy vs time at different M_A (flow speed $0.7\,c$)
M_A = 82.83 (Blue), 41.41 (Red), 20.70 (Green), 10.34 (Magenta), 5.145 (Cyan)
$v_{z0}(x)$ = $0.7\,c\,\mathrm{sech}^2(x/r_0)$

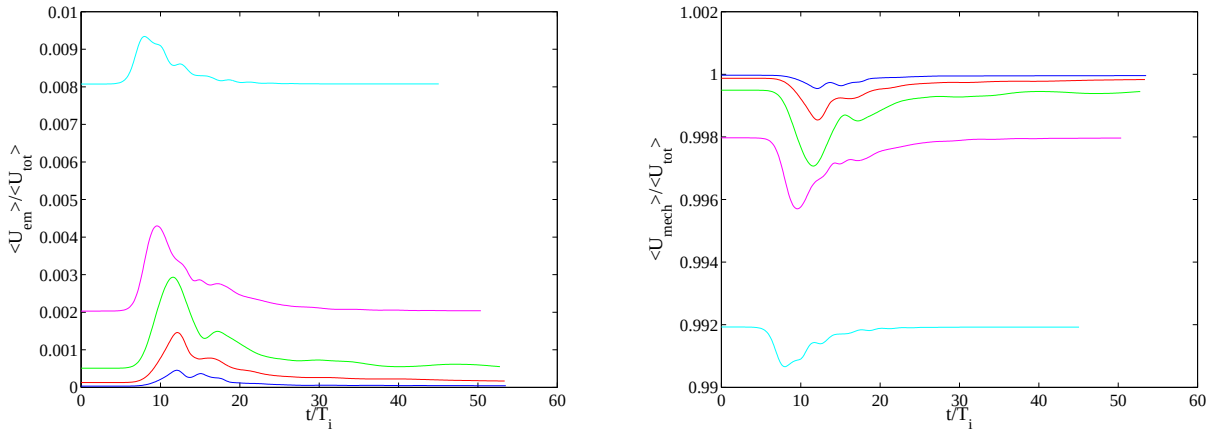

(a) average electromagnetic to total energy (b) average thermo-mechanical to total energy

Figure 9.41: EM and mechanical energy vs time at different M_A (flow speed $0.5\,c$)
M_A = 82.83 (Blue), 41.41 (Red), 20.70 (Green), 10.34 (Magenta), 5.145 (Cyan)
$v_{z0}(x)$ = $0.5\,c\,\mathrm{sech}^2(x/r_0)$

9.7 Conclusion

We have examined the growth of the fluctuations in primitive variables (density, pressure, velocity, and magnetic field) in the linear and nonlinear regimes. We have seen that in the linear regime, the fluctuations grow at approximately the expected growth rate of the linear mode, and that deviations are due to evanescent modes introduced by diffusion. In particular, we have seen that the diffusion in longitudinal momentum introduces a pair of linear transverse pressure waves that propagate between the central axis and transverse boundaries. The density diffusion introduces a narrow density depletion layer (i.e., a region of expelled mass) around the central axis, also seen in Frank et al. (1996) and Mignone et al. (2009). The fluctuations saturate after about 8 to 10 growth times, at 7 to 10 powers of e, with the magnetic field components saturating at a later time, and at a higher level, than the density, pressure, and velocity components, probably due to field amplification at the extremities of large vortices whose formation closely coincides with saturation. After saturation, the fluctuations either remain at a roughly constant level (often seen in the density, pressure, and velocity components) or gradually decrease (often seen in the magnetic field components). The density, pressure, and transverse velocity fluctuations exhibit nonlinear oscillations due to nonlinear transverse sound waves propagating between the jet axis and transverse boundaries. These oscillations are typically not seen in the nonlinear fluctuations in longitudinal velocity and magnetic field components. The exception is the vortex-suppressing field ($M_A = 5$), for which the fluctuations in transverse and longitudinal velocity remain at a roughly constant value after saturation, and exhibit little oscillation, while there is a noticeable decrease in the fluctuation level of the other quantities, and no-

ticeable nonlinear oscillatory behavior. The fluctuation level, in a given quantity, generally decreases as we increase the magnetic field strength, with the exception being the fluctuation in longitudinal velocity. It should be emphasized that although these nonlinear acoustic oscillations are influenced by the location of the transverse boundaries of the system, they do not in turn significantly influence the evolution of the flow and its interaction with the magnetic field, as we will show in sections 11.3 through 11.5.

We have also examined the spatially-averaged, RMS, and maximum values of certain quantities as a function of time, particularly in the nonlinear regime. We have found that the average (and maximum) velocity components, and Lorentz factor, decrease with time, while the average pressure and density both increase with time. This corresponds to the viscous dissipation, into thermal energy, of electromagnetic energy and mechanical energy in the bulk flow, resulting in deceleration of the jet. Much of the deceleration occurs shortly after saturation, corresponding to the extraction of electromagnetic energy from the bulk flow as newly formed vortices expel magnetic field lines to their extremities, resulting in field amplification. There is also a bifurcation in the dependence of these processes on field strength. The maximum amount of deceleration, and dissipation into thermal energy, occurs for the intermediate vortex-disruptive fields for which $M_A = 41$ or $M_A = 21$, which are weak enough to allow extensive vortex formation, but strong enough to drive rapid vortex disruption. The resulting turbulent breakdown, into smaller-scale structures, is sufficiently complex to optimize the rate of viscous dissipation of energy into thermal form. In particular, for complex turbulent breakdown, the smaller-scale turbulent structures are more comparable to the length scales set by diffusion, and the vorticity decreases to frequencies

which are comparable to the frequencies of modes introduced by diffusion, as we will discuss in chapter 10. The aforementioned average quantities also undergo oscillations associated with nonlinear transverse sound waves.

We have further examined the time-dependence of certain quantities which reach a maximum at or shortly after the saturation stage, followed by gradual decay as energy is dissipated into thermal form. These include the RMS vorticity, RMS current density, average and maximum electromagnetic-to-thermal energy ratio, and average electromagnetic longitudinal momentum. The peak, immediately following saturation, corresponds to field amplification at the extremities of newly formed vortices, whose rotation expels the field lines. This behavior, which we explore in chapter 10, is consistent with the MHD results of Malagoli et al. (1996) and Baty et al. (2003), along with the RMHD results of Bucciantini and Del Zanna (2006). There is also a bifurcation in the dependence of peak amplitude on field strength. The RMS current density has the largest amplification for the intermediate vortex-disruptive field corresponding to $M_A = 41$, indicating that current density is maximized through vortex formation and development. This is because the current density is the curl of the magnetic field, and is therefore maximized for maximum shear in field line concentration, as occurs when field lines are expelled by rotating vortices.

The remaining quantities, however, (vorticity, maximum electromagnetic-to-thermal pressure, electromagnetic longitudinal momentum) are maximized for a strongly vortex-disruptive field corresponding to $M_A = 10$. This indicates that the extraction of electromagnetic energy is maximized not through extensive vortex formation but by rapid vortex disruption. Put another way, this conversion process is less responsive to amplification by rotational kinetic

energy, and more responsive to the extraction of electromagnetic energy directly from the bulk flow by the tension in the field lines. However, some vortex formation must occur in order to extract the largest possible amount of electromagnetic energy from the bulk flow, as seen by the reduction in peak values for the vortex-suppressing field $M_A = 5.1$. We will discuss this further in chapter 10. Here, we must distinguish between electromagnetic energy and *amplification* of electromagnetic energy (i.e., maximum value divided by background value). Maximum *amplification* of electromagnetic energy occurs for the weakest fields, and decreases for stronger fields, as in figure 9.36(b.), so here there is no bifurcation.

Finally, we have verified that the total z-momentum and total energy are conserved to a high order of numerical accuracy for each field strength, as we show in table 9.1. In chapters 10 and 11, we use other methods to validate the accuracy and reliability of our numerical algorithm.

Having examined the time-dependence of spatial averages (or maximum values) of various quantities, we now refine our insights, in chapter 10, by examining two-dimensional displays of some of these quantities.

Chapter 10

Displays of Simulation Results

Having explored the time-dependence of various spatially-averaged quantities, we seek to further develop these insights by examining spatial displays of some of these quantities at different times in the simulations. In particular, the displays will deepen our understanding of (i) the nonlinear evolution for an unmagnetized case, (ii) the intricate process by which the magnetic field inhibits vortex development, and (iii) the sensitivities of this process to background field strength. We describe four stages of vortex inhibition by a magnetic field, which are qualitatively similar to processes described in MHD literature. We examine in detail how and to what extent these stages manifest in RMHD for a set of representative field strengths.

At the start of the simulation, the system is launched in the fastest-growing numerical eigenmode corresponding to the wave vector of the perturbation (computed using the method described in chapter 5). As we demonstrated analytically in section 9.2, the real-valued initial perturbation distribution consists of only one positive growth rate, namely that of the selected eigenmode. At the start of the linear regime of evolution, the perturbations therefore ideally grow at this growth rate. Additional deviations from ideal growth are due to evanescent modes introduced by artificial viscosity, as discussed in chapter 9.

The system then transitions into the nonlinear regime, followed shortly by saturation of the perturbations, followed by nonlinear evolution. The early nonlinear regime generally corresponds to the formation of two large, counter-rotating vortices on either side of the central axis. The half-wavelength separation between the vortices is correlated with the symmetries of the shear profiles of the perturbations (discussed in chapter 7). Driven by mechanical torques, the vortices rotate in the direction of fluid circulation within them. Section 10.1 discusses the evolution of an unmagnetized (RHD) case. Here, we see that in the early stages of vortex rotation, the vortices become alternately elongated in the longitudinal and transverse directions, and undergo angular acceleration. Further into the nonlinear development, the angular velocity relaxes to a roughly constant value. The vortices also assume a much more circular shape, with less elongation. This corresponds to the conversion of some of the mechanical stress into thermal stress.

In section 10.2, we introduce a vortex-disruptive field, which is not strong enough to suppress vortex formation, and discuss the stages of vortex inhibition. The first such stage is field amplification, where the fluid circulation within the vortices results in expulsion of the plasma and magnetic field, resulting in regions of amplified field (along with amplified alternating current layers) at the vortex extremities. As the vortices rotate, they twist the magnetic field lines, leading to magnetic reconnection. The second stage is vortex disruption by the field, in which magnetic stresses at the vortex boundaries result in vortex deformation, and shedding of amplified filamentary features of hybrid vorticity. The third stage corresponds to vortex breakdown into smaller-scale hybrid structures, resulting in a transition to a turbulent regime. In the fourth stage, the system gradually relaxes to an equilibrium

state consisting of flow-aligned vortex and current filaments, in which the field is once again aligned with the flow. Similar stages of vortex inhibition are described in Baty et al. (2003), Malagoli et al. (1996), and Bucciantini and Del Zanna (2006). The equilibrium filament width is about 1/4 the width of the initial jet. The jet has also decelerated, and widened to about 4.5 times its initial width, corresponding to viscous dissipation, into thermal energy, of mechanical and electromagnetic energy. There is a central region of persistent vortex structures, which coincides with the central flow region. Throughout the evolution, there is a remarkable complementarity between fluid and magnetic field behavior, as illustrated by the displays.

In section 10.5, we consider a field which is strong enough to suppress vortex formation, and show that this case corresponds to a rapid transition to an equilibrium flow-aligned filamented state. Here, the filaments are narrower (only about 1/6 the width of the initial flow), and the jet only widens to about 2.25 times its initial width. In the equilibrium state, there is a central region of relatively high flow speed, and relatively low density, whose width is about 1/5 of the initial jet width. Similar low-density regions were also found in Frank et al. (1996) and Mignone et al. (2009).

The flow also generates nonlinear acoustic waves which reverberate from the transverse boundaries, and are therefore partly a numerical phenomenon. However, we will show in sections 11.3 through 11.5 of chapter 11 that these back and forth oscillations have an insignificant effect on the nonlinear development of the flow and its interaction with the magnetic field.

The stages of vortex inhibition, by a vortex-disruptive field, are qualitatively consistent

with observations of numerous jets, including M87, Centaurus A, 3C 120, 3C 273, and Herbig-Haro jets such as HH 30. These phenomena include vortex formation, field twisting and amplification, shedding of filamentary features, turbulent breakdown, jet widening, and jet deceleration associated with viscous dissipation. In particular, the extragalactic radio jet M87 has a background field which is aligned with the flow (as in our simulations), except in large knots, where it is believed to be transverse (Hines et al. 1989). Stawarz et al. 2005 deduced that the field in knot A is amplified (at least 300 μG) relative to its value elsewhere, which is less than about 100 μG (Hines et al. 1989). These knots may well be exhibiting vortex-like behavior, twisting the field lines as they rotate, resulting in a partially transverse configuration, and centrifugally expelling the field lines to the vortex extremities, resulting in field amplification. This corresponds to the amplification stage of vortex disruption. We discuss this at the end of the chapter.

We also discuss, in section 10.8, the differences between nonlinear evolution in the RMHD and MHD regimes. Even for moderately relativistic flows, for which numerical simulations can be sustained, relativistic effects destabilize the system in certain ways. For highly relativistic flows, the system cannot be stabilized by any combination or amount of diffusion.

Finally, in section 10.9, we examine the accuracy with which the vorticity displays exhibit alternating symmetry. This results from the symmetric background velocity and antisymmetric pressure perturbations.

For each display, there is a corresponding legend to the immediate right of that display, which indicates the correspondence between colors and values of the given quantity, where the minimum value corresponds to dark blue, the maximum value corresponds to dark red,

and intermediate values are assigned colors according to the visible spectrum. Each section displays results for a given simulation. It should be noted that within a given section, displays of a given quantity may use different scales at different times, in order to maintain the contrast between the features being displayed. Therefore, the correspondence between colors and values may not be the same from one display to the next. This is particularly true of the displays of the magnetized cases, for which, over the course of nonlinear evolution, a given quantity often decays considerably from its maximum value.

We often display the vorticity, i.e., curl of the velocity, which tends to exaggerate the spatial contrast of the nonlinear features, making them easier to examine. However, it should be noted that one does not directly observe vorticity, but rather the components of the flow velocity.

Also, many physical mechanisms are discussed in reference to the displays in this chapter, and it should be noted that these mechanisms are reasoned conjectures that have not been proven.

10.1 Evolution in RHD

We begin by considering an unmagnetized relativistic case. The background density and pressure are both uniform, and the background flow has the following shear variation:

$$v_{z0}(x) \;=\; 0.7\,c\,\mathrm{sech}^2(x/r_0). \tag{10.1}$$

The sound speed is $c_s = 0.576\,c$, which is near its relativistic maximum value of $c/\sqrt{3}$ (corresponding to a pressure-dominated system). The system is launched in a numerical

eigenmode with wave number $k_z = 0.8/r_0$ along the flow direction, and complex frequency $\omega = (0.278 + i\,0.099)\,c/r_0$. We use a viscosity of $0.0002\,r_0 c$ in the density and momentum components. The input parameters are as follows:

$$
\begin{aligned}
v_{z0}(x) &= 0.7\,c\,\mathrm{sech}^2(x/r_0), \\
c_s &= 0.576\,c, \\
k_z &= 0.8/r_0, \\
L_x &= 31.5\,r_0, \qquad -L_x/2 \le x \le L_x/2, \qquad 0 \le z \le 2\pi/k_z, \\
N_x &= 1001, \qquad N_z = 201, \\
\Delta t &= 0.032\,r_0/c, \qquad \Delta x = 0.0315\,r_0, \qquad \Delta z = 0.0393\,r_0, \\
L_x/c_s &= 54.7\,r_0/c, \qquad \text{sound transit time}, \\
\eta_\rho &= \eta_x = \eta_z = 0.0002\,r_0 c.
\end{aligned}
\tag{10.2}
$$

The eigenmode parameters, emerging from the numerical linear analysis described in chapter 6, are as follows, where T_i is the growth time:

$$
\begin{aligned}
\omega &= (0.278 + i\,0.099)\,c/r_0, \\
T_i &= 1/\omega_i = 10.06\,r_0/c, \qquad \text{growth time}, \\
T &= \frac{2\pi}{\omega_r} = 22.61\,r_0/c.
\end{aligned}
\tag{10.3}
$$

In the linear regime, the perturbations grow at the approximate growth rate of $0.099\,c/r_0$, where deviations are due to evanescent modes introduced by viscosity. After about 7 growth

times, the perturbation amplitudes become comparable to the background values, and other modes are introduced into the system. Energy is diverted from the initial mode into these other modes, resulting in saturation of the perturbations after 8 to 9 growth times (the different quantities saturate at slightly different times).

Each row of displays below corresponds to a given time in the simulation, where the left display is of the vorticity, i.e., curl of the velocity, and the right display is of the longitudinal velocity. The x-direction is the shear direction. The z-direction (vertical), is the flow direction, where the flow is directed upward, and the displays show only one longitudinal wavelength of the perturbation, although the system spans two perturbation wavelengths (for the cases shown). In some simulations, not shown in this chapter, the system spans up to five perturbation wavelengths, however in each case the system remains spatially periodic in the flow direction, with negligible differences in behavior from one wavelength to the next.

Figures 10.1 and 10.2 depict the early stages of vortex formation, which coincide with saturation. As discussed in chapter 7, this process is closely correlated with the antisymmetry of the pressure perturbation, and the symmetry of the transverse velocity perturbation. These symmetries govern the buildup, during the linear regime, of an antisymmetric thermal stress, a symmetric transverse momentum, and symmetric transverse mechanical stresses of the form $w\gamma^2 v_z v_x$ and $w\gamma^2 v_x^2$. These stresses become large enough, at the start of the nonlinear regime, to bend the flow. Although the system is pressure-dominated, it is the mechanical stresses, not the thermal stresses, which govern the initial deformation of the flow. We first examine the flow velocity shown in figures 10.1(b) and 10.2(b). Where the transverse velocity (and therefore transverse mechanical stresses) have maximum amplitude

in the positive x-direction, the flow has maximum lateral displacement in the positive x-direction. A quarter-wavelength upstream from this point, the transverse velocity is zero, and the flow is not displaced. A quarter-wavelength further upstream, the transverse velocity and mechanical stresses have maximum amplitude in the negative x-direction, and the flow has maximum lateral displacement in the negative x-direction. These stresses vary continuously along the flow, and therefore the flow assumes a continuous shape as it is bent. This bending increases the transverse momentum of the flow, in turn resulting in larger mechanical stresses, which enhance the transverse deformations, as shown by comparing the flow velocities in figures 10.1(b) and 10.2(b).

The mechanical stress components, together with $w\gamma^2 v_z^2$, also modulate the deformation, resulting in a larger amount of curvature in the central region of high flow velocity (which experiences a greater amount of mechanical stress), and smaller curvature to the wider region of slower-moving flow (which experiences less mechanical stress). This is shown in figure 10.1(b). The coupling between transverse and longitudinal momentum, which are now comparable, together with the inertial resistance of the bulk flow, result in a buildup of angular momentum, leading to the formation of two counter-rotating vortices on either side of the flow axis. This vortex formation is shown in the vorticity displays in figures 10.1(a) and 10.2(a). The vortices form around existing regions of low density and pressure associated with the distributions of the density and pressure perturbations. In the vorticity displays, the red coloration corresponds to clockwise fluid circulation, and the blue coloration to counterclockwise fluid circulation. This is due to the fact that the vorticity is in the y-direction, which points into the page. As described above, the half-wavelength separation of

the two vortices is a direct consequence of the symmetries of the perturbations, corresponding to a sinuous mode (Drazin and Howard 1966). The vortex formation also corresponds to a rapid deceleration of the longitudinal flow speed from $0.7\,c$ to $0.5\,c$, as translational kinetic energy is converted into rotational kinetic energy. Driven by torques exerted by mechanical stresses, the vortices rotate in the direction of fluid circulation within them.

As the vortices rotate, they change shape, alternately being elongated in the transverse and longitudinal directions, as seen by comparing figures 10.2 through 10.6. In the early stages of vortex rotation (from 7.94 growth times to 16.49 growth times), the vortices exhibit substantial variation in their angular velocity. In figures 10.2 through 10.6, there is substantial variation in the time intervals between successive states of longitudinal and transverse elongation, indicating rotational acceleration. Also, vortex rotation corresponds to an oscillation in longitudinal velocity, which is minimized during transverse elongation and maximized during longitudinal elongation. The time-varying angular velocity, and noticeable changes in vortex shape, indicate that the early vortex rotation is dominated by mechanical stresses, as opposed to thermal stresses.

However, in the later nonlinear regime, mechanical energy is dissipated viscously into thermal energy. As a result, mechanical stresses become less dominant, and thermal stresses become more dominant. Upon inspection of figures 10.7 through **??**, we notice that after about 25 growth times, the vortex shape has become considerably less elongated and more circular, due to the isotropic nature of thermal pressure. In particular, the thermal stresses are modulated by nonlinear transverse sound waves, which propagate between the jet axis and transverse boundaries. This decelerates the vortex rotation to a nearly constant angular

speed. Between figures 10.7 and 10.8, corresponding respectively to about 5 and 6 sound transit times, the vortices have completed almost exactly one revolution.

Initially, the primary vortices are connected by dual filaments which are reminiscent of filamentary features observed in various jets, including the cosmic double-helix observed in the extragalactic jet 3C 273 (Lobanov and Zensus 2001). As the simulation progresses, these filaments gradually dissipate due to diffusion. During the linear regime, the flow moves at approximately the phase velocity of $\omega_r/k_z = 0.347\,c$. During the early nonlinear regime, the primary vortices only move downstream at 1/2 to 3/4 of the flow speed (their downstream translational movement, like their rotation, is not constant during this time). During the latter stages of the nonlinear regime, when the vortices have relaxed to a more circular shape, and are rotating at roughly constant angular speed, their downstream movement also relaxes to a roughly constant value of about 60% of the linear phase velocity. The slower pattern speed is due partly to deceleration of the flow, as kinetic energy is converted from translational into rotational form, and as this energy undergoes viscous dissipation. After about 17 growth times, we notice the formation, at the outskirts of either side of the flow, of a pair of smaller adjacent secondary vortices of opposite vorticity. These vortices do not move downstream with the flow, perhaps because they lack the size, and therefore inertia, of the primary vortices.

The rotation speed of the vortices, and their shapes after about 16 growth times, are therefore influenced, through boundary reverberations of nonlinear acoustic waves, by the transverse width of the system. However, we show in section 11.5 of chapter 11 that most aspects of the unmagnetized flow are uninfluenced by the system width. These include the

transverse location and size of the primary and secondary vortices, the average pattern speed of the primary vortices, the lack of downstream movement of the secondary vortices, and the equilibrium shape of the primary vortices, which is slightly ellipsoidal with a small aspect ratio. When the system is made wider, the primary vortices attain this equilibrium shape somewhat more quickly.

Having considered the nonlinear evolution of an unmagnetized case, in the next section we examine how this evolution is modified in the presence of a weak magnetic field.

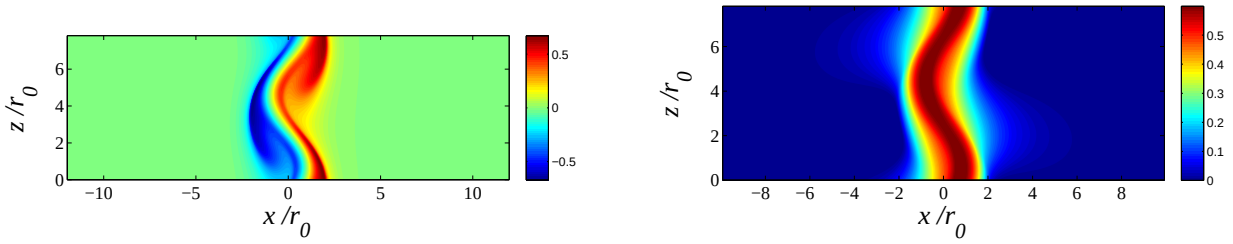

(a) vorticity (b) longitudinal velocity

Figure 10.1: Unmagnetized evolution: $t = 7.33\,T_i = 3.26\,T = 73.7\,r_0/c = 1.35\,L_x/c_s$

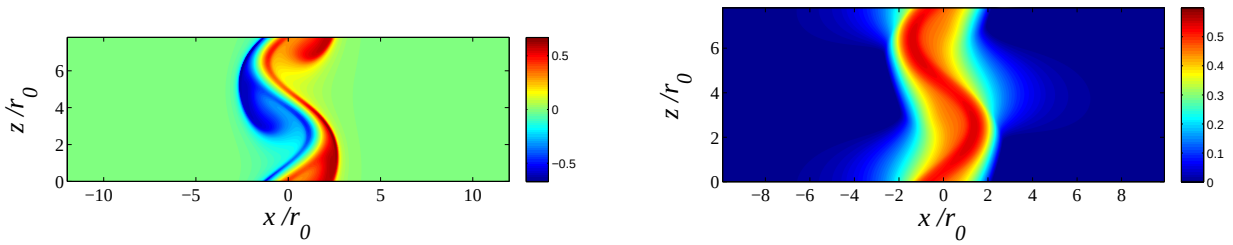

(a) vorticity (b) longitudinal velocity

Figure 10.2: Unmagnetized evolution: $t = 7.94\,T_i = 3.53\,T = 79.9\,r_0/c = 1.46\,L_x/c_s$

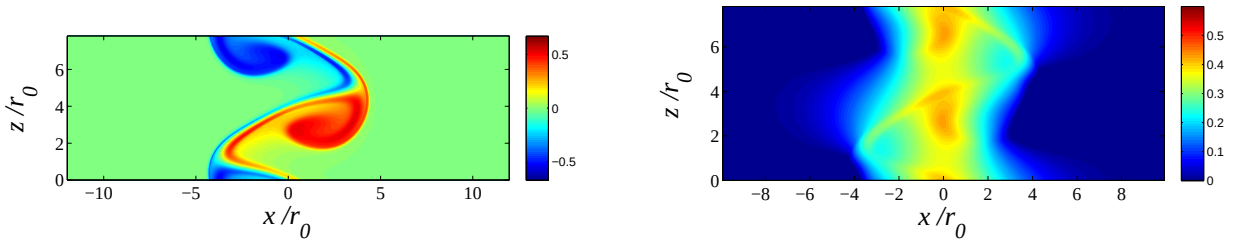

(a) vorticity (b) longitudinal velocity

Figure 10.3: Unmagnetized evolution: $t = 9.16\,T_i = 4.08\,T = 92.2\,r_0/c = 1.68\,L_x/c_s$

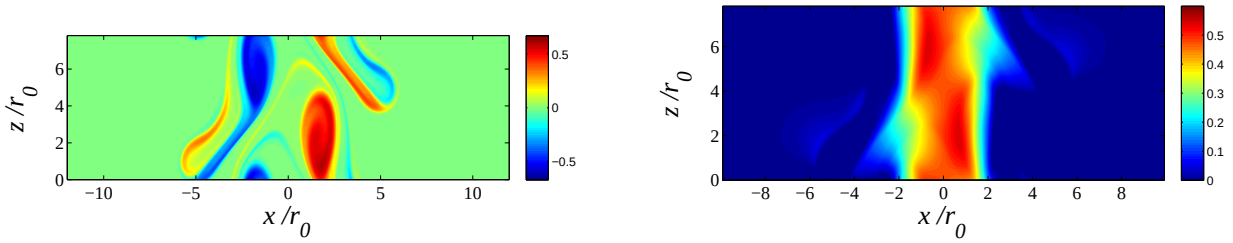

(a) vorticity (b) longitudinal velocity

Figure 10.4: Unmagnetized evolution: $t = 12.21\,T_i = 5.44\,T = 122.9\,r_0/c = 2.25\,L_x/c_s$

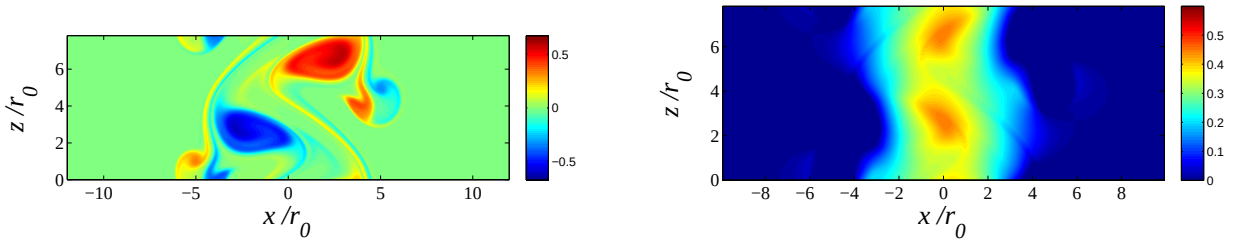

(a) vorticity (b) longitudinal velocity

Figure 10.5: Unmagnetized evolution: $t = 14.04\,T_i = 6.25\,T = 141.3\,r_0/c = 2.58\,L_x/c_s$

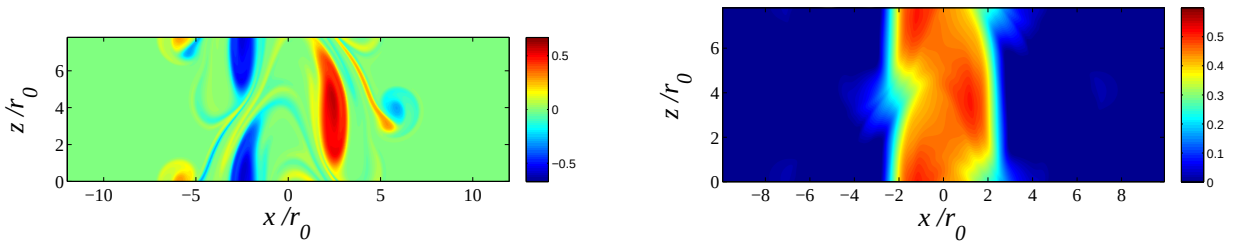

(a) vorticity (b) longitudinal velocity

Figure 10.6: Unmagnetized evolution: $t = 16.49\,T_i = 7.34\,T = 165.9\,r_0/c = 3.03\,L_x/c_s$

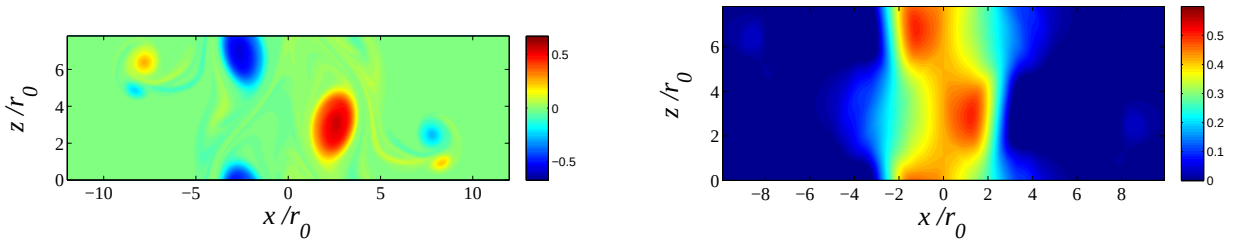

(a) vorticity (b) longitudinal velocity

Figure 10.7: Unmagnetized evolution: $t = 27.48\,T_i = 12.23\,T = 276.5\,r_0/c = 5.05\,L_x/c_s$

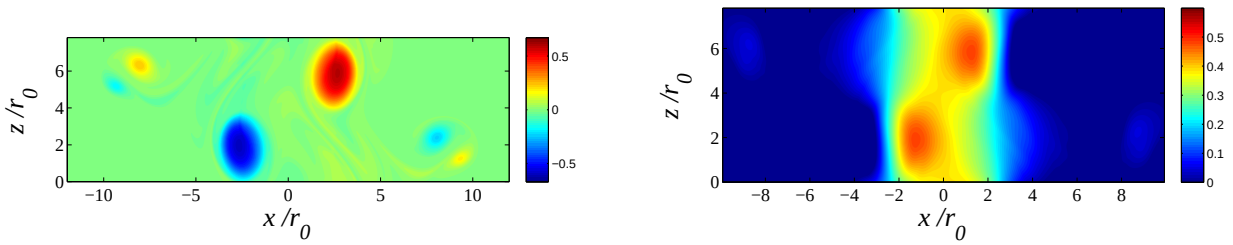

(a) vorticity (b) longitudinal velocity

Figure 10.8: Unmagnetized evolution: $t = 32.97\,T_i = 14.67\,T = 331.8\,r_0/c = 6.07\,L_x/c_s$

10.2 Weak Vortex-disruptive Field ($M_A = 41.4$)

We now consider the same system as above, but we introduce a magnetic field which is not strong enough to suppress vortex formation but is strong enough to disrupt and inhibit nonlinear vortices after they have formed. The influence of the magnetic field is closely correlated with a relativistic extension of the Alfvenic Mach number, which we have defined as follows:

$$\begin{aligned} M_A &= \frac{\gamma v_{z0}}{\gamma_A v_A}, \qquad \text{where} \\ \gamma &= \frac{1}{\sqrt{1 - v_{z0}^2/c^2}}, \\ \gamma_A &= \frac{1}{\sqrt{1 - v_A^2/c^2}}. \end{aligned} \tag{10.4}$$

v_{z0} is the amplitude of the background flow speed, and v_A is the background Alfven speed. γ and γ_A are the Lorentz factors corresponding, respectively, to the flow speed and Alfven speed. Our definition of M_A is analogous to the manner in which Bodo et al. (2004) defined a relativistic version of the sonic Mach number. For a "sech^2" background velocity profile, the vortex-disruptive regime corresponds to M_A larger than about 6. For this test case, we use a field for which $M_A = 41.4$, corresponding to a plasma β of 888 and an Alfven velocity of $0.0237\,c$. Note that these are background values, and the plasma β decreases to order unity as the field is amplified during the nonlinear regime. As with the RHD case in the previous section, we assume uniform background density and pressure. We also assume a uniform background magnetic field which is aligned with the flow. As shown by the parameter listing below, all parameters not related to the magnetic field are the same as in the RHD case from

the previous section. The magnetic field is also not strong enough to appreciably change the frequency ω, for which the growth rate is 99.65% of the growth rate of the RHD case (denoted ω_{i0} below). The parameters related to the magnetic field are M_A, β, v_A, the Alfven transit time, and the magnetic viscosities (i.e., resistivities) η_{Bx} and η_{Bz}. The input parameters are as follows:

$$
\begin{aligned}
v_{z0}(x) &= 0.7\,c\,\mathrm{sech}^2(x/r_0), \\
c_s &= 0.576\,c, \\
(M_A, \beta, v_A/c) &= (41.41,\ 888.3,\ 0.0237), \qquad \text{background values}, \\
k_z &= 0.8/r_0, \\
L_x &= 31.5\,r_0, \qquad -L_x/2 \le x \le L_x/2, \qquad 0 \le z \le 2\pi/k_z, \\
N_x &= 1001, \qquad N_z = 201, \\
\Delta t &= 0.032\,r_0/c, \qquad \Delta x = 0.0315\,r_0, \qquad \Delta z = 0.0393\,r_0, \\
L_x/c_s &= 54.7\,r_0/c, \qquad \text{sound transit time}, \\
L_x/v_A &= 1329\,r_0/c, \qquad \text{Alfven transit time}, \\
\eta_\rho &= \eta_x = \eta_z = 0.0002\,r_0 c, \\
\eta_{Bx} &= \eta_{Bz} = 0.0012\,r_0 c.
\end{aligned}
\tag{10.5}
$$

The eigenmode parameters, emerging from the numerical linear analysis described in chapter 6, are as follows:

$$
\begin{aligned}
\omega &= (0.278 + i\,0.099)\, c/r_0, \\
\omega_i &= 0.0990\, c/r_0 \;=\; 0.9965\, \omega_{i0}, \\
T_i &= 1/\omega_i \;=\; 10.10\, r_0/c, \qquad \text{growth time}, \\
T &= \frac{2\pi}{\omega_r} \;=\; 22.63\, r_0/c.
\end{aligned}
\tag{10.6}
$$

Figures 10.9 through 10.11 each show displays of the vorticity, at a given time in the simulation, for the (a) unmagnetized case considered in the previous section, and (b) magnetized case described above. In the magnetized case, the display is overlaid with contours of the magnetic field lines, which demonstrates the close complementarity between flow and magnetic field behavior. The unmagnetized and magnetized displays have slightly different sizes, due to the fact that the unmagnetized displays span a larger transverse width of the system. An important feature of the magnetized evolution, that should be noted in the displays in this section and other sections discussing magnetized evolution, is the remarkable complementarity between the fluid behavior and the behavior of the magnetic field. This can be seen in the close correspondence between the field lines and various flow-related quantities (vorticity, flow velocity, etc.), shown in the displays onto which the field lines are overlaid. Physically, the fluid is driving the field via thermal and mechanical stresses, and in turn, the tension in the field lines is constraining the fluid via electromagnetic stresses.

The evolution in the early nonlinear regime is almost identical to the evolution for the RHD case, as shown in figure 10.9. For $M_A = 41.4$, the case shown, this close agreement persists through 10 or 11 growth times, i.e., until just after the saturation stage. This period of agreement corresponds to the field amplification stage of vortex inhibition, during which

the counter-rotating vortices expel plasma and magnetic field lines, resulting in low density and pressure in the vortices, and field amplification at the vortex extremities, along the filaments connecting the vortices. As the vortices rotate, they twist the field lines, which will lead to magnetic reconnection. In their studies of the extragalactic radio jet M87, Hines et al. (1989) observed that while the field is generally aligned with the jet flow, there are large knots in which the field has a transverse component. Stawarz et al. (2005) deduced that the magnetic field inside knot A of M87 has an amplified value of at least 300 μG, where the field elsewhere is less than about 100 μG (Hines et al. 1989). These observations are consistent with the knots of M87 exhibiting vortex-like behavior, twisting the field lines into configurations with transverse components, and centrifugally expelling them to vortex extremities, thereby amplifying them. We will discuss this further in section 10.7.

This amplification results in vortex-shedding of amplified hybrid filamentary features, which signals the start of the next stage of vortex inhibition, i.e., vortex disruption, where we begin to see deviations between the magnetized and unmagnetized cases. In figure 10.10, at 12.2 growth times, the magnetized case contains enhanced filamentary features, and hybridization, not seen in the unmagnetized case. In figure 10.11, at 13.4 growth times, we see greater deviation between the two cases. The vortex disruption has progressed, and there is a greater population of features of enhanced vorticity. Also, the unmagnetized vortices have undergone more rotation than the magnetized vortices. The amplified magnetic field therefore exerts stresses that substantially decelerate the overall vortex rotation. At the same time, these stresses result in vortex deformation. Again from examining figure 10.11, the magnetic field also suppresses the formation of the pairs of secondary vortices seen in

the unmagnetized case. In their place, we instead see magnetic reconnection occurring in pocket-like regions on either side of the flow. Filamentary features, as described above, have been observed in numerous jets, including the cosmic double-helix in 3C 273 (Lobanov and Zensus 2001), the ribbons and threads in 3C 120 (Hardee 2003, 2005), and the filaments in the radio lobes of M87 (Hines et al. 1989). These filaments may be the result of field-induced vortex shedding during the disruptive stage, or may possibly be similar to the dual filaments connecting the vortices throughout vortex evolution, i.e., the filaments along which the field is amplified, as discussed in section 10.7.

After vortex-disruption, the next stage of inhibition is turbulent breakdown into smaller-scale structures, which corresponds to further broadening and deceleration of the jet as electromagnetic and mechanical energy are viscously dissipated into thermal energy. The jet then relaxes to an equilibrium configuration consisting of flow-aligned vortex and current filaments. We will discuss these stages in more detail in what follows. We should mention that the small-scale features in the turbulent regime are influenced to some extent by reverberations of acoustic waves from the transverse boundaries of the system. However, as we show in sections 11.3 through 11.5 of chapter 11, the vortex-disruptive phase (up to about 16 growth times) is independent of system width, and in the turbulent and equilibrium phases, the system width does not significantly influence the evolution of the flow or the magnetic field.

The initial jet width is about $3.6\, r_0$. Figures 10.12 through 10.17 each show displays of the (a) vorticity, (b) current density, and (c) longitudinal flow velocity at a sequence of times in the simulation, tracing through the successive stages of vortex inhibition by the magnetic

field (amplification, vortex disruption, turbulent breakdown, and relaxation to equilibrium). Similar stages of vortex inhibition are described in the MHD analyses of Baty et al. (2003) and Malagoli et al. (1996), and in the RMHD analysis of Bucciantini and Del Zanna (2006). Each display is overlaid with contours of the magnetic field lines. The current density and vorticity are the curl of the magnetic field and velocity field, respectively, and are therefore directed in the positive or negative y-direction, perpendicular to the plane of the page. Because the y-axis is directed into the page, where current density (vorticity) is positive (orange or red), the current (vorticity) is directed into the page, and where current density (vorticity) is negative (blue), the current (vorticity) is directed out of the page.

Figures 10.12, at 7.91 growth times, correspond to the early stages of vortex formation, at which point, as we saw in the previous discussion, the evolution is almost identical to the unmagnetized case. However, thin amplified layers of alternating current (only about 1/10 the initial jet width) are already developing at the vortex extremities, indicating that fluid circulation within the vortices is already expelling the field lines, which concentrate in bundles along the filaments connecting the vortices. As shown in figure 10.12(c), the central field lines also closely border the narrow region of central flow that separates the vortices. The vorticity, current density, and electromagnetic energy are all still increasing.

In figures 10.13, at 11.56 growth times (note change in longitudinal velocity scale), the vortices have expelled the field lines, resulting in amplified field, along with amplified alternating current layers, at the vortex extremities, and along the filaments connecting the vortices. These current layers have widened, compared to figure 10.12(b). There is almost no current in the vortex interiors, but the current diffuses into the regions into which the

field lines are being twisted by vortex rotation, i.e., the regions where magnetic reconnection will take place. Vortex rotation is closely correlated with the deformation of the flow, as seen in figure 10.13(c). This is the approximate time when the vorticity, current density, and electromagnetic energy reach their maximum values. The minimum plasma β at this time is 2.09, which is close to the smallest value that occurs for this simulation, and is less than 1/400 of the background plasma β. There is minimal vortex disruption by the field, and therefore the evolution of the flow, until this point, very closely resembles the evolution for the corresponding unmagnetized case. Although the central flow has not widened noticeably, the region of non-zero vorticity has widened to almost 3 times the initial jet width, indicating a broadening of the outer slower-moving regions.

In figures 10.14, at 13.39 growth times, magnetic stresses at the vortex boundaries have resulted in significant vortex disruption. This disruption takes the form of significant vortex shedding of amplified hybrid filamentary features (seen in the vorticity display), and deformation of the vortex shape. By examining the previous comparison, in figure 10.11, of the vorticity display with the corresponding unmagnetized case, we can isolate the vortex deformation which is due specifically to magnetic stresses, as opposed to mechanical and thermal stresses. Specifically, magnetic stresses have not yet caused significant deformation, but are gradually making the vortices narrower, more elongated, and more irregular in shape, as will be seen more clearly in the next display. As shown in figure 10.14(a), the hybrid filamentary features take the form of thin layers at the vortex boundaries, and a complex structure that emerges between the vortices. Magnetic stresses also cause rapid angular deceleration, halting vortex rotation at the orientations shown in the vorticity display. Magnetic reconnection

has occurred in the pocketed regions into which the vortices have twisted the field lines (i.e., the regions into which the current has diffused). The field, and current layers, are still amplified along the interconnecting filaments. From the display of longitudinal velocity, we see that the vortex disruption closely complements the disruption of the flow, due to magnetic stresses exerted by amplified field lines. The jet has widened to about $10.8\,r_0$ (i.e., about 3 times its initial width), and has decelerated to about $0.4\,c$.

In figures 10.15, at 16.43 growth times (note change in longitudinal velocity scale), the vortices are almost completely inhibited (barely noticeable), and the system is transitioning from the disruptive regime to the regime of turbulent breakdown into smaller-scale structures. The vorticity display shows that the primary vortex filaments have been expelled to the left and right boundaries of the flow, and narrowed into two amplified vortex filaments. These filaments will persist throughout the remainder of the evolution. As shown in figure 10.15(b), the current sheets are also undergoing turbulent breakdown, and the current is greatest in areas of reconnection within densely packed field lines, not along the aforementioned vortex filaments. The current is also amplified along a central strip of concentrated field lines, which zig-zags across the jet, and traces the upper boundaries of what remains of the primary vortices. From the display of longitudinal velocity, we see that the flow has been significantly disrupted. However, now that the vortices are almost completely inhibited, we also notice regions where the flow is no longer skewed by vortex rotation, and has therefore aligned itself with the downstream direction. The jet has widened to about $12.0\,r_0$ (i.e., about 3.5 times its initial width), and its maximum flow speed is now about $0.35\,c$, only half its initial maximum speed of $0.7\,c$.

In figures 10.16, at 27.38 growth times (note change in color scales), the system is well into the turbulent regime. The boundaries of many features have been smeared by viscous dissipation. Two factors are likely involved in the enhancement of viscous dissipation. Turbulent breakdown results in structures whose length scales are more comparable to the length scales associated with diffusion. Also, the average vorticity has decreased by a factor of almost 4, which means that it now corresponds to frequencies which are closer to the frequencies of modes introduced by diffusion. The system therefore has a higher correlation with viscous processes, enabling a greater amount of energy transfer via viscous interactions. The field and current have lost much of their amplification, however there are numerous areas of magnetic reconnection in the central region. Two large central reconnected regions appear to drive persistent vortical behavior. Filaments of enhanced vorticity are concentrating in layers on the left and right boundaries of the flow. A downstream-aligned central flow, of about $7.0\,r_0$ in width, i.e., twice the initial jet width, is in the process of forming, and over time, is becoming more spatially uniform. This process began as soon as the vortices were inhibited, and the magnetic field began to lose its amplification. The flow has continued to decelerate, due to viscous dissipation, and now has a maximum flow speed of about $0.25\,c$. The central flow is still somewhat heterogeneous, and contains components with flow speeds ranging from about $0.15\,c$ to about $0.25\,c$. The regions of minimum flow speed tend to be located between vortex filaments of opposite vorticity. The central flow region is a region of low density, from which plasma has been expelled.

In figures 10.17, at 56.59 growth times (note change in color scales), the system is now approaching an equilibrium state consisting of flow-aligned vortex and current filaments.

The width of these filaments is, on average, about $0.9\,r_0$ (i.e., 1/4 the initial jet width). The filaments are somewhat smeared due to diffusion, partly for the reasons mentioned in the previous paragraph (the vorticity is now only about 1/8 of its initial value, and is therefore more closely tuned to the frequencies of modes associated with diffusion). The filaments surround a central region of persistent vortical behavior, driven by magnetic reconnection, though both the field lines and vortical filaments are gradually becoming aligned with the flow. These reconnected regions correspond to locally amplified current density. We can now see that this coincides with the low-density central flow region, which has a width of about $7.0\,r_0$ (about twice the initial jet width). Meanwhile, the jet has widened to about $16.0\,r_0$, which is roughly 4.5 times its initial width. If the simulation uses less magnetic viscosity (resistivity), the central flow region is wider, though the overall jet width is the same, as are the filament widths (see chapter 11). The jet has continued to decelerate, and the central flow region has become more homogeneous, so that the central flow speeds range from roughly $0.15\,c$ to $0.2\,c$. While the current filaments alternate spatially, the vortex filaments have more spatial uniformity, with the filaments of positive vorticity to the right of the flow, and the filaments of negative vorticity to the left of the flow. The flow is maximized in the central region, and undergoes a continuous transition to zero flow speed at the transverse boundaries. Though the jet has widened, these equilibrium distributions of vorticity, and longitudinal flow, are qualitatively similar to their distributions at the start of the simulation. That is to say, despite the complex intermediate reorganization brought on by magnetic and mechanical stresses, the flow retains a memory of its initial configuration. Similar results were also seen in the MHD studies of Ryu et al. (2000) and Frank et al. (1996).

We see that for a fairly weak vortex-disruptive field $M_A = 41.4$, there is considerable magnetic reconnection. This results from extensive vortex twisting of the field lines, as the field is sufficiently weak to allow extensive vortex rotation prior to disruption. The magnetic reconnection, in turn, enhances the complexity of the turbulent regime after the vortices have been inhibited, and drives persistent vortical behavior in the central region. Extensive magnetic reconnection was also observed in the MHD studies of Frank et al. (1996), Baty et al. (2003), and Otto and Fairfield (2000). Otto and Fairfield studied the interaction of the Earth's magnetosphere with the solar wind. In this simulation, the perturbation has an input wave number $k_z = 0.8/r_0$, corresponding to an input wavelength of $7.85\, r_0$. The jet widens to about $16.0\, r_0$, or about 2 times the input wavelength. If we decrease the input wave number (i.e., increase the input wavelength), the equilibrium jet width is proportionally larger (see chapter 11). We can therefore say, more generally, that the jet widens to about twice the wavelength of the initial perturbation. This applies to weak vortex-disruptive fields, though, as we shall see, it is not true of fields which are strong enough to suppress vortex formation, for which we will discover that equilibrium jet width seems to be independent of the input wavelength.

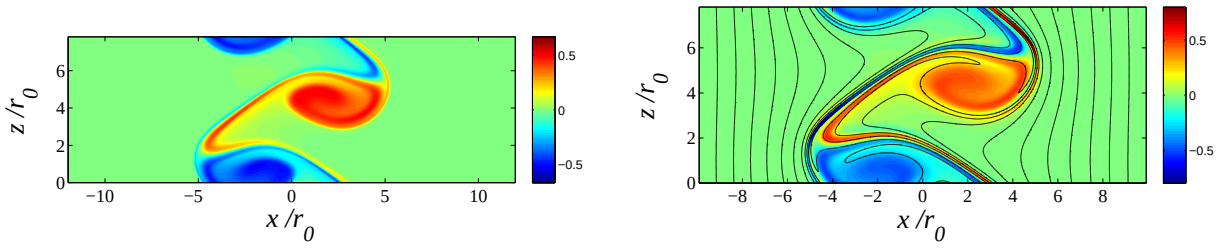

(a) $t = 9.77\,T_i = 4.35\,T = 98.3\,r_0/c = 1.80\,L_x/c_s$ (b) $t = 9.74\,T_i = 4.34\,T = 98.3\,r_0/c = 1.80\,L_x/c_s$, $\beta_{\min} = 4.56$

Figure 10.9: Vorticity for $B = 0$ (left) and $M_A = 41.41$ (right) at $9.8\,T_i$

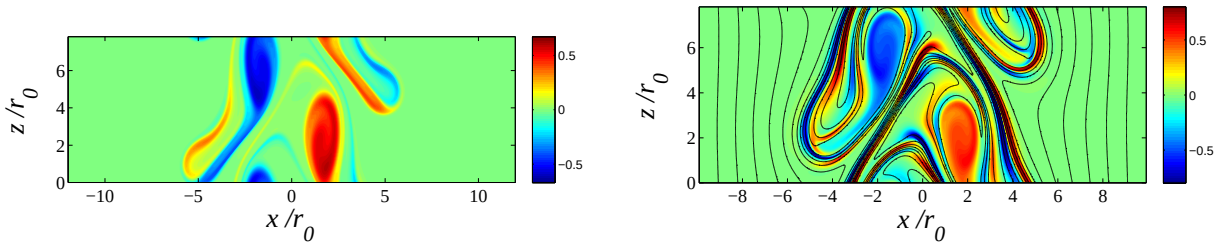

(a) $t = 12.21\,T_i = 5.44\,T = 122.9\,r_0/c = 2.25\,L_x/c_s$ (b) $t = 12.17\,T_i = 5.43\,T = 122.9\,r_0/c = 2.25\,L_x/c_s$, $\beta_{\min} = 1.94$

Figure 10.10: Vorticity for $B = 0$ (left) and $M_A = 41.41$ (right) at $12.2\,T_i$

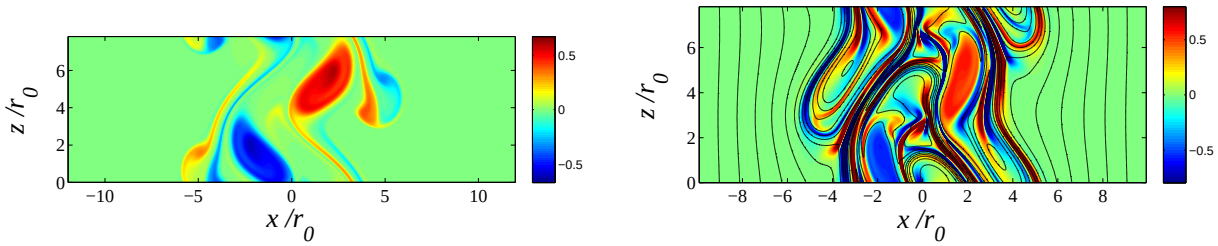

(a) $t = 13.43\,T_i = 5.98\,T = 135.2\,r_0/c = 2.47\,L_x/c_s$ (b) $t = 13.39\,T_i = 5.97\,T = 135.2\,r_0/c = 2.47\,L_x/c_s$, $\beta_{\min} = 3.38$

Figure 10.11: Vorticity for $B = 0$ (left) and $M_A = 41.41$ (right) at $13.4\,T_i$

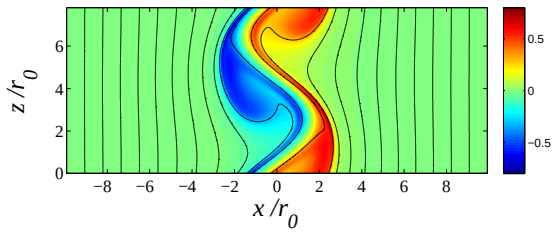

(a) vorticity

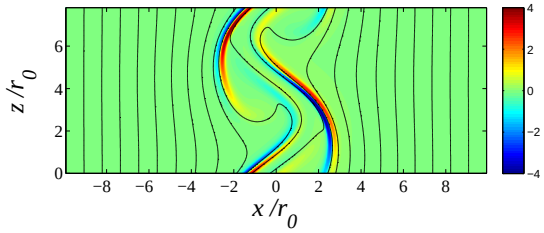

(b) current density

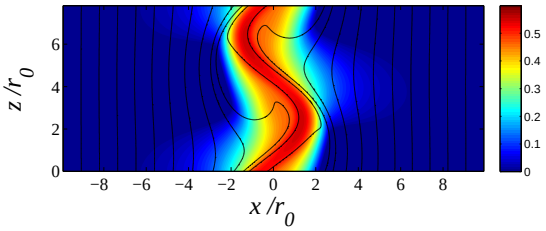

(c) longitudinal velocity

Figure 10.12: Various quantities at $t = 7.91\,T_i = 3.53\,T$, $M_A = 41.4$
$(M_A, v_{Az}/c, \beta, v_{z0}/c) = (41.4, 0.024, 888, 0.7)$, $\quad \beta_{\min} = 26.4$

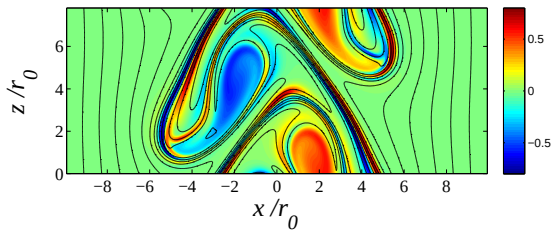

(a) vorticity

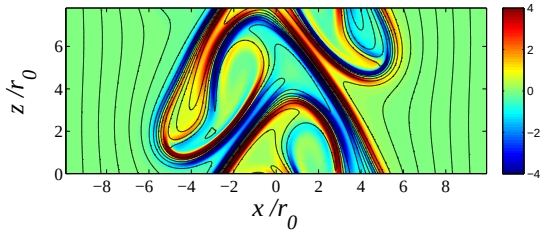

(b) current density

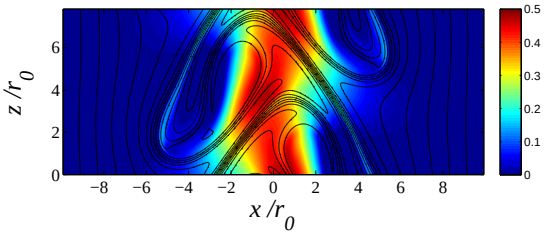

(c) longitudinal velocity

Figure 10.13: Various quantities at $t = 11.6\,T_i = 5.16\,T$, $M_A = 41.4$
$(M_A, v_{Az}/c, \beta, v_{z0}/c) = (41.4, 0.024, 888, 0.7)$, $\quad \beta_{\min} = 2.09$

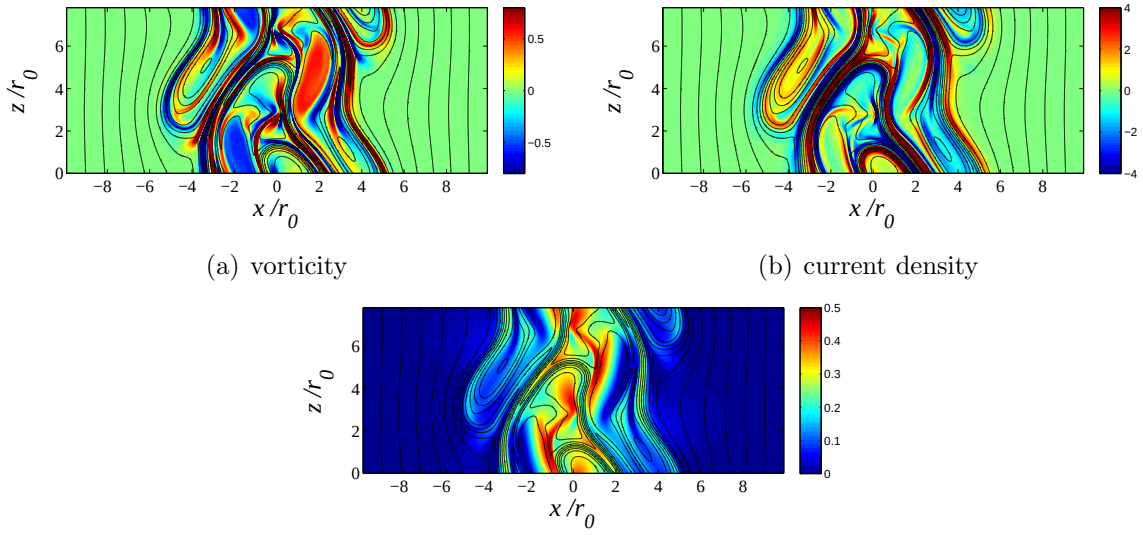

(a) vorticity

(b) current density

(c) longitudinal velocity

Figure 10.14: Various quantities at $t = 13.4\,T_i = 5.97\,T$, $M_A = 41.4$
$(M_A, v_{Az}/c, \beta, v_{z0}/c) = (41.4, 0.024, 888, 0.7)$, $\quad \beta_{\min} = 3.38$

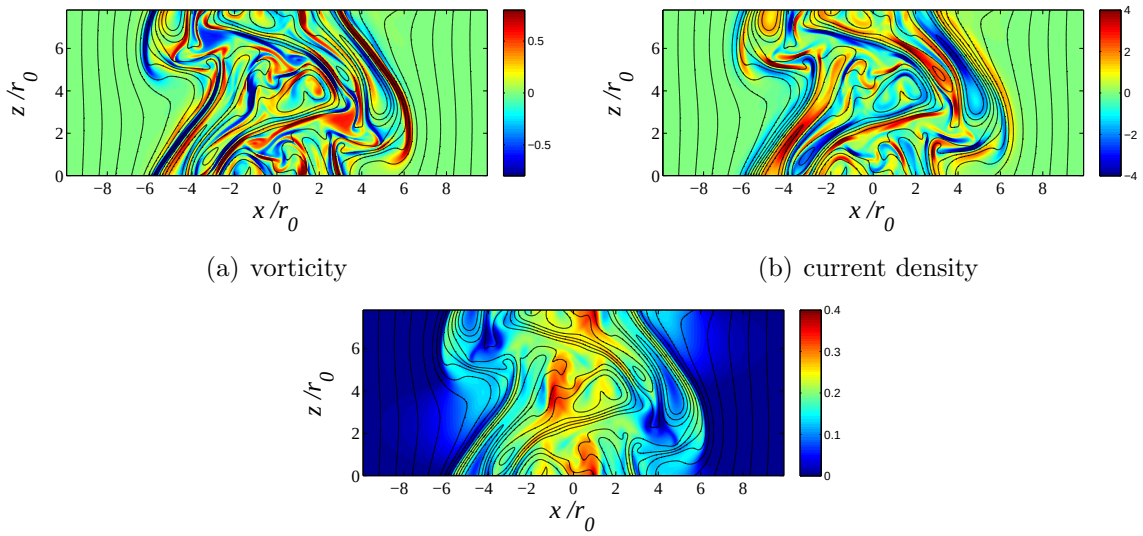

(a) vorticity

(b) current density

(c) longitudinal velocity

Figure 10.15: Various quantities at $t = 16.4\,T_i = 7.33\,T$, $M_A = 41.4$
$(M_A, v_{Az}/c, \beta, v_{z0}/c) = (41.4, 0.024, 888, 0.7)$, $\quad \beta_{\min} = 10.9$

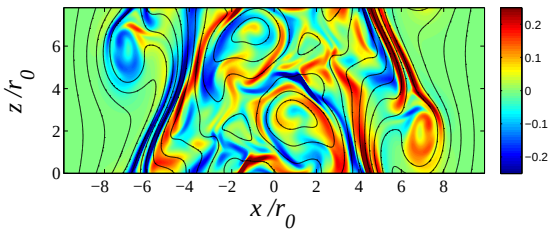

(a) vorticity

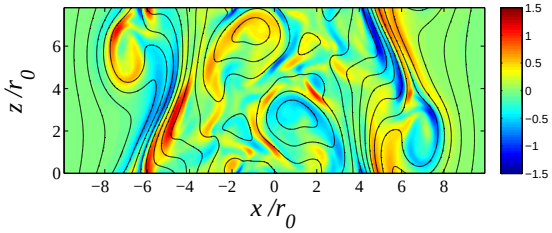

(b) current density

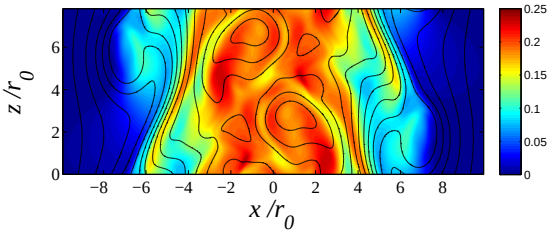

(c) longitudinal velocity

Figure 10.16: Various quantities at $t = 27.4\,T_i = 12.2\,T$, $M_A = 41.4$
$(M_A, v_{Az}/c, \beta, v_{z0}/c) = (41.4, 0.024, 888, 0.7)$, $\quad \beta_{\min} = 27.2$

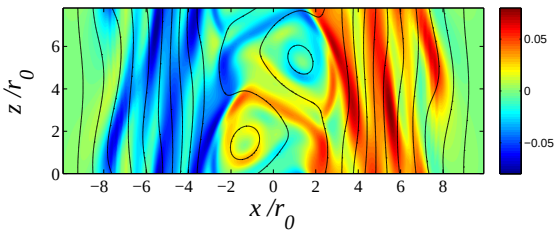

(a) vorticity

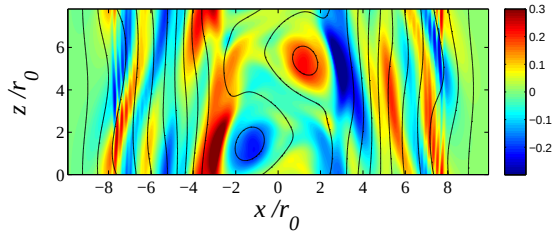

(b) current density

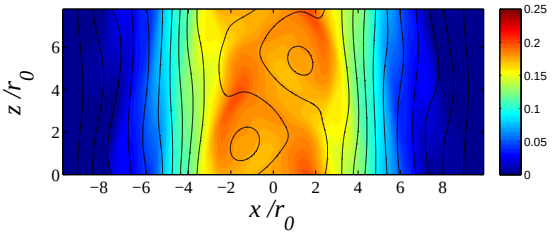

(c) longitudinal velocity

Figure 10.17: Various quantities at $t = 56.6\,T_i = 25.3\,T$, $M_A = 41.4$
$(M_A, v_{Az}/c, \beta, v_{z0}/c) = (41.4, 0.024, 888, 0.7)$, $\quad \beta_{\min} = 182$

10.3 Intermediate Vortex-disruptive Field ($M_A = 20.7$)

We have examined the stages of vortex inhibition for a fairly weak vortex-disruptive field for which $M_A = 41.4$. We now examine how this process is modified for stronger fields. In general, any field in the vortex-disruptive regime (M_A larger than about 6) inhibits vortex development through the processes described above (field amplification, vortex disruption, turbulent breakdown into smaller-scale structures, and relaxation to an equilibrium state consisting of flow-aligned vortex and current filaments). However, for stronger fields, these processes occur more rapidly (i.e., after a smaller number of growth times), and the jet does not widen by as large a factor. In the above case ($M_A = 41.4$), vortex disruption is not noticeable until 12 growth times, and even after 60 growth times, the system has not completely relaxed to its equilibrium state, due to the persistent vortical behavior in the central region. Figures 10.18 through 10.20 show the stages of vortex inhibition for a field corresponding to $M_A = 20.7$. Here, vortex disruption is noticeable after 10 growth times (see figure 10.18(a)), versus about 13 growth times for $M_A = 41.4$, and the system has almost reached an equilibrium filamented state after 37 growth times (see figure 10.20), with an equilibrium jet width of about $15\, r_0$ (about 4 times the initial jet width). Recall that for $M_A = 41.4$, even after almost 60 growth times, the system still has not reached an equilibrium state. In the case for which $M_A = 20.7$, there is less magnetic reconnection, and vortices therefore do not persist in the central region. In particular, for $M_A = 20.7$, the vortices are inhibited at an earlier point in their rotation, before they can twist the field lines to the point where they reconnect in pocket-like regions along the sides of the flow (see figure 10.18 (b)).

We now examine the displays for $M_A = 20.7$ in more detail. Figure 10.18(a), at 10.24 growth times, displays the vorticity when the electromagnetic energy is approaching its approximate maximum value. The primary vortices have formed (the orange and blue regions), and as they rotate are expelling the field lines, which as a result are concentrated along the central filaments. Electromagnetic energy, electromagnetic momentum, current density, and vorticity are all maximized along the central filaments. The vortices are twisting the field lines as they rotate. Even though electromagnetic energy, current density, etc. have not yet reached their maximum values, magnetic stresses have already begun to disrupt the vortices, as seen by narrow filaments of the opposite vorticity which extend into each primary vortex. Through vortex twisting and diffusion, the field lines are beginning to infiltrate the regions between the vortices.

We now proceed to figure 10.18(b), which displays the vorticity at 13.85 growth times. The electromagnetic energy density and vorticity have previously reached their peak values, and are now decreasing, as seen by the fact that the field lines are less concentrated. Magnetic stresses have brought vortex rotation to a halt, so that they remain in the orientations shown. These stresses also deform the vortices into the irregular shapes shown, and result in the emergence of enhanced hybrid filamentary features. These include the narrow layers of opposite vorticity at the vortex boundaries, and the complex hybrid structure in the interior region between the vortices, which is formed by layers of filament which magnetic stresses have peeled from the primary filament and the base of the vortex. This latter structure is modulated by magnetic reconnection occurring among field lines which have infiltrated the interior, as a result of vortex twisting and field diffusion. Note that the vortices fail to twist

the field lines to the point where they reconnect in pocket-like regions along the sides of the jet, as occurs for the weaker field $M_A = 41.4$. The vorticity and electromagnetic energy are still maximized in the primary filaments, which are still intact, although these have detached from the bases of the vortices. The jet has widened to about 3 times its initial width.

We now proceed to figure 10.19(a), which displays the vorticity at 16.26 growth times. The system has transitioned from the disruptive to the turbulent regime, as the primary vortices are no longer visible. Electromagnetic and mechanical energy are being viscously dissipated into thermal energy. Viscous dissipation has smeared the hybrid structures that emerged in the interior regions, so that these are much less sharply defined, though magnetic reconnection persists. The dissipation of these hybrid structures is due to their smaller length scales and smaller vorticity, which are more comparable, respectively, to the length scales and frequencies associated with diffusion. Vorticity and electromagnetic energy are still maximized along the primary filaments, which are narrower and have been expelled from the central region by mechanical stresses, and by magnetic stresses associated with reconnection. These filaments still retain much of the initial curvature that developed during formation of the primary vortices. The jet has now widened to about 3.4 times its initial width.

We now proceed to figure 10.19(b), which displays the vorticity at 23.48 growth times (note change in color scale). The system is well into the turbulent regime. About 2/3 of the peak electromagnetic energy has been viscously dissipated from the system, resulting in a loss of field line concentration, and a decrease in vorticity in the primary filaments, which have now been expelled to the left and right boundaries, and have lost their curvature and become aligned with the flow. The primary filaments have also shed fragments of enhanced

vorticity which lie along the central axis, and are interspersed elsewhere in the interior. Throughout the interior are small turbulent structures, which have been viscously smeared due to the close correlation between the small length scales and vorticity of these structures, and the length scales and frequencies introduced by diffusion. The turbulent features are partly driven by persistent magnetic reconnection. The jet has now widened to about 3.6 times its initial width, and decelerated from a flow speed of $0.7\,c$ to about $0.3\,c$.

We now consider figures 10.20(a) and (b), which display the vorticity and longitudinal velocity, respectively, of the system at 37.93 growth times, as it approaches an equilibrium state consisting of flow-aligned filaments (note change in vorticity color scale). The vorticity is maximized in the outer filaments, but has decreased to about a quarter of its peak value, and is therefore more closely tuned to frequencies of modes introduced by diffusion, resulting in widening of the filaments due to viscous smearing. The magnetic field lines are more closely aligned with the flow, as are the turbulent features, which are developing into vortex filaments. The jet has broadened to about 4 times its initial width (based on the vorticity display), while the central flow region is about 3 times the initial jet width, and is much broader and more heterogeneous than the equilibrium central flow for the weaker field $M_A = 41.4$. The central flow consists of several regions whose flow speed is about $0.2\,c$ interspersed with a background flow whose speed is about $0.12\,c$. In particular, there is a narrow strip, along the central axis, whose flow speed is about $0.18\,c$. For stronger fields, we will also observe narrow central strips of relatively high flow speed. However, these central channels will be surrounded by much slower uniform background flows. The central channel in a broad heterogeneous flow, as shown in figure 10.20(b), represents an intermediate configuration

between the broad, more homogeneous equilibrium flow of a weak field, with no central channel, and the equilibrium flow of a strong field, which has a relatively fast central channel surrounded by a slower background flow. Recall that a weak field, such as $M_A = 41.4$, has more magnetic reconnection, resulting in vortical behavior that persists for many more growth times, than the present case ($M_A = 20.7$).

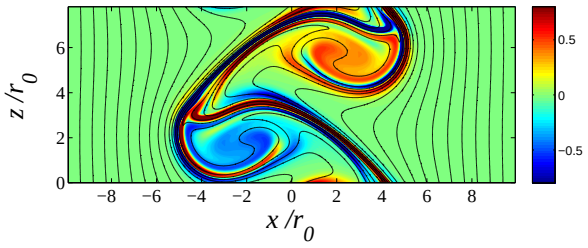

(a) $t = 10.24\,T_i = 4.61\,T = 104.4\,r_0/c = 1.91\,L_x/c_s, \quad \beta_{\min} = 1.43$

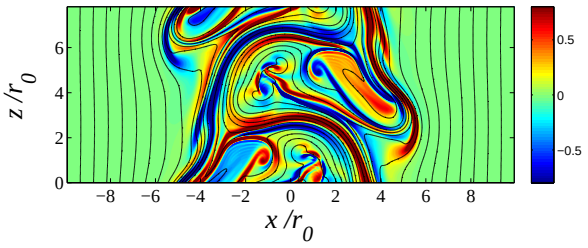

(b) $t = 13.85\,T_i = 6.23\,T = 141.3\,r_0/c = 2.58\,L_x/c_s, \quad \beta_{\min} = 4.26$

Figure 10.18: Vorticity at (a) $10.2\,T_i$ and (b) $13.9\,T_i$
$(M_A, v_{Az}/c, \beta, v_{z0}/c) = (20.7, 0.047, 222, 0.7)$

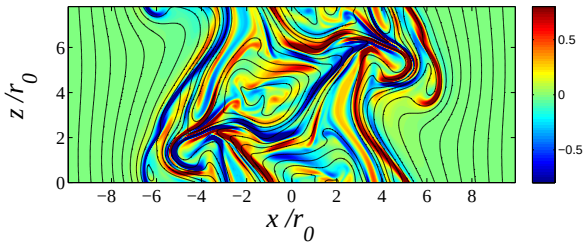

(a) $t = 16.26\,T_i = 7.31\,T = 165.9\,r_0/c = 3.03\,L_x/c_s, \quad \beta_{\min} = 5.79$

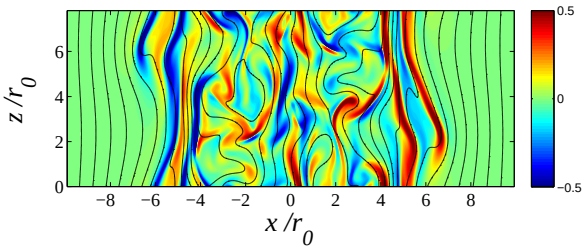

(b) $t = 23.48\,T_i = 10.56\,T = 239.6\,r_0/c = 4.38\,L_x/c_s, \quad \beta_{\min} = 15.4$

Figure 10.19: Vorticity at (a) $16.3\,T_i$ and (b) $23.5\,T_i$
$(M_A, v_{Az}/c, \beta, v_{z0}/c) = (20.7, 0.047, 222, 0.7)$

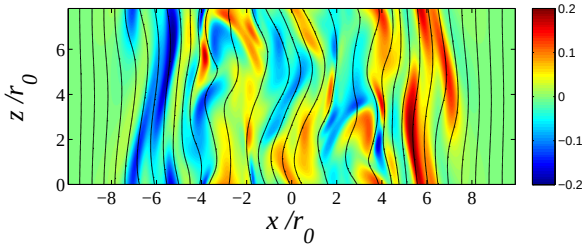

(a) $t = 37.93\,T_i = 17.07\,T = 387.1\,r_0/c = 7.08\,L_x/c_s, \quad \beta_{\min} = 35.9$

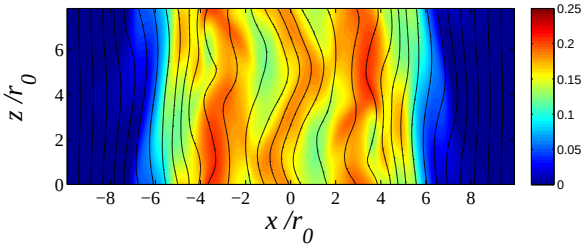

(b) $t = 37.93\,T_i = 17.07\,T = 387.1\,r_0/c = 7.08\,L_x/c_s, \quad \beta_{\min} = 35.9$

Figure 10.20: (a) Vorticity and (b) longitudinal velocity at $t = 37.9\,T_i$
$(M_A, v_{Az}/c, \beta, v_{z0}/c) = (20.7, 0.047, 222, 0.7)$

10.4 Strong Vortex-disruptive Field ($M_A = 10.3$)

We now consider the nonlinear evolution of a strong vortex-disruptive field for which $M_A = 10.34$. Figures 10.21 through 10.23 show the stages of vortex inhibition. Here, vortex disruption is noticeable after 8.5 growth times, i.e., almost immediately after the vortices begin to form (see figure 10.21), and the system has reached an equilibrium filamented state after about 25 growth times (see figure 10.23). The field $M_A = 10.34$ also inhibits magnetic reconnection, which occurs to a minimal extent after about 12 growth times, as the field lines diffuse into the partially-formed vortices (see figure 10.22(a)). The equilibrium jet width is about $12\,r_0$, which is about 3.2 times the initial jet width. The equilibrium flow contains a narrow central region of high flow speed, low density, and width about 1/5 the initial jet width, along with a background flow whose width is about 1.5 times the width of the initial flow (see figure 10.23(b)). We will observe very similar equilibrium flow properties in section 10.5, when we consider a field which is strong enough to suppress vortex formation ($M_A = 5.145$). For this field, equilibrium is reached after about 20 growth times, and the jet only widens to about $8\,r_0$, which is about 2.25 times its initial width.

We now examine the displays for $M_A = 10.34$ in more detail. Figure 10.21(a), at 8.64 growth times, displays the vorticity at the approximate saturation stage in the early nonlinear regime. The partially-formed vortices have already been disrupted by strong magnetic stresses. As these stresses oppose the rotation of the flow, it develops large shear variations where the magnetic tension is greatest, resulting in amplified filaments of high vorticity, and a large amount of electromagnetic energy being extracted directly from the bulk flow, energy that would otherwise be diverted into rotational form. The magnetic stresses also cause

the interiors of the partially-formed vortices to separate into regions of opposite vorticity, resulting in extensive hybridization before the vortices have the opportunity to acquire a well-defined clockwise or counterclockwise vorticity. The field lines have begun to diffuse into the partially-formed vortices. We now proceed to figure 10.21(b), after 10.94 growth times. Maximum vorticity has been reached (after about 10 growth times), along with maximum electromagnetic energy. The filaments of maximum vorticity have thickened. The aforementioned regions of hybrid vorticity, which had permeated the vortical regions, are now compressed by magnetic tension into densely packed hybrid filament layers. The ends of these filaments curl sharply in response to the resistance exerted by magnetic stresses. This high curvature enhances the diffusion of magnetic field lines into the vortical regions, whose vorticity is almost entirely concentrated in the filaments at the boundaries. The jet has broadened to slightly over twice its initial width.

We now proceed to figure 10.22(a), after 13.24 growth times. The electromagnetic and mechanical energy are now being viscously dissipated into thermal energy. As a result, the vorticity has decreased considerably, and correspondingly, the central filaments have been viscously "smeared" into broader, more gradually sheared regions. As the magnetic stresses have decreased, the tips of the outer filaments have lost much of their previous curvature. A portion of densely packed filament became aligned with the central axis after about 12 growth times, and now, this filament is separating into a thick hybrid structure in the central region. A small amount of magnetic reconnection is now visible in the vortical regions into which the field lines have diffused. Note that for a strong field such as this one, the movement of magnetic field lines is dominated not by vortex twisting, but by diffusion, which leads

to much weaker reconnection, if any. The jet has broadened to almost 3 times its initial width. All of these processes signify the transition of the system into a turbulent regime. We now proceed to figure 10.22(b), after 16.70 growth times. The system is now well into the turbulent regime, and the vorticity has continued to decrease as more electromagnetic energy is viscously dissipated. The outer filaments have lost more of their curvature, and are becoming aligned with the flow, signifying the inhibition of the vortices that partially emerged in the early nonlinear regime. The central trunk, however, has spread into a larger central region of curved filaments surrounded by almost circular regions of newly emergent vortical behavior.

Finally, we proceed to figures 10.23(a) and (b), which display the vorticity and longitudinal velocity, respectively, after 27.06 growth times, as the system is approaching an equilibrium state consisting of flow-aligned filaments (note change in vorticity color scale). The filament width is about 1/5 the initial jet width, and the filaments are interspersed with viscously smeared regions of smaller vorticity of the opposite sign. These viscous regions formed at the boundaries of the jet in the early turbulent regime, as seen in figures 10.22(a) and (b). The jet has now broadened to about 3.2 times its initial width, which is its approximate equilibrium width. The flow consists of a narrow central strip of relatively high flow speed of about $0.4\,c$, and whose width is about 1/4 the initial jet width. Surrounding this narrow flow are two vortex filaments, which show that this flow channel has relatively high shear at its boundaries. Also surrounding the flow channel is a background flow whose width is about 1.5 times the initial jet width, and whose flow speed has a nearly uniform value of about $0.2\,c$. This background flow coincides with the central vortical region described in

figure 10.22(b). We will see that in the case of a vortex-suppressing field, the width of this background flow is nearly identical to the initial jet width.

We see that for stronger background fields, the vortices are inhibited at an earlier point in their rotation, and there is therefore less twisting of the field lines, which results in less magnetic reconnection. As the amount of reconnection diminishes, the reconnection that does occur is driven less by vortex twisting and to a greater extent by diffusion of the field lines. With less magnetic reconnection, the turbulent reorganization of the system is less complex, and the transition to a flow-aligned filamented state is more rapid. Apart from more rapid vortex inhibition, stronger fields also result in a suppression of both magnetic reconnection and of the complexity of turbulent breakdown. Correspondingly, for stronger background fields, the filament widths are narrower, and the equilibrium jet widths are narrower. Let W_0 denote the initial jet width, and W_f the equilibrium jet width. For $M_A = 41.4$, $W_f \approx 4.5\,W_0$. For $M_A = 20.7$, $W_f \approx 4\,W_0$. For $M_A = 10.3$, $W_f \approx 3.2\,W_0$. And for the vortex-suppressing field $M_A = 5.15$, $W_f \approx 2.25\,W_0$. These equilibrium widths correspond to an input perturbation wavelength of $7.85\,r_0$. As we will see in chapter 11, the equilibrium width seems to scale with input wavelength for weaker fields, but not for stronger fields.

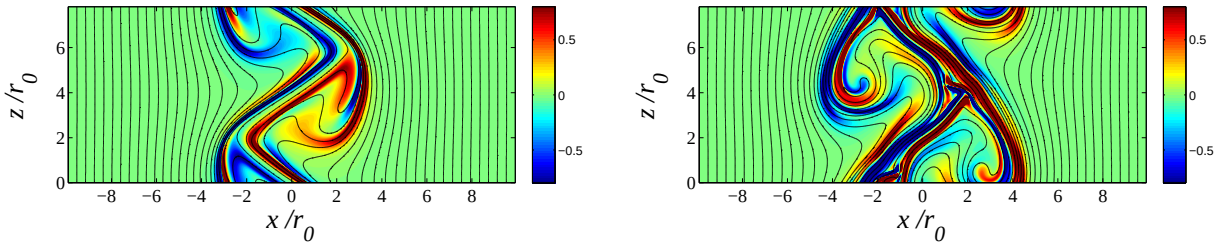

(a) $t = 8.64\,T_i = 4.03\,T = 92.2\,r_0/c = 1.68\,L_x/c_s, \quad \beta_{\min} = 0.87$

(b) $t = 10.94\,T_i = 5.10\,T = 116.7\,r_0/c = 2.13\,L_x/c_s, \quad \beta_{\min} = 2.79$

Figure 10.21: Vorticity at (a) $8.6\,T_i$ and (b) $10.9\,T_i$
$(M_A, v_{Az}/c, \beta, v_{z0}/c) = (10.3, 0.095, 55.5, 0.7)$

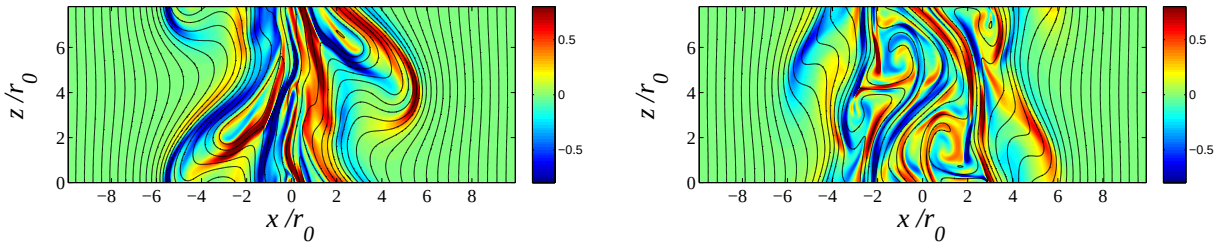

(a) $t = 13.24\,T_i = 6.17\,T = 141.3\,r_0/c = 2.58\,L_x/c_s, \quad \beta_{\min} = 4.05$

(b) $t = 16.70\,T_i = 7.78\,T = 178.2\,r_0/c = 3.26\,L_x/c_s, \quad \beta_{\min} = 5.76$

Figure 10.22: Vorticity at (a) $13.2T_i$ and (b) $16.7\,T_i$
$(M_A, v_{Az}/c, \beta, v_{z0}/c) = (10.3, 0.095, 55.5, 0.7)$

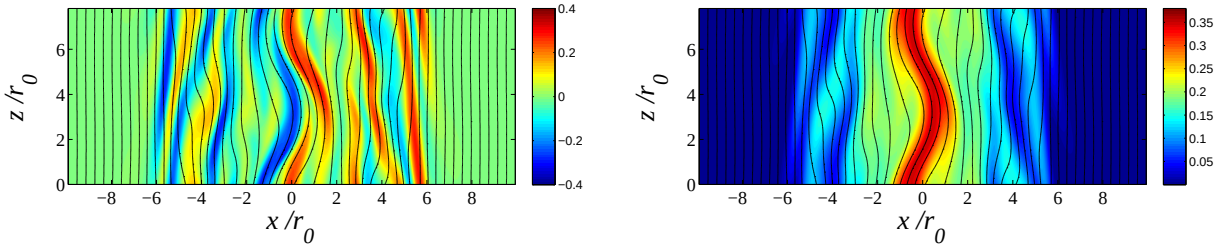

(a) $t = 27.06\,T_i = 12.61\,T = 288.8\,r_0/c = 5.28\,L_x/c_s, \quad \beta_{\min} = 20.9$

(b) $t = 27.06\,T_i = 12.61\,T = 288.8\,r_0/c = 5.28\,L_x/c_s, \quad \beta_{\min} = 20.9$

Figure 10.23: (a) Vorticity and (b) longitudinal velocity at $t = 27.1\,T_i$
$(M_A, v_{Az}/c, \beta, v_{z0}/c) = (10.3, 0.095, 55.5, 0.7)$

10.5 Vortex-suppressing Field ($M_A = 5.145$)

We now consider a magnetic field which is strong enough to suppress vortex formation, which means that M_A is less than about 6. Specifically, $M_A = 5.145$. The input parameters for this case are

$$
\begin{aligned}
v_{z0}(x) &= 0.7\, c\, \mathrm{sech}^2(x/r_0), \\
c_s &= 0.576\, c, \\
(M_A, \beta, v_A/c) &= (5.145,\ 13.88,\ 0.1893): \quad \text{background values}, \\
k_z &= 0.8/r_0, \\
L_x &= 31.5\, r_0, \qquad -L_x/2 \le x \le L_x/2, \qquad 0 \le z \le 2\pi/k_z, \\
N_x &= 1001, \qquad N_z = 201, \\
\Delta t &= 0.032\, r_0/c, \qquad \Delta x = 0.0315\, r_0, \qquad \Delta z = 0.0393\, r_0, \\
L_x/c_s &= 54.7\, r_0/c, \qquad \text{sound transit time}, \\
L_x/v_A &= 166\, r_0/c, \qquad \text{Alfven transit time}, \\
\eta_\rho &= \eta_x = \eta_z = 0.0002\, r_0 c, \\
\eta_{Bx} &= \eta_{Bz} = 0.0012\, r_0 c.
\end{aligned}
\tag{10.7}
$$

The eigenmode parameters, emerging from the numerical linear analysis described in chapter 6, are as follows:

$$
\begin{aligned}
\omega &= (0.265 + i\,0.074)\, c/r_0, \\
\omega_i &= 0.0738\, c/r_0 \;=\; 0.743\, \omega_{i0}, \\
T_i &= 1/\omega_i \;=\; 13.55\, r_0/c, \qquad \text{growth time}, \\
T &= \frac{2\pi}{\omega_r} \;=\; 23.70\, r_0/c.
\end{aligned}
\tag{10.8}
$$

As before, the initial jet width is about $3.6\, r_0$. Figures 10.24 through 10.26 show the suppression of vortex formation, and the rapid transition to a flow-aligned filamented state. As before, each color display (vorticity, current density, and longitudinal velocity) is overlaid with contours of the magnetic field lines. Recall that the current density is the curl of the magnetic field, and is therefore directed in the positive or negative y-direction, perpendicular to the plane of the page. Because the y-axis is directed into the page, where current density is positive (orange or red), the current is directed into the page, and where current density is negative (blue), the current is directed out of the page.

We begin by examining figures 10.24. In figures 10.24 (a) and (b), at 8.62 growth times, we are approximately at the saturation stage of the early nonlinear regime, where vortices would ordinarily develop. However, the magnetic tension resists vortex formation, resulting in filaments of enhanced vorticity and enhanced current density. The translational kinetic energy extracted from the flow is converted mostly into electromagnetic energy, with very little rotational energy, since the vortices fail to form. As shown in figure 10.24(c), this results in a deceleration of much of the flow, in particular, the regions of flow that perform the most work against the magnetic tension in the field lines, i.e., the background flow surrounding a narrow channel of high flow speed.

We continue to examine figures 10.24. There remains a central channel of maximum flow velocity ranging from $0.5\,c$ to $0.6\,c$, whose width is about 1/5 the initial jet width, outside of which the flow speed drops abruptly to an average of about $0.3\,c$. The abrupt shear at the channel boundaries accounts for the central filaments of high vorticity. The outer high-vorticity filaments are produced by an abrupt shear in the background flow. However this background flow is very heterogeneous, varying from about $0.2\,c$ to about $0.35\,c$. The complementarity between vorticity and current filaments arises from the complementarity between the flow and the magnetic field. As seen in figure 10.24(c), the field lines bend in response to the flow, and are concentrated where the flow exhibits rapid shear. This behavior gives rise to a large curl of the field, producing the high-density current filaments seen in figure 10.24(b). Certain field-influenced quantities (vorticity, current density, electromagnetic pressure, etc.) are enhanced by the direct conversion of bulk flow energy into electromagnetic energy. Neither the vorticity in figure 10.24(a) nor the current density in figure 10.24(b) have yet reached their peak values. Both are still increasing.

However, the increase in electromagnetic energy is limited by the complete suppression of vortex formation, since developing vortices would expel the field lines, providing further field amplification at the vortex boundaries. This is why, as seen in the time-dependent graphs in section 9.6 of chapter 9, electromagnetic energy is not maximized for a strong vortex-suppressing field. Rather, vorticity and electromagnetic pressure are maximized for the strongest fields that still allow some vortex formation. This indicates that although the enhancement of these quantities is heavily dependent on mechanical energy extracted directly from the field lines (proportional to the strength of the background field), this enhancement

also has some dependence on field amplification due to vortex-induced centrifugal expulsion of field lines.

We return to the case $M_A = 5.145$, and progress to 13.15 growth times, for which the relevant displays are shown in figures 10.25. The vorticity and current density have already peaked, after about 10 growth times, and are now decreasing, as electromagnetic energy is now being viscously dissipated into thermal energy. From figures 10.25 (a) and (b), the vortex and current filaments have become more closely aligned with the flow, and the jet has widened to about twice its initial width. There are now more filaments of alternating vorticity and alternating current density. The filaments alternate not only in the direction of vorticity (or current density) but also in the magnitudes of these quantities. That is, the vortex filaments in figure 10.25(a) alternate spatially between well-defined, narrow filaments of high vorticity, and less well-defined, viscously "smeared out" filaments of larger width and smaller vorticity in the opposite direction. The same happens with the current filaments in figure 10.25(b). This is a striking manifestation of the viscous dissipation of electromagnetic energy. The more sharply defined filaments have also narrowed, relative to figures 10.24 (a) and (b), from 1/5 of the initial jet width to only about 1/8 the initial jet width. The vorticity is maximized around the narrow central flow region, which has also become more closely aligned with the flow direction. As shown in figure 10.25(c), the flow within this central strip has become more homogeneous, with a nearly uniform flow speed of $0.5\,c$. The background flow surrounding the central strip is still fairly heterogeneous, with flow speeds ranging from $0.2\,c$ to $0.3\,c$.

In figures 10.26, we see that after 21.77 growth times (note change in color scales), the

flow has relaxed to an equilibrium state in which the filaments are aligned with the flow direction, and the jet has further widened to about $8\,r_0$, or 2.25 times its initial width. As shown in figures 10.26(a) and (b), the vorticity and current density are now only about 1/3 of their peak values. The filaments of relatively high vorticity (and current density) are now located at the left and right boundaries, and along the central axis. The enhanced vortex filaments have a width of about $0.6\,r_0$, i.e., 1/6 of the initial jet width, while the current filaments are only about 1/8 the initial jet width. Viscous dissipation has smeared the vorticity in the region between the central axis and the boundaries. This is likely due to the same mechanism discussed in the vortex-disruptive case. In particular, the vorticity has decreased by a factor of about 4, from its initial average value, and is now closer to the frequencies of modes associated with diffusion. The system therefore has a higher correlation with viscous processes, enabling a greater amount of energy transfer via viscous interactions. By comparing figures 10.26(a) and (b), we see that each filament of high vorticity corresponds to a pair of current filaments of alternating current density. A comparison of figures 10.26(a) and (c) shows that filaments of high vorticity correspond to locations of large and abrupt shear variation in the flow.

As shown in figure 10.26(c), the flow speed within the narrow central flow remains at a uniform value of $0.5\,c$. Since its formation in the early nonlinear regime, this central flow region has maintained a nearly constant width of about $0.7\,r_0$, or 1/5 the initial jet width, and corresponds to a narrow region of low density (i.e., a density undershoot, which we also observed in the vortex-disruptive case, but with a wider flow). Similar density undershoots were observed in the MHD simulation of Frank et al. (1996) and the RMHD simulation of

Mignone et al. (2009). This narrow central flow region occurs for stronger fields ($M_A = 5.145$ and $M_A = 10.3$), and is a consequence of the field lines having sufficient magnetic tension to extract large amounts of electromagnetic energy directly from the translational kinetic energy of the flow, without allowing more of this energy to be diverted into the rotational kinetic energy of developing vortices. Surrounding this narrow central flow is a region in which the flow speed is about $0.3\,c$ and whose width is very nearly equal to the initial flow width (about $3.6\,r_0$). The background flow is also much more homogeneous than at earlier times. These same flow properties are also observed in the equilibrium state of the strongly vortex-disruptive field $M_A = 10.3$ (see figure 10.23). As with the weaker vortex-disruptive fields, the system has relaxed to an equilibrium configuration which retains a memory of its initial configuration. In the initial jet, and the equilibrium configurations of vortex-disruptive and vortex-suppressing fields, we have vortex filaments of positive vorticity to the right of the axis, and filaments of negative vorticity to the left of the axis, along with flow velocity falling off with distance from the central axis, asymptotically approaching zero. However, unlike the vortex-disruptive case $M_A = 41.4$, the relaxation to equilibrium occurs after about 20 growth times, whereas in the $M_A = 41.4$ case, equilibrium still has not been reached after 60 growth times. There is also greater enhancement of vorticity, along the axis and at the boundaries, for the vortex-suppressing case than the vortex-disruptive cases. Only the vortex-suppressing case, and the strongly vortex-disruptive case $M_A = 10.3$, contain a narrow central region that retains high flow speed. Only the vortex-suppressing case develops a background flow region of uniform flow speed whose width very nearly coincides with the width of the initial jet, as shown in figure 10.26(c).

We see that maximum flow deceleration, from $0.7\,c$ to about $0.2\,c$, occurs for the intermediate vortex-disruptive fields $M_A = 41.4$ and $M_A = 20.7$, whereas the stronger fields only decelerate the jet to about $0.4\,c$ ($M_A = 10.3$) or $0.5\,c$ ($M_A = 5.13$). The intermediate vortex-disruptive fields allow a sufficient amount of vortex development to result in a complex reorganization process associated with vortex disruption, partly driven by extensive magnetic reconnection. This maximizes the complexity and number of smaller-scale structures arising from turbulent breakdown, which in turn enhances the amount of correlation with the small length scales set by diffusion. This maximizes the viscous dissipation of mechanical energy into thermal energy. We also discussed this in section 9.5 of chapter 9, in which we saw this effect in plots of pressure and velocity-related quantities as functions of time.

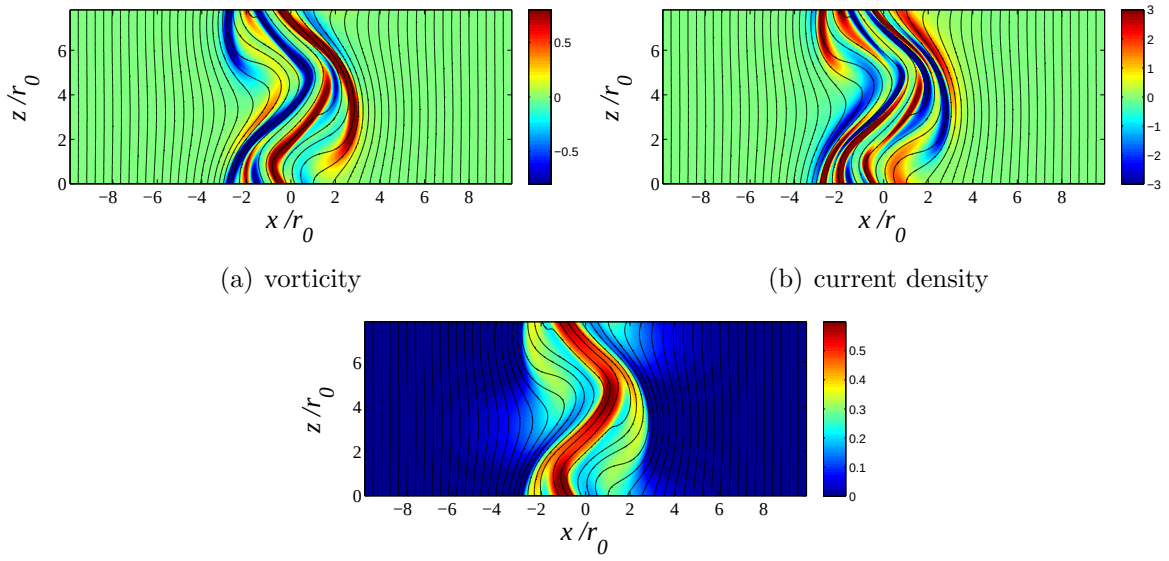

(a) vorticity

(b) current density

(c) longitudinal velocity

Figure 10.24: Various quantities at $t = 8.62\,T_i = 4.93\,T$, $M_A = 5.15$
$(M_A, v_{Az}/c, \beta, v_{z0}/c) = (5.15, 0.189, 13.9, 0.7)$, $\quad \beta_{\min} = 1.62$

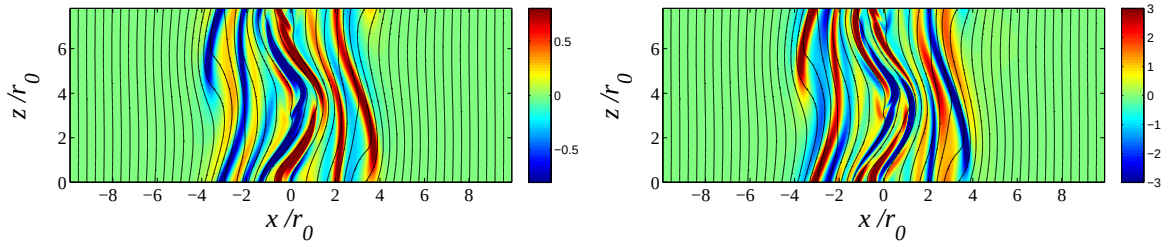

(a) vorticity (b) current density

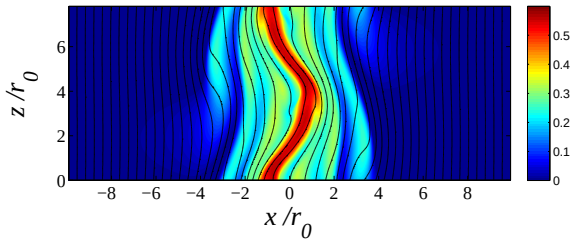

(c) longitudinal velocity

Figure 10.25: Various quantities at $t = 13.2\,T_i = 7.52\,T$, $M_A = 5.15$
$(M_A, v_{Az}/c, \beta, v_{z0}/c) = (5.15, 0.189, 13.9, 0.7)$, $\quad \beta_{\min} = 3.97$

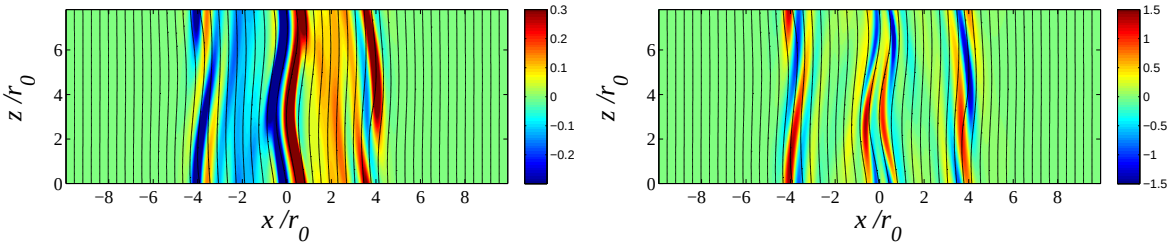

(a) vorticity (b) current density

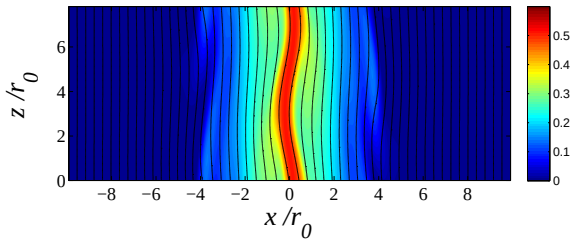

(c) longitudinal velocity

Figure 10.26: Various quantities at $t = 21.8\,T_i = 12.5\,T$, $M_A = 5.15$
$(M_A, v_{Az}/c, \beta, v_{z0}/c) = (5.15, 0.189, 13.9, 0.7)$, $\quad \beta_{\min} = 8.75$

10.6 Evolution with Periodic Boundary Conditions

The evolution we have shown retains longitudinal periodicity, with one spatial period equal to one wavelength of the perturbation, and these results are independent of the number of longitudinal wavelengths spanned by the simulation. We wish to relate our temporal progression of longitudinally periodic snapshots to a single image of an entire jet. A good example of such an image is shown in figure 10.27, taken from Van Dyke (1982), in which an axisymmetric jet is formed from a laminar stream of air being injected into a circular tube. This jet becomes Kelvin-Helmholtz unstable due to the interaction of its boundaries with the ambient medium, leading to the formation of vortices, followed by turbulent breakdown. Note that the vortices in this image are symmetric, whereas the vortices in our simulations are antisymmetric. This is a consequence of our use of a slab geometry, in which symmetric modes are more stable. In a cylindrical geometry, as with the air stream in figure 10.27, symmetric modes have higher growth rates. The jet in figure 10.27 is, of course, unmagnetized, non-relativistic, and not astrophysical, and therefore evolves according to different mechanisms than are being considered in our models. However, the image provides a good illustration of how to combine a sequence of spatially periodic snapshots, shown at a sequence of times, into a single image of the entire jet, comprising all time steps. As our simulation progresses, our simulation box moves along the jet, away from its point of origin. This is the relationship we should keep in mind when, in section 10.7, we suggest potential applications of our simulation results to images of astrophysical jets, each of which shows a snapshot of an entire jet.

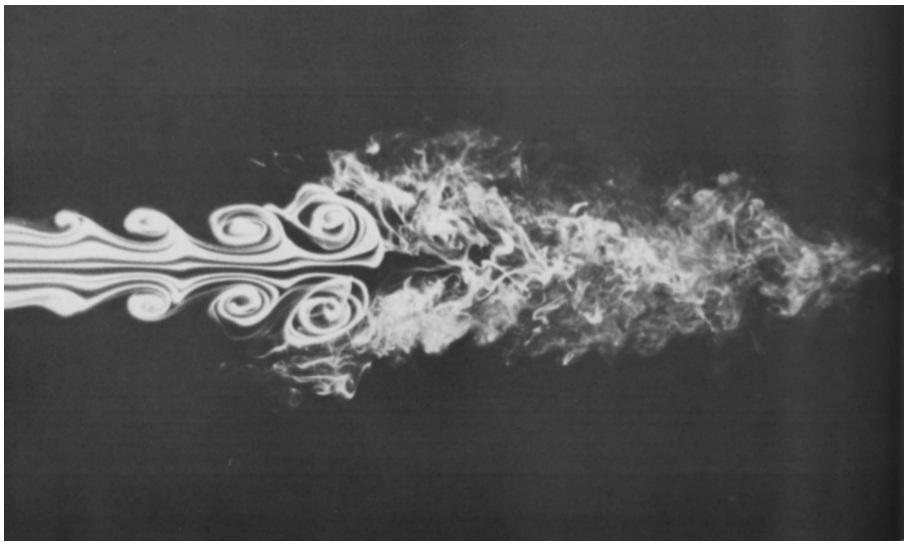

Figure 10.27: Laminar stream of air, Van Dyke (1982)

10.7 Comparison with Jet Observations

In this section we offer potential applications of our simulation results to jet observations. However, we do not make any claims as to the accuracy or completeness of our model in describing the physical mechanisms behind any of the jets mentioned. Other mechanisms (e.g., radiative cooling, jet precession) are undoubtedly present.

Several extragalactic jets show qualitative agreement with vortex formation, followed by vortex inhibition by a disruptive magnetic field (including M87, Centaurus A, 3C 120, 3C 273, HH 30, HH 49, etc.). Closer to the nucleus, we often observe features resembling vortices. This is often followed by a disruptive stage in which these features break into smaller-scale structures, qualitatively resembling vortex disruption and turbulent breakdown. Filaments are observed in such jets as M87 (Hines et al. 1989), 3C 273 (Lobanov and Zensus 2001) and 3C120 (Hardee 2003, 2005). These might be produced by vortex-shedding during the

disruptive stage, or might be associated with the dual filamentary structure connecting the vortices throughout their development. Many images also show significant jet widening, consistent with the widening observed in the simulations. In the outer regions of the jet, this widening seems to be coupled with the viscous dissipation and flow deceleration also observed in the simulations. Note that for the model we are using, a magnetic field is required in order to qualitatively reproduce these observed features. In particular, the field should be vortex-disruptive, and not vortex-suppressing, since the features are closely correlated with the stages of vortex inhibition. In the absence of a magnetic field, the simulation predicts that the vortices persist almost indefinitely.

Figure 10.28 shows three images of the extragalactic radio jet M87, also known as Virgo A, and NGC 4486. The X-ray image is produced by Chandra, the radio image by the VLA (Very Large Array), and the optical image by the Hubble Space Telescope. M87 is a highly energetic plasma jet extending 1.5 kpc, and which emanates from a supermassive central black hole in a supergiant elliptical galaxy. As in our simulations, the background magnetic field is believed to be primarily aligned with the flow (Hines et al. 1989). However, in certain knots (i.e., knot A and knot C), the field is believed to be primarily transverse to the flow (Hines et al. 1989), which might be consistent with vortex-twisting of field lines within these knots, resulting in field amplification. Stawarz et al. (2005) estimated an amplified field of at least 300 μG within knot A, where the field elsewhere in the jet is believed to be less than about 100 μG (Hines et al. 1989). So the knots may indeed behave like vortices, twisting the magnetic field lines into partially transverse configurations, and centrifugally expelling them to the vortex extremities, resulting in field amplification. As shown in section 8.2 of chapter

8, the above magnetic fields yield a conductivity, governed by electron and ion gyrations, which is consistent with the magnetic viscosity used in the simulations. Furthermore, the field outside the knots is believed to be aligned with the flow (Hines et al. 1989), which is the equilibrium, and background, field configuration used in our numerical simulations.

Figure 10.29 shows the extragalactic jet Centaurus A, which is the only extragalactic jet closer to us than M87. Figure 10.30 shows the mildly relativistic jet HH30 (Herbig-Haro 30). The Herbig-Haro objects are within our own galaxy, and most likely arise from protostellar systems. These are much less relativistic than the aforementioned extragalactic jets. As with the images of M87, these images show features which indicate possible vortex disruption, turbulent breakdown, jet widening, and viscous dissipation, all of which would be consistent with the stages of vortex inhibition by a vortex-disruptive field.

It should be emphasized that these comparisons only suggest possible physical mechanisms that might offer insight into the observed jet features. Other mechanisms (radiative cooling, etc.) are undoubtedly present. Another important point is that the field strengths examined in our study are separated by roughly an order of magnitude, which falls well within the uncertainty in estimates of field strength in astrophysical jets. These estimates are obtained from synchrotron emission observations.

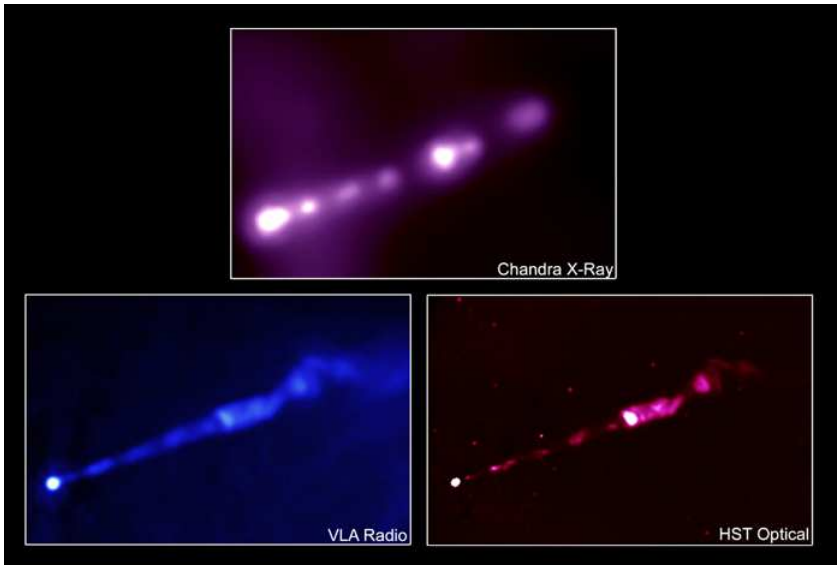

Figure 10.28: M87 (a.k.a. Virgo A, NGC 4486)

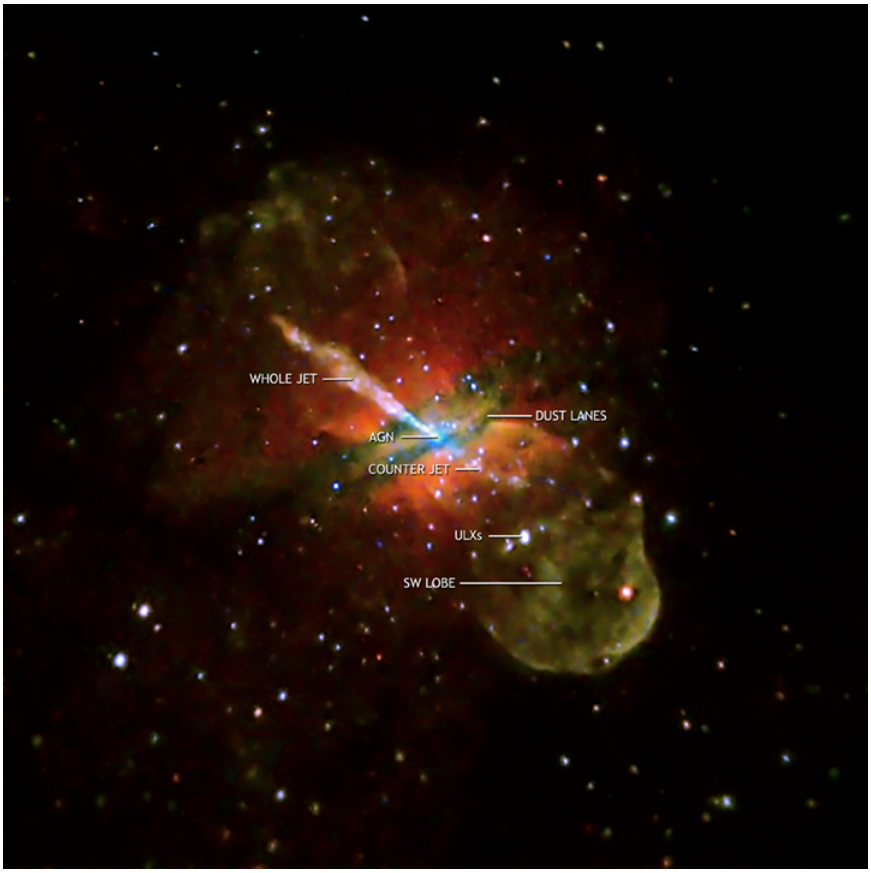

Figure 10.29: Centaurus A, imaged with Chandra in X-ray

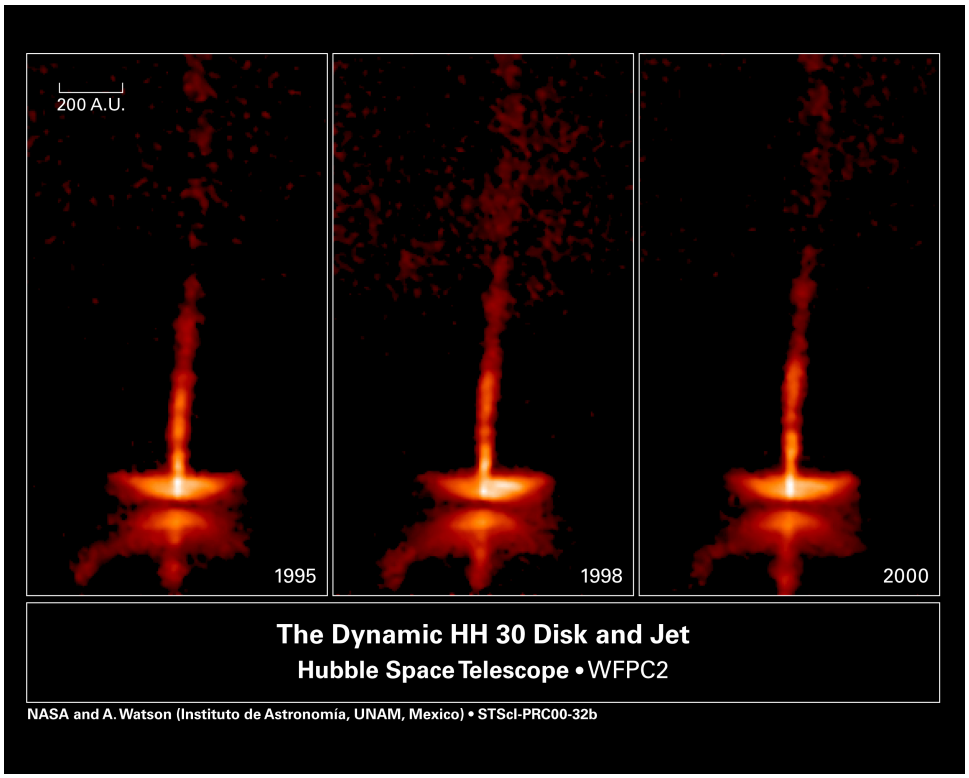

Figure 10.30: Herbig-Haro 30

10.8 RMHD Versus MHD Results

These relativistic MHD simulation results are qualitatively similar within a range of moderately relativistic flow speeds from $0.5\,c$ to $0.8\,c$. However, when compared with MHD simulations (non-relativistic flow speeds and sound speeds), there are certain differences. The growth rates are considerably lower in the MHD case, owing partly to the much smaller sound speed, for which the rest energy density ρc^2 is much larger than the pressure, so that the background flow has considerably more inertia against extraction of energy from the bulk flow. Another effect, particularly for more relativistic sound speeds, is that growth rate tends to increase with flow speed, due to the increase in velocity shear between the jet and ambient medium (seen in the linear growth rate analysis of chapter 6). However, for highly relativistic flow speeds, the system is KH-stable, though other instabilities emerge. RMHD simulations also produce nonlinear transverse sound waves propagating between the jet axis and transverse boundaries, and the amplitude of these waves increases with increasing flow speed, creating large-amplitude oscillations in the time-dependence of certain quantities (discussed in chapter 9). We have seen, particularly for the unmagnetized RHD case, how these waves modulate vortex rotation, for which the rotational period is approximately the sound transit time. In the magnetized cases, these waves influence vortex rotation and orientation prior to disruption. In sections 11.3 through 11.5 of chapter 11, we show that these acoustic waves do not significantly influence the evolution of the flow. In the MHD case, these nonlinear sound waves, if present, have much smaller amplitudes.

Relativistic effects also introduce a desynchronization between longitudinal and transverse motions, where relativistic boosting exerts a strong preference in the longitudinal di-

rection. This has the effect of destabilizing the system. In the simulation results, relativistic desynchronization tends to introduce more complexity into vortex disruption and turbulent breakdown, particularly in the weak-field regime. This occurs because modes with smaller wavelengths emerge (see discussion in chapter 6), so that smaller length scales emerge in the hybrid features arising from vortex disruption. Due to the emergence of smaller length scales, a considerably larger amount of diffusion is required in order to stabilize relativistic systems than non-relativistic ones. Above a Lorentz factor of about 2, no amount or combination of diffusion can stabilize the system. Modes with small wavelength can also give rise to shock-like phenomena, which are more frequently observed in more relativistic simulations. As we will see in chapter 11, the RMHD and MHD regimes are convergent in the limit of non-relativistic flow speeds and sound speeds.

We see that even in the moderately relativistic regime, for which numerical simulations can be sustained, relativistic effects destabilize the system through nonlinear sound waves, desynchronization of longitudinal and transverse motions, and modes with small length scales. These effects are enhanced for more relativistic flows, leading to unconditional instability for Lorentz factors exceeding about 2.

We now examine the alternating symmetry of the vorticity displays of our simulation results.

10.9 Alternating Symmetry of the Vorticity

We notice throughout our vorticity displays that the vorticity satisfies a certain condition of alternating symmetry, which is dictated by the symmetry of the background velocity

profile and the antisymmetry of the pressure perturbation profiles. Specifically, we have equal and opposite vorticity on either side of the central axis at locations separated by half the longitudinal perturbation wavelength. If we denote the vorticity $\Omega(x, z, t)$, then mathematically, this condition reads

$$\Omega(x, z, t) \;=\; -\Omega(-x, z + \lambda/2, t). \tag{10.9}$$

where $\lambda = 2\pi/k_z$ is the wavelength of the input perturbation. This condition is a mathematical interpretation of the half-wavelength separation of counter-rotating vortices that form in the early nonlinear evolution, but is maintained throughout the evolution, in both the magnetized and unmagnetized cases. The accuracy with which this condition is satisfied provides a measure of the numerical accuracy of our results. Specifically, we compute the ratio

$$f \;=\; \frac{|\Omega(x, z, t) + \Omega(-x, z + \lambda/2, t)|}{|\Omega(x, z, t)|}. \tag{10.10}$$

The average value of this ratio is roughly 10^{-5} during the nonlinear evolution of a magnetized case. This provides one method of validation of the numerical accuracy of our simulations, which we will verify in other ways in chapter 11.

10.10 Conclusion

We have explored the nonlinear evolution of the simulations in the unmagnetized and magnetized cases, and found qualitative agreement between observations of several jets and the stages of vortex inhibition associated with vortex-disruptive magnetic fields (including M87, Centaurus A, 3C 120, 3C 273, HH 30, etc.). In the unmagnetized case, we found that upon

saturation of the perturbations, the transverse momentum has built to a point where the flow is deformed due to transverse components of the mechanical stresses. The growth of this deformation, along with the interaction of comparable transverse and longitudinal momentum, lead to the formation of two large counter-rotating vortices on opposite sides of the jet axis. These vortices are connected by a dual filamentary structure, and form around regions of low density and pressure. Initially driven by mechanical torques, the vortices rotate in the same direction as fluid circulation within them. However, the flow decelerates as mechanical energy is dissipated into thermal energy. Correspondingly, some of the mechanical stress is replaced by thermal stress. Consequently, the vortex rotation is eventually modulated by thermal stresses associated with nonlinear transverse sound waves propagating between the jet axis and transverse boundaries. In the latter stages of the nonlinear regime (after about 20 growth times), the vortex rotation has relaxed to a constant angular velocity whose rotation period is equal to the sound transit time. The buildup of thermal stresses also causes the vortices to become less elongated, and assume a more circular shape. The vortices are also separated, along the flow direction, by half the perturbation wavelength, which is a consequence of the antisymmetry of the pressure perturbation profile, and the symmetry of the transverse velocity profile, discussed in chapter 7. Apart from viscous losses, the vortices persist essentially indefinitely. Although intermediate vortex shape and rotation are influenced by reverberations of acoustic waves from the transverse system boundaries, we show in section 11.5 of chapter 11 that most aspects of the unmagnetized evolution are unaffected by system width.

When the system is magnetized, the vortices are inhibited through a series of stages,

namely, field amplification, vortex disruption, turbulent breakdown, and approach to an equilibrium state. These stages have been discussed in prior literature for MHD flows (Malagoli et al. 1996; Baty et al. 2003, etc.). We have examined in detail how and to what extent these stages manifest in the RMHD regime for a set of representative field strengths. These field strengths are within an order of magnitude of one another, which falls within the uncertainty in estimates of field strengths in astrophysical jets. We have found that the influence of the magnetic field is closely correlated with a relativistic version of the Alfvenic Mach number M_A, which we have defined analogously to how Bodo et al. (2004) defined a relativistic version of the sonic Mach number. This close correlation with M_A is shown in the linear analysis in chapter 6 and in the nonlinear evolution in chapter 11. Our expression for M_A is given by (6.3) in chapter 6.

We first examined a weak vortex-disruptive field corresponding to $M_A = 41.4$, which allows vortex formation, and then inhibits the vortices through a series of stages. In stage 1, field amplification occurs when the field lines are centrifugally expelled to the vortex boundaries. In stage 2, the field disrupts the vortices, resulting in further deformation due to magnetic stresses, and vortex shedding of amplified hybrid filamentary features. In stage 3, the vortices undergo turbulent breakdown into smaller-scale structures. In stage 4, the system relaxes to an equilibrium state consisting of flow-aligned vortex and current filaments. The width of these filaments is about 1/4 the initial jet width. Similar stages of vortex inhibition were described in Baty et al. (2003), Malagoli et al. (1996), and Bucciantini and Del Zanna (2006).

Throughout the evolution, there is remarkable complementarity between the flow and

the field lines, which is partly due to the fact that the transverse velocity and field both have symmetric perturbation profiles, while the longitudinal velocity and field both have antisymmetric perturbation profiles. This complementarity is seen in the displays, in which the contours of the magnetic field lines correspond closely to the vorticity and flow velocity distributions onto which they are overlaid. This complementarity describes the close interaction between the field and the flow, whereby the mechanical energy of the flow initially drives the field, seen in vortex-induced amplification and twisting of the field lines. In response, the field constrains the flow through electromagnetic stresses, resulting in vortex deformation and disruption. Vortex rotation also leads to magnetic reconnection, which in turn enhances the turbulent breakdown, and viscous dissipation, of the faster-moving components of the flow.

For the weak vortex-disruptive field $M_A = 41.4$, the jet widens to about 4.5 times its initial width, and decelerates from flow speed amplitudes of $0.7\,c$ to about $0.2\,c$. During stages 1 and 2, vortex-twisting of the field lines leads to considerable magnetic reconnection, which drives much of the complexity of the turbulent breakdown, along with persistent vortical behavior in the central region, where the flow is fairly uniform. For stronger vortex-disruptive fields, these stages of vortex inhibition occur more rapidly, and at earlier times in the simulation. Stronger fields also correspond to less magnetic reconnection, and less widening of the jet. In the later stages of evolution, particularly with weaker fields, the nonlinear features have boundaries which are less sharply defined, indicating that viscosity has more of an effect on the system. At least two factors are involved. First, turbulent breakdown results in structures with smaller length scales, which are therefore more compa-

rable to the length scales set by diffusion. Second, the vorticity decreases by a factor of at least 5, from its maximum value, and is therefore more comparable to frequencies of modes associated with diffusion. These two factors lead to a higher correlation with diffusive processes, and therefore a larger transfer of energy to viscous dissipation. We then considered a vortex-suppressing field ($M_A = 5.145$) which is strong enough to suppress vortex formation, resulting in a rapid transition to a filamented flow-aligned state. The filaments are only 1/6 of the initial jet width, and the equilibrium jet width is about 2.25 times its initial value. Both of these are smaller than the corresponding values for the weaker field $M_A = 41.4$.

After complete vortex-disruption, small-scale turbulent structures are influenced to some extent by reverberations of acoustic waves from the transverse boundaries of the system. However, in sections 11.3 through 11.5, we compare nonlinear evolution for two transverse system widths at different magnetic field strengths, and find that the system width does not significantly influence the evolution of the flow and the manner in which it interacts with the magnetic field. Furthermore, these nonlinear acoustic oscillations are suppressed by fields which are strong enough to suppress complex turbulent reorganization.

We also observed that weaker fields allow further vortex twisting of the field lines, leading to a greater amount of magnetic reconnection, which in turn drives a more complex turbulent reorganization of the system, leading to intermediate states that persist for many growth times before the filaments finally become aligned with the flow. Stronger fields, which allow less vortex twisting, exhibit less reconnection, and this reconnection is instead dominated by diffusion of the field lines. Stronger fields therefore suppress intermediate turbulence.

Maximum flow deceleration (from $0.7\,c$ to about $0.2\,c$) occurs for intermediate vortex-

disruptive fields $M_A = 41.4$ and $M_A = 20.7$. This field regime allows enough vortex development, and disrupts the vortices rapidly enough, to generate a complex turbulent breakdown, partly driven by extensive magnetic reconnection, thereby maximizing viscous dissipation into thermal energy (also driven in part by the two factors mentioned above, namely, closer correlation with length scales and frequencies associated with diffusion). We discussed this in section 9.5 of chapter 9, in which we saw this effect in graphs of pressure and velocity-related quantities as functions of time. On the other hand, the largest field-related quantities (i.e., the highest electromagnetic energy, vorticity, etc.) are generated for the strongly vortex-disruptive field $M_A = 10.3$, not the vortex-suppressing field $M_A = 5.145$. Apart from the size of the background field, whereby the tension in the field lines extracts energy directly from the flow, some vortex-induced field amplification is required for optimum field enhancement. We also discussed this in section 9.6 of chapter 9, in which we saw that strongly vortex-disruptive fields correspond to maximum amplification of such quantities as vorticity and electromagnetic energy. We have therefore identified two fundamental bifurcations in field behavior, arising from maximization of two sets of quantities at two different intermediate field strengths. These are, specifically, maximum viscous dissipation for intermediate vortex-disruptive fields ($20 \leq M_A \leq 42$), and maximum enhancement of field-related quantities for strong fields that still allow vortex formation ($M_A \approx 10$).

The intermediate vortex-disruptive fields $M_A = 41.4$ and $M_A = 20.7$ have wide equilibrium flow widths (about twice the initial jet width), which is correlated with the maximum jet deceleration observed for these cases. Equilibrium flow width is smaller for stronger background fields, due to more rapid longitudinal filament alignment by the magnetic tension.

The stronger fields $M_A = 10.3$ and $M_A = 5.145$, on the other hand, each have equilibrium states with a narrow central channel of relatively high flow speed, and low density (flow speed of about $0.4\,c$ to $0.5\,c$, and width about 1/5 the initial jet width). The narrow central flow is correlated with early vortex inhibition due to high magnetic tension. Stronger fields suppress intermediate turbulence, and viscous dissipation of mechanical energy. The aforementioned narrow central flow channel is where this residual mechanical energy resides. In each regime of field strength, the vorticity, flow, and field assume equilibrium configurations which indicate that the system has retained a memory of its initial configuration (also seen in the MHD analyses of Frank et al. 1996 and Ryu et al. 2000). For the vortex-suppressing field $M_A = 5.145$, this central flow is surrounded by a background flow whose width is very nearly equal to the initial jet width. This indicates that in the vortex-suppressing case, the system retains not only a qualitative, but also a quantitative, memory of its initial configuration.

These relativistic MHD simulation results are qualitatively similar for moderately relativistic flow speeds from $0.5\,c$ to $0.8\,c$. However, when compared with MHD simulations (non-relativistic flow speeds and sound speeds), there are certain differences, each of which illustrate how relativistic effects tend to destabilize the system. The growth rates are considerably higher in the RMHD case, due partly to the larger shear in flow speed between jet and ambient medium, and partly to the larger (more relativistic) sound speed, which gives the bulk flow less inertial resistance to perturbation. It should be noted, however, that the system is linearly less KH-unstable in the highly relativistic regime, although other instabilities emerge. RMHD simulations also produce large-amplitude nonlinear transverse sound waves propagating between the jet axis and transverse boundaries, and the amplitude

of these waves increases with increasing flow speed, creating large-amplitude oscillations in the time-dependence of certain quantities (discussed in chapter 9). These effects are much less visible in MHD simulations.

Relativistic effects also desynchronize longitudinal and transverse motions, due to preferential boosting in the longitudinal direction. This destabilizes the system. In simulations for weak fields, relativistic desynchronization introduces more complexity into vortex disruption and turbulent breakdown. This is the result of modes with smaller wavelengths (see chapter 6), so that hybrid features with smaller length scales arise from vortex disruption. Due to the emergence of smaller length scales, a greater amount of diffusion is required to stabilize relativistic systems than non-relativistic ones. Above a Lorentz factor of about 2, no amount or combination of diffusion can stabilize the system. Modes with small wavelength can also give rise to shock-like phenomena, which are more frequently observed in more relativistic simulations. We will show in chapter 11that the RMHD and MHD results exhibit the expected convergence.

We have observed qualitative agreement with numerous jet observations, including M87, Centaurus A, 3C 120, 3C 273, HH 30, and HH 49. These jets contain features resembling vortices and filamentary features, and appear to exhibit turbulent breakdown, jet widening, and jet deceleration. In particular, some of the knots in the extragalactic radio jet M87 are believed to contain amplified fields (Stawarz et al. 2005) with transverse components (Hines et al. 1989). This suggests possible vortex-like behavior in these knots, which would result in field amplification due to vortex expulsion of the field lines as they are twisted into transverse configurations. This behavior is probably most consistent with a weakly vortex-disruptive

field ($M_A = 41.4$). Furthermore, the field outside these knots is believed to be aligned with the flow (Hines et al. 1989), which is the equilibrium (and background) field configuration in our simulations. In addition, Hines et al. (1989) deduced field strengths of less than 100 μG, which, as shown at the end of chapter 8, are consistent with conductivities corresponding to the magnetic viscosity used in our simulations. This assumes that the conductivity emerges from electron and ion gyration. While we may have found possible mechanisms underlying these jet observations, other mechanisms are undoubtedly present (radiative cooling, etc.).

Finally, in section 10.9, we verified that the vorticity has an alternating symmetry, which is due to the symmetric background velocity profile and the antisymmetric pressure perturbation profiles. This provides one method of validation of the accuracy of our simulation. Another was to determine the accuracy with which certain quantities are conserved, which we did in table 9.1 of chapter 9. In chapter 11, we will use other methods of examining the accuracy and reliability of our results.

We have studied the basic properties of the simulation results in various regimes of magnetic field strength, and seen how our simulations reproduce certain observed features and behavior in various astrophysical jets. In chapter 11, we examine the parameter-dependence of these results. This includes spatial and temporal convergence, convergence between the RMHD regime and the MHD and RHD regimes, and sensitivity to viscosity, flow speed, and perturbation wavelength.

Chapter 11

Sensitivity of Results to Input Parameters

Having examined various plots and displays of our simulation results, we now examine the sensitivity of these results to various input parameters. We first verify that, to within reasonable accuracy, the magnetic field remains divergenceless throughout the evolution. We then examine convergence with respect to time step, with a fixed spatial grid, and find that the results have indeed converged temporally. We next examine convergence with respect to refinement of the numerical mesh. We find that the results are not yet converged for a 501x101 mesh, but, upon comparison between this, the 751x151 mesh, and the 1001x201 mesh, we find that the results show good convergence through the early stages of nonlinear evolution, and in the later stages show good agreement in terms of the nature of the behavior. They deviate from one another in the latter stages of evolution in terms of the small-scale structures emerging from turbulent breakdown. However, we observe convergence in the turbulent evolution on larger scales.

We next consider the dependence of the simulation results on the transverse width of the system, which, as we have seen, influences the oscillations of transverse acoustic waves.

We compare results for two different system widths for both magnetized and unmagnetized cases. In the magnetized case, we find that the results are almost identical through the vortex-disruptive stage, and then, after about 16 growth times, begin to show differences in the small-scale features emerging in the turbulent regime. However, the large-scale structure of the flow, and its interaction with the magnetic field, are not significantly affected by system width, in either the turbulent regime or the approach to equilibrium. In the unmagnetized case, the evolution is nearly identical through the early nonlinear stages, through about 16 growth times. The nonlinear acoustic waves then exert an influence on vortex shape and rotation rate. However, numerous properties of the flow are unaffected by system width, including the sizes and transverse locations of primary and secondary vortices, average pattern speeds, and the ellipsoidal shape to which the primary vortices eventually relax. There is also close agreement, between the two system widths, in the time-dependence of various spatially-averaged or maximized quantities, including flow speed and electromagnetic energy. This collectively demonstrates that, for magnetized and unmagnetized systems, the evolution of the flow and magnetic field are not significantly influenced by the transverse boundaries of the system. The nonlinear evolution also is not affected when we change the number of wavelengths of the perturbation spanned in the longitudinal direction. Therefore, the evolution is approximately convergent with respect to time step, spatial step, and transverse and longitudinal system dimensions.

We next consider an RMHD case with a low flow speed and low sound speed, which is approximately non-relativistic. We compare results generated with the MHD source code to those generated with the RMHD source code, and find excellent convergence, thereby

demonstrating convergence between the RMHD and MHD regimes in the non-relativistic limit. We then demonstrate convergence between the RHD and RMHD regimes by comparing an unmagnetized and a weakly magnetized case, both having the same relativistic flow speed.

We examine sensitivity to magnetic viscosity (resistivity) and to momentum viscosity for several different field strengths ($M_A = 41, 21$, and 5). We find general agreement in the time-dependence of various quantities, and that increasing momentum viscosity tends to reduce quantities related to flow velocity, while increasing magnetic viscosity tends to reduce quantities related to the magnetic field. There is good qualitative agreement between the displays corresponding to different viscosities, with deviations in the turbulent regime, although the equilibrium jet width seems to be unaffected by viscosity. However, in the $M_A = 41$ case, the equilibrium central flow width is narrower in the case with higher magnetic viscosity. For a given value of M_A, we compare results for background flow speed amplitudes of $0.7\,c$ and $0.5\,c$, juxtaposing displays corresponding to a given number of growth times. We find good agreement, indicating that the relativistic Alfvenic Mach number M_A is indeed closely correlated with the extent to which the magnetic field influences the evolution, and also that the growth time is a fundamentally important unit for characterizing the temporal progression of the evolution.

We then examine the sensitivity of the results to the input wavelength of the perturbation. We find that for a weaker field ($M_A = 41$), the equilibrium jet width is equal to roughly twice this wavelength, and the equilibrium flow width is slightly larger than one wavelength (which is to say that both of these are proportional to the input wavelength). For the stronger field ($M_A = 5$), the equilibrium jet width is approximately 4 times the initial width, independent

of the wavelength, while there is an amplified central flow whose width is about 1/10 of the wavelength. Quantities related to the magnetic field are larger for longer wavelengths, for both field strengths. However, quantities related to flow velocity are smaller for longer wavelengths at $M_A = 41$, and larger for longer wavelengths at $M_A = 5$. We will examine these trends in terms of length scales set by viscous dissipation.

We demonstrate in this chapter that the magnetic field remains divergenceless, and that our results are convergent with respect to such parameters as time step, spatial step, system dimensions, viscosity, and between the RHD, MHD, and RMHD regimes.

Throughout this chapter, we make use of the following quantities. The influence of the magnetic field is characterized by the relativistic Alfvenic Mach number, given by

$$M_A \;=\; \frac{v_{z0}\gamma}{v_{Az,0}\gamma_A} \;=\; \frac{v_{z0}}{v_{Az,0}}\sqrt{\frac{1-v_{Az,0}^2/c^2}{1-v_{z0}^2/c^2}}, \tag{11.1}$$

where v_{z0} is the amplitude of the background flow speed, $v_{Az,0}$ is the background relativistic Alfven speed, and γ and γ_A are the respective Lorentz factors. The Alfven speed is given by

$$v_{Az} \;=\; (c)\frac{B_z}{\sqrt{w}} \;=\; \frac{B_z}{\sqrt{\rho + (P/c^2)\Gamma/(\Gamma-1)}}, \tag{11.2}$$

where Γ is the adiabatic index, generally assumed to be 4/3, owing to the sound speed, in most cases, being approximately at its relativistic maximum value of $c/\sqrt{3}$. w is the enthalpy. The aforementioned relativistic adiabatic sound speed is given by

$$c_s \;=\; c\sqrt{\frac{\Gamma P}{w}} \;=\; \sqrt{\frac{\Gamma P}{\rho + (P/c^2)\Gamma/(\Gamma-1)}}. \tag{11.3}$$

We begin by demonstrating that the magnetic field remains divergenceless throughout the simulation.

11.1 Zero Divergence of Magnetic Field

We verify that as the simulations progress, the magnetic field remains divergenceless, so that the solenoidal condition is preserved. Because the magnetic field is restricted to the $x-z$ plane, its divergence is given by

$$\boldsymbol{\nabla}\cdot\mathbf{B} \;=\; \frac{\partial B_x}{\partial x}+\frac{\partial B_z}{\partial z}. \tag{11.4}$$

A good measure of satisfaction of the solenoidal condition is to compare the divergence of the field to each of the spatial derivatives on the right side of (11.4). That is, we define the ratios

$$\begin{aligned}\epsilon_x \;&=\; \frac{|\boldsymbol{\nabla}\cdot\mathbf{B}|}{|\partial B_x/\partial x|},\\ \epsilon_z \;&=\; \frac{|\boldsymbol{\nabla}\cdot\mathbf{B}|}{|\partial B_z/\partial z|}.\end{aligned} \tag{11.5}$$

The solenoidal condition is accurately satisfied if $\epsilon_x << 1$ and $\epsilon_z << 1$. For $c_s = 0.576\,c$ and $v_{z0} = 0.7\,c$, and for several field strengths (values of M_A) used in our simulations, we present the average and maximum values of ϵ_x and ϵ_z for a series of representative time intervals, in units of the growth time, which is 10 clock times. The averages are performed over the entire spatial grid, and over the indicated time interval. The maximization is performed over regions where $|\partial B_x/\partial x|$ and $|\partial B_z/\partial z|$ are at least 10^{-6} of B_{z0}/r_0, as ϵ_x and ϵ_z can be deceptively large where these spatial derivatives vanish. The results are shown in table 11.1.

These results show that for the field strengths used in the simulation, the divergence of the field is many orders of magnitude lower than either of the spatial derivatives from which it is computed. This accuracy generally improves somewhat as the simulation progresses, and is somewhat better for weaker fields (larger M_A) than stronger fields.

M_A	time interval	$< \epsilon_x >$	$< \epsilon_z >$	Max(ϵ_x)	Max(ϵ_z)
41.4	$7.6\,T_i < t < 9.1\,T_i$	1.34×10^{-7}	1.34×10^{-7}	2.59×10^{-5}	2.59×10^{-5}
41.4	$12.2\,T_i < t < 13.7\,T_i$	2.54×10^{-8}	2.54×10^{-8}	6.41×10^{-6}	6.41×10^{-6}
41.4	$24.3\,T_i < t < 25.9\,T_i$	4.58×10^{-9}	4.58×10^{-9}	6.54×10^{-6}	6.54×10^{-6}
41.4	$36.5\,T_i < t < 38.0\,T_i$	2.69×10^{-9}	2.69×10^{-9}	3.17×10^{-6}	3.17×10^{-6}
41.4	$48.7\,T_i < t < 50.2\,T_i$	1.91×10^{-9}	1.91×10^{-9}	1.10×10^{-5}	1.10×10^{-5}
20.7	$7.6\,T_i < t < 9.1\,T_i$	2.41×10^{-7}	2.46×10^{-7}	1.75×10^{-5}	1.75×10^{-5}
20.7	$15.1\,T_i < t < 16.6\,T_i$	2.03×10^{-8}	2.03×10^{-8}	8.61×10^{-6}	8.61×10^{-6}
20.7	$25.6\,T_i < t < 27.1\,T_i$	6.13×10^{-9}	6.13×10^{-9}	1.13×10^{-5}	1.13×10^{-5}
20.7	$37.6\,T_i < t < 39.1\,T_i$	6.43×10^{-9}	6.43×10^{-9}	2.37×10^{-5}	2.37×10^{-5}
10.3	$7.2\,T_i < t < 8.6\,T_i$	2.51×10^{-7}	2.51×10^{-7}	9.77×10^{-5}	9.77×10^{-5}
10.3	$24.5\,T_i < t < 25.9\,T_i$	3.30×10^{-9}	3.30×10^{-9}	5.84×10^{-5}	5.84×10^{-5}
10.3	$36.0\,T_i < t < 37.4\,T_i$	6.01×10^{-9}	6.00×10^{-9}	4.53×10^{-5}	4.53×10^{-5}
5.1	$5.7\,T_i < t < 6.8\,T_i$	1.92×10^{-6}	1.88×10^{-6}	8.60×10^{-4}	8.60×10^{-4}
5.1	$13.6\,T_i < t < 14.7\,T_i$	2.06×10^{-8}	2.06×10^{-8}	2.90×10^{-4}	2.90×10^{-4}
5.1	$23.8\,T_i < t < 24.9\,T_i$	2.65×10^{-8}	2.66×10^{-8}	1.60×10^{-4}	1.60×10^{-4}

Table 11.1: Divergence of magnetic field

Having verified that the magnetic field satisfies the solenoidal condition, we now assess the convergence of the simulation results with respect to such parameters as time step, spatial step, and system dimensions.

11.2 Spatio-temporal Convergence of Simulation Results

In this section, we demonstrate convergence of the simulation results first with respect to time step, then with respect to refinement of the numerical grid (along with the time step). In the next sections, we will then demonstrate convergence with respect to system dimensions, between the RHD, MHD, and RMHD regimes, and with respect to viscosity. This provides not only further validation of the numerical algorithm, but also greater physical significance of the results.

We begin by demonstrating convergence with respect to time step. We compare two

magnetized cases ($M_A = 41.41$) which differ only in the time step used in the simulation. Case 1 uses $\Delta t = 0.032\, r_0/c$, while case 2 uses $\Delta t = 0.016\, r_0/c$. The parameters common to both cases are as follows:

$$
\begin{aligned}
\rho_0 c^2 &= 0.1\,\epsilon, \qquad P_0 = 5\,\epsilon, \\
c_s &= 0.576c, \qquad v_{z0}(x) = 0.7\, c\, \mathrm{sech}^2(x/r_0), \\
k_z &= 0.8\, r_0^{-1}, \\
v_A &= 0.0237\, c, \qquad \beta = 888.3, \\
M_A &= \infty : \qquad \omega_{i0} = 0.0994\, c/r_0, \\
M_A &= 41.41 : \qquad \omega_i = 0.0990\, c/r_0 = 0.9965\, \omega_{i0}, \\
\text{phase period :} \qquad T &= \frac{2\pi}{\omega_r} = 22.63\, r_0/c, \\
\text{growth time :} \qquad T_i &= \frac{1}{\omega_i} = 10.10\, r_0/c, \\
-15.75\, r_0 \le x \le 15.75\, r_0, &\qquad 0 \le z \le \frac{2\pi}{k_z}, \\
N_x &= 1001, \qquad N_z = 201, \qquad \text{one wavelength}, \\
\Delta x &= 0.0315\, r_0, \qquad \Delta z = 0.0393\, r_0, \\
\eta_\rho &= \eta_x = \eta_z = 0.0002\, r_0 c, \\
\eta_{Bx} &= \eta_{Bz} = 0.0012\, r_0 c.
\end{aligned}
\tag{11.6}
$$

In figures 11.1, we compare graphs showing the time-dependence of certain quantities, where at each time step, we compute either the spatially averaged value or the maximum value over the grid. The black curve corresponds to the larger time step, and the red curve to the smaller time step. In each case, the two curves almost exactly overlay one another, thereby showing excellent convergence with respect to time step.

In figures 11.2, the display on the left is case 1, at $\Delta t = 0.032\, r_0/c$, while the display on the right is case 2, at $\Delta t = 0.016\, r_0/c$. The displays show close agreement, even well into the nonlinear evolution. This shows temporal convergence of the simulation for time steps less than $0.032\, r_0/c$. Each vorticity display is overlaid with the contours of the magnetic field

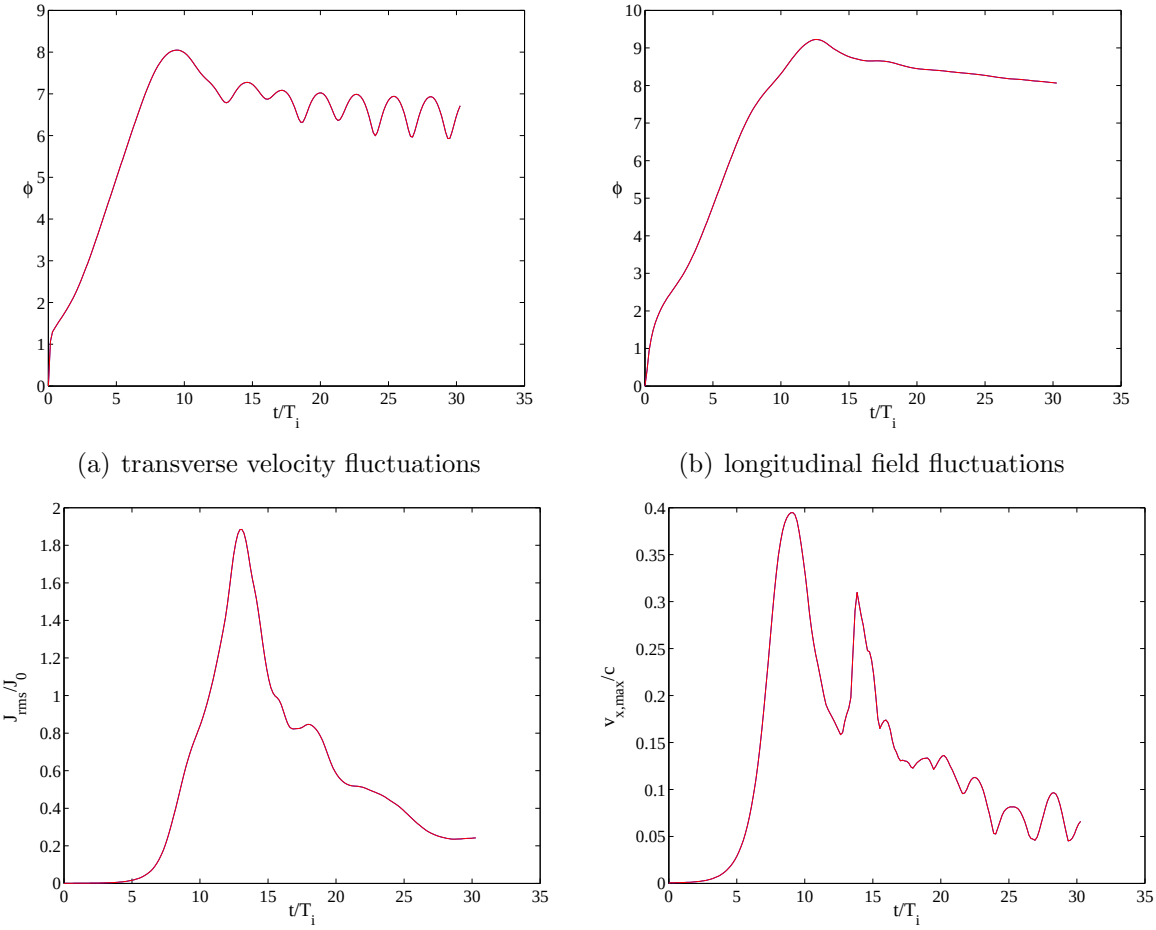

(a) transverse velocity fluctuations

(b) longitudinal field fluctuations

(c) RMS current density

(d) maximum transverse velocity

Figure 11.1: Time-dependencies for $\Delta t = 0.032\, r_0/c$ and $\Delta t = 0.016\, r_0/c$
$v_{z0} = 0.7\, c \qquad M_A = 41.41, \qquad v_{Az} = 0.0237c$
$c\Delta t/r_0 = 0.032$ (black), 0.016 (red)

lines.

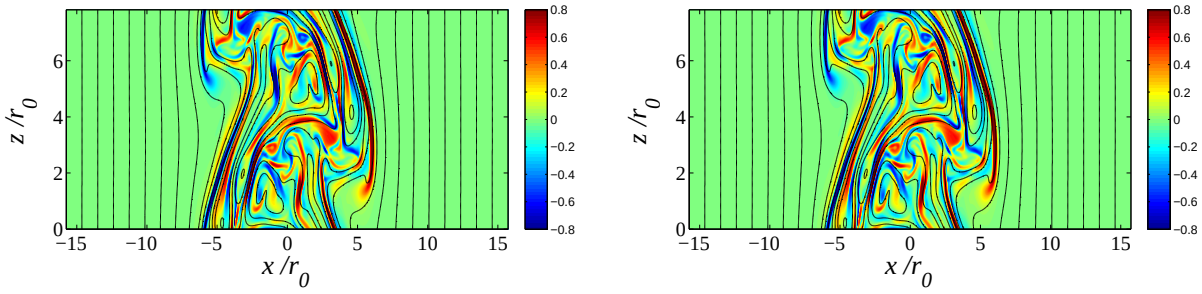

(a) $\Delta t \;=\; 0.032\, r_0/c$ (b) $\Delta t \;=\; 0.016\, r_0/c$

Figure 11.2: Vorticity displays for two time increments: $t = 17.0\, T_i$
$t = 172.0\, r_0/c = 7.603\, T = 17.04\, T_i$
$v_{z0}(x) \;=\; 0.7\, c \qquad M_A \;=\; 41.41, \qquad v_{Az} = 0.0237\, c$

We next examine the spatio-temporal convergence of the simulations, as we refine both the mesh and time step. We use the same case as above, and compare simulation results for meshes of 501×201, 751×151, and 1001×501. For the 501×201 mesh, we consider two different values of the viscosity coefficients, in order to assess the influence of artificial diffusion. The ratio of spatial increment to time step is the same in all cases. The parameters for the three mesh sizes are as follows:

$$
\begin{aligned}
501 \times 101: \qquad & \Delta t \;=\; 0.064\, r_0/c, \\
751 \times 151: \qquad & \Delta t \;=\; 0.04267\, r_0/c, \\
1001 \times 201: \qquad & \Delta t \;=\; 0.032\, r_0/c, \\
501 \times 101,\ \text{less diffusion}: \qquad & (\eta_\rho, \eta_x, \eta_z, \eta_{Bx}, \eta_{Bz}) \;=\; (0.0001)(2.8, 2.8, 2.8, 24, 24)\, r_0 c, \\
501 \times 101,\ \text{more diffusion}: \qquad & (\eta_\rho, \eta_x, \eta_z, \eta_{Bx}, \eta_{Bz}) \;=\; (0.0001)(4, 4, 4, 24, 24)\, r_0 c, \\
751 \times 151: \qquad & (\eta_\rho, \eta_x, \eta_z, \eta_{Bx}, \eta_{Bz}) \;=\; (0.0001)(2.4, 2.4, 2.4, 18, 18)\, r_0 c, \\
1001 \times 201: \qquad & (\eta_\rho, \eta_x, \eta_z, \eta_{Bx}, \eta_{Bz}) \;=\; (0.0001)(2, 2, 2, 12, 12)\, r_0 c. \qquad (11.7)
\end{aligned}
$$

For each grid resolution, the initial eigenmode is approximately the same, with the complex eigenfrequencies agreeing to within a fractional difference of about 10^{-6}, which demonstrates convergence of the numerical eigenmodes. The relevant displays are shown in figures

11.3 through 11.5. At a given time, there are four displays, each corresponding to a certain grid resolution used in the numerical simulations. Displays (a) and (b) both correspond to a 501 by 101 spatial grid, but display (a) uses less momentum and density diffusion than display (b). Display (c) corresponds to a 751 by 151 grid. Display (d) corresponds to a 1001 by 201 grid. Each vorticity display is overlaid with the contours of the magnetic field lines. The numerical simulations show good agreement that persists through the early stages of vortex formation and evolution. However, once the vortices are disrupted by the magnetic field, the three grids show divergent behavior, seen in the displays at the latest time ($156.7\, r_0/c$). This may be partly due to the larger amounts of artificial viscosity necessary to sustain the simulations using the coarser meshes.

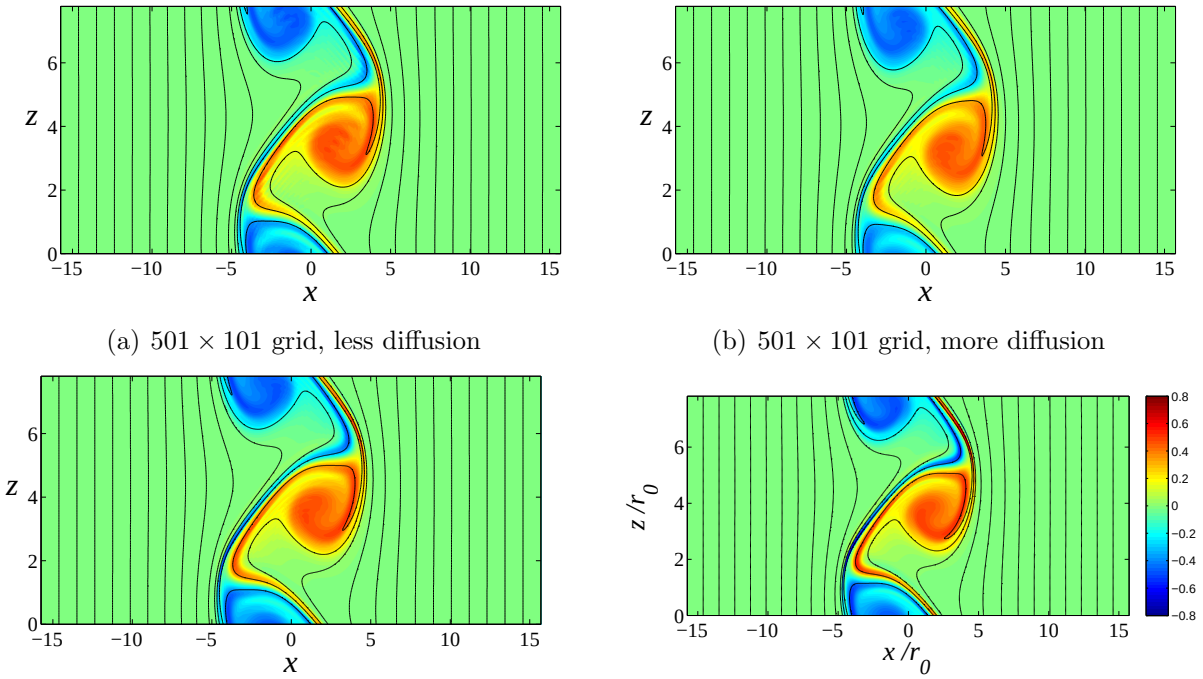

(a) 501×101 grid, less diffusion

(b) 501×101 grid, more diffusion

(c) 751×151 grid points

(d) 1001×201 grid points

Figure 11.3: Vorticity displays at different grid resolutions: $t = 9.43\, T_i$
$t = 95.2\, r_0/c = 4.209\, T = 9.432\, T_i, \qquad v_{z0} = 0.7\, c, \quad M_A = 41.41, \quad v_{Az} = 0.0237\, c$

Having examined the spatial and temporal convergence of the simulations, we now wish

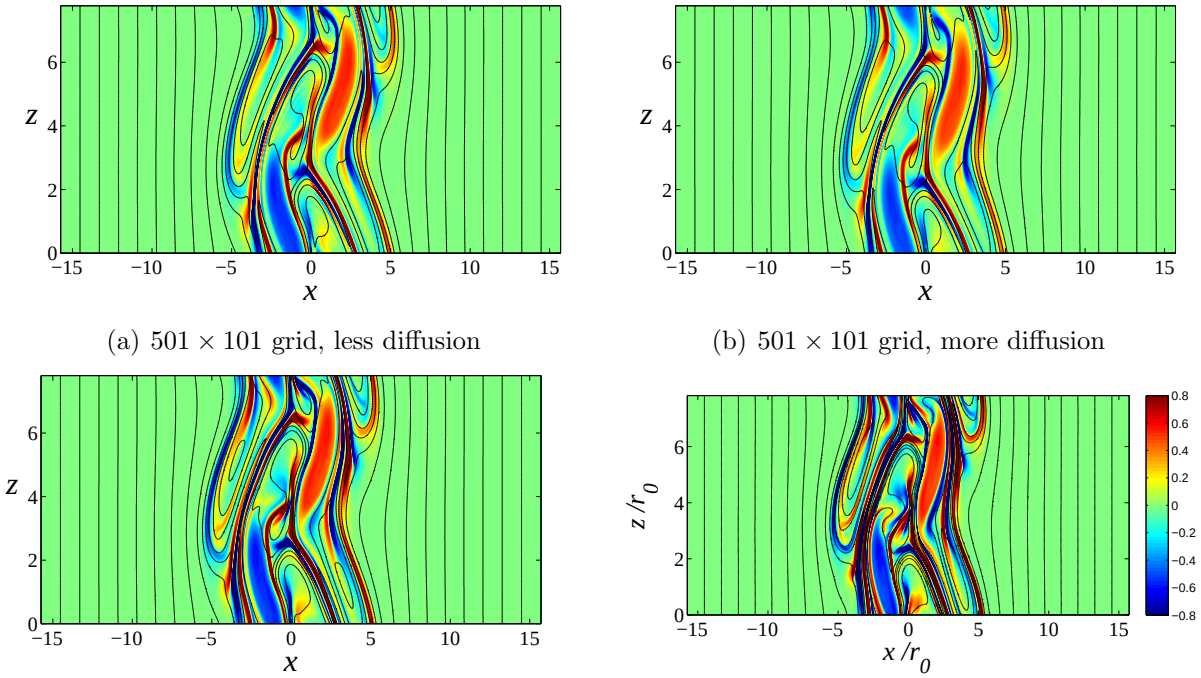

(a) 501×101 grid, less diffusion

(b) 501×101 grid, more diffusion

(c) 751×151 grid points

(d) 1001×201 grid points

Figure 11.4: Vorticity displays at different grid resolutions: $t = 13.7\,T_i$
$t = 138.2\,r_0/c = 6.110\,T = 13.69\,T_i, \qquad v_{z0} = 0.7\,c, \qquad M_A = 41.41, \quad v_{Az} = 0.0237\,c$

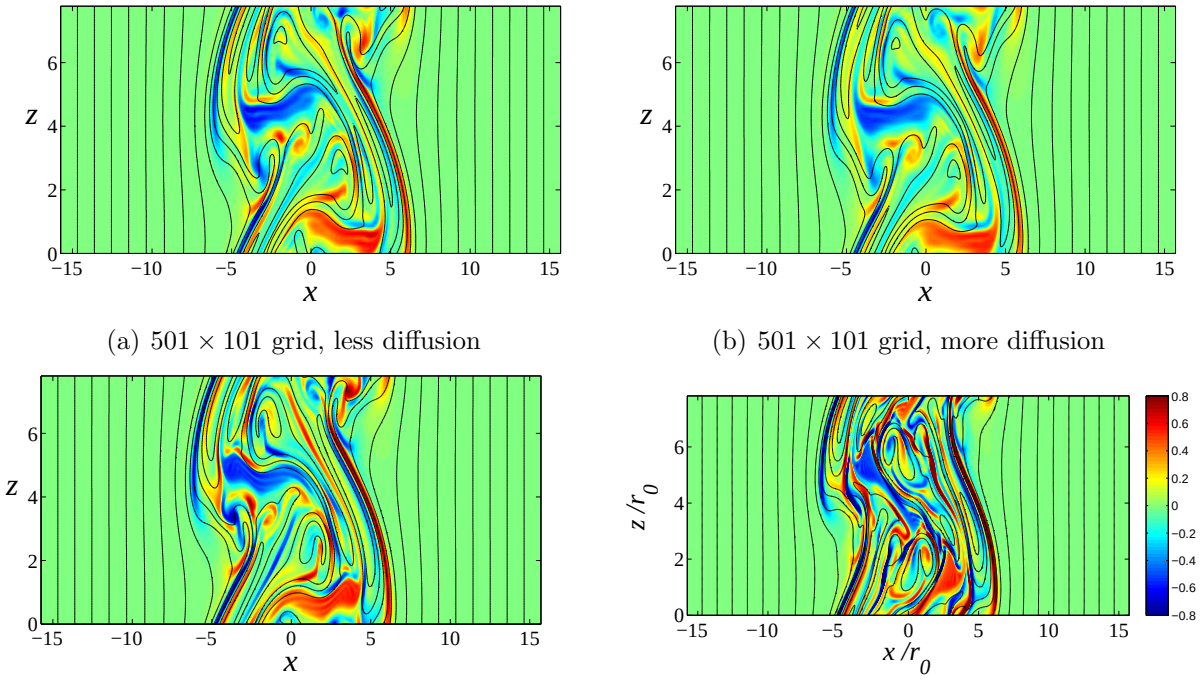

(a) 501×101 grid, less diffusion

(b) 501×101 grid, more diffusion

(c) 751×151 grid points

(d) 1001×201 grid points

Figure 11.5: Vorticity displays at different grid resolutions: $t = 15.5 T_i$
$t = 156.7\,r_0/c = 6.924\,T = 15.52\,T_i, \qquad v_{z0} = 0.7\,c, \qquad M_A = 41.41, \quad v_{Az} = 0.0237c$

to examine the dependence of the simulation results on the system dimensions. In particular, we wish to assess the influence of transverse boundary reflections on the development of the flow.

11.3 Dependence on System Dimensions

We now consider the dependence of our simulation results on the transverse and longitudinal dimensions of the system. Periodic boundary conditions are used in both directions. To examine the longitudinal dimension, we have compared results obtained for numerical grids spanning one wavelength, three wavelengths, and five wavelengths of the input perturbation, where all other input parameters are the same. The results are indistinguishable between the three cases, and moreover, the system retains a longitudinal spatial period of one perturbation wavelength. The results are therefore unaffected by the number of perturbation wavelengths spanned longitudinally. We now consider the influence of the transverse width of the system.

We have observed nonlinear oscillatory behavior in our simulation results, and noted that these oscillations correspond to nonlinear transverse acoustic waves propagating between the central axis and transverse boundaries. The period of the pressure waves is equal to the sound transit time across the width of the system, indicating that these waves are influenced by reverberations from the transverse boundaries (where periodic boundary conditions are used). We wish to assess the influence of these boundary reflections on the development of the flow, in order to verify that the nonlinear flow evolution is governed by physical processes rather than numerical constraints. To make this assessment, we compare results for numerical simulations using two different transverse system widths, namely $L_x = 31.5\, r_0$

and $L_x = 47.25\, r_0$, with all other parameters kept the same.

We begin with the case corresponding to the intermediate field $M_A = 20.7$. Figures 11.6 through 11.11 show the time-dependence of various spatially averaged and maximized quantities. In each plot, there are two curves simultaneously displayed. The blue curve corresponds to a transverse width $L_x = 31.5\, r_0$, while the red curve corresponds to a transverse width $L_x = 47.25\, r_0$. These curves show very close agreement well into the nonlinear regime, with fractional deviations not exceeding about 5%. In figures 11.10 and 11.11, the magnetic field remains slightly stronger for the larger system width, indicating that more frequent boundary reverberations tend to dissipate slightly more electromagnetic energy from the system.

We then display the vorticity, overlaid with contours of the magnetic field lines, for each system width. In each row, the display on the left corresponds to a width of $31.5\, r_0$, while the display on the right corresponds to $47.25\, r_0$. The displays show almost exact agreement well into the vortex-disruptive phases of nonlinear evolution (figures 11.12 and 11.13), and we only begin to notice differences after about 17 growth times, during the turbulent breakdown. The differences occur with the smaller-scale structures in the interior of the jet, while the larger-scale structure, including the enhanced filaments, remains fairly unchanged. Consequently, the equilibrium of the system, shown in figures 11.16, has the same basic properties in terms of equilibrium jet width, approximate filament width, exterior filaments, and jet alignment. For $M_A = 20.7$, boundary reflections do not significantly influence the evolution of the flow.

In the next section, we consider the influence of boundary reflections on a more weakly magnetized flow in which there is more extensive vortex development.

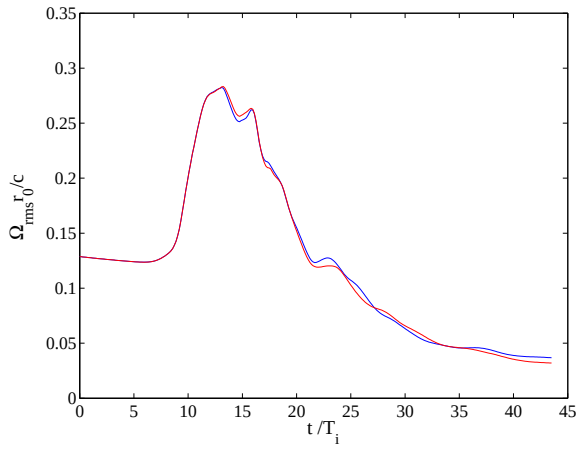

(a) RMS vorticity, $-15.8\,r_0 \le x \le 15.8\,r_0$

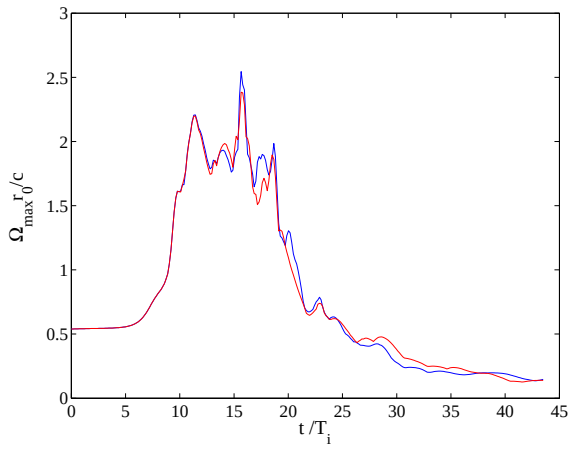

(b) Max. vorticity

Figure 11.6: RMS and max. vorticity for $M_A = 20.7$ for $L_x = 31.5$ (blue) and 47.25 (red)

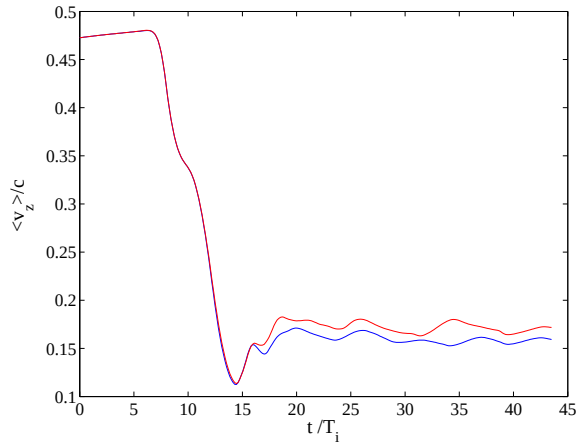

(a) Avg. z-velocity, $-1.3\,r_0 \le x \le 1.3\,r_0$

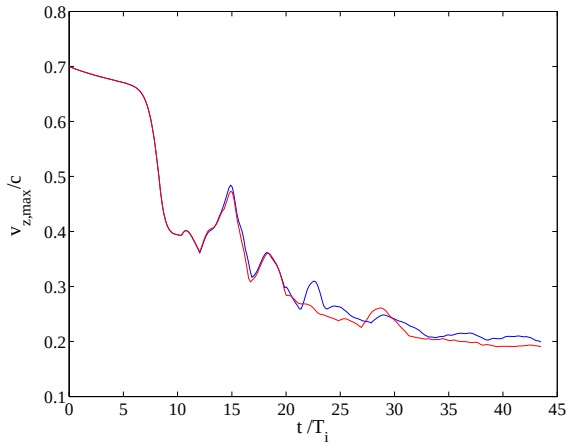

(b) Max. z-velocity

Figure 11.7: Avg. and max. v_z for $M_A = 20.7$ for $L_x = 31.5$ (blue) and 47.25 (red)

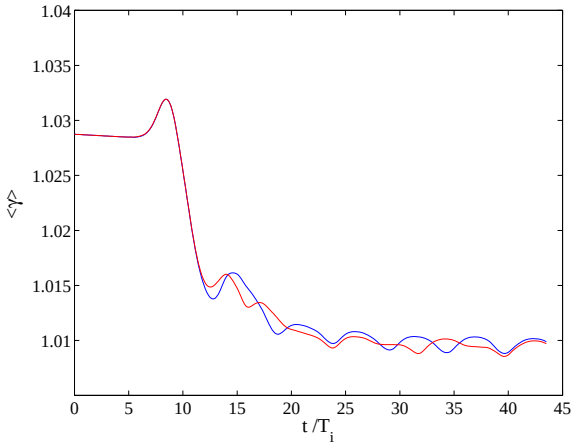

(a) Avg. Lorentz fct., $-7.9\,r_0 \leq x \leq 7.9\,r_0$

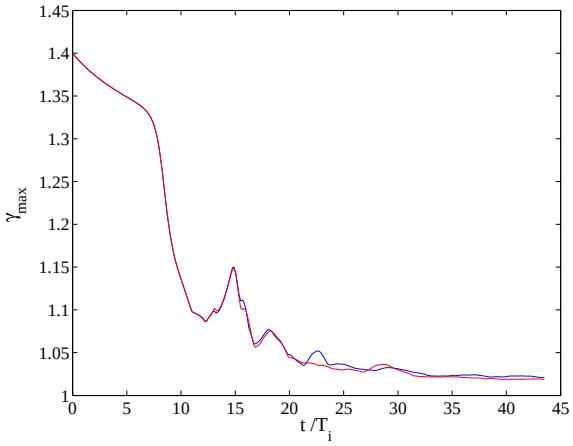

(b) Max. Lorentz fct.

Figure 11.8: Avg. and max. γ for $M_A = 20.7$ for $L_x = 31.5$ (blue) and 47.25 (red)

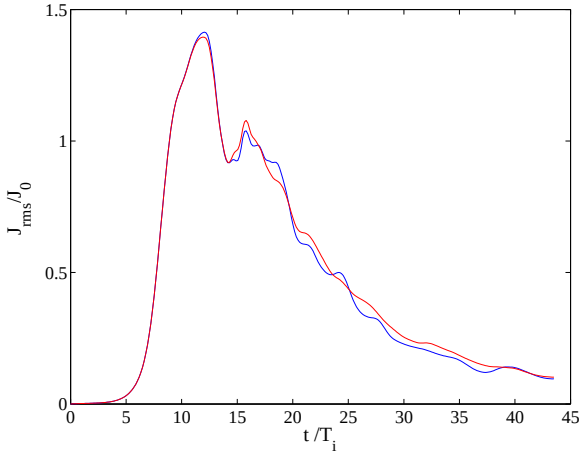

(a) RMS current density, $-15.8\,r_0 \leq x \leq 15.8\,r_0$

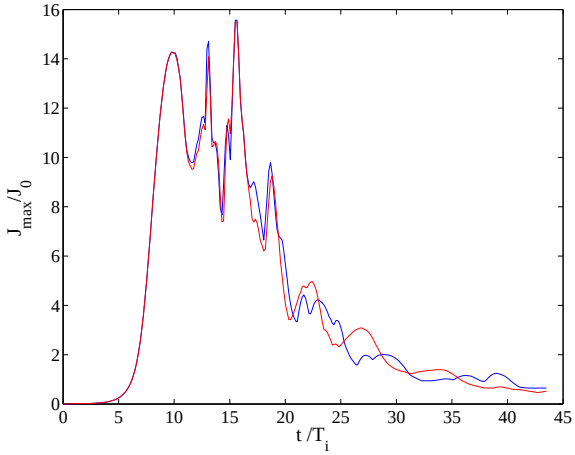

(b) Max. current density

Figure 11.9: RMS and max. J for $M_A = 20.7$ for $L_x = 31.5$ (blue) and 47.25 (red)

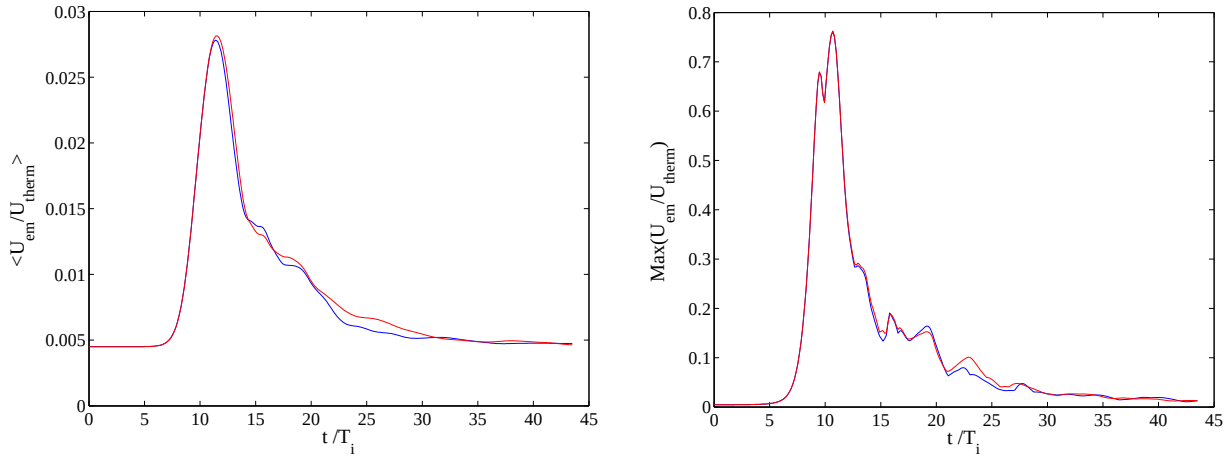

(a) Avg. $U_{\rm EM}/U_{\rm therm}$, $\quad -15.8\,r_0 \le x \le 15.8\,r_0$ (b) Max. $U_{\rm EM}/U_{\rm therm}$

Figure 11.10: Avg. and max. EM energy for $M_A = 20.7$ for $L_x = 31.5$ (blue), 47.25 (red)

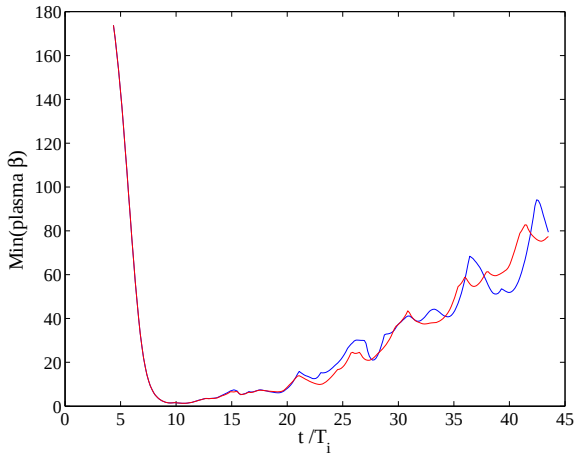

Figure 11.11: Min. plasma β for $M_A = 20.7$ for $L_x = 31.5$ (blue) and 47.25 (red)

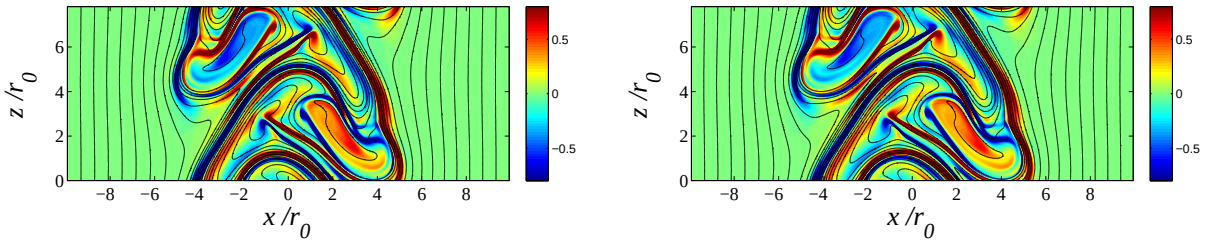

(a) $L_x = 31.5 \quad \beta_{\rm min} = 3.52$ (b) $L_x = 47.25 \quad \beta_{\rm min} = 3.45$

Figure 11.12: $M_A = 20.70, \qquad t = 12.6\,T_i = 5.69\,T = 129.0\,r_0/c$

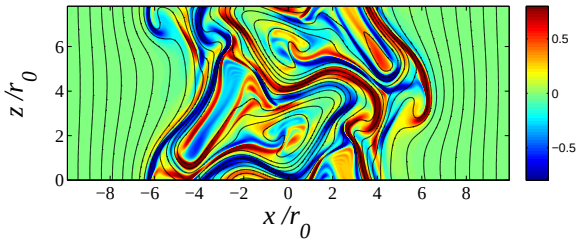

(a) $L_x = 31.5 \quad \beta_{\min} = 7.21$

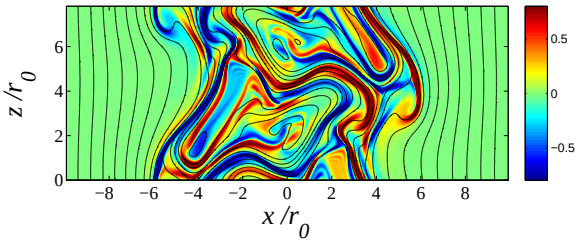

(b) $L_x = 47.25 \quad \beta_{\min} = 6.50$

Figure 11.13: $M_A = 20.70, \qquad t = 15.1\,T_i = 6.77\,T = 153.6\,r_0/c$

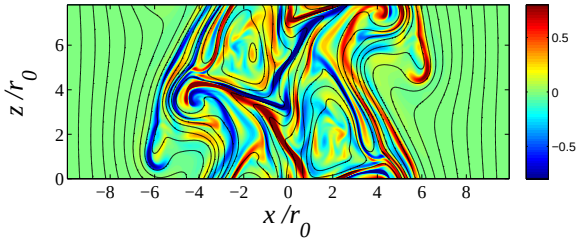

(a) $L_x = 31.5 \quad \beta_{\min} = 7.38$

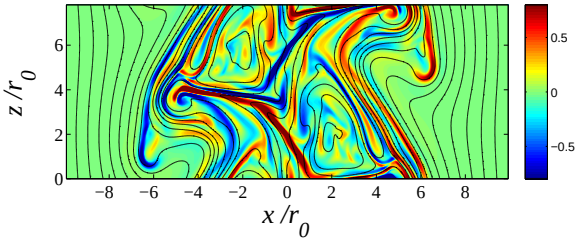

(b) $L_x = 47.25 \quad \beta_{\min} = 7.26$

Figure 11.14: $M_A = 20.70, \qquad t = 17.5\,T_i = 7.86\,T = 178.2\,r_0/c$

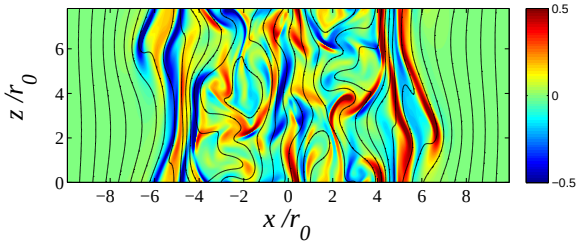

(a) $L_x = 31.5 \quad \beta_{\min} = 15.4$

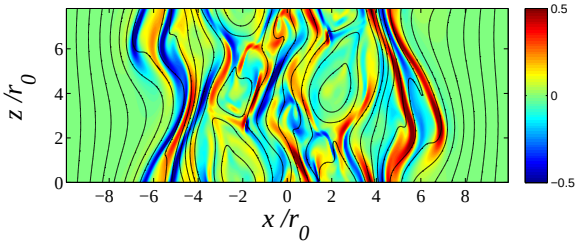

(b) $L_x = 47.25 \quad \beta_{\min} = 11.1$

Figure 11.15: $M_A = 20.70, \qquad t = 23.5\,T_i = 10.6\,T = 239.6\,r_0/c$

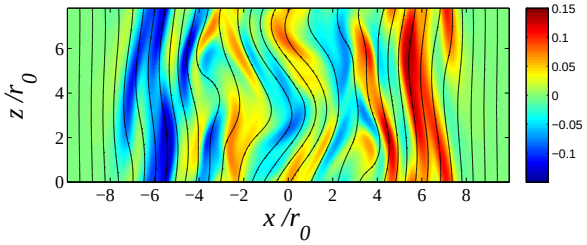

(a) $L_x = 31.5 \quad \beta_{\min} = 92.3$

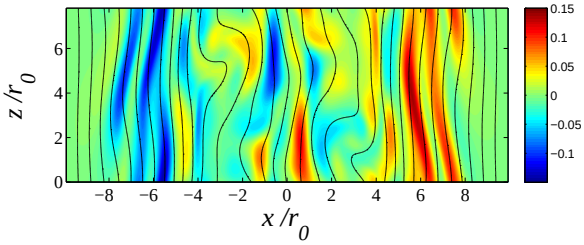

(b) $L_x = 47.25 \quad \beta_{\min} = 75.4$

Figure 11.16: $M_A = 20.70, \qquad t = 42.8\,T_i = 19.2\,T = 436.2\,r_0/c$

11.4 Dependence on System Width: Weaker field

We now consider the influence of boundary reverberations for a weaker field corresponding to $M_A = 41.4$. As before, in each of the plots of time-dependence, the blue curve corresponds to a transverse system width of $31.5\, r_0$ and the red curve to a system width of $47.25\, r_0$.

In figures 11.17 to 11.22, we display the vorticity for each system width. In each row, the display on the left corresponds to a width of $31.5\, r_0$, while the display on the right corresponds to $47.25\, r_0$. Again, the two simulations remain almost identical well into the vortex-disruptive stage, and only begin to deviate after about 16 growth times, during the transition to the turbulent regime. However, figure 11.21 shows that the large-scale filamentary structure remains unaffected, as is the overall jet width at any given time, and that the differences are in the small-scale turbulent features in the interior of the flow. From figures 11.22, we see that the system width does not affect the equilibrium jet width and equilibrium filamentary structure, and also does not influence the nature of the persistent vortical behavior (including the width of this central region, which corresponds to the equilibrium width of the flow).

We have determined that boundary reverberations do not significantly alter the behavior of the flow in magnetized cases. We now seek to show that the same holds in the absence of a magnetic field.

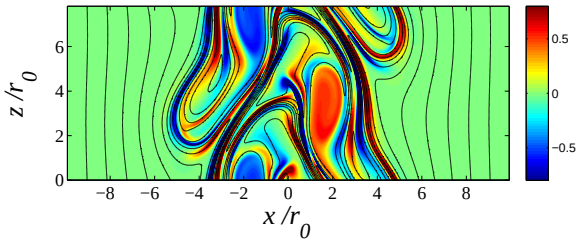

(a) $L_x = 31.5 \quad \beta_{\min} = 2.10$

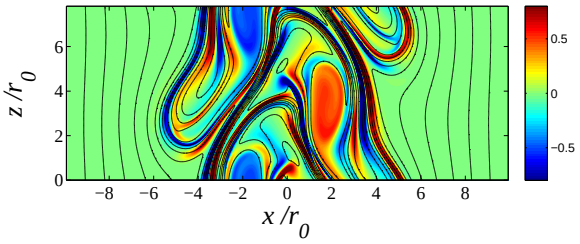

(b) $L_x = 47.25 \quad \beta_{\min} = 2.05$

Figure 11.17: $M_A = 41.41, \qquad t = 12.78\, T_i = 5.70\, T = 129.0\, r_0/c$

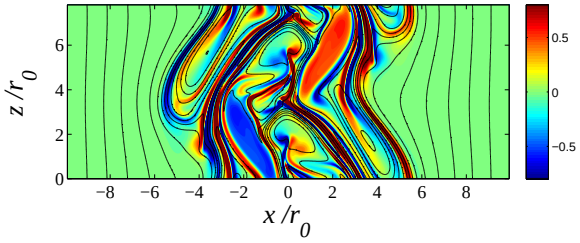

(a) $L_x = 31.5 \quad \beta_{\min} = 4.36$

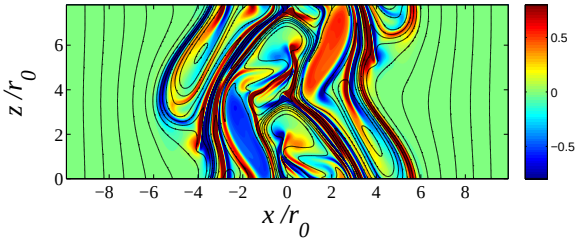

(b) $L_x = 47.25 \quad \beta_{\min} = 4.05$

Figure 11.18: $M_A = 41.41, \qquad t = 14.00\, T_i = 6.25\, T = 141.3\, r_0/c$

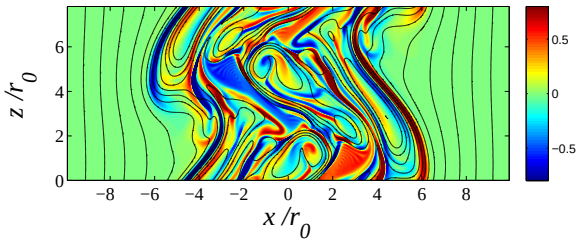

(a) $L_x = 31.5 \quad \beta_{\min} = 7.35$

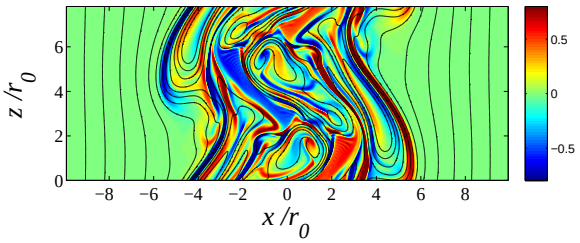

(b) $L_x = 47.25 \quad \beta_{\min} = 7.80$

Figure 11.19: $M_A = 41.41, \qquad t = 15.21\, T_i = 6.79\, T = 153.6\, r_0/c$

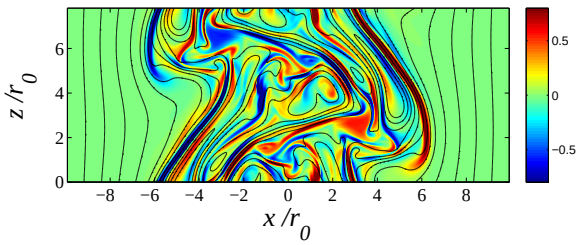

(a) $L_x = 31.5 \quad \beta_{\min} = 10.9$

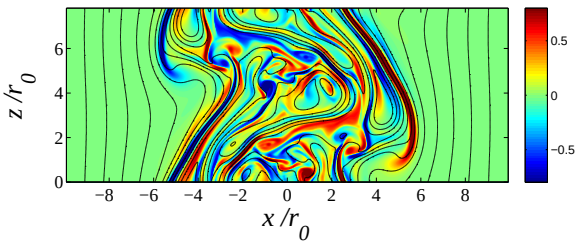

(b) $L_x = 47.25 \quad \beta_{\min} = 11.1$

Figure 11.20: $M_A = 41.41, \qquad t = 16.43\, T_i = 7.33\, T = 165.9\, r_0/c$

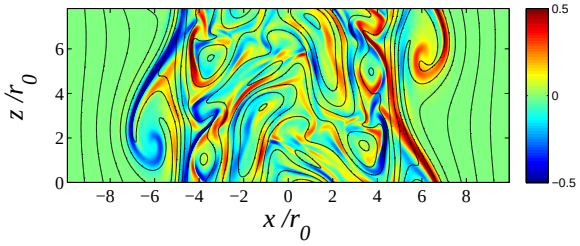

(a) $L_x = 31.5 \quad \beta_{\min} = 26.6$

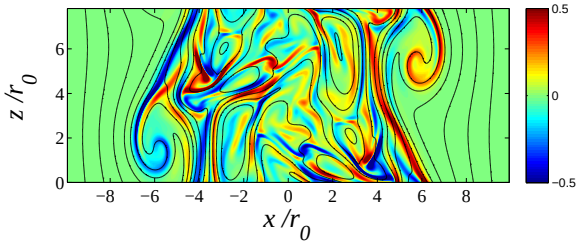

(b) $L_x = 47.25 \quad \beta_{\min} = 19.4$

Figure 11.21: $M_A = 41.41, \qquad t = 21.30\, T_i = 9.50\, T = 215.0\, r_0/c$

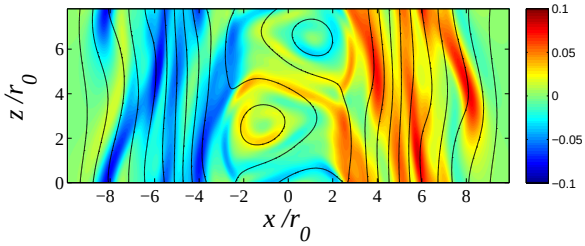

(a) $L_x = 31.5 \quad \beta_{\min} = 173.8$

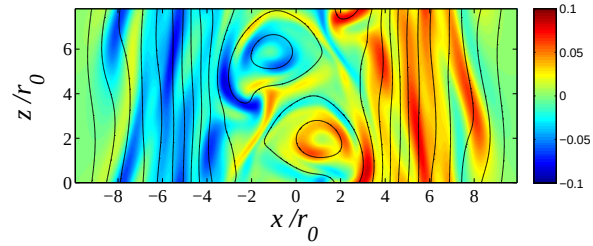

(b) $L_x = 47.25 \quad \beta_{\min} = 127.0$

Figure 11.22: $M_A = 41.41, \qquad t = 52.94\, T_i = 23.62\, T = 534.5\, r_0/c$

11.5 Dependence on System Width: RHD Case

We now consider the influence of boundary reverberations for the unmagnetized case, i.e., the simulation for which $B = 0$. As before, in each of the plots of time-dependence, the blue curve corresponds to a transverse system width of $31.5\, r_0$ and the red curve to a system width of $47.25\, r_0$. Because the system is unmagnetized, the acoustic oscillations are more pronounced, and the curves oscillate with different frequencies which are determined by the system widths. However, the time-averaged behavior of each of the quantities is approximately the same. Recall that in chapter 9 we compared the unmagnetized case to the different magnetized cases, and the relevant parameters to compare were the average values of such quantities as velocity, Lorentz factor, etc. Our conclusions regarding the influence of a magnetic field were not based on amplitudes or frequencies of oscillations in these values.

In figures 11.27 to 11.31, we display the vorticity for each system width. In each row, the display on the left corresponds to a width of $31.5\, r_0$, while the display on the right corresponds to $47.25\, r_0$. The displays show almost exact agreement through about 15 growth times, at which time the vortices begin to rotate at different rates, and assume different shapes, for the two system widths. In both cases, the vortices eventually relax to a more circular shape dominated by thermal stresses, though this occurs more quickly for the larger system width. Also, both cases exhibit agreement in the (i) transverse locations and (ii) average sizes of the larger primary vortices and of the smaller secondary vortices. Moreover, even as the secondary vortices move farther from the central axis, each row of figures shows agreement in their translational positions at a given instant in time. The average pattern speeds of the large primary vortices are approximately the same in both cases, while in both cases the

secondary vortices exhibit almost no longitudinal movement. Figure 11.31 shows that for both system widths, the vortices relax to a smooth ellipsoidal shape of roughly the same size and aspect ratio.

We have shown that, as long as the transverse system width is sufficient to allow asymptotic vanishing of the flow speed, the nonlinear evolution of the flow is not significantly altered by the system width, i.e., by the presence of boundary reverberations which take the form of nonlinear acoustic waves. In the presence of a magnetic field, we observe closer quantitative agreement between results for the two system widths examined. A magnetic field therefore has the effect of further suppressing the influence of reflected acoustic waves on the flow. We therefore have approximate convergence of the nonlinear evolution of the flow with respect to the transverse system width. This demonstrates that our conclusions from chapters 9 and 10 have physical significance, and are not simply artifacts of numerical constraints.

We have demonstrated convergence with respect to time step, spatial step, and system dimensions. In the next section, we proceed to examine convergence between the RMHD, MHD, and RHD regimes.

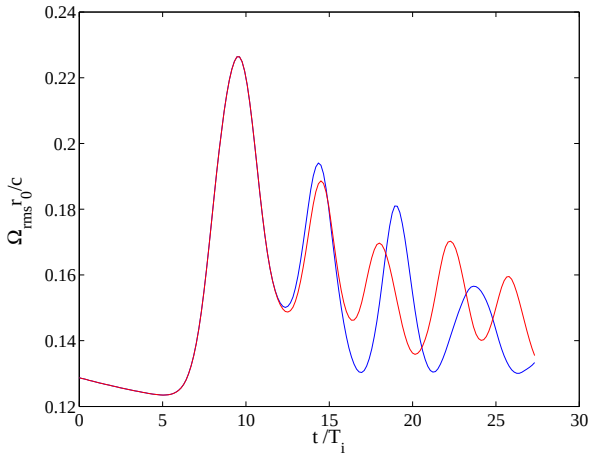

(a) RMS vorticity, $-15.8\,r_0 \le x \le 15.8\,r_0$

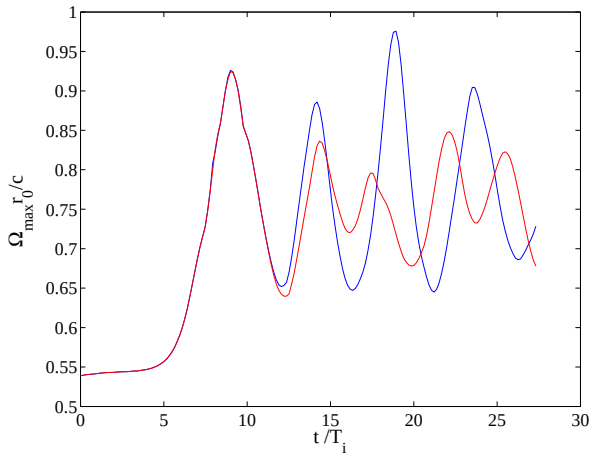

(b) Max. vorticity

Figure 11.23: RMS and max. vort. for $B = 0$ for $L_x = 31.5$ (blue) and 47.25 (red)

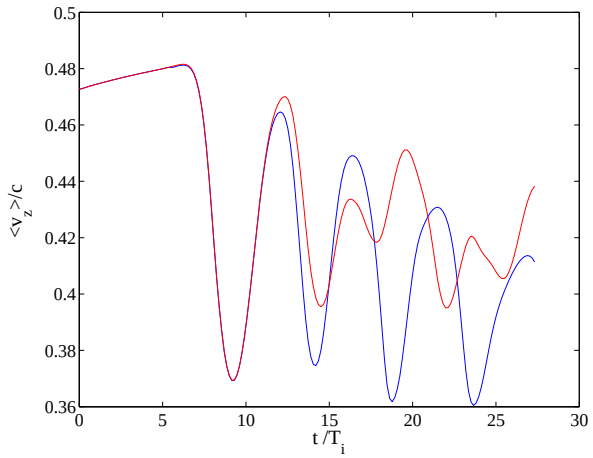

(a) Avg. z-velocity, $-1.3\,r_0 \le x \le 1.3\,r_0$

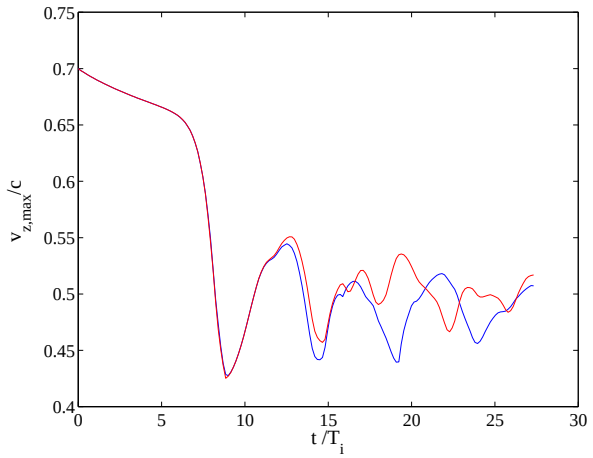

(b) Max. z-velocity

Figure 11.24: Avg. and max. v_z for $B = 0$ for $L_x = 31.5$ (blue) and 47.25 (red)

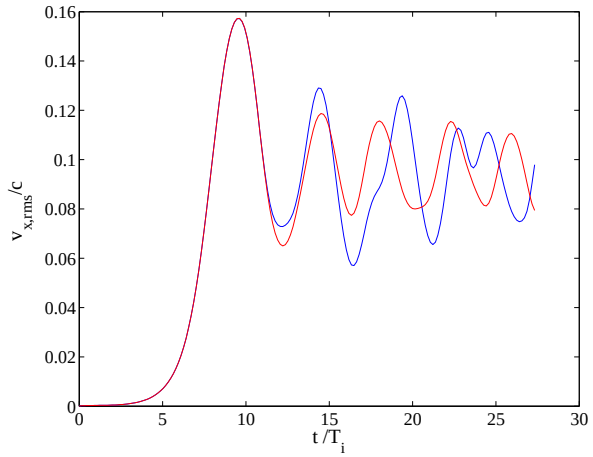

(a) RMS x-velocity, $\quad -1.3\,r_0 \le x \le 1.3\,r_0$

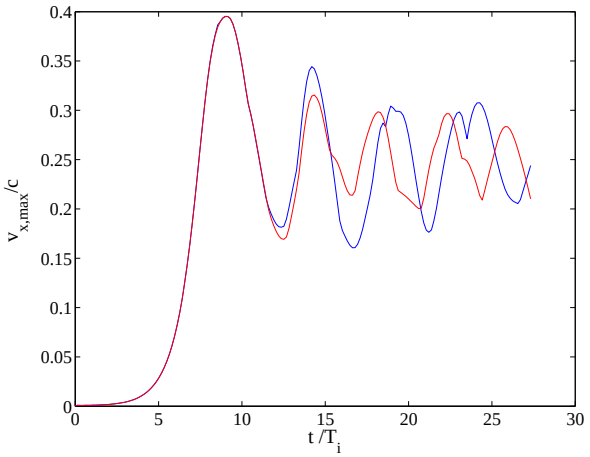

(b) Max. x-velocity

Figure 11.25: RMS and max. v_x for $B = 0$ for $L_x = 31.5$ (blue) and 47.25 (red)

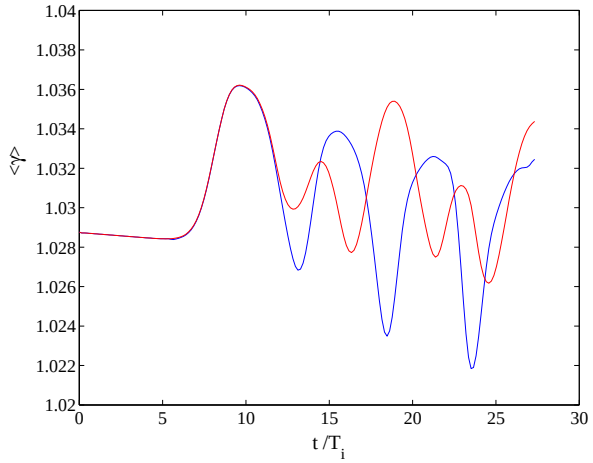

(a) Avg. γ, $\quad -7.9\,r_0 \le x \le 7.9\,r_0$

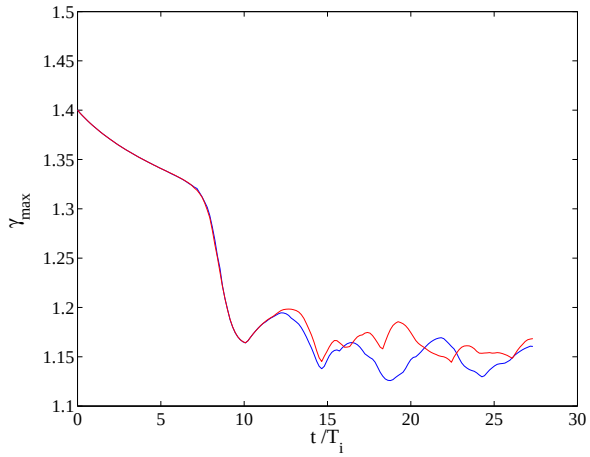

(b) Max. γ

Figure 11.26: Avg. and max. γ for $B = 0$ for $L_x = 31.5$ (blue) and 47.25 (red)

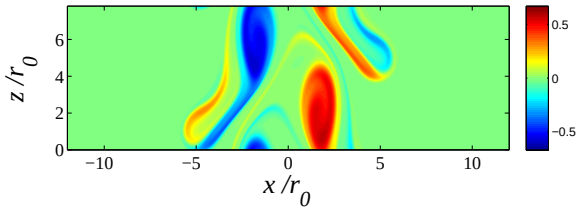

(a) $L_x = 31.5$

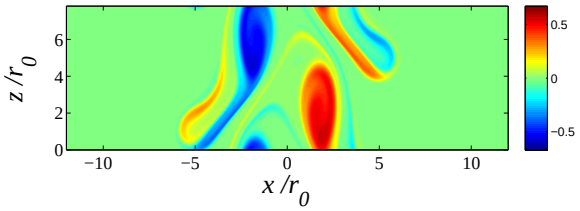

(b) $L_x = 47.25$

Figure 11.27: $B = 0, \qquad t = 12.21\,T_i = 5.44\,T = 122.9\,r_0/c$

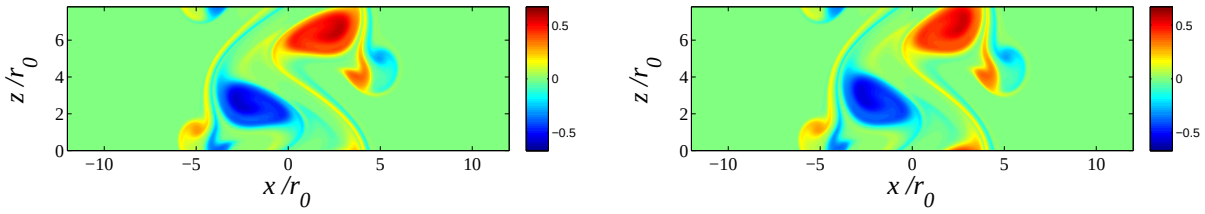

(a) $L_x = 31.5$ (b) $L_x = 47.25$

Figure 11.28: $B = 0$, $t = 14.04\,T_i = 6.25\,T = 141.3\,r_0/c$

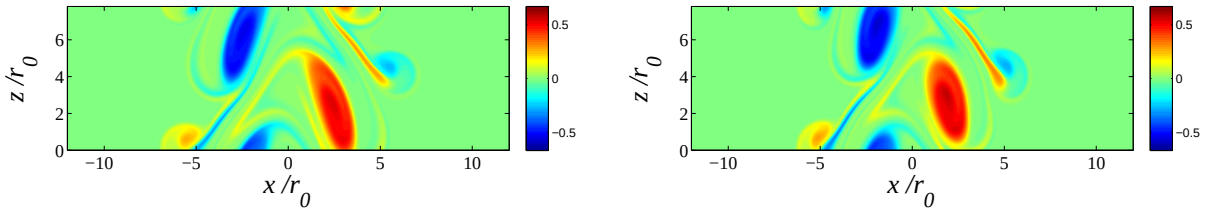

(a) $L_x = 31.5$ (b) $L_x = 47.25$

Figure 11.29: $B = 0$, $t = 15.88\,T_i = 7.07\,T = 159.7\,r_0/c$

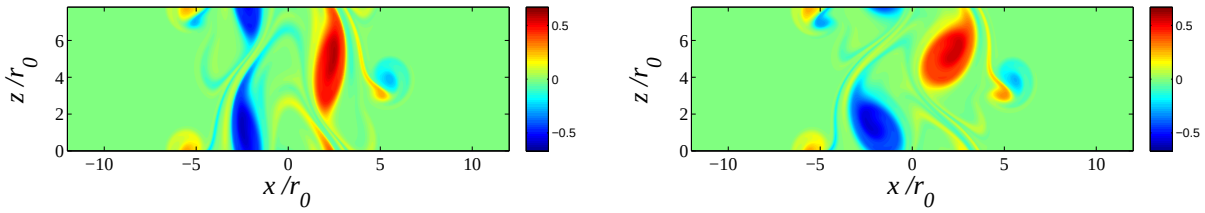

(a) $L_x = 31.5$ (b) $L_x = 47.25$

Figure 11.30: $B = 0$, $t = 17.10\,T_i = 7.61\,T = 172.0\,r_0/c$

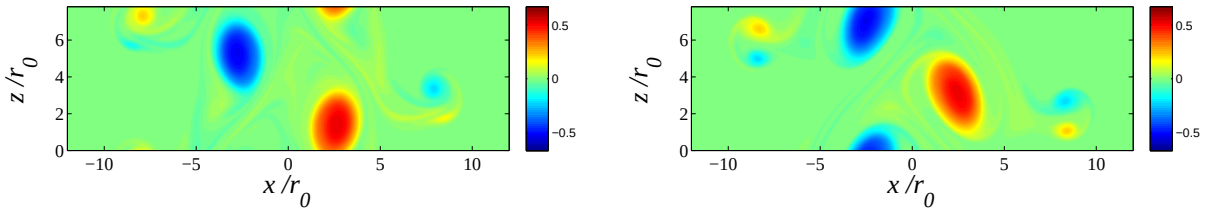

(a) $L_x = 31.5$ (b) $L_x = 47.25$

Figure 11.31: $B = 0$, $t = 26.87\,T_i = 11.96\,T = 270.3\,r_0/c$

11.6 Convergence Between RMHD, MHD, and RHD Regimes

We now wish to demonstrate convergence between the RMHD and MHD regimes. For a non-relativistic flow speed and sound speed, we compare results obtained from an RMHD simulation and an MHD simulation. We use a non-relativistic adiabatic constant of $\Gamma = 5/3$. The parameters for both cases are as follows, where ϵ has units of energy density, r_0 has units of length, and the scale velocity $c_0 = c$ in the RMHD case, but is much less than c in the MHD case:

$$\begin{aligned}
\rho_0 c_0^2 &= 200\,\epsilon, \qquad P_0 = 5\,\epsilon, \\
v_{z0}(x) &= 0.16\,c_0\,\mathrm{sech}^2(x/r_0), \\
k_z &= 0.8\,r_0^{-1}, \\
-15.75\,r_0 \le x \le 15.75\,r_0, &\qquad 0 \le z \le \frac{2\pi}{k_z}, \\
N_x &= 1001, \qquad N_z = 201, \\
\Delta t &= 0.032\,r_0/c_0, \qquad \Delta x = 0.0315\,r_0, \qquad \Delta z = 0.0393\,r_0, \\
\eta_\rho &= \eta_x = \eta_z = \eta_\epsilon = 0.00018\,r_0 c_0, \\
\eta_{Bx} &= \eta_{Bz} = 0.0006\,r_0 c_0.
\end{aligned} \tag{11.8}$$

The parameters specific to the RMHD simulation are as follows:

$$
\begin{aligned}
\beta &= \frac{2P_0}{B_{z0}^2} = 969, \\
w_0 &= \rho_0 c^2 + P_0\Gamma/(\Gamma-1) = 200 + (5)(2.5) = 212.5\,\epsilon, \\
v_{Az} &= (c)\frac{B_{z0}}{\sqrt{w_0}} = \frac{0.1016\,c}{\sqrt{212.5}} = 0.007\,c, \\
M_A &= \frac{v_{z0}\gamma}{v_{Az}\gamma_A} = \frac{v_{z0}}{v_{Az}}\sqrt{\frac{1-v_{Az}^2/c^2}{1-v_{z0}^2/c^2}} = 23.3, \\
c_s &= c\sqrt{\frac{\Gamma P_0}{w_0}} = 0.198\,c, \\
\omega &= (0.0553 + i\,0.0235)\,\frac{c}{r_0}, \\
T_i &= \frac{1}{\omega_i} = 42.57\,\frac{r_0}{c}.
\end{aligned}
\tag{11.9}
$$

The parameters specific to the MHD simulation are as follows:

$$
\begin{aligned}
\beta &= \frac{2P_0}{B_{z0}^2} = 1031, \\
v_{Az} &= \frac{B_{z0}}{\sqrt{\rho_0}} = \frac{0.0985}{\sqrt{200}} = 0.007\,c_0, \\
M_A &= \frac{v_{z0}}{v_{Az}} = 23.0, \\
c_s &= \sqrt{\frac{\Gamma P_0}{\rho_0}} = 0.204\,c_0, \\
\omega &= (0.0550 + i\,0.0235)\,\frac{c_0}{r_0}, \\
T_i &= \frac{1}{\omega_i} = 42.57\,\frac{r_0}{c_0}.
\end{aligned}
\tag{11.10}
$$

Note that the eigenfrequencies agree very closely between the two cases, indicating convergence between the RMHD and MHD algorithms for computing numerical linear eigenmodes in which to launch the simulations. Figures 11.32 display the growth curves of the primitive variables for the RMHD case (left figure) and the MHD case (right figure). These show close agreement. Figures 11.33 through 11.36 each simultaneously display the time-dependence of

a certain spatially-averaged or maximum quantity for the RMHD case (blue curve) and the MHD case (red curve).

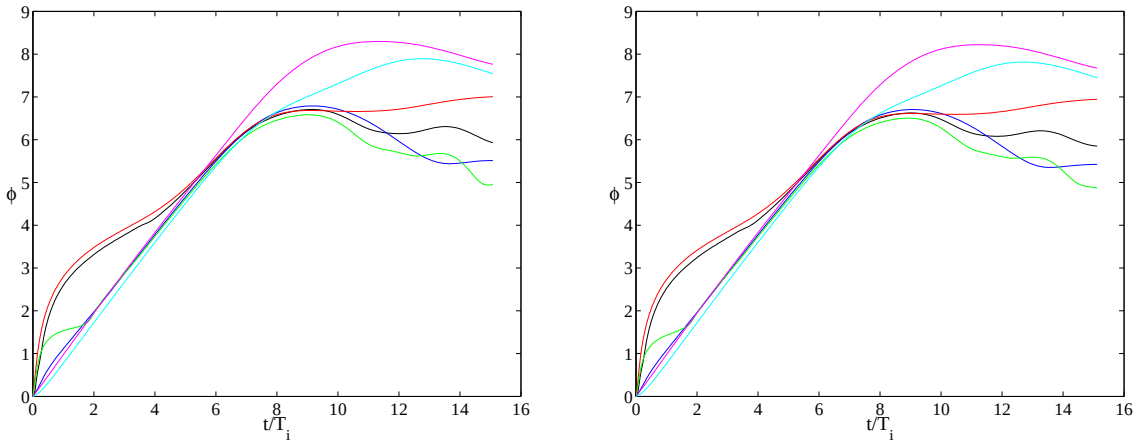

(a) RMHD case (b) MHD case

Figure 11.32: Growth curves for RMHD and MHD cases
ρ (black), v_x (blue), v_z (red), P (green), B_x (magenta), B_z (cyan)
$M_A = 23, \qquad v_{Az} = 0.007\, c_0, \qquad v_{z0} = 0.16\, c_0$

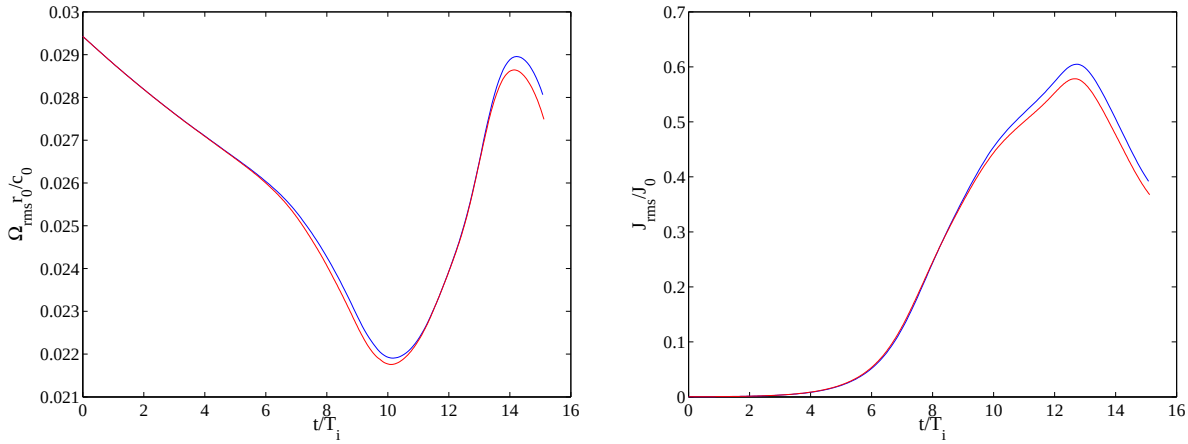

(a) RMS vorticity (b) RMS current density

Figure 11.33: Vorticity and current density for RMHD (blue) and MHD (red) cases
$M_A = 23, \qquad v_{Az} = 0.007\, c_0, \qquad v_{z0} = 0.16\, c_0$

Displays of the simulation results are shown in figures 11.37 through 11.39. These are displays of the vorticity, i.e., the curl of the velocity field, superimposed with contours of the magnetic field. Although the grid used in the simulations spans two wavelengths

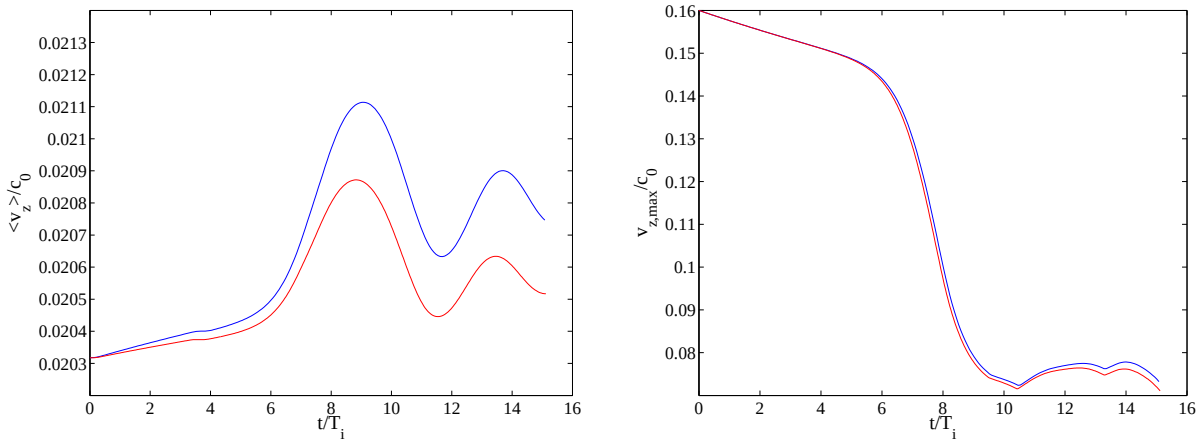

(a) average longitudinal velocity

(b) maximum longitudinal velocity

Figure 11.34: Average and max. longit. veloc. for RMHD (blue) and MHD (red) cases $M_A = 23, \qquad v_{Az} = 0.007\, c_0, \qquad v_{z0} = 0.16\, c_0$

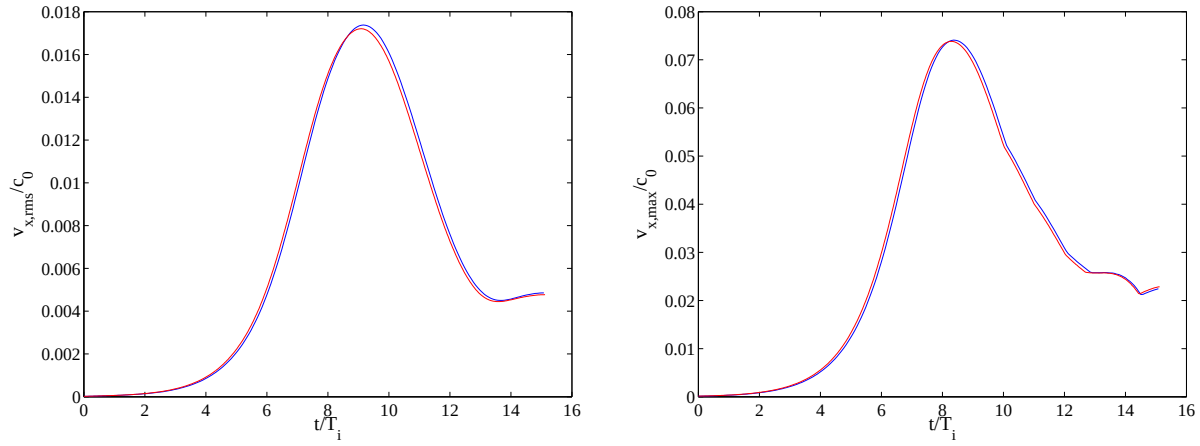

(a) RMS transverse velocity

(b) maximum transverse velocity

Figure 11.35: RMS and max. transverse velocity for RMHD (blue) and MHD (red) cases $M_A = 23, \qquad v_{Az} = 0.007\, c_0, \qquad v_{z0} = 0.16\, c_0$

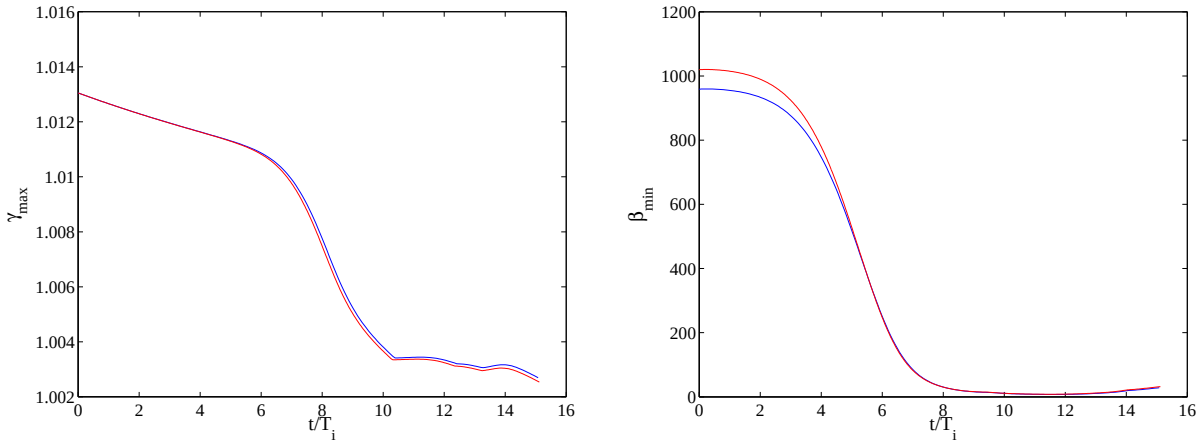

(a) maximum Lorentz factor

(b) minimum plasma β

Figure 11.36: Max. γ and min. plasma β for RMHD (blue) and MHD (red) cases
$M_A = 23, \qquad v_{Az} = 0.007\, c_0, \qquad v_{z0} = 0.16\, c_0$

of the perturbation in the flow direction, the displays span only one wavelength, as the system remains spatially periodic. Each row of displays corresponds to a specific time in the evolution (the growth time is approximately the same for both cases), where the display on the left corresponds to the RMHD simulation and the display on the right corresponds to the MHD simulation. The displays agree very closely, indicating that the RMHD regime converges to the MHD regime in the limit of non-relativistic flow speed and sound speed.

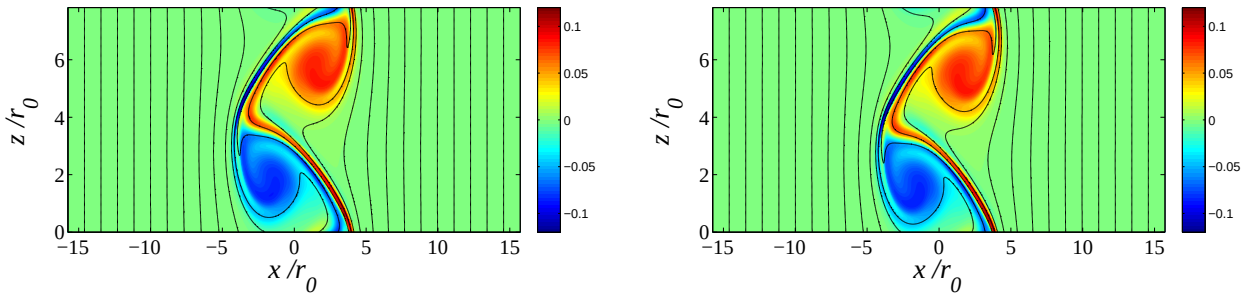

(a) RMHD $\quad \beta_{\min} = 14.0$

(b) MHD $\quad \beta_{\min} = 14.8$

Figure 11.37: Vorticity displays for RMHD and MHD cases: $t = 9.38\, T_i$
$M_A = 23, \qquad v_{Az} = 0.007\, c_0, \qquad v_{z0} = 0.16\, c_0, \qquad t = 9.382\, T_i = 399.4\, r_0/c_0$

We now wish to demonstrate convergence between the RMHD and RHD regimes. We

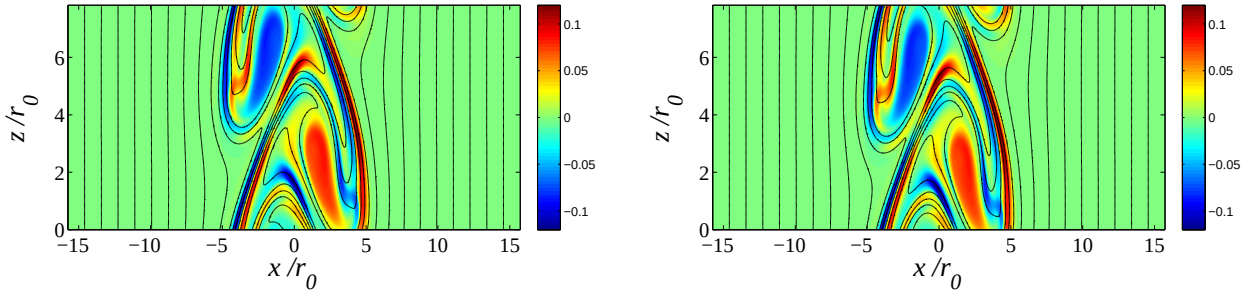

(a) RMHD $\beta_{\min} = 8.14$ (b) MHD $\beta_{\min} = 9.02$

Figure 11.38: Vorticity displays for RMHD and MHD cases: $t = 12.3\,T_i$
$M_A = 23, \qquad v_{Az} = 0.007\,c_0, \qquad v_{z0} = 0.16\,c_0, \qquad t = 12.27\,T_i = 522.2\,r_0/c_0$

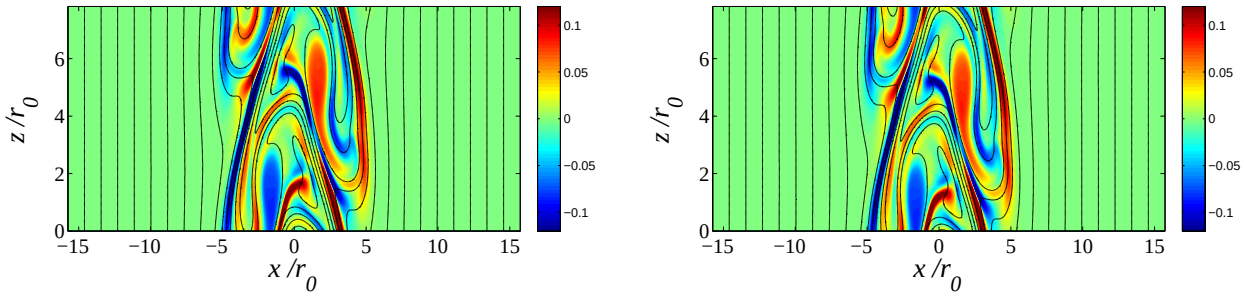

(a) RMHD $\beta_{\min} = 18.9$ (b) MHD $\beta_{\min} = 21.3$

Figure 11.39: Vorticity displays for RMHD and MHD cases: $t = 14.0\,T_i$
$M_A = 23, \qquad v_{Az} = 0.007\,c_0, \qquad v_{z0} = 0.16\,c_0, \qquad t = 14.00\,T_i = 596.0\,r_0/c_0$

compare an unmagnetized RHD case with a weakly magnetized RMHD case for which the Alfvenic Mach number $M_A = 82.83$. The parameters common to both cases are as follows:

$$\begin{aligned}
v_{z0}(x) &= 0.5\,c\,\mathrm{sech}^2(x/r_0), \\
\rho_0 c^2 &= 0.1\,\epsilon, \qquad P_0 = 5\,\epsilon, \\
c_s &= 0.576\,c, \\
k_z &= 0.8\,r_0^{-1}, \\
L_x/c_s &= 31.5\,r_0/(0.576\,c) = 54.70\,r_0/c, \qquad \text{(sound transit time)}, \\
-15.75\,r_0 \le x \le 15.75\,r_0, &\qquad 0 \le z \le \frac{2\pi}{k_z}, \\
N_x &= 1001, \qquad N_z = 201, \\
\Delta t &= 0.032\,r_0/c, \qquad \Delta x = 0.0315\,r_0, \qquad \Delta z = 0.0393\,r_0.
\end{aligned} \tag{11.11}$$

The parameters specific to the unmagnetized case are as follows:

$$\begin{aligned}
\omega_{r0} &= 0.2779\,c/r_0, \\
\omega_{i0} &= 0.0994\,c/r_0, \\
T_0 &= \frac{2\pi}{\omega_{r0}} = 22.61\,r_0/c, \\
T_{i0} &= \frac{1}{\omega_{i0}} = 10.06\,r_0/c, \\
\eta_\rho &= \eta_x = \eta_z = 0.00025\,r_0 c.
\end{aligned} \tag{11.12}$$

The parameters specific to the magnetized case are as follows:

$$\begin{aligned}
(M_A, \beta, v_A/c) &= (82.83,\ 3553,\ 0.0118), \\
\omega_r &= 0.2779\,c/r_0, \\
\omega_i &= 0.0993\,c/r_0 = 0.9991\,\omega_{i0}, \\
T &= \frac{2\pi}{\omega_r} = 22.61\,r_0/c, \\
T_i &= \frac{1}{\omega_i} = 10.07\,r_0/c, \\
\eta_\rho &= \eta_x = \eta_z = 0.0002\,r_0 c, \\
\eta_{Bx} &= \eta_{Bz} = 0.0012\,r_0 c.
\end{aligned} \tag{11.13}$$

We see that the complex eigenfrequencies are approximately the same, thereby demonstrating convergence between the RMHD and RHD regimes in the computation of numerical

linear eigenmodes. Consequently, the real and growth periods are also very nearly the same. Displays of the simulation results are shown in figures 11.40 through 11.41. These are displays of the vorticity, which in the magnetized case are superimposed with contours of the magnetic field lines. Each row corresponds to a given time in the simulations, with the displays on the left and right representing the unmagnetized and magnetized cases, respectively. The displays show close agreement in the early stages of vortex formation and evolution, and begin to diverge only when the magnetic field begins to disrupt and strain the vortices, accompanied by enhanced filamentation, which is not seen in the RHD case.

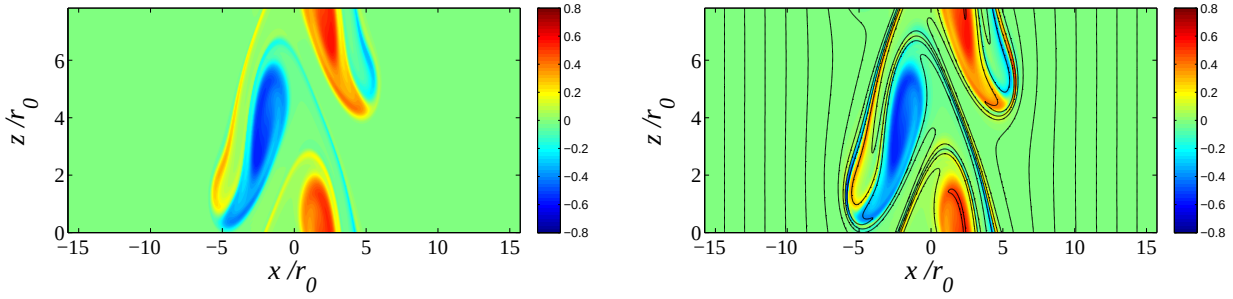

(a) $B_{z0} = 0$,

(b) $M_A = 82.83$, $v_{Az}/c = 0.0118$, $\beta = 3553$, $\beta_{\min} = 8.81$

Figure 11.40: Vorticity displays for RHD and RMHD cases: $t = 11.3\,T_i$
$t = 11.3\,T_i = 113.7\,r_0/c = 2.08\,L_x/c_s$, $v_{z0}(x) = 0.7\,c\,\mathrm{sech}^2(x/r_0)$

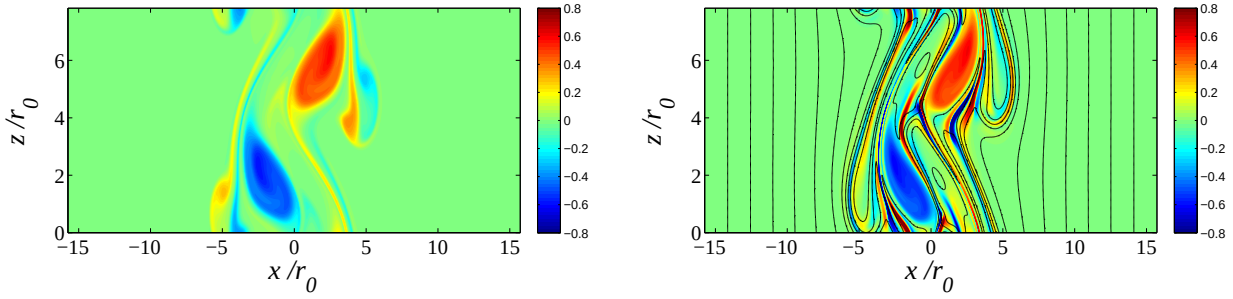

(a) $B_{z0} = 0$,

(b) $M_A = 82.83$, $v_{Az}/c = 0.0118$, $\beta = 3553$, $\beta_{\min} = 4.44$

Figure 11.41: Vorticity displays for RHD and RMHD cases: $t = 13.7\,T_i$
$t = 13.7\,T_i = 138.2\,r_0/c = 2.53\,L_x/c_s$, $v_{z0}(x) = 0.7\,c\,\mathrm{sech}^2(x/r_0)$

Having established convergence of our results between the RHD, MHD, and RMHD regimes. In the next section, we examine the sensitivity of our results to the artificial viscosity used in the simulations. Throughout the remainder of this chapter, we assume the following parameters for all cases:

$$\begin{aligned}
\rho_0 c^2 &= 0.1\,\epsilon, \qquad P_0 = 5\,\epsilon, \\
c_s &= 0.576\,c, \\
L_x/c_s &= 31.5\,r_0/(0.576\,c) = 54.70\,r_0/c, \qquad \text{(sound transit time)}, \\
-15.75\,r_0 \le x \le 15.75\,r_0, &\qquad 0 \le z \le \frac{2\pi}{k_z}, \\
N_x &= 1001, \qquad N_z = 201, \\
\Delta t &= 0.032\,r_0/c, \qquad \Delta x = 0.0315\,r_0, \qquad \Delta z = 0.0393\,r_0.
\end{aligned} \tag{11.14}$$

11.7 Influence of Viscosity on Nonlinear Evolution

We now wish to assess the influence of viscosity on the simulation results. Viscosity is included in our simulation for purposes of numerical stability, but also has physical significance. Momentum viscosity models viscous momentum transfer between microscopic eddies. As discussed in section 8.2 of chapter 8, magnetic viscosity models a conductivity which is consistent with electron and ion gyrations in relevant astrophysical environments. We begin with two cases for which $M_A = 41.41$, and compare results for magnetic viscosities of $\eta_B = 0.0012\,r_0 c$ and $\eta_B = 0.0006\,r_0 c$. We use the following parameters for both cases:

$$\begin{aligned}
c_s &= 0.576\,c, \qquad v_{z0}(x) = 0.7\,c\,\mathrm{sech}^2(x/r_0), \\
M_A &= \infty, \qquad \beta = \infty : \qquad \omega_{i0} = 0.0994\,c/r_0, \\
(M_A, \beta, v_A/c) &= (41.41,\ 888.3,\ 0.0237) : \quad \omega_i = 0.0990\,c/r_0 = 0.9965\,\omega_{i0}, \\
T_i &= 1/\omega_i = 10.10\,r_0/c, \qquad k_z = 0.8\,r_0^{-1}, \\
\eta_\rho &= \eta_x = \eta_z = 0.0002\,r_0 c.
\end{aligned} \tag{11.15}$$

We first examine the time-dependent behavior of certain quantities which at each time

step are spatially averaged or maximized over the numerical grid. The blue curve corresponds to $\eta_B = 0.0012\, r_0 c$ and the red curve to $\eta_B = 0.0006\, r_0 c$. Figures 11.42 through 11.43 compare the time-dependence of the growth in fluctuations of the primitive variables. We see very close agreement in each of these graphs, indicating that magnetic viscosity has little influence on the behavior of the fluctuations. Figures 11.44 through 11.45 show the time-dependence of average (or RMS) vorticity, current density, Lorentz factor, and velocity components, along with the maximum Lorentz factor and velocity components, and minimum plasma β. The RMS vorticity and current density are consistently higher, and the minimum plasma β consistently lower, for the lower magnetic viscosity, indicating that the effective magnetic field is generally stronger for lower magnetic viscosities. The quantities related to velocity agree very closely, indicating that these are not significantly influenced by the magnetic viscosity.

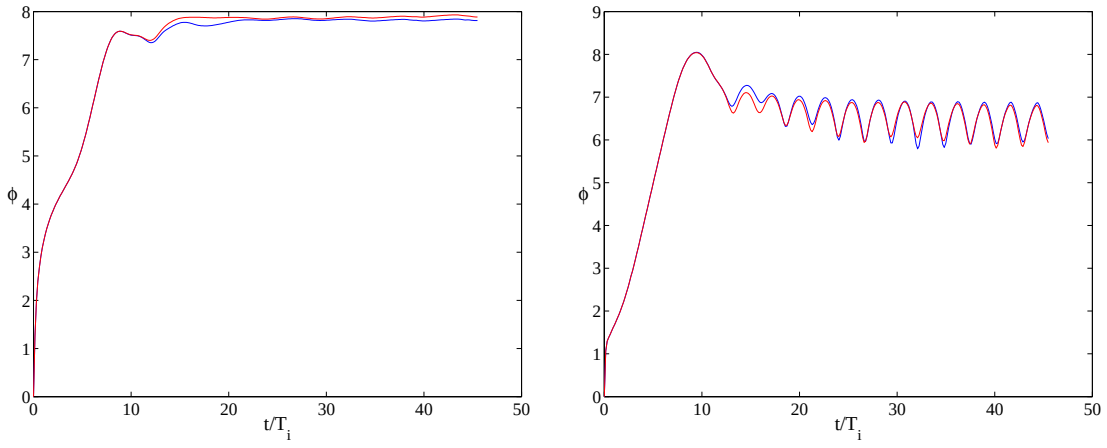

(a) longitudinal velocity fluctuations (b) transverse velocity fluctuations

Figure 11.42: Viscosity-dependence of growth in velocity components: $M_A = 41$ $\eta_B/(r_0 c) = 0.0012$ (blue), 0.0006 (red)

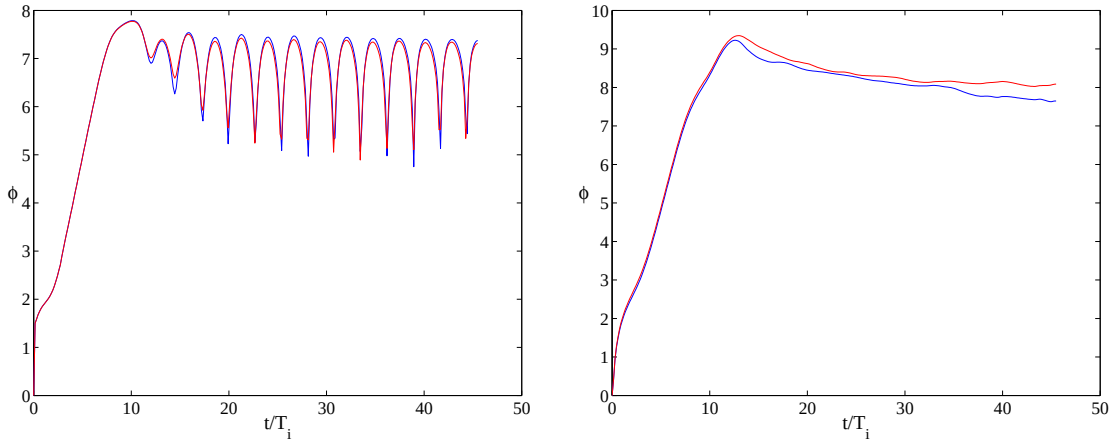

(a) pressure fluctuations (b) longitudinal field fluctuations

Figure 11.43: Viscosity-dependence of growth in P and B_z: $M_A = 41$ $M_A = 41, \quad \eta_B/(r_0 c) = 0.0012$ (blue), 0.0006 (red)

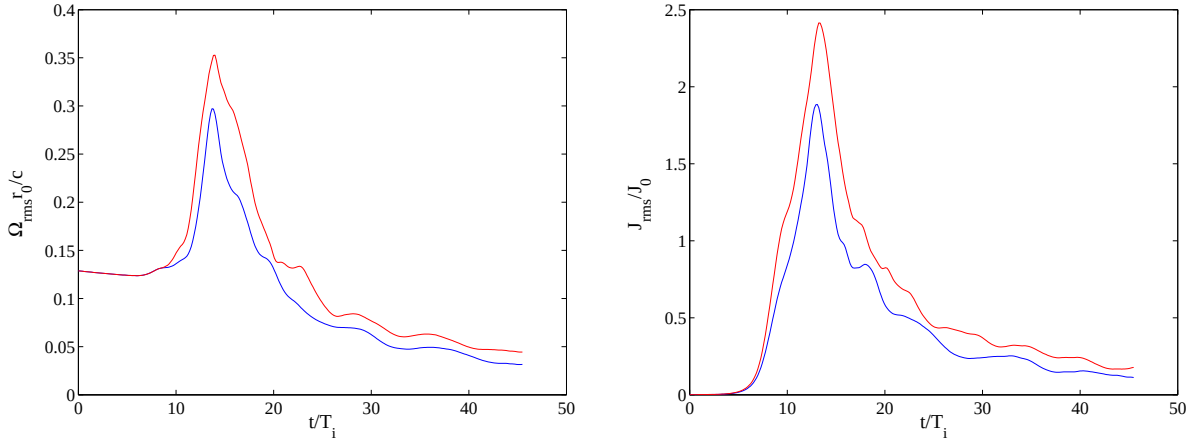

(a) RMS vorticity (b) RMS current density

Figure 11.44: Viscosity-dependence of RMS vorticity and current density: $M_A = 41$ $M_A = 41, \quad \eta_B/(r_0 c) = 0.0012$ (blue), 0.0006 (red)

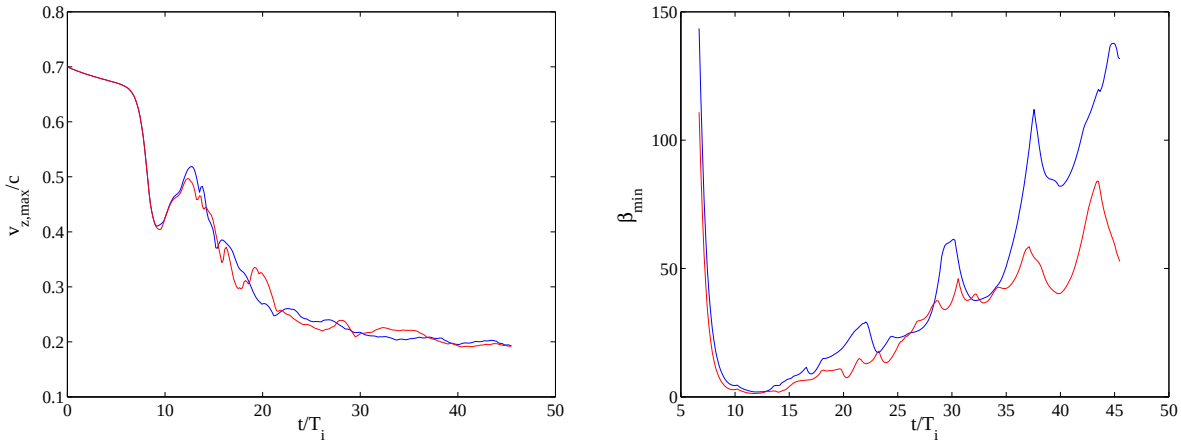

(a) maximum longitudinal velocity

(b) minimum plasma β

Figure 11.45: Viscosity-dependence of Max. v_z, min. plasma β: $M_A = 41$
$M_A = 41, \qquad \eta_B/(r_0 c) = 0.0012$ (blue), 0.0006 (red)

We now compare displays of the vorticity, in figures 11.46 through 11.49, where each display is overlaid with contours of the magnetic field lines. Each row corresponds to a given time step in the simulation, where the display on the left corresponds to $\eta_B = 0.0012\, r_0 c$ and the display on the right to $\eta_B = 0.0006\, r_0 c$. We observe close agreement that persists through the linear regime and through the early stages of vortex formation and development. However, the results begin to diverge in the latter stages of vortex disruption by the field, indicating that this disruption is sensitive to the magnetic viscosity. This seems to emerge from the complexity of the processes leading to the transition to a turbulent regime, namely, vortex deformation, filamentation, magnetic reconnection, and reorganization of smaller eddy structures. For both viscosities, however, the jet widens to an equilibrium width of about $16\, r_0$.

Figures 11.50 and 11.51 show comparisons of displays of the longitudinal velocity, again superimposed with contours of the magnetic field lines. We see that the flow widens in both cases, but that in the latter stages of evolution, the equilibrium width of the central flow

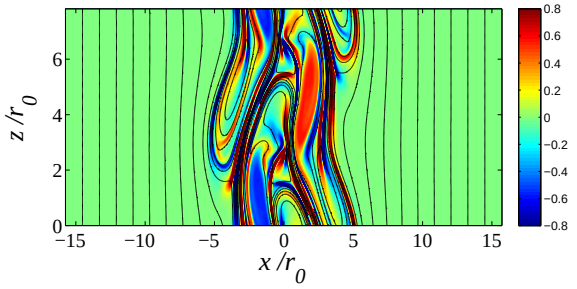

(a) $\eta_B = 0.0012\, r_0 c, \quad \beta_{\min} = 3.38$

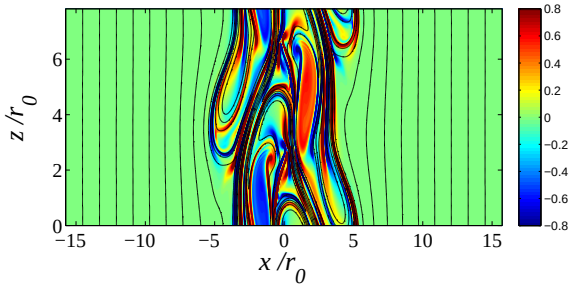

(b) $\eta_B = 0.0006\, r_0 c, \quad \beta_{\min} = 2.20$

Figure 11.46: Viscosity-dependence of vorticity for $M_A = 41$: $t = 13.4\, T_i$
$t = 135\, r_0/c = 5.97\, T = 13.4\, T_i = 2.47\, L_x/c_s, \quad (M_A, v_{Az}/c, v_{z0}/c) = (41.4, 0.0237, 0.7)$

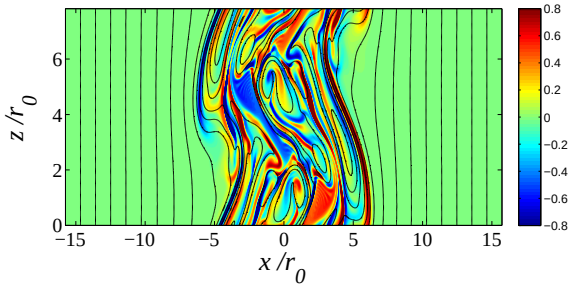

(a) $\eta_B = 0.0012\, r_0 c, \quad \beta_{\min} = 7.35$

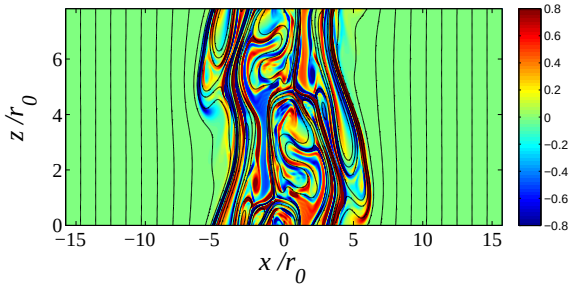

(b) $\eta_B = 0.0006\, r_0 c, \quad \beta_{\min} = 4.72$

Figure 11.47: Viscosity-dependence of vorticity for $M_A = 41$: $t = 15.2\, T_i$
$t = 154\, r_0/c = 6.79\, T = 15.2\, T_i = 2.81\, L_x/c_s, \quad (M_A, v_{Az}/c, v_{z0}/c) = (41.4, 0.0237, 0.7)$

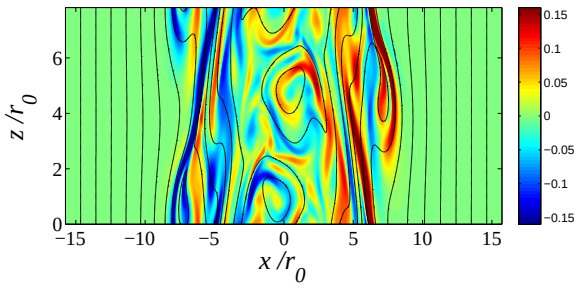

(a) $\eta_B = 0.0012\, r_0 c, \quad \beta_{\min} = 38.34$

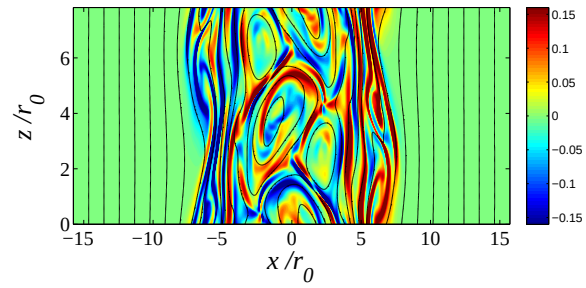

(b) $\eta_B = 0.0006\, r_0 c, \quad \beta_{\min} = 36.58$

Figure 11.48: Viscosity-dependence of vorticity for $M_A = 41$: $t = 32.9\, T_i$
$t = 332\, r_0/c = 14.7\, T = 32.9\, T_i = 6.07\, L_x/c_s, \quad (M_A, v_{Az}/c, v_{z0}/c) = (41.4, 0.0237, 0.7)$

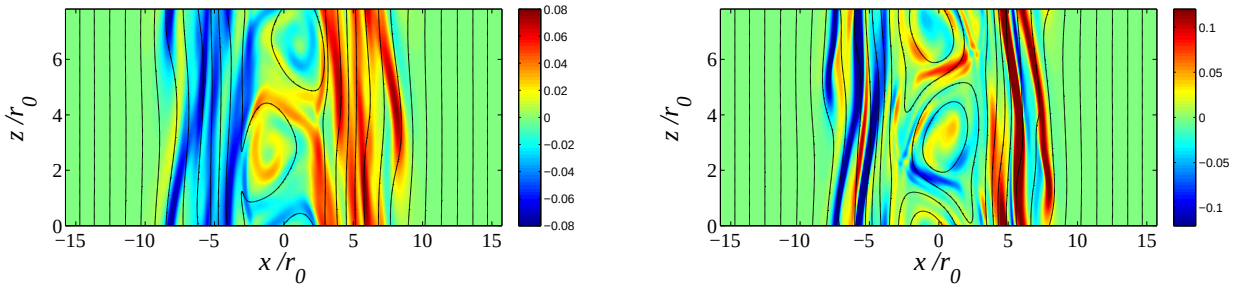

(a) $\eta_B = 0.0012\, r_0 c, \quad \beta_{\min} = 173.8$ (b) $\eta_B = 0.0006\, r_0 c, \quad \beta_{\min} = 70.23$

Figure 11.49: Viscosity-dependence of vorticity for $M_A = 41$: $t = 52.9\, T_i$
$t = 535\, r_0/c = 23.6\, T = 52.9\, T_i \;=\; 9.77\, L_x/c_s, \quad (M_A, v_{Az}/c, v_{z0}/c) = (41.4, 0.0237, 0.7)$

is about 10% wider in the case with lower magnetic viscosity than in the case with higher viscosity. However, the equilibrium width of the jet (about $16\, r_0$) is approximately the same for both viscosities, as is the overall structure of the flow.

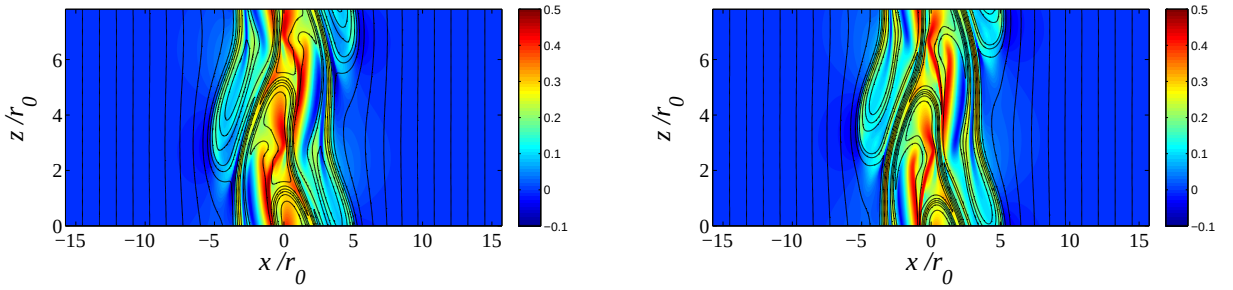

(a) $\eta_B = 0.0012\, r_0 c, \quad \beta_{\min} = 3.38$ (b) $\eta_B = 0.0006\, r_0 c, \quad \beta_{\min} = 2.20$

Figure 11.50: Viscosity-dependence of longitudinal velocity for $M_A = 41$: $t = 13.4\, T_i$
$t = 135\, r_0/c = 5.97\, T = 13.4\, T_i \;=\; 2.47\, L_x/c_s, \quad (M_A, v_{Az}/c, v_{z0}/c) = (41.4, 0.0237, 0.7)$

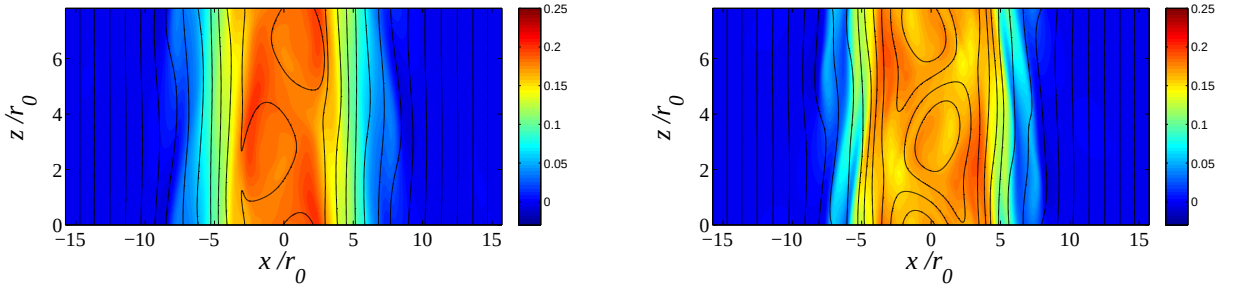

(a) $\eta_B = 0.0012\, r_0 c, \quad \beta_{\min} = 173.8$ (b) $\eta_B = 0.0006\, r_0 c, \quad \beta_{\min} = 70.23$

Figure 11.51: Viscosity-dependence of longitudinal velocity for $M_A = 41$: $t = 52.9 T_i$
$t = 535\, r_0/c = 23.6\, T = 52.9\, T_i \;=\; 9.77\, L_x/c_s, \quad (M_A, v_{Az}/c, v_{z0}/c) = (41.4, 0.0237, 0.7)$

We now consider a stronger magnetic field corresponding to $M_A = 21$, and compare two cases with respective magnetic viscosities of $0.0012\, r_0 c$ and $0.0008\, r_0 c$. The parameters for both cases are as follows:

$$
\begin{aligned}
c_s &= 0.576\, c, \qquad v_{z0}(x) = 0.7\, c\, \mathrm{sech}^2(x/r_0), \\
k_z &= 0.8\, r_0^{-1}, \\
M_A &= \infty : \qquad \omega_{i0} = 0.0994\, c/r_0, \\
M_A &= 20.70 : \qquad \omega_i = 0.0980\, c/r_0 = 0.986\, \omega_{i0}, \\
\text{growth time :} \qquad T_i &= \frac{1}{\omega_i} = 10.20\, r_0/c, \\
\text{period :} \qquad T &= \frac{2\pi}{\omega_r} = 22.68\, r_0/c, \\
v_A &= 0.0473\, c, \qquad \beta = 222.1, \\
L_x/v_A &= 31.5\, r_0/(0.0473\, c) = 666.0\, r_0/c, \qquad \text{(Alfven transit time)}, \\
\eta_\rho &= \eta_x = \eta_z = 0.0002\, r_0 c. \qquad (11.16)
\end{aligned}
$$

As before, we compare the time-dependence of certain quantities which, at each time step, are either spatially averaged or maximized over the numerical grid. In each of figures 11.52 through 11.56, the black curve corresponds to momentum and field viscosities of $0.0002\, r_0 c$ and $0.0012\, r_0 c$, respectively. The blue curve corresponds to momentum and field viscosities of $0.0002\, r_0 c$ and $0.0008\, r_0 c$, respectively. The red curve corresponds to momentum and field viscosities of $0.00013\, r_0 c$ and $0.0012\, r_0 c$, respectively. As with the previous cases for $M_A = 41$, figures 11.52 through 11.53 show that there is excellent agreement in the growth in fluctuations of primitive variables (density, velocity, pressure, magnetic field), indicating that, once again, the growth in fluctuations is not sensitive to field or momentum viscosity. Figures 11.54 through 11.56 show the time-dependence of the RMS vorticity, RMS current density, maximum longitudinal velocity and Lorentz factor, minimum plasma β, and average pressure. There is close agreement between quantities related to velocity, indicating that these, again,

are not heavily affected by momentum and field viscosity. The RMS vorticity and current density are consistently higher in the cases with more viscosity, while the minimum plasma β values are about the same. It appears that in the regime of strongly vortex-disruptive fields ($M_A = 21$), these viscosities suppress enhancement of vortices and current sheets, but have little effect on the magnetic pressure itself.

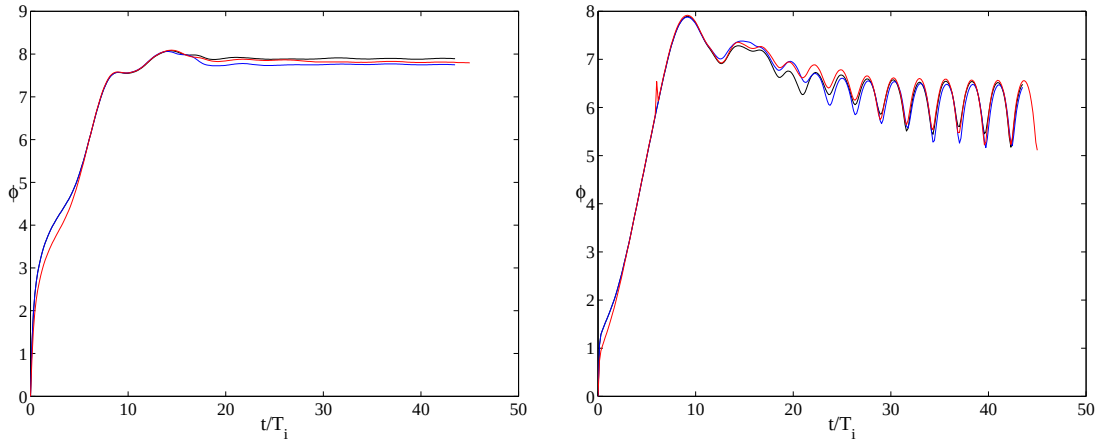

(a) longitudinal velocity fluctuations (b) transverse velocity fluctuations

Figure 11.52: Viscosity-dependence of growth in velocity components: $M_A = 21$ $10000\,(\eta_v, \eta_B)/(r_0 c)$ = (2,12) (black), (2,8) (blue), (1.3,12) (red)

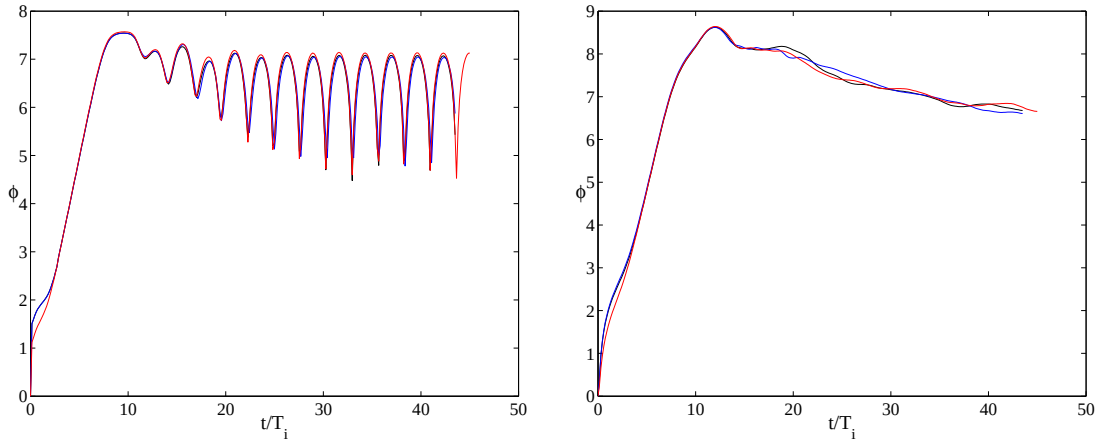

(a) pressure fluctuations (b) longitudinal field fluctuations

Figure 11.53: Viscosity-dependence of growth in P and B_z: $M_A = 21$ $10000\,(\eta_v, \eta_B)/(r_0 c)$ = (2,12) (black), (2,8) (blue), (1.3,12) (red)

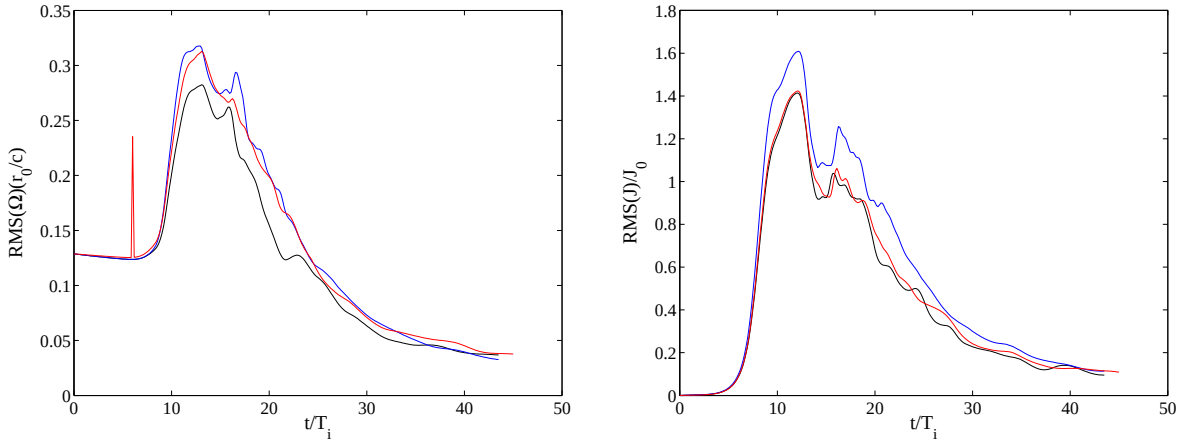

(a) RMS vorticity

(b) RMS current density

Figure 11.54: Viscosity-dependence of RMS vorticity and current density: $M_A = 21$ 10000 $(\eta_v, \eta_B)/(r_0 c)$ = (2,12) (black), (2,8) (blue), (1.3,12) (red)

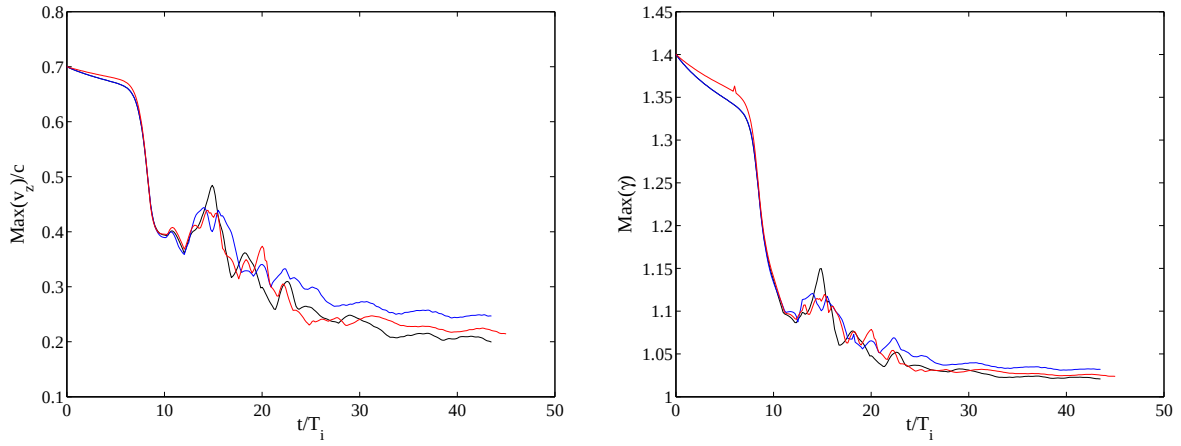

(a) maximum longitudinal velocity

(b) maximum Lorentz factor

Figure 11.55: Viscosity-dependence of max. longit. veloc. and Lorentz factor: $M_A = 21$ 10000 $(\eta_v, \eta_B)/(r_0 c)$ = (2,12) (black), (2,8) (blue), (1.3,12) (red)

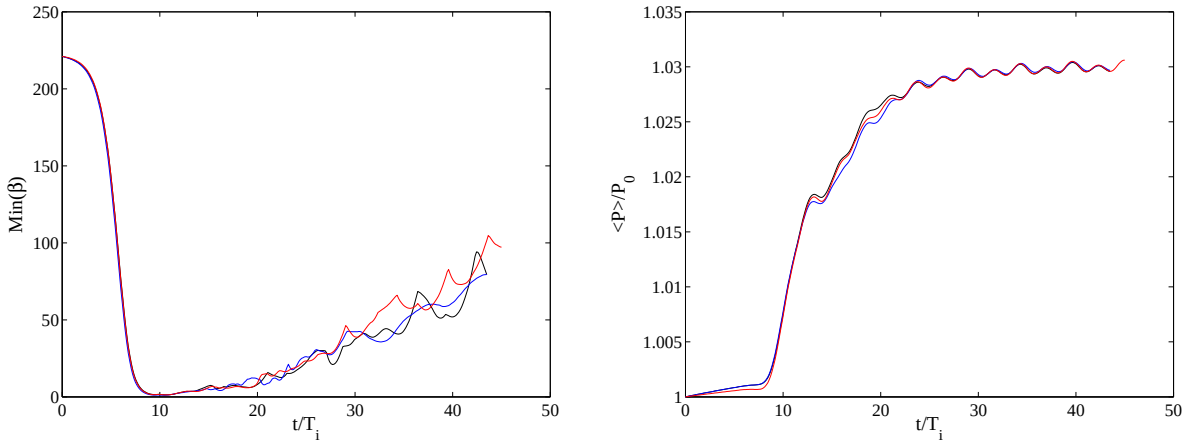

(a) minimum plasma β (b) average pressure

Figure 11.56: Viscosity-dependence of min. plasma β and avg. pressure: $M_A = 21$ 10000 $(\eta_v, \eta_B)/(r_0 c)$ = (2,12) (black), (2,8) (blue), (1.3,12) (red)

Figures 11.57 through 11.59 present displays of the vorticity, overlaid with contours of the magnetic field lines. Each row corresponds to a given time step, and the displays on left and right correspond to respective magnetic viscosities of $0.0012\, r_0 c$ and $0.0008\, r_0 c$. As with $M_A = 41$, there is good agreement through the linear regime and early stages of vortex evolution. However, as before, the two cases diverge in the later stages of vortex disruption and the transition to a filamented state. Nevertheless, the equilibrium jet width is about $15\, r_0$ in both cases, and the flow-aligned vortex filaments have the same qualitative features, particularly in the exterior regions (1 r_0 in width, positive vorticity for $x > 0$, negative for $x < 0$). Close to the axis, the filamentary behavior differs somewhat between the two viscosities, though the difference is not as great as was the case for the weaker field $M_A = 41$. This leads to several conclusions. As we move further from the jet axis, there is a decrease in sensitivity, to magnetic viscosity, of the equilibrium configuration. Also, weaker fields correspond to a more complex and turbulent reorganization, and therefore have greater sensitivity to such input parameters as magnetic viscosity.

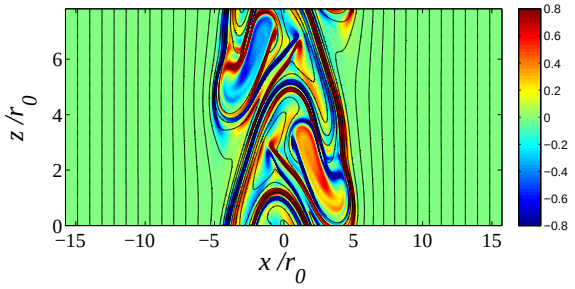

(a) $\eta_B = 0.0012\, r_0 c, \quad \beta_{\min} = 3.524$

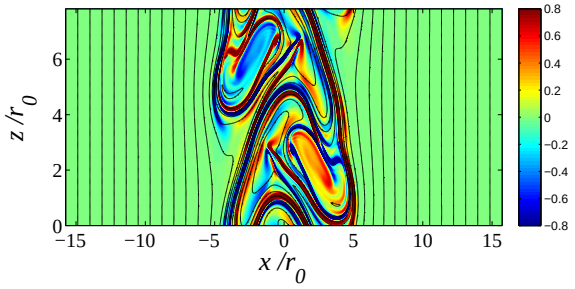

(b) $\eta_B = 0.0008\, r_0 c, \quad \beta_{\min} = 3.113$

Figure 11.57: Viscosity-dependence of vorticity for $M_A = 21$: $t = 12.6\, T_i$
$t = 129\, r_0/c = 5.69\, T = 12.6\, T_i = 2.36\, L_x/c_s, \quad (M_A, v_{Az}/c, v_{z0}/c) = (20.7, 0.0473, 0.7)$

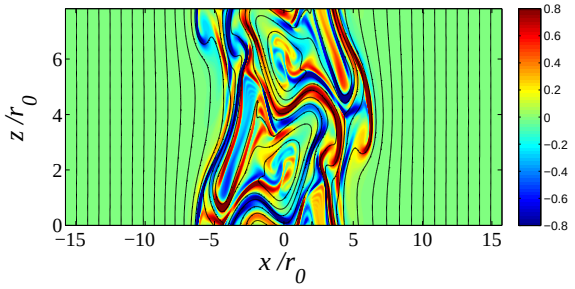

(a) $\eta_B = 0.0012\, r_0 c, \quad \beta_{\min} = 7.208$

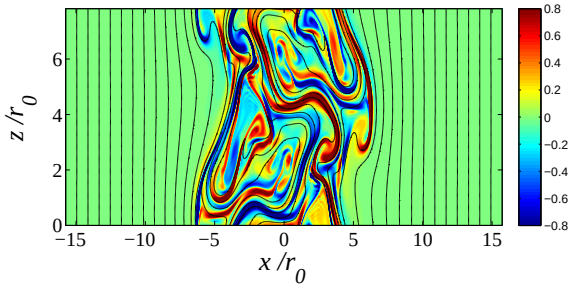

(b) $\eta_B = 0.0008\, r_0 c, \quad \beta_{\min} = 4.783$

Figure 11.58: Viscosity-dependence of vorticity for $M_A = 21$: $t = 15.1\, T_i$
$t = 154\, r_0/c = 6.77\, T = 15.1\, T_i = 2.81\, L_x/c_s, \quad (M_A, v_{Az}/c, v_{z0}/c) = (20.7, 0.0473, 0.7)$

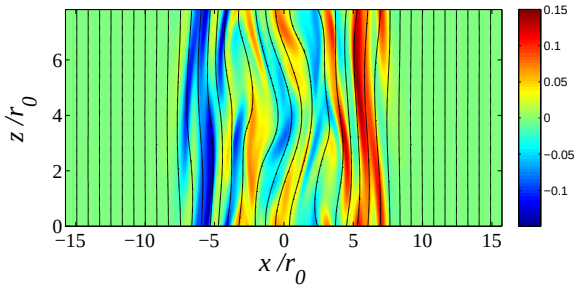

(a) $\eta_B = 0.0012\, r_0 c, \quad \beta_{\min} = 82.01$

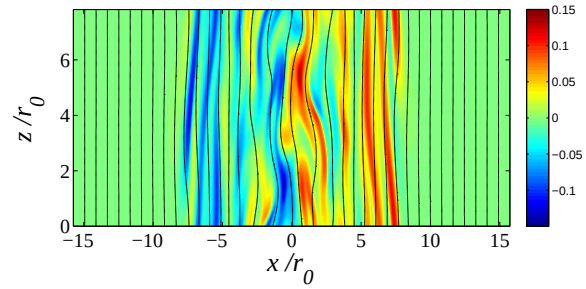

(b) $\eta_B = 0.0008\, r_0 c, \quad \beta_{\min} = 79.33$

Figure 11.59: Viscosity-dependence of vorticity for $M_A = 21$: $t = 43.4\, T_i$
$t = 442\, r_0/c = 19.5\, T = 43.4\, T_i = 8.09\, L_x/c_s, \quad (M_A, v_{Az}/c, v_{z0}/c) = (20.7, 0.0473, 0.7)$

In figure 11.60, we display the longitudinal velocity for the two viscosities, again overlaid with contours of the magnetic field lines, in a near-equilibrium configuration. The flow width is about $15\,r_0$ in both cases. In each case, there is also a filamentary region of higher flow speed, about 1 r_0 in width, localized around the jet axis. In the less viscous case, $0.0008\,r_0c$, the flow speed in this region oscillates along the axis between $0.2\,c$ and $0.25\,c$. In the more viscous case, $0.0012\,r_0c$, the flow speed is only about $0.17\,c$, and remains uniform along the filament, though this filament is less aligned with the central axis than in the $0.0008\,r_0c$ case.

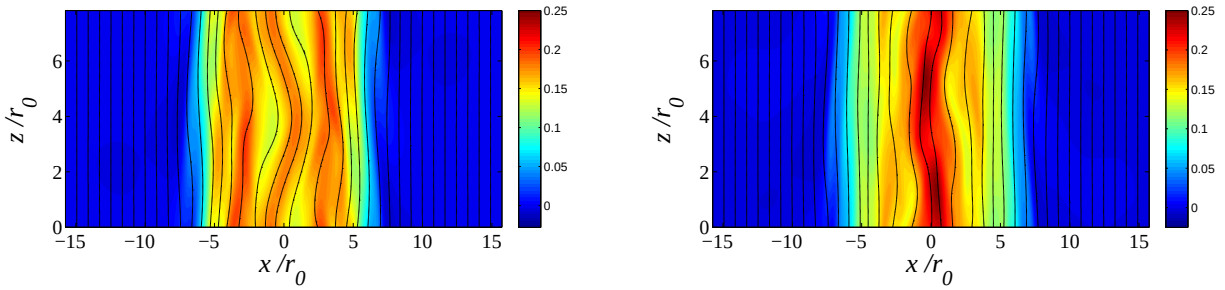

(a) $\eta_B = 0.0012\,r_0c$, $\beta_{\min} = 82.01$ (b) $\eta_B = 0.0008\,r_0c$, $\beta_{\min} = 79.33$

Figure 11.60: Viscosity-dependence of longitudinal velocity for $M_A = 21$: $t = 43.4\,T_i$ $t = 442\,r_0/c = 19.5\,T = 43.4\,T_i = 8.09\,L_x/c_s$, $(M_A, v_{Az}/c, v_{z0}/c) = (20.7, 0.0473, 0.7)$

We finally consider a strong vortex-suppressing magnetic field corresponding to $M_A = 5.145$, with a smaller background flow speed amplitude of $0.5\,c$, and compare two cases with respective momentum viscosities of $0.0002\,r_0c$, $0.0002\,r_0c$, and $0.00015\,r_0c$, and respective magnetic field viscosities of $0.0012\,r_0c$, $0.0008\,r_0c$, and $0.0008\,r_0c$. Unlike the previous two fields, this field suppresses vortex formation, resulting in a more rapid transition to a filamented state. Because this transition is less complex, we will see, from the vorticity displays, that the three cases give results which are qualitatively much more similar than was observed in the weaker-field cases. The parameters for this magnetic field are as follows:

$$
\begin{aligned}
c_s &= 0.576\,c, \qquad v_{z0}(x) = 0.5\,c\,\mathrm{sech}^2(x/r_0), \\
k_z &= 0.8\,r_0^{-1}, \\
M_A &= \infty : \qquad \omega_{i0} = 0.0760\,c/r_0, \\
M_A &= 5.145 : \qquad \omega_i = 0.0565\,c/r_0 = 0.744\,\omega_{i0}, \\
\text{growth time :} \qquad T_i &= \frac{1}{\omega_i} = 17.69\,r_0/c, \\
\text{period :} \qquad T &= \frac{2\pi}{\omega_r} = 35.34\,r_0/c, \\
v_A &= 0.1115\,c, \qquad \beta = 40, \\
L_x/v_A &= 31.5\,r_0/(0.1115\,c) = 282.5\,r_0/c, \qquad \text{(Alfven transit time).}
\end{aligned}
\tag{11.17}
$$

As before, we compare the time-dependence of certain quantities which, at each time step, are either spatially averaged or maximized over the numerical grid. Figures 11.61 through 11.62 show the time-dependence of the growth in fluctuations of the primitive variables (density, velocity, pressure, magnetic field). The largest discrepancies occur with the growth of the magnetic field components in the nonlinear regime, which is consistent with the fact that only the magnetic viscosities are different. Figures 11.63 through 11.65 show the time-dependence of the RMS vorticity, RMS current density, velocity components, minimum plasma β, and pressure. As with the weaker-field cases, quantities related to velocity are in close agreement. The vorticity and current density are higher, and the minimum plasma β is lower, for the lower viscosity case, indicating that, as in the weaker-field $M_A = 41$ case, a lower viscosity generally corresponds to a stronger magnetic field. The black, blue, and red curves correspond to respective momentum viscosities of $0.0002\,r_0c$, $0.0002\,r_0c$, and $0.00015\,r_0c$, and to respective magnetic field viscosities of $0.0012\,r_0c$, $0.0008\,r_0c$, and $0.0008\,r_0c$.

Figures 11.66 through 11.68 present displays of the vorticity, overlaid with contours of the magnetic field lines. Each row corresponds to a given time step, and the displays on

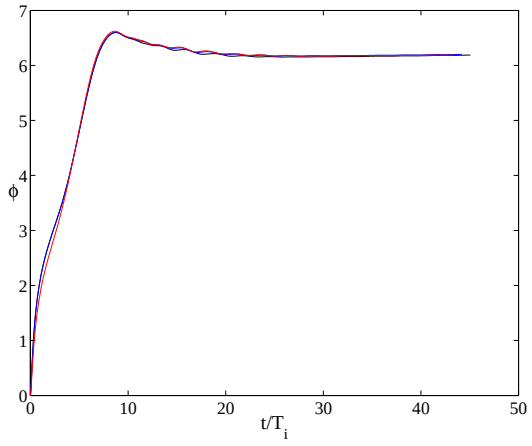

(a) longitudinal velocity fluctuations

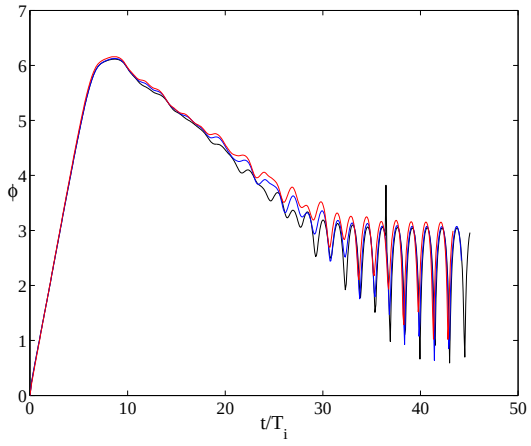

(b) transverse velocity fluctuations

Figure 11.61: Viscosity-dependence of growth in velocity components: $M_A = 5.1$ $10000\,(\eta_v, \eta_B)/(r_0 c)$ = (2,12) (black), (2,8) (blue), (1.5,8) (red)

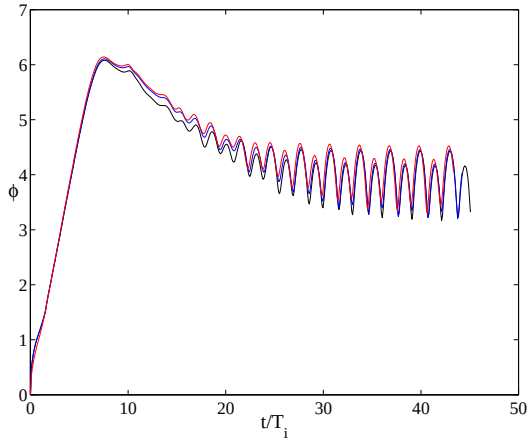

(a) pressure fluctuations

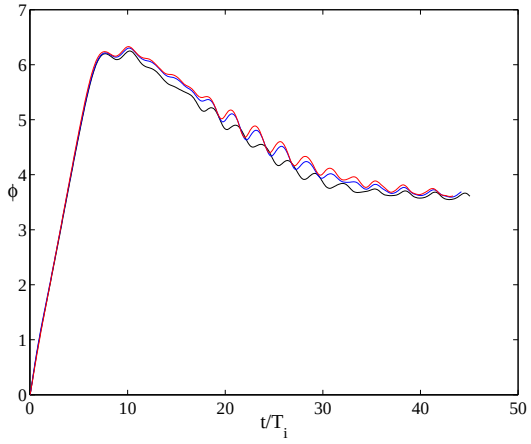

(b) longitudinal field fluctuations

Figure 11.62: Viscosity-dependence of growth in P and B_z: $M_A = 5.1$ $10000\,(\eta_v, \eta_B)/(r_0 c)$ = (2,12) (black), (2,8) (blue), (1.5,8) (red)

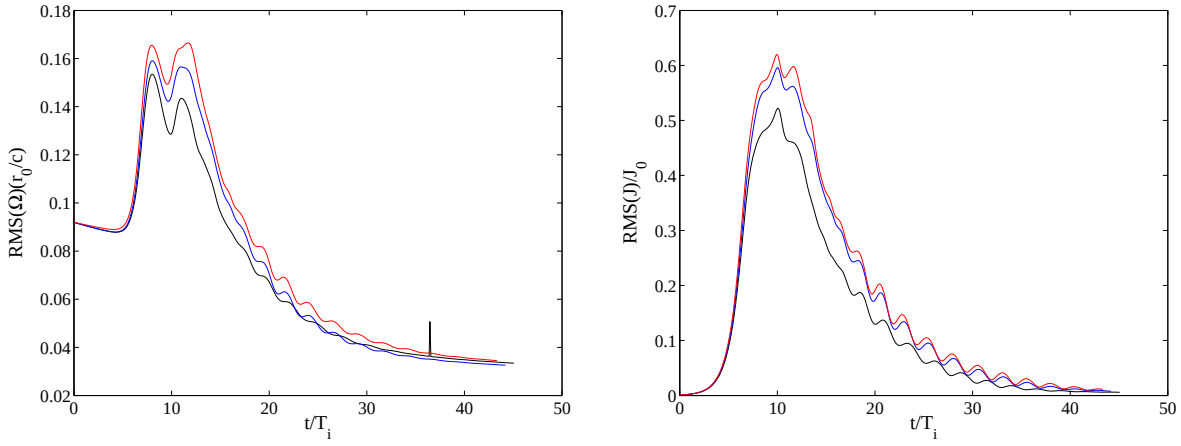

(a) RMS vorticity

(b) RMS current density

Figure 11.63: Viscosity-dependence of vorticity and current density: $M_A = 5.1$ 10000 $(\eta_v, \eta_B)/(r_0 c)$ = (2,12) (black), (2,8) (blue), (1.5,8) (red)

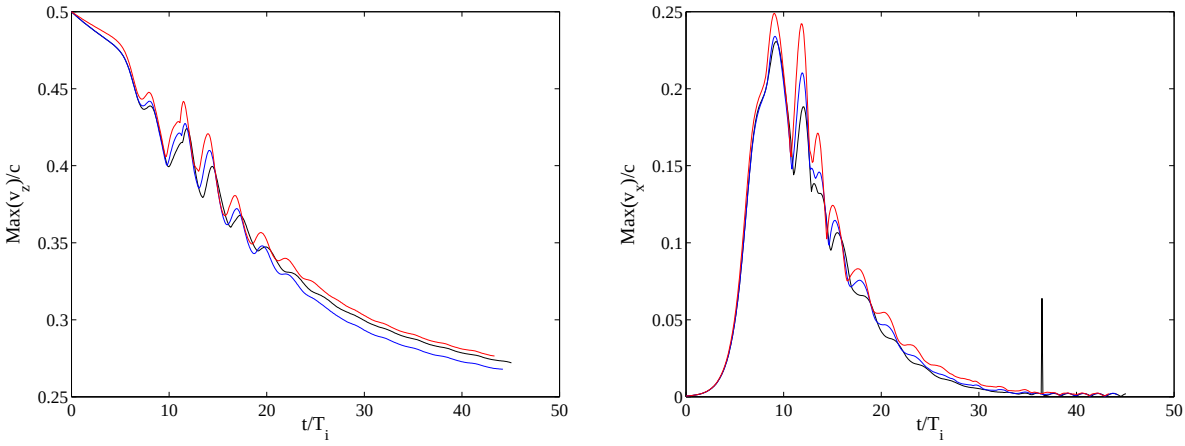

(a) maximum longitudinal velocity

(b) maximum transverse velocity

Figure 11.64: Viscosity-dependence of maximum velocity components: $M_A = 5.1$ 10000 $(\eta_v, \eta_B)/(r_0 c)$ = (2,12) (black), (2,8) (blue), (1.5,8) (red)

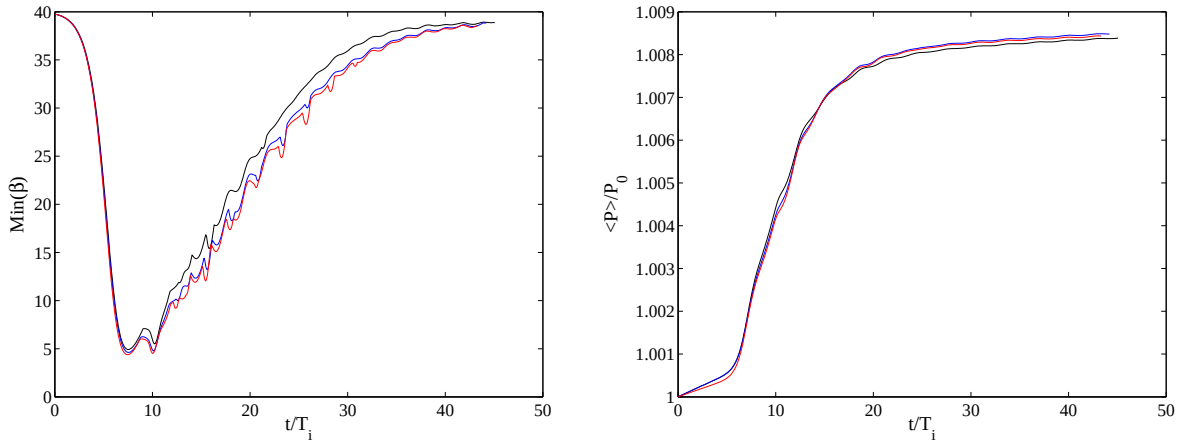

(a) minimum plasma β (b) average pressure

Figure 11.65: Viscosity-dependence of minimum plasma β and avg. pressure: $M_A = 5.1$ $10000\,(\eta_v, \eta_B)/(r_0 c)$ = (2,12) (black), (2,8) (blue), (1.5,8) (red)

left and right correspond to respective magnetic viscosities of $0.0006\,r_0 c$ and $0.0004\,r_0 c$. As with $M_A = 41$ and $M_A = 21$, there is good agreement through the linear regime. The displays are generally in close qualitative agreement, indicating that the vorticity behavior has little qualitative dependence on the magnetic viscosity, unlike the weaker-field cases. The stronger field, corresponding to $M_A = 5.145$, suppresses vortex formation, resulting in a rapid transition to a filamented state, a transition process which is much less turbulent, and less complex than in the weaker-field cases that allow vortex formation. With a less complex evolution, the system can be expected to have less qualitative sensitivity to magnetic viscosity. However, as the time-dependent curves show, the quantitative sensitivity is about the same as for the weaker-field cases.

Having examined the sensitivity of our results to viscosity, in the next section we examine their sensitivity to the background flow speed.

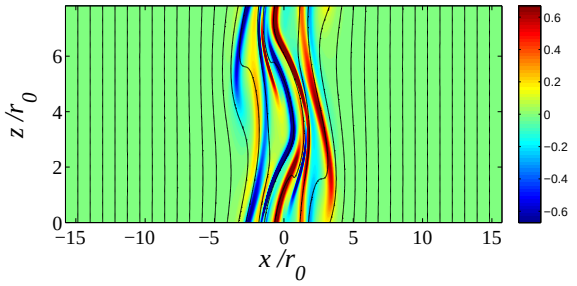

(a) $(10^4\eta_B, \Omega_{\rm rms}, \beta_{\rm min}) = (6\,r_0c, 0.15\,c/r_0, 4.73)$

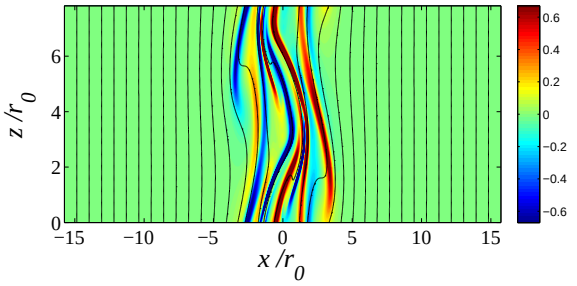

(b) $(10^4\eta_B, \Omega_{\rm rms}, \beta_{\rm min}) = (4\,r_0c, 0.17\,c/r_0, 4.36)$

Figure 11.66: Viscosity-dependence of vorticity for $M_A = 5.1$: $t = 10.3\,T_i$
$t = 10.3\,T_i = 5.13\,T = 181\,r_0/c = 3.31\,L_x/c_s, \quad (M_A, v_{Az}/c, \beta, v_{z0}/c) = (5.2, 0.11, 40, 0.5)$

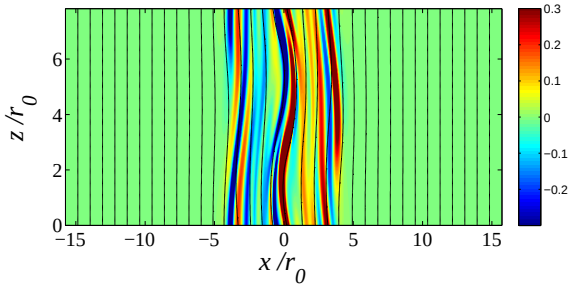

(a) $(10^4\eta_B, \Omega_{\rm rms}, \beta_{\rm min}) = (6\,r_0c, 0.09\,c/r_0, 18.1)$

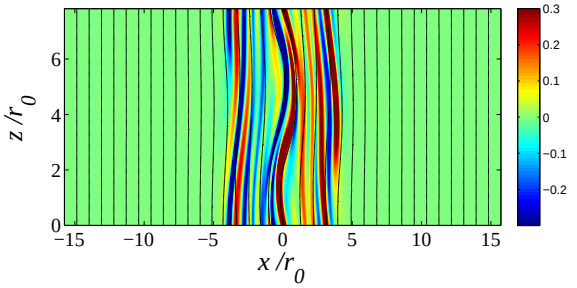

(b) $(10^4\eta_B, \Omega_{\rm rms}, \beta_{\rm min}) = (4\,r_0c, 0.10\,c/r_0, 14.8)$

Figure 11.67: Viscosity-dependence of vorticity for $M_A = 5.1$: $t = 17.5\,T_i$
$t = 17.5\,T_i = 8.78\,T = 310\,r_0/c = 5.67\,L_x/c_s, \quad (M_A, v_{Az}/c, \beta, v_{z0}/c) = (5.2, 0.11, 40, 0.5)$

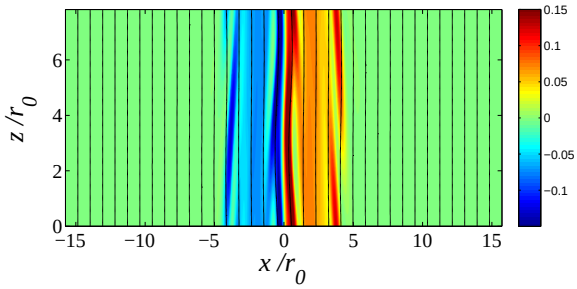

(a) $(10^4\eta_B, \Omega_{\rm rms}, \beta_{\rm min}) = (6\,r_0c, 0.04\,c/r_0, 33.1)$

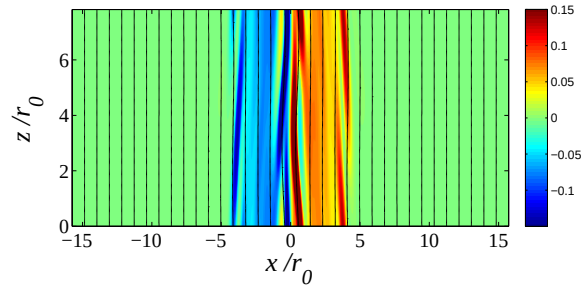

(b) $(10^4\eta_B, \Omega_{\rm rms}, \beta_{\rm min}) = (4\,r_0c, 0.04\,c/r_0, 32.9)$

Figure 11.68: Viscosity-dependence of vorticity for $M_A = 5.1$: $t = 28.3\,T_i$
$t = 28.3\,T_i = 14.2\,T = 501\,r_0/c = 9.15\,L_x/c_s, \quad (M_A, v_{Az}/c, \beta, v_{z0}/c) = (5.2, 0.11, 40, 0.5)$

11.8 Dependence on Flow Speed

In chapter 9, we plotted the time-dependence of certain spatially-averaged quantities, for background flow speed amplitudes of both $0.7\,c$ and $0.5\,c$, specifically as a function of the number of growth times. We observed that, at each Alfvenic Mach number M_A, corresponding curves were very similar for both flow speeds when plotted as a function of growth time, and that this agreement persisted well into the nonlinear regime. In figures 11.69 through 11.71, we compare vorticity displays, again overlaid with contours of the magnetic field lines, for the two flow speeds, at $M_A = 10.34$. Each row corresponds to a given number of growth times, where the display on the left corresponds to a flow speed amplitude of $0.7\,c$ and the display on the right to a flow speed amplitude of $0.5\,c$. We observe close agreement between corresponding displays, i.e., after a given number of growth times. The main discrepancy between these figures is a longitudinal phase shift arising from differences in the pattern speeds, which would be expected for different background flow speeds. Linear phase velocity, and hence nonlinear pattern speed, are both dependent on the background flow speed. However, the influence of the magnetic field on the flow remains roughly the same at both flow speeds. This supports two important conclusions. First, the relativistic Alfvenic Mach number M_A is indeed the governing parameter that, within a regime of moderately relativistic flow speeds, characterizes the influence of the magnetic field on the evolution of the system. Second, it is the growth time (not acoustic transit time, Alfven transit time, or period) that serves as the fundamental time unit for characterizing the development of the instability. Notice, in the parameters below, that for both flow speeds, the fractional reduction in growth rate is about 94 %, relative to the unmagnetized case. Recall the observation made in an earlier

chapter, in which we plotted linear growth rate as a function of magnetic field strength. We concluded that for moderately relativistic flow speeds, the fractional reduction in growth rate, by the field, is a function of Alfvenic Mach number, not flow speed.

The parameters specific to $v_{z0}(x) \;=\; 0.7\,c\,\mathrm{sech}^2(x/r_0)$ are as follows:

$$\begin{aligned}
M_A \;&=\; \infty: \qquad \omega_{i0} \;=\; 0.0994\,c/r_0, \\
M_A \;&=\; 10.34: \qquad \omega_i \;=\; 0.0937\,c/r_0 \;=\; 0.943\,\omega_{i0}, \\
\text{growth time}: \qquad T_i \;&=\; \frac{1}{\omega_i} \;=\; 10.67\,r_0/c, \\
\text{period}: \qquad T \;&=\; \frac{2\pi}{\omega_r} \;=\; 22.89\,r_0/c, \\
v_A \;&=\; 0.0947\,c, \qquad \beta \;=\; 55.52, \\
L_x/v_A \;&=\; 31.5\,r_0/(0.0947c) \;=\; 332.6\,r_0/c, \qquad \text{(Alfven transit time)}, \\
\eta_\rho \;&=\; \eta_x \;=\; \eta_z \;=\; 0.0002\,r_0 c, \\
\eta_{Bx} \;&=\; \eta_{Bz} \;=\; 0.0012\,r_0 c. \qquad (11.18)
\end{aligned}$$

The parameters specific to $v_{z0}(x) \;=\; 0.5\,c\,\mathrm{sech}^2(x/r_0)$ are as follows:

$$\begin{aligned}
M_A \;&=\; 10.34: \qquad \omega_i \;=\; 0.0715\,c/r_0 \;=\; 0.940\,\omega_{i0}, \\
\text{growth time}: \qquad T_i \;&=\; \frac{1}{\omega_i} \;=\; 14.00\,r_0/c, \\
\text{period}: \qquad T \;&=\; \frac{2\pi}{\omega_r} \;=\; 34.73\,r_0/c, \\
v_A \;&=\; 0.0557\,c, \qquad \beta \;=\; 160.0, \\
L_x/v_A \;&=\; 31.5\,r_0/(0.0557\,c) \;=\; 564.9\,r_0/c, \qquad \text{(Alfven transit time)}, \\
\eta_\rho \;&=\; \eta_x \;=\; \eta_z \;=\; 0.00025\,r_0 c, \\
\eta_{Bx} \;&=\; \eta_{Bz} \;=\; 0.0006\,r_0 c. \qquad (11.19)
\end{aligned}$$

We now make the same comparison of flow speeds, but this time at twice the Alfvenic Mach number, $M_A = 20.70$, i.e., half the field strength. As before, we display the vorticity, overlaid with the magnetic field lines. In figures 11.72 through 11.74, each row of displays corresponds to a given number of growth times, where the display on the left corresponds

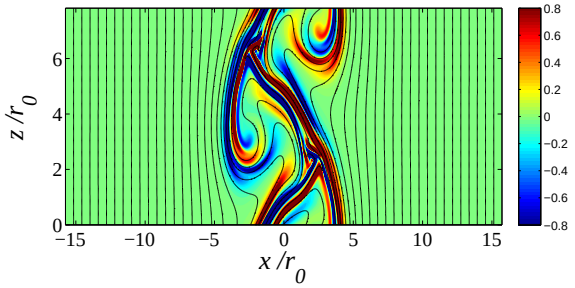

(a) $v_{z0} = 0.7\,c$, $v_A/c = 0.0947$,
$\beta = 55.52$, $\beta_{\min} = 1.89$
$t = 10.36\,T_i = 4.83\,T = 110.6\,r_0/c$
$= 2.02\,L_x/c_s = 0.332\,L_x/v_A$

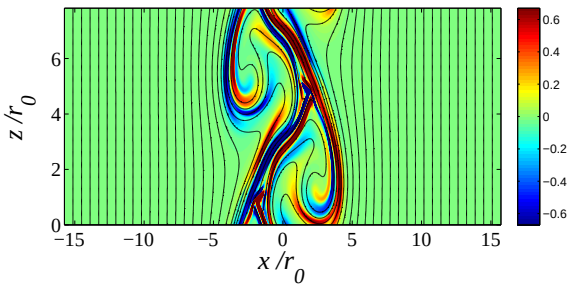

(b) $v_{z0} = 0.5\,c$, $v_A/c = 0.0557$,
$\beta = 16$, $\beta_{\min} = 8.09$
$t = 10.32\,T_i = 4.16\,T = 144.4\,r_0/c$
$= 2.64\,L_x/c_s = 0.255\,L_x/v_A$

Figure 11.69: Vorticity at two flow speeds, $M_A = 10.3$: $t = 10.3\,T_i$

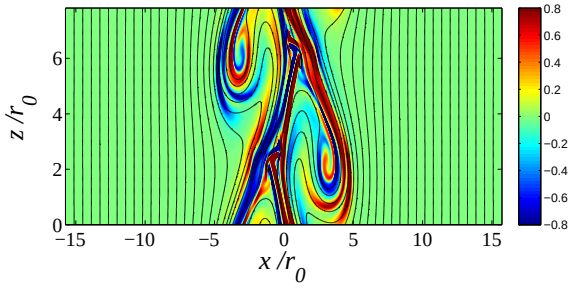

(a) $v_{z0} = 0.7\,c$, $v_A/c = 0.0947$,
$\beta = 55.52$, $\beta_{\min} = 3.09$
$t = 11.66\,T_i = 5.43\,T = 124.4\,r_0/c$
$= 2.27\,L_x/c_s = 0.374\,L_x/v_A$

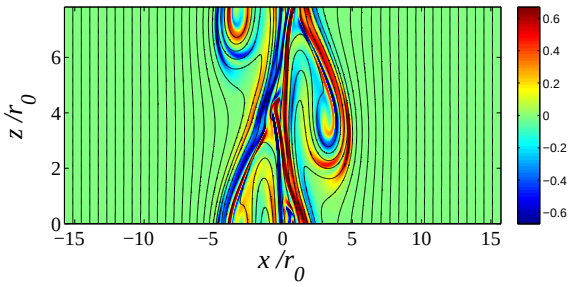

(b) $v_{z0} = 0.5\,c$, $v_A/c = 0.0557$,
$\beta = 160$, $\beta_{\min} = 8.74$
$t = 11.63\,T_i = 4.69\,T = 162.8\,r_0/c$
$= 2.98\,L_x/c_s = 0.288\,L_x/v_A$

Figure 11.70: Vorticity at two flow speeds, $M_A = 10.3$: $t = 11.6\,T_i$

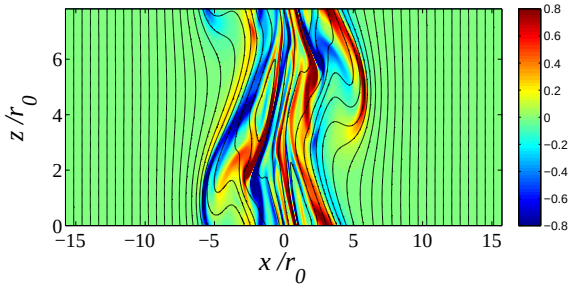

(a) $v_{z0} = 0.7\,c$, $v_A/c = 0.0947$,
$\beta = 55.52$, $\beta_{\min} = 4.84$
$t = 13.82\,T_i = 6.44\,T = 147.5\,r_0/c$
$= 2.70\,L_x/c_s = 0.443\,L_x/v_A$

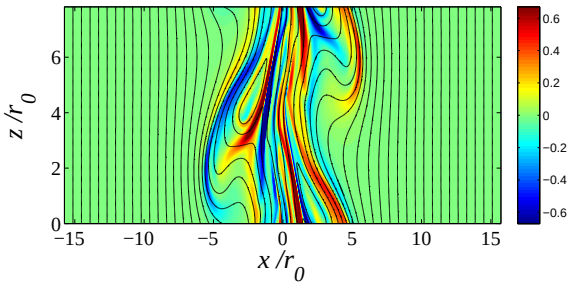

(b) $v_{z0} = 0.5\,c$, $v_A/c = 0.0557$,
$\beta = 160$, $\beta_{\min} = 13.32$
$t = 13.83\,T_i = 5.57\,T = 193.5\,r_0/c$
$= 3.54\,L_x/c_s = 0.342\,L_x/v_A$

Figure 11.71: Vorticity at two flow speeds, $M_A = 10.3$: $t = 13.8\,T_i$

to a flow speed amplitude of $0.7\,c$ and the display on the right to a flow speed amplitude of $0.5\,c$. Here again, we observe close agreement between corresponding displays, i.e., after a given number of growth times. As with $M_A = 10.34$, the main discrepancy is a longitudinal phase shift associated with differing pattern speeds resulting from the different background flow speeds. This reinforces the conclusions reached above for $M_A = 10.34$ with regard to the fundamental importance of Alfvenic Mach number and growth time in characterizing the evolution of the system. Notice, in the parameters below, that for both flow speeds, the fractional reduction in growth rate is about 98.5%, relative to the unmagnetized case. Again, for moderately relativistic flow speeds, the fractional reduction in growth rate, by the field, is a function of Alfvenic Mach number, not flow speed.

We have examined the sensitivity of our simulation results to background flow speed, and within a regime of moderately relativistic flow speeds, have found little such sensitivity, which reinforces the fundamental importance of the relativistic Alfvenic Mach number in characterizing the influence of the magnetic field on the flow. In the next section we examine the sensitivity of our results to the wavelength of the initial perturbation.

The parameters specific to $v_{z0}(x) \;=\; 0.7\,c\,\mathrm{sech}^2(x/r_0)$ are as follows:

$$
\begin{aligned}
M_A \;&=\; \infty: \qquad \omega_{i0} \;=\; 0.0994\,c/r_0, \\
M_A \;&=\; 20.70: \qquad \omega_i \;=\; 0.0980\,c/r_0 \;=\; 0.986\,\omega_{i0}, \\
\text{growth time}: \qquad T_i \;&=\; \frac{1}{\omega_i} \;=\; 10.20\,r_0/c, \\
\text{period}: \qquad T \;&=\; \frac{2\pi}{\omega_r} \;=\; 22.68\,r_0/c, \\
v_A \;&=\; 0.0473\,c, \qquad \beta \;=\; 222.1, \\
L_x/v_A \;&=\; 31.5\,r_0/(0.0473\,c) \;=\; 666.0\,r_0/c, \qquad \text{(Alfven transit time)}, \\
\eta_\rho \;&=\; \eta_x \;=\; \eta_z \;=\; 0.0002\,r_0 c, \\
\eta_{Bx} \;&=\; \eta_{Bz} \;=\; 0.0012\,r_0 c. \qquad (11.20)
\end{aligned}
$$

The parameters specific to $v_{z0}(x) \;=\; 0.5\,c\,\mathrm{sech}^2(x/r_0)$ are as follows:

$$
\begin{aligned}
M_A \;&=\; \infty: \qquad \omega_{i0} \;=\; 0.0760\,c/r_0, \\
M_A \;&=\; 20.70: \qquad \omega_i \;=\; 0.0749\,c/r_0 \;=\; 0.985\;\omega_{i0}, \\
\text{growth time}: \qquad T_i \;&=\; \frac{1}{\omega_i} \;=\; 13.36\,r_0/c, \\
\text{period}: \qquad T \;&=\; \frac{2\pi}{\omega_r} \;=\; 34.57\,r_0/c, \\
v_A \;&=\; 0.0279\,c, \qquad \beta \;=\; 640, \\
L_x/v_A \;&=\; 31.5\,r_0/(0.0279\,c) \;=\; 1129\,r_0/c, \qquad \text{(Alfven transit time)}, \\
\eta_\rho \;&=\; \eta_x \;=\; \eta_z \;=\; 0.00025\,r_0 c, \\
\eta_{Bx} \;&=\; \eta_{Bz} \;=\; 0.0006\,r_0 c. \qquad (11.21)
\end{aligned}
$$

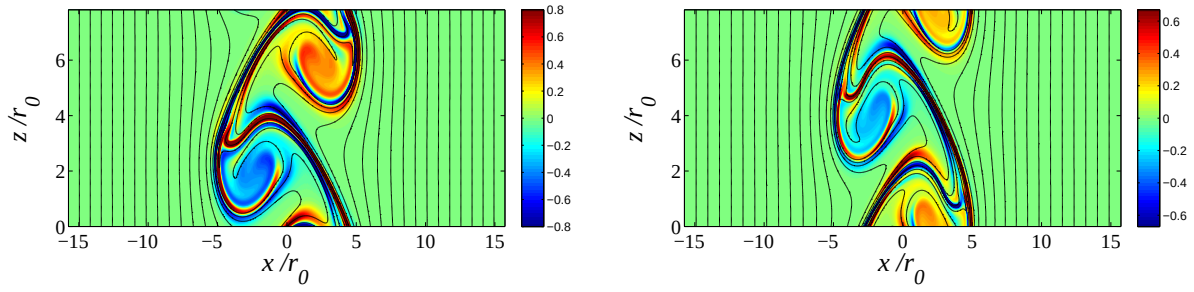

(a) $v_{z0} = 0.7\,c, \quad v_A/c = 0.0473,$
$\beta = 222, \quad \beta_{\min} = 1.37$
$t = 10.39\,T_i = 4.67\,T = 106.0\,r_0/c$
$= 1.94\,L_x/c_s = 0.159\,L_x/v_A$

(b) $v_{z0} = 0.5\,c, \quad v_A/c = 0.0279,$
$\beta = 640, \quad \beta_{\min} = 3.72$
$t = 10.35\,T_i = 4.00\,T = 138.2\,r_0/c$
$= 2.53\,L_x/c_s = 0.122\,L_x/v_A$

Figure 11.72: Vorticity at two flow speeds, $M_A = 20.7$: $t = 10.4\,T_i$

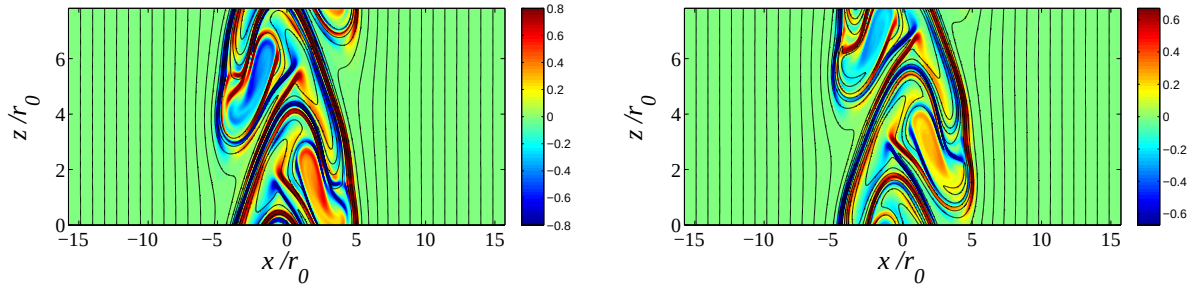

(a) $v_{z0} = 0.7\,c, \quad v_A/c = 0.0473,$
$\beta = 222, \quad \beta_{\min} = 2.92$
$t = 12.19\,T_i = 5.49\,T = 124.4\,r_0/c$
$= 2.27\,L_x/c_s = 0.187\,L_x/v_A$

(b) $v_{z0} = 0.5\,c, \quad v_A/c = 0.0279,$
$\beta = 640, \quad \beta_{\min} = 8.29$
$t = 12.19\,T_i = 4.71\,T = 162.8\,r_0/c$
$= 2.98\,L_x/c_s = 0.144\,L_x/v_A$

Figure 11.73: Vorticity at two flow speeds, $M_A = 20.7$: $t = 12.2\,T_i$

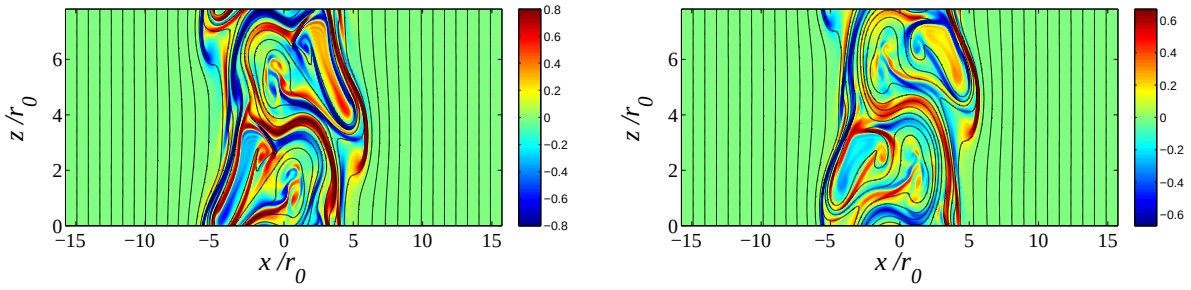

(a) $v_{z0} = 0.7\,c$, $\quad v_A/c = 0.0473$,
$\beta = 222$, $\quad \beta_{\min} = 5.72$
$t = 14.45\,T_i = 6.50\,T = 147.5\,r_0/c$
$= 2.70\,L_x/c_s = 0.221\,L_x/v_A$

(b) $v_{z0} = 0.5\,c$, $\quad v_A/c = 0.0279$,
$\beta = 640$, $\quad \beta_{\min} = 10.7$
$t = 14.49\,T_i = 5.60\,T = 193.5\,r_0/c$
$= 3.54\,L_x/c_s = 0.171\,L_x/v_A$

Figure 11.74: Vorticity at two flow speeds, $M_A = 20.7$: $t = 14.5\,T_i$

11.9 Dependence on Perturbation Wavelength

We now wish to determine the dependence of the simulation results on the wavelength ($\lambda = 2\pi/k_z$) of the initial perturbation in which the system is launched. We consider two cases, both at Alfvenic Mach number $M_A = 41.41$ (a weak field), where one has an initial perturbation corresponding to $k_z = 0.8\,r_0^{-1}$, $\lambda = 7.85\,r_0$, and the other has an initial perturbation corresponding to $k_z = 0.6\,r_0^{-1}$, $\lambda = 10.47\,r_0$.

The parameters for both cases are as follows, where ϵ has units of energy density, and r_0 has units of length:

$$\begin{aligned}
c_s &= 0.576\,c, \qquad v_{z0}(x) = 0.7\,c\,\mathrm{sech}^2(x/r_0), \\
v_A &= 0.0237\,c, \qquad \beta = 888.3, \\
L_x/v_A &= 31.5\,r_0/(0.0237\,c) = 1329\,r_0/c, \qquad \text{(Alfven transit time)}, \\
\eta_\rho &= \eta_x = \eta_z = 0.0002\,r_0 c \qquad \text{magnetized}, \\
\eta_{Bx} &= \eta_{Bz} = 0.0012\,r_0 c. \qquad (11.22)
\end{aligned}$$

The parameters specific to $k_z = 0.8/r_0$ are as follows:

$$\begin{aligned} \Delta z &= 0.0393\, r_0, \\ M_A &= 41.41: \qquad \omega_i = 0.0990\, c/r_0, \\ \text{growth time}: \qquad T_i &= \frac{1}{\omega_i} = 10.10\, r_0/c, \\ \text{period}: \qquad T &= \frac{2\pi}{\omega_r} = 22.63\, r_0/c. \end{aligned} \tag{11.23}$$

The parameters specific to $k_z = 0.6/r_0$ are as follows:

$$\begin{aligned} \Delta z &= 0.0524\, r_0, \\ M_A &= 41.41: \qquad \omega_i = 0.0920\, c/r_0, \\ \text{growth time}: \qquad T_i &= \frac{1}{\omega_i} = 10.87\, r_0/c, \\ \text{period}: \qquad T &= \frac{2\pi}{\omega_r} = 34.17\, r_0/c. \end{aligned} \tag{11.24}$$

We first examine the time-dependent behavior of certain quantities which at each time step are spatially averaged or maximized over the numerical grid. The blue curve corresponds to $k_z = 0.8/r_0$ and the red curve to $k_z = 0.6/r_0$. Figures 11.75 through 11.76 compare the time-dependence of the growth in fluctuations of the primitive variables. Figures 11.77 through 11.80 show the time-dependence of average (or RMS) vorticity, current density and Lorentz factor, along with the maximum Lorentz factor and velocity components, and minimum plasma β. These displays show that for larger perturbation wavelengths, electromagnetic energy dissipates more slowly, allowing the magnetic field to remain stronger. This is seen in the larger vorticity, larger current density, and smaller plasma β after vortex-disruption. However, for larger perturbation wavelengths, the system also decelerates to slower speeds, indicating greater dissipation of mechanical energy from the bulk flow.

In figures 11.81 through 11.84, we display the vorticity overlaid with contours of the

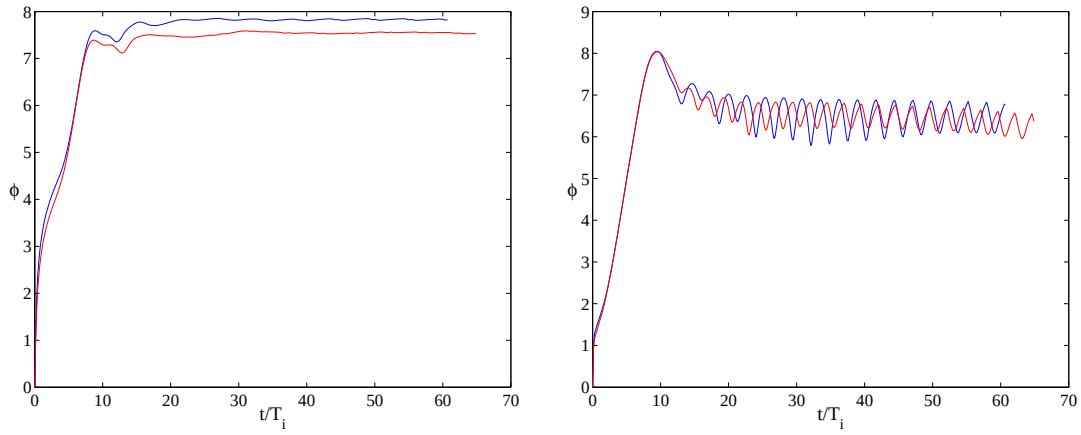

(a) longitudinal velocity fluctuations (b) transverse velocity fluctuations

Figure 11.75: Wavelength-dependence of growth in velocity components: $M_A = 41$ $k_z r_0 = 0.8$ (blue), 0.6 (red)

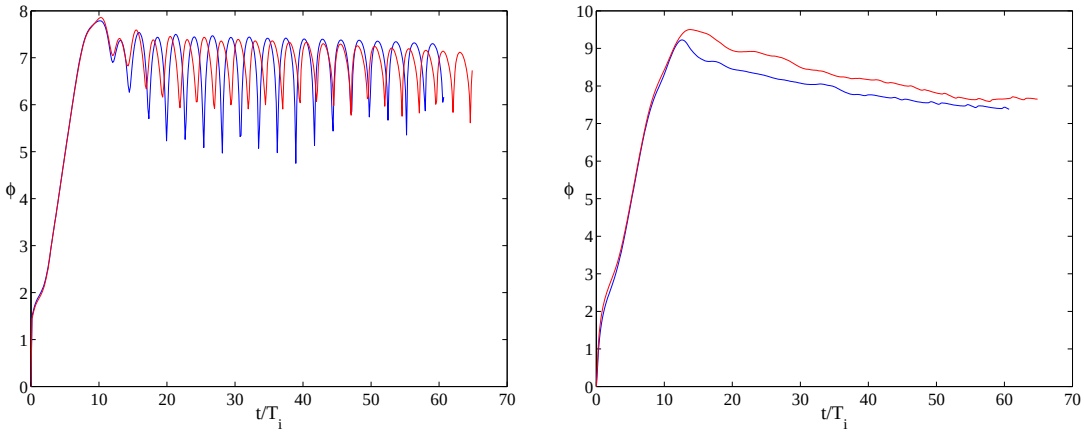

(a) pressure fluctuations (b) longitudinal field fluctuations

Figure 11.76: Wavelength-dependence of growth in P and B_z: $M_A = 41$ $k_z r_0 = 0.8$ (blue), 0.6 (red)

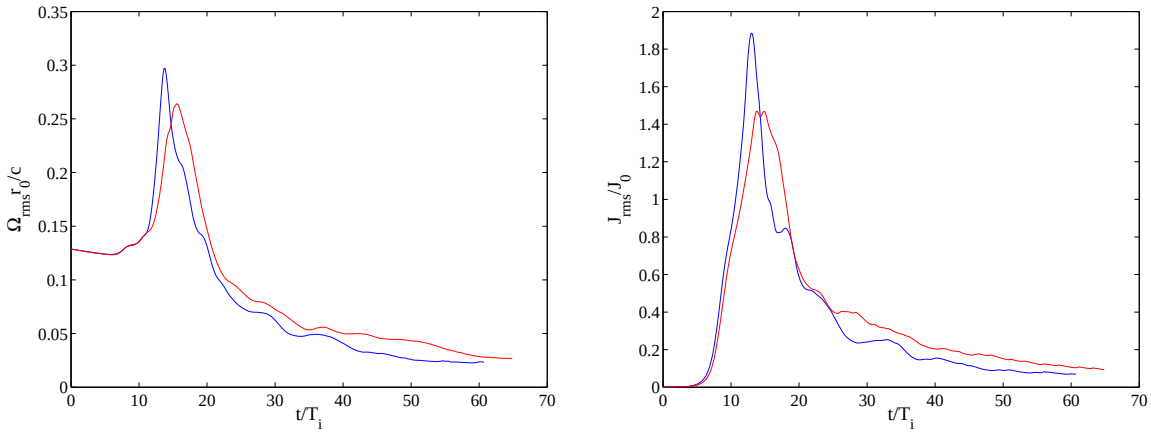

(a) RMS vorticity (b) RMS current density

Figure 11.77: Wavelength-dependence of RMS vorticity and current density: $M_A = 41$ $k_z r_0 = 0.8$ (blue), 0.6 (red)

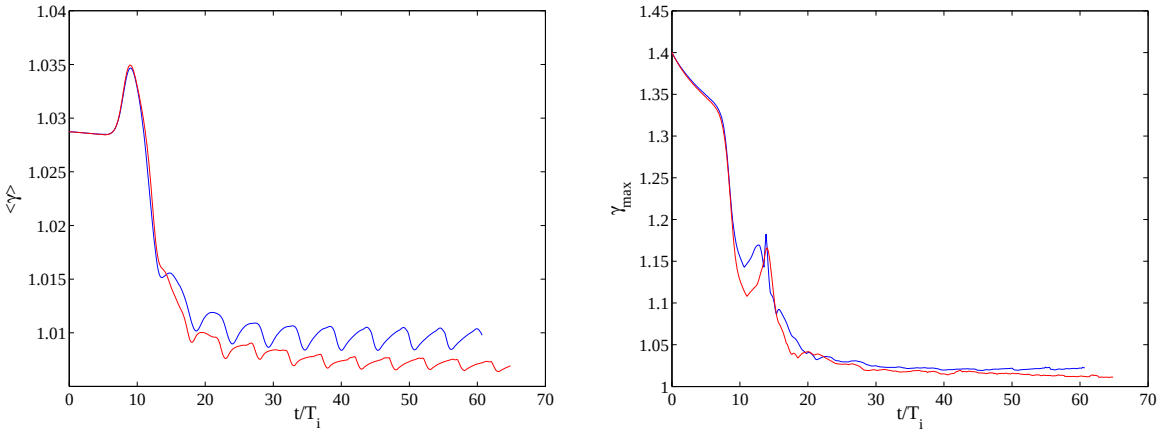

(a) average Lorentz factor (b) maximum Lorentz factor

Figure 11.78: Wavelength-dependence of Lorentz factor: $M_A = 41$ $k_z r_0 = 0.8$ (blue), 0.6 (red)

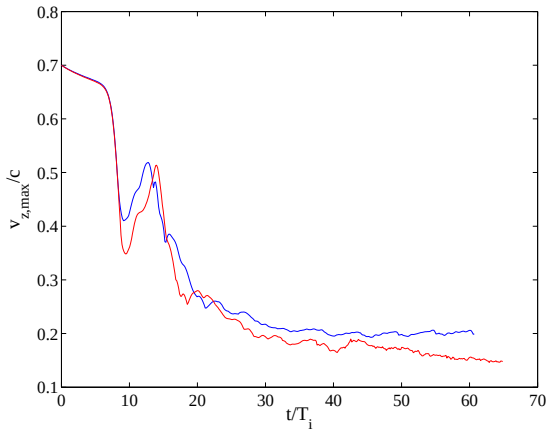

(a) maximum longitudinal velocity

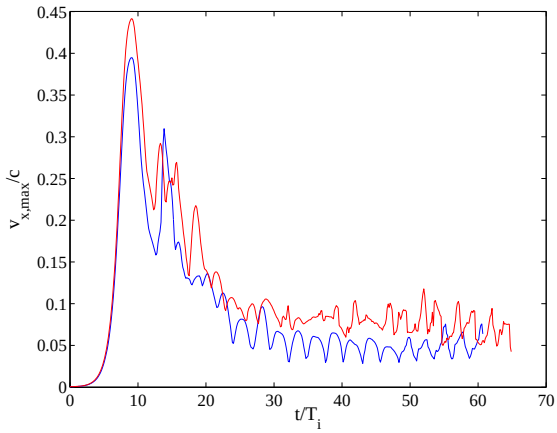

(b) maximum transverse velocity

Figure 11.79: Wavelength-dependence of maximum velocity components: $M_A = 41$ $k_z r_0 = 0.8$ (blue), 0.6 (red)

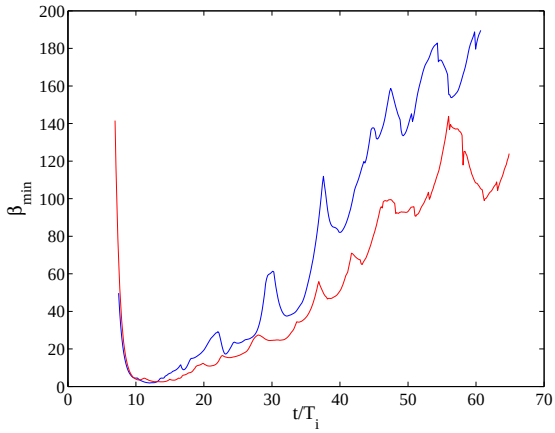

(a) minimum plasma β

Figure 11.80: Wavelength-dependence of minimum plasma β: $M_A = 41$ $k_z r_0 = 0.8$ (blue), 0.6 (red)

magnetic field lines. Each row of displays corresponds to a given number of growth times, where the display on the left corresponds to $k_z = 0.8\, r_0^{-1}$ and the display on the right corresponds to $k_z = 0.6\, r_0^{-1}$. The behavior exhibits fairly close agreement through the linear regime and early stages of vortex formation, but diverges in the early stages of vortex disruption, and the transition to the nonlinear regime. The equilibrium states also differ, particularly near the central jet axis. In the outer jet, we observe vortex filaments of positive vorticity for $x > 0$ and negative vorticity for $x < 0$. In the $k_z = 0.6\, r_0^{-1}$ case, the vortex filaments in the outer region exhibit more curvature (less aligned with the flow direction), and are less densely clustered.

In this weak-field regime, the complexity of vortex disruption and turbulent transition result in a strong sensitivity to perturbation wavelength. Earlier in the chapter, we saw very much the same effect for magnetic viscosity. However, the equilibrium jet width is larger (about $21.3\, r_0$) for the larger wavelength, and smaller (about $16\, r_0$) for the smaller wavelength. In particular, the ratio of equilibrium jet widths is approximately equal to the ratio of input wavelengths, which in this case is $4/3$. For $M_A = 41.41$, the ratio of equilibrium jet width to input wavelength is about

$$\frac{W_{\rm eq}}{\lambda} \;=\; \frac{(16)(0.8)}{2\pi} \;=\; \frac{6.4}{\pi} \;\approx\; 2.04. \tag{11.25}$$

There is also an approximate $4/3$ ratio in the equilibrium central flow widths, i.e., the width of the central region surrounded by vortex filaments. Here, the flow width is about $8\, r_0$ for the $k_z = 0.8\, r_0^{-1}$ case, and about $10.7\, r_0$ for the $k_z = 0.6\, r_0^{-1}$ case. Therefore, for $M_A = 41.41$, the ratio of equilibrium flow width to input wavelength is about

$$\frac{W_{\text{cent,eq}}}{\lambda} \;=\; \frac{(8)(0.8)}{2\pi} \;=\; \frac{3.2}{\pi} \;\approx\; 1.02. \tag{11.26}$$

It should also be noted that in the longer-wavelength case, the effective field is stronger (the minimum plasma β is consistently lower). Consequently, there is more magnetic reconnection, leading to a more complex, turbulent reorganization process during vortex disruption.

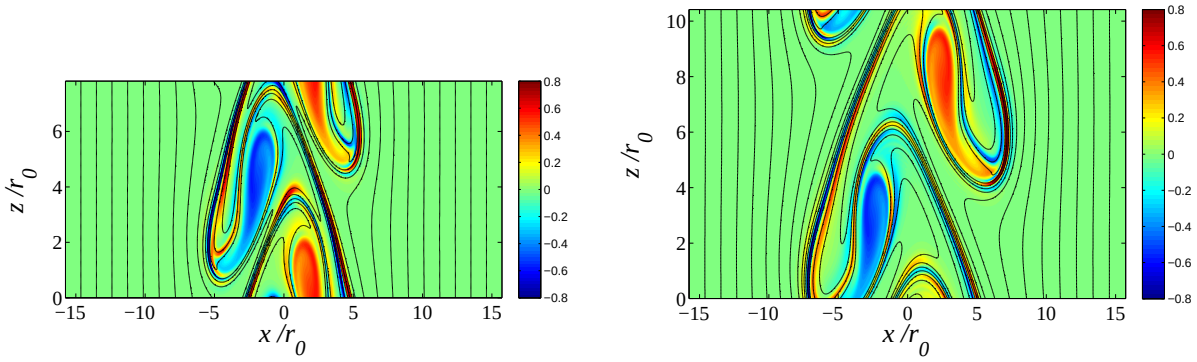

(a) $t = 11.6\,T_i = 5.16\,T = 116.7\,r_0/c$
$= 2.13\,L_x/c_s = 0.088\,L_x/v_A$,
$\beta_{\min} = 2.09, \quad k_z = 0.8\,r_0^{-1}$

(b) $t = 11.9\,T_i = 3.78\,T = 129.0\,r_0/c$
$= 2.36\,L_x/c_s = 0.097\,L_x/v_A$,
$\beta_{\min} = 3.40, \quad k_z = 0.6\,r_0^{-1}$

Figure 11.81: Wavelength-dependence of vorticity for $M_A = 41.4$: $t = 12\,T_i$
$M_A = 41.41, \qquad v_{Az}/c = 0.0237, \qquad \beta = 888.3, \qquad v_{z0} = 0.7\,c$

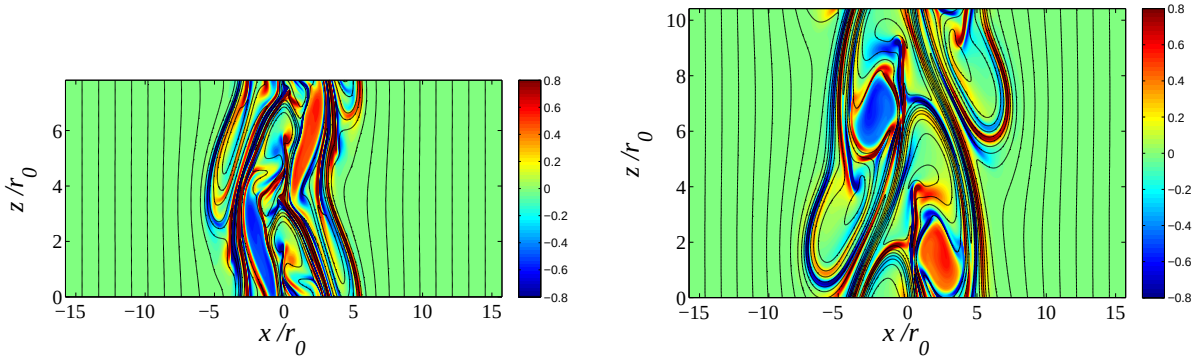

(a) $t = 14.0\,T_i = 6.25\,T = 141.3\,r_0/c$
$= 2.58\,L_x/c_s = 0.106\,L_x/v_A$,
$\beta_{\min} = 4.36, \quad k_z = 0.8\,r_0^{-1}$

(b) $t = 14.1\,T_i = 4.50\,T = 153.6\,r_0/c$
$= 2.81\,L_x/c_s = 0.116\,L_x/v_A$,
$\beta_{\min} = 2.54, \quad k_z = 0.6\,r_0^{-1}$

Figure 11.82: Wavelength-dependence of vorticity for $M_A = 41.4$: $t = 14\,T_i$
$M_A = 41.41, \qquad v_{Az}/c = 0.0237, \qquad \beta = 888.3, \qquad v_{z0} = 0.7\,c$

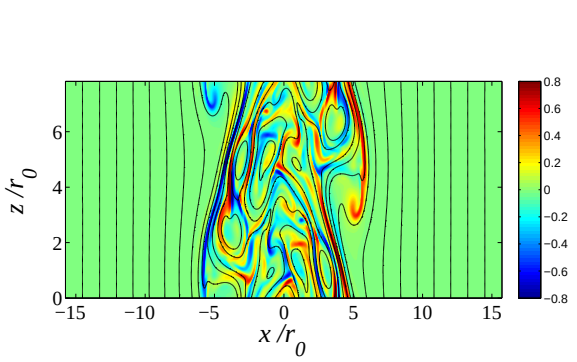

(a) $t = 18.9\,T_i = 8.42\,T = 190.5\,r_0/c$
$= 3.48\,L_x/c_s = 0.143\,L_x/v_A$,
$\beta_{\min} = 15.8, \quad k_z = 0.8\,r_0^{-1}$

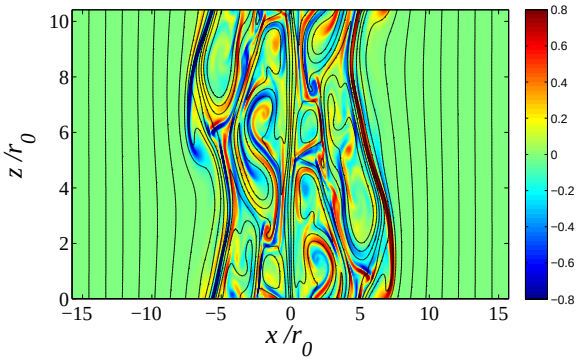

(b) $t = 18.7\,T_i = 5.93\,T = 202.8\,r_0/c$
$= 3.71\,L_x/c_s = 0.153\,L_x/v_A$,
$\beta_{\min} = 9.58, \quad k_z = 0.6\,r_0^{-1}$

Figure 11.83: Wavelength-dependence of vorticity for $M_A = 41.4$: $t = 19\,T_i$
$M_A = 41.41, \qquad v_{Az}/c = 0.0237, \qquad \beta = 888.3, \qquad v_{z0} = 0.7\,c$

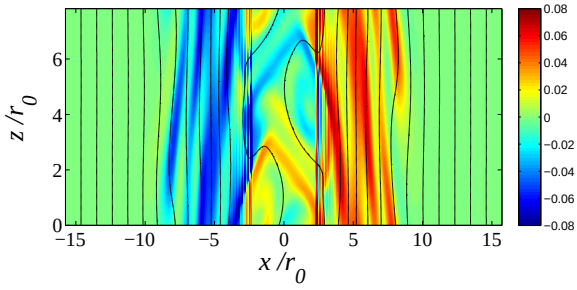

(a) $t = 60.2\,T_i = 26.9\,T = 608.3\,r_0/c$
$= 11.1\,L_x/c_s = 0.458\,L_x/v_A$,
$\beta_{\min} = 185.1, \quad k_z = 0.8\,r_0^{-1}$

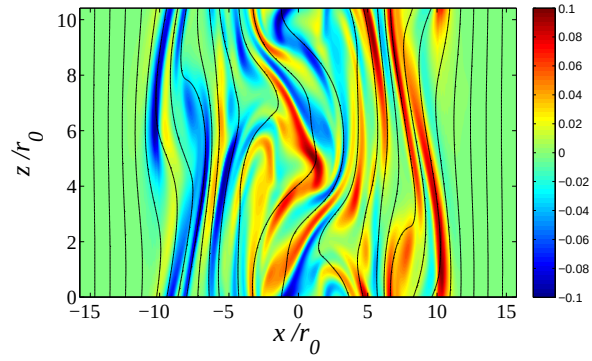

(b) $t = 60.5\,T_i = 19.2\,T = 608.3\,r_0/c$
$= 11.1\,L_x/c_s = 0.458\,L_x/v_A$,
$\beta_{\min} = 106.5, \quad k_z = 0.6\,r_0^{-1}$

Figure 11.84: Wavelength-dependence of vorticity for $M_A = 41.4$: $t = 60\,T_i$
$M_A = 41.41, \qquad v_{Az}/c = 0.0237, \qquad \beta = 888.3, \qquad v_{z0} = 0.7\,c$

Figure 11.85 displays the longitudinal velocity, with magnetic field lines superimposed, of the two cases as the system approaches the equilibrium state. As with the vorticity displays, the jet widths and central widths each have a ratio of 4/3, equal to the wavelength ratio. The central region, in particular, is seen to be the region of upstream flow, and the flow speed is considerably less in the outer regions composed of vortex filaments. The flow in the central region is noticeably more heterogeneous in the $k_z = 0.6\, r_0^{-1}$ case than in the $k_z = 0.8\, r_0^{-1}$ case. That is, the equilibrium flow is more uniform in the shorter-wavelength case, and is also more closely aligned in the vertical direction. In the equilibrium configuration of the longer-wavelength case, both the flow and the vortex filaments exhibit more curvature.

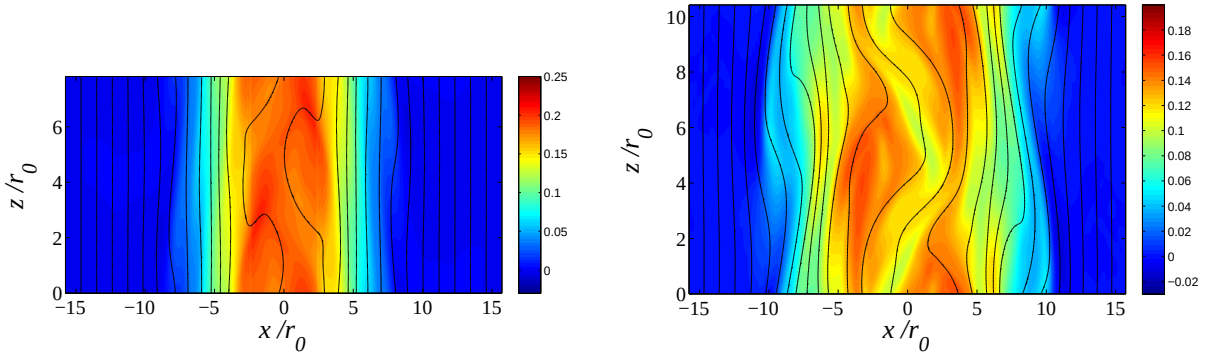

(a) $t = 60.2\, T_i = 26.9\, T = 608.3\, r_0/c$
$= 11.1\, L_x/c_s = 0.458\, L_x/v_A$,
$\beta_{\min} = 185.1, \quad k_z = 0.8\, r_0^{-1}$

(b) $t = 60.5\, T_i = 19.2\, T = 608.3\, r_0/c$
$= 11.1\, L_x/c_s = 0.458\, L_x/v_A$,
$\beta_{\min} = 106.5, \quad k_z = 0.6\, r_0^{-1}$

Figure 11.85: Wavelength-dependence of longitudinal velocity for $M_A = 41.4$: $t = 60\, T_i$
$M_A = 41.41, \qquad v_{Az}/c = 0.0237, \qquad \beta = 888.3, \qquad v_{z0} = 0.7\, c$

We perform the same comparison as above, except this time for a strong magnetic field for which $M_A = 5.145$, corresponding to immediate vortex suppression and rapid transition to a filamented state. The parameters for all cases are as follows, where ϵ has units of energy density, and r_0 has units of length:

$$
\begin{aligned}
c_s &= 0.576\,c, \qquad v_{z0}(x) = 0.7\,c\,\mathrm{sech}^2(x/r_0), \\
v_A &= 0.1893\,c, \qquad \beta = 13.88, \\
L_x/v_A &= 31.5\,r_0/(0.1893\,c) = 166.4\,r_0/c, \qquad \text{(Alfven transit time)}, \\
\eta_\rho &= \eta_x = \eta_z = 0.0002\,r_0 c \qquad \text{magnetized}, \\
\eta_{Bx} &= \eta_{Bz} = 0.0012\,r_0 c.
\end{aligned} \tag{11.27}
$$

The parameters specific to $k_z = 0.8/r_0$ are as follows:

$$
\begin{aligned}
\Delta z &= 0.0393\,r_0, \\
M_A &= 5.145: \qquad \omega_i = 0.0738\,c/r_0, \\
\text{growth time}: \qquad T_i &= \frac{1}{\omega_i} = 13.55\,r_0/c, \\
\text{period}: \qquad T &= \frac{2\pi}{\omega_r} = 23.70\,r_0/c.
\end{aligned} \tag{11.28}
$$

The parameters specific to $k_z = 0.6/r_0$ are as follows:

$$
\begin{aligned}
\Delta z &= 0.0524\,r_0, \\
M_A &= 5.145: \qquad \omega_i = 0.0688\,c/r_0, \\
\text{growth time}: \qquad T_i &= \frac{1}{\omega_i} = 14.53\,r_0/c, \\
\text{period}: \qquad T &= \frac{2\pi}{\omega_r} = 35.59\,r_0/c.
\end{aligned} \tag{11.29}
$$

The parameters specific to $k_z = 0.5/r_0$ are as follows:

$$
\begin{aligned}
\Delta z &= 0.0628\,r_0, \\
M_A &= 5.145: \qquad \omega_i = 0.0625\,c/r_0, \\
\text{growth time}: \qquad T_i &= \frac{1}{\omega_i} = 16.01\,r_0/c, \\
\text{period}: \qquad T &= \frac{2\pi}{\omega_r} = 46.41\,r_0/c.
\end{aligned} \tag{11.30}
$$

We first examine the time-dependent behavior of certain quantities which at each time step are spatially averaged or maximized over the numerical grid. The black curve corresponds to $k_z = 0.8/r_0$, the blue curve to $k_z = 0.6/r_0$, and the red curve to $k_z = 0.5/r_0$.

Figures 11.86 through 11.87 compare the time-dependence of the growth in fluctuations of the primitive variables. Figures 11.88 through 11.92 show the time-dependence of average (or RMS) vorticity, current density, and Lorentz factor, along with the maximum Lorentz factor and velocity components, minimum plasma β, and average density and pressure. We can make an important observation by comparing the three curves in the later stages of nonlinear evolution. Specifically, with increasing k_z, i.e., decreasing wavelength, there is a general decrease in quantities associated with the velocity components (v_z, v_x, Lorentz factor), and a general decrease in quantities influenced by the magnetic field (and a corresponding increase in the plasma β). As wavelength decreases, there is a corresponding increase in the average pressure and density, i.e., quantities related to viscous or thermal processes. As we decrease the wavelength of the perturbation, we decrease the length scales associated with the emergent nonlinear features of the flow (e.g., the filaments), thereby making them slightly more comparable to (i.e., not as much larger than) the length scales associated with diffusion. This enables a greater amount of viscous dissipation of mechanical and electromagnetic energy into thermal energy.

As before, each row of displays below corresponds to a given number of growth times, and in each row, the display on the left corresponds to $k_z = 0.8\, r_0^{-1}$ while the display on the right corresponds to $k_z = 0.6\, r_0^{-1}$. We begin, in figures 11.93 through 11.94, by showing displays of the vorticity overlaid with contours of magnetic field lines. In figure 11.95, we display the longitudinal velocity overlaid with magnetic field lines. In both cases, the equilibrium width of the jet is the same, equal to about $8\, r_0$. However, from the longitudinal velocity displays, there is in both cases a central region where the flow remains at about $0.5\, c$. For

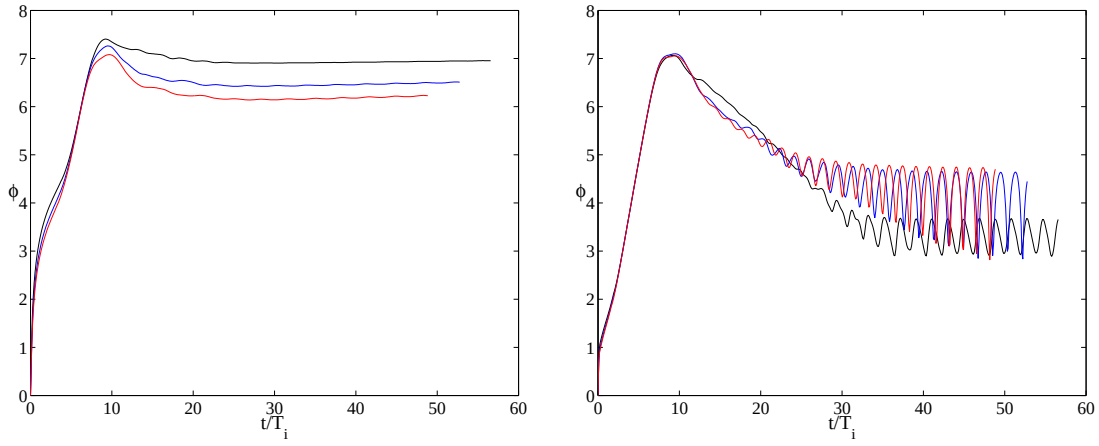

(a) longitudinal velocity fluctuations (b) transverse velocity fluctuations

Figure 11.86: Wavelength-dependence of growth in velocity components: $M_A = 5.1$ $k_z r_0 = 0.8$ (black), 0.6 (blue), 0.5 (red)

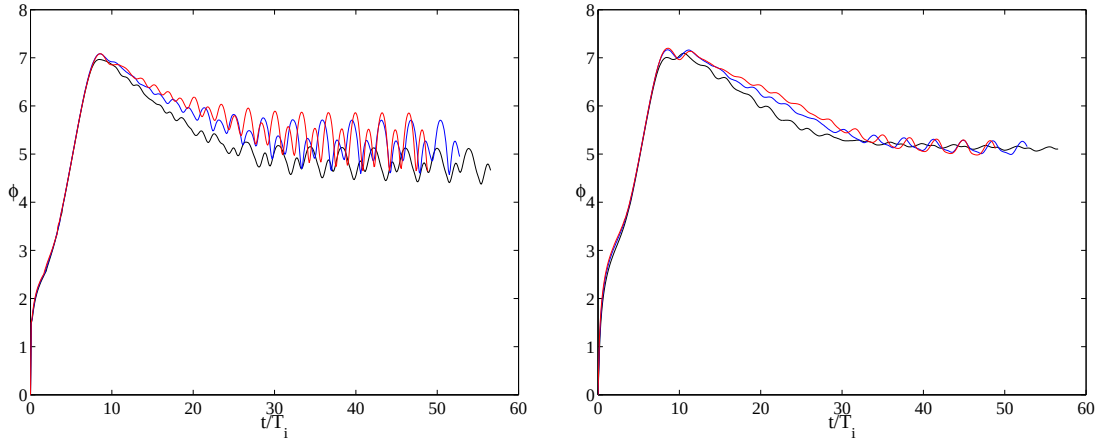

(a) pressure fluctuations (b) longitudinal field fluctuations

Figure 11.87: Wavelength-dependence of growth in P and B_z: $M_A = 5.1$ $k_z r_0 = 0.8$ (black), 0.6 (blue), 0.5 (red)

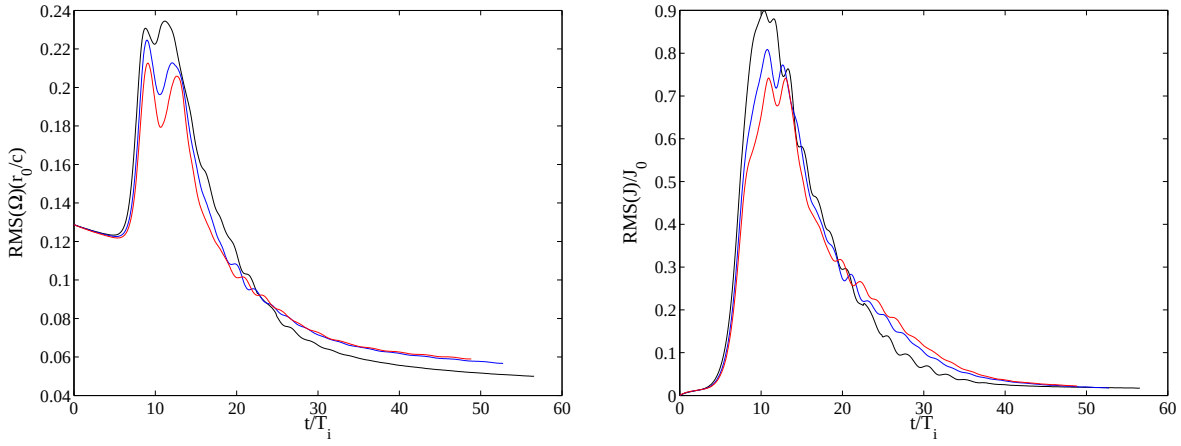

(a) RMS vorticity

(b) RMS current density

Figure 11.88: Wavelength-dependence of RMS vorticity and current density: $M_A = 5.1$ $k_z r_0 = 0.8$ (black), 0.6 (blue), 0.5 (red)

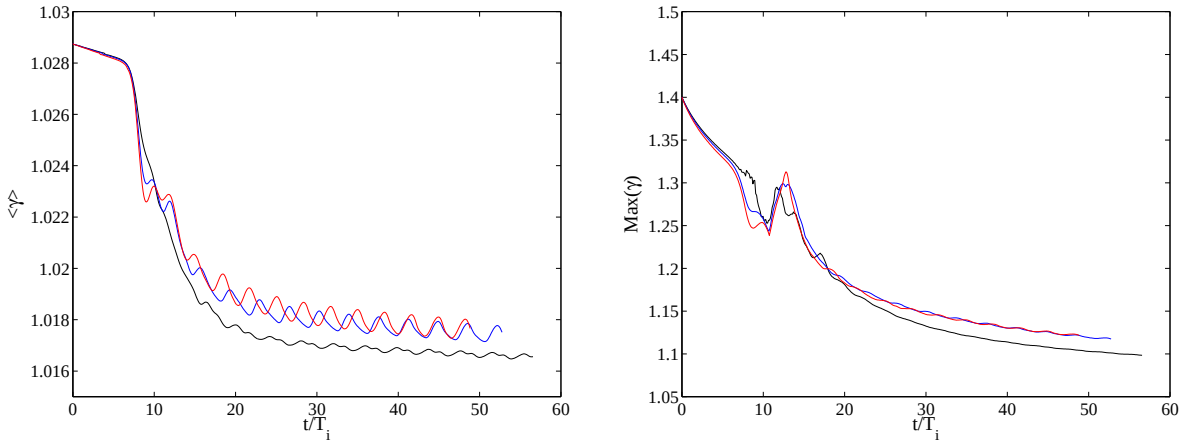

(a) average Lorentz factor

(b) maximum Lorentz factor

Figure 11.89: Wavelength-dependence of Lorentz factor: $M_A = 5.1$ $k_z r_0 = 0.8$ (black), 0.6 (blue), 0.5 (red)

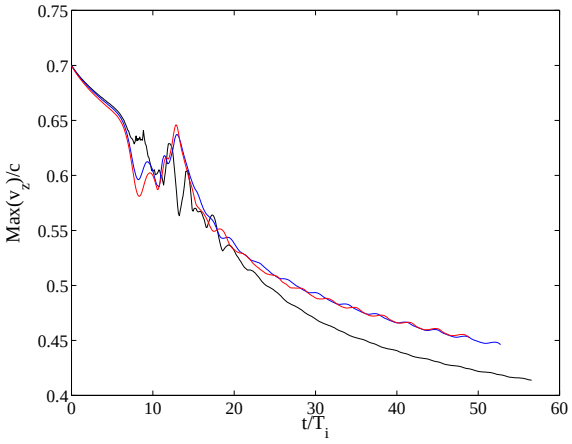

(a) maximum longitudinal velocity

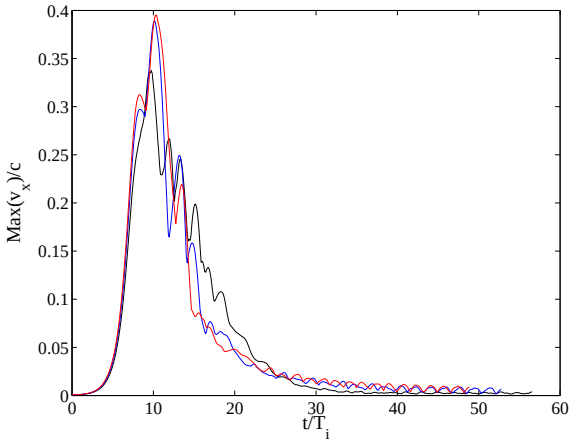

(b) maximum transverse velocity

Figure 11.90: Wavelength-dependence of maximum velocity components: $M_A = 5.1$ $k_z r_0 = 0.8$ (black), 0.6 (blue), 0.5 (red)

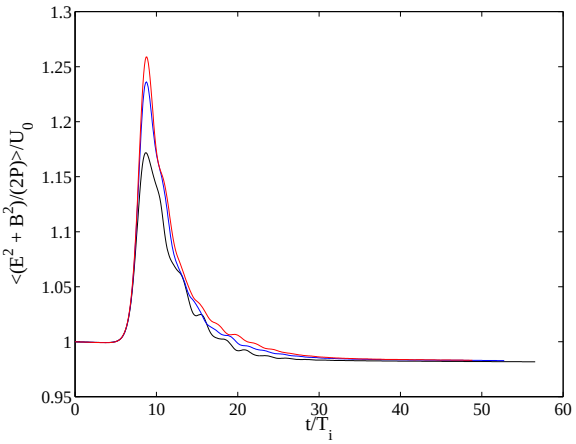

(a) average inverse plasma β

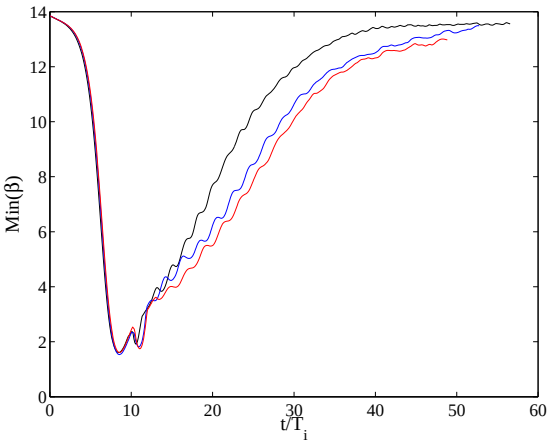

(b) minimum plasma β

Figure 11.91: Wavelength-dependence of plasma β: $M_A = 5.1$ $k_z r_0 = 0.8$ (black), 0.6 (blue), 0.5 (red)

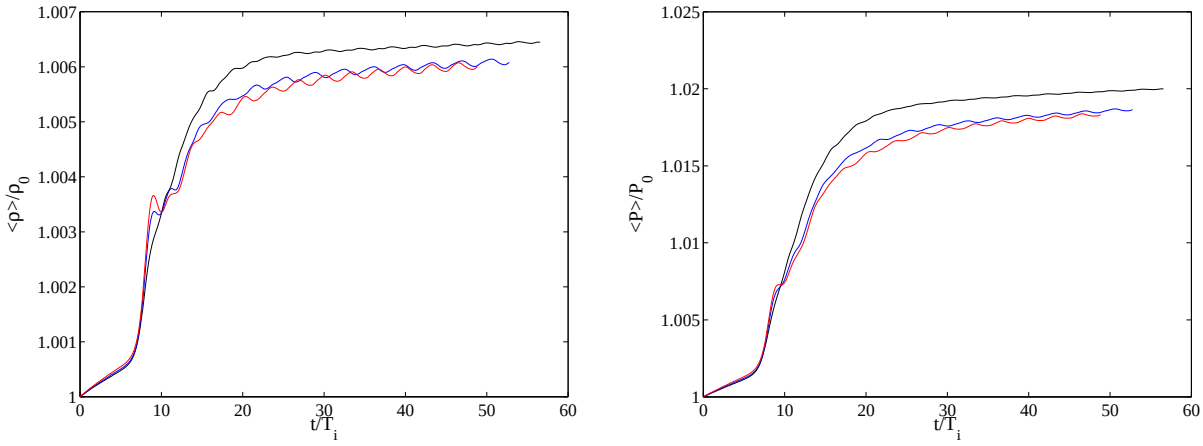

(a) average density

(b) average pressure

Figure 11.92: Wavelength-dependence of avg. density and pressure: $M_A = 5.1$ $k_z r_0 = 0.8$ (black), 0.6 (blue), 0.5 (red)

$k_z = 0.8\, r_0^{-1}$, the width of the central flow is about $0.85\, r_0$. For $k_z = 0.6\, r_0^{-1}$, the central flow width is about $1.1\, r_0$. The ratio of flow widths is about 1.3, which is approximately equal to the ratio 4/3 of input perturbation wavelengths. The filament widths are also larger, by a ratio of about 4/3, in the longer-wavelength case. This indicates that for a strong magnetic field, the overall jet width is roughly independent of perturbation wavelength, while the equilibrium central flow width, and the equilibrium filament width, both scale linearly with the perturbation wavelength. For the flow width, the scale factor is about

$$\frac{W_{\text{flow}}}{\lambda} \approx \frac{(0.85)(0.8)}{2\pi} = \frac{0.34}{\pi} \approx 0.11. \tag{11.31}$$

For the filament width, the scale factor is about

$$\frac{W_{\text{filament}}}{\lambda} \approx \frac{(0.6)(0.8)}{2\pi} = \frac{0.24}{\pi} \approx 0.08. \tag{11.32}$$

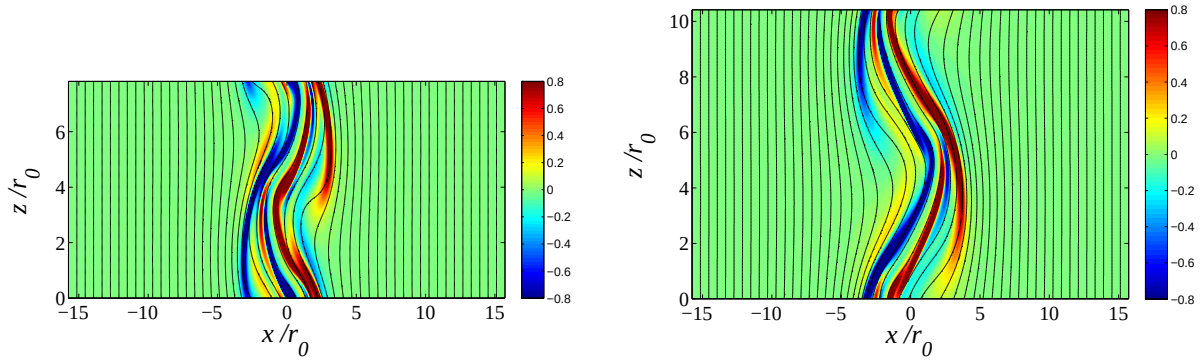

(a) $t = 9.30\,T_i = 5.32\,T = 126.0\,r_0/c$
$= 2.30\,L_x/c_s = 0.757\,L_x/v_A$,
$\beta_{\min} = 1.95, \quad k_z = 0.8\,r_0^{-1}$

(b) $t = 9.30\,T_i = 3.80\,T = 135.2\,r_0/c$
$= 2.47\,L_x/c_s = 0.812\,L_x/v_A$,
$\beta_{\min} = 1.83, \quad k_z = 0.6\,r_0^{-1}$

Figure 11.93: Wavelength-dependence of vorticity for $M_A = 5.1$: $t = 9.3\,T_i$
$v_{Az}/c = 0.1893, \qquad \beta = 13.88, \qquad v_{z0} = 0.7\,c$

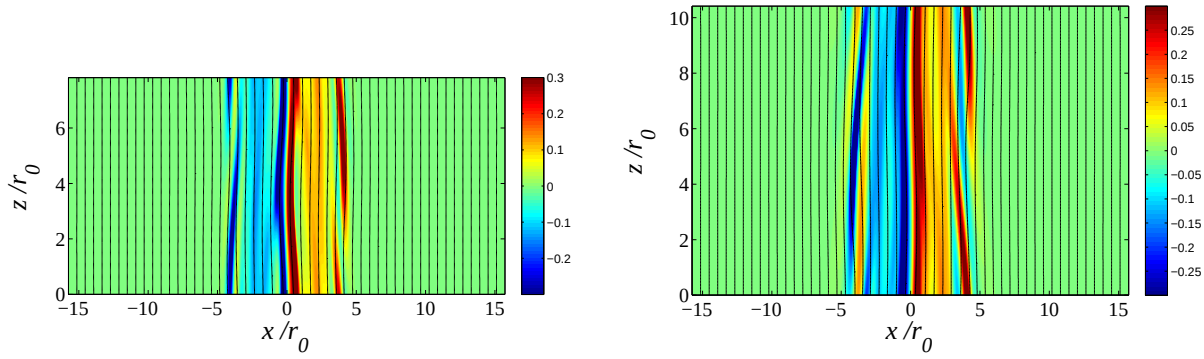

(a) $t = 24.49\,T_i = 14.00\,T = 331.8\,r_0/c$
$= 6.07\,L_x/c_s = 1.99\,L_x/v_A$,
$\beta_{\min} = 10.06, \quad k_z = 0.8\,r_0^{-1}$

(b) $t = 24.53\,T_i = 10.01\,T = 356.4\,r_0/c$
$= 6.52\,L_x/c_s = 2.14\,L_x/v_A$,
$\beta_{\min} = 8.37, \quad k_z = 0.6\,r_0^{-1}$

Figure 11.94: Wavelength-dependence of vorticity for $M_A = 5.1$: $t = 24.5\,T_i$
$v_{Az}/c = 0.1893, \qquad \beta = 13.88, \qquad v_{z0} = 0.7\,c$

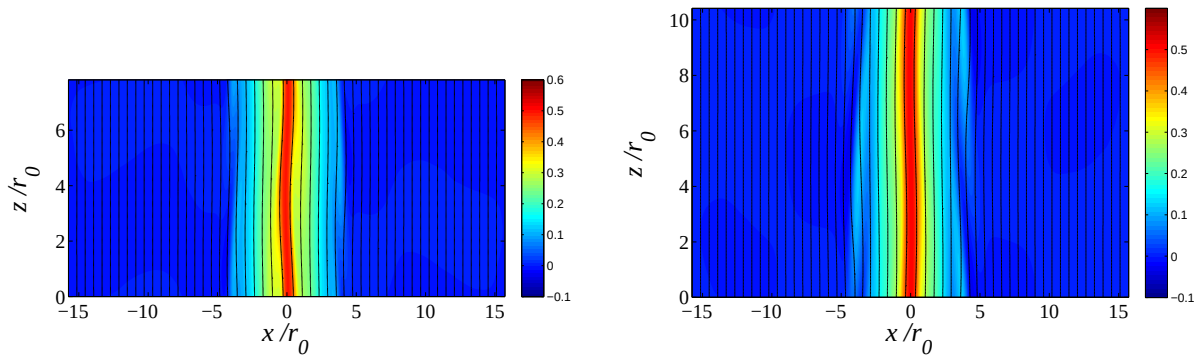

(a) $t = 24.49\,T_i = 14.00\,T = 331.8\,r_0/c$
$= 6.07\,L_x/c_s = 1.99\,L_x/v_A$,
$\beta_{\min} = 10.06, \quad k_z = 0.8\,r_0^{-1}$

(b) $t = 24.53\,T_i = 10.01\,T = 356.4\,r_0/c$
$= 6.52\,L_x/c_s = 2.14\,L_x/v_A$,
$\beta_{\min} = 8.37, \quad k_z = 0.6\,r_0^{-1}$

Figure 11.95: Wavelength-dependence of longitudinal velocity for $M_A = 5.1$: $t = 24.5\,T_i$
$v_{Az}/c = 0.1893, \qquad \beta = 13.88, \qquad v_{z0} = 0.7\,c$

11.10 Conclusion

We have examined the sensitivity of our simulation results to various input parameters. Apart from validating our numerical algorithm, our findings have lent further insight into the physical mechanisms underlying our model. We first demonstrated that the magnetic field remains approximately divergenceless. We next showed that our results are convergent with respect to time step (keeping the spatial grid constant). With respect to refinement of the numerical grid, our simulation exhibits convergence for an adequately refined grid (at least 751 points in the shear direction, and at least 151 points spanning a wavelength in the flow direction). In the latter stages of the nonlinear evolution, this convergence is preserved in terms of the overall structure of the flow, though there are differences in the smaller-scale structures emerging from turbulent breakdown. We then demonstrated that, in both magnetized and unmagnetized cases, the system width does not significantly impact the nonlinear evolution of the flow and of the magnetic field. This is also true of the system length, as demonstrated by comparing results for different numbers of wavelengths spanned

in the flow direction, and finding that in this direction the system remains spatially periodic. In short, we have demonstrated convergence of our results with respect to spatial step, time step, and system dimensions.

We compared results, using a non-relativistic flow speed and sound speed, obtained by evolving the (i) RMHD equations and (ii) MHD equations. We found convergence between the RMHD and MHD regimes. We also demonstrated convergence between the RMHD and RHD regimes. We then assessed the viscosity-sensitivity of simulations using several different field strengths. From time-dependent graphs of various spatially-averaged or maximized quantities, we determined that an increase in viscosity generally leads to a slight decrease in quantities related to magnetic field and velocity, and a corresponding increase in pressure. This is not surprising, when considering that diffusion represents the dissipation of mechanical and electromagnetic energy into thermal energy. When comparing two-dimensional displays at different viscosities, we found the largest differences for simulations using weaker fields, as these are the cases for which the vortex inhibition is more complex. For the weak vortex-disruptive field $M_A = 41.4$, when we use less magnetic viscosity, we see that the equilibrium central flow region, in which vortices persist for many growth times, is wider, less spatially uniform, and contains more magnetic reconnection. For all field strengths examined, the equilibrium jet width, and filament width, are approximately viscosity-independent, though viscosity sometimes results in a loss of sharpness of the filament boundaries, so that the width is less well-defined.

For magnetic fields corresponding to $M_A = 10.3$ and 20.7, we compared simulation results for background flow speed amplitudes of $0.7\,c$ and $0.5\,c$, and found close agreement that

persists well into the nonlinear regime. This indicates that, within a regime of moderately relativistic flow speeds, the relativistic Alfvenic Mach number M_A is indeed closely correlated with the influence of the magnetic field on vortex development. This is consistent with our observation in chapter 6 that M_A is closely correlated with the fractional reduction in linear growth rate, compared to the case with no magnetic field. However, this correlation breaks down for mildly relativistic, or ultra-relativistic, flow speeds.

We then examined the sensitivity of our results to the wavelength of the perturbation in which the simulation is launched. For the vortex-disruptive case $M_A = 41.4$, we found that when the perturbation wavelength is increased by a certain factor, the equilibrium jet width, and equilibrium central flow width, both increase by roughly this same factor. This leads to the conclusion that in the equilibrium state for $M_A = 41.4$, the jet width is roughly twice the input perturbation wavelength, and the central flow width is roughly equal to the perturbation wavelength. For the vortex-suppressing case $M_A = 5.145$, the equilibrium jet width is about 2.25 times the initial jet width, independent of the input wavelength. Therefore, the equilibrium jet width has far more dependence on input wavelength for weaker fields than strong fields. One possible explanation is that this input wavelength is longitudinal, and therefore influences longitudinal dimensions of such features as emerging vortices. For a weak field, these vortices are allowed to develop extensively, and vortex rotation has the effect of coupling these longitudinal dimensions to transverse dimensions, thereby influencing the equilibrium flow width. Strong fields suppress vortex rotation, and therefore inhibit this coupling between longitudinal and transverse lengths.

However, for the case $M_A = 5.145$, the widths of many characteristic features seem to

scale with the input wavelength. These include the width of the narrow central region of relatively high flow speed, which is about 11% of the wavelength, and the filament width, which is about 8% of the input wavelength. Again for $M_A = 5.145$, we plotted the time-dependence of various spatially-averaged and maximized quantities, and found that when wavelength is increased, there is a corresponding increase in quantities related to velocity and magnetic field, and a decrease in average density and pressure. A larger wavelength tends to generate features with larger length scales, which are therefore less comparable to the smaller length scales associated with diffusion, so that there is less correlation with viscous dissipation of mechanical and electromagnetic energy. In the simulations discussed in chapters 9 and 10, we use a wavelength of $(2\pi/0.8)\, r_0 \approx 7.85\, r_0$, which is close to the wavelength of maximum growth, as shown in chapter 6.

We have examined, through numerical simulation, the manner in which a magnetic field inhibits the KH instability, and we have verified that our magnetic field remains divergence-less, and that our results are convergent with respect to time step, spatial step, system dimensions, viscosity, and between the RHD, MHD, and RMHD regimes. We have also discovered that for background flow speeds exceeding about $0.9\, c$ (corresponding to a Lorentz factor of about 2), the simulation undergoes early unphysical breakdown (speeds exceeding the speed of light, negative densities, etc.). This is a problem that has plagued artificial viscosity simulations for over 20 years (Marti and Muller 2003). Whereas magnetic fields have a stabilizing effect, we see that relativistic effects are destabilizing.

In chapter 12, we explore a mathematical anomaly associated with diffusion in highly relativistic systems.

Chapter 12

Diffusion in Relativistic Flows: A Mathematical Anomaly

In our studies of the KH instability, we have used artificial viscosity to stabilize the numerical system, and also to model physical processes. The exact single-fluid RMHD equations are marginally stable. However, when we discretize the spatial and temporal derivatives in a numerical scheme, these equations become unstable, and therefore diffusion is needed in order to restore stability to the system. In chapter **??**, we verified the convergence of our results with respect to viscosity, which demonstrates that our results are not significantly influenced by diffusion. Diffusion also preserves the conservative nature of the RMHD equations. We have also used a velocity shear which establishes a stationary frame of reference with respect to the flow. Therefore, we have operated in a single reference frame, and the validity of our results does not require that the diffusion operator preserve the Lorentz-invariance of the RMHD equations. In this chapter, we mathematically demonstrate an anomaly that arises from the lack of Lorentz-invariance of the diffusion operator, but we should emphasize that the results of this chapter do not in any way undermine the results of our study of the KH instability.

The diffusion operator is not Lorentz-invariant in relativistic systems, as we demonstrate in section 12.1 using the telegraph equation, also used in Morse and Feshbach (1953). This can produce anomalous results in models which do not establish a well-defined frame of reference. In this chapter, we consider one such model, in which we perturb the RMHD single-fluid conservation-diffusion equations in the presence of a uniform background flow. Because diffusion does not preserve the Lorentz-invariance of the RMHD equations, this uniform-flow model predicts anomalous growing modes in reference frames in which the flow speed is highly relativistic. This occurs whether or not a magnetic field is present, as we demonstrate by first analyzing the RHD case in section 12.2 and then the RMHD case in section 12.3. One important result of this analysis is that we obtain a dispersion relation whose diffusionless limit recovers familiar results, including relativistic acoustic waves in the RHD limit, and the Alfven and magnetoacoustic modes of LRN09 in the RMHD regime. We have therefore recovered these results using an entirely different method, in a limit in which the system is marginally stable. However, when we introduce diffusion, the resulting modes appear to grow rapidly in frames corresponding to highly relativistic flow speeds, but decay in reference frames corresponding to non-relativistic flow speeds, for which the co-moving reference frame corresponds to the limit of zero flow speed.

This result, of course, does not make physical sense, since it contradicts two expectations, namely, that the growth or decay of a mode should not be frame-dependent, and that diffusion should introduce decaying modes in order to stabilize a system, as it does in our numerical simulations. Therefore, this analysis can be considered an academic exercise that reveals the anomalies that can arise from the manner in which current mathematical models

handle diffusion in relativistic systems. Hence, the results of this chapter have mathematical implications, but cannot be given physical significance, and do not in any way harm the validity of our simulation results. It should also be noted that in this chapter when we speak of a "uniform background flow," the flow speed is with respect to an arbitrarily chosen frame of reference, and that a change in flow speed is tantamount to changing the reference frame. This is in contrast to our studies of the KH instability, in which a well-defined reference frame is established by the velocity shear.

We begin, in section 12.1, by describing the manner in which linear modes should behave under Lorentz transformations, and then demonstrating the lack of Lorentz-invariance of the diffusion operator. This lays the groundwork for the anomalous behavior we will later observe in modes introduced by diffusion in a model with uniform flow.

12.1 Lorentz-invariance and Diffusion

In this section, we describe certain properties we expect linear modes to have in the presence of a relativistic uniform flow, one of which is Lorentz-invariance. In the diffusionless case, these properties are satisfied. We then show that the diffusion operator is not Lorentz-invariant, which means that when diffusion is introduced into a system with uniform background flow, we can expect to encounter anomalous frame-dependent results.

We begin by demonstrating the Lorentz-invariance of the linear modes arising from the uniform-flow model. We do this by demonstrating the Lorentz-invariance of the overall phase of these linear perturbations, which shows that modal behavior is frame-independent when examined with respect to the co-moving space and time coordinates of the frame under consideration. In the absence of diffusion, the modes are indeed Lorentz-invariant and

marginally stable, and we show in the later sections of this chapter that these correspond to familiar results (the acoustic and magnetosonic modes of LRN09). We then show that we expect Lorentz-invariance to be qualitatively preserved when the modal frequencies are complex, i.e., that the temporal growth or decay of such a mode should be Lorentz-invariant with respect to the co-moving time coordinate. In a uniform-flow model, diffusion has the effect of making the frequencies complex, and therefore preserves Lorentz-invariance with respect to the co-moving time coordinate. However, the diffusion operator, proportional to ∇^2, is not itself Lorentz-invariant, as we show using the telegraph equation, which is discussed in Morse and Feshbach (1953). Therefore, the growth or decay of a mode introduced by diffusion is not Lorentz-invariant when measured with respect to a fixed time coordinate. This lays the groundwork for later sections, in which the uniform-flow model yields anomalous modes which decay in some reference frames and appear to grow rapidly in other reference frames.

Consider a uniform background flow which moves at a relativistic speed v_{z0}, where $\hat{z}$ is the flow direction and $\hat{x}$ is the shear direction. We wish to relate the derivatives $\partial/\partial z$ and $\partial/\partial t$ in the stationary frame to the derivatives $\partial/\partial z'$ and $\partial/\partial t'$ in the co-moving frame of the flow. We begin by noting that the primed and unprimed quantities are related by a simple Lorentz transformation:

$$z' = \gamma(z - v_{z0}t), \tag{12.1}$$

$$t' = \gamma\left(t - \frac{v_{z0}z}{c^2}\right), \tag{12.2}$$

$$z = \gamma(z' + v_{z0}t'), \tag{12.3}$$

$$t = \gamma\left(t' + \frac{v_{z0}z'}{c^2}\right). \tag{12.4}$$

$\gamma = (1 - v_{z0}^2/c^2)^{-1/2}$ is the Lorentz factor. Using equations (12.1) and (12.2), the unprimed derivatives can be related as follows to the primed derivatives:

$$\begin{aligned} \frac{\partial}{\partial z} &= \frac{\partial}{\partial z'}\frac{\partial z'}{\partial z} + \frac{\partial}{\partial t'}\frac{\partial t'}{\partial z} = \gamma\left(\frac{\partial}{\partial z'} - \frac{v_{z0}}{c^2}\frac{\partial}{\partial t'}\right), \\ \frac{\partial}{\partial t} &= \frac{\partial}{\partial t'}\frac{\partial t'}{\partial t} + \frac{\partial}{\partial z'}\frac{\partial z'}{\partial t} = \gamma\left(\frac{\partial}{\partial t'} - v_{z0}\frac{\partial}{\partial z'}\right). \end{aligned} \tag{12.5}$$

Similarly, using equations (12.3) and (12.4), the primed derivatives can be related as follows to the unprimed derivatives:

$$\begin{aligned} \frac{\partial}{\partial z'} &= \frac{\partial}{\partial z}\frac{\partial z}{\partial z'} + \frac{\partial}{\partial t}\frac{\partial t}{\partial z'} = \gamma\left(\frac{\partial}{\partial z} + \frac{v_{z0}}{c^2}\frac{\partial}{\partial t}\right), \\ \frac{\partial}{\partial t'} &= \frac{\partial}{\partial t}\frac{\partial t}{\partial t'} + \frac{\partial}{\partial z}\frac{\partial z}{\partial t'} = \gamma\left(\frac{\partial}{\partial t} + v_{z0}\frac{\partial}{\partial z}\right). \end{aligned} \tag{12.6}$$

Suppose we have a linear mode which, in the stationary frame, is given by

$$f(x, z, t) = f_0 + f_1 \exp[i(k_x x + k_z z - \omega t)]. \tag{12.7}$$

In the co-moving frame, this mode is given by

$$f(x, z', t') = f_0 + f_1 \exp[i(k_x x + k'_z z' - \omega' t')]. \tag{12.8}$$

We would like to demonstrate that these two representations are consistent, i.e., that the overall phase of the linear perturbation is Lorentz-invariant. We first apply the derivative relations in equations (12.5) to equation (12.8), and obtain

$$\begin{aligned} k_z &= \gamma\left(k'_z + \frac{\omega' v_{z0}}{c^2}\right), \\ \omega &= \gamma(\omega' + k'_z v_{z0}). \end{aligned} \tag{12.9}$$

We then apply the derivative relations in equations (12.6) to equation (12.7), and obtain

$$
\begin{aligned}
k'_z &= \gamma\left(k_z - \frac{\omega v_{z0}}{c^2}\right), \\
\omega' &= \gamma(\omega - k_z v_{z0}).
\end{aligned}
\tag{12.10}
$$

We have recovered the simple Lorentz transformation of the spatial and temporal frequencies, employed numerous times in this and previous chapters (k_x and x are untransformed). By combining equations (12.1) through (12.4) with equations (12.9) and (12.10), we wish to demonstrate that the overall phase of the linear perturbation is Lorentz-invariant. We begin by writing the phase in the co-moving frame:

$$
\begin{aligned}
k'_z z' - \omega' t' &= \gamma^2\left(k_z - \frac{\omega v_{z0}}{c^2}\right)(z - v_{z0}t) - \gamma^2(\omega - k_z v_{z0})\left(t - \frac{v_{z0} z}{c^2}\right) \\
&= \gamma^2\left[k_z z\left(1 - \frac{v_{z0}^2}{c^2}\right) - \omega t\left(1 - \frac{v_{z0}^2}{c^2}\right)\right] \\
&= k_z z - \omega t.
\end{aligned}
\tag{12.11}
$$

We therefore have Lorentz-invariance of the overall phase:

$$
k_x x + k'_z z' - \omega' t' = k_x x + k_z z - \omega t. \tag{12.12}
$$

This means that the overall behavior of a linear mode should not be frame-dependent, as long as we transform not only the frequencies but also the space and time coordinates, so that we always measure coordinates in the co-moving frame of the system. In the absence of diffusion, the modes are indeed Lorentz-invariant, and marginally stable. We show in sections 12.2 and 12.3 that in the diffusionless limit we recover relativistic acoustic modes in RHD and the Alfven and magnetoacoustic modes derived in LRN09 in RMHD.

We now wish to verify that if the frequency ω is complex, we still expect the mode to satisfy qualitative Lorentz-invariance, i.e., we expect the growth or decay of a mode to be

invariant under a Lorentz transformation. When, in section 12.3, we linearize the RMHD equations in the presence of a uniform background flow, we use a temporal approach, and therefore the x and z-components of the wave vector are both real. When we solve the polynomial dispersion relation in ω, the presence of diffusion results in complex roots for ω, where they would otherwise be purely real. Suppose that in the stationary frame, a wave vector with real components k_x and k_z corresponds to a linear mode with complex frequency

$$\omega = \omega_r + i\omega_i, \tag{12.13}$$

where $\omega_i > 0$, so that the mode is growing. The fluid flows at a background speed v_{z0}. In the co-moving frame of the fluid, the frequency and wave vector are given by equation (12.10):

$$\begin{aligned} \omega' &= \gamma(\omega - k_z v_{z0}), \\ k'_z &= \gamma\left(k_z - \frac{\omega v_{z0}}{c^2}\right), \\ k'_x &= k_x. \end{aligned} \tag{12.14}$$

In particular, ω' is also complex, so we have

$$\begin{aligned} (\omega')_i &= \gamma\omega_i, \\ (\omega')_r &= \gamma(\omega_r - k_z v_{z0}). \end{aligned} \tag{12.15}$$

Therefore, if in the stationary frame we have a mode growing at a rate ω_i with respect to time t, then in the co-moving frame we have a mode growing at a rate $(\omega')_i = \gamma\omega_i$ with respect to time t', where t and t' are the time measured in the stationary and co-moving frames, respectively. These are related by equations (12.1) through (12.4). This tells us that if a mode is growing in one frame, it is also growing in any other frame, with respect to the co-moving time-coordinate of that frame. Furthermore, the ratios t'/t and $(\omega')_i/\omega_i$ are

both approximately equal to the Lorentz factor, which tells us that the growth rates in each frame are roughly equal. Following the same reasoning, we can make precisely the same statement about the frame-independence of decaying modes. In summary, when we have complex eigenfrequencies, the temporal growth or decay of a mode is Lorentz-invariant with respect to the co-moving time coordinate.

In the presence of a uniform flow, the introduction of diffusion has the effect of making the frequencies complex. Therefore, the linear modes introduced by diffusion are Lorentz-invariant with respect to the co-moving time coordinate of each frame. That is, a mode that decays with respect to time t' in the co-moving reference frame also decays with respect to time t in the stationary reference frame. The next question is whether the same is true of a mode that decays with respect to time t in the co-moving reference frame, i.e., if we transform reference frames without transforming the time coordinate. The answer is: not necessarily. This is because, as we show below, the diffusion operator, proportional to ∇^2, does not itself preserve Lorentz-invariance. Using equation (12.5), we can write the diffusion operator ∇^2 in terms of the coordinates of the co-moving frame:

$$\begin{aligned}
\nabla^2 &= \frac{\partial^2}{\partial x^2} + \frac{\partial^2}{\partial z^2} \\
&= \frac{\partial^2}{\partial x^2} + \left(\frac{\partial}{\partial z'} - \frac{v_{z0}}{c^2} \frac{\partial}{\partial t'} \right)^2 \\
&= \frac{\partial^2}{\partial x^2} + \frac{\partial^2}{\partial (z')^2} - \frac{1}{c^2} \frac{\partial^2}{\partial (t')^2} + \frac{1}{c^2} \frac{\partial^2}{\partial t^2}.
\end{aligned} \tag{12.16}$$

This demonstrates the Lorentz-invariance of the operator

$$\nabla^2 - \frac{1}{c^2} \frac{\partial^2}{\partial t^2} = (\nabla')^2 - \frac{1}{c^2} \frac{\partial^2}{\partial (t')^2}, \tag{12.17}$$

which is of course the operator that governs the wave equation, and can be considered a covariant extension of the diffusion operator. However, the diffusion operator itself is not Lorentz-invariant. To see this, consider the telegraph equation (Morse and Feshbach 1953), which we employ in one dimension (i.e., restricted to the flow direction), and which governs the time-dependence of the diffusion of some quantity f. In terms of stationary coordinates and a diffusion coefficient η, the telegraph equation reads as follows:

$$\frac{\partial f}{\partial t} \;=\; \eta \frac{\partial^2 f}{\partial z^2}. \tag{12.18}$$

We see that in the telegraph equation, the time and diffusion operators act on f in the same way that they act on the conserved quantities in the RMHD conservation-diffusion equations. In terms of the co-moving coordinates of the flow, the telegraph equation reads

$$\frac{\partial f}{\partial t'} - v_{z0}\frac{\partial f}{\partial z'} \;=\; \eta\gamma \left(\frac{\partial}{\partial (z')} - \frac{v_{z0}}{c^2}\frac{\partial}{\partial (t')} \right)^2 f. \tag{12.19}$$

We see that in the stationary frame, the rate of diffusion of f has only a spatial dependence, whereas in the co-moving frame, the diffusion rate has a spatial and a temporal dependence. This demonstrates that the diffusion operator is not invariant to Lorentz transformation. This must also be true of the conservation-diffusion equations, which can be thought of as the telegraph equation onto which we add the divergence of a flux term. We therefore cannot expect Lorentz-invariance of the growth or decay of a mode introduced by diffusion in a fluid with uniform flow. That is, we know that a mode that decays with respect to time t' in the co-moving frame decays with respect to time t in the stationary frame. However, a mode

that decays with respect to time t in the co-moving frame may in fact appear to *grow* with respect to time t in the stationary frame. This is the type of anomalous behavior we will observe in the upcoming sections, in particular when the stationary frame is with respect to a highly relativistic flow.

We again emphasize that these results pertain to a model with uniform background flow speed, and do not in any way undermine our studies of the KH instability, for which we remain in a stationary frame of reference which is established by the background velocity shear, and for which diffusion always introduces decaying modes and stabilizes the system, as expected. Diffusion introduces decaying modes even in the highly relativistic regime of our KH-unstable simulations. The aforementioned anomalies can only emerge when performing frame transformations in the presence of a uniform background flow, for which there is no externally-imposed velocity shear.

In the next section, in which we analyze a uniform flow in RHD, we will obtain results which bear out the predictions of the analysis we have just performed. Specifically, in the absence of diffusion, we recover familiar marginally stable modes, but in the presence of diffusion, we obtain anomalous modes whose growth or decay is not Lorentz-invariant. In the forthcoming sections, the aforementioned co-moving frame is the zero-velocity limit of the reference frames corresponding to non-relativistic flow speed.

12.2 RHD Stability Analysis with Diffusion

In this section, we analyze a uniform flow in RHD. We will see that in the absence of diffusion, we recover familiar marginally stable modes, namely, the relativistic acoustic modes seen in

Bodo et al. (2004). However, in the presence of diffusion, we will obtain anomalous modes which decay in a frame of non-relativistic flow speed, but appear to rapidly grow in a frame of highly relativistic flow speed.

We wish to linearize the RHD conservation-diffusion equations in two dimensions. There is a uniform unperturbed density ρ_0 and pressure P_0, and a uniform unperturbed velocity v_{z0} in the z-direction. From the linearization, we derive a dispersion relation which is a fourth-order polynomial in ω. We then show that the growth or decay of these roots is in fact dependent on the uniform flow speed, i.e., on the frame of reference.

12.2.1 Derivation of RHD Dispersion Relation with Diffusion

We derive the RHD dispersion relation by linearizing the conservation-diffusion equations, which are

$$\begin{aligned}
\frac{1}{c}\frac{\partial}{\partial t}(\gamma\rho) + \frac{\partial}{\partial x}(\gamma\rho\beta_x) + \frac{\partial}{\partial z}(\gamma\rho\beta_z) &= \eta_\rho\left(\frac{\partial^2}{\partial x^2} + \frac{\partial^2}{\partial z^2}\right)(\gamma\rho), \\
\frac{1}{c}\frac{\partial}{\partial t}(w\gamma^2\beta_x) + \frac{\partial}{\partial x}(P + w\gamma^2\beta_x^2) + \frac{\partial}{\partial z}(w\gamma^2\beta_x\beta_z) &= \eta_x\left(\frac{\partial^2}{\partial x^2} + \frac{\partial^2}{\partial z^2}\right)(w\gamma^2\beta_x), \\
\frac{1}{c}\frac{\partial}{\partial t}(w\gamma^2\beta_z) + \frac{\partial}{\partial x}(w\gamma^2\beta_z\beta_x) + \frac{\partial}{\partial z}(P + w\gamma^2\beta_z^2) &= \eta_z\left(\frac{\partial^2}{\partial x^2} + \frac{\partial^2}{\partial z^2}\right)(w\gamma^2\beta_z), \\
\frac{1}{c}\frac{\partial}{\partial t}\left(w\gamma^2 - P\right) + \frac{\partial}{\partial x}(w\gamma^2\beta_x) + \frac{\partial}{\partial z}(w\gamma^2\beta_z) &= \eta_\epsilon\left(\frac{\partial^2}{\partial x^2} + \frac{\partial^2}{\partial z^2}\right)\left(w\gamma^2 - P\right), \quad (12.20)
\end{aligned}$$

where the enthalpy is

$$w = \rho c^2 + \frac{\Gamma}{\Gamma - 1}(P), \quad (12.21)$$

where Γ is the adiabatic constant. We define dimensionless heat capacities at constant volume C_v and at constant pressure C_p, which are given by

$$
\begin{aligned}
C_v &= \frac{1}{\Gamma - 1}, \\
C_p &= \frac{\Gamma}{\Gamma - 1} = C_v + 1.
\end{aligned} \tag{12.22}
$$

The first equation in (12.20) describes mass transport, the second and third equations momentum transport, and the fourth equation energy transport. We assume the following linearized forms of the variables, corresponding to plane waves:

$$
\begin{aligned}
\rho(x,z,t) &= \rho_0 + \rho_1 \exp[i(k_x x + k_z z - \omega t)], \\
\beta_x(x,z,t) &= \beta_{x1} \exp[i(k_x x + k_z z - \omega t)], \\
\beta_z(x,z,t) &= \beta_{z0} + \beta_{z1} \exp[i(k_x x + k_z z - \omega t)], \\
P(x,z,t) &= P_0 + P_1 \exp[i(k_x x + k_z z - \omega t)].
\end{aligned} \tag{12.23}
$$

We now separately linearize each term of the conservation-diffusion equations. For the density transport equation, we have

$$
\begin{aligned}
\frac{\partial}{\partial t}(\gamma\rho) &= -i\omega \left(\gamma\rho_1 + \gamma^3 \beta_{z0}\beta_{z1}\rho_0\right), \\
\frac{\partial}{\partial x}(\gamma\rho\beta_x) &= ik_x \gamma\rho_0\beta_{x1}, \\
\frac{\partial}{\partial z}(\gamma\rho\beta_z) &= ik_z \left(\gamma\rho_0\beta_{z1} + \gamma\rho_1\beta_{z0} + \gamma^3\beta_{z0}^2\beta_{z1}\rho_0\right), \\
\eta_\rho \left(\frac{\partial^2}{\partial x^2} + \frac{\partial^2}{\partial z^2}\right)(\gamma\rho) &= -\eta_\rho k^2 \left(\gamma\rho_1 + \gamma^3\beta_{z0}\beta_{z1}\rho_0\right).
\end{aligned} \tag{12.24}
$$

For the transport of x-momentum, we have

$$
\begin{aligned}
\frac{\partial}{\partial t}(w\gamma^2\beta_x) &= -i\omega w_0 \gamma^2 \beta_{x1}, \\
\frac{\partial}{\partial x}(P + w\gamma^2\beta_x^2) &= ik_x P_1, \\
\frac{\partial}{\partial z}(w\gamma^2\beta_x\beta_z) &= ik_z w_0 \gamma^2 \beta_{z0}\beta_{x1}, \\
\eta_x \left(\frac{\partial^2}{\partial x^2} + \frac{\partial^2}{\partial z^2}\right)(w\gamma^2\beta_x) &= -\eta_x k^2 w_0 \gamma^2 \beta_{x1}.
\end{aligned} \tag{12.25}
$$

For the transport of z-momentum, we have

$$\begin{aligned}
\frac{\partial}{\partial t}(w\gamma^2\beta_z) &= -i\omega\left(w_0\gamma^2\beta_{z1} + w_1\gamma^2\beta_{z0} + 2w_0\gamma^4\beta_{z0}^2\beta_{z1}\right), \\
\frac{\partial}{\partial x}(w\gamma^2\beta_x\beta_z) &= ik_x w_0\gamma^2\beta_{z0}\beta_{x1}, \\
\frac{\partial}{\partial z}(P + w\gamma^2\beta_z^2) &= ik_z\left(P_1 + w_1\gamma^2\beta_{z0}^2 + 2w_0\gamma^2\beta_{z0}\beta_{z1} + 2w_0\gamma^4\beta_{z0}^3\beta_{z1}\right), \\
\eta_z\left(\frac{\partial^2}{\partial x^2} + \frac{\partial^2}{\partial z^2}\right)(w\gamma^2\beta_z) &= -\eta_z k^2\left(w_0\gamma^2\beta_{z1} + w_1\gamma^2\beta_{z0} + 2w_0\gamma^4\beta_{z0}^2\beta_{z1}\right). \qquad (12.26)
\end{aligned}$$

For the transport of energy, we have

$$\begin{aligned}
\frac{\partial}{\partial t}\left(w\gamma^2 - P\right) &= -i\omega\left(w_1\gamma^2 + 2w_0\gamma^4\beta_{z0}\beta_{z1} - P_1\right), \\
\frac{\partial}{\partial x}(w\gamma^2\beta_x) &= ik_x w_0\gamma^2\beta_{x1}, \\
\frac{\partial}{\partial z}(w\gamma^2\beta_z) &= ik_z\left(w_0\gamma^2\beta_{z1} + w_1\gamma^2\beta_{z0} + 2w_0\gamma^4\beta_{z0}^2\beta_{z1}\right), \\
\eta_\epsilon\left(\frac{\partial^2}{\partial x^2} + \frac{\partial^2}{\partial z^2}\right)\left(w\gamma^2 - P\right) &= -\eta_\epsilon k^2\left(w_1\gamma^2 + 2w_0\gamma^4\beta_{z0}\beta_{z1} - P_1\right). \qquad (12.27)
\end{aligned}$$

Upon collecting terms, we arrive at the following four linearized equations:

$$\begin{aligned}
0 &= \bar{\omega}_\rho\gamma\left(w_1 - \frac{\Gamma P_1}{\Gamma - 1}\right) - \gamma\rho_0 c^3 k_x\beta_{x1} + \left(\bar{\omega}_\rho\rho_0\gamma^3\beta_{z0} - \gamma\rho_0 c k_z\right)c^2\beta_{z1}, \\
0 &= -ck_x P_1 + \bar{\omega}_x w_0\gamma^2\beta_{x1}, \\
0 &= \gamma^2\beta_{z0}\bar{\omega}_z w_1 - ck_z P_1 - ck_x w_0\gamma^2\beta_{z0}\beta_{x1} + C_0\beta_{z1}, \\
0 &= \gamma^2\bar{\omega}_\epsilon w_1 - \omega_\epsilon P_1 - ck_x w_0\gamma^2\beta_{x1} + w_0\gamma^2\left(-ck_z + 2\gamma^2\beta_{z0}\bar{\omega}_\epsilon\right)\beta_{z1}, \qquad (12.28)
\end{aligned}$$

where we have made the following definitions:

$$\begin{aligned}
\bar{\omega} &= \omega - ck_z\beta_{z0}, \\
\bar{\omega}_\rho &= \bar{\omega} + i\eta_\rho k^2, \\
\bar{\omega}_x &= \bar{\omega} + i\eta_x k^2, \\
\bar{\omega}_z &= \bar{\omega} + i\eta_z k^2, \qquad \omega_z = \bar{\omega}_z + k_z v_{z0}, \\
\bar{\omega}_\epsilon &= \bar{\omega} + i\eta_\epsilon k^2, \qquad \omega_\epsilon = \bar{\omega}_\epsilon + k_z v_{z0}, \\
C_0 &= \omega_z w_0\gamma^2\left(1 + 2\gamma^2\beta_{z0}^2\right) - 2w_0\gamma^2 ck_z\beta_{z0}\left(1 + \gamma^2\beta_{z0}^2\right). \qquad (12.29)
\end{aligned}$$

We see that the above four linearized equations can be written in the following matrix form:

$$M \begin{pmatrix} w_1 \\ P_1 \\ \beta_{x1} \\ \beta_{z1} \end{pmatrix} \;=\; 0, \tag{12.30}$$

where M is a 4 by 4 matrix. By equating the determinant of this matrix to zero, we obtain a polynomial dispersion relation which is fourth-order in ω:

$$F_4\omega^4 + F_3\omega^3 + F_2\omega^2 + F_1\omega + F_0 \;=\; 0. \tag{12.31}$$

Suppose we introduce the following definitions:

$$\begin{aligned} \chi_j &= \frac{\eta_j k}{c}, \qquad \Omega = \frac{\omega}{ck}, \\ h &= \frac{w_0}{\rho_0}, \qquad f = \frac{\rho_0}{w_0}, \\ \zeta_z &= \frac{k_z}{k}, \qquad \zeta_x = \frac{k_x}{k}, \\ \tau_z &= \beta\zeta_z = \frac{v_{z0}k_z}{ck}. \end{aligned} \tag{12.32}$$

Then the dispersion relation can be written in the following dimensionless form:

$$G_4\Omega^4 + G_3\Omega^3 + G_2\Omega^2 + G_1\Omega + G_0 \;=\; 0. \tag{12.33}$$

The general solution for Ω is given by the quartic formula, which is determined as follows (Nickalls 2009). We first define

$$\begin{aligned} \alpha &= -\frac{3G_3^2}{8G_4^2} + \frac{G_2}{G_4}, \\ \alpha_2 &= \frac{G_3^3}{8G_4^3} - \frac{G_3G_2}{2G_4^2} + \frac{G_1}{G_4}, \\ \alpha_3 &= -\frac{3G_3^4}{256G_4^4} + \frac{G_2G_3^2}{16G_4^3} - \frac{G_3G_1}{4G_4^2} + \frac{G_0}{G_4}. \end{aligned} \tag{12.34}$$

We then define

$$\begin{aligned}
P &= -\frac{\alpha^2}{12} - \alpha_3, \\
Q &= -\frac{\alpha^3}{108} + \frac{\alpha\alpha_3}{3} - \frac{\alpha_2^2}{8}, \\
R &= -\frac{Q}{2} \pm \sqrt{\frac{Q^2}{4} + \frac{P^3}{27}}, \\
U &= R^{1/3}, \\
y &= \frac{-5}{6}\alpha + U - \frac{P}{3U}, \qquad \text{if } U \neq 0, \\
y &= \frac{-5}{6}\alpha + U - Q^{1/3}, \qquad \text{if } U = 0, \\
W &= \sqrt{\alpha + 2y}.
\end{aligned} \tag{12.35}$$

The desired roots are then given by

$$\omega = -\frac{G_3}{4G_4} + \frac{\pm_1 W \mp_2 \sqrt{-(3\alpha + 2y \pm_1 2\alpha_2/W)}}{2}, \qquad \alpha_2 \neq 0, \tag{12.36}$$

$$\omega = -\frac{G_3}{4G_4} \pm_1 \sqrt{\frac{-\alpha \pm_2 \sqrt{\alpha^2 - 4\alpha_3}}{2}}, \qquad \alpha_2 = 0, \tag{12.37}$$

where $\pm_1$ and $\pm_2$ can vary independently of one another, so that each of the above expressions corresponds to four solutions.

The coefficients G_j are as follows, first without diffusion:

$$\begin{aligned}
G_{40} &= -\beta^2\gamma^2(2-f) - 1 + C_p\gamma^2, \\
&= \gamma^2[1 - f + \gamma^2(-2 + C_p + f)], \\
G_{30} &= 2\tau_z[-1 + f - 2\gamma^2(-2 + C_p + f)], \\
G_{20} &= (-1+f)\zeta_x^2 + \zeta_z^2[(-1+f)(1-\beta^2) + 6\gamma^2\beta^2(-2 + C_p + f)], \\
G_{10} &= 2\tau_z[-(-1+f)\zeta_x^2 + \zeta_z^2(-3 + 2C_p + f - 2(-2 + C_p + f)\gamma^2)], \\
G_{00} &= \tau_z^2[(-1+f)\zeta_x^2 + \zeta_z^2(1 - C_p + \gamma^2(-2 + C_p + f))].
\end{aligned} \tag{12.38}$$

In the presence of diffusion, the G_j are given by

$$
\begin{aligned}
G_4 &= G_{40} = -\beta^2\gamma^2(2-f) - 1 + C_p\gamma^2, \\
G_3 &= G_{30} + i(\chi_x + \chi_z + \chi_\epsilon + \chi_\rho)[-\beta^2\gamma^2(2-f) - 1 + C_p\gamma^2], \\
G_2 &= G_{20} + i\chi_x\tau_z[3 - f + \gamma^2(2 - f - 3C_p + 2(2-f)\beta^2)] \\
&\quad + i\chi_z\tau_z[2 - f + \gamma^2(-2C_p + 2(2-f)\beta^2)] \\
&\quad + i\chi_\epsilon\tau_z[4 - f + \gamma^2(2 - f - 4C_p + 3(2-f)\beta^2)] \\
&\quad + i\chi_\rho\tau_z[3 + \gamma^2(2 - f - 3C_p + 2(2-f)\beta^2)] \\
&\quad - [\chi_\rho(\chi_x + \chi_z + \chi_\epsilon) + \chi_\epsilon(\chi_x + \chi_z) + \chi_x\chi_z][-\beta^2\gamma^2(2-f) - 1 + C_p\gamma^2], \qquad (12.39)
\end{aligned}
$$

$$
\begin{aligned}
G_1 &= G_{10} + i\chi_x[(-1+f)\zeta_z^2 + (f-2)\tau_z^2 + \tau_z^2\gamma^2(3C_p + 2f - 4 + (f-2)\beta^2)] \\
&\quad + i\chi_z[(-1+f)(\zeta_x^2 + \tau_z^2) + \beta^2\gamma^2((-2+f)\zeta_x^2 + C_p\zeta_z^2 + (f-2)\tau_z^2)] \\
&\quad + i\chi_\epsilon[f + \beta^2[(-5+2f)\zeta_z^2 + \gamma^2((2-f)(\zeta_x^4 - \zeta_x^2\zeta_z^2 - 2\zeta_z^4 - 3\tau_z^2) + 5C_p\zeta_z^2)]] \\
&\quad + i\chi_\rho[-1 - 2\tau_z^2 + \gamma^2\tau_z^2(3C_p + (f-2)(2+\beta^2))] \\
&\quad + \chi_x\chi_z\tau_z[-1 + f + C_p\gamma^2 + (f-2)\beta^2\gamma^2] \\
&\quad + \chi_x\chi_\epsilon\tau_z[-3 + f + \gamma^2(3C_p + (f-2)(1+2\beta^2))] + \chi_z\chi_\epsilon\tau_z[f - 2 + 2\gamma^2(C_p + (f-2)\beta^2)] \\
&\quad + \chi_x\chi_\rho\tau_z[-2 + \gamma^2(2C_p + (f-2)(1+\beta^2))] + \chi_z\chi_\rho\tau_z[-1 + \gamma^2(C_p + (f-2)\beta^2)] \\
&\quad + \chi_\epsilon\chi_\rho\tau_z[-3 + \gamma^2(3C_p + (f-2)(1+2\beta^2))] \\
&\quad + i[\chi_x\chi_z(\chi_\epsilon + \chi_\rho) + \chi_\epsilon\chi_\rho(\chi_x + \chi_z)][1 - C_p\gamma^2 + (2-f)\beta^2\gamma^2], \qquad (12.40)
\end{aligned}
$$

$$
\begin{aligned}
G_0 &= G_{00} + i\chi_x\tau_z\zeta_z^2[1 - f + \beta^2\gamma^2(2 - f - C_p)] \\
&\quad + i\chi_z\tau_z\zeta_x^2[1 - f + \beta^2\gamma^2(2-f)] \\
&\quad + i\chi_\epsilon\tau_z\{-f + \beta^2[(2-f)\zeta_z^2 + \gamma^2[(2-f)(\zeta_z^2 - \zeta_x^2 + \tau_z^2) - 2C_p\zeta_z^2]]\} \\
&\quad + i\chi_\rho\tau_z[1 + \tau_z^2\gamma^2(2 - f - C_p)] \\
&\quad + \chi_x\chi_\epsilon\zeta_z^2[-f + (2-f)\beta^2 + \beta^2\gamma^2(-2C_p + (2-f)(1+\beta^2))] \\
&\quad + \chi_z\chi_\epsilon[-f\zeta_x^2 + (1-f)\tau_z^2 + \tau_z^2\gamma^2(-C_p + (2-f)\beta^2)] \\
&\quad + \chi_x\chi_\rho\zeta_z^2[1 + \beta^2\gamma^2(2 - f - C_p)] + \chi_z\chi_\rho\zeta_x^2[1 + (2-f)\beta^2\gamma^2] \\
&\quad + \chi_\epsilon\chi_\rho\beta^2[2\zeta_z^2 + \gamma^2(-2C_p\zeta_z^2 + (2-f)(\zeta_z^2 - \zeta_x^2 + \tau_z^2))] \\
&\quad + i\chi_x\chi_z\chi_\epsilon\tau_z[f - 1 + \gamma^2(C_p - (2-f)\beta^2)] + i\chi_x\chi_\epsilon\chi_\rho\tau_z[-2 + \gamma^2(2C_p + (f-2)(1+\beta^2))] \\
&\quad + \chi_z\chi_\epsilon\chi_\rho(i\tau_z + \chi_x)[-1 + C_p\gamma^2 - \beta^2\gamma^2(2-f)]. \qquad (12.41)
\end{aligned}
$$

Through the normalization with respect to kc, we eliminate any dependence on the wave number k. Therefore, we see that the roots in ω have a simple linear dependence on k.

12.2.2 RHD Dispersion Relation in Diffusionless Case

We seek to solve the dispersion relation for the RHD case with no diffusion, and recover the familiar Lorentz-shifted and acoustic modes. We will then take the non-relativistic limit and recover the Doppler-shifted and non-relativistic acoustic modes. The dispersion relation for the diffusionless case can be written in the form

$$C_4\Omega^4 + C_3\Omega^3 + C_2\Omega^2 + C_1\Omega + C_0 \;=\; 0, \tag{12.42}$$

where

$$\begin{aligned} Q &= \frac{2+f}{1-f} \;=\; \frac{2w_0 + \rho_0 c^2}{w_0 - \rho_0 c^2}, \\ C_4 &= \gamma^2 Q + 1, \\ C_3 &= -2\tau_z\left(2\gamma^2 Q + 1\right), \\ C_2 &= 6\tau_z^2\gamma^2 Q - 1 + \tau_z^2, \\ C_1 &= -2\tau_z(2\tau_z^2\gamma^2 Q - 1), \\ C_0 &= \tau_z^2(\tau_z^2\gamma^2 Q - 1). \end{aligned} \tag{12.43}$$

This polynomial can be simplified to read

$$\begin{aligned} (\Omega - \zeta_z\beta)^2[Q\gamma^2(\Omega - \tau_z)^2 + \Omega^2 - 1] \;&=\; 0, \qquad \text{or} \\ (\Omega - \zeta_z\beta)^2[(Q\gamma^2 + 1)\Omega^2 - 2Q\gamma^2\tau_z\Omega + Q\gamma^2\tau_z^2 - 1] \;&=\; 0. \end{aligned} \tag{12.44}$$

The corresponding roots are

$$\begin{aligned} \Omega_1 &= \tau_z \\ \Omega_2 &= \frac{\tau_z Q\gamma^2 + \sqrt{1 + Q\gamma^2(1-\tau_z^2)}}{1 + Q\gamma^2}, \\ \Omega_3 &= \frac{\tau_z Q\gamma^2 - \sqrt{1 + Q\gamma^2(1-\tau_z^2)}}{1 + Q\gamma^2}, \end{aligned} \tag{12.45}$$

or, in terms of ω,

$$
\begin{aligned}
\omega_1 &= k_z v_{z0}, \\
\omega_2 &= (k_z v_{z0}) \frac{Q\gamma^2 + \sqrt{1 + Q\gamma^2(1-\tau_z^2)}}{1 + Q\gamma^2}, \\
\omega_3 &= (k_z v_{z0}) \frac{Q\gamma^2 - \sqrt{1 + Q\gamma^2(1-\tau_z^2)}}{1 + Q\gamma^2}.
\end{aligned}
\tag{12.46}
$$

The first root corresponds to the Lorentz shift, and has a multiplicity of two, which is why we only have three distinct roots. The second and third roots correspond to relativistic acoustic waves traveling at the relativistic sound speed

$$
\begin{aligned}
c_s &= \sqrt{\left(\frac{4}{3}\right)\frac{P_0}{w_0}} \\
&= c\sqrt{\frac{w_0 - \rho_0}{3w_0}} = c\sqrt{\frac{1-f}{3}} = \frac{c}{\sqrt{Q+1}}.
\end{aligned}
\tag{12.47}
$$

We can therefore write the acoustic roots in terms of the sound speed:

$$
\begin{aligned}
a_s^2 &\equiv \frac{c_s^2}{c^2}, \\
Q &= \frac{c^2}{c_s^2} - 1 = \frac{1 - a_s^2}{a_s^2}, \\
\Omega_2 &= \frac{\beta\zeta_z Q + \sqrt{(1-\beta^2)[1 - \beta^2 + Q(1-\tau_z^2)]}}{1 - \beta^2 + Q} \\
&= \frac{\beta\zeta_z(1-a_s^2) + a_s\sqrt{(1-\beta^2)[a_s^2(1-\beta^2) + (1-a_s^2)(1-\tau_z^2)]}}{a_s^2(1-\beta^2) + 1 - a_s^2} \\
&= \frac{\beta\zeta_z(1-a_s^2) + a_s\sqrt{(1-\beta^2)[a_s^2(1-\beta^2) + (1-a_s^2)(1-\tau_z^2)]}}{1 - \beta^2 a_s^2}, \\
\omega_2 &= (ck)\frac{\tau_z(1-a_s^2) + a_s\sqrt{(1-\beta^2)[a_s^2(1-\beta^2) + (1-a_s^2)(1-\tau_z^2)]}}{1 - \beta^2 a_s^2}, \qquad (12.48) \\
\omega_3 &= (ck)\frac{\tau_z(1-a_s^2) - a_s\sqrt{(1-\beta^2)[a_s^2(1-\beta^2) + (1-a_s^2)(1-\tau_z^2)]}}{1 - \beta^2 a_s^2}. \qquad (12.49)
\end{aligned}
$$

In particular, the dispersion relation satisfied by the acoustic roots can be written in a more illuminating form:

$$Q\gamma^2(\Omega - \tau_z)^2 + \Omega^2 - 1 \;=\; 0. \tag{12.50}$$

Writing the dimensionless variables in terms of their definitions in (12.32), we have

$$\frac{c^2 - c_s^2}{c_s^2}\gamma^2(\omega - k_z v_{z0})^2 + \omega^2 - c^2k^2 \;=\; 0. \tag{12.51}$$

We can also make use of the Lorentz invariance of the quantity $\omega^2 - c^2k^2$, by which we mean that this quantity is the same regardless of the frame in which it is evaluated. That is, we have

$$\omega^2 - c^2k^2 \;=\; \gamma^2(\omega - k_z v_{z0})^2 - c^2\left[k_x^2 + \gamma^2\left(k_z - \frac{\omega v_{z0}}{c^2}\right)^2\right]. \tag{12.52}$$

Inserting (12.52) into the dispersion relation (12.51), we have

$$\frac{c^2 - c_s^2}{c_s^2}\gamma^2(\omega - k_z v_{z0})^2 + \gamma^2(\omega - k_z v_{z0})^2 - c^2\left[k_x^2 + \gamma^2\left(k_z - \frac{\omega v_{z0}}{c^2}\right)^2\right] \;=\; 0. \tag{12.53}$$

Multiplying both sides of (12.53) by c_s^2/c^2, we obtain a more transparent version of the dispersion relation for relativistic acoustic waves, which simply equates the frequency squared to the product of sound speed squared and wave vector squared:

$$\gamma^2(\omega - k_z v_{z0})^2 \;=\; c_s^2\left[\gamma^2\left(k_z - \frac{\omega v_{z0}}{c^2}\right)^2 + k_x^2\right]. \tag{12.54}$$

This is similar to the dispersion relation for non-relativistic acoustic waves. However, in the relativistic case, the frequency and wave vector are both Lorentz-shifted. Taking into account Lorentz-shifted and acoustic modes, we recover the familiar RHD diffusionless dispersion relation:

$$(\omega - k_z v_{z0})^2 \left\{ \gamma^2 (\omega - k_z v_{z0})^2 - c_s^2 \left[\gamma^2 \left(k_z - \frac{\omega v_{z0}}{c^2} \right)^2 + k_x^2 \right] \right\} \;=\; 0. \tag{12.55}$$

This is identical to the dispersion relation appearing in Bodo et al. (2004), with notational differences. In the non-relativistic limit, we have

$$\begin{aligned} \beta \;&<<\; 1, \\ a_s \;&=\; \frac{c_s}{c} \;<<\; 1. \end{aligned} \tag{12.56}$$

We can therefore make the following approximations for the two terms in the numerator of expressions (12.48) and (12.49) for the acoustic roots ω_2 and ω_3:

$$\begin{aligned} 1 - a_s^2 \;&\approx\; 1, \\ \sqrt{(1-\beta^2)[a_s^2(1-\beta^2) + (1-a_s^2)(1-\tau_z^2)]} \;&\approx\; 1, \\ 1 - \beta^2 a_s^2 \;&\approx\; 1. \end{aligned} \tag{12.57}$$

The non-relativistic acoustic roots therefore have the expected form:

$$\begin{aligned} \omega_2 \;&\approx\; (ck)(\tau_z + a_s) \;=\; k_z v_{z0} + k c_s, \\ \omega_3 \;&\approx\; (ck)(\tau_z + a_s) \;=\; k_z v_{z0} - k c_s. \end{aligned} \tag{12.58}$$

These satisfy the dispersion relation

$$(\omega - k_z v_{z0})^2 \;=\; c_s^2 k^2 \;=\; c_s^2 (k_z^2 + k_x^2). \tag{12.59}$$

Taking into account the Doppler-shifted mode $\omega = k_z v_{z0}$, we recover the familiar HD diffusionless dispersion relation:

$$(\omega - k_z v_{z0})^2 [(\omega - k_z v_{z0})^2 - c_s^2 (k_z^2 + k_x^2)] \;=\; 0. \tag{12.60}$$

This is simply the non-relativistic limit of the corresponding RHD dispersion relation. Because $c_s << c$, we can also make approximations associated with a non-relativistic sound speed:

$$\begin{aligned} \rho_0 c^2 &>> \frac{\Gamma}{\Gamma - 1} P_0, \\ w_0 &= \rho_0 c^2 + \frac{\Gamma P_0}{\Gamma - 1} \approx \rho_0 c^2, \\ c_s &= (c)\sqrt{\frac{\Gamma P_0}{w_0}} \approx \sqrt{\frac{\Gamma P_0}{\rho_0}}. \end{aligned} \tag{12.61}$$

In the next section, we show that

12.2.3 Decaying Modes in Non-relativistic Regime

We again consider the non-relativistic limit, this time including diffusion, and seek to show that in a reference frame in which the flow speed is non-relativistic, the uniform-flow model generally does not predict that diffusion introduces growing modes. Note that the limit of zero flow speed corresponds to the co-moving frame discussed in section 12.1.

The momentum viscosities are $0.00025\, c/k$. Our reference frame is such that the flow speed is $v_{z0} = 0.08\, c$. We plot maximum growth rate verses $\eta_\epsilon - \eta_\rho$, the difference between energy viscosity and density viscosity. The momentum viscosity is $0.00025\, c/k$, and the density viscosity is $0.0002\, c/k$. Figure 12.1 simultaneously plots curves for several different values of the sound speed. In each case, there is a nearly linear decrease of growth rate for $\eta_\epsilon < \eta_\rho$, and a nearly linear increase of growth rate for $\eta_\epsilon > \eta_\rho$. When $\eta_\epsilon = \eta_\rho$, the rate of decay is $0.0002\, ck$, equal to the density viscosity multiplied by k^2. As the sound speed increases, there is a decrease in the rate of change of growth rate with viscosity ratio, and a widening of the interval of energy viscosities corresponding to stability (negative growth

rate). We obtain these same qualitative results when we alter the values of the viscosities.

Therefore, we obtain decaying modes as long as we relate the energy and density viscosities in a manner which is consistent with the sound speed of the system. We can interpret this in terms of frame-invariant properties of the single-fluid equations. Specifically, for non-relativistic sound speeds, we have $\rho c^2 >> P$, and the density of the system is much more comparable to the energy. In the non-relativistic limit of the fluid equations in chapter 3, we can make the approximation $w \approx \rho c^2$ in the momentum equations, and thus we see that density plays a larger role in the evolution of the system. Thus, it makes sense that in the regime of non-relativistic flow speed and sound speed, the density and energy viscosity ought to be comparable (if either of these is nonzero, which generally is not the case). However, as the sound speed becomes more relativistic, P dominates over ρc^2, so that the density plays much less of a role in the fluid equations, and is further decoupled from the evolution of the system, which is now more heavily influenced by the pressure, in part via the enthalpy. It therefore makes sense that as sound speed becomes more relativistic, there is also a decoupling between density and energy viscosities, which no longer need to be equal in order for stability.

This shows that in a reference frame corresponding to non-relativistic or mildly relativistic flow speeds, the modes introduced by diffusion are decaying modes, as we would expect. However, in the next subsection, we transform into reference frames corresponding to highly relativistic flow speeds, and observe that these decaying modes now look like growing modes.

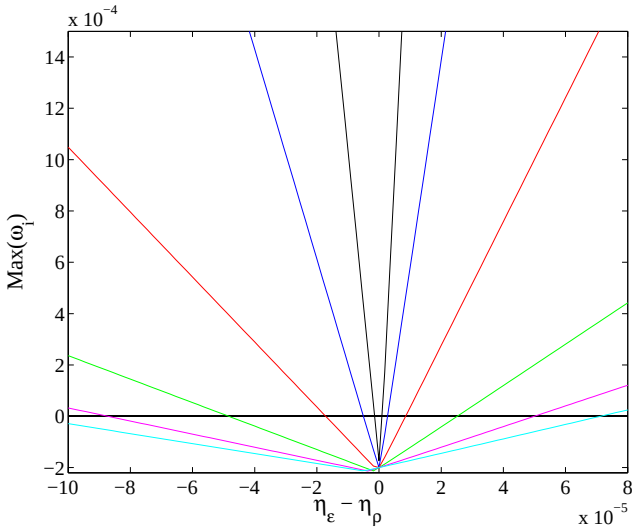

Figure 12.1: Growth rate vs. energy viscosity for different sound speeds c_s/c = 0.05 (black), 0.09 (blue), 0.16 (red), 0.27 (green), 0.37 (magenta), 0.42 (cyan) $v_{z0} = 0.08\,c, \qquad \eta_x = \eta_z = 0.00025\,c/k, \qquad \eta_\rho = 0.0002\,c/k$

12.2.4 Anomalous Growing Modes in Highly Relativistic Regime

We now present a mathematical analysis showing that in a reference frame corresponding to highly relativistic flow speeds, the uniform-flow model predicts anomalous growing modes introduced by diffusion, due to the frame-dependence of the diffusion operator in relativistic systems. For highly relativistic velocities, $\gamma >> 1$, and the terms in the coefficients which dominate are those with the highest power of γ, which is γ^4. In the relativistic regime, the adiabatic constant is $\Gamma = 4/3$, the heat capacity at constant volume is $C_v = 3$, and the heat capacity at constant pressure is $C_p = 4$. We now introduce the dimensionless quantity

$$\alpha \;=\; \frac{2-f}{2+f}. \tag{12.62}$$

In this limit, the coefficients without viscosity are as follows:

$$
\begin{aligned}
G_{40} &= 1, \\
G_{30} &= -4\zeta_z, \\
G_{20} &= 6\zeta_z^2, \\
G_{10} &= -4\zeta_z^3, \\
G_{00} &= \zeta_z^4.
\end{aligned} \tag{12.63}
$$

When we include viscosity, we have

$$
\begin{aligned}
G_4 &= 1, \\
G_3 &= -4\zeta_z + (i)(\chi_x + \chi_z + \chi_\epsilon + \chi_\rho), \\
G_2 &= 6\zeta_z^2 - [\chi_\epsilon\chi_\rho + \chi_x\chi_z + (\chi_x + \chi_z)(\chi_\rho + \chi_\epsilon)] - \\
&\quad i\zeta_z(4\chi_\epsilon + 3\chi_\rho + 3\chi_x + 2\chi_z), \\
G_1 &= -4\zeta_z^3 + i[-\chi_x\chi_z(\chi_\epsilon + \chi_\rho) - (\chi_x + \chi_z)\chi_\epsilon\chi_\rho] + \\
&\quad \zeta_z[\chi_x(\chi_z + 2\chi_\rho + 3\chi_\epsilon) + \chi_z(2\chi_\epsilon + \chi_\rho) + 3\chi_\rho\chi_\epsilon] + \\
&\quad i[(3\chi_x + \chi_z + 3\chi_\rho + 5\chi_\epsilon)\zeta_z^2 + (-\chi_z + \chi_\epsilon)\zeta_x^2\alpha], \\
G_0 &= \zeta_z^4 + \chi_x\left[\zeta_z^2(-i\zeta_z - \chi_\rho) + \chi_\epsilon[2\zeta_z(-\zeta_z + i\beta\chi_\rho)]\right] + \\
&\quad \chi_z\left[\zeta_x^2\alpha(i\zeta_z + \chi_\rho) + \chi_\epsilon\left(-\zeta_z^2 + i\zeta_z\chi_\rho\right)\right] - \\
&\quad [i\zeta_z\chi_\rho + 2\chi_\epsilon(\chi_\rho + i\zeta_z)]\zeta_z^2 - \chi_\epsilon(\chi_\rho + i\zeta_z)\zeta_x^2\alpha.
\end{aligned} \tag{12.64}
$$

Suppose we make the following definition:

$$
s = \frac{\Omega}{\zeta_z} = \frac{\omega}{k_z c}. \tag{12.65}
$$

Then in the diffusionless case, the dispersion relation reduces to

$$
0 \approx s^4 - 4s^3 + 6s^2 - 4s + 1 = (s-1)^4 \equiv f(s). \tag{12.66}
$$

The function $f(s)$ has the root $s = 1$, corresponding to $\omega = k_z c \approx k_z v_{z0}$, which is the expected mode corresponding to a Lorentz shift. The relativistic acoustic modes, evidently, are no longer present in the extreme relativistic case.

Suppose now we have a sufficiently small amount of diffusion that only terms of order χ_j are important. Letting $\psi_j = \chi_j \zeta_z$, and $\alpha_{xz} = \alpha \zeta_x / \zeta_z$, the polynomial reduces to

$$\begin{aligned}
0 &= (s-1)^4 + (i)(\psi_3 s^3 + \psi_2 s^2 + \psi_1 s + \psi_0), \qquad \text{where} \\
\psi_3 &= \psi_x + \psi_z + \psi_\epsilon + \psi_\rho, \\
\psi_2 &= -(3\psi_x + 2\psi_z + 4\psi_\epsilon + 3\psi_\rho), \\
\psi_1 &= 3\psi_x + \psi_z + 5\psi_\epsilon + 3\psi_\rho + (-\psi_z + \psi_\epsilon)\alpha_{xz}, \\
\psi_0 &= -\psi_x - 2\psi_\epsilon - \psi_\rho + (\psi_z - \psi_\epsilon)\alpha_{xz}.
\end{aligned} \tag{12.67}$$

If we now write $s = 1 + \delta$, we have

$$\begin{aligned}
0 &= \delta^4 + (i)[\psi_3(1+\delta)^3 + \psi_2(1+\delta)^2 + \psi_1(1+\delta) + \psi_0] \\
&= \delta^4 + (i)(\psi_3 \delta^3 + \psi_{b2}\delta^2 + \psi_{b1}\delta + \psi_{b0}), \qquad \text{where} \\
\psi_{b2} &= 3\psi_3 + \psi_2 \;=\; \psi_z - \psi_\epsilon, \\
\psi_{b1} &= 3\psi_3 + 2\psi_2 + \psi_1 \;=\; -(\psi_z - \psi_\epsilon)\alpha_{xz}, \\
\psi_{b0} &= \psi_3 + \psi_2 + \psi_1 + \psi_0 \;=\; 0.
\end{aligned} \tag{12.68}$$

The polynomial therefore simplifies to

$$\begin{aligned}
0 &= \delta^4 + (i)[\psi_3 \delta^3 + (\psi_z - \psi_\epsilon)(\delta^2 - \alpha_{xz}\delta)], \quad \text{or} \\
0 &= \delta^4 + (i)[(\psi_x + \psi_z + \psi_\epsilon + \psi_\rho)\delta^3 + (\psi_z - \psi_\epsilon)(\delta^2 - \alpha_{xz}\delta)].
\end{aligned} \tag{12.69}$$

This yields the trivial solution $\delta_0 = 0$ multiplied by a third-order polynomial in δ.

Because $\delta << 1$, we can make the approximations

$$\psi_3 \delta^2 \;<<\; \psi_{b1}, \qquad \psi_{b2}\delta \;<<\; \psi_{b1}. \tag{12.70}$$

The polynomial then reduces to

$$\begin{aligned}
\delta^4 + \psi_{b1}\delta &= 0, \qquad \text{or} \\
\delta^4 - i\alpha_{xz}(\psi_z - \psi_\epsilon)\delta &= 0.
\end{aligned} \tag{12.71}$$

which has the roots

$$\begin{aligned}
\delta_0 &= 0, \qquad \text{and} \\
\delta_{123} &= \alpha_{xz}(\psi_z - \psi_\epsilon) i^{1/3} \\
&= \alpha_{xz}(\psi_z - \psi_\epsilon) \left\{ \exp(i\pi/6), \exp(i5\pi/6), \exp(i3\pi/2) \right\} \\
&= \alpha_{xz}(\psi_z - \psi_\epsilon) \left\{ \frac{\sqrt{3}+i}{2}, \ \frac{-\sqrt{3}+i}{2}, \ -i \right\} \\
&= \frac{k_x}{k_z} \left(\frac{w_0 - 2\rho_0 c^2}{w_0 + 2\rho_0 c^2} \right) (\psi_z - \psi_\epsilon) \left\{ \frac{\sqrt{3}+i}{2}, \ \frac{-\sqrt{3}+i}{2}, \ -i \right\}. \qquad (12.72)
\end{aligned}$$

The corresponding frequencies are

$$\begin{aligned}
\omega_0 &= k_z v_{z0} \approx k_z c, \qquad \text{and} \\
\omega_{123} &= k_z v_{z0} + k_x v_{z0} \left(\frac{w_0 - 2\rho_0 c^2}{w_0 + 2\rho_0 c^2} \right) (\psi_z - \psi_\epsilon) \left\{ \frac{\sqrt{3}+i}{2}, \ \frac{-\sqrt{3}+i}{2}, \ -i \right\} \\
&\approx k_z c + k_x c \left(\frac{w_0 - 2\rho_0}{w_0 + 2\rho_0} \right) (\psi_z - \psi_\epsilon) \left\{ \frac{\sqrt{3}+i}{2}, \ \frac{-\sqrt{3}+i}{2}, \ -i \right\}. \qquad (12.73)
\end{aligned}$$

Two of these roots have positive imaginary parts, and are therefore growing roots that lead to instability. Local stability analysis therefore predicts that in reference frames for which the flow speed is highly relativistic, any diffusion coefficients satisfying $\psi_z \neq \psi_\epsilon$ will produce anomalous modes which appear to grow.

Consider again the polynomial with all coefficients retained:

$$0 = \delta^4 + (i)[(\psi_x + \psi_z + \psi_\epsilon + \psi_\rho)\delta^3 + (\psi_z - \psi_\epsilon)(\delta^2 - \alpha_{xz}\delta)]. \qquad (12.74)$$

If $\psi_z = \psi_\epsilon$, we have the trivial solution, along with the decaying root given by

$$\begin{aligned}
\delta_1 &= -i\psi_3 = -i(\psi_x + \psi_z + \psi_\epsilon + \psi_\rho) = -i(\psi_x + 2\psi_z + \psi_\rho), \\
s_1 &= 1 + \delta_1 = 1 - i(\psi_x + 2\psi_z + \psi_\rho). \qquad (12.75)
\end{aligned}$$

In this case only, diffusion does not introduce growing modes in the extreme relativistic limit.

We have presented a mathematical demonstration that in a frame in which the flow speed is highly relativistic, the uniform-flow model predicts that diffusion introduces anomalous growing modes. In the highly relativistic regime of our simulations, diffusion can no longer stabilize the system numerically, however, diffusion itself does not introduce growing modes. The anomalous results of the uniform-flow model are a consequence of the fact that the diffusion operator, proportional to ∇^2, is fundamentally not Lorentz-invariant.

Specifically, anomalous growing modes generally emerge in a reference frame in which the flow speed exceeds the sound speed. In figure 12.2, we plot the maximum growth rate as a function of the apparent flow speed. The variation of flow speed along the horizontal axis corresponds to a continuous change of the frame of reference. We see that for each curve, the critical flow speed is nearly equal to the sound speed; $0.58\,c$ for $P/(\rho c^2) = 50$ (black curve), $0.436\,c$ for $P/(\rho c^2) = 1/3$ (blue curve), $0.365\,c$ for $P/(\rho c^2) = 1/6$ (red curve), $0.289\,c$ for $P/(\rho c^2) = 1/12$ (green curve), and $0.236\,c$ for $P/(\rho c^2) = 1/20$ (magenta curve). This illustrates that in the absence of energy diffusion, anomalous growing modes are predicted to emerge in reference frames for which the flow speed exceeds the sound speed of the system.

For the same parameters and sound speeds just considered, we now plot the maximum growth rate as a function of the covariant flow speed $u_{z0} = \gamma v_{z0}$, where $\gamma = (1 - v_{z0}^2/c^2)^{-1/2}$ is the Lorentz factor. This is shown in figure 12.3. In this regime of flow speeds, the covariant flow speed and Lorentz factor are approximately equal. For each sound speed, the maximum growth rate increases rapidly with u_{z0} for γ on the order of 20 or less, and then tapers off to an asymptotic value in the ultra-relativistic regime. For smaller sound speeds, the transition

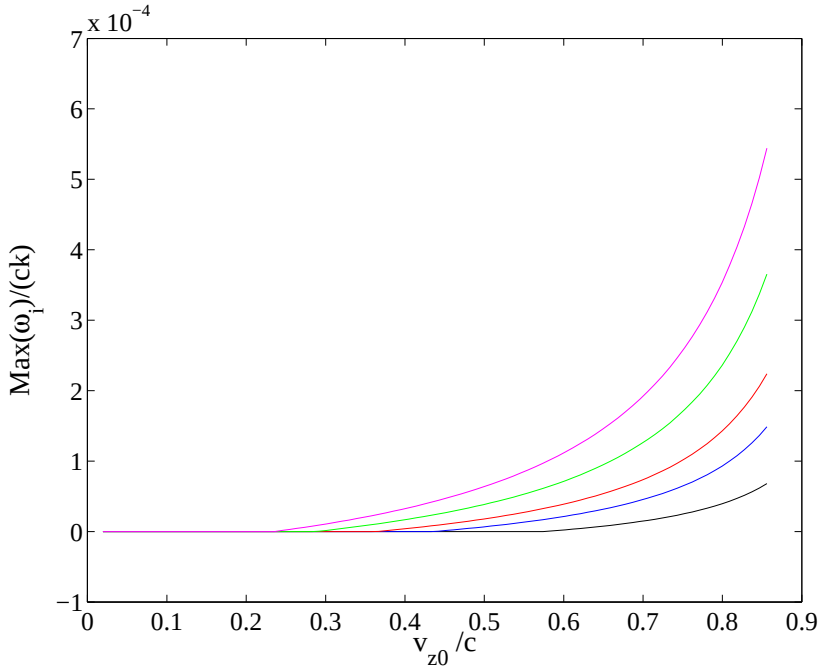

Figure 12.2: Max. growth rate vs. flow speed for different sound speeds
$c_s/c = 0.58$ (Black), 0.44 (Blue), 0.37 (Red), 0.29 (Green), 0.24 (Magenta)
$\eta_\rho = 0, \qquad (\eta_x, \eta_z) = (0.00025, 0.00005)\, c/k$

to asymptotic behavior occurs at a smaller value of γ, and the asymptotic growth rate is smaller. This is consistent with our above observation that at smaller sound speeds, modes appear to grow in reference frames corresponding to a smaller flow speed, so it makes sense that subsequent transitions would also occur in frames corresponding to less relativistic flow speeds.

Another interesting feature of figure 12.3 is the common intersection point of every growth curve at a Lorentz factor of roughly 20. At this flow speed, the curves are at different stages in their transition to asymptotic behavior, however they all have roughly the same growth rate. This Lorentz factor of 20 may well have some transitional mathematical significance which is independent of sound speed. Keep in mind that because these results are frame-dependent, we cannot give them physical significance.

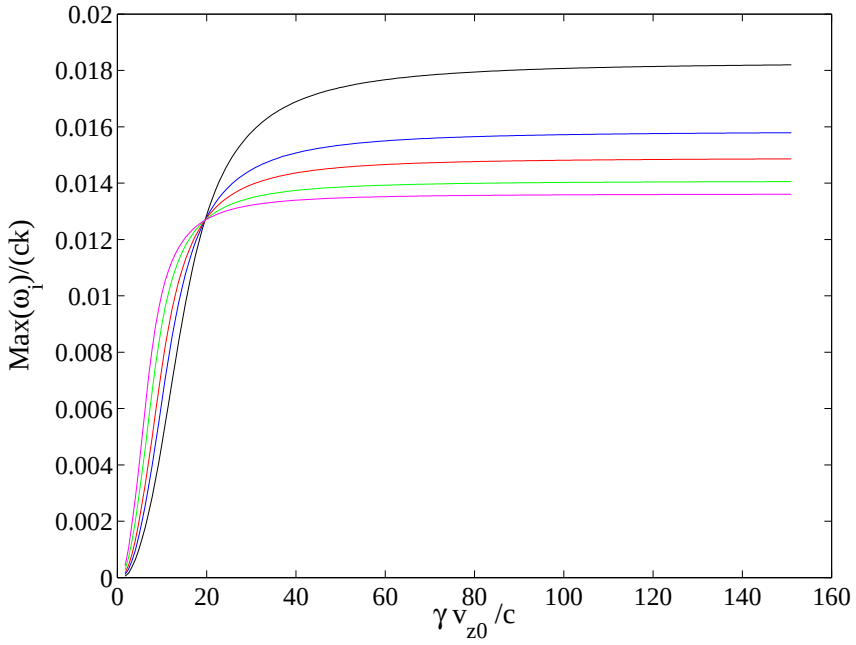

Figure 12.3: Max. growth rate vs. covariant flow speed for different sound speeds $c_s/c = 0.57$ (Black), 0.44 (Blue), 0.37 (Red), 0.29 (Green), 0.24 (Magenta) $\eta_\rho = 0, \qquad (\eta_x, \eta_z) = (0.00025, 0.00005)\, c/k$

12.2.5 Summary of RHD Results

In this section, we derived the RHD dispersion relation for a uniform-flow model with diffusion. We showed that in the diffusionless limit of this dispersion relation, we recover the relativistic acoustic waves seen in Bodo et al. (2004) and the unmagnetized limit of the result of LRN09. We then demonstrated that in a frame in which the flow speed is highly relativistic, diffusion appears to introduce rapidly-growing modes, which in a non-relativistic frame are decaying modes. We then showed that the uniform-flow model generally predicts these anomalous growing modes when the flow speed exceeds the sound speed in the given frame of reference.

Recall that these results are mathematical, and cannot be given physical significance, as they arise from a model in which the diffusion operator is not Lorentz-invariant, and therefore

does not preserve the Lorentz-invariance of the single-fluid equations. In the next section, we introduce a magnetic field, and show that this has very little effect on the predictions of the uniform-flow model. Again, this is only an academic exercise intended to illustrate what can happen with diffusion in certain highly relativistic systems.

12.3 RMHD Stability Analysis with Diffusion

We have seen that, in the uniform-flow model, modes introduced by diffusion appear to grow in a frame in which the flow is highly relativistic. We now want to see what effect, if any, the presence of a magnetic field has on these results. We first linearize the RMHD conservation-diffusion equations in two dimensions. There is a uniform unperturbed density ρ_0 and pressure P_0, a uniform unperturbed velocity v_{z0} in the z-direction, and a uniform unperturbed magnetic field B_{z0}, also in the z-direction. From the linearization, we derive a dispersion relation which is a sixth-order polynomial in ω. In the diffusionless limit of this dispersion relation, we recover the Alfven and magnetosonic modes derived in LRN09. We then characterize the influence of the magnetic field on the anomalous behavior introduced by diffusion. We find that, as with the unmagnetized RHD case, we observe decaying modes in reference frames corresponding to non-relativistic flow speed, and anomalous growing modes in reference frames corresponding to relativistic flow speed. Because these results are frame-dependent, they have mathematical implications, but cannot be given physical significance.

12.3.1 Derivation of RMHD Dispersion Relation with Diffusion

We derive the RMHD dispersion relation by linearizing the RMHD conservation-diffusion equations. We first define the enthalpy:

$$w \;=\; \rho c^2 + \frac{\Gamma P}{\Gamma - 1}. \tag{12.76}$$

The conservation-diffusion equations are

$$
\begin{aligned}
\frac{1}{c}\left(\frac{\partial}{\partial t}-\eta_\rho\boldsymbol{\nabla}^2\right)(\gamma\rho) &= -\frac{\partial}{\partial x}(\gamma\rho\beta_x)-\frac{\partial}{\partial z}(\gamma\rho\beta_z),\\
\frac{1}{c}\left(\frac{\partial}{\partial t}-\eta_x\boldsymbol{\nabla}^2\right)f_{2x} &= -\frac{\partial}{\partial x}g_{2xx}-\frac{\partial}{\partial z}g_{2xz},\\
\frac{1}{c}\left(\frac{\partial}{\partial t}-\eta_z\boldsymbol{\nabla}^2\right)f_{2z} &= -\frac{\partial}{\partial x}g_{2xz}-\frac{\partial}{\partial z}g_{2zz},\\
\frac{1}{c}\left(\frac{\partial}{\partial t}-\eta_\epsilon\boldsymbol{\nabla}^2\right)f_{3} &= -\frac{\partial}{\partial x}g_{3x}+\frac{\partial}{\partial z}g_{3z},\\
\frac{1}{c}\left(\frac{\partial}{\partial t}-\eta_{bx}\boldsymbol{\nabla}^2\right)B_x &= \frac{\partial E_y}{\partial z} = -\frac{\partial}{\partial z}(\beta_z B_x-\beta_x B_z),\\
\frac{1}{c}\left(\frac{\partial}{\partial t}-\eta_{bz}\boldsymbol{\nabla}^2\right)B_z &= -\frac{\partial E_y}{\partial x} = \frac{\partial}{\partial x}(\beta_z B_x-\beta_x B_z),
\end{aligned}
\tag{12.77}
$$

where

$$
\begin{aligned}
f_1 &= \gamma\rho,\\
g_{1x} &= \gamma\rho\beta_x,\\
g_{1z} &= \gamma\rho\beta_z,\\
f_{2x} &= w\gamma^2\beta_x+E_yB_z = w\gamma^2\beta_x+(B_z\beta_x-B_x\beta_z)B_z,\\
f_{2z} &= w\gamma^2\beta_z-E_yB_x = w\gamma^2\beta_z-(B_z\beta_x-B_x\beta_z)B_x,\\
g_{2xx} &= P+\frac{1}{2}\left[B^2+(B_z\beta_x-B_x\beta_z)^2\right]+w\gamma^2\beta_x^2-B_x^2,\\
g_{2xz} &= w\gamma^2\beta_x\beta_z-B_xB_z,\\
g_{2zz} &= P+\frac{1}{2}\left[B^2+(B_z\beta_x-B_x\beta_z)^2\right]+w\gamma^2\beta_z^2-B_z^2,\\
f_3 &= w\gamma^2-P+\frac{E^2+B^2}{2},\\
g_{3x} &= w\gamma^2\beta_x+E_yB_z = w\gamma^2\beta_x+(B_z\beta_x-B_x\beta_z)B_z,\\
g_{3z} &= w\gamma^2\beta_z-E_yB_x = w\gamma^2\beta_z-(B_z\beta_x-B_x\beta_z)B_x.
\end{aligned}
\tag{12.78}
$$

The first conservation-diffusion equation describes mass transport, and in the absence of diffusion, is the mass-continuity equation. The second and third equations describe momentum transport, the fourth equation energy transport, and the fifth and sixth equations Faraday's law. We assume the following linearized forms of the variables, corresponding to plane waves:

$$
\begin{aligned}
\rho(x,z,t) &= \rho_0 + \rho_1 \exp[i(k_x x + k_z z - \omega t)], \\
\beta_x(x,z,t) &= \beta_{x1} \exp[i(k_x x + k_z z - \omega t)], \\
\beta_z(x,z,t) &= \beta_{z0} + \beta_{z1} \exp[i(k_x x + k_z z - \omega t)], \\
P(x,z,t) &= P_0 + P_1 \exp[i(k_x x + k_z z - \omega t)], \\
B_x(x,z,t) &= B_{x1} \exp[i(k_x x + k_z z - \omega t)], \\
B_z(x,z,t) &= B_{z0} + B_{z1} \exp[i(k_x x + k_z z - \omega t)].
\end{aligned} \tag{12.79}
$$

We now separately linearize each term of the conservation-diffusion equations. For the mass transport equation, we have

$$
\begin{aligned}
f_{1,1} &= (\gamma\rho)_1 = \gamma\rho_1 + \gamma^3 \beta_{z0}\beta_{z1}\rho_0, \\
g_{1x,1} &= (\gamma\rho\beta_x)_1 = \gamma\rho_0\beta_{x1}, \\
g_{1z,1} &= (\gamma\rho\beta_z)_1 = \gamma\rho_0\beta_{z1} + \gamma\rho_1\beta_{z0} + \gamma^3\beta_{z0}^2\beta_{z1}\rho_0, \\
\left(\frac{\partial}{\partial t} - \eta_\rho \boldsymbol{\nabla}^2\right) f_1 &= \left(-i\omega + \eta_\rho k^2\right) f_{1,1}, \\
\frac{\partial}{\partial x}(\gamma\rho\beta_x) &= ik_x g_{1x,1}, \\
\frac{\partial}{\partial z}(\gamma\rho\beta_z) &= ik_z g_{1z,1}, \\
\left(-i\omega + \eta_\rho k^2\right) f_{1,1} &= -ick_x g_{1x,1} - ick_z g_{1z,1}, \qquad \text{or} \\
0 &= \left(\omega + i\eta_\rho k^2\right) f_{1,1} - ck_x g_{1x,1} - ck_z g_{1z,1}.
\end{aligned} \tag{12.80}
$$

For the transport of x-momentum, we have

$$
\begin{aligned}
f_{2x,1} &= w_0\gamma^2\beta_{x1} + B_{z0}^2\beta_{x1} - B_{z0}\beta_{z0}B_{x1}, \\
g_{2xx,1} &= P_1 + B_{z0}B_{z1}, \\
g_{2xz,1} &= w_0\gamma^2\beta_{z0}\beta_{x1} - B_{z0}B_{x1}, \\
\left(\frac{\partial}{\partial t} - \eta_x \boldsymbol{\nabla}^2\right) f_{2x} &= \left(-i\omega + \eta_x k^2\right) f_{2x,1}, \\
\frac{\partial}{\partial x} g_{2xx,1} &= ik_x g_{2xx,1}, \\
\frac{\partial}{\partial z} g_{2xz,1} &= ik_z g_{2xz,1}, \qquad \text{which gives} \\
\left(-i\omega + \eta_x k^2\right) f_{2x,1} &= -ick_x g_{2xx,1} - ick_z g_{2xz,1}, \qquad \text{or} \\
0 &= \left(\omega + i\eta_x k^2\right) f_{2x,1} - ck_x g_{2xx,1} - ck_z g_{2xz,1}.
\end{aligned} \tag{12.81}
$$

For the transport of z-momentum, we have

$$\begin{aligned}
f_{2z,1} &= w_0\gamma^2\beta_{z1} + w_1\gamma^2\beta_{z0} + 2w_0\gamma^4\beta_{z0}^2\beta_{z1} \\
&\qquad - \left[(B_z\beta_x - B_x\beta_z)B_x\right]_1 \\
&= w_0\gamma^2\beta_{z1} + w_1\gamma^2\beta_{z0} + 2w_0\gamma^4\beta_{z0}^2\beta_{z1}, \\
g_{2xz,1} &= w_0\gamma^2\beta_{z0}\beta_{x1} - B_{z0}B_{x1}, \\
g_{2zz,1} &= P_1 - B_{z0}B_{z1} + w_1\gamma^2\beta_{z0}^2 + 2w_0\gamma^2\beta_{z0}\beta_{z1} + 2w_0\gamma^4\beta_{z0}^3\beta_{z1}, \\
\left(\frac{\partial}{\partial t} - \eta_z\boldsymbol{\nabla}^2\right) f_{2z} &= \left(-i\omega + \eta_z k^2\right) f_{2z,1}, \\
\frac{\partial}{\partial x} g_{2xz,1} &= ik_x g_{2xz,1}, \\
\frac{\partial}{\partial z} g_{2zz,1} &= ik_z g_{2zz,1}, \qquad \text{which gives} \\
\left(-i\omega + \eta_z k^2\right) f_{2z,1} &= -ick_x g_{2xz,1} - ick_z g_{2zz,1}, \qquad \text{or} \\
0 &= \left(\omega + i\eta_z k^2\right) f_{2z,1} - ck_x g_{2xz,1} - ck_z g_{2zz,1}.
\end{aligned} \tag{12.82}$$

For the transport of energy, we have

$$\begin{aligned}
f_{3,1} &= w_1\gamma^2 + 2w_0\gamma^4\beta_{z0}\beta_{z1} - P_1 + B_{z0}B_{z1}, \\
g_{3x,1} &= w_0\gamma^2\beta_{x1} + B_{z0}^2\beta_{x1} - B_{z0}\beta_{z0}B_{x1}, \\
g_{3z,1} &= w_0\gamma^2\beta_{z1} + w_1\gamma^2\beta_{z0} + 2w_0\gamma^4\beta_{z0}^2\beta_{z1}, \\
\left(\frac{\partial}{\partial t} - \eta_\epsilon\boldsymbol{\nabla}^2\right) f_3 &= \left(-i\omega + \eta_\epsilon k^2\right) f_{3,1}, \\
\frac{\partial}{\partial x} g_{3x,1} &= ik_x g_{3x,1}, \\
\frac{\partial}{\partial z} g_{3z,1} &= ik_z g_{3z,1}, \qquad \text{which gives} \\
\left(-i\omega + \eta_\epsilon k^2\right) f_{3,1} &= -ick_x g_{3x,1} - ick_z g_{3z,1}, \qquad \text{or} \\
0 &= \left(\omega + i\eta_\epsilon k^2\right) f_{3,1} - ck_x g_{3x,1} - ck_z g_{3z,1}.
\end{aligned} \tag{12.83}$$

For the x-component of Faraday's law, we have

$$\begin{aligned}
\left(\frac{\partial}{\partial t} - \eta_{bx}\boldsymbol{\nabla}^2\right) B_x &= \left(-i\omega + \eta_{bx}k^2\right) B_{x1}, \\
-\frac{\partial}{\partial z}(\beta_z B_x - \beta_x B_z) &= -ik_z(\beta_{z0}B_{x1} - \beta_{x1}B_{z0}), \qquad \text{which gives} \\
(-i\omega + \eta_{bx}k^2)B_{x1} &= -ick_z(\beta_{z0}B_{x1} - \beta_{x1}B_{z0}), \qquad \text{or} \\
0 &= (\omega + i\eta_{bx}k^2)B_{x1} - ck_z(\beta_{z0}B_{x1} - \beta_{x1}B_{z0}).
\end{aligned} \tag{12.84}$$

For the z-component of Faraday's law, we have

$$\begin{aligned}
\left(\frac{\partial}{\partial t} - \eta_{bz}\boldsymbol{\nabla}^2\right) B_z &= \left(-i\omega + \eta_{bz}k^2\right) B_{z1}, \\
\frac{\partial}{\partial x}(\beta_z B_x - \beta_x B_z) &= ik_x(\beta_{z0}B_{x1} - \beta_{x1}B_{z0}), \qquad \text{which gives} \\
\left(-i\omega + \eta_{bz}k^2\right) B_{z1} &= ick_x(\beta_{z0}B_{x1} - \beta_{x1}B_{z0}), \qquad \text{or} \\
0 &= \left(\omega + i\eta_{bz}k^2\right) B_{z1} + ck_x(\beta_{z0}B_{x1} - \beta_{x1}B_{z0}).
\end{aligned} \tag{12.85}$$

We can now make the following definitions:

$$\begin{aligned}
\bar{\omega} &= \omega - ck_z\beta_{z0}, \\
\bar{\omega}_\rho &= \bar{\omega} + i\eta_\rho k^2, \qquad \omega_\rho = \omega + i\eta_x k^2, \\
\bar{\omega}_x &= \bar{\omega} + i\eta_x k^2, \qquad \omega_x = \omega + i\eta_x k^2, \\
\bar{\omega}_z &= \bar{\omega} + i\eta_z k^2, \qquad \omega_z = \omega + i\eta_z k^2, \\
\bar{\omega}_\epsilon &= \bar{\omega} + i\eta_\epsilon k^2, \qquad \omega_\epsilon = \omega + i\eta_\epsilon k^2, \\
\bar{\omega}_{bx} &= \bar{\omega} + i\eta_{bx} k^2, \qquad \omega_{bx} = \omega + i\eta_{bx} k^2, \\
\bar{\omega}_{bz} &= \bar{\omega} + i\eta_{bz} k^2, \qquad \omega_{bz} = \omega + i\eta_{bz} k^2.
\end{aligned} \tag{12.86}$$

In summary, we have the following linearized equations:

$$\omega_\rho f_{1,1} - k_x g_{1x,1} - k_z g_{1z,1} = 0, \tag{12.87}$$

$$\omega_x f_{2x,1} - ck_x g_{2xx,1} - ck_z g_{2xz,1} = 0, \tag{12.88}$$

$$\omega_z f_{2z,1} - ck_x g_{2xz,1} - ck_z g_{2zz,1} = 0, \tag{12.89}$$

$$\omega_\epsilon f_{3,1} - ck_x g_{3x,1} - ck_z g_{3z,1} = 0, \tag{12.90}$$

$$\omega_{bx} B_{x1} - ck_z(\beta_{z0}B_{x1} - \beta_{x1}B_{z0}) = 0, \tag{12.91}$$

$$\omega_{bz} B_{z1} + ck_x(\beta_{z0}B_{x1} - \beta_{x1}B_{z0}) = 0. \tag{12.92}$$

The above linearized equations can be written in the following matrix form:

$$M \begin{pmatrix} w_1 \\ P_1 \\ \beta_{x1} \\ \beta_{z1} \\ B_{x1} \\ B_{z1} \end{pmatrix} = 0, \tag{12.93}$$

where M is a 6 by 6 matrix with the following elements:

$$\begin{aligned}
M_{1j} &= \left(\gamma\bar{\omega}_\rho, \quad -4\gamma\bar{\omega}_\rho, \quad -\gamma c^3 k_x \rho_0, \quad \gamma^3\beta_{z0}\rho_0 c^2\bar{\omega}_\rho - \gamma k_z\rho_0, \quad 0, \quad 0\right), \\
M_{2j} &= \left(0, \quad -ck_x, \quad w_0\gamma^2\bar{\omega}_x + B_{z0}^2\omega_x, \quad 0, \quad cB_{z0}\left(k_z - \frac{\omega_x v_{z0}}{c^2}\right), \quad -ck_x B_{z0}\right), \\
M_{3j} &= \left(\gamma^2\beta_{z0}\bar{\omega}_z, \quad -ck_z, \quad -w_0\gamma^2 ck_x\beta_{z0}, \quad M_{34}, \quad ck_x B_{z0}, \quad ck_z B_{z0}\right), \\
M_{34} &= w_0\gamma^2\left[\left(1+2\gamma^2\beta_{z0}^2\right)\bar{\omega}_z - ck_z\beta_{z0}\right], \\
M_{4j} &= \left(\gamma^2\bar{\omega}_\epsilon, \quad -\omega_\epsilon, \quad -ck_x\left(w_0\gamma^2 + B_{z0}^2\right), \quad M_{44}, \quad B_{z0}ck_x\beta_{z0}, \quad B_{z0}\omega_\epsilon\right), \\
M_{44} &= w_0\gamma^2\left(2\gamma^2\beta_{z0}\bar{\omega}_\epsilon - ck_z\right), \\
M_{5j} &= (0, \quad 0, \quad ck_z B_{z0}, \quad 0, \quad \bar{\omega}_{bx}, \quad 0), \\
M_{6j} &= (0, \quad 0, \quad -ck_x B_{z0}, \quad 0, \quad ck_x\beta_{z0}, \quad \omega_{bz}).
\end{aligned} \tag{12.94}$$

We now non-dimensionalize the variables as follows:

$$\begin{aligned}
\Omega &= \frac{\omega}{ck}, \qquad f = \frac{\rho c^2}{w}, \qquad q = \frac{P}{w}, \\
\beta_A &= \frac{B_{z0}}{\sqrt{w_0}}, \\
\zeta_z &= \frac{k_z}{k}, \qquad \zeta_x = \frac{k_x}{k}, \\
tau_z &= \beta\zeta_z, \qquad \chi_j = \frac{\eta_j k}{c}, \\
\Omega_j &= \Omega + i\chi_j, \qquad \bar{\Omega}_j = \Omega_j - \zeta_z\beta.
\end{aligned} \tag{12.95}$$

The matrix equation is now

$$M'\begin{pmatrix} f_1 \\ q_1 \\ \beta_{x1} \\ \beta_{z1} \\ \beta_{A,x1} \\ \beta_{A,z1} \end{pmatrix} = 0, \tag{12.96}$$

where the elements of M' are given by

$$
\begin{aligned}
M'_{1j} &= \left(\gamma\bar{\Omega}_\rho, \quad -4\gamma\bar{\Omega}_\rho, \quad -\gamma\zeta_x f, \quad \gamma^3\beta f\bar{\Omega}_\rho - \gamma\zeta_z f, \quad 0, \quad 0\right), \\
M'_{2j} &= \left(0, \quad -\zeta_x, \quad \gamma^2\bar{\Omega}_x + \beta_A^2\Omega_x, \quad 0, \quad \beta_A\left(\zeta_z - \Omega_x\beta\right), \quad -\zeta_x\beta_A\right), \\
M'_{3j} &= \left(\gamma^2\beta\bar{\Omega}_z, \quad -\zeta_z, \quad -\gamma^2\zeta_x\beta, \quad M'_{34}, \quad \zeta_x\beta_A, \quad \zeta_z\beta_A\right), \\
M'_{34} &= \gamma^2\left[\left(1 + 2\gamma^2\beta^2\right)\bar{\Omega}_z - \zeta_z\beta\right], \\
M'_{4j} &= \left(\gamma^2\bar{\Omega}_\epsilon, \quad -\Omega_\epsilon, \quad -\zeta_x\left(\gamma^2 + \beta_A^2\right), \quad \gamma^2\left(2\gamma^2\beta\bar{\Omega}_\epsilon - \zeta_z\right), \quad \beta_A\zeta_x\beta, \quad \beta_A\Omega_\epsilon\right), \\
M'_{5j} &= \left(0, \quad 0, \quad \zeta_z\beta_A, \quad 0, \quad \bar{\Omega}_{bx}, \quad 0\right), \\
M'_{6j} &= \left(0, \quad 0, \quad -\zeta_x\beta_A, \quad 0, \quad \zeta_x\beta, \quad \Omega_{bz}\right).
\end{aligned} \tag{12.97}
$$

By taking the determinant of M', and equating this to zero, we obtain a dispersion relation which can be written as a sixth-order polynomial in $\Omega = \omega/(kc)$:

$$
C_6\Omega^6 + C_5\Omega^5 + C_4\Omega^4 + C_3\Omega^3 + C_2\Omega^2 + C_1\Omega + C_0 \;=\; 0. \tag{12.98}
$$

In the absence of diffusion, the coefficients are as follows (where $\tau_z = \zeta_z\beta$):

$$
\begin{aligned}
C_{60} &= (\beta_A^2+\gamma^2)[-1+C_p\gamma^2-\beta^2\gamma^2(2-f)],\\
C_{50} &= \tau_z[\beta_A^2(3+(2-3C_p)\gamma^2+4\beta^2\gamma^2)+\gamma^2(5+(2-5C_p)\gamma^2+8\beta^2\gamma^2)]-\\
&\quad \tau_z f[\beta_A^2(1+\gamma^2(1+2\beta^2))+\gamma^2(1+\gamma^2(1+4\beta^2))],\\
C_{40} &= R_1+R_2+f(R_3+R_4), \qquad \text{where}\\
R_1 &= \gamma^2[-1-12\zeta_z^2\beta^4\gamma^2+\tau_z^2(-9+2(-4+5C_p)\gamma^2)],\\
R_2 &= \beta_A^2[-2\zeta_z^2\beta^4\gamma^2+\zeta_x^2-C_p\gamma^2+\beta^2(-2\zeta_z^2+\gamma^2(2\zeta_x^2+(-2+3C_p)\zeta_z^2))],\\
R_3 &= \gamma^2[1+6\zeta_z^2\beta^4\gamma^2+\tau_z^2(3+4\gamma^2)],\\
R_4 &= \beta_A^2[\zeta_z^2(1+\beta^4\gamma^2)+\beta^2(\zeta_z^2+\gamma^2(-\zeta_x^2+\zeta_z^2))],\\
\\
C_{30} &= \tau_z[S_1+S_2+f(S_3+S_4)], \qquad \text{where}\\
S_1 &= \gamma^2[3+8\zeta_z^2\beta^4\gamma^2+\tau_z^2(7+2(6-5C_p)\gamma^2)],\\
S_2 &= \beta_A^2[-\beta^2\gamma^2(4\zeta_x^2+(2+C_p)\zeta_z^2)-3\zeta_x^2-2\zeta_z^2+(-2+3C_p)\gamma^2],\\
S_3 &= -\gamma^2[3+4\zeta_z^2\beta^4\gamma^2+3\tau_z^2(1+2\gamma^2)],\\
S_4 &= \beta_A^2[\beta^2\gamma^2(2\zeta_x^2+\zeta_z^2)+\zeta_x^2+\gamma^2],\\
\\
C_{20} &= \zeta_z^2[Q_1+Q_2+f(Q_3-Q_4)], \qquad \text{where}\\
Q_1 &= \beta^2\gamma^2[-3-2\zeta_z^2\beta^4\gamma^2-\tau_z^2(2+(8-5C_p)\gamma^2)],\\
Q_2 &= \beta_A^2[1+2\beta^4\gamma^2+\beta^2(2+(4-3C_p)\gamma^2)],\\
Q_3 &= \beta^2\gamma^2[3+\zeta_z^2\beta^4\gamma^2+\tau_z^2(1+4\gamma^2)],\\
Q_4 &= \beta_A^2[1+\beta^4\gamma^2+\beta^2(1+2\gamma^2)],\\
\\
C_{10} &= \zeta_z^3\beta(T_1+fT_2), \qquad \text{where}\\
T_1 &= \beta^2\gamma^2-(-2+C_p)\zeta_z^2\beta^4\gamma^4+\beta_A^2[-1+(-2+C_p)\beta^2\gamma^2],\\
T_2 &= -\beta^2\gamma^2-\zeta_z^2\beta^4\gamma^4+\beta_A^2(1+\beta^2\gamma^2),\\
\\
C_{00} &= 0.
\end{aligned}
\tag{12.99}
$$

We now introduce a small amount of diffusion, allowing us to retain only terms up to order χ_j. Letting $\tau_z = \zeta_z\beta$, the coefficients are given by

$$
\begin{aligned}
C_6 &= C_{60} = (\beta_A^2+\gamma^2)[-1+C_p\gamma^2-\beta^2\gamma^2(2-f)],\\
C_5 &= C_{50}+i(\chi_x+\chi_z+\chi_\epsilon+\chi_\rho)[\beta_A^2(-1+C_p\gamma^2-2\beta^2\gamma^2)-\gamma^2+C_p\gamma^4-2\beta^2\gamma^4]\\
&\quad +i(\chi_x+\chi_z+\chi_\epsilon+\chi_\rho)f\beta^2\gamma^2(\beta_A^2+\gamma^2)\\
&\quad +i(\chi_{bx}+\chi_{bz})(\beta_A^2+\gamma^2)[\beta^2\gamma^2(f-2)-1+C_p\gamma^2],\\
\\
C_4 &= C_{40}+i(\chi_{bx}+\chi_x)\tau_z[\beta_A^2(3-f+(2-f-3C_p)\gamma^2+2(2-f)\beta^2\gamma^2)\\
&\quad +\gamma^2(4-f+(2-f-4C_p)\gamma^2+3(2-f)\beta^2\gamma^2)]\\
&\quad +i(\chi_{bz}+\chi_\epsilon)\tau_z[\beta_A^2(3-f+(2-f-3C_p)\gamma^2+2(2-f)\beta^2\gamma^2)\\
&\quad +\gamma^2(5-f+(2-f-5C_p)\gamma^2+4(2-f)\beta^2\gamma^2)]\\
&\quad +i\chi_z\tau_z[\beta_A^2(1-f-C_p\gamma^2+(2-f)\beta^2\gamma^2)+\gamma^2(3-f-3C_p\gamma^2+3(2-f)\beta^2\gamma^2)]\\
&\quad +i\chi_\rho\tau_z[\beta_A^2(2+(2-f-2C_p)\gamma^2+(2-f)\beta^2\gamma^2)\\
&\quad +\gamma^2(4+(2-f-4C_p)\gamma^2+3(2-f)\beta^2\gamma^2)], \qquad (12.100)
\end{aligned}
$$

$$
\begin{aligned}
C_3 &= C_{30}+i\beta_A^2[\zeta_x^2-\zeta_z^2-2\tau_z^2-C_p\zeta_x^2\gamma^2+\beta^2\gamma^2(2\zeta_x^4-2\zeta_x^2\zeta_z^2-4\zeta_z^4+3C_p\zeta_z^2-2\tau_z^2)]\chi_{bx}\\
&\quad +i\beta_A^2f[\zeta_z^2+\tau_z^2+\beta^2\gamma^2(-\zeta_x^4+\zeta_x^2\zeta_z^2+2\zeta_z^4+\tau_z^2)]\chi_{bx}\\
&\quad +i\gamma^2[-1-5\tau_z^2+6\tau_z^2\gamma^2(-1+C_p-\beta^2)]\chi_{bx}\\
&\quad +i\gamma^2f[1+2\tau_z^2+3\tau_z^2\gamma^2(1+\beta^2)]\chi_{bx}\\
&\quad +i\beta_A^2[-\zeta_x^2-2\tau_z^2-C_p\zeta_z^2\gamma^2+\beta^2\gamma^2(-2\zeta_x^4+(-4+3C_p)\zeta_x^2\zeta_z^2+(-2+3C_p)\zeta_z^4-2\tau_z^2)]\chi_{bz}\\
&\quad +i\gamma^2[-1-9\tau_z^2+\tau_z^2\gamma^2(-8+10C_p-12\beta^2)]\chi_{bz}\\
&\quad +i\beta_A^2f[\zeta_z^2+\tau_z^2+\beta^2\gamma^2(1+\tau_z^2)]\chi_{bz}+i\gamma^2f[1+3\tau_z^2+\tau_z^2\gamma^2(4+6\beta^2)]\chi_{bz}\\
&\quad +i\beta_A^2[-\zeta_z^2-2\tau_z^2+\tau_z^2\gamma^2(-4+3C_p-2\beta^2)]\chi_x\\
&\quad +i\gamma^2[-\zeta_z^2-5\tau_z^2+6\tau_z^2\gamma^2(-1+C_p-\beta^2)]\chi_x\\
&\quad +i\beta_A^2f[\zeta_z^2+\tau_z^2+\tau_z^2\gamma^2(2+\beta^2)]\chi_x+i\gamma^2f[\zeta_z^2+2\tau_z^2+3\tau_z^2\gamma^2(1+\beta^2)]\chi_x\\
&\quad +i\beta_A^2(1-C_p\gamma^2+2\beta^2\gamma^2)\chi_z+i\gamma^2[-\zeta_x^2-3\tau_z^2+\beta^2\gamma^2(-2\zeta_x^2+3C_p\zeta_z^2-6\tau_z^2)]\chi_z\\
&\quad +i\gamma^2f[-\beta_A^2+\zeta_x^2+2\tau_z^2+\beta^2\gamma^2(\zeta_x^2+3\tau_z^2)]\chi_z\\
&\quad +i\beta_A^2[2\zeta_x^4+3\zeta_x^2\zeta_z^2+\zeta_z^4-2\tau_z^2-C_p\gamma^2+\beta^2\gamma^2(4\zeta_x^2+2C_p\zeta_z^2-2\tau_z^2)]\chi_\epsilon\\
&\quad +i\beta_A^2f[\zeta_z^2+\tau_z^2+\beta^2\gamma^2(-2\zeta_x^2+\tau_z^2)]\chi_\epsilon\\
&\quad +i\gamma^2[9\tau_z^2(-1+C_p\gamma^2)+\beta^2\gamma^2(2\zeta_x^4-4\zeta_x^2\zeta_z^2-6\zeta_z^4-12\tau_z^2)]\chi_\epsilon\\
&\quad +i\gamma^2f[1+3\tau_z^2+\beta^2\gamma^2(-\zeta_x^4+2\zeta_x^2\zeta_z^2+3\zeta_z^4+6\tau_z^2)]\chi_\epsilon\\
&\quad +i\beta_A^2[\zeta_x^2-C_p\gamma^2+\gamma^2\beta^2(2\zeta_x^2+C_p\zeta_z^2)]\chi_\rho+i\gamma^2[-1-5\tau_z^2+6\tau_z^2\gamma^2(-1+C_p-\beta^2)]\chi_\rho\\
&\quad +i\beta^2\gamma^2f[-\beta_A^2\zeta_x^2+3\zeta_z^2\gamma^2(1+\beta^2)]\chi_\rho, \qquad (12.101)
\end{aligned}
$$

$$
\begin{aligned}
C_2 \;=\; & C_{20} + i\beta_A^2\tau_z[-3\zeta_x^4 - 2\zeta_x^2\zeta_z^2 + \zeta_z^4 + (-4+3C_p)\zeta_x^2\gamma^2 \\
& + \beta^2\gamma^2(-4\zeta_x^4 + 2\zeta_z^2(\zeta_z^2 - \zeta_x^2) - C_p\zeta_z^2)]\chi_{bx} \\
& + i\tau_z f\beta_A^2[\zeta_x^4 - \zeta_z^4 + 2\gamma^2\zeta_x^2 + \gamma^2\beta^2(2\zeta_x^4 + \zeta_x^2\zeta_z^2 + \zeta_z^4)]\chi_{bx} \\
& + i\gamma^2\tau_z[2 + 2\tau_z^2 + \tau_z^2\gamma^2(6 - 4C_p + 2\beta^2)]\chi_{bx} \\
& + i\tau_z f\gamma^2[-2 - \tau_z^2 - \tau_z^2\gamma^2(3+\beta^2)]\chi_{bx} \\
& + i\beta_A^2\tau_z[3\zeta_x^4 + \zeta_x^2\zeta_z^2 - 2\zeta_z^4 \\
& + \gamma^2(2\zeta_x^4 + 3C_p\zeta_x^2\zeta_z^2 + (-2+3C_p)\zeta_z^4 + \beta^2(4\zeta_x^4 + (2-C_p)\zeta_x^2\zeta_z^2 - (2+C_p)\zeta_z^4))]\chi_{bz} \\
& + i\tau_z f\beta_A^2[-\zeta_x^2 + \gamma^2(\zeta_z^4 - \zeta_x^4) + \beta^2\gamma^2(-2\zeta_x^4 - \zeta_x^2\zeta_z^2 + \zeta_z^4)]\chi_{bz} \\
& + i\gamma^2\tau_z[3 + 7\tau_z^2 + \tau_z^2\gamma^2(12 - 10C_p + 8\beta^2)]\chi_{bz} \\
& + i\tau_z f\gamma^2[-3 - 3\tau_z^2 - \tau_z^2\gamma^2(6+4\beta^2)]\chi_{bz} \\
& + i\tau_z[\beta_A^2(\zeta_z^2 + (2-C_p)\tau_z^2\gamma^2) + \gamma^2(2\zeta_z^2 + 2\tau_z^2 + \tau_z^2\gamma^2(6 - 4C_p + 2\beta^2))]\chi_x \\
& + i\tau_z f[\beta_A^2(-\zeta_z^2 - \tau_z^2\gamma^2) + \gamma^2(-2\zeta_z^2 - \tau_z^2 - \tau_z^2\gamma^2(3+\beta^2))]\chi_x \\
& + i\tau_z[\beta_A^2(-1 + C_p\gamma^2 - 2\beta^2\gamma^2) + \gamma^2(2\zeta_x^2 + \tau_z^2 \\
& \qquad + \gamma^2\beta^2(4\zeta_x^4 - C_p\zeta_z^4 + (4-C_p)\zeta_x^2\zeta_z^2 + 2\tau_z^2))]\chi_z \\
& + i\tau_z f[\beta_A^2(1+\beta^2\gamma^2) + \gamma^2(-2\zeta_x^2 - \tau_z^2 - \beta^2\gamma^2(2\zeta_x^2 + \tau_z^2))]\chi_z \\
& + i\tau_z\beta_A^2[-6\zeta_x^4 - 9\zeta_x^2\zeta_z^2 - 3\zeta_z^4 + (-2+3C_p)\gamma^2 + \beta^2\gamma^2(-8\zeta_x^4 - 12\zeta_x^2\zeta_z^2 - 4\zeta_z^4)]\chi_\epsilon \\
& + i\tau_z f\beta_A^2[(1+2\beta^2\gamma^2)(2\zeta_x^4 + 3\zeta_x^2\zeta_z^2 + \zeta_z^4) + \gamma^2]\chi_\epsilon \\
& + i\tau_z\gamma^2[7\tau_z^2 + \beta^2\gamma^2(-4\zeta_x^4 + (2-7C_p)\zeta_x^2\zeta_z^2 + (6-7C_p)\zeta_z^4 + 8\tau_z^2)]\chi_\epsilon \\
& + i\tau_z f\gamma^2[-2 - 3\tau_z^2 + \beta^2\gamma^2(2\zeta_x^4 - \zeta_x^2\zeta_z^2 - 3\zeta_z^4 - 4\tau_z^2)]\chi_\epsilon \\
& + i\tau_z[\beta_A^2(-2 + 2(-1+C_p)\gamma^2 - 2\beta^2\gamma^2) + \gamma^2(2 + 2\tau_z^2 + \tau_z^2\gamma^2(6 - 4C_p + 2\beta^2))]\chi_\rho \\
& + i\tau_z f\gamma^2[\beta_A^2(1+\beta^2) - \tau_z^2\gamma^2(3+\beta^2)]\chi_\rho, \qquad (12.102)
\end{aligned}
$$

$$
\begin{aligned}
C_1 &= C_{10} + i\beta_A^2\zeta_x^2\zeta_z^2[2(1+\beta^2) + (8-3C_p)\beta^2\gamma^2 + 2\beta^4\gamma^2]\chi_{bx} \\
&+ i\gamma^2\tau_z^2(-1 + (-2+C_p)\tau_z^2\gamma^2)\chi_{bx} \\
&- if\zeta_x^2\zeta_z^2\beta_A^2[2+\beta^2+\beta^2\gamma^2(4+\beta^2)]\chi_{bx} + if\gamma^2\tau_z^2(1+\tau_z^2\gamma^2)\chi_{bx} \\
&+ i\beta_A^2[(1+2\beta^2)(-\zeta_x^4\zeta_z^2 + \zeta_z^6) - \tau_z^2\gamma^2(4\zeta_x^4 + 3C_p\zeta_x^2\zeta_z^2 + (3C_p-4)\zeta_z^4 + 2\beta^2(\zeta_x^4 - \zeta_z^4))]\chi_{bz} \\
&+ i\gamma^2\tau_z^2[-3 - 2\tau_z^2 + \tau_z^2\gamma^2(5C_p - 8 - 2\beta^2)]\chi_{bz} \\
&+ if\beta_A^2(\zeta_x^4 - \zeta_z^4)[\zeta_z^2 + \tau_z^2 + \tau_z^2\gamma^2(2+\beta^2)]\chi_{bz} + if\tau_z^2\gamma^2[3 + \tau_z^2 + \tau_z^2\gamma^2(4+\beta^2)]\chi_{bz} \\
&+ i\gamma^2\tau_z^2(-\zeta_z^2 + (C_p-2)\tau_z^2\gamma^2)\chi_x - i\gamma^2\tau_z^2(\zeta_x^2 + 2\zeta_x^2\beta^2\gamma^2)\chi_z \\
&+ if\gamma^2\tau_z^2\zeta_z^2(1+\beta^2\gamma^2)\chi_x + if\gamma^2\tau_z^2\zeta_x^2(1+\beta^2\gamma^2)\chi_z \\
&+ i\beta_A^2\tau_z^2[(1+\gamma^2\beta^2)(4\zeta_x^4 + 6\zeta_x^2\zeta_z^2 + 2\zeta_z^4) + (2-2C_p)\gamma^2]\chi_\epsilon \\
&+ if\beta_A^2(1+\beta^2\gamma^2)[-\zeta_z^2 - \tau_z^2(2\zeta_x^4 + 3\zeta_x^2\zeta_z^2 - \zeta_z^4)]\chi_\epsilon \\
&+ i\gamma^2\tau_z^2\beta^2[-2\zeta_z^2 + \gamma^2(2\zeta_x^4 + 2C_p\zeta_x^2\zeta_z^2 + 2(-1+C_p)\zeta_z^4 - 2\tau_z^2)]\chi_\epsilon \\
&+ if\gamma^2\tau_z^2[1 + \tau_z^2 + \beta^2\gamma^2(\zeta_z^4 - \zeta_x^4 + \tau_z^2)]\chi_\epsilon \\
&+ i\zeta_z^2[\beta_A^2(1 + (2-C_p)\beta^2\gamma^2) + \tau_z^2\gamma^2(-1 + (C_p-2)\tau_z^2\gamma^2)]\chi_\rho \\
&+ if\gamma^2\tau_z^2(-\beta_A^2 + \tau_z^2\gamma^2)\chi_\rho
\end{aligned} \tag{12.103}
$$

$$
\begin{aligned}
C_0 &= i\tau_z\zeta_z^2\zeta_x^2\beta_A^2[-2 + \beta^2\gamma^2(C_p-4)]\chi_{bx} \\
&+ 2if\tau_z\zeta_z^2\zeta_x^2\beta_A^2(1+\beta^2\gamma^2)\chi_{bx} \\
&+ i\tau_z\zeta_z^2[\beta_A^2(\zeta_x^4 - \zeta_z^4 + \beta^2\gamma^2(2(\zeta_x^2 - \zeta_z^2) + C_p\zeta_z^2)) + \beta^2\gamma^2(1 + (2-C_p)\tau_z^2\gamma^2)]\chi_{bz} \\
&+ if\tau_z\zeta_z^2[\beta_A^2(1+\beta^2\gamma^2)(\zeta_z^4 - \zeta_x^4) - \beta^2\gamma^2(1+\tau_z^2\gamma^2)]\chi_{bz}.
\end{aligned} \tag{12.104}
$$

If we retain all terms, we must first make the following definitions:

$$
\begin{aligned}
\psi_j &= -\tau_z + i\chi_j, \\
D_1 &= -2\tau_z(1+\gamma^2\beta^2) + i(1+2\gamma^2\beta^2)\chi_z, \\
D_2 &= -\zeta_z\gamma^2 + 2\beta\gamma^4(-\tau_z + i\chi_\epsilon), \\
D_3 &= -\zeta_z\gamma + \beta\gamma^3(-\tau_z + i\chi_\rho).
\end{aligned} \tag{12.105}
$$

The coefficient C_0 is then given by

$$
\begin{aligned}
C_0 \;=\; & -i\beta_A^2\zeta_x^2\zeta_z\beta\gamma^3 D_1\psi_\rho\chi_{bz} - i\zeta_x^2\gamma^3(\beta_A^2+\gamma^2)\psi_{bx}D_1\psi_\rho\chi_{bz} \\
& + 2i\beta_A^2\zeta_x^2\tau_z\gamma^3 D_1\psi_\rho\chi_\epsilon + 2i\beta_A^2\zeta_x^2\gamma^3 D_1\psi_\rho\psi_{bx}\chi_\epsilon - \beta_A^2\zeta_z\gamma^3(\zeta_z - i\beta\chi_x)D_1\psi_\rho\chi_{bz}\chi_\epsilon \\
& + \gamma^3\psi_x\chi_{bz}(i\beta_A^2\chi_x + \gamma^2\psi_x)D_1\psi_\rho\chi_\epsilon + 4\beta_A^2\zeta_x^2\tau_z\gamma^5 D_1\psi_\rho\psi_\epsilon \\
& - 4\beta_A^2\zeta_x^2\gamma^5 D_1\psi_\rho\psi_\epsilon\psi_{bx} - 4i\beta_A^2\zeta_z\gamma^5\chi_{bz}\psi_x D_1\psi_\rho\psi_\epsilon \\
& + 4i\gamma^5\chi_{bz}\psi_{bx}(i\beta_A^2\chi_x + \gamma^2\psi_x)D_1\psi_\rho\psi_\epsilon - 2\beta_A^2\zeta_x^2\zeta_z^2\beta\gamma D_2\psi_\rho + i\beta_A^2\zeta_x^2\zeta_z\gamma\chi_{bz}D_2\psi_\rho \\
& + i\zeta_x^2\beta\gamma^3\psi_{bx}\chi_{bz}D_2\psi_\rho - i\beta_A^2\zeta_z^2\gamma\chi_{bz}(\zeta_z - i\beta\chi_x)D_2\psi_\rho + i\zeta_z\gamma\psi_{bx}\chi_{bz}(i\beta_A^2\chi_x + \gamma^2\psi_x)D_2\psi_\rho \\
& + 4\beta_A^2\zeta_x^2\zeta_z\beta^2\gamma^3\psi_z D_2\psi_\rho + 4\beta_A^2\zeta_x^2\beta\gamma^3\psi_{bx}\psi_z D_2\psi_\rho + 4i\beta_A^2\tau_z\gamma^3\chi_{bz}(\zeta_z - i\beta\chi_x)\psi_z D_2\psi_\rho \\
& - 4i\beta\gamma^3\psi_{bx}\chi_{bz}(i\beta_A^2\chi_x + \gamma^2\psi_x)\psi_z D_2\psi_\rho + i\zeta_x^2\gamma^5 f\psi_{bx}\chi_{bz}D_2\psi_\epsilon \\
& - i\zeta_x^2\beta\gamma^3 f\psi_{bx}\chi_{bz}\psi_z D_2 + \beta_A^2\zeta_x^2\zeta_z\gamma^2\psi_{bx}D_3\psi_\epsilon f + i\beta_A^2\zeta_x^2\zeta_z\beta^2\gamma^2\chi_{bz}D_3\psi_z f \\
& + i\zeta_x^2\beta\gamma^2(\beta_A^2+\gamma^2)\psi_{bx}\chi_{bz}D_3\psi_z f + \beta_A^2\gamma^2\chi_\epsilon D_3\psi_z f[-2i\zeta_x^2\zeta_z\beta^2 - 2i\zeta_x^2\beta\psi_{bx} \\
& + \tau_z\chi_{bz}(\zeta_z - i\beta\chi_x)] - \beta\gamma^2\psi_{bx}\chi_{bz}(i\beta_A^2\chi_x + \gamma^2\psi_x)\chi_\epsilon D_3\psi_z f + 2\beta_A^2\zeta_x^2\zeta_z^2\beta\gamma^2 D_3\psi_\epsilon f \\
& + \beta_A^2\zeta_x^2\zeta_z\gamma^2\psi_{bx}D_3\psi_\epsilon f - i\beta_A^2\zeta_x^2\zeta_z\gamma^2\chi_{bz}D_3\psi_\epsilon f - i\zeta_x^2\beta\gamma^4\psi_{bx}\chi_{bz}D_3\psi_\epsilon f \\
& + i\beta_A^2\zeta_z^2\gamma^2\chi_{bz}(\zeta_z - i\beta\chi_x)D_3\psi_\epsilon f - i\zeta_z\gamma^2\psi_{bx}\chi_{bz}(i\beta_A^2\chi_x + \gamma^2\psi_x)D_3\psi_\epsilon f. \qquad (12.106)
\end{aligned}
$$

The dimensionless relativistic sound speed is given by

$$
\begin{aligned}
\beta_s \;&=\; \frac{c_s}{c} \;=\; \sqrt{\frac{\Gamma P}{w}} \\
&=\; \sqrt{\Gamma\left(\frac{\Gamma-1}{\Gamma}\right)\frac{w-\rho c^2}{w}} \\
&=\; \sqrt{(\Gamma-1)(1-f)}. \qquad (12.107)
\end{aligned}
$$

We also denote the Lorentz-shifted wave vector as follows:

$$
\begin{aligned}
\bar{k}_x \;&=\; k_x, \\
\gamma\bar{k}_z \;&=\; \gamma\left(k_z - \frac{\omega\beta_{z0}}{c}\right). \qquad (12.108)
\end{aligned}
$$

Correspondingly, we define $\bar{\zeta}_z$, the dimensionless version of $\bar{k}_z$, as

$$
\bar{\zeta}_z \;=\; \zeta_z - \Omega\beta. \qquad (12.109)
$$

With these definitions, the above dispersion relation is equivalent to the following:

$$\Omega\bar{\Omega}f_4(\Omega) \;=\; 0, \qquad \text{where}$$

$$f_4(\Omega) \;=\; \gamma^2\bar{\Omega}^4 - [\beta_s^2(\zeta_x^2+\gamma^2\bar{\zeta}_z^2)+\beta_A^2(1-\Omega^2)]\bar{\Omega}^2 + \beta_s^2(1-\Omega^2)\beta_A^2\bar{\zeta}_z^2. \tag{12.110}$$

Using definitions (12.95) to write (12.110) in terms of the original variables, the dispersion relation reads as follows:

$$\omega\bar{\omega}g_4(\omega) \;=\; 0, \qquad \text{where}$$

$$g_4(\omega) \;=\; \gamma^2\bar{\omega}^4 - \left[c_s^2(k_x^2+\gamma^2\bar{k}_z^2)+v_{Az}^2\left(k^2-\frac{\omega^2}{c^2}\right)\right]\bar{\omega}^2 + c_s^2\left(k^2-\frac{\omega^2}{c^2}\right)v_{Az}^2\bar{k}_z^2. \tag{12.111}$$

The solutions are $\Omega = 0$ ($\omega = 0$), $\Omega = \zeta_z\beta$ ($\omega = k_z v_{z0}$), and the four magnetosonic modes to which $g_4(\omega)$ corresponds. The non-relativistic limit of $g_4(\omega)$ is in agreement with the dispersion relation for magnetosonic modes presented in LRN09.

LRN09 also present Alfven modes corresponding to

$$f_2(\omega) \;=\; \bar{\omega}^2 - v_{Az}^2\left(k_z^2-\frac{\omega^2}{c^2}\right) \;=\; 0. \tag{12.112}$$

Alfven waves occur when the total stress is spatially uniform, i.e., when we have

$$\boldsymbol{\nabla}\left(P+\frac{E^2+B^2}{2}\right) \;=\; 0. \tag{12.113}$$

Substituting the linearized forms (12.79) for P and $\mathbf{B}$ into (12.113), we obtain

$$i\mathbf{k}\,(P_1 + B_{z0}B_{z1}) \;=\; 0. \tag{12.114}$$

To show how this corresponds to the familiar Alfven modes, we need an expression for B_{z1} in terms of P_1, in the absence of diffusion. We obtain this as follows. From the diffusionless version of equation (12.91), we can solve for B_{x1} in terms of v_{x1}:

$$B_{x1} \;=\; \frac{-k_z B_{z0}}{\bar{\omega}} v_{x1}. \tag{12.115}$$

Substituting (12.115) into (12.92) (diffusionless versions), we can solve for B_{z1} in terms of v_{x1}:

$$B_{z1} \;=\; \frac{k_x B_{z0}}{\bar{\omega}} v_{x1}. \tag{12.116}$$

The second element of the diffusionless version of (12.93), describing transport of x-momentum, can be written as follows:

$$-k_x P_1 + \left(w_0 \gamma^2 \bar{\omega} + \frac{B_{z0}^2}{c^2} \omega \right) v_{x1} + B_{z0} \left(k_z - \frac{\omega v_{z0}}{c^2} \right) B_{x1} - k_x B_{z0} B_{z1} \;=\; 0. \tag{12.117}$$

We now substitute expressions (12.115) and (12.116) into equation (12.117). This yields the following expression for v_{x1} in terms of P_1:

$$v_{x1} \;=\; \frac{c^2 k_x \bar{\omega} P_1}{w_0 \gamma^2 \bar{\omega}^2 - B_{z0}^2 (k^2 - \omega^2/c^2)} \;=\; \frac{c^2 k_x \bar{\omega} P_1}{w_0 (\gamma^2 \bar{\omega}^2 - v_{Az}^2 (k^2 - \omega^2/c^2))}. \tag{12.118}$$

Substituting (12.118) into (12.116), we obtain the following expression for B_{z1} in terms of P_1:

$$B_{z1} \;=\; \frac{k_x B_{z0}}{\bar{\omega}} v_{x1} \;=\; \frac{c^2 k_x^2 B_{z0} P_1}{w_0(\gamma^2\bar{\omega}^2 - v_{Az}^2(k^2 - \omega^2/c^2))}. \tag{12.119}$$

Substituting this result into (12.114), we obtain

$$i\mathbf{k}P_1 \left[1 + \frac{c^2 k_x^2 B_{z0}^2}{w_0(\gamma^2\bar{\omega}^2 - v_{Az}^2(k^2 - \omega^2/c^2))}\right] \;=\; 0. \tag{12.120}$$

Using $v_{Az}^2 = c^2 B_{z0}^2/w_0$ and multiplying (12.120) by the denominator, we obtain

$$\gamma^2\bar{\omega}^2 - v_{Az}^2\left(k^2 - \frac{\omega^2}{c^2}\right) + k_x^2 v_{Az}^2 \;=\; 0, \tag{12.121}$$

which, upon combining the second and third term, gives the familiar dispersion relation for Alfven modes:

$$\gamma^2\bar{\omega}^2 - v_{Az}^2\left(k_z^2 - \frac{\omega^2}{c^2}\right) \;=\; 0. \tag{12.122}$$

The non-relativistic limit of (12.122) is in agreement with the result of LRN09. In summary, in the absence of diffusion, we recover the marginally stable Alfven and magnetosonic modes derived in LRN09.

12.3.2 Stability for Equal Diffusion Coefficients

Suppose now that the diffusion is non-zero, and that all viscosity coefficients are equal to a common value χ. This amounts to simply replacing Ω with $\Omega + i\chi$ in the diffusionless

version of the linearized system (12.97). We therefore make the substitution $y = \Omega + i\chi$ in the dispersion relation (12.110) for the diffusionless case:

$$y(y - \tau_z) f_4(y) \;=\; 0, \tag{12.123}$$

where

$$f_4(y) \;=\; \gamma^2 (y - \tau_z)^4 - [\beta_s^2 (\zeta_x^2 + \gamma^2 \bar{\zeta}_z^2) + \beta_A^2 (1 - y^2)](y - \tau_z)^2 + \beta_s^2 (1 - y^2) \beta_A^2 \bar{\zeta}_z^2. \tag{12.124}$$

Let y_j, for $j = 1, ..., 4$, denote the four magnetosonic modes satisfying $f_4(y_j) = 0$. The y_j are all purely real, as are the solutions $y = 0$ and $y = \tau_z$ corresponding to the other two modes. The corresponding solutions for Ω are therefore

$$\begin{aligned} \Omega_j &= y_j - i\chi, \qquad j = 1, ..., 4 \\ \Omega_5 &= -i\chi \\ \Omega_6 &= \tau_z - i\chi \end{aligned} \tag{12.125}$$

The imaginary part of each solution is $-\chi$, which indicates that each solution corresponds to a decaying mode. This leads to an important conclusion, namely, that when all viscosity coefficients are the same, the uniform-flow model yields decaying modes in all reference frames.

12.3.3 Decaying Modes in Non-relativistic Regime

We now include diffusion, and show that in reference frames for which the flow speed is non-relativistic, the uniform-flow model generally yields decaying modes. Note that the limit of zero flow speed corresponds to the co-moving frame discussed in section 12.1.

In the non-relativistic limit, the Lorentz factor has the following Taylor expansions:

$$\begin{aligned}\gamma^2 &\approx 1+\beta^2+....,\\ \gamma^4 &\approx 1+2\beta^2+.... .\end{aligned} \tag{12.126}$$

The sound speed can be written as

$$\begin{aligned}\frac{c_s^2}{c^2} &= \frac{\Gamma P_0}{w_0} = (\Gamma-1)(1-f), \qquad \text{so that}\\ 1-f &= \frac{1}{\Gamma-1}\left(\frac{c_s^2}{c^2}\right) = \frac{\beta_s^2}{\Gamma-1} = C_v\beta_s^2,\\ f &= 1-C_v\beta_s^2,\end{aligned} \tag{12.127}$$

where we have defined the dimensionless sound speed $\beta_s = c_s/c$ and a dimensionless version of the heat capacity at constant volume, $C_v = (\Gamma-1)^{-1}$. The usual heat capacity is $C_v' = k_B C_v$, where k_B is Boltzmann's constant. Assuming non-relativistic sound speeds, we can make the approximation $f \approx 1$ only in the absence of terms such as $1-f$ and $f-1$. When these terms appear, the sound speed must be retained.

We retain only terms up to order β^2, and invoke the approximations of a non-relativistic sound speed, $f \approx 1$ and (12.127) for $1-f$. Recalling that $C_p = C_v + 1$, we have, for the coefficients of the diffusionless polynomial,

$$\begin{aligned}C_{60} &\approx (\beta_A^2+2\beta^2+1)C_v,\\ C_{50} &\approx -\tau_z C_v(3\beta_A^2+\beta_s^2-10\beta^2+5),\\ C_{40} &\approx C_v(-\beta_s^2-\beta_A^2+10\tau_z^2),\\ C_{30} &\approx \tau_z C_v(3\beta_s^2+3\beta_A^2-10\tau_z^2),\\ C_{20} &\approx \zeta_z^2 C_v[\beta^2(-3\beta_s^2+5\tau_z^2)+\beta_A^2(\beta_s^2-3\beta^2)],\\ C_{10} &\approx C_v\beta\zeta_z^3[\beta_s^2\beta^2+\beta_A^2(-\beta_s^2+\beta^2)],\\ C_{00} &= 0.\end{aligned} \tag{12.128}$$

We seek the roots of the diffusionless dispersion relation in the non-relativistic limit. From the factorization (12.110), we know that two of these roots are $\Omega_1 = 0$ and $\Omega_2 = \tau_z$. The remaining four roots are magnetosonic modes, and can be obtained from the non-relativistic limit of the dispersion relation for magnetosonic waves, $f_4(\Omega) = 0$, where $f_4(\Omega)$ is given by (12.110). The non-relativistic limit of this is as follows, where, as before, $\bar{\Omega} = \Omega - \tau_z$:

$$\bar{\Omega}^4 - (\beta_s^2 + \beta_A^2)\bar{\Omega}^2 + \beta_s^2\beta_A^2\zeta_z^2 \;=\; 0. \tag{12.129}$$

The magnetosonic roots are as follows:

$$\bar{\Omega}_+^2 \;=\; \beta_{s+}^2 \;=\; \frac{\beta_s^2 + \beta_A^2 + \sqrt{\beta_s^4 + \beta_A^4 + 2(1-2\zeta_z^2)\beta_s^2\beta_A^2}}{2}, \tag{12.130}$$

$$\bar{\Omega}_-^2 \;=\; \beta_{s-}^2 \;=\; \frac{\beta_s^2 + \beta_A^2 - \sqrt{\beta_s^4 + \beta_A^4 + 2(1-2\zeta_z^2)\beta_s^2\beta_A^2}}{2}. \tag{12.131}$$

The diffusionless polynomial can now be written in terms of its non-relativistic roots:

$$\Omega(\Omega - \tau_z)\left[(\Omega-\tau_z)^2 - \beta_{s+}^2\right]\left[(\Omega-\tau_z)^2 - \beta_{s-}^2\right] \;=\; 0, \tag{12.132}$$

whose roots are

$$\begin{aligned} \Omega_1 &= 0, \qquad \Omega_2 = \tau_z, \\ \Omega_3 &= \tau_z + \beta_{s+}, \qquad \Omega_4 = \tau_z - \beta_{s+}, \\ \Omega_5 &= \tau_z + \beta_{s-}, \qquad \Omega_6 = \tau_z - \beta_{s-}. \end{aligned} \tag{12.133}$$

We now wish to introduce a small amount of diffusion into the non-relativistic polynomial, and write this polynomial in terms of a perturbation δ to the diffusionless roots. That is, for each Ω_j which is a root of the diffusionless polynomial, $\Omega_j + \epsilon\delta_j$ is the corresponding root of

the polynomial with diffusion. For a given Ω_j, we begin by writing the diffusion-containing polynomial in the form

$$\sum_{h=0}^{6} C_h(\Omega_j + \epsilon\delta_j)^h \;=\; 0. \tag{12.134}$$

Assuming sufficiently small viscosities, we retain only terms up to order χ_j. We invoke the approximations of a non-relativistic sound speed, namely, $f \approx 1$ and expression (12.127) for $1 - f$. Also, recall that $C_p = C_v + 1$. The coefficients with diffusion can now be written as

$$\begin{aligned}
C_6 &\approx C_{60} \;=\; (\beta_A^2 + 2\beta^2 + 1)C_v, \\
C_5 &\approx C_{50} + i(\chi_x + \chi_z + \chi_\epsilon + \chi_\rho + \chi_{bx} + \chi_{bz})C_v(1 + \beta_A^2 + 2\beta^2), \\
C_4 &\approx C_{40} + i(\chi_{bx} + \chi_x)\tau_z C_v(-3\beta_A^2 + 2\beta_s^2 - 8\beta^2 - 4) \\
&\quad + i(\chi_{bz} + \chi_\epsilon)\tau_z C_v(-3\beta_A^2 + 2\beta_s^2 - 10\beta^2 - 5) \\
&\quad + i\chi_z\tau_z[\beta_A^2(-1 - C_v) + C_v\beta_s^2 - (1 + 6C_v)\beta^2 - 1 - 3C_v] \\
&\quad + i\chi_\rho\tau_z[\beta_A^2(1 - 2C_v) + C_v\beta_s^2 + (1 - 8C_v)\beta^2 + 1 - 4C_v],
\end{aligned}$$

$$\begin{aligned}
C_3 &\approx C_{30} + i[6C_v\tau_z^2 - C_v\beta_s^2 + \beta_A^2(-C_v\zeta_x^2 - C_v\zeta_z^2\beta_s^2 + 3C_v\tau_z^2 - (C_v + 2)\zeta_x^2\beta^2)]\chi_{bx} \\
&\quad + i[-C_v\beta_s^2 + 10C_v\tau_z^2 + \beta_A^2(-C_v\zeta_z^2 - \zeta_x^2)]\chi_{bz} \\
&\quad + iC_v(-\zeta_z^2\beta_s^2 + 6\tau_z^2)\chi_x + i[-C_v\zeta_x^2\beta_s^2 + (2 + 3C_v)\tau_z^2 - \beta^2\zeta_x^2 - (1 + C_v)\beta_A^2]\chi_z \\
&\quad + i[1 + \beta_A^2(1 - C_v)]\chi_\epsilon + i[-1 - \beta_A^2(1 + C_v)]\chi_\rho,
\end{aligned}$$

$$\begin{aligned}
C_2 &\approx C_{20} + i\tau_z[2C_v\beta_s^2 - 4C_v\tau_z^2 + (-1 + 3C_v)\zeta_x^2\beta_A^2]\chi_{bx} \\
&\quad + i\tau_z[3C_v\beta_s^2 - 10C_v\tau_z^2 + 3\beta_A^2(C_v\zeta_z^2 + \zeta_x^2)]\chi_{bz} \\
&\quad + i\tau_z C_v[C_v\zeta_z^2\beta_s^2 - 4\tau_z^2 + \beta_A^2(2C_v\zeta_z^2\beta_s^2 - \tau_z^2)]\chi_x \\
&\quad + i\tau_z[2C_v\zeta_x^2\beta_s^2 + (-(1 + C_v)\zeta_z^2 + 2\zeta_x^2)\beta^2 + (1 + C_v)\beta_A^2]\chi_z \\
&\quad + i\tau_z[-2 + (-2\zeta_x^2 + 3C_v)\beta_A^2]\chi_\epsilon + i\tau_z[2 + (-1 + 2C_v)\beta_A^2]\chi_\rho,
\end{aligned}$$

$$\begin{aligned}
C_1 &\approx C_{10} + i[\tau_z^2(-C_v\beta_s^2 + C_v\tau_z^2) + \beta_A^2\zeta_x^2\zeta_z^2[2C_v\beta_s^2 + 3\beta^2(4 - C_v)]]\chi_{bx} \\
&\quad + i\tau_z^2[-3C_v\beta_s^2 + 5C_v\tau_z^2 + ((-2 - 3C_v)\zeta_z^2 - \zeta_x^2)\beta_A^2]\chi_{bz} \\
&\quad + i\tau_z^2[C_v\zeta_z^2(-\beta_s^2 + \beta^2)\chi_x - \zeta_x^2(C_v\beta_s^2 + \beta^2)\chi_z] + i(\tau_z^2 - \zeta_z^2\beta_A^2)\chi_\epsilon + i\zeta_z^2(-\tau_z^2 + \beta_A^2)\chi_\rho,
\end{aligned}$$

$$\begin{aligned}
C_0 &\approx i\beta\zeta_z^3\zeta_x^2\beta_A^2[-2C_v\beta_s^2 + \beta^2(-1 + C_v)]\chi_{bx} \\
&\quad + i\tau_z\zeta_z^2[C_v\beta^2(\beta_s^2 - \tau_z^2) + (-C_v\beta_s^2(\zeta_z^2 - \zeta_x^2) + \beta^2(\zeta_x^2 + C_v\zeta_z^2))\beta_A^2]\chi_{bz}.
\end{aligned} \tag{12.135}$$

Each coefficient C_j can be written in the form

$$C_j \;=\; C_{j0} + i\epsilon H_j. \tag{12.136}$$

The imaginary parts of the C_j are given by ϵH_j, where

$$\begin{aligned}
H_6 &= 0,\\
H_5 &= (S_x + S_z + S_\epsilon + S_\rho + S_{bx} + S_{bz})C_v(\beta_A^2 + 1),\\
H_4 &= (S_{bx} + S_x)\tau_z C_v(-3\beta_A^2 - 4) + (S_{bz} + S_\epsilon)\tau_z C_v(-3\beta_A^2 - 5)\\
&\quad + S_z\tau_z[\beta_A^2(-1 - C_v) - 1 - 3C_v] + S_\rho\tau_z[\beta_A^2(1 - 2C_v) + 1 - 4C_v],\\
H_3 &= [6C_v\tau_z^2 - C_v\beta_s^2 + \beta_A^2(-C_v\zeta_x^2 - C_v\zeta_z^2\beta_s^2 + 3C_v\tau_z^2)]S_{bx}\\
&\quad + [-C_v\beta_s^2 + 10C_v\tau_z^2 + \beta_A^2(-C_v\zeta_z^2 - \zeta_x^2)]S_{bz}\\
&\quad + C_v(-\zeta_z^2\beta_s^2 + 6\tau_z^2)S_x + [-C_v\zeta_x^2\beta_s^2 + (2 + 3C_v)\tau_z^2 - \beta^2\zeta_x^2 - (1 + C_v)\beta_A^2]S_z\\
&\quad + [1 + \beta_A^2(1 - C_v)]S_\epsilon + [-1 - \beta_A^2(1 + C_v)]S_\rho,\\
H_2 &= \tau_z[2C_v\beta_s^2 - 4C_v\tau_z^2 + (-1 + 3C_v)\zeta_x^2\beta_A^2]S_{bx}\\
&\quad + \tau_z[3C_v\beta_s^2 - 10C_v\tau_z^2 + 3\beta_A^2(C_v\zeta_z^2 + \zeta_x^2)]S_{bz}\\
&\quad + \tau_z C_v[C_v\zeta_z^2\beta_s^2 - 4\tau_z^2 + \beta_A^2(2C_v\zeta_z^2\beta_s^2 - \tau_z^2)]S_x\\
&\quad + \tau_z[2C_v\zeta_x^2\beta_s^2 + (-(1 + C_v)\zeta_z^2 + 2\zeta_x^2)\beta^2 + (1 + C_v)\beta_A^2]S_z\\
&\quad + \tau_z[-2 + (-2\zeta_x^2 + 3C_v)\beta_A^2]S_\epsilon + \tau_z[2 + (-1 + 2C_v)\beta_A^2]S_\rho,\\
H_1 &= [\tau_z^2(-C_v\beta_s^2 + C_v\tau_z^2) + \beta_A^2\zeta_x^2\zeta_z^2[2C_v\beta_s^2 + 3\beta^2(4 - C_v)]]S_{bx}\\
&\quad + \tau_z^2[-3C_v\beta_s^2 + 5C_v\tau_z^2 + ((-2 - 3C_v)\zeta_z^2 - \zeta_x^2)\beta_A^2]S_{bz}\\
&\quad + \tau_z^2[C_v\zeta_z^2(-\beta_s^2 + \beta^2)S_x - \zeta_x^2(C_v\beta_s^2 + \beta^2)S_z] + (\tau_z^2 - \zeta_z^2\beta_A^2)S_\epsilon + \zeta_z^2(-\tau_z^2 + \beta_A^2)S_\rho,\\
H_0 &= \beta\zeta_z^3\zeta_x^2\beta_A^2[-2C_v\beta_s^2 + \beta^2(-1 + C_v)]S_{bx}\\
&\quad + \tau_z\zeta_z^2[C_v\beta^2(\beta_s^2 - \tau_z^2) + (-C_v\beta_s^2(\zeta_z^2 - \zeta_x^2) + \beta^2(\zeta_x^2 + C_v\zeta_z^2))\beta_A^2]S_{bz}.
\end{aligned} \tag{12.137}$$

where we define $\chi_j = \epsilon S_j$ for the viscosities. If we further assume $\beta_A^2 << 1$, the H_j reduce to

$$\begin{aligned}
H_6 &= 0,\\
H_5 &= (S_x + S_z + S_\epsilon + S_\rho + S_{bx} + S_{bz})C_v,\\
H_4 &= -4(S_{bx} + S_x)\tau_z C_v + (S_{bz} - 5S_\epsilon)\tau_z C_v + S_z\tau_z(-1 - 3C_v) + S_\rho\tau_z(1 - 4C_v),\\
H_3 &= S_\epsilon - S_\rho,\\
H_2 &= -2\tau_z(S_\epsilon - S_\rho),\\
H_1 &= (\tau_z^2 - \zeta_z^2\beta_A^2)S_\epsilon + \zeta_z^2(-\tau_z^2 + \beta_A^2)S_\rho,\\
H_0 &= \beta\zeta_z^3\zeta_x^2\beta_A^2[-2C_v\beta_s^2 + \beta^2(-1 + C_v)]S_{bx}\\
&\quad + \tau_z\zeta_z^2[C_v\beta^2(\beta_s^2 - \tau_z^2) + (-C_v\beta_s^2(\zeta_z^2 - \zeta_x^2) + \beta^2(\zeta_x^2 + C_v\zeta_z^2))\beta_A^2]S_{bz}.
\end{aligned} \tag{12.138}$$

If we now assume β is much smaller than other terms, we can further simplify the expressions for H_1 and H_0:

$$\begin{aligned} H_1 &= -\zeta_z^2 \beta_A^2 (S_\epsilon - S_\rho), \\ H_0 &= -C_v \beta \zeta_z^3 \beta_s^2 \beta_A^2 [2\zeta_x^2 S_{bx} + (\zeta_z^2 - \zeta_x^2) S_{bz}]. \end{aligned} \tag{12.139}$$

Substituting expressions (12.136) and (12.138) for the C_j into the dispersion relation (12.134), we have

$$C_{60}(\Omega_j + \epsilon\delta_j)^6 + \sum_{h=0}^{5} (C_{h0} + i\epsilon H_h)(\Omega_j + \epsilon\delta_j)^h \;=\; 0. \tag{12.140}$$

(12.140) can be written in the form

$$\sum_{i=0}^{6} F_i \epsilon^i \;=\; 0, \tag{12.141}$$

where

$$F_0 \;=\; \sum_{h=0}^{6} C_{h0} \Omega_j^h, \tag{12.142}$$

$$F_1 \;=\; \delta_j \sum_{h=1}^{6} h C_{h0} \Omega_j^{h-1} + i \sum_{h=0}^{5} H_h \Omega_j^h. \tag{12.143}$$

In order for (12.141) to hold, each of the F_i must vanish individually. F_0 vanishes automatically, since this is simply the diffusionless polynomial whose roots are the Ω_j. By setting F_1 equal to zero, we arrive at an expression for δ_j:

$$\delta_j \;=\; (-i) \left[\sum_{h=0}^{5} H_h \Omega_j^h \right] \left[\sum_{h=1}^{6} h C_{h0} \Omega_j^{h-1} \right]^{-1}. \tag{12.144}$$

Because the unperturbed roots Ω_j are all real, the stability of a perturbed root is dictated by the sign of the imaginary part of the perturbation δ_j, which is purely imaginary. If Im

$(\delta_j) > 0$, we have a growing mode, and instability. If Im $(\delta_j) < 0$, we have a decaying mode that does not contribute instability. To explicitly compute each δ_j below, we use expression (12.144), substituting expressions (12.128) for the C_{j0} and expressions (12.138) and (12.139) for the H_j. We consider cases for which $\beta << \beta_s$ and $\beta << \beta_A$.

Consider the unperturbed root $\Omega_1 = 0$. From (12.144), the corresponding perturbation is

$$\begin{aligned}
\delta_1 &= (-i)\frac{H_0}{C_{10}} \\
&= (i)\frac{C_v\beta\zeta_z^3\beta_s^2\beta_A^2[2\zeta_x^2 S_{bx} + (\zeta_z^2 - \zeta_x^2)S_{bz}]}{C_v\beta\zeta_z^3[\beta_s^2\beta^2 + \beta_A^2(-\beta_s^2 + \beta^2)]} \\
&\approx (-i)\frac{C_v\beta\zeta_z^3\beta_s^2\beta_A^2[2\zeta_x^2 S_{bx} + (\zeta_z^2 - \zeta_x^2)S_{bz}]}{C_v\beta\zeta_z^3\beta_A^2\beta_s^2} \\
&= (-i)[2\zeta_x^2 S_{bx} + (\zeta_z^2 - \zeta_x^2)S_{bz}]. \qquad (12.145)
\end{aligned}$$

As long as S_{bz} is not significantly larger than S_{bx}, we have Im $\delta_1 < 0$, and root 1 does not contribute instability.

Consider the unperturbed root $\Omega_2 = \tau_z$. Using (12.144), and retaining only the largest terms, the corresponding perturbation is

$$\begin{aligned}
\delta_2 &\approx \frac{H_1\tau_z}{2C_{20}\tau_z + C_{10}} \\
&\approx (-i)\frac{-\zeta_z^3\beta\beta_A^2(S_\epsilon - S_\rho)}{\zeta_z^3 C_v\beta_A^2\beta_s^2\beta} = (i)\frac{S_\epsilon - S_\rho}{C_v\beta_s^2}. \qquad (12.146)
\end{aligned}$$

As long as $S_\rho > S_\epsilon$, we have Im $\delta_2 < 0$, and root 2 does not contribute instability.

Consider the unperturbed roots having the form $\Omega_r = \tau_z \pm \beta_r$, where $\beta_r = \beta_{s,\pm}$. Because $\tau_z << \beta_r$, we can say that $\Omega_r \approx \pm\beta_r$. Using (12.144), and retaining only the largest terms, the corresponding perturbation is

$$\begin{aligned}
\delta_r &\approx (-i)\frac{H_3\Omega_r^3 + H_1\Omega_r}{6C_{60}\Omega_r^5 + 4C_{40}\Omega_r^3 + 2C_{20}\Omega_r} \\
&\approx (-i)\frac{(S_\epsilon - S_\rho)(\pm\beta_r^3 \mp \zeta_z^2\beta_A^2\beta_r)}{C_v[\pm 6\beta_r^5 \mp 4(\beta_s^2+\beta_A^2)\beta_r^3 \pm 2\zeta_z^2\beta_A^2\beta_s^2\beta_r]} \\
&= (-i)\frac{(S_\epsilon - S_\rho)(\beta_r^2 - \zeta_z^2\beta_A^2)}{C_v[6\beta_r^4 - 4(\beta_s^2+\beta_A^2)\beta_r^2 + 2\zeta_z^2\beta_A^2\beta_s^2]}.
\end{aligned} \tag{12.147}$$

From expression (12.130), we see that $\beta_{s+} \geq \beta_s$ and $\beta_{s+} \geq \beta_A$. From expression (12.131), on the other hand, we see that $\beta_{s-} \leq \beta_s$ and $\beta_{s-} \leq \beta_A$. We define the ratios

$$\begin{aligned}
R_+ &= \frac{\beta_{s+}^2 - \zeta_z^2\beta_A^2}{C_v[6\beta_{s+}^4 - 4(\beta_s^2+\beta_A^2)\beta_{s+}^2 + 2\zeta_z^2\beta_A^2\beta_s^2]}, \\
R_- &= \frac{\beta_{s-}^2 - \zeta_z^2\beta_A^2}{C_v[6\beta_{s-}^4 - 4(\beta_s^2+\beta_A^2)\beta_{s-}^2 + 2\zeta_z^2\beta_A^2\beta_s^2]}.
\end{aligned} \tag{12.148}$$

Given that $\Omega_r \approx \beta_{s,\pm}$, these two quantities both satisfy the diffusionless magnetosonic dispersion relation (12.129). That is,

$$\beta_{s,\pm}^4 - (\beta_s^2+\beta_A^2)\beta_{s,\pm}^2 + \beta_s^2\beta_A^2\zeta_z^2 = 0. \tag{12.149}$$

Therefore, R_+ and R_- can be rewritten as

$$\begin{aligned}
R_+ &= \frac{\beta_{s+}^2 - \zeta_z^2\beta_A^2}{C_v[4\beta_{s+}^2 - 2(\beta_s^2+\beta_A^2)]}, \\
R_- &= \frac{\beta_{s-}^2 - \zeta_z^2\beta_A^2}{C_v[4\beta_{s-}^2 - 2(\beta_s^2+\beta_A^2)]},
\end{aligned} \tag{12.150}$$

where, again,

$$\beta_{s+}^2 = \frac{\beta_s^2+\beta_A^2 + \sqrt{\beta_s^4+\beta_A^4+2(1-2\zeta_z^2)\beta_s^2\beta_A^2}}{2}, \tag{12.151}$$

$$\beta_{s-}^2 = \frac{\beta_s^2+\beta_A^2 - \sqrt{\beta_s^4+\beta_A^4+2(1-2\zeta_z^2)\beta_s^2\beta_A^2}}{2}. \tag{12.152}$$

The magnetosonic perturbations can be written as

$$\begin{aligned} \delta_+ &= (-i)(S_\epsilon - S_\rho)R_+ \\ \delta_- &= (-i)(S_\epsilon - S_\rho)R_- \end{aligned} \tag{12.153}$$

We use (12.151) and (12.152) in conjunction with the expressions for R_+ and R_-. The numerator and denominator of R_+ are both greater than or equal to zero, so that R_+ is always positive. This means that δ_+ yields stability as long as $S_\epsilon \geq S_\rho$. The denominator of R_- is less than or equal to zero. However, the numerator of R_- can be either positive or negative. If it's positive, then $R_- < 0$, and stability requires $S_\epsilon \leq S_\rho$. If the numerator is negative, then $R_- > 0$, and stability requires $S_\epsilon \leq S_\rho$. We see that in some cases stability requires $S_\epsilon \geq S_\rho$, while in other cases stability requires $S_\epsilon \leq S_\rho$. Combining these, we see that as long as $S_\epsilon = S_\rho$, i.e., we have equal energy and density viscosities, we observe decaying or marginally stable modes in the reference frame corresponding to non-relativistic flow speed. We now consider reference frames corresponding to highly relativistic flow speed, and show that this is the limit in which the anomalies emerge. This is identical to the condition obtained in subsection 12.2.3 of the corresponding RHD (unmagnetized) analysis.

12.3.4 Extreme Relativistic Limit

We now seek to demonstrate that in reference frames for which the flow speed approaches the speed of light, diffusion yields anomalous growing modes in almost all circumstances. In the extreme relativistic limit, we retain only terms with the highest power of γ, which is γ^4. The coefficients without diffusion then become

$$
\begin{aligned}
C_{60} &= 4-\beta^2(2-f),\\
C_{50} &= \tau_z[-18-f+4\beta^2(2-f)],\\
C_{40} &= \tau_z^2[4(8+f)-6\beta^2(2-f)],\\
C_{30} &= \tau_z^3[-28-6f+4\beta^2(2-f)],\\
C_{20} &= \tau_z^4[12+4f-\beta^2(2-f)],\\
C_{10} &= -\tau_z^5(2+f),\\
C_{00} &= 0.
\end{aligned}
\tag{12.154}
$$

The coefficients with diffusion are now given by

$$
\begin{aligned}
C_6 &= C_{60} = 4-\beta^2(2-f),\\
C_5 &= C_{50}+i(\chi_x+\chi_z+\chi_\epsilon+\chi_\rho+\chi_{bx}+\chi_{bz})[4-(2-f)\beta^2],\\
C_4 &= C_{40}+i\tau_z[-14-f+3(2-f)\beta^2](\chi_{bx}+\chi_x+\chi_\rho)\\
&\quad +i\tau_z[-18-f+4(2-f)\beta^2](\chi_{bz}+\chi_\epsilon)+i\tau_z[-12+3(2-f)\beta^2)]\chi_z,\\
C_3 &= C_{30}+i\tau_z^2[3(6+f)-3(2-f)\beta^2](\chi_{bx}+\chi_x+\chi_\rho)\\
&\quad +i\tau_z^2[4(8+f)-6(2-f)\beta^2]\chi_{bz}\\
&\quad +i\beta^2[-2\zeta_x^4+10\zeta_x^2\zeta_z^2+12\zeta_z^4+f\zeta_x^2-3(2-f)\tau_z^2]\chi_z\\
&\quad +i\beta^2[(2-f)\zeta_x^4+2(16+f)\zeta_x^2\zeta_z^2+3(10+f)\zeta_z^4-6(2-f)\tau_z^2]\chi_\epsilon,\\
C_2 &= C_{20}+i\tau_z^3[-10-3f+(2-f)\beta^2](\chi_{bx}+\chi_x+\chi_\rho)\\
&\quad +i\tau_z^3[-28-6f+4(2-f)\beta^2]\chi_{bz}\\
&\quad +i\tau_z\beta^2[-4\zeta_z^2+(2-f)(\tau_z^2+2\zeta_x^2)]\chi_z\\
&\quad +i\tau_z\beta^2[-(26+f)\zeta_x^2\zeta_z^2-(22+3f)\zeta_z^4+2(2-f)(2\tau_z^2-\zeta_x^4)]\chi_\epsilon,\\
C_1 &= C_{10}+i\tau_z^4(2+f)(\chi_{bx}+\chi_x+\chi_\rho)\\
&\quad +i\tau_z^4[4(3+f)-(2-f)\beta^2]\chi_{bz}-i\tau_z^2\zeta_x^2\beta^2(2-f)\chi_z\\
&\quad +i\tau_z^2\beta^2[8\zeta_x^2\zeta_z^2+(6+f)\zeta_z^4+(2-f)(-\tau_z^2+\zeta_x^4)]\chi_\epsilon,\\
C_0 &= -i\tau_z^5(2+f)\chi_{bz}.
\end{aligned}
\tag{12.155}
$$

To first order, the effect of the diffusion is to add an imaginary component to C_0 through C_5, so that each of these takes on the form

$$
C_j = C_{j0}+iC_{ji}. \tag{12.156}
$$

We now have, for the diffusionless dispersion relation,

$$\Omega[C_{60}\Omega^5 + C_{50}\Omega^4 + C_{40}\Omega^3 + C_{30}\Omega^2 + C_{20}\Omega + C_{10}] \;=\; 0, \tag{12.157}$$

with expressions (12.154) for the C_{j0}. It can be easily verified that $\Omega_0 = \tau_z = \zeta_z\beta$ is a solution of (12.157). This corresponds to the angular frequency $\omega_0 = k_z v_{z0}$. When we introduce a small amount of diffusion, we expect this root to be shifted by a small amount δ. That is, we have

$$\sum_{j=0}^{6} C_j(\Omega_0 + \delta)^j \;=\; \sum_{j=0}^{6} C_j(\tau_z + \delta)^j \;=\; 0, \tag{12.158}$$

where the C_j are given by (12.155). Equation (12.158) can be written as a polynomial in δ:

$$\sum_{j=0}^{6} D_j\delta^j \;=\; 0, \tag{12.159}$$

where the D_j are as follows:

$$\begin{aligned}
D_6 &= C_6,\\
D_5 &= C_5 + 6C_6\tau_z,\\
D_4 &= C_4 + 5C_5\tau_z + 15C_6\tau_z^2,\\
D_3 &= C_3 + 4C_4\tau_z + 10C_5\tau_z^2 + 20C_6\tau_z^3,\\
D_2 &= C_2 + 3C_3\tau_z + 6C_4\tau_z^2 + 10C_5\tau_z^3 + 15C_6\tau_z^4,\\
D_1 &= C_1 + 2C_2\tau_z + 3C_3\tau_z^2 + 4C_4\tau_z^3 + 5C_5\tau_z^4 + 6C_6\tau_z^5,\\
D_0 &= C_0 + C_1\tau_z + C_2\tau_z^2 + C_3\tau_z^3 + C_4\tau_z^4 + C_5\tau_z^5 + C_6\tau_z^6.
\end{aligned} \tag{12.160}$$

Because τ_z is a solution of (12.157), D_{0i} is purely imaginary:

$$D_0 \;=\; iD_{0i} \;=\; (i)\sum_{j=1}^{5} C_{ji}\tau_z^j. \tag{12.161}$$

We consider first the general case, for which the D_j are non-vanishing. Note that C_6 has no imaginary part. Because we are in a reference frame corresponding to the extreme relativistic regime, τ_z is of order unity, which means that we have

$$|D_j \delta^j| \; << \; |D_0|, \qquad \text{for} \quad j = 1, 2, ..., 6. \tag{12.162}$$

This means that equation (12.159) can be approximated as

$$D_6 \delta^6 + D_0 \; = \; 0. \tag{12.163}$$

Because $D_6 = C_6$ is purely real, and D_0 is purely imaginary, we have

$$\delta^6 \; = \; \frac{-D_0}{D_6} \; = \; \frac{-iD_{0i}}{C_6} \; = \; \frac{|D_{0i}|}{C_6} \exp\left(\frac{\pm i\pi}{2}\right). \tag{12.164}$$

We include the $\pm$ in the exponent because D_{0i} can be either negative or positive. Taking the six roots of (12.164), we have, for $j = 1, 2, ..., 6$,

$$\delta_j \; = \; \left(\frac{|D_{0i}|}{C_6}\right)^{1/6} \exp\left(\frac{\pm i\pi}{12}\right) \exp\left(\frac{2\pi ij}{6}\right). \tag{12.165}$$

These are six distinct roots, at least two of which are guaranteed to have positive imaginary parts, and therefore correspond to growing modes. This demonstrates that in the extreme relativistic magnetized regime, a small amount of diffusion leads to growing modes. This is identical to the condition obtained in the corresponding RHD (unmagnetized) analysis. This analysis assumes that the D_j are non-vanishing, which is true in almost all circumstances.

As described earlier, there is a special case corresponding to the χ_j being equal to one another. In this case, several of the D_j vanish, and the resulting polynomial in δ yields only

decaying modes, with imaginary part equal to $-\chi_j$. For almost all other cases, the D_j are non-vanishing, and diffusion yields anomalous growing modes.

We have shown that the presence of a magnetic field does not suppress the anomalies of the uniform-flow model. In particular, the modes introduced by diffusion still appear to grow in reference frames for which the flow speed is highly relativistic.

12.4 Conclusion

The exact single-fluid RMHD equations are marginally stable. However, when these equations are discretized in a numerical simulation, they become slightly unstable. We therefore need to include artificial viscosity in order to curtail these effects, and restore stability to the system. In our studies of the KH instability, diffusion has precisely this effect. The anomaly introduced by diffusion in no way undermines the results of our numerical simulations.

In particular, we have provided analytical and graphical demonstrations that in the case of a uniform background flow, the modes introduced by diffusion appear to exhibit anomalous rapid growth in reference frames for which the flow speed is highly relativistic. To demonstrate this, we linearized the RHD and RMHD equations, with diffusion, for a uniform-flow, and in each case derived a dispersion relation which is a polynomial in ω (fourth-order in the RHD case, sixth-order in the RMHD case). In the diffusionless limit of the RHD polynomial, we recovered the relativistic acoustic modes of Bodo et al. (2004). In the non-relativistic diffusionless limit of the RMHD polynomial, we recovered the Alfven and magnetosonic modes of LRN09. We then demonstrated that the presence of a magnetic field does not suppress the anomalous modes predicted by the uniform-flow model. Diffusion introduces modes which decay in frames corresponding to non-relativistic flows, but appear

to grow in frames corresponding to highly relativistic flows. These results cannot be given physical significance, as they exhibit frame-dependence which arises from a model in which the diffusion operator does not preserve the Lorentz-invariance of the system.

However, this academic exercise sheds light on a shortcoming of current mathematical models of diffusion. In particular, the diffusion operator does not preserve the Lorentz-invariance of the single-fluid RMHD equations, which reveals that these models do not adequately address the influence of diffusion in the relativistic regime.

We again emphasize that these results do not in any way undermine the results of our study of the KH instability. Throughout this study, we remained in the rest frame of the system, for which diffusion introduces decaying modes and provides numerical stability. We also demonstrated in chapter 11 that our numerical results are convergent with respect to viscosity. The anomalies encountered in the present chapter are the result of attempting to Lorentz-transform between different reference frames in a model with uniform background flow.

We have examined both the stabilizing effects of a magnetic field and an anomaly associated with diffusion and relativistic flows. In the next chapter, we discuss an opportunity for further research of the KH instability using what is known as a high-resolution shock-capturing (HRSC) scheme.

Chapter 13

Further Research Using High Resolution Shock-capturing Methods

For the results obtained in this study, the numerical scheme employs artificial viscosity (AV) in combination with explicit finite-differencing. This scheme has the advantage of being absolutely convergent, and more rapidly convergent than other schemes. This scheme also allows greater flexibility in terms of being able to explicitly control the diffusion of mass, momentum, energy, and magnetic field. However, many of the simulation results have a possible sensitivity to viscosity, which can potentially undermine their significance if an excessive amount of viscosity, or physically unrealistic combination of viscosity coefficients, is used. As we have seen, artificial viscosity schemes also have difficulty handling high Lorentz factors (larger than 2). Another class of numerical schemes, the so-called shock-capturing schemes, have emerged as a possible alternative. High-resolution shock-capturing (HRSC) schemes are able to stabilize the numerical system without the need for explicit artificial viscosity, and in RHD, have been able to handle Lorentz factors of up to 1000. However, most such schemes have at best second-order convergence (compared with fourth-order convergence in space and time for our AV scheme), and have numerous difficulties handling the relativistic magnetized hydrodynamic (RMHD) regime. Nevertheless, Mignone

et al. (2009) have developed an HRSC scheme that overcomes many of these difficulties, and in future research, could provide results with which to compare the results obtained in this study. In the next section, we present an overview of the history of the development of AV and HRSC schemes (along with a few other schemes), and discuss the sequence of advances that have led to the development of the HRSC scheme of Mignone et al. (2009). In future research, this scheme could potentially be applied to our model in order to generate results with which to compare the results of this study.

We begin with an overview of the development of various numerical schemes for solving RHD and RMHD equations, in particular artificial viscosity (AV) and high-resolution shock-capturing (HRSC) schemes, culminating in the development of the scheme of Mignone et al. (2009).

Wilson (1972, 1979) was among the first efforts to solve the RHD equations. He used an explicit finite-differencing scheme with explicit artificial viscosity. Almost all numerical codes developed in the 1980s for special and general RHD relied on this scheme (Piran 1980; Stark and Piran 1987; Nakamura 1980, 1981, and 1982; Evans 1986; Centrella and Wilson 1984). However, such a scheme is unable to accurately simulate ultra-relativistic flows (Lorentz factors larger than 2). Norman and Winkler (1986) reported on these difficulties, and proposed a scheme using implicit artificial viscosity along with adaptive mesh refinement. They were able to obtain accurate results at high Lorentz factors, but only in one dimension. Our scheme uses explicit finite-differencing and artificial viscosity, and suffers from very much the same problem with regard to high Lorentz factors. As discussed below, more recent schemes (e.g. shock-capturing) have been able to obtain accurate results at high Lorentz

factors in RHD, but are less rapidly convergent than our scheme, and much more difficult to extend to RMHD regimes, and multiple dimensions.

Starting in the early 1990s, many attempts were made to integrate the RHD equations without the use of artificial viscosity. Dubal (1991) used a flux-corrected transport (FCT) algorithm, along with an explicit second-order Lax-Wendroff scheme. Mann (1991) adapted smoothed particle hydrodynamics (SPH) techniques to the numerical solution of GRHD equations, and in 1993 applied this method to relativistic spherical collapse. Van Putten (1993) was among the pioneering efforts in simulating an RHD jet. He used a 2D slab geometry with a Lorentz factor of 3.25. He also developed an RMHD scheme that uses Maxwell's equations in divergence form. However, his method led to oscillations for strong shocks, which requires a smoothing algorithm, and is limited to moderate Lorentz factors. In 1D relativistic shock tube tests, these methods performed similarly to Wilson's approach, and had little success with high Lorentz factors.

High-resolution shock-capturing (HRSC) methods, which are designed specifically to solve conservative hyperbolic systems, provide a tremendous improvement to the simulation of ultra-relativistic flows in RHD. Early versions of HRSC methods were developed in Marti et al. (1991) and Marquina et al. (1992). Eulderink (1993) developed a relativistic HD version of a Roe-type solver, which applies an approximate Riemann solver locally to each grid cell, by diagonalizing a Jacobian relating the flux variables to the conserved quantities. Marti and Muller (1996) developed what they called a relativistic piecewise parabolic method (rPPM) for 1D RHD, which used an exact Riemann solver, although exact solvers tend to be more computationally expensive (Marti and Muller 2003). Colella and Woodward

(1984) were among the first to develop and describe the piecewise parabolic method (PPM).

Harten, Lax, and van Leer (1983) proposed a shock-capturing scheme (the HLL scheme) using a Riemann solver that only requires approximate knowledge of the slow and fast wave speeds associated with the shocks, and therefore does not require diagonalization of a Jacobian. Schneider et al. (1993) adapted this method to the relativistic regime. This method was used by Duncan and Hughes (1994) in the simulation of relativistic extragalactic jets with Lorentz factors of 10. They were also among the first to simulate an RHD jet in cylindrical geometry. They used a Newton-Raphson method to compute primitive variables. They noted from their results that the relativistic nature of the flow inhibits the development of the KH instability, with no KH instability visible for a Lorentz factor of 10, and hypothesized that this might explain the smoother structure of QSOs (quasi-stellar objects), which have more relativistic flows than the more turbulent BL Lacertae objects. Duncan and Hughes used a small Mach number, while Marti et al. (1995) performed an RHD simulation in cylindrical geometry with a highly supersonic Mach number. They used an HRSC scheme with a Riemann solver and Runge-Kutta time discretization to integrate the equations, and, as with Duncan and Hughes, used a Newton-Raphson method to recover primitive variables. They observed a jet surrounded by a cocoon with distinct Kelvin-Helmholtz vortices, and noted that the conclusions of Duncan and Hughes do not apply to jets with high Mach numbers.

Koide et al. (1996) were among the first efforts to extend HRSC schemes to the simulation of RMHD fluids, using a simplified total variation diminishing (STVD) scheme developed by Davis (1984) for HD fluids, rather than a Riemann solver. This can be thought of as the Lax-

Wendroff method coupled with the formal use of diffusion. As with the other simulations, they use a Newton-Raphson method to recover primitive variables. They concluded that a strong magnetic field, coupled with relativistic effects, may explain the collimated, faster, and smoother flows observed in quasars, in contrast to the bending observed in BL Lacertae objects and extragalactic jets such as 3C 279 and 3C 454.3, which is largely caused by propagation into an oblique magnetic field. Nishikawa et al. (1998) performed a 3D RMHD jet simulation. These studies used a second-order Lax-Wendroff scheme, which has several disadvantages compared to a Godunov-type scheme. The second-order Lax-Wendroff scheme incurs a large amount of implicit numerical viscosity. Also, there have been no published results of a comprehensive set of standard numerical tests to validate the properties of these codes (convergence, etc.), according to Del Zanna and Bucciantini (2003). This scheme is limited to moderate Lorentz factors.

Komissarov (1999a) and Balsara (2001) also made important advances toward extending HRSC schemes to the simulation of RMHD fluids, this time using linearized Riemann solvers incorporated into second-order Godunov-type schemes. However, these schemes rely on Roe-type solvers which require complicated diagonalization. Furthermore, they require the solution of systems of equations in order for primitive variable recovery from conserved quantities. Del Zanna and Bucciantini (2003) applied the HLL scheme to the RMHD problem, requiring only the estimation of wave speeds rather than matrix diagonalization. They also used a third-order essentially non-oscillatory (ENO) central-type scheme. This scheme has third-order overall accuracy, and is an extension of an RHD scheme presented in Del Zanna and Bucciantini (2002) and the 3D MHD shock-capturing scheme presented in Lon-

drillo and Del Zanna (2000). They also reduced the primitive variable recovery process to the solution of just one nonlinear equation in terms of the enthalpy. The primitive variable recovery algorithm of Newman (2002) uses a single equation in terms of the pressure.

Bucciantini and Del Zanna (2006) used their shock-capturing scheme to numerically simulate the growth of the KH instability in RMHD, comparing their results to observed synchrotron emission spectra in pulsar wind nebulae (PWN). They concluded that the KH instability might be responsible for time-dependent filamentary structure in the main torus of a PWN.

Mignone and Bodo (2006) solved the RMHD equations using an HLLC approximate Riemann solver, which improves upon HLL schemes by resolving the intermediate wave associated with the contact discontinuity. Mignone and Bodo (2009) improved upon their HLLC scheme with a so-called HLLD scheme which resolves several other characteristics in RMHD. Zrake and MacFadyen (2011) used the HLLD Riemann solver in their simulations of RMHD turbulence. To recover primitive variables, they used a 2D Newton-Raphson algorithm to solve a system of two equations in two unknowns. These RMHD studies only considered moderate Lorentz factors.

Newman (2002) introduced an improvement over the above RMHD schemes by presenting a rapidly convergent, accurate approach for recovering the primitive variables (density, pressure, velocity) from the conserved quantities at each time step of a simulation, which is a vast improvement over other methods, such as the Newton-Raphson method. The scheme of Newman (2002) is used in our simulations. Furthermore, our numerical integration scheme has fourth-order convergence in space and time. Our use of explicit finite-differencing and

artificial viscosity has advantages and disadvantages over shock-capturing schemes. Where the latest HRSC schemes are able to handle Lorentz factors of up to 1000 in RHD, our scheme undergoes early numerical breakdown for Lorentz factors larger than around 2. However, while shock-capturing schemes have at most second-order accuracy, our scheme has fourth-order accuracy. Also, our scheme can be much more easily extended to the RMHD regimes, and to multiple dimensions, whereas shock-capturing schemes must address a number of complications associated with the magnetic field and relativistic effects. There are more characteristics to identify at each spatial point, and a method needs to be developed to ensure that the magnetic field remains divergenceless (typically the so-called constrained transport (CT) method developed for MHD by Evans and Hawley (1988)). Nevertheless, the HLLD Riemann solver of Mignone et al. (2009) does an effective job of addressing many of these difficulties, and for purposes of further research into our model, would be a good scheme against which to compare our results.

We have discussed a high-resolution shock-capturing scheme which could potentially provide a basis for further exploration of the KH instability problem being studied in this dissertation. In the next chapter, we summarize the salient results discussed in this dissertation, and discuss other opportunities for further exploration.

Chapter 14

Summary

We have explored, via numerical and analytical methods, the evolution of the KH instability in magnetized relativistic astrophysical flows with a velocity shear, with applications to astrophysical jets. The exact RMHD single-fluid equations are marginally stable, however they become unstable when discretized in a numerical scheme. We therefore need artificial viscosity in order to restore stability to the system. Viscosity also models physical processes, such as momentum transfer and conductivity. Due to relativistic effects, viscosity can lead to anomalous behavior, however we explain in chapter 12 why this behavior does not emerge in our numerical simulations.

We find that while the magnetic field tends to stabilize the system, relativity tends to destabilize the system. Through both linear and nonlinear analysis, we have found that the magnetic field tends to stabilize the system to the KH instability. Through linear analysis, we demonstrate that the magnetic field has the effect of reducing the linear growth rate, and also reducing the region of instability. Through nonlinear analysis of the numerical simulations, we demonstrate that the magnetic field tends to inhibit vortex development through a series of stages that show qualitative agreement with observations of numerous jets, namely, field amplification, vortex disruption, turbulent breakdown, and relaxation to an equilibrium

filamented state. Qualitatively similar processes have been discussed in MHD literature. In our study, we examine in detail how and to what extent these stages manifest in RMHD for a set of representative field strengths. These field strengths are within an order of magnitude of one another, and therefore within the uncertainty in field estimates of astrophysical jets. We find that in the moderately relativistic regime, the influence of the magnetic field, both on the linear growth rate and on the nonlinear evolution, is closely correlated with a relativistic extension of the Alfvenic Mach number, which we define analogously (see equation (6.3)) to the manner in which Bodo et al. (2004) defined a relativistic version of the sonic Mach number.

We also find that relativistic effects tend to destabilize the system. In our linear analyses of the KH instability for the continuous velocity profile used in the simulations (chapter 6), we find that highly relativistic flows tend to support modes with near-maximum growth at wavelengths which are shorter than the width of the velocity shear.

Through our linear and nonlinear studies, we have successfully unified the HD, MHD, RHD, and RMHD regimes. Here are some of the many ways in which we have done this. In chapter 4, we examined the KH instability in the presence of a tangential discontinuity, and demonstrated convergence between these four regimes in our dispersion relations and growth rate results. In chapter 5, we derived a second-order ODE in the perturbation to total pressure for a system with shear in the background velocity, and demonstrated that this ODE has the same underlying structure in each of the above four regimes. In chapter 6, we found convergence between the four regimes in our numerical growth rate results obtained by solving the above second-order ODE. In chapter 11, we demonstrated convergence between

the four regimes in the nonlinear evolution of the system. In chapter 12, we demonstrated that when we take the diffusionless limit of the dispersion relations arising from the uniform-flow model, we recover familiar modes in each of these regimes (Alfven and magnetosonic modes in MHD and RMHD, along with acoustic modes in RHD and HD).

Below, we summarize our findings. We first discuss our basic model of the system, followed by the stabilizing influence of a magnetic field, followed by the destabilizing influence of relativity. We then proceed to discuss some possible limitations of our model, and opportunities for further research of this problem.

14.1 Our Model of the System

Our numerical simulations solve the RMHD single-fluid equations in conservative form. In chapter 3, we demonstrate the mathematical equivalence of three formulations of these equations which commonly appear in the literature. The first formulation is not written in conservative form, but instead explicitly includes the Lorentz force in terms of the charge and current densities, along with electric and magnetic fields in the stationary frame. This is closest in form to the equations used to model laboratory plasmas with multiple fluids, which employ a separate force equation for each fluid. The second formulation, used by Koide et al. (1996) and Nishikawa et al. (1997), is in conservative form, but is written in terms of the electric and magnetic fields in the stationary frame. The third formulation, the one used in the simulations, is in conservative form, and written in the covariant form of Anile (1989), for which the magnetic fields are given in the co-moving frame of the fluid, and the velocity and magnetic field are represented as relativistic four-vectors. This is the form most commonly used in RMHD single-fluid simulations.

Upon surveying the salient literature of prior MHD and RMHD single-fluid simulations of the KH instability, we have developed a model for our numerical simulations. We assume a fluid which is compressible, adiabatic, has infinite conductivity, and has an isotropic pressure tensor. We assume a two-dimensional slab geometry, with periodic boundary conditions in the flow (z) direction, and the shear (x) direction. We assume a uniform background density and pressure, and a uniform background magnetic field which is aligned with the flow. The background flow velocity has a sech^2 shear profile, which peaks at the central axis, and vanishes asymptotically at the boundaries. This profile is also known as a Bickley jet (Bickley 1937). We evolve the simulation by numerically solving the single-fluid RMHD equations of Anile (1989) in conservative form, using a method which is fourth-order accurate in space and time, and which exploits a rapidly convergent, highly accurate algorithm developed by Newman (2002) for recovering the primitive variables from the conserved quantities (significantly better than methods used in many prior studies, such as the Newton-Raphson method). The exact RMHD single-fluid equations are marginally stable, but become unstable when we discretize the spatial and temporal derivatives in a numerical scheme. We therefore need to include artificial viscosity for numerical stability, but also to model viscous exchanges of momentum and energy between microscopic eddies, and, in the case of magnetic viscosity, to model conductivities associated with electron and ion gyration in relevant astrophysical environments. In first and second-order methods, viscosity is implicitly present as a truncation error. By using fourth-order methods in space and time, we are able to explicitly control the viscosity coefficients. Viscosity can introduce anomalous results in relativistic systems, however we explain in chapter 12 why these anomalies are not observed in our simulations.

We construct a numerical eigenmode of the system by numerically solving a second-order ODE in the perturbation to total pressure. This ODE has the same underlying structure in the HD, RHD, MHD, and RMHD regimes, as discussed in chapter 5. We numerically solve the ODE using the shooting method, also used in Blumen (1970). For a given frequency, we construct left and right pressure profiles by integrating inward from the outer transverse boundaries. In this way, the physical solution prevails over the unphysical one. We repeat this process over an array of complex frequencies. The frequency of the eigenmode is the frequency for which the left and right pressure profiles converge smoothly at a point close to the central axis.

The numerical growth rates increase with increasing velocity within the moderately relativistic regime, but the system is KH-stable for highly relativistic flow speeds exceeding about $0.95\,c$. The growth rate is also larger for larger sound speeds, as the perturbation performs less work in order to extract energy from the background flow. There are also several differences between the numerical growth rates, for a velocity profile with continuous shear variation, and the growth behavior for a velocity profile with a tangential discontinuity (TD), as studied, for example, by Bodo et al. (2004). In the case of a TD, the growth rate increases linearly with the wave number of the perturbation. With a shear variation, there is a wave number above which the growth rate ceases to grow, and a larger wave number above which the system is stabilized. This is discussed in section 6.5 of chapter 6. In the case of a TD, we show in chapter 4, and in agreement with Bodo et al. (2004), that the flow is KH-stabilized to flow-aligned perturbations when the Mach number exceeds 4 (in the frame in which one fluid is stationary). However, for a shear variation, we see in section 6.4 of

chapter 6 that the flow can be KH-unstable to flow-aligned perturbations at Mach numbers much larger than this, particularly at low sound speeds.

It should be noted that the numerical eigenfrequencies are about 10 orders of magnitude smaller than the Larmor frequency. Therefore, it is highly unlikely that the KH-unstable modes being studied would generate resonance with gyrating particles. We discuss this in section 8.2 of chapter 8.

Once we have obtained a numerical eigenmode, we launch the simulation by perturbing the system in this eigenmode. The system then evolves through a linear regime in which the perturbations grow at approximately the numerical growth rate. Deviations from linear agreement are due to evanescent modes introduced by artificial diffusion. After about 8 to 10 growth times, the perturbations become comparable to the corresponding background (unperturbed) values, and energy is diverted from the linear mode into newly emergent nonlinear modes. This results in saturation of the perturbed quantities. At about this time, transverse mechanical stresses have become large enough to twist the flow into two large counter-rotating vortices on either side of the central axis, separated longitudinally by half the perturbation wavelength. This half-wavelength separation is a direct consequence of the transverse symmetry of the perturbation profiles of transverse velocity, and the transverse antisymmetry of the pressure perturbation profiles (as discussed in chapters 7 and 10). These symmetries are those of a sinuous mode. For a varicose mode, which has the opposite symmetries, the two vortices would be longitudinally colocated. The terms "sinuous" and "varicose" are used by Drazin and Howard (1966). In our slab geometry, the fastest-growing modes are sinuous, while the varicose modes are much more stable.

The vortices form around regions of low density and pressure, and each rotate in the direction of fluid circulation within them. In the early nonlinear regime, this rotation is dominated by mechanical stresses, so that the angular velocity varies irregularly, and the vortices assume irregular shapes, alternately being elongated in the longitudinal and transverse directions. In the absence of a magnetic field, the vortices persist, and over time, thermal stresses become more dominant over mechanical stresses. Because thermal stresses are isotropic, the vortices gradually relax to a more circular shape, and their angular velocity relaxes to a roughly constant value, for which the rotation period is roughly equal to one sound transit time. This is due to modulation by nonlinear transverse sound waves which propagate between the jet axis and transverse boundaries. These sound waves cause nonlinear oscillations in the graphs, versus time, of the spatially-averaged density, pressure, and velocity components. These oscillations also appear in the graphs, versus time, of the perturbations of density, pressure, and transverse velocity, though not longitudinal velocity, as discussed in chapter 9. At a given pressure peak, the pressure is maximized around the central axis of the flow, and the flow speed is at a local minimum. At the next pressure peak, the pressure is maximized at the transverse boundaries, and the flow speed is at a local maximum, and so on. The oscillations in average flow speed therefore have twice the period of the oscillations in average pressure and density. Sufficiently strong fields suppress these nonlinear oscillations. Although these acoustic oscillations are influenced by the transverse width of the system, we show in sections 11.3 through 11.5 of chapter 11 that they do not significantly influence the evolution of the flow.

14.2 Stabilizing Influence of a Magnetic Field

The presence of a magnetic field has the general effect of inhibiting the KH instability, both in its linear and nonlinear development. In section 4.7 of chapter 4, we show that for a tangential discontinuity between two relativistic flows, a flow-aligned magnetic field stabilizes the system to flow-aligned perturbations when the magnetic pressure exceeds the thermal pressure. In section6.3 of chapter 6, we show that for a given flow speed, growth rate decreases with increasing field strength, and that stronger magnetic fields are required to stabilize systems with higher flow speeds and higher densities. In particular, we find that within a regime of moderately relativistic flow speeds, the fractional reduction in growth rate, due to a magnetic field, is closely correlated with a relativistic version of the Alfvenic Mach number M_A, which we have defined analogously to the manner in which Bodo et al. (2004) defined a relativistic sonic Mach number (see equation (6.3)). The system is stabilized when M_A is less than about 3. However, this correlation breaks down somewhat for flow speeds less than about $0.3\,c$ or larger than about $0.8\,c$.

In the nonlinear regime, the magnetic field inhibits vortex development through a series of stages, described in chapter 10. First, the rotating vortices centrifugally expel the field lines, resulting in field amplification within the filaments connecting the vortices. The vortices twist the field lines, and this, in combination with magnetic resistivity, results in magnetic reconnection. Second, the field disrupts the vortices. Magnetic stresses on the vortex boundaries inhibit vortex rotation, and deform the vortices into irregular shapes, accompanied by vortex shedding of amplified hybrid filamentary features. Third, the vortices undergo turbulent breakdown into smaller-scale structures, partly driven by magnetic re-

connection, and the jet continues to broaden as electromagnetic and mechanical energy are viscously dissipated into thermal energy. In the fourth and final stage, the system gradually relaxes to an equilibrium state consisting of flow-aligned vortex and current filaments. These stages of inhibition are qualitatively similar to those discussed in the MHD simulations of Malagoli et al. (1996) and Baty et al. (2003), and the mildly relativistic MHD simulations of Bucciantini and Del Zanna (2006). Miura and Pritchett (1982) also noticed the presence of field-aligned currents in the equilibrium state of their MHD results. We examine in detail how and to what extent these stages manifest in RMHD for a set of representative field strengths. These field strengths are separated by roughly an order of magnitude, which falls well within the uncertainty in estimates of field strength in astrophysical jets (obtained from synchrotron emission observations).

The final equilibrium state consists of a wide equilibrium flow (broader than the initial jet width) with an average longitudinal velocity of only about $0.2\,c$ (where it was initially $0.7\,c$), as shown by the displays in section 10.2. For fields which are stronger than this intermediate range (i.e., $M_A < 20$), there is less viscous dissipation and jet deceleration, because there is less intermediate turbulence. In this regime, the magnetic tension converts a larger amount of mechanical bulk flow energy directly into electromagnetic form, with incomplete vortex formation, and minimal magnetic reconnection, if any. This results in an equilibrium state with a narrow central channel of relatively high flow speed (about $0.4\,c$ for $M_A = 10.3$, and about $0.5\,c$ for $M_A = 5.15$), whose width is about 1/5 the initial jet width. This narrow channel is bordered on either side by filaments of enhanced vorticity (i.e., large velocity shear), and corresponds to a region of low density (see the displays in

sections 10.3, for the strong vortex-disruptive field, and 10.5, for the vortex-suppressing field). Similar density undershoots were observed in the MHD study of Frank et al. (1996) and the RMHD study of Mignone et al. (2009). In summary, when fields are strong enough to reduce the rate of viscous dissipation, most of the residual bulk flow energy resides in a narrow region surrounding the central flow axis. Fields with this strength also tend to suppress the propagation of nonlinear transverse sound waves, as seen in the plots in sections 9.4 and 9.5 of chapter 9, in which nonlinear oscillations are suppressed for sufficiently strong fields.

Another observation is the close complementarity between the flow and magnetic field, seen in the displays in chapter 10, in which the vorticity is overlaid with contours of the magnetic field lines. This complementarity can be viewed in terms of an interaction between mechanical energy and electromagnetic stresses. When the vortices form shortly after saturation, the flow initially drives the field, through field amplification by centrifugal vortex expulsion of field lines, and subsequent twisting of the field lines through vortex rotation. Then, the field builds up sufficient electromagnetic stresses to constrain the flow, as the tension in the field lines halts vortex rotation while deforming and disrupting the vortices. Vortex behavior also leads to magnetic reconnection, which in turn enhances the turbulent breakdown of the faster-moving components of the flow.

The extent and rapidness of vortex inhibition are closely characterized by M_A, our aforementioned relativistic extension of the Alfvenic Mach number. We demonstrate this correlation in section 11.8 of chapter 11, in which we compare results for a given M_A at two different background flow speeds, $0.7\,c$ and $0.5\,c$, and find very close agreement well into the nonlinear regime. Baty et al. (2003) performed non-relativistic MHD simulations in which they found

close correlation of vortex inhibition with the non-relativistic Alfvenic Mach number. In chapter 10, we see that for stronger magnetic fields (smaller M_A), the vortices are disrupted at an earlier point in their rotation, and after fewer growth times, resulting in less twisting of the field lines, and therefore less magnetic reconnection. Consequently, the breakdown of the vortices is less complex, and there is less intermediate turbulence, so that the system reaches an equilibrium filamented state after fewer growth times. For stronger fields, the equilibrium jet is not as wide, and the filaments tend to be narrower. Fields for which M_A is less than about 6 suppress vortex formation entirely, resulting in an immediate transition to an equilibrium filamented state. At all field strengths, the nonlinear features tend to have less sharply-defined (i.e., more gradually sheared) boundaries in the latter stages of the non-linear regime (turbulent breakdown, the approach to equilibrium). This is partly due to the decay of the vorticity to about $0.2\,c/r_0$, which is only about one quarter of its initial value. The smaller vorticity is more closely correlated with frequencies of modes introduced by diffusion, which more strongly couples the evolution to viscous dissipation. Another important property of the equilibrium flow, and corresponding vorticity, is that they are qualitatively similar to the initial flow. This indicates that, regardless of the intermediate turbulence and complexity of vortex disruption, the system retains a memory of its initial configuration, an observation that was also made in the MHD study of Ryu et al. (2000). In particular, for the vortex-suppressing field, the equilibrium flow contains a nearly uniform background flow region whose width is almost identical to the width of the initial jet (see figure 10.26(c) in section 10.5). In the vortex-suppressing case, the flow therefore retains not just a qualitative but also a quantitative memory of its initial configuration.

We see that the extent and rapidness of vortex inhibition are directly correlated with the field strength. However, there are certain energy-conversion processes for which we observe bifurcations, i.e., processes which are optimized for intermediate field strengths. We observe two important bifurcations. The first corresponds to the viscous dissipation of mechanical energy into thermal energy, which is optimized for intermediate vortex-suppressing fields ($20 \leq M_A \leq 42$). We observe this bifurcation in the plots in section 9.5 of chapter 9, for which the intermediate fields $M_A = 21$ and $M_A = 41$ correspond to minimum longitudinal velocity, minimum Lorentz factor, and maximum pressure in the latter stages of the nonlinear regime. These fields allow a sufficient amount of vortex development to lead to a large amount of bulk flow mechanical energy being diverted into rotational form, a large amount of field amplification by vortex expulsion of field lines, and sufficient vortex twisting to lead to magnetic reconnection. This, in turn, results in a complex turbulent breakdown, partly driven by persistent magnetic reconnection. The turbulence generates small-scale structures whose lengths are comparable to the length scales set by diffusion. This optimizes viscous dissipation of non-thermal energy into thermal form, and therefore maximizes jet deceleration. Another consequence of intermediate turbulence is greater broadening of the jet as directional bulk flow energy is diverted into random motions, which contributes to the deceleration. For fields which are too weak to optimize viscous dissipation (e.g., $M_A = 82$), the vortex disruption is too gradual, and therefore the emergent features are dissipated before they have the opportunity to interact in a turbulent manner. This bifurcation is not observed in the *transverse* velocity, which is correlated with the amount of bulk flow energy diverted into rotational form, and therefore simply decreases with increasing field strength. For fields which are too strong to optimize viscous dissipation, the residual mechanical energy

is concentrated in a narrow central flow channel.

The second bifurcation corresponds to extraction of electromagnetic energy from the bulk flow in the early nonlinear regime. At this stage, certain field-dependent quantities (e.g., electromagnetic energy density, electromagnetic momentum, vorticity) reach a peak near the onset of vortex disruption by the magnetic field, followed by gradual decay that asymptotically approaches equilibrium values. The peak in each of these quantities is maximized for the strongest vortex-disruptive fields, and is smaller for the vortex-suppressing field, as shown by the plots in section 9.6 of chapter 9. The strongest vortex-disruptive field studied corresponds to $M_A = 10.3$. The early extraction of electromagnetic energy is therefore heavily correlated with the ability of the magnetic tension to extract this energy directly from the bulk flow, and is less correlated with field amplification due to vortex rotation, associated with weaker vortex-suppressing fields. However, in order to optimize conversion into electromagnetic energy, some of the bulk flow energy must also be diverted into rotational form, as seen by the observation that the peaks are substantially smaller for the vortex-suppressing field $M_A = 5.15$. The strong vortex-disruptive field regime, which optimizes extraction of electromagnetic energy, is also correlated with the emergence of the aforementioned narrow central channel of relatively high flow speed and low density.

The current density also reaches a peak in the early nonlinear regime, followed by gradual decay. However, maximum peak current density occurs for *weak* vortex-disruptive fields (among the fields sampled, $M_A = 41.4$ gives maximum current density). One explanation is that the current density is given by the curl of the magnetic field, and therefore depends on the shear in the field, rather than on the strength of the field itself. The greatest shear in field

strength occurs when we optimize the shear in field line concentration. This occurs when field lines are expelled by rotating vortices. Strong vortex-disruptive fields suppress vortex rotation, thereby reducing the current density. Also, although we maximize the *amount* of extracted electromagnetic energy with a strong vortex-disruptive field, this is not how we maximize the *amplification* of electromagnetic energy, relative to its background value. This amplification is due to field line concentration, and is correlated with the amount of vortex development. It therefore simply decreases with increasing field strength, and does not exhibit a bifurcation.

There are qualitative similarities between our simulation results and certain jet observations, suggesting that our model might offer insight into some of the physical mechanisms taking place in these jets. We discuss this in section 10.7. The formation of vortices, turbulent breakdown, jet broadening, and jet deceleration are all qualitatively consistent with observations (see figure 10.28 of the radio jet M87, figure 10.29 of the jet Centaurus A, and figure 10.30 of the jet from Herbig-Haro 30). Filamentary features, seen in our vorticity and current displays, are also consistent with observations. Lobanov and Zensus (2001) used the KH instability to model the filamentary double-helix in the extragalactic jet 3C 273. Hardee (2003; 2005) used the KH instability to model filamentary features in the extragalactic jet 3C 120. In our simulations, we observe that the large vortices are initially connected by a dual filamentary structure, and that for all field strengths, the system relaxes to an equilibrium state consisting of flow-aligned vortex and current filaments. All of the aforementioned jets are extragalactic, though these qualitative similarities are also observed with jets in our galaxy, such as the Herbig-Haro object HH 30.

Another potential comparison involves some of the knots in the radio jet M87. Stawarz et al. (2005) reported amplified fields of at least 300 μG in knot A, and Hines et al. (1989) reported transverse field components in this knot, among others, and that the field outside the knots has a smaller value of less than 100 μG. These knots may exhibit vortical behavior, whereby vortex rotation could expel the field lines, resulting in amplified field with transverse components near the knot boundaries, as occurs in our simulations for weak vortex-disruptive fields. Furthermore, Hines et al. (1989) deduced that the magnetic field outside the knots is primarily aligned with the flow, which is consistent with the background field in our simulations. This is, of course, only one of many possible explanations of these observations.

There are many ways in which we verify the reliability of our numerical results. At the end of chapter 9, we verify that the total longitudinal momentum and energy are in fact very nearly constant in time, as we expect, given that these are conserved quantities in the conservative RMHD equations, and there is no net flux of these quantities through the system boundaries. At the end of chapter 10, we verify that, to a high level of accuracy, the vorticity results satisfy the condition of alternating vorticity, which arises from the symmetry of the background velocity profile and the antisymmetry of the pressure perturbations. In chapter 11, we demonstrate the convergence of our simulation results. For each magnetic field studied, the field remains approximately divergenceless throughout the evolution of the system. Our simulations are rapidly convergent with respect to time step. With respect to spatial step, convergence is more difficult, and requires a mesh of at least 751 points in the transverse direction and 151 points per wavelength in the flow direction. Even then, the evolution diverges somewhat in the latter nonlinear regime in the turbulent features emerging

within the jet. Our simulations use 1001 points in the transverse direction, and 201 points per wavelength in the flow direction. Our results are essentially independent of the number of perturbation wavelengths spanned by the system in the flow direction. The transverse width has minor effects on the latter nonlinear evolution via boundary reverberations of nonlinear acoustic waves. However, the vortex-disruptive stage in essentially unaffected, as is the equilibrium state, and the intermediate turbulent regime is affected only in the details of the emergent turbulent features interior to the jet. Relevant spatially-averaged or maximized physical quantities do not vary with system width by more than about 5% or 10%. These effects are further reduced for strong fields, which suppress nonlinear acoustic oscillations. In the limit of vanishingly weak magnetic fields, our simulations show good convergence between the RMHD and RHD regimes. For non-relativistic flow speeds and sound speeds, our simulations show good convergence between the RMHD and MHD regimes, which we demonstrate by comparing results from the RMHD and MHD versions of our numerical code.

Our results show a slight sensitivity to the amount of viscosity used. An increase in viscosity results in a decrease in flow speeds and an increase in density and pressure, which are consistent with an increased rate of viscous dissipation into thermal energy. Qualitative sensitivity, with respect to the displays, is higher for weaker magnetic fields, due to the increased complexity of the small-scale structures arising from vortex disruption. For vortex-suppressing fields, which suppress small-scale turbulence, the displays exhibit little qualitative sensitivity to viscosity. For the weak-field case, less magnetic viscosity results in a broader, more heterogeneous background flow, with somewhat more magnetic reconnection. However, for all field strengths examined, the equilibrium jet width, and filament width, are

approximately viscosity-independent, though viscosity sometimes results in a loss of sharpness of the filament boundaries, so that the width is less well-defined. For each case, within a range of physically reasonable viscosities, the results do not vary by more than about 5%.

We also examine, in chapter 11, the sensitivity of our results to the wavelength of the input perturbation. We find that for weak fields, the equilibrium jet width is roughly twice the input wavelength, and therefore increases linearly with wavelength. For the wavelength of $7.85\,r_0$ used in the simulations (a wavelength of maximum growth for typical parameters), the equilibrium jet width is about 4.5 times the initial jet width. For strong vortex-suppressing fields, on the other hand, the equilibrium jet width is 2.25 times the initial jet width, independent of the input wavelength. Therefore, equilibrium jet width becomes independent of wavelength for strong fields. One possible explanation is that weak fields allow extensive vortex development and intermediate turbulence. The longitudinal dimensions of various features, including the initial vortices, are dependent on the input wavelength ($2\pi/k_z$, which is longitudinal). The resulting vortex rotation has the effect of coupling longitudinal dimensions to transverse dimensions, and hence to the overall width of the jet, so that for weak fields, equilibrium jet width scales with input wavelength. Stronger fields inhibit vortex formation and development, thereby inhibiting the coupling between longitudinal and transverse lengths, and the dependence of jet width on input wavelength. However, for strong fields, the equilibrium central flow width and equilibrium filament width seem to both increase linearly with wavelength, with respective values of roughly $0.11\,\lambda$ and $0.08\,\lambda$. For strong fields, shorter input wavelengths tend to result in slower flow speeds and higher pressures. One possible explanation is that these shorter wavelengths are more comparable

to the length scales set by diffusion, so that nonlinear evolution is more strongly coupled to viscous dissipation into thermal energy.

14.3 Destabilizing Influence of Relativistic Effects

We have seen that magnetic fields tend to suppress the KH instability, both in the linear growth and in the nonlinear evolution. Highly relativistic flows, on the other hand, tend to destabilize the system. For Lorentz factors exceeding about 2, no amount or combination of diffusion can sustain a numerical simulation using artificial viscosity, which is a problem that has plagued such simulations for over 20 years (Marti and Muller 2003). We first see evidence of relativistic destabilization in chapter 4, for a tangential discontinuity between two relativistic flows. Such a system is KH-stable when the Mach number (specifically, its projection onto the perturbation wave vector) exceeds a critical value. However, as the flow speed approaches the speed of light within this regime, we see that in one of the fluids the wavelengths approach infinite lengths, while in the other fluid the wavelengths approach zero, suggesting the emergence of modes with vanishingly small length scales. In chapter 6, in which we analyze the linear growth of the KH instability for the Bickley jet ("sech^2") velocity profile used in the simulations, we notice a similar result. In particular, when we plot growth rate as a function of wave number, we notice that for moderately relativistic flows there is a wave number corresponding to maximum growth and a larger wave number above which the system is KH-stable. This larger wave number is roughly equal to the width of the velocity shear across the initial jet. However, for highly relativistic background flow speeds, instability at near-maximum growth extends to higher values of k_z, and therefore to wavelengths which are smaller than the length scale set by the velocity shear. This is

another manifestation of the tendency of relativistic effects to destabilize the system.

In chapter 12, we present an anomaly associated with diffusion in highly relativistic flows. Recall that the exact RMHD single-fluid equations are marginally stable, but become slightly unstable when we discretize the derivative operators in a numerical implementation. This requires the use of artificial viscosity in order to restore stability to the system, which is how viscosity behaves in our studies of the KH instability. However, in the presence of a uniform flow, viscosity can introduce anomalous behavior associated with relativistic effects. We show this by linearizing the single-fluid equations, including artificial viscosity in each equation, for a fluid with a uniform background flow. What results is a polynomial in the eigenfrequency, which can be solved with the aid of suitable approximations. By taking the diffusionless limit of this polynomial, we recover familiar modes. In the RHD regime, we recover the dispersion relation for relativistic adiabatic sound waves, which is found, for example, in Bodo et al. (2004). In the MHD regime, we recover the magnetosonic and Alfven modes found in LRN09 and PK83 and KP84. By analytically solving this polynomial in the presence of diffusion, we encounter modes which exhibit the expected decay in frames with non-relativistic flow speeds, but appear to grow rapidly in frames with highly relativistic flow speeds. This result is unaffected by the presence of a magnetic field, and is a consequence of the fact that the diffusion operator does not preserve the Lorentz-invariance of the single-fluid RMHD equations. Our demonstration sheds light on a shortcoming of current mathematical models to adequately address the behavior of diffusion in highly relativistic systems. However, these results do not in any way undermine the results of our studies of the KH instability. Our simulations of the KH instability are always performed in the rest frame of the system, in

which diffusion only introduces decaying modes and has the expected effect of stabilizing the evolution. We also verify in chapter 11 that our simulation results are convergent with respect to viscosity.

14.4 Opportunities for Future Research

There are numerous opportunities for further research into the influence of the Kelvin-Helmholtz instability on relativistic magnetized astrophysical flows. One possibility is to explore the influence of density and pressure shears between the jet and ambient medium. Another possibility is to introduce a shear in the magnetic field. The linearization of the RMHD equations is more complicated, as there are now four sheared background quantities (density, pressure, velocity, and magnetic field), and this introduces additional complications into the computation of a numerical eigenmode. Prior studies have used some of these shears in non-relativistic environments, though these have not been adapted to the more complicated RMHD equations with the same level of accuracy, convergence, and computational efficiency as is used in our model. Once these difficulties are overcome, however, we can examine how these additional shears influence nonlinear evolution, and model astrophysical environments with potentially higher fidelity. It will also be useful to adapt our model to more complex geometries, e.g., a three-dimensional slab or cylindrical geometry. Reconnecting field lines can, for example, experience forces which push them in a direction orthogonal to the plane in which they reconnect, thereby resulting in more complicated relationships between field and fluid behavior. In three-dimensional space, field lines can wrap around vortex filaments, rather than coinciding with their contours. See the three-dimensional MHD study of Ryu et al. (2000). Although MHD studies have been performed in these geome-

tries, RMHD studies have not, as yet, overcome the difficulties of the RMHD equations to model the KH instability in a highly accurate, efficient, rapidly-convergent manner. These difficulties would need to be overcome in order to model each dimension with sufficient grid resolution.

As mentioned previously, schemes using artificial viscosity, such as this one, encounter numerical breakdown when the Lorentz factor of the flow exceeds roughly 2. Another class of schemes, namely, high-resolution shock-capturing (HRSC) schemes, has been developed as a remedy to this problem. These schemes have been able to handle Lorentz factors of up to 1000 in RHD (relativistic hydrodynamics). Komissarov (1999a) extended such a scheme to the RMHD (relativistic magnetohydrodynamic) regime. However, the convergence of this HRSC scheme, as with most others, is only second-order, while our scheme is fourth-order in space and time. Also, HRSC schemes face many more difficulties in order to accurately evolve a complex flow in RMHD, such as a flow that can be subjected to the KH instability. Nevertheless, Mignone et al. (2009) have recently developed an HRSC scheme in RMHD that overcomes many of these difficulties, and for purposes of further research into our model, would be a good scheme against which to compare our results.

14.5 Conclusion

We have examined, both analytically and numerically, the role of the Kelvin-Helmholtz instability in the evolution of relativistic magnetized plasmas, with applications to astrophysical jets. We numerically solved the single-fluid RMHD equations of Anile (1989) using a scheme which is fourth-order in space and time, and uses the highly accurate, rapidly-convergent relaxation scheme of Newman (2002) to invert the RMHD equations. These equations are

marginally stable in their exact form, but become unstable when discretized in a numerical scheme. Therefore, artificial viscosity was included to restore numerical stability to the system, but also to model physical processes (momentum transfer, conductivity). As we discuss in chapter 12, there can be situations in which diffusion introduces anomalous behavior associated with relativistic effects, however this behavior does not occur in our numerical simulations. As discussed in chapter 11, we have verified the convergence of our results with respect to time step, spatial step, system dimensions, viscosity, and between the RHD, MHD, and RMHD regimes. We also verified that the magnetic field remains divergenceless. We found generally that a magnetic field has a stabilizing effect, while relativistic effects are destabilizing.

We examined the manner in which a magnetic field inhibits the KH instability. We see this in the linear analysis, where a stronger magnetic field results in a lower growth rate. We also find that in the nonlinear evolution, the magnetic field inhibits the development KH-unstable vortices. We have identified stages of vortex inhibition which are qualitatively similar to what has been discussed in MHD literature. However, we have examined in detail the complex mechanisms by which these stages manifest in RMHD for a set of representative field strengths. We have found that the extent of vortex inhibition, along with the fractional reduction in linear growth rate, are closely correlated with a relativistic extension of the Alfvenic Mach number M_A, which we have defined analogously to the definition of a relativistic sonic Mach number found in Bodo et al. (2004). We have found that intermediate fields ($20 < M_A < 45$) are weak enough to allow extensive vortex formation and magnetic reconnection, which then drives a complex turbulent breakdown and intermediate reorganization of the system, along with maximum viscous dissipation and jet deceleration.

For fields which are weaker than this, the vortex disruption is too gradual, and therefore the emergent features are dissipated too quickly to interact in a turbulent manner. For fields which are stronger than this, the vortices are inhibited while partially formed, which suppresses magnetic reconnection, intermediate turbulence and viscous dissipation. In these strong-field cases, the residual mechanical energy is found in a narrow central flow channel of relatively high speed. We also found that maximum electromagnetic energy is extracted from the bulk flow by the strongest background fields which still allow partial vortex formation. Electromagnetic energy extraction is substantially reduced for vortex-suppressing fields. We have seen remarkable complementarity between the behavior of the fluid and magnetic field, i.e., between the flow driving the field, and the field constraining the flow. In all cases, the jet broadens, however jet-broadening is correlated with vortex-development, and is therefore greater for weaker fields. We have also found potential comparisons with numerous jet observations, particularly some of the knots in the extragalactic radio jet M87.

In our linear analyses and examinations of nonlinear evolution, we have demonstrated convergence of our results between the RMHD, RHD, MHD, and HD regimes, thereby unifying these four regimes (see the last paragraph of the introduction to this chapter). We look forward to extending our exploration of this problem in the ways outlined in section 14.4.

References

Anile, A.M. 1989. *Relativistic Fluids and Magneto-fluids.* Cambridge, U.K.: Cambridge University Press.

Balsara, D.S. 2001. Total variation diminishing scheme for relativistic magnetohydrodynamics. *Astrophys. J. Suppl. Ser.*, **132**, 83-101

Batchelor, G.K. 1967. *An introduction to fluid dynamics.* Cambridge, U.K.: Cambridge University Press.

Baty, H., Keppens, R., and Comte, P. 2003. The two-dimensional magnetohydrodynamic Kelvin-Helmholtz instability: compressibility and large-scale coalescence effects. *Phys. Plasmas*, **10**(12), 4661-4674

Bicknell, B., and Begelman, M. 1996. Understanding the Kiloparsec-Scale Structure of M87. *Astrophys. J.*, **467**, 597-621

Bickley, W.G. 1937. The plane jet. *Philos. Mag.*, **23**, 727

Birkinshaw, M. 1991. The Kelvin-Helmholtz instability for relativistic particle beams - II. Flows bounded by a simple shear layer. *Mon. Not. R. Astron. Soc.*, **252**, 505-527

Biretta, J.A. 1993. The M87 Jet. in Burgurella, D., Livio, M., and O'Dea, C.P. (eds.) *Astrophysical Jets*, 263-304, Cambridge, U.K.: Cambridge University Press.

Bittencourt, J.A. 2004. *Fundamentals of Plasma Physics.* 3rd edn. New York, NY: Springer-Verlac New York, Inc.

Blandford, R.D., and Payne, D.G. 1982. Hydromagnetic flows from accretion discs and the production of radio jets. *Mon. Not. R. Astron. Soc.*, **199**, 883-903

Blandford, R.D., and Rees, M.J. 1974. A 'twin-exhaust' model for double radio sources. *Mon. Not. R. Astron. Soc.*, **169**, 395-415

Blumen, W. 1970. Shear layer instability of an inviscid compressible fluid. Part 1. *J. Fluid Mech.*, **40**(1), 769

Blumen, W., Drazin, P.G., and Billings, D.F. 1975. Shear layer instability of an inviscid compressible fluid. Part 2. *J. Fluid Mech.*, **71**(2), 305-316

Bodo, G., Mignone, A., and Rosner, R. 2004. Kelvin-Helmholtz Instability for Relativistic Fluids. *Phys. Rev.*, **70**, [036304-1]-[036304-4]

Bucciantini, N., and Del Zanna, L. 2006. Local Kelvin-Helmholtz instability and synchrotron modulation in Pulsar Wind Nebulae. *Astron. Astrophys.*, **454,2**, 393-400

Case, K.M. 1960. Stability of an idealized atmosphere. I. Discussion of results. *The Physics of Fluids*, **3**, 149-154

Centrella, J., and Wilson, J.R. 1984. Planar numerical cosmology II: the difference equations and numerical tests. *Astrophys. J. Suppl. Ser.*, **54**, 229-249

Chandrasekhar, S. 1961. *Hydrodynamic and Hydromagnetic Stability.* Clarendon, Oxford

Choudhury, S.R., and Lovelace, R.V.E. 1984. On the Kelvin-Helmholtz instabilities of supersonic shear layers. *Astrophys. J.*, **283**, 331-342

Choudhury, S.R., and Lovelace, R.V.E. 1986. On the Kelvin-Helmholtz instabilities of high-velocity magnetized shear layers. *Astrophys. J.*, **302**, 188-199

Colella, P., and Woodward, P.R. 1984. The piecewise parabolic method (PPM) for gas-dynamical simulations. *J. Comput. Phys.*, **54**, 174-201

Davis, R.J. 1984. *A simplified TVD finite difference scheme via artificial viscosity.* Report no. 84-20. Virginia, U.S.A.: ICASE

Davis, R.J., and Booth, R.S., eds. 1993. *Sub-Arcsecond Radio Astronomy.* Cambridge: Cambridge University Press

Del Zanna, L., and Bucciantini, N. 2002. An efficient shock-capturing central-type scheme for multi-dimensional relativistic flows. I. Hydrodynamics. *Astron. Astrophys.*, **390**, 1177-1186

Del Zanna, L., Bucciantini, N., and Londrillo, P. 2003. An efficient shock-capturing central-type scheme for multi-dimensional relativistic flows. II. Magnetohydrodynamics. *Astron. Astrophys.*, **400**, 397-414

Drazin, P.G. 1958. The stability of a shear layer in an unbounded heterogeneous inviscid fluid. *J. Fluid Mech.*, **4**, 214-224

Drazin, P.G., and Howard, L.N. 1966. Hydrodynamic Stability of Parallel Flow of Inviscid Fluid. *Adv. Appl. Mech.*, **9**, 1-89

Drazin, P.G. 2002. *Introduction to hydrodynamic stability.* Cambridge, U.K.: Cambridge University Press.

Drazin, P.G and Reid, W. H. 2004. *Hydrodynamic Stability.* 2nd edn. Cambridge, U.K.: Cambridge University Press.

Dubal, M.R. 1991. Numerical simulations of special relativistic, magnetic gas flows. *Comput. Phys. Commun.*, **64**, 221-234

Duncan, G.C., and Hughes, P.A. 1994. Simulations of relativistic extragalactic jets. *Astrophys. J.* , **436**, L119-L122

Dyson, F.J. 1960. Stability of an idealized atmosphere. II. Zeros of the confluent hypergeometric function. *The Physics of Fluids*, **3**, 155-157

Eulderink, F. 1993. *Numerical relativistic hydrodynamics.* Ph.D. Thesis. Rijksuniverteit te Leiden, Leiden, Netherlands

Evans, C.R. 1986. An approach for calculating axisymmetric gravitational collapse. in Centrella, J. (ed.) *Dynamical Space-Times and Numerical Relativity*, 3-39, Cambridge, U.K.: Cambridge University Press

Evans, C.R., and Hawley, J.F. 1988. Simulations of magnetohydrodynamic flows: a constrained transport method. *Astrophys. J.*, **332**, 659-677

Faganello, M., Califano, F., and Pegoraro, F. 2008. Competing Mechanisms of Plasma Transport in Inhomogeneous Configurations with Velocity Shear: The Solar-Wind Interaction with Earth's Magnetosphere. *Phys. Rev. Lett.*, **100**, 015001(1)-015001(4)

Ferrari, A., Trussoni, E., and Zaninetti, L. 1978. Relativistic Kelvin-Helmholtz Instabilities in Extragalactic Radio-sources. *Astron. Astrophys.*, **64**, 43-52

Ferrari, A., Trussoni, E., and Zaninetti, L. 1980. Magnetohydrodynamic Kelvin-Helmholtz instabilities in astrophysics - I. Relativistic flows - plane boundary layer in vortex sheet approximation. *Mon. Not. R. Astron. Soc.*, **193**, 469-486

Francis, J.R.D. 1954. Wave motions and aerodynamic drag on a free oil surface. *Phil. Mag.*, Ser. 7, **45**, 695-702

Frank, A., Jones, T.W., Ryu, D., and Gaalaas, J.B. 1996. The magnetohydrodynamic Kelvin-Helmholtz instability: a two-dimensional numerical study. *Astrophys. J.*, **460**, 777-793

Hardee, P.E. 1987. Spatial stability of relativistic jets: application to 3C 345. *Astrophys. J.*, **318**, 78-92

Hardee, P.E. 2000. On three-dimensional structures in relativistic hydrodynamic jets. *Astrophys. J.*, **533**, 176-193

Hardee, P.E. 2003. Modeling helical structures in relativistic jets. *Astrophys. J.*, **597**, 798-808

Hardee, P.E. 2005. Modeling the 3C 120 radio jet from 1 to 30 milliarcseconds. *Astrophys. J.*, **620**, 646-664

Harten, A., Lax, P.D., and van Leer, B. 1983. On upstream differencing and Godunov-type schemes for hyperbolic conservation laws. *SIAM Rev.*, *25*, 35-61

Helmholtz, H. 1868. Uber discontinuierliche Flussigkeits-bewegungen [On the discontinuous movements of fluids]. *Monatsberichte der Koniglichen Preussische Akademie der Wissenschaften zu Berlin* [Monthly Reports of the Royal Prussian Academy of Philosophy in Berlin], **23**, 215-228

Helmholtz, H. 1882. Ueber discontinuierliche Flussigkeits-bewegungen [On the discontinuous movements of fluids]. *Wissenschaftliche Abhandlungen*, 146-157; translation by Guthrie 1868. *Phil. Mag.*, Ser. 4, **36**, 337-346

Hines, D.C., Owen, F.N., and Eilek, J.A. 1989. Filaments in the radio lobes of M87. *Astrophys. J.*, **347**, 713-726

Howard, L.N., and Drazin, P.G. 1964. On the instability of parallel shear flow of inviscid fluid in a rotating system with variable Coriolis parameter. *J. Math. Phys.*, **43**, 83

Hunter, J.H., Whitaker, R.W., and Lovelace, R.V.E. 1998. Stability of interfaces with self-gravity, relative flow, and B-field. *Astrophys. J.*, **508**, 680-689

Jackson, J.D. 1975. *Classical Electrodynamics.* 2nd edn. New York: Wiley

Kelvin, Lord 1871. Hydrokinetic solutions and observations. *Phil. Mag.*, **42**, 362-377

Kelvin, Lord 1910. Influence of wind and capillarity on waves in water supposed frictionless. *Mathematical and Physical Papers*, iv, *Hydrodynamics and General Dynamics*, Cambridge, England

Keppens, R., Toth, G., Westermann, R.H.J., and Goedbloed, J.P. 1999. Growth and saturation of the Kelvin-Helmholtz instability with parallel and anti-parallel magnetic fields. *J. Plasma Physics*, **61**(1), 1-19

Kivelson, M.G., and Pu, Z.-Y. 1984. The Kelvin-Helmholtz instability on the magnetopause. *Planet. Space. Sci.*, **32**(1), 1335-1341

Koide, S. Nishikawa, K.-I., and Mutel, R.L. 1996. A two-dimensional simulation of a relativistic magnetized jet. *Astrophys. J.*, **463**, L71-L74

Komissarov, S.S. 1999. A Godunov-type scheme for relativistic magnetohydrodynamics. *Mon. Not. R. Astron. Soc.*, **303**, 343-366

Komissarov, S.S. 1999. Numerical simulations of relativistic magnetized jets. *Mon. Not. R. Astron. Soc.*, **308**, 1069-1076

Lai, S.H., and Lyu, L.H. 2006. Nonlinear evolution of the MHD Kelvin-Helmholtz instability in a compressible plasma. *J. Geophys. Res.*, **111**, A01202

Landau, L.D., and Lifshitz, E.M. 1959a. *Fluid mechanics.* 1st edn. Course of Theoretical Physics, vol. 6. Elmsford, New York: Pergamon Press

Landau, L.D., and Lifshitz, E.M. 2004. *Fluid mechanics.* 2nd, 2nd english ed., rev edn. Course of theoretical physics, vol. 6. Burlington, MA: Elsevier Butterworth-Heinemann.

Leismann, T., Anton, L., Aloy, M.A., Muller, E., Marti, J.M., Miralles, J.A., and Ibanez, J.M. 2005. Relativistic MHD simulations of extragalactic jets. *Astron. Astrophys.* , **436**, 503-526

Lipps, F.B. 1962. The barotropic stability of the mean winds in the atmosphere. *J. Fluid Mech.* , **12**, 397

Lobanov, A.P., and Zensus, J.A. 2001. A cosmic double helix in the archetypal quasar 3C273. *Science* , **294**, 128-130

Londrillo, P., and Del Zanna, L. 2000. High-order upwind schemes for multidimensional magnetohydrodynamics. *Astrophys. J.*, **530**(1), 508-541

Lovelace, R.V.E. 1976. Dynamo model of double radio sources. *Nature*, **262**, 649-652

Lovelace, R., Romanova, M., and Newman, W. 2009. Kelvin-Helmholtz instability of the magnotopause of disc-accreting stars. *Mon. Not. R. Astron. Soc.*, **402**, 2575-2582

Malagoli, A., Bodo, G., and Rosner, R. 1996. On the nonlinear evolution of magnetohydrodynamic Kelvin-Helmholtz instabilities. *Astrophys. J.*, **456**, 708-716

Mann, P.J. 1991. A relativistic smoothed particle hydrodynamics method tested with the shock tube. *Computer. Phys. Commun.*, **67**, 245-260

Marquina, A., Marti, J.M., Ibanez, J.M., Miralles, J.A., and Donat, R. 1992. Ultrarelativistic hydrodynamics: high-resolution shock-capturing methods. *Astron. Astrophys.*, **258**, 566-571

Marscher, A.P., and Jorstad, S.G. 2011. The Megaparsec-Scale X-ray Jet of the BL Lac Object OJ287. *Astrophys. J.*, **728**, 26-33

Marti, J.M., Ibanez, J.M., and Miralles, J.A. 1991. Numerical relativistic hydrodynamics: local characteristic approach. *Phys. Rev. D*, **43**, 3794-3801

Marti, J.M., Muller, E., Font, J.A., and Ibanez, J.M. 1995. Morphology and dynamics of highly supersonic relativistic jets. *Astrophys. J.*, **448**, L105-L108

Marti, J.M., and Muller, E. 1996. Extension of the piecewise parabolic method to one-dimensional relativistic hydrodynamics. *J. Comput. Phys.*, **123**, 1-14

Marti, J.M., and Muller, E. 2003. Numerical hydrodynamics in special relativity. *Living Rev. Relativity*, **6**, 7-106

Maslowe, S.A. 1991. Barotropic instability of the Bickley jet. *J. Fluid Mech.*, **229**, 417-426

Mattingly, G.E., and Criminale, W.O. 1972. The stability of an incompressible two-dimensional wake. *J. Fluid Mech.*, **51**, 233

McKelvey, J.P. 1984. Simple transcendental expressions for the roots of cubic equations. *Amer. J. Phys.* **52**(3), 269-270

Melatos, A., and Melrose, D.B. 1996. Energy transport in a rotation-modulated pulsar wind. *Mon. Not. R. Astron. Soc.*, **279**, 1168-1190

Mignone, A., and Bodo, G. 2006. An HLLC Riemann solver for relativistic flows-II. Magnetohydrodynamics. *Mon. Not. R. Astron. Soc.*, **368**, 1040-1054

Mignone, A., Rossi, P., Bodo, G., Ferrari, A., and Massaglia, S. 2010. High-resolution 3D relativistic MHD simulations of jets. *Mon. Not. R. Astron. Soc.*, **402**, 7-12

Mignone, A., Ugliano, M., and Bodo, G. 2009. A five-wave Harten-Lax-van Leer Riemann solver for relativistic magnetohydrodynamics. *Mon. Not. R. Astron. Soc.*, **393**(4), 1141-1156

Miura, A., and Pritchett, P.L. 1982. Nonlocal Stability Analysis of the MHD Kelvin-Helmholtz Instability in a Compressible Plasma. *J. Geophys. Res.*, **87**(A9), 7431-7444

Morse, P.M., and Feshbach, H. 1953. *Methods of Theoretical Physics.* New York: McGraw-Hill.

Munk, W.H. 1947. A critical wind speed for air-sea boundary processes. *J. Marine Research*, **6**, 203-218

Nakamura, T. 1981. General relativistic collapse of axially symmetric stars leading to the formation of rotating black holes. *Prog. Theor. Phys.*, **65**, 1876-1890

Nakamura, T., Maeda, K., Miyama, S., and Sasaki, M. 1980. General relativistic collapse of an axially symmetric star.I. *Prog. Theor. Phys.*, **63**, 1229-1244

Nakamura, T., and Sato, H. 1982. General relativistic collapse of non-rotating axisymmetric stars. *Prog. Theor. Phys.*, **67**, 1396-1405

Newman, W.I. 2002. A fast approach for determining primitive variables in conservative relativistic MHD simulations. Personal Communication.

Newman, W.I., and Newman, A.L. 1999. The interaction of a strong magnetic field with a cold plasma: the evolution of a magnetic bubble. *Astrophys. J.*, **515**, 685-695

Nickalls, R.W.D. 1993. A new approach to solving the cubic; Cardan's solution revealed. *The Mathematical Gazette*, **77**(480), 354-359

Nickalls, R.W.D. 2009. The quartic equation: invariants and Euler's solution revealed. *The Mathematical Gazette*, **93**(526), 66-75

Nishikawa, K.-I., Koide, S., Sakai, J.-I., Christodoulou, D.M., Sol, H., and Mutel, R.L. 1997. Three-dimensional magnetohydrodynamic simulations of relativistic jets injected along a magnetic field. *Astrophys. J.*, **483**, L45-L48

Nishikawa, K.-I., Frank, J., Christodoulou, D.M., Koide, S., Sakai, J.-I., Sol, H., and Mutel, R.L. 1998. Dynamics of relativistic jets. *New Astron. Rev.*, **42**, 633-636

Norman, M.L., and Winkler, K.-H.A. 1986. Why ultrarelativistic hydrodynamics is difficult. in Norman, M.L., and Winkler, K.-H.A. (eds.) *Astrophysical Radiation Hydrodynamics: Proceedings of the NATO Advanced Workshop held in Garching, August 2-13, 1982*, *NATO ASI Series C*, **188**, 449-476. Dordrecht, Netherlands: Reidel

Nykyri, K., and Otto, A. 2001. Plasma transport at the magnetospheric boundary due to reconnection in Kelvin-Helmholtz vortices. *Geophys. Res. Let.*, **28**(18), 3565-3568

Otto, A., and Fairfield, D.H. 2000. Kelvin-Helmholtz instability at the magnetotail boundary: MHD simulation and comparison with Geotail observations. *J. Geophys. Res.*, **105**(A9), 21,175-21,190

Perucho, M., Lobanov, A.P., Marti, J.-M., and Hardee, P.E. 2006. The role of Kelvin-Helmholtz instability in the internal structure of relativistic outflows. The case of the jet in 3C 273. *Astron Astrophys.*, **456**, 493-504

Piran, T. 1980. Numerical codes for cylindrical general relativistic systems. *J. Comput. Phys.*, **35**, 254-283

Pu, Z.-Y., and Kivelson, M.G. 1983. Kelvin-Helmholtz Instability at the Magnetopause: Solution for Compressible Plasmas. *J. Geophys. Res.*, **88**, 841-852

Ralston, A., and Rabinowitz, P. 2001. *A First Course in Numerical Analysis.* 2nd edn. Mineola, N.Y.: Dover Publications.

Ray, T.P. 1982. The effects of a simple shear layer on the growth of Kelvin-Helmholtz instabilities. *Mon. Not. R. Astron. Soc.*, **198**, 617-625

Ray, T.P. 1981. Kelvin-Helmholtz instabilities in radio jets. *Mon. Not. R. Astron. Soc.*, **196**, 195-207

Readhead, A.C.S. 1993. See Davis and Booth 1993

Rees, M.J. 1971. New interpretation of extragalactic radio sources. *Nature*, **229**, 312-317

Ryu, D., Jones, T.W., and Frank, A. 2000. The magnetohydrodynamic Kelvin-Helmholtz instability: a three-dimensional study of nonlinear evolution. *Astrophys. J.*, **545**, 475-493

Savic, P. 1941. On acoustically effective vortex motion in gaseous jets. *Mag.*, **32**, 245

Scheuer, P.A.G. 1974. Models of extragalactic radio sources with a continuous energy supply from a central object. *Mon. Not. R. Astron. Soc.*, **166**, 513-528

Schiesser, W.E. 1991. *The numerical method of lines: integration of partial differential equations.* San Diego: Academic Press.

Schneider, V., Katscher, U., Rischke, D.H., Waldhauser, B., Maruhn, J.A., and Munz, C.-D. 1993. New algorithms for ultra-relativistic numerical hydrodynamics. *J. Comput. Phys.*, **105**, 92-107

Southwood, D.J. 1968. The Hydromagnetic Stability of the Magnetospheric Boundary. *Planet. Space Sci.*, **16**, 587-605

Stark, R.F., and Piran, T. 1987. A general relativistic code for rotating axisymmetric configurations and gravitational radiation: numerical methods and tests. *Comput. Phys. Rep.*, **5**, 221-264

Stawarz, L., Siemiginowska, A., Ostrowski, M., and Sikora, M. 2005. On the magnetic field in the kiloparsec-scale jet of radio galaxy M87. *Astrophys. J.*, **626**, 120-127

Stern, M.E. 1960. The "salt fountain" and thermohaline convection. *Tellus*, **12**, 172-175

Stern, M.E. 1961. The stability of thermocline jets. *Tellus*, **13**, 503

Swaters, G.E. 1999. On the evolution of near-singular modes of the Bickley jet. *Physics of Fluids*, **11**(9), 2546-2555

Tennekes, H., and Lumley, John L. 1972. *A first course in turbulence.* Cambridge, Mass.: MIT Press.

Turland, B.D., and Scheuer, P.A.G. 1976. Instabilities of Kelvin-Helmholtz type for relativistic streaming. *Mon. Not. R. Astron. Soc.*, **176**, 421-441

Van Dyke, Milton. 1982. *An Album of Fluid Motion.* Stanford, California: The Parabolic Press.

van Putten, M.H.P.M. 1993. A two-dimensional relativistic ($\Gamma = 3.25$) jet simulation. *Astrophys. J.*, **408**, L21-L23

Wilson, J.R. 1972. Numerical study of fluid flow in a Kerr space. *Astrophys. J.*, **173**, 431-438

Wilson, J.R. 1979. A numerical method for relativistic hydrodynamics. in Smarr, L.L. (ed.) *Sources of gravitational radiation*, 423-446, Cambridge, U.K.: Cambridge University Press

Zensus, J.A. 1997. Parsec-scale jets in extragalactic radio sources. *Annu. Rev. Astron. Astrophys.*, **35**, 607-636

Zensus, J.A., and Pearson, T.J., eds. 1987. *Superluminal Radio Sources.* Cambridge: Cambridge Univ. Press

Zrake, J., and MacFadyen, A.I. 2012. Numerical Simulations of Driven Relativistic MHD Turbulence. *Astrophys. J.*, **744**, 32-42